Imperial College London

# Fixation of Unicondylar Knee Prostheses

by

**Mahmut Tuncer**

**A thesis submitted for the degree of Doctor of Philosophy of Imperial College London and the Diploma of Imperial College**

**Mechanical Engineering Department**

**Imperial College London**

**June 2012**

# Statement of Originality

I declare that:

(i) the content of this thesis is original and of my own work;

(ii) all assistance received and sources of materials (data, theoretical analysis, figures, and text) have been acknowledged; and

(iii) the work has not been submitted to any other Institution for any degree or diploma.

*Dedicated to*

*my wife Katy and*

*my sons Hector and Alaric.*

# Abstract

There is increasing use of Unicondylar or Unicompartmental Knee Replacements (UKR), especially following publication of good survival data and a trend towards ‘minimally invasive surgery’. The UKR preserves one of the femoral condyles and its meniscus, plus both of the cruciate ligaments. Therefore, the knee functions more normally following UKR than after Total Knee Replacement (TKR). However, the odds for failure of the UKR are higher than the TKR, and a principal reason is loosening of the tibial and femoral components. There is a need for the development of more reliable UKR fixation designs.

The overall aim of this research was to understand fixation of UKR and make recommendations for improvement to designers and surgeons. Since the Oxford mobile-bearing UKR is most widely used in the UK, it was used as the benchmark in this study.

To assess initial fixation, in-vitro bone-constructs were prepared from ten cadavers implanted with the Oxford mobile-bearing UKR and tested for bone strain and bone-implant interface motion with the implants fixed using first cementless and then cemented methods. Cementless fixation produced higher proximal tibia strain and bone-implant displacement than cemented fixation. Peak bone strain increased with reduced bone density, such that the lowest density specimen fractured when implanted with the cementless UKR.

To assess long-term fixation, an in-vivo prospective follow-up study of 11 Oxford UKR patients was developed and conducted for one-year, taking measurements of bone density using Dual X-Ray Absorptiometry (DXA) scanning. The average bone resorption under the tibial implant was found to be low; while it was higher under the femoral component and very high under the tibial intercondylar eminence. The fixation of the Oxford UKR implant was considered to be adequate at 1-year.

Finite Element (FE) simulation techniques were reviewed and developed to simulate the UKR knee for investigation of bone strain, bone-implant interface micromotion and bone remodelling to assess initial and long-term fixation performance. Computer simulations of the tibiae and femora of 2 patients and 4 cadaveric specimens (obtained from the in-vivo and in-vitro studies) were developed and validated for bone strain, bone-implant interface micromotion and bone remodelling.

Comparative multi-specimen computational studies were conducted to understand how particular design features affected fixation. Good fixation was indicated for cementless UKRs when implanted in dense bone, but bone strains were very high in low density tibia. Cementation of the implants spread the loads more evenly and reduced bone strains. The

cementless tibial implant caused less bone resorption (compared to the cemented equivalent) but the difference in the femur was small. Bone resorption was highest at the anterior tibia and posterior to the femoral peg. Bone density was an important factor in the fixation performance of implant design features. Less bulky fixation features reduced bone resorption, provided that the underlying bone was sufficiently dense to maintain bone strains below the failure limit of bone. For patients with dense bone, fixation could be improved with shorter tibial keels and less stiff femoral implants. For patients with low density bone, fixation could be improved with cementation and bone resection that avoids creating stress-raisers.

# Acknowledgement

I have dedicated my PhD to my wife Katy for her personal support and encouragement. During the course of my PhD, she married me and gave birth to my two sons Hector and Alaric. In fact, Alaric was born the day after I completed this thesis!

I also owe sincere thanks for the privilege I have had of working with esteemed and eminent academics and surgeons. My most warm thanks go to my principal supervisor Professor Andrew Amis who has inspired me with his pragmatic approach and unrivalled knowledge of biomechanics of the knee. His advice has been instrumental in all aspects of my research, and I greatly appreciate his patience, guidance and support. Dr Ulrich Hansen has provided constructive guidance and critical thought-provoking analysis regarding development of credible computer simulations. Professor Justin Cobb has shown me clinical insights that I never imagined I would have the opportunity to see and be part of, as well as ideas and thoughts regarding the direction of this research, and essential resources to be able to collaborate with clinicians. Rajesh Patel has been instrumental, offering advice and support in setting up my clinical patient study. Amgad Nakhla has shaped my laboratory study of cadaveric knees by applying his surgical skills and clinical perspective on unicompartmental knee replacements.

This PhD study is strongly founded on the results of the clinical study, and I would like to acknowledge all the other clinicians who supported this work, in particular Wendy Wallis and Lesley Honeyfield from Charing Cross Hospital, and Johann Henckel. It was also dependent on all the patients who were so kind to give up their time, consistent participation and support.

Many past and present colleagues at Imperial College have inspired and helped develop my thinking. In particular: Desmond Chong, Camilla Halewood, Richard Keller, Joanna Stephen, Pam Lumpaopong, Sarah Junaid, Bidyut Pal, Ryo Kashihara, Tian Seah and Philip Wilson.

I am extremely grateful for the financial support of the Arthritis Research UK charity, without which this research would have never happened.

# Contents

# List of Figures

# List of Tables

# Nomenclature

ACL Anterior Cruciate Ligament

BMD Bone Mineral Density

cm Centimetre

DXA Dual X-Ray Absorptiometry

FE Finite Element

FEA Finite Element Analysis

FEM Finite Element Method

g Gram

HU Hounsfield Unit

Hz Hertz

Kg Kilogram

LCL Lateral Collateral Ligament

Ltd Limited Company

LVDT Linear Variable Displacement Transducer

m Metre

MCL Medial Collateral Ligament

MIS Minimally Invasive Surgery

PCL Posterior Cruciate Ligament

PE Poly-Ethylene

Plc Public Limited Company

SG Strain Gauge

THA Total Hip Arthroplasty

THR Total Hip Replacement

TKA Total Knee Arthroplasty

TKR Total Knee Arthroplasty

UK United Kingdom

UKA Unicompartmental Knee Arthroplasty

UKR Unicompartmental Knee Replacement

USA United States of America

# 1 Introduction and Background

## 1.1 Unicompartmental Knee Replacement in Treatment of Osteoarthritis

Osteoarthritis (OA) is a degenerative joint disease in which the homeostasis of articular cartilage chondrocytes, extracellular matrix and subchondral bone is damaged mechanically and biologically. It is the most common musculoskeletal disease particularly in people over 50 years of age and can severely impair mobility and reduce quality of life. It is estimated that 15% of people of age 55- 64, 23% of age 65-74, and 40% of age over 75 years suffer from OA (Odding et al., 1998, 2006, Helmick et al., 2008). Symptomatic knee OA occurs in about 10-38% of people of age over 60 years (Buckwalter et al., 2004, Takeda et al., 2011). There are numerous early-stage treatments available to relieve the symptoms; however, the disease is progressive and Total Knee Replacement (TKR) is performed as the last resort for end-stage OA.

The knee has three compartments (medial, lateral and patellofemoral). If the joint disease is confined to a single compartment then partial knee replacement provides another treatment option before TKR. Since OA usually begins in the medial compartment, medial Unicondylar or Unicompartmental Knee Replacement (UKR) is the most popular form of partial knee replacement.

## 1.2 Current Demand for UKR

Knee Arthroplasty is widespread and growing in Europe, Australia and the Unites States of America (USA). On average, 0.2% of these populations have knee arthroplasty per year (Kurtz et al., 2011) and the number of procedures is growing by 5-17% (Kurtz et al., 2011). The number of primary TKRs, among patients less than 65 years old, is expected to double in 2016 compared to the total number of TKR patients of all ages in 2009 (Kurtz et al., 2009b). The number of patients requiring revision surgery is also expected to rise similarly (Kurtz et al., 2009b). The ageing populations of Europe and the USA pose further challenges for more cost-effective solutions. Currently TKR is preferred and only 8% of all knee arthroplasties are UKR (Fitz, 2009, Willis-Owen et al., 2009).

For patients that are suitable, UKR provides distinct benefits over TKR. Post-operatively the knee kinematics are more natural (Cameron and Jung, 1988, Kozinn and Scott, 1989) with improved range of motion (Griffin et al., 2007) and no shortening of the patellar tendon (Weale et al., 1999). The functional outcome of UKR knees do not differ significantly from

normal, non-operative age- and sex-matched knees (Willis-Owen et al., 2009) and are better than TKR outcomes (Laurencin et al., 1991). The bone stock is preserved (Vorlat et al., 2006) enabling future revision surgery to be easier (Saldanha et al., 2007, Chakrabarty et al., 1998, Becker et al., 2004, Kozinn and Scott, 1989). UKR is minimally-invasive and it is associated with reduced risk of infection. In comparison, TKR is associated with high infection rates and a significant economic burden (Kurtz et al., 2007). Operating and patient recovery times are reduced with UKR and it is cheaper (Shakespeare and Jeffcote, 2003). For the younger group, minimal bone resection, minimal disruption to knee kinematics; and easier revision are important factors.

Patient expectations for knee arthroplasty differ greatly, with more demanding expectations from the increasing proportion of younger patients. Patients not only want pain relief, they want to resume sporting activities such as swimming, jogging and even skiing. Fixation of the implant to the bone is a more important issue with the next generation of implant designs. The dissatisfaction rates of TKR patients are high at up to 20% (Scott et al., 2010) and alternative solutions must be considered to meet these challenging demands.

The potential benefits of UKR are available to far more patients than current practice, with estimates suggesting that up to 45% of patients requiring knee arthroplasty are suitable for UKR (Goodfellow, 2006, Willis-Owen et al., 2009).

The following trends within the orthopaedic community are responsible for the increasing demand of UKR: the development of a spectrum of smaller procedures to treat arthritic joints at an earlier stage; the use of smaller surgical incisions (‘minimally invasive surgery’, MIS); and pressure to reduce hospital recovery times. As described above, surgeons are performing TKR in cases that may be suitable for the lesser UKR procedure. The surgeons contend that this situation is largely a result of their knowledge of the relative survival rates of TKR versus UKR. This is a vicious circle, in which surgeons do not use UKR, so the manufacturers do not invest in developing them as they have for TKR, so they have remained relatively undeveloped and unreliable.

## 1.3 The State of UKR Research

Although the potential advantages of UKR are widely recognised, there is still debate over its reliability (Furnes et al., 2007) and cost-effectiveness (Koskinen et al., 2008). Early in the evolution of UKR, conflicting reports cast doubt on its efficacy (Kozinn and Scott, 1989). Two influential early studies of UKR reported poor results (Insall and Aglietti, 1980, Laskin, 1978). As a consequence, UKR was abandoned by many practices. Therefore many trained orthopaedic surgeons (especially in the USA) have little or no exposure to UKR.

Revision rates are often used as a measure of outcome. A major confounding factor in the measure of revision rates and outcome of UKR patients is surgical experience and surgical approach to treatment of OA. In general, good UKR outcomes are repeated by practices that perform large numbers of UKRs while the poorer outcomes come from small practices that do not have the benefit of surgical routine (Robertsson et al., 2001a). A study of UK practices of UKR (Schindler et al., 2010) identified a big difference in surgical approaches between surgeons. For example: only 52% were minimally invasive; 30-40% allowed squash and jogging post-operatively: and 96% of all surgeons prefer cemented fixation (even though there is no real clinical evidence for this). Therefore, the clinical evidence for using UKR often seems contradictory and confusing.

Revision of failed UKRs has also been reported to be more difficult with less favourable outcomes compared to a primary TKR (Froimson et al., 2009). However, revision from UKR is easier (Weale et al., 2001) and has a better outcome than TKR revision (Saldanha et al., 2007) with reduced re-revision rate (4% compared to 6.7%) (Robertsson et al., 2001b).

UKR components are considered to be poorly designed (Fitz, 2009) with poor fit, particularly for the lateral compartment. Experienced surgeons use tricks to compensate for the inadequate designs (Fitz, 2009) and surgical experience may explain the diversity of survival results (Robertsson et al., 2001a). Furthermore, the majority of today's clinical results are from elderly patients who have low activity levels, and these good survival results are not being duplicated in younger, more active patients (Price et al., 2005a, Deshmukh and Scott, 2002).

One of the principal reasons for revision of UKR is aseptic loosening of the tibial and femoral implants (Koskinen et al., 2007, Lindstrand and Stenstrom, 1992, Skyrme et al., 2002, Bohm and Landsiedl, 2000, Price and Svard, 2011, Berger et al., 2004). Based on Swedish, Finnish and Norwegian and USA arthroplasty registers, 25-45% of failures are due to aseptic loosening (Lewold et al., 1998, Koskinen et al., 2007, Furnes et al., 2007, Gioe et al., 2003). Since 1993, the National Swedish Arthroplasty Register has consistently reported that ~45% of all UKR revisions were due to loosening compared to ~25% of all TKRs (osteoarthritis patients) (Goodfellow, 2006, Lund, 2011). Loosening is a significant issue in UKRs and there is a requirement to improve fixation and surgical techniques to achieve the full benefits of UKR.

Progression of arthritis (most commonly to the patellofemoral joint) is also a common reason for revision (Berger et al., 2004, Koskinen et al., 2007). Based on Swedish, Finnish and Norwegian arthroplasty registers, 20-40% are due to progression of arthritis (Lewold et al., 1998, Koskinen et al., 2007, Furnes et al., 2007). Based on a USA registry of over 500

UKRs, progression of arthritis was reported to account for 51% of revisions (Gioe et al., 2003). Revision due to progression of arthritis is mainly a consequence of poor patient selection while aseptic loosening is due to insufficient fixation research dedicated to UKR.

Over the past 20 years, clinical survival studies from varied groups of international authors have demonstrated good results (Goodfellow et al., 1987, Knutson et al., 1986, Marmor, 1988, Mackinnon et al., 1988, Murray et al., 1998, Vorlat et al., 2000, Svard and Price, 2001, Pandit et al., 2006). The prostheses continue to survive ten years post-operation (Skowronski et al., 2005, Price and Svard, 2011). Although, there are still some mixed reports, Nuffield hospital, Oxford have consistently demonstrated excellent survival results of 98% (Murray et al., 1998) at ten years and 91% at twenty years (Price et al., 2005b, Price and Svard, 2011). Clinical evidence suggests that, of those UKRs revised, most tend to occur within the first 5 years of arthroplasty (average 3 years (Price and Svard, 2011)).

Over the past ten years, there has been a resurgence of interest in UKR (as evident by an increase of published papers). However published literature concentrates on clinical studies and there are unanswered questions (Laskin, 2001). Clinical studies are often inconclusive because: (1) there are often confounding factors in the cohorts of patients; (2) studies are often poorly done (do not follow CONSORT) with little evidence supporting the conclusions (Price, 2000); and (3) the measure of revision/survival rate is not an indicator of performance (Goodfellow et al., 2010).

Most UKR survival studies are retrospective, and confounding factors have been managed ineffectively such that like-for-like is not compared. For example, comparing revision rates of UKR to TKR may be inappropriate because UKR patients may be younger, more active and have higher expectations.

The traditional objective of pain relief is often disregarded. For example, a study by Gleeson et al. (2004) reported that although the Oxford UKR has a better survival rate, a fixed bearing (St George Sled) has better pain relief scores. Note also that loosening can be undetected for long periods of time and it can cause significant pain to the patient; therefore, loosening can be a bigger problem than results show. The literature is limited on credible UKR implant fixation and implant design studies.

## 1.4 History of the UKR Design

McKeever and Elliot developed the concept of uni-condylar resurfacing in the 1950s and used it in the 1960s. Fixed bearing knee designs using cemented hemiarthroplasty were first reported in the 1970s by Gunston and Marmor. Unfortunately, the Gunston failed early because it was highly constrained with straight tracks. It was learnt that less constraint was

needed which helped develop two types of design: (1) fixed bearing tibial component; (2) mobile-bearing bearing tibial component.

A successful fixed bearing design, right from the onset was the St George Sled (Waldemar-Link GmbH & Co., Hamburg, Germany), introduced in 1970s and with a survivorship of 86% at up to 20 years (Steele et al., 2006). The Sled (Figure 1) has a flat fixed bearing (either fully PE or metal backed) and a femoral component designed to fit the profile of the femoral condyle.

**Figure 1 - The St George Sled UKR by Waldemar-Link GmbH & Co (image from www.linkorthopaedics.com, 2011).**

The Oxford mobile-bearing, designed by Goodfellow and O'Connor in 1975, was a significant development step, with subsequent contributions by Buechel and Pappas in contact stress kinematics and wear. Sixty-two percent of orthopaedic practices in the UK use the Oxford UKR; it is by far the most popular design (Schindler et al., 2010).

The Oxford mobile meniscal bearing UKR, as illustrated in Figure 2, has a single radius cobalt chrome alloy femoral component that is fully congruent with an ultra-high molecular-weight polyethylene (UHMWPE) mobile-bearing. The bearing slides on a flat tibial cobalt chrome component with a short keel. The cemented designs are fixed using polymethylmethacrylate (PMMA) cement and the cementless designs are coated with hydroxyapatite.

Since its introduction, the Oxford design has had three development phases (current version is phase 3). For medial UKR, it has demonstrated excellent clinical results. For lateral UKR, the incidence of bearing dislocations is high; therefore, Oxford UKR in the lateral condyle is uncommon. Lateral condyle UKR is more challenging (Heyse and Tibesku, 2010). Currently most lateral UKRs utilise fixed bearings and, due to the increased kinematic movement of the lateral condyle, these would benefit most from the reduced wear rates of the mobile-bearing. Based on research that a domed implant would perform better on the lateral

condyle (Baré et al., 2006), Biomet Ltd (Swindon, UK) have released a new lateral tibial tray, in order to make UKR of the lateral condyle a more viable option.


**Figure 2 - The Oxford mobile meniscal bearing UKR phase 3 range offered by Biomet Ltd, Swindon, UK (images from www.biomet.co.uk, 2011).**

A further iteration on the design of the Oxford mobile-bearing UKR, has been the Uniglide mobile-bearing by Corin Group Plc (Cirencester, UK). Since the profile of the natural femoral condyle does not conform to a single radius, the Uniglide design has a tri-radius femoral component. It is designed so that the bearing is congruent at flexion angles that bear the greatest loads during everyday activities.


**Figure 3 - The Uniglide mobile-bearing UKR range offered by Corin Group Plc, Cirencester, UK (images from www.coringroup.com, 2011).**

## 1.5 Competition between UKR Designs

The most common fixed bearing UKRs have either all-polyethylene or metal backed polyethylene tibial components. Most are onlay implants i.e. the implant is fixed over the rim of the sagittal and transverse cuts of the proximal tibia.

The difference in 10-year survival rates of mobile-bearings and fixed bearings is small (Emerson et al., 2002). The Oxford mobile-bearing design has 10-year survival rates of 84-

100% (Price et al., 2005b, Murray et al., 1998, Emerson et al., 2002, Rajasekhar et al., 2004, Keys et al., 2004, Vorlat et al., 2006) while fixed bearing designs (Marmor, St George Sled, Brigham, PCA, MBUKA, Miller-Galante) have survival rates of 80-100% (Heck et al., 1993, Cartier et al., 1996, Squire et al., 1999, Ansari et al., 1997, Scott et al., 1991, Hasegawa et al., 1998, Bert, 1998, Berger et al., 1999, Argenson et al., 2002). Of the fixed bearing cohort studies that had data up to 15 years (Marmor and St George Sled), the survivorship reduced below 90% while the Oxford mobile-bearing design is reported to maintain survivorship above 90%. A study by Emerson et al. (Emerson et al., 2002), compared a cohort of mobile and fixed bearing UKR patients and reported that although the survivorship was similar, the fixed bearings tended to fail by tibial loosening while the Oxford knees fail due to progression of arthritis.

Over 20 different UKRs are available in the market, the majority of which are fixed bearing designs. Implant companies tend to offer modular designs so that the surgeon can be flexible at surgery. Some common UKRs are the Oxford (Biomet Ltd, Swindon, UK); Uniglide (Corin Group Plc, Cirencester, UK), Miller-Galante and Replica (Zimmer Holdings Inc., Warsaw, USA ); EIUS (Stryker Inc., USA); Advance and St George Sled (Waldemar-Link GmbH & Co., Hamburg, Germany); Accuris (Smith and Nephew, London, UK); Align 360 (Cardo Medical Inc., USA); Preservation (DePuy Orthopaedics Inc., Warsaw, USA); Unix and PCA (Howmedica Osteonics, Stryker Inc., USA); Advance (Wright Medical Technology Inc., USA); and Uni Evolution (Tornier Inc., USA).

## 1.6 TKR Research and Understanding

Since significantly less research has been conducted on the UKR compared to the TKR, the TKR knowledge base has been important in the design of UKRs. The following summarises relevant TKR knowledge and describes the limitations of such an approach.

Some relevant knowledge from TKR research is that (1) the tibial subchondral bone strength decreases with depth below the tibial plateau, related to reducing cancellous bone density (Goldstein et al., 1983); (2) tibial components are more secure if they rest on the cortical rim (Bourne and Finlay, 1986); (3) load onto one edge of a component tends to cause tilting, so that the far edge lifts off from the bone, leading to loosening (Kaiser and Whiteside, 1990).

One could also speculate, based on TKR research, that fixation would improve by using broadly-spaced fixation features that stabilise the components against tilting/rocking micromotion and transfer loads into the cortical shell of the tibia and femur. Although this is relevant, it must be noted that the mechanisms that cause rocking, tilting and translational movements in UKRs are not the same as TKRs. The UKR has a single condylar contact

point while the TKR has bi-condylar contact points and the implant-bone interface area is more than double in TKRs.

There is also the need to minimise component size, both to aid MIS and to reduce bone loss during the event of revision surgery. There is therefore an inherent trade-off to be made between using bulky implants and the need for MIS surgical procedures. Finding a solution to this trade-off cannot be merely borrowed from TKR knowledge but requires dedicated investigation and optimisation of the UKR.

Recent experience has also highlighted critical differences in surgical procedure: UKRs are thought to be more difficult to align accurately (Fisher et al., 2003) and correct soft-tissue balancing (Emerson and Higgins, 2008) during surgery (to ensure good knee kinematics) is far more critical to outcome. These factors must also be included in UKR design.

There is evidence in the literature that UKR design features that have been inherited from TKRs require further optimisation and development. For example the metal backing of TKR tibial components has been implemented into many UKR designs but there is limited literature on the theoretical evaluation of metal backing in UKR and clinical results are inconclusive (Heck et al., 1993). Hyldahl et al. (2001) recommends that metal backing should be avoided in UKR. Another example is that polyethylene TKR fixed bearings are recommended to be thick to reduce wear rates (Marmor, 1976). Although this is a feasible design recommendation for TKRs where extensive bone removal for use of a thicker tibial tray is possible, this is not practical for UKRs where preservation of bone stock and minimally invasive operative techniques are higher priorities.

UKR designs must be considered independently of recommendations made for TKRs. There is a requirement to reassess these TKR design features with a UKR perspective. Since one of the primary failure mechanisms of UKRs is loosening, the aim of this research is to make recommendations to improve fixation. The three distinct factors that contribute to successful implant fixation are (1) initial fixation, (2) long-term fixation and (3) implant durability. The failure modes are not entirely mechanical and are commonly inter-related with biological factors. Osteolysis, for example, may be initiated by implant wear particles and the body's response causes dissolution of bone and eventual loosening. An implant designed without due consideration of all three factors will not have a successful fixation outcome.

## 1.7 Clinical Observations of UKR Fixation Performance

There is also inconsistent evidence in the literature regarding which designs are the best performing UKRs. Based on published literature and on analysis of national joint arthroplasty registry data, the St Georg Sled, Miller Galante and Oxford UKRs are most consistent and

popular in their performance (Robertsson et al., 2001b, 2011, Lund, 2011). As described above, implant loosening is a principal reason for UKR failure (Goodfellow, 2006); therefore the following section includes a comprehensive review of the clinical observations concerning loosening.

Much of the literature on UKR is based on clinical studies, often retrospective (not prospective randomised controlled trials) and they attempt to answer questions which are multifactorial and intertwined with confounding factors (Price, 2000). They are rarely supported by any theoretical analysis and laboratory studies. The reader should be aware that these studies often assess fixation performance by revision rate which is not a credible indicator (Goodfellow et al., 2010) because it neglects mobility, pain and achievable activity levels.

**Radiolucencies**

Radiolucent lines tend to appear in most UKR patients irrespective of cemented or cementless implant fixation; however there are distinct characteristics that can help identify pathological and physiological cases (Gulati et al., 2009a). Radiographs have traditionally been used as a method for assessing fixation (Mukherjee et al., 2008). In a study by Tibrewal et al. (1984), 96% of cemented Oxford UKRs showed radiolucencies. Other studies have reported 62-75% of cases (Gulati et al., 2009a, Pandit et al., 2009), with nearly half of those complete radiolucencies; however, none required revision surgery. They tend to appear a few weeks post-surgery and develop to be stable after 1-year. For cemented Oxford UKR, the most common sites tend to be around the keel (mostly towards the medial side in medial UKRs and vice-versa in lateral UKRs). As presented in Figure 4, these radiolucencies tend to be less than 1 mm thick and do not usually exceed 3 mm.

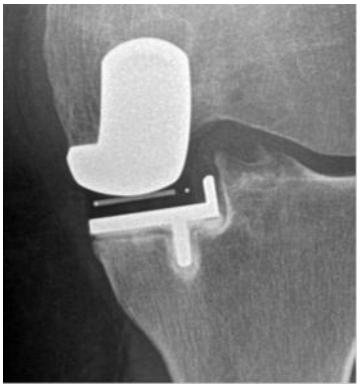

**Figure 4 - Radiograph at year-1 of a cemented Oxford UKR, showing complete radiolucency around the tibial component (Pandit et al., 2009).**

The occurrence of radiolucent lines in cementless Oxford UKRs tends to be significantly less at one year post-arthroplasty (Pandit et al., 2009). Radiolucencies are thought to be regions of fibro-cartilage tissue.

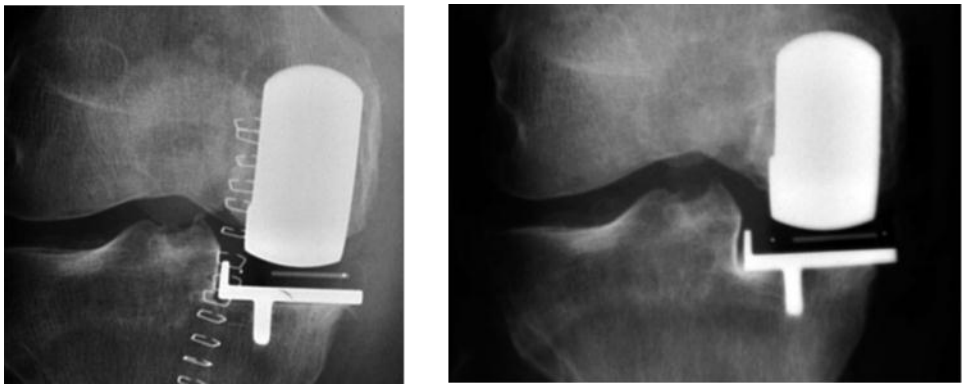

**Figure 5 - Radiograph of a cementless Oxford UKR showing radiolucency around the tibial component immediately post-surgery (left) which disappeared at year-1 (Right) (Pandit et al., 2009).**

Although the reasons for its occurrence and its significance are unclear for UKRs (Gulati et al., 2009a), it is indicative of areas of low fixation and compliance. Radiolucencies are either a layer of osteoporotic bone or fibrous tissue (Kwong et al., 1992). In cases where loosening occurs, radiolucencies tend to be thick and appear to engulf the implant (Figure 6). Pathological radiolucencies tend to be greater than 2 mm thick, don't have a radiodense line and are progressive whilst "physiological" radiolucencies are defined as "narrow and well defined" (Gulati et al., 2009a). Potential factors could be (1) high hydrostatic bone strains remodelling bone into fibrous tissue (Gray et al., 2010); (2) bone-implant interface motion (Jasty et al., 1997a); (3) lysis initiated by wear particles (Huang et al., 2002); (4) thermal necrosis of bone (Berman et al., 1984, Ahlberg and Linden, 1977).

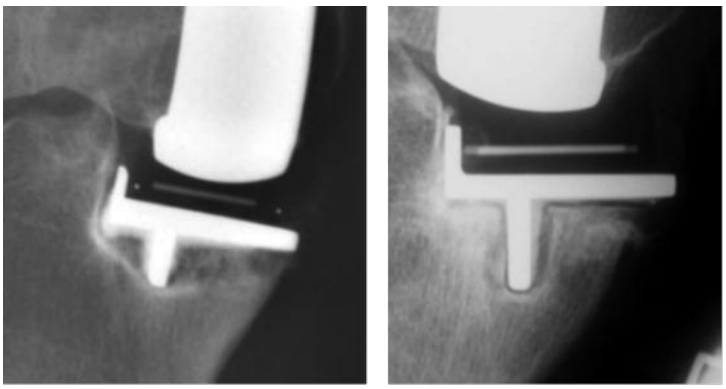

**Figure 6 - Radiograph of cemented Oxford UKRs showing pathological radiolucency (left) and extreme physiological radiolucency (right)(Gulati et al., 2009a).**

Radiodense lines tend to appear immediately adjacent to the radiolucencies (Tibrewal et al., 1984), as illustrated in Figure 6. The formation of radiodense lines can be signs of bone in-growth and osseointegration (Tibrewal et al., 1984). Osseointegration tends to occur 6-16 weeks post-surgery (Jasty et al., 1997a, Soballe et al., 1992, Prendergast et al., 1997, Cameron et al., 1973).

Radiodense lines showing immediately post-surgery could also suggest a layer of poor quality dense bone (sclerotic bone) into which cement has not integrated (poor fixation) (Tibrewal et al., 1984). Sclerotic lines can also appear later on. It is postulated that this is because of formation of a soft tissue layer at the cement-mantle, causing high shear strains on the bone immediately under it, and leading to bone densification (Gray et al., 2010). This appears as high density bone regions under regions of radiolucency.

Radiographs can be very useful to the experienced surgeon for characterising the success of UKRs; however these claims are unsatisfactorily supported with clear evidence especially because it is widely accepted that distinguishing between physiological and pathological radiolucency is difficult (Kalra et al., 2011). The knowledge gained from the study of TKRs links radiolucencies to loose implants (Ritter et al., 1999, Hvid and Nielsen, 1984, Ahlberg and Linden, 1977). This conflicts with the claims made for UKRs; therefore, UKR research clearly has to be studied independently.

**Bone Resorption**

Based on knowledge gained from TKRs and Total Hip Replacements (THRs), it is widely accepted that bone resorption can lead to bone loss and eventual loosening of implants. There is evidence that this can also occur in UKRs (Tibrewal et al., 1984). Bone resorption tends to occur due to ‘stress shielding’ of the underlying bone by the stiff implant. This can eventually lead to component failure, as displayed by radiographs in Figure 7.

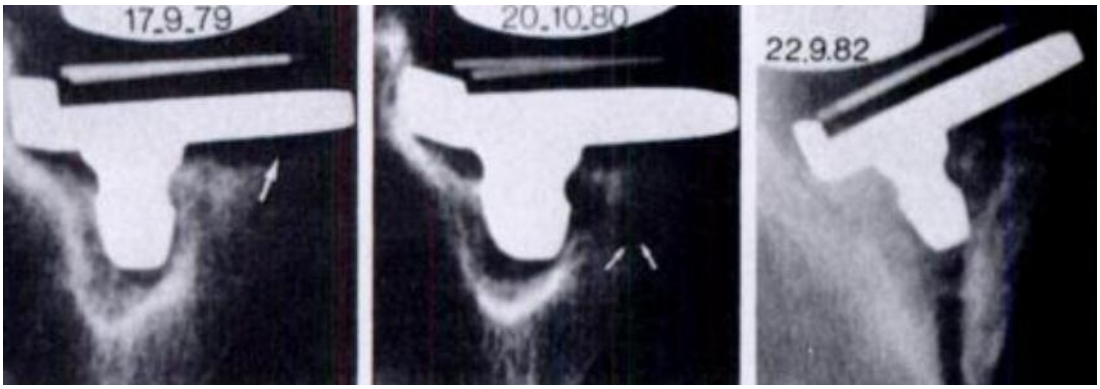


**Figure 7 - The radiodense line between the radiolucent cement and the bone is incomplete (left). The patient complained of pain. One year later the bone had resorbed (middle) and the component failed eventually (right) (Tibrewal et al., 1984).**

### Migration

Progressive 'sinking' (migration) of the tibial implant occurs in most UKR patients. It tends to be 0.4-1.0 mm in the first year and it tends to level off over a few years (Hyldahl et al., 2005, Ryd et al., 1983, Rea et al., 2007). In Oxford UKRs, it has been reported that there is some anterior migration coupled with this distal migration (Rea et al., 2007). There is also evidence that the femoral implant migrates distally by a similar amount (Rea et al., 2007). No correlation has been found between radiolucency and migration for UKRs (Ryd et al., 1983, Rea et al., 2007). Excessive migration, particularly in osteoporotic patients who have very soft bone at the proximal tibia, can cause tilt to one side and eventual loosening (Ryd et al., 1995). High cancellous bone stresses under the implant are thought to be responsible for the migration (Taylor et al., 1998), but have never been quantified for the UKR.

### Perioperative Fractures

A small number of patients may experience fracture of the tibia, mostly propagating from either the base of the keel (Vardi and Strover, 2004) or the tip of the sagittal cut. Fractures tend to occur perioperatively (Seon et al., 2007, Kumar et al., 2008) and are likely to be due to errors in operative technique (Clarius et al., 2009a, Clarius et al., 2009b). The errors tend to be related to extended cuts. A study by Clarius et al. (2009a) found that inexperienced surgeons produce vertical cutting errors of more than 4mm in 18% of cases.

### Misalignment

Misalignment of TKRs increases the risk of loosening and the same conclusion has been associated with medial UKRs (Kasodekar et al., 2006, Keene et al., 2006, Kennedy and White, 1987). Correct alignment of UKRs, particularly mobile-bearing designs, is more

difficult than TKRs (Fisher et al., 2003) and the routine of performing UKR surgery improves accuracy and the likelihood of survival (Robertsson et al., 2001a).

Hernigou and Deschamps, in a clinical follow-up study of 212 fixed bearing UKR patients (Hernigou and Deschamps, 2004), concluded that tibial cuts with anteroposterior slopes greater than 7 degrees could cause loosening, particularly for unconstrained implants. Assor and Aubaniac (2006), in a 7-15 year clinical follow-up study of 276 patients, showed that, of the 52 failures, 45 had loosening of the tibial component due to femoral component rotational misalignment. The radiograph in Figure 8 shows how rotation of the femoral component can cause the bearing to be on the medial extent. Assor and Aubaniac (2006) concluded that that femoral rotational misalignment causes increased mediolateral translation of the contact point, leading to abrasion and excessive pressure on the medial portion of the plateau.

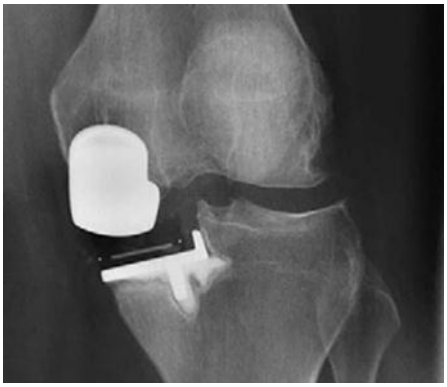

**Figure 8 - Radiograph of a cemented Oxford UKR, showing how tilt of the femoral component can cause the mobile-bearing to be on the medial edge of the tibial tray.**

Implant superoinferior alignment directly affects the varus/valgus knee angle and influences the medial-lateral compartment load-split. Based on clinical studies, there are conflicting reports about how and whether the knee should be corrected. Studies by Ridgeway et al. (2002) and Cartier et al. (1996) recommend that under-correction should be avoided (particularly for thin polyethylene metal backed tibial components). This was supported by Emerson et al. (2007) who recommended the correction of varus/valgus deformity using the Oxford ligament balancing technique. Gulati et al. (2009b), based on a study of 160 Oxford UKR patients, found that 25% had varus deformity and that the level of deformity was unrelated to the outcome.

The translational position of the tibial component, such as an overhang (in an onlay compared to an inlay design), also makes a difference to outcome. Overhang can cause irritation of soft tissues and pain, whereas an underhang can cause loosening. Chau et al. (2009) analysed 172 Oxford UKR knee overhangs and found that patients with an overhang

of 3 mm or more exhibited significantly worse Oxford Knee Scores and pain scores at 5 year post-arthroplasty. No difference was found in knee scores in patients with minor overhang and underhang. Inlay UKRs, such as the Replicci UKR by Biomet, require an incision into the tibial plateau followed by insertion of a polyethylene tibial component. The survival rates of onlay UKRs tend to be lower (Goodfellow, 2006).

**Femoral Implant Loosening**

Loosening of the tibial implant is easier to detect than the femoral implant (Monk et al., 2009, Kalra et al., 2011); therefore, there is more evidence in the literature for tibial loosening than femoral loosening and it is unclear which component is more susceptible. Some studies have reported that femoral implants are more likely to fail (Weale et al., 2001) particularly at the tip of the peg (Kalra et al., 2011). One failure mechanism of the femoral component is that the resected profile no longer matches the implant underside, so the implant rocks on the surface showing wedge shaped radiolucency at the posterior femur during extension (Monk et al., 2009).

**Implant Materials**

Results of clinical studies have produced mixed results for recommendations on materials in UKR design. For example, on the question of whether full-polyethylene bearings or metal-backed bearings are better (Hyldahl et al., 2001, Heck et al., 1993). A recent clinical study by Arastu et al. (2009) highlighted a 21% failure rate of the Depuy Preservation mobile-bearing UKR (DePuy Orthopaedics, Inc., Warsaw, Poland) at a mean of 22 months. Although the cause is unconfirmed, the Preservation UKR is constrained in the mediolateral direction, which, it is speculated, is responsible for the loosening.

**Bearing Dislocations**

With the introduction of the mobile-bearing UKR came some unexpected problems that were identified very clearly with clinical studies. Bearing dislocation was a common cause of complications, particularly for the lateral condyle (Verhaven et al., 1991). As a result, they now tend not to be implanted in the lateral condyle. The designs have improved, incidences have reduced and a new mobile-bearing UKR specifically designed for the lateral condyle was introduced into the market by Biomet in 2011.

**Wear**

Wear particles can lead to osteolysis and eventual loosening due to the immunological response of tissue cells to the wear particles. Osteolysis was responsible for many of the TKR failures in the past (Robinson et al., 1995). The immunological response is sensitive to

both particle size and quantity (Huang et al., 2002); therefore it is important that the particles are sufficiently small and sparse, so that they do not generate an immunological response.

Based on clinical studies of TKR, it is recommended that, to minimise wear, polyethylene bearing thicknesses should be greater than 6 mm (Engh et al., 1992c, Bartley et al., 1994) and have a limited shelf age (Bohl et al., 1999), and a design allowing large areas of contact mediolaterally and anteroposteriorly (Argenson and Parratte, 2006). The developments that have occurred in reducing wear have been significant and have filtered into UKRs. Although wear was a common failure mode in early UKRs (Engh et al., 1992c), it is significantly less frequent, particularly in mobile-bearings which have been shown to have annual wear rates less than 0.08mm (Psychoyios et al., 1998). That said, 15% of all failures since 2000, reported in the Swedish National Joint Registry (Lund, 2011) were due to wear.

## 1.8 Initial Fixation

Initial fixation is a measure of the immediate post-operative stability of the implant. Currently the majority of UKR implants are cemented with known values of 96% in the UK (Schindler et al., 2010), 99% in Sweden (Lund, 2011), 75% in Australia (Australian National Joint Replacement Registry, 2011). Although cementless fixation is very low, there is a trend evident in the Australian National Joint Replacement Registry that surgeons are increasingly using cementless and even hybrid fixation (Figure 9). Analysis of the joint registries shows that cementless fixation is more popular for the femoral component (compared to the tibial implant), such that some patients are having a cemented tibial implant with a cementless femoral implant (Australian National Joint Replacement Registry, 2011).

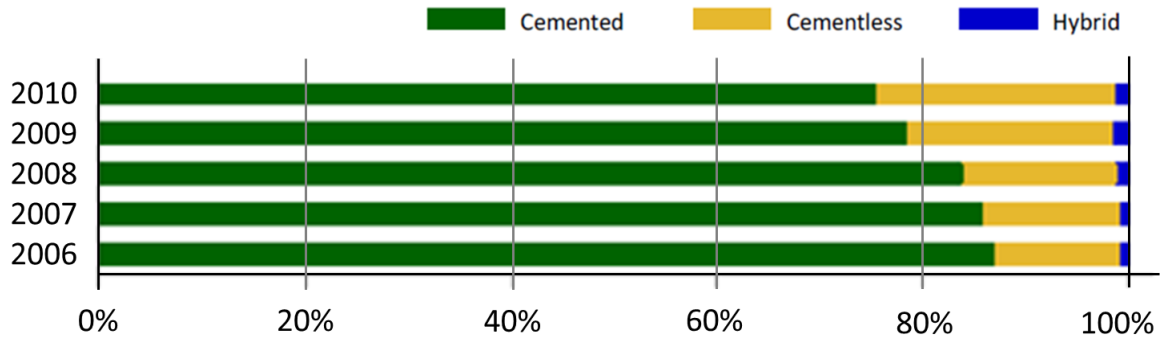


**Figure 9 - The fixation methods used in UKRs published in the Australian National Joint Replacement Registry (2011).**

Under daily activities, good initial fixation will exhibit low bone strains (within 50% of the failure limit of bone) and low micro-movements between the bone and implant at the interface (micromotion). Micromotion is particularly important during osseointegration of the

bone-implant interface of cementless prosthesis. Micromotions, parallel to the implant-bone interface (surface-tangent micromotion), greater than 50μm are likely to inhibit osseointegration (Pilliar et al., 1986, Jasty et al., 1997a, Burke et al., 1991).

Since assessment of initial fixation only requires short-term results, clinical survival results can be valuable; however, it is difficult to isolate variables that are causing the adverse effects. Micromotion can not be measured accurately in-vivo (radiostereometric analysis is too inaccurate for daily micromotions); therefore, mechanical testing and FE modelling methods are commonly used. FE modelling offers the potential to test numerous scenarios quickly and efficiently. A literature search revealed only four papers specific to initial fixation of UKRs of which none were based on computer simulations.

A theoretical based paper on fixation of generic design features was published by O'Connor et al. (1982). However, it lacks a long-term fixation perspective and it is aimed at promoting the Oxford UKR.

Kaiser and Whiteside (1990) compared initial fixation stability of screwed and pegged cementless implants on cadaveric specimens. Although they recommended the use of screws which was supported by long-term clinical studies (Epinette and Manley, 2008), the industry has been reluctant to use screws due to reports in TKR patients of radiolucent lines (Whiteside, 1994).

Miskovsky et al. (1992) mechanically tested 3 different cementation techniques and concluded that cementing to a smooth subchondral bone or "unlavaged" cancellous bone is unreliable for initial fixation. Based on a cadaveric study of 24 UKR femurs, Clarius et al. (2010) reported that a rough surface (with drilled holes) is important for a strong cemented interface and that the posterior of the femoral implant was most susceptible to improper fixation.

Rosa et al. (2002) compared initial fixation strength of a peg and a rim on the cemented all-polyethylene Advance UKR (by Wright Medical Technology) with a series of mechanical tests on polyurethane foam blocks. The paper is focussed on promoting the Advance UKR and lacks a thorough analysis.

Recently, a couple of relevant computer simulation-based papers were published: Simpson et al. (2011) reported that there was minimal load transfer through the lateral wall of the tibial implant. Chang et al. (2011) reported that a radial corner could help to alleviate the high strains at the resected corner of tibial implants.

## 1.9 Long-term Fixation

There are increasingly higher longevity expectations for UKRs; therefore, it is important to understand how implant design can be improved for increased long-term fixation. Although studies have been published for long-term fixation for TKRs, the literature is limited for UKRs.

There is considerable evidence to suggest that a reduction in the local stress distribution will, due to bone resorption, cause a decrease in bone mineral density (BMD). This can jeopardise implant fixation and lead to revision surgery. Computational bone remodelling techniques are sufficiently developed to provide useful fixation assessments of implants (Huiskes et al., 1987, Bitsakos et al., 2005, Kerner et al., 1999). However, limited resources have been placed on UKR simulation, particularly for the purposes of improving long-term fixation designs. A literature search revealed only six papers specific to long-term fixation of UKRs, of which only two use modelling based approaches.

Hyldahl et al. (2001) assessed 2-year post-arthroplasty migration of 45 patients, comparing a metal tibial backed UKR with an all-polyethylene UKR tibial component. They found that there was no enhanced fixation provided by the metal-backed UKR and recommended the use of all-polyethylene UKRs.

Lindstrand et al. (1988) compared cemented and cementless fixation in a cohort of 93 PCA (by Howmedica) UKR patients over a period of 1-4 years. There were no statistical differences in radiolucencies or any other fixation parameters. However, the report recommends cemented UKRs because they have a higher likelihood of complete pain relief.

Epinette et al. (2008) assessed the fixation capabilities of hydroxyapatite on cementless Unix (by Howmedica) UKRs based on a 5-13 year follow-up study of 125 knees. Note that the Unix tibial component has four screws into the bone. Only 3% of patients had radiolucencies under the tibial plateau and there were no instances of radiographic loosening. The study concluded that cementless UKRs can be successful in the long-term and promoted the use of screws.

Pandit et al. (2009) compared radiolucencies of 62 Oxford UKR knees at 1-year post-arthroplasty and found that cementless implants showed significantly less radiolucencies compared to cemented implants. If radiolucencies can be assumed to be indicative of fixation, then this shows that short-term fixation of cementless Oxford UKRs is better than cemented UKRs.

Gillies et al. (2007) investigated the long-term fixation effects of two polyethylene tibial implants, with and without a keel, using FE modelling. Post-arthroplasty, they predicted bone resorption of less than 8% with the keel and up to 10% bone apposition without the keel.

A study by Simpson et al. (2009) investigated tibial strain caused by the Oxford UKR in various alignments. Although the study was used primarily to explain tibial pain as a result of elevated tibial bone strains anteromedially, strain is also an indicator of bone remodelling. The study lacks a perspective on fixation.

Recently, Gray et al. (2010) reported the results of a computer simulation of the region beneath the tibial implant. They demonstrated that the radiolucencies observed in the clinic may be due to differentiation of the bone tissue into fibrous tissue and the sclerotic line due to bone apposition in this underlying region.

## 1.10 Component Durability

In order to maintain good fixation, the implant must remain intact. There is sufficient literature for designers to make conservative loading assumptions for implant design. For this reason failure of the component by yielding or fracture is rarely seen. Failure due to fatigue, and in particular due to wear is more common.

Design features that reduce wear often affect the fixation capability of the implant. For example the Oxford UKR, which, to enable greater tibiofemoral surface conformity, has a single curvature femoral component, that curvature does not follow the femoral geometry as closely as its counterparts. This may have adverse effects on long-term fixation.

A review of the current understanding of wear in UKR is discussed by Argenson and Parratte (2006). Since many of the developments associated with materials used in other implants can be transferred to UKRs, and wear modelling is computationally very different to the modelling performed in this study, component durability was considered to be outside the scope of this research thesis.

## 1.11 Finite Element Analysis Studies

Finite Element (FE) analysis of bone and bone-implant constructs is a powerful tool for biomechanics research of implants. If correctly performed, the method can help to isolate specific design factors and assess the implications of design changes while avoiding the high costs and time expenses inherent in traditional in-vivo and in-vitro studies. However, verification and validation using in-vivo and in-vitro studies are vital for the results to be meaningful.

Bone material properties are complex and modelling a bone accurately depends on the level of detail required for the intended purpose of the analysis. Tissue-level simulations help to analyse trabecular micro-mechanisms such as at the cement-bone interface of THRs (Waanders et al., 2009). Whole bone-level models (of whole joints) help to determine muscle forces and kinematics of joints (Hopkins et al., 2009). Architectural-level models require data from both the whole-bone level and tissue-level models in order to simulate the macro processes of whole bones such as remodelling in the tibia (Chong et al., 2011). Incorporating these into a single multi-scale model is a challenge for the biomechanics community. Until that is achievable careful assessment of assumptions is required, followed by verification and validation processes in order to produce meaningful results.

## 1.12 Objectives and Scope

The overall aim of this research was to understand fixation of the UKR and make recommendations for improvement. This was to be accomplished via a sequence of intermediate aims:

1. Gathering of detailed bone geometry and density distributions of UKR patient knees by computed tomography (CT) scanning;
2. Development of Finite Element (FE) computer models of implanted UKRs for investigation of initial and long-term fixation;
3. Undertaking of in-vitro mechanical testing of implant/bone constructs to validate FE stress/strain results;
4. Undertaking of a 12-patient clinical study to investigate post-arthroplasty bone adaptation and to validate computer predictions;
5. Investigation of initial and long-term fixation of the UKRs and how they are affected by changes in implant alignment, implant design and bone excision.

## 1.13 Structure of Thesis

This thesis is structured into ten sections. The first three sections (including this section) provide a comprehensive review of UKR both in the clinic and within the biomechanics community. The subsequent seven chapters describe the development of the tools to assess UKR fixation and present the findings of the studies conducted.

Section One (this section) is the introduction and details a literature review of mechanical fixation of UKRs. Section Two describes the current methods used to simulate bone properties in FE models of the knee, including a detailed literature review of the material property of bone, and a study on the sensitivity of material parameters on modelling bone.

Section Three is a literature review of knee forces and the rationale for assembling a new database of knee forces specific for UKRs and detaching from previous methods employed for TKRs.

Section Four describes the FE modelling approach used in this thesis and presents findings of studies used to investigate the uncertainties associated with modelling of the UKR, and how these challenges were overcome.

Section Five outlines the mechanical tests conducted in-vitro on ten cadaveric knees, and the results. The validation of four of these UKR cadaveric knees is presented in Section Six.

Section Six presents a detailed validation of multiple UKR tibiae and femora FE models, for bone strain and bone-implant displacement. It demonstrates the reliability of the method developed in Section Four.

Section Seven presents the in-vivo DXA study on 12 UKR patients and the year-1 results. The validation of two UKR patient knee models is presented in Section Eight.

Section Eight describes the development of the bone remodelling simulations of patient-specific FE models and evaluates their performance against in-vivo clinical data obtained from the DXA study.

Section Nine presents the findings of comparative studies using computer simulations of UKR fixation features. The studies are based on UKR fixation questions identified in the literature and the clinic.

Section Ten presents a summary of the conclusions of this thesis with recommendations for improving UKR fixation and for future work.

# 2 Modelling Bone for Computer Simulations

## 2.1 Introduction

Finite Element (FE) analysis of bone is a very powerful tool for biomechanics research, particularly for implant design. Bone material properties are complex and modelling a bone accurately depends on the level of detail required for the intended purpose of the analysis. This Section presents a detailed literature review of material properties of bone; the current methods for developing subject-specific bone FE models; and includes a study to conclude the most appropriate method to model fixation of Unicompartmental Knee Replacements (UKRs).

## 2.2 Background

It is important to consider the microstructure of bone to understand its mechanical properties (Rice et al., 1988). By weight, bone is made up of 60% inorganic mineral, 30% organic and 10% water. The inorganic mineral phase of bone is a ceramic crystalline-type mineral; an impure form of hydroxyapatite, primarily composed of calcium carbonate and calcium phosphate, and it gives bone its characteristic rigidity and compressive strength. The organic phase is primarily type I collagen and osteoid.

The material properties of bone are dependent on the level of interest: whole-bone level; architectural level (>1mm); tissue level (0.1-0.5mm); lamellar level (1-10μm); and collagen fibril level (0.1μm).

At the architectural level, bone is classified as either cortical or cancellous (also called trabecular) depending on its porosity. Cortical bone is formed of tightly packed lamellar, Haversian, or woven bone and has a porosity of 5-30%. Cancellous bone is highly porous (greater than 30% porosity) and is of cellular structure (Keaveny et al., 2003).

Tissue level bone models have shown to accurately mimic architectural level bone characteristics measured in the laboratory (Gibson, 1985). These models assume that the mineral phase of bone is homogenous and isotropic and the level of detail within the models incorporate trabecular architecture, alignment and porosity. Unfortunately there are computational challenges with scaling the models to the architectural level. Due to insufficient computational power to model whole bones from tissue level properties, simplified architectural level material properties are required. Keaveny and Hayes (1993) provide a good summary of the mechanical properties of trabecular bone.

Bone has a cellular solid structure with mineralised connecting walls/struts (100-300μm thick and 500-1500μm spacing) known as trabeculae. As the porosity reduces, the structural interconnectivity increases and cell struts (open cell porous structure) begin to look more like cell walls (closed porous cell structure). The alignment of the walls/struts determines whether the structure transfers load by axial deformation (high alignment) or by bending (low alignment); therefore it determines the degree of anisotropy. The structure is stiffest in axial deformation because the porous cells are aligned in this direction. There are four deformation mechanisms in a porous structure: (1) open cell structure with pure bending; (2) open cell structure with pure axial deformation; (3) closed cell structure with pure bending; (4) closed cell structure with pure axial. The overall deformation of cancellous bone is made up of a combination of these mechanisms, depending on the porosity, bone architecture and alignment of the cell walls. Based on the theoretical study of cellular structures, Gibson and Ashby (1982) proposed a square relationship (between elastic modulus and density) for open cell materials (high porosity, cortical bone) and a cubic relationship for closed cell materials (low porosity, cancellous bone).

At the architectural level, the mechanical properties of bone are heterogeneous and anisotropic, and porosity and trabecular architecture are dependent on species and anatomy (Keaveny and Hayes, 1993). Differences in trabecular architecture are often defined using measurements of trabecular spacing, wall-thickness and trabecular number; for example, trabecular spacing is 30% higher in human proximal tibia compared with bovine proximal tibia and the trabecular walls are 50% thicker in the human femoral neck compared to the human proximal tibia (Morgan et al., 2004). The bone epiphysis (proximal tibia and distal femur) tend to display relatively low anisotropy with increasing anisotropy towards the stem (mid-diaphysis) (Pope and Outwater, 1974). The porosity and density are related to the elastic modulus and derivation of empirical relationships has been instrumental in development of FE modelling capabilities of whole-bone.

The early work of Carter and Hayes (1977) proposed a single relationship for the whole porosity range of bone. They tested bones of various species and various anatomical sites and assumed that bone elastic modulus was isotropic. This work is well established in the biomechanics community and is commonly used in FE studies because it is convenient and easy to implement.

Recent developments have demonstrated that the Carter and Hayes relationship is simplistic: Orthotropic properties of bone have been published (Rho et al., 1995); studies have shown species dependence (Rice et al., 1988, Ciarelli et al., 1991) and anatomic site dependence (Morgan et al., 2003). That said, the Carter and Hayes relationship may be adequate for the purposes of this Thesis. This Section presents a detailed review of current

methods for obtaining elastic moduli from density of bone and presents a comparative study of different relationships published in the literature that are relevant to the knee.

## 2.3 Bone Density from CT

Material property relationships in the literature normally relate elastic moduli to bone density; therefore, the density of bone must first be determined.

A wide range of scanning methods are available and Computed Tomography (CT) is the most suitable for generating patient-specific whole-bone scale models. Although μCT produces higher resolution (tissue level) images, the maximum specimen length is limited to 15cm and the high radiation dose is a barrier for obtaining ethical approval on living human subjects. CT is well established and widely available in hospitals and research centres. The image resolution (0.6 mm) captures architectural level detail – it is not sufficiently detailed to resolve individual trabeculae but has fine enough resolution that it does not omit bone topography. Two-dimensional X-ray images, measuring attenuation coefficient, are taken around a single axis of rotation. Three-dimensional arrays of greyscale values (called voxels) are then generated by computational processing of these images. The data is organised in slices perpendicular to the axis of rotation. These values can vary depending on equipment and the settings; therefore, the radiologist will usually calibrate the CT scan against a phantom (usually water HU=0 and air HU=-1000), giving Hounsfield Unit (HU).

The empirical relationship between HU and density is linear (Rho et al., 1995, McBroom et al., 1985, Ciarelli et al., 1991). The linear relationship between HU and apparent density ($\rho$) depends on the composition of the material filling the voids and the density of this material. Studies in the literature have used different measures of density and it is important to define a consistent approach. Density measures can be grouped into (1) Ash density, (2) Wet density, or (3) Dry density. There is no consistent definition of apparent density through the literature; however, recent studies have tended to define it as dry density (including Carter and Hayes) and this is the definition used in this thesis. These density measures can be converted using equations empirically derived by Keyak et al. (1994) (and substantiated by Schileo et al. (2008a)):

$\rho_{dry}=1.66\rho_{ash} + 0.00457$

$\rho_{dry}=0.913\rho_{wet} - 0.00336$

The material that fills the bone voids is bone marrow. The bone marrow is composed of a variety of cells (blood cells in all stages of development, fat cells and reticulum cells) and connective tissue. If we assume that the material that fills the bone voids is two-phase, composed of water and fat, then we know that the linear relationship is somewhere between

an upper and lower bound: (1) If the material that fills the voids is just water, and water has a Hounsfield value of 0 HU, then the apparent density of bone at 0 HU must be 0 g/cm$^3$. (2) If the material that fills the voids is fat, and fat has a Hounsfield value of approximately -120 HU, then the apparent density of bone at -120 HU must be 0 g/cm$^3$.

Over the years there have been developments in CT scanning equipment and measurement techniques; and it is unclear in the literature which relationships (between HU and apparent density) are most appropriate to this study. Therefore, a new relationship has been derived from the CT data set of actual cadaveric knees analysed in this study. Based on the analysis of ten cadaveric knees, the average upper value of 1860 HU was assumed to correspond to an average upper apparent density value for cortical bone of 1.75 g/cm$^3$.The average lower value of -40 HU corresponded to bone marrow and the lower apparent density limit of 0 g/cm$^3$. Note that all these scans were performed on a “Definition AS+” Computed Tomography (CT) scanner (Siemens Healthcare, Germany) which is the same scanner used to scan the UKR patients (described in Section 7), and cadavers used to develop FE models (described in Section 5). The following relationship between HU and the apparent dry bone density (ρ, g/cm$^3$) was developed and used in the study:

$$\rho = 0.04 + (9.2 \times 10^{-4})HU$$

where apparent density ρ is in g/cm$^3$.

As illustrated in Figure 10, this is similar to relationships used in the literature (Rho et al., 1995).

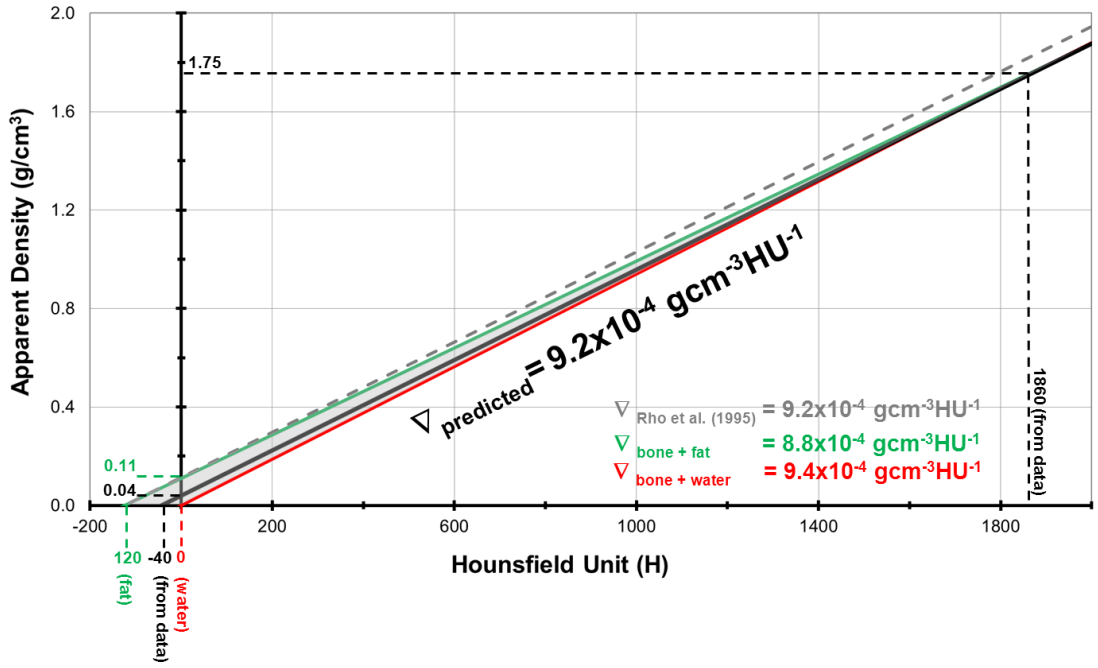


**Figure 10 - Relationship between Apparent Density of bone and Hounsfield Unit**

There are two different approaches in the literature for deriving apparent density from CT data: (1) calibrate HU numbers to ash density using a phantom and then use another relationship to obtain apparent density (Barker et al., 2005, Dalstra et al., 1995, Keyak et al., 2005, Keyak et al., 1998), or (2) calibrate HU numbers to apparent density directly (Bitsakos et al., 2005, Chong et al., 2010, Cody et al., 1999, Gupta et al., 2004, Peng et al., 2006, Taddei et al., 2004). The latter is usually done based on the assumption that apparent density is 0 g/cm$^3$ for 0 HU; and the maximum estimated cortical density corresponds to the maximum HU in the dataset. Schileo et al. (2008a) reported that a subject-specific correction factor to the relationship reduces the error in a femur model. The method used in this thesis maintains a consistent approach, so that differences of densities between specimens are maintained and not normalised against average bone values from the literature.

## 2.4 Elastic Modulus from Bone Density

In 1977, Carter and Hayes (1977) proposed a single relationship between apparent bone density and elastic modulus, covering both cancellous and cortical bone. The relationship was empirically derived independent of species and anatomy.

$$E = 3.79\rho^3$$

where elastic modulus E is in GPa, and apparent density ρ is in g/cm$^3$.

This significant development opened opportunities in the computational modelling of the heterogeneous nature of bone; however, the study has its limitations and further development have been made.

The literature contains over 40 studies (26 studies were reviewed by Linde et al. (1992) and another 15 by Helgasson et al. (2008)) and a tenfold difference in elastic-modulus predictions for cancellous bone at a particular density. It is therefore important to carefully consider what to use in computer simulations.

As described in Sub-section 2.2, Gibson (1982) and Ashby (1985) demonstrated that elastic modulus is proportional to the square of apparent density for open cell materials (high porosity) and cube of apparent density for closed cell materials (low porosity). No theory exists for the middle range of porosity. In the late 1980s, new studies were conducted by analysing cancellous and cortical bone separately (Rice et al., 1988, Rho et al., 1997, Schaffler and Burr, 1988) and appreciating the anisotropic nature of bone by assuming orthotropy.

The elastic modulus of bone is strain rate dependent with most studies showing an increase in stiffness with increasing strain rate (Hansen et al., 2008, Carter et al., 1981). Hansen et al. (2008) showed that increasing compressive strain rate from 0.14-29 $s^{-1}$, the elastic modulus of femoral cortical bone increased from 16-30 GPa. These high strain rates are representative of impact loading from falls and not of loading experienced during daily activities such as walking and stair climbing. For low strain rates, representative of daily activities, the variation of elastic modulus is small (Currey, 1988) and has therefore been assumed to have negligible effect on computer simulations presented in this thesis.

It is also important to consider the development of material testing methods. The platen-technique, used in early studies such as Carter and Hayes, involved resecting bone into cylinders/cubes and using an anvil to apply a load and measure its deformation. This method is known to be prone to errors arising from: machine compliance errors (due to the very small deformations measured); and structural end-effects (high strains near the platens) – these can lead to underestimations of elastic modulus of 20-40% (Keaveny et al., 1997, Linde et al., 1992). Another source of error in early studies is due to misalignment of specimens. Modern methods (extensometer and the end-cap technique) use extensometers to focus on strain measurements at the centre of the specimens (Keaveny et al., 1997, Turner and Cowin, 1988, Odgaard and Linde, 1991). Alternative methods are also used in the literature: Snyder and Schneider (1991) conducted three point bend experiments on slices of cortical bone resected from the human tibia. Their results for elastic modulus of the tibia were higher than those previously measured for the femur (Currey, 1975); therefore,

they concluded that their method was inaccurate. However, with further developments since their study, particularly on the tibia, we now know that the modulus of tibial bone is higher than that of the femur (Morgan et al., 2003), and their results have been corroborated by other studies done on cortical bone (Hansen et al., 2008).

Since 2000, research on bone architecture (Keaveny and Yeh, 2002) has suggested that bone property relationships are species and anatomical site dependent (Morgan et al., 2003). The study by Morgan et al. (2003) demonstrated differences of elastic modulus of cancellous bone in various anatomical sites including the vertebra, proximal tibia, femoral neck and greater trochanter:

$$E_{proximal\ tibia} = 15.52\rho_{wet}^{1.93}$$

$$E_{greater\ trochanter} = 15.01\rho_{wet}^{2.18}$$

$$E_{femoral\ neck} = 8.92\rho_{wet}^{1.49}$$

where E is in GPa and ρ is in g/cm$^3$.

These relationships must not be extrapolated further than their appropriate density range. Cortical bone was not assessed in the study and has been considered separately. Snyder and Schneider (1991) conducted a study specifically on tibial cortical bone and proposed the following relationship for apparent densities greater than 1.5 g/cm$^3$:

$$E_{proximal\ tibia} = 4.83\rho_{dry}^{2.39}$$

where E is in GPa and ρ is in g/cm$^3$.

Since the variation of cortical bone modulus is small within the diaphysis and metaphysis regions, an average modulus may be adequate. Measurements vary from 12-20 GPa (Rho et al., 1993), including specific anatomical measurements of 17.5 GPa for the tibia (Snyder and Schneider, 1991) and 17.7-17.8 GPa for the femur (Bayraktar et al., 2004b, Turner et al., 1999).

The findings of the literature review have been considered with the practicalities and objectives of the computer simulations described in this thesis. Bone material properties applicable for the proximal tibia and distal femur were explored further with a material sensitivity study presented in Section 3.5. Although computer simulations of bone would be more accurate if orthotropic properties were used (Keyak et al., 1994), the literature is limited for the proximal tibia and distal femur, but the effect on results has been demonstrated to be small (Peng et al., 2006). The proximal tibia exhibits some anisotropy (Ciarelli et al., 1991); however, since the tibia is principally loaded along the anatomical axis (and provided material properties were obtained from samples orientated along this axis), the assumption

of isotropy is considered satisfactory. The principal loading direction of the distal femur is however not always along the anatomical axis - it varies with knee flexion angle. For walking gait, it is loaded mainly along the anatomical axis (maximum flexion angle is 30 degrees); but for stair-climbing and chair-rise activities the distal femur is off-axis loaded at mid-flexion (60-90 degrees) with high tibiofemoral and patellofemoral contact loads (refer to Section 4). The transverse elastic modulus can be less than 50% of the anatomical axis modulus (Kaneko et al., 2004). It is therefore important to keep in mind the limitations of assuming isotropy in simulations of the femur during stair-climbing.

## 2.5 Bone Strength

Simulating bone failure is important in computer simulations of implants. It will identify how close bone is to failure, highlighting hotspots and possible failure mechanisms. A review of the literature was conducted to determine the most appropriate method for calculating a safety factor for bone.

Early studies of bone failure criteria concentrated on finding a relationship between density and failure stress (Carter and Hayes, 1977, Rice et al., 1988, Hvid et al., 1989, Keyak et al., 1994). Figure 11 compares the most cited relationships (Carter and Hayes, 1977, Rice et al., 1988, Hvid et al., 1989, Morgan and Keaveny, 2001, Keyak et al., 1994). The difference increases with bone density and becomes significant at densities greater than 0.5 g/cm$^3$.

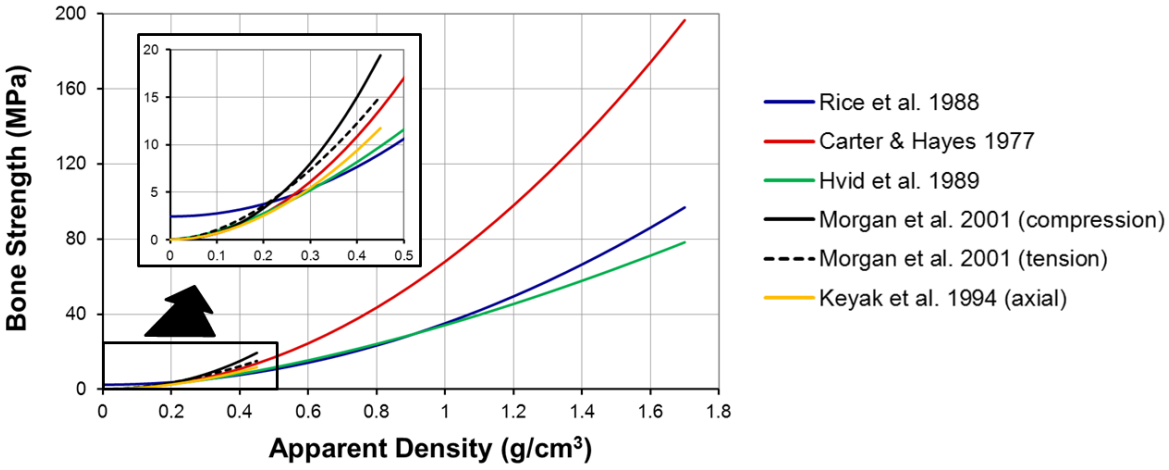


**Figure 11 - Apparent Density to Yield Stress relationships published in the literature**

Recent literature suggests that the failure of bone is better defined using a yield strain criterion (Morgan and Keaveny, 2001, Bayraktar et al., 2004b). Morgan and Keaveny (2001) conducted multi-specimen multi-donor uniaxial mechanical tests on proximal tibia, greater trochanter, femoral neck and vertebra, to determine yield strain in these regions. They demonstrated that yield strain varies across anatomical sites and the yield strain is mostly

uniform within a given site despite substantial variation of elastic modulus and yield stress. In a follow up study, Morgan et al. (2004) showed that the inter-site variation was due to differences in bone architecture (trabecular spacing and wall thickness). The following yield strains were reported:

**Table 1 - Human cancellous bone yield strains published in the literature.**

| Anatomic Site | Compressive Strain | Tensile Strain |
|---|---|---|
| Proximal Tibia | 7300 με | 6500 με |
| Greater Trochanter | 7000 με | 6100 με |
| Femoral Neck | 8500 με | 6100 με |

The femoral neck compression yield strain is higher than that of the proximal tibia and the tensile yield strains are similar between regions. Bayraktar et al. (2004b) conducted a study with samples taken from the femoral neck and supported the conclusions for a strain based failure criterion. Another study (Bayraktar and Keaveny, 2004) concluded that, while compressive yield strains are dependent on anatomical site, tensile yield strains are independent of anatomical site - this matches the similarity in tensile properties reported by Morgan and Keaveny (2001). The compressive yield strain of cortical bone is unreported but under tension it has been measured as 7300 με (Bayraktar et al., 2004b).

In 2000, Niebur et al. (2000) simulated bone failure with high-resolution FE models. They compared predictions with mechanical tests of bone in-vitro; and demonstrated that the strain failure criterion was accurate. Whole-bone level computational models have also successfully predicted reliable results: Schileo et al. (2008b) compared stress and strain yield criteria against experimental results and concluded that the strain criterion was more accurate.

Since arthroplasty is usually performed on patients of 60-80 years, age is a factor to consider in the analysis of bone failure. McCalden et al. (1993) showed that ultimate bone strain halves from 3.5% to 1.75% between the ages of 20 and 80 years. Older bone has reduced mechanical properties due to the presence and susceptibility of developing microcracks that initiate at strains as low as 1500με; as a consequence, bone yield stress is lower in the elderly (Courtney et al., 1996).

## 2.6 Material Sensitivity Study

### *2.6.1 Introduction*

Since there is such a large variation of material property relationships in the literature, it was deemed necessary to do a study to understand the sensitivity of FE models to such uncertainty. It was hypothesised that, modelling the different elastic-modulus versus density relationships of bone and comparing them against a failure criterion, it would at least be

possible to identify unlikely relationships i.e. those that lead to predictions of bone failure under normal daily activity loads.

### *2.6.2 Method*

A ‘strong’ tibia and ‘weak’ tibia were chosen from 10 fresh frozen cadavers that were mechanically tested in the laboratory (specimens CAD01 and CAD04 respectively, as described in Section 5), modelled using FE analysis and validated (Section 6). The matching femur of the ‘strong’ tibia was also analysed.

As described in Sub-section 4.3.1, the tibiae were scanned using the “Definition AS+” Computed Tomography (CT) scanner (Siemens Healthcare, Germany) and phantom-calibrated. The long axes of the bones were aligned with the scanner axis; the slice thicknesses were 0.6 mm and the cross-section voxels were 0.5x0.5 mm.

The CT scans were segmented (as described in Sub-section 4.3.2), the surface meshed and smoothened with triangular mesh using AVIZO 6.1 software (Visualization Sciences Group, USA), and solid meshed with tetrahedral elements using MARC Mentat software (MSC Software Corporation, USA). As recommended in the literature (Polgar et al., 2001) and supported by our own sensitivity studies of element type (refer to Sub-section 4.5), 10-node quadratic tetrahedral elements were used and adequate mesh convergence was achieved (refer to Section 7.2). The proximal tibial and femoral distal cortices are too thin to be modelled with solid elements; hence, quadratic shell elements were included around the cancellous bone. The proximal 150mm of the tibia and distal 200mm of the femur were modelled with the base of the shafts fully constrained.

Single elastic moduli of 18 GPa and 14 GPa were assigned to the cortical bone regions of the ‘strong’ and ‘weak’ bones, respectively. A single cortical elastic modulus produced the best correlation and the value was chosen based on the specimen specific average CT value. The thin proximal tibial cortex was modelled with 0.2 mm thick shell elements of equivalent elastic moduli (sensitivity assessments described in Sub-section 4.6.2 showed that the uncertainty of the cortex shell thickness and elastic modulus had only local strain effects and did not disrupt the global response of the model).

Density-modulus relationships from the literature that were most appropriate for the tibia are listed in Table 2. All apparent densities were converted to dry apparent density (Keyak et al., 1994). Each study covered a range of bone densities, but these were mostly of low density cancellous bone or high density cortical bone, leaving few data to cover intermediate values. Because a model of a complete bone has to cover the density range, linear relationships were assumed across the gaps between published low and high density data. This

assumption was supported by prior work (Ciarelli et al., 1991, Bessho et al., 2004), leading to ten sets of density-modulus relationships for the tibia (Figure 12). The plot shows differences of an order of magnitude in predicted elastic moduli for bone densities below 10 g/cm$^3$.

**Table 2 - Material bone property relationship groups modelled in tibia study.**

| | ρ Range (g/cm$^3$) | ρ-E Equation (GPa) | Source |
|---|---|---|---|
| **1** | 0.1-1.73 | $E=3.79\rho^3$ | Carter and Hayes (1977) |
| **2** | 0.1-0.6<br>>0.8 | $E=2.56\rho^{1.47}$<br>$E=3.79\rho^3$ | Hvid et al. (1989)<br>(Carter and Hayes, 1977) |
| **3** | 0.1-0.95<br>1.9-2.2 | $E=0.06+0.9\rho^2$<br>$E=0.9\rho^{7.4}$ | Rice et al. (1988)<br>Schaffler et al. (1988) |
| **4** | 0.1-0.95<br>>1.5 | $E=0.06+0.9\rho^2$<br>$E=4.83\rho^{2.39}$ | Rice et al. (1988)<br>Snyder and Schneider (1991) |
| **5** | 0.1-0.95<br>>1.5 | $E=-0.16+4\rho+1.1\rho^2$<br>$E=4.83\rho^{2.39}$ | Rho et al. (1993)<br>Snyder and Schneider (1991) |
| **6** | 0.1-1.56<br>>1.56 | $E=-0.16+4\rho+1.1\rho^2$<br>$E=4.83\rho^{2.39}$ | Rho et al. (1993)<br>Snyder and Schneider (1991) |
| **7** | 0.1-0.778<br>>0.778 | $E=2.003\rho^{1.56}$<br>$E=2.875\rho^{3.0}$ | Perillo-Marcone et al. (2003)<br>Perillo-Marcone et al. (2003) |
| **8** | 0.1-0.37<br>>1.5 | $E=11.12^{2.2}$<br>$E=4.83^{2.39}$ | Keyak et al. (1994)<br>Snyder and Schneider (1991) |
| **9** | 0.1-0.37<br>>1.5 | $E=18.49\rho^{1.93}$<br>$E=4.83\rho^{2.39}$ | Morgan et al. (2003)<br>Snyder and Schneider (1991) |
| **10** | 0.1-0.37<br>>1.2 | $E=18.49\rho^{1.93}$<br>$E=3.89\rho^{2.39}$ | Morgan et al. (2003)<br>Carter and Hayes (1977) |

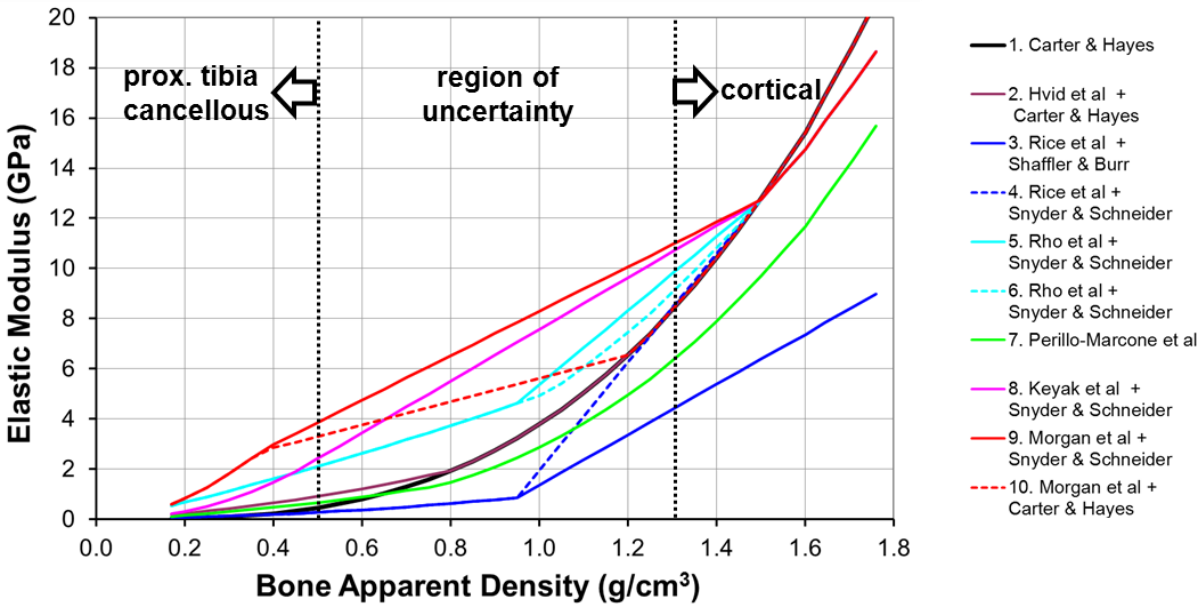


**Figure 12 - Comparison of published tibia density-modulus relationships assessed in the study**

The relationships included for the femur are detailed in Table 3 – these are less extensive and serve the purpose of supporting the conclusions of the tibia assessments for the femur.

**Table 3 - Material bone property relationship groups modelled in femur study**

| | ρ Range (g/cm$^3$) | ρ-E Equation (GPa) | Source |
|---|---|---|---|
| **1** | 0.1-1.73 | $E=3.79\rho^{3}$ | Carter and Hayes (1977) |
| **2** | 0.17-0.58<br>>1.5 | $E=4.782\rho^{1.61}$<br>$E=4.83\rho^{2.39}$ | Distal Femur, Kaneko et al. (2004)<br>Snyder and Schneider (1991) |
| **3** | 0.23-0.70<br>>1.5 | $E=7.845^{1.49}$<br>$E=4.83\rho^{2.39}$ | Femoral Neck, Morgan et al. (2003)<br>Snyder and Schneider (1991) |
| **4** | 0.1-0.37<br>>1.5 | $E=18.49\rho^{1.93}$<br>$E=4.83\rho^{2.39}$ | Proximal Tibia. Morgan et al. (2003)<br>Snyder and Schneider (1991) |

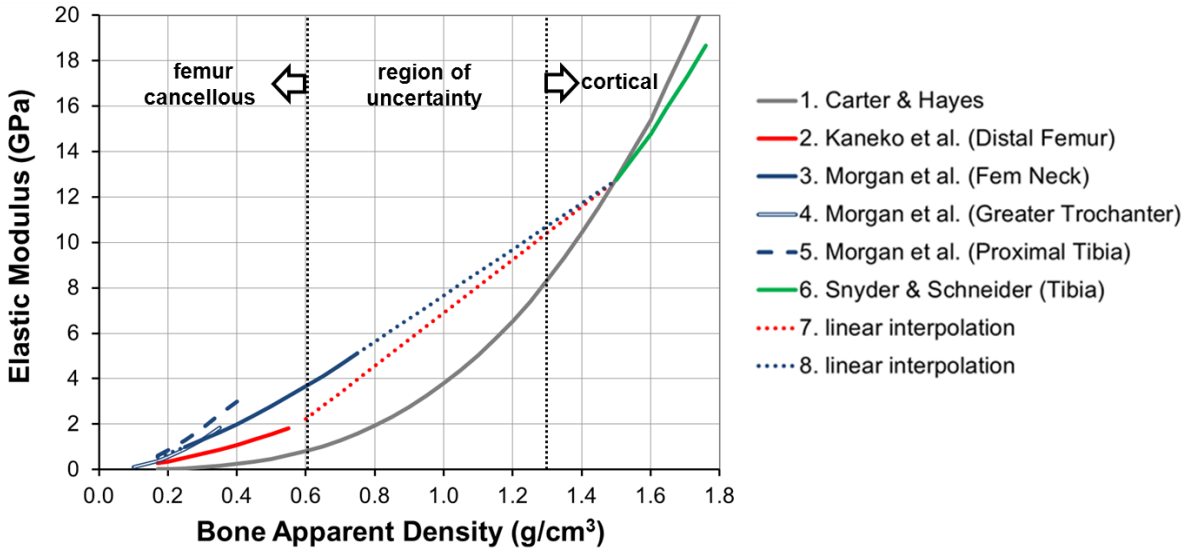


**Figure 13 - Comparison of published femur density-modulus relationships assessed in the study**

Material properties were assigned on an element-by-element basis assuming heterogeneity and isotropy and assuming a Poisson's ratio of 0.3 (Van Rietbergen et al., 1996). Radiographic grey scale values were obtained from CT data by averaging nine sampling points for each element. The CT scans were phantom calibrated to water and air to give Hounsfield Units (HU). The relationship between HU and tissue density was assumed to be linear as described in sub-Section 3.2 above.

A database of tibiofemoral joint contact forces with muscle and ligament forces for walking and stair ascent were determined from analysis of the literature, as presented in Section 4.

The loads were applied directly to the tibial and femoral cortices based on anatomical data for ligament attachment areas (as). The two peak forces, at 15% and 50% of the gait cycle were analysed.

The loads were scaled to body weight (64 kg for ‘strong’ tibia and 81 kg for ‘weak’ tibia) and applied directly to the nodes based on anatomical data for ligament attachment areas (Amis et al., 2006; Edwards et al., 2007) and tibio-femoral contact areas (Walker and Hajek, 1972) and positions (Wretenberg et al., 2002), as Sub-section 3.2. Simple representations of the medial meniscus were modelled in order to distribute the high medial contact loads accurately. Although the elastic modulus of the meniscus is non-linear (at 20% strain elastic modulus is 20 MPa and increases to 300 MPa with increased strain (Leslie et al., 2000)), a single linear elastic modulus of 20 MPa was assigned because it produced strains of approximately 20%. Two peak forces, at 15% of walking and stair-descent activities (refer to Section 3 for details of the knee forces during daily activities) were analysed.

A Regions of Interest (ROI), represented by 163 nodes, was defined at the medial condyle, 10 mm below the medial tibial plateau, defined by a mediolateral width of 10 mm, anteroposterior length of 20 mm and depth of 10 mm.

The static implicit FE models were solved using the MARC 2010 multifrontal direct sparse solver; analysed for tibial stress and strains; and assessed against a strain failure limit, as described in Section 3.4.

The results were post-processed to display plots of safety factor calculated against a bone yield strain criterion proposed by Morgan et al. (2004). Since there is no yield strain criterion available for the distal femur, the femur was assessed against criteria for both the proximal tibia and femoral neck. Refer to Sub-section 3.3 for further discussion of the strain criteria and Sub-section 4.6.9 for details of how the criterion was implemented as a MARC subroutine.

### *2.6.3 Results*

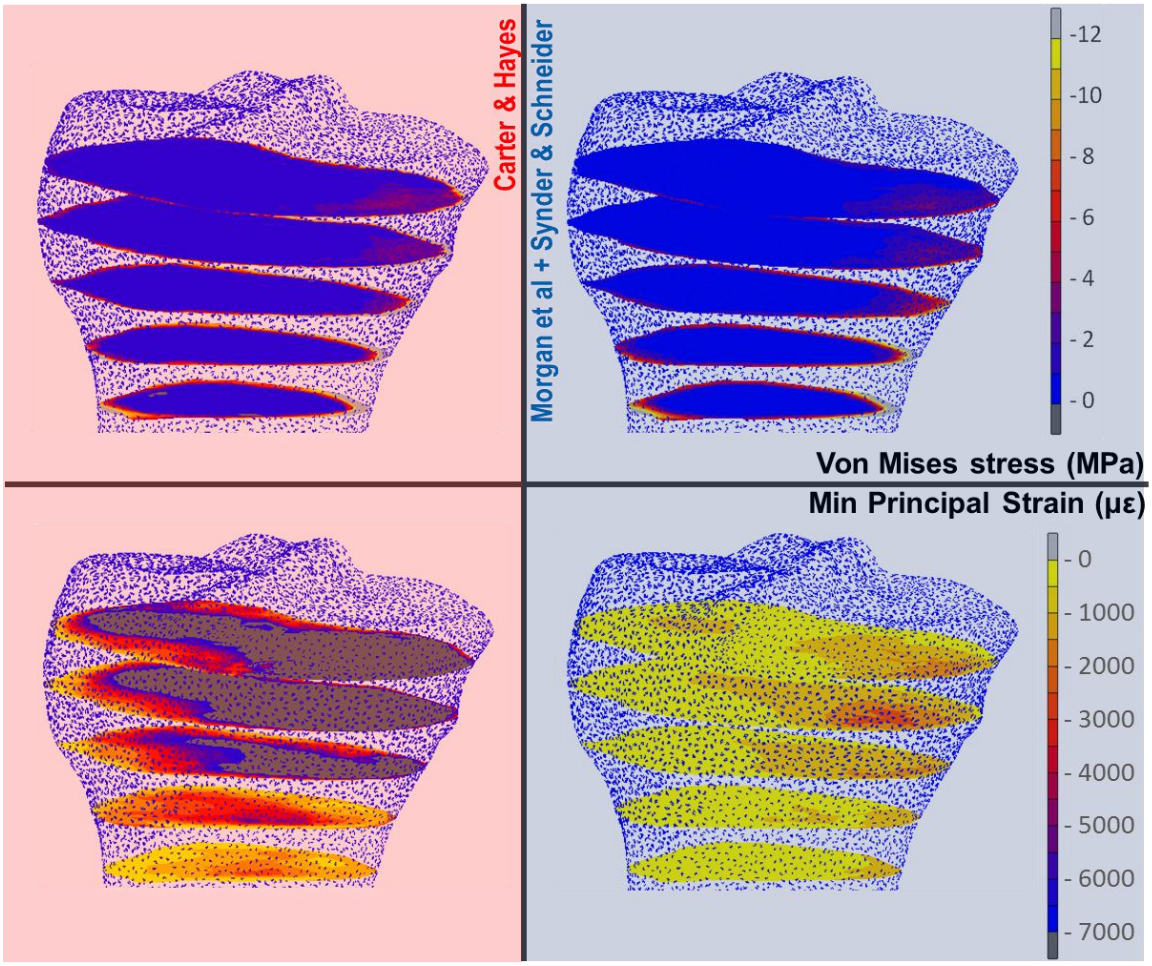


**Figure 14 - Plots of minimum principal stress and strain at 15% of the walking gait cycle comparing material relationships by Carter & Hayes against Morgan et al and Snyder & Schneider.**

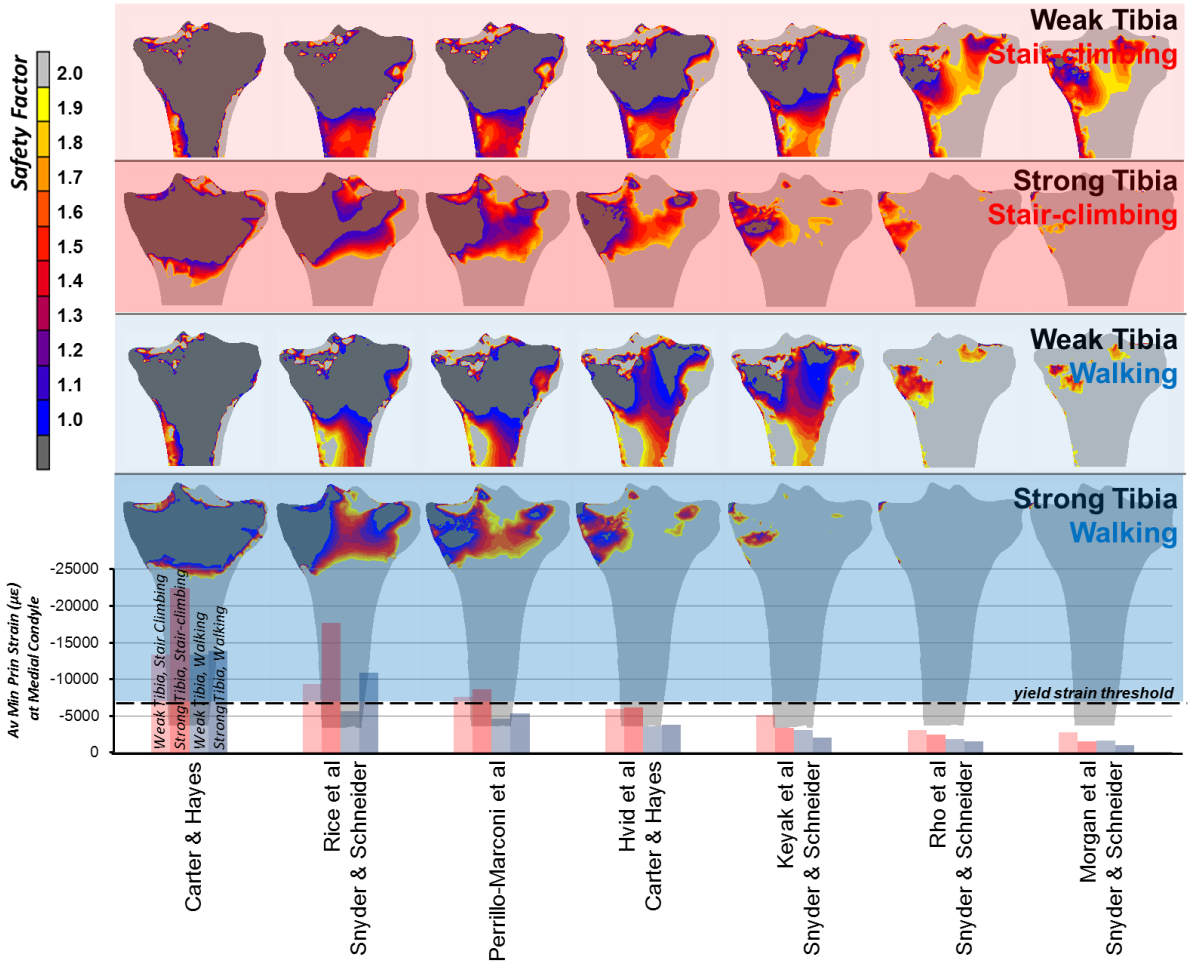


**Figure 15 - Bone failure plots at 15% of the walking and 50% of the stair ascent activity cycles. The legend scale 1.0-2.0 indicates the safety factors, with dark grey indicating failure and light grey indicating less than 50% of failure limit. The superimposed plot indicates the average minimum principal strain at the ROI defined at the medial condyle.**

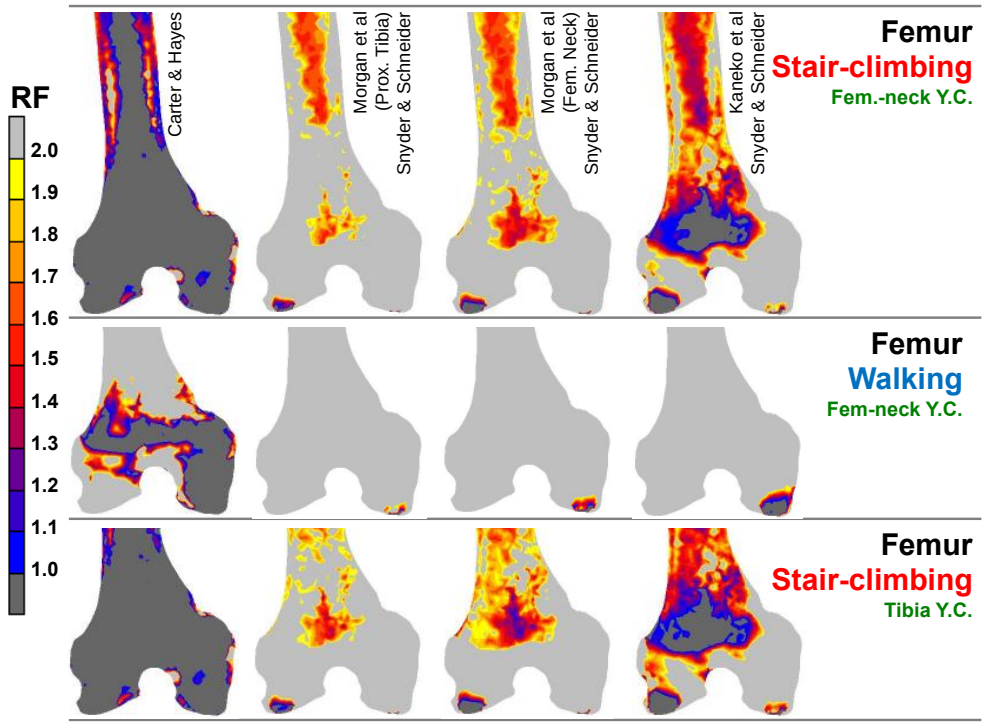


**Figure 16 - Bone failure plots at 15% of the walking and 15% of the stair ascent activity cycles. The legend scale 1.0-2.0 indicates the reserve factors, with dark grey indicating failure and light grey indicating less than 50% of failure limit. The plots also compare the difference in using yield criteria of the femoral-neck and tibia.**

### *2.6.4 Discussion and Conclusions*

The most important finding of this study is that some of the published apparent bone density to elastic modulus relationships led to predictions of bone strains in the proximal tibia which exceeded published failure criteria under loads imposed by normal activities. There have been a number of studies which based their density-modulus relationships on measurements of low density cancellous bone and/or high-density cortical bone specimens, which suggests that they were unrealistic, leaving a scarcity of data to describe intermediate bone densities. This study found that both the relatively low density and high density bones had approximately 30% of their volume which fell within the range of uncertainty – from 0.4 to 1.2 g/cm$^3$. Thus, in addition to casting doubt on the use of some of the published density-modulus relationships for analysis of the human proximal tibia, this study highlights the need for further experimental work to characterise the behaviour of bone with intermediate densities.

There are numerous FE studies of the tibia in the literature; however we are not aware of a single study that has used the relationships that we propose. Most recently, experimental validation of a human cadaveric tibia, was reported by Gray et al. (2008). They used orthotropic material relationships, proposed by Rho et al. (1995), for which the dominant

superior-inferior elastic modulus according to our study would be under-predicted. This may explain why their regression gradient was 25 % above unity. Varghese et al. (2011) conducted a multi-specimen tibia validation and demonstrated excellent correlation; however, they did not use any material property relationships published in the literature. They avoided the problem of uncertainty in these material relationships by optimising elastic moduli value in order to produce the most favourable correlation. Although they obtained excellent correlations against in-vitro cortex mounted strain gauges, it is uncertain as to whether the cancellous bone strains they predicted were realistic.

Schileo et al. (2007) conducted a validation study of the human femur and investigated 3 different material property relationships including the generic Carter & Hayes and a species and anatomy specific relationship proposed by Morgan et al. They concluded that the species and anatomy specific relationship produced the most accurate results for the femur. In a follow up study, Schileo et al. (2008b) concluded that the strain failure criteria produced the most accurate predictions of bone failure. Our study on validated femoral bones supports the findings of Schileo et al. In addition, our study highlights the large potential inaccuracies produced by using inappropriate material properties.

Bone in the proximal tibia predominantly has apparent dry densities of 0.1-0.4 g/cm$^3$ (68-73% by volume as presented in Table 4) and, as illustrated in Figure 1, the literature displays significant variability in elastic modulus predictions for this density range. The variability is an order of magnitude between Carter and Hayes and Morgan et al at 0.4 g/cm$^3$. This was responsible for the large variability in the strain predictions.

**Table 4- Proportion of bone densities in proximal 100 mm of tibia.**

| Density Region | 'Strong' Tibia | 'Weak' Tibia |
|---|---|---|
| 0.0 - 0.4 g/cm$^3$ | 68% | 73% |
| 0.4 - 1.2 g/cm$^3$ | 32% | 27% |
| 1.2 - 2.0 g/cm$^3$ | 0.03% | 0.04% |

The variability in cortical bone density-modulus relationships in the literature had less impact on strain predictions because (1) the cortical bone region was separated and a single elastic modulus assigned, and (2) the proportion of cortical bone (in the proximal 100 mm of the tibia) was very low (0.3-0.4%). Note that although the global response of the model changed with variations in cortical elastic modulus values, the results had negligible effect on the conclusions of this study.

The wide spread of bone elastic modulus data in the literature, across the density range 0.1-1.2 gcm$^{-3}$ (Figure 12), is compounded by the sparcity of experimental data in this range, so there is uncertainty as to which is the most accurate relationship. Note that 27-32% of the tibial bone volumes were composed of densities in this range.

The safety factor plots (Figures 15 and 16) illustrate that the strain failure criteria proposed by Morgan et al. are not compatible with the density-modulus relationship proposed by Carter and Hayes for the tibia. The Carter and Hayes model under-predicted elastic moduli of the proximal tibia and, based on the strain failure criteria, over one-third of the proximal tibia was then predicted to fail under daily activity loads. One reason for this discrepancy may be because, as Morgan et al. (2003) demonstrated, bone material properties are species and anatomical site specific and we must use specific bone property data in computational models. A counter-argument for this discrepancy may be that the strain failure criteria used in this study are not appropriate in this case. However, there is evidence that strain failure criteria model bone behaviour more accurately than stress based criteria (Morgan and Keaveny, 2001). A constant strain failure criterion under uniaxial loading for the proximal tibia has produced acceptable results (Morgan and Keaveny, 2001). Bayraktar et al. (2004a) showed that human trabecular bone failure is nearly isotropic and homogeneous, providing further evidence that a simple strain failure criterion would be adequate in assessing bone failure. Schileo et al. (2008b) have successfully demonstrated that such a criterion can predict failure accurately for the femur. A limitation of this study is that all the results of density-modulus relationships were compared against a single failure criterion, which was proposed by Morgan et al, who also proposed the density-modulus relationship which this study demonstrates to be most appropriate.

It is important to consider the limitations of this study. The modelling technique used in this study is common in the analysis of bones and the models used in this study were validated against in-vitro tests. Partial volume effects at the tibia boundary can cause geometric and material inaccuracies; however, sensitivity assessments of boundary material properties and geometric uncertainties showed negligible effect on the conclusions of this study. Since the precise knee loads experienced by these specimens is unknown, the loads were derived from various literature sources. The largest ligament and muscle contributors during peak walking and stair-descent loads are the ACL and patellar tendon. Sensitivity assessments on the ACL and patellar tendon loads revealed that uncertainties in these values made no difference to the conclusions of this study. Although there are an abundance of sources (using three principal methods: telemetry from instrumented knee prostheses, optimisation and inverse dynamic analysis of gait) supporting the magnitude of the knee load assessed, there is some uncertainty in the medial-lateral load-split. The load-split under walking loads was obtained from optimisation methods (Shelburne et al., 2004, Shelburne et al., 2006) and this is supported by more simple inverse dynamics (Morrison, 1970a) and telemetry (Zhao et al., 2007). The stair-descent loads were determined from simple inverse dynamics (Morrison, 1969) and the load-split was calculated from a study of adduction moments

(Kowalk et al., 1996, Andriacchi et al., 1980). The load-split is dependent on the adduction moment at the knee (Zhao et al., 2007), and although predictions are available for normal subjects it does vary depending on gait patterns and hip-knee-ankle alignment (Kowalk et al., 1996, Erhart et al., 2010). That said, neither specimen showed any geometric abnormalities and their knee alignment was probably relatively normal. It should also be considered that other activities, including chair-rise, can impart greater loads than those assessed (D'Lima et al., 2006) and these would further exacerbate the discrepancies observed. Sensitivity checks on other parameters (including uncertainty in CT-density relationship) revealed relative insensitivity compared to density-modulus relationship.

The Carter and Hayes (1977) relationship is convenient; however, this study concludes that this relationship, including those by Perillo-Marcone et al. (2003) and Hvid et al. (1986), are unsuitable for the proximal tibia. The relationships proposed by (Morgan et al., 2003) produced acceptable tibial strains that did not predict bone failure under loads imposed during daily activities. This study also demonstrates how sensitivity assessments can provide a means to reduce uncertainty by eliminating unlikely candidates. The uncertainty present in computer models of the tibia highlights the need for validation of such models.

Although the relationship proposed by Kaneko et al. (2004) is specific to the distal femur, it predicts yielding under daily loads, as presented by Figure 16. Note that the low safety factors at the condyle edges are artefacts of the nodal forces applied and can be ignored. Unfortunately Morgan et al. (2003) did not investigate the distal femur but did investigate the femoral neck and greater trochanter. Since both relationships were similar for their range of bone densities and the femoral neck relationship covered a wider range, the femoral neck relationship (combined with that of Snyder and Schneider (1991)) was used to predict femoral elastic moduli. Despite this relationship being the stiffest relationship available for the femur, the minimum principal strains are close to the compressive tibial bone yield strain limit and exhibit low safety margins. The tibia yield strain limit seems to be too low for these daily loads imposed on the femur. Although the femoral yield criterion (Morgan and Keaveny, 2001) was derived from the femoral neck, it displays acceptable safety margins. Similar to the proximal femur, the distal femur loading is multi-directional, while the proximal tibia loading, on the other hand, is primarily on-axis. Trabecular architecture of the distal femur should resemble that of the proximal femur more closely than that of the proximal tibia (both loaded multi-directionally); therefore, using the femoral yield criterion on the distal femur is most appropriate, with the limitations of the literature in mind.

Based on the findings of this study, Table 5 presents the density-modulus relationships and yield strains that were concluded to be the most suitable for the proximal tibia and distal femur.

**Table 5 - Density to elastic modulus relationships for the proximal tibia and distal femur deemed most suitable.**

| | ρ Range ($g/cm^3$) | ρ-E Equation (GPa) | Source | Yield Strain $\varepsilon_y$ (με) |
|---|---|---|---|---|
| Proximal Tibia | 0.1-0.37<br>>1.5 | $E=18.49\rho^{1.93}$<br>$E=4.83\rho^{2.39}$ | Prox. tib., Morgan et al. (2003)<br>Snyder and Schneider (1991) | Tensile: 6500με<br>Compression: 7300με |
| Distal Femur | 0.23-0.70<br>>1.5 | $E=7.85\rho^{1.49}$<br>$E=4.83\rho^{2.39}$ | Fem. Neck, Morgan et al. (2003)<br>Snyder and Schneider (1991) | Tensile: 6100με<br>Compression: 8500με |

This study demonstrates the uncertainty of bone elastic moduli predictions used in FE models of the tibia and femur. It also highlights the variability of bone properties of human tibiae and femora. For successful implant design, the extremes must be considered, as it is the extremes that are likely to create undesirable outcomes. A recent study by Laz et al. (2007) incorporated the uncertainty of material property data into computer models using probabilistic methods. Although a statistical analysis is outside the scope of this thesis, based on variability of the samples measured by Morgan et al. (2003) and Snyder and Schneider (1991), upper and lower bounds have been predicted for the tibia, as presented in Table 6.

**Table 6 - Upper and lower bounds of density to elastic modulus relationships for the proximal tibia.**

| | ρ Range ($g/cm^3$) | ρ-E Equation (GPa) Upper | ρ-E Equation (GPa) Lower | Source |
|---|---|---|---|---|
| Proximal Tibia | 0.1-0.37<br>>1.5 | $E=26.48\rho^{1.93}$<br>$E=5.23\rho^{2.39}+1$ | $E=12.90\rho^{1.93}$<br>$E=4.43\rho^{2.39}-1$ | Prox. tib., Morgan et al. (2003)<br>Snyder and Schneider (1991) |

# 3 Simulating Knee Forces, Kinematics & Contact

## 3.1 Introduction

This section describes a literature review of knee forces, kinematics and contact between the tibia, femur and patella; and how a database of knee forces (boundary conditions for the computer models described in Section 4) was assembled. The database contains forces (magnitudes and directions) of tibiofemoral and patellofemoral contact, muscles and ligaments for the full activity cycles of walking, stair-ascent and stair-descent.

Although walking locomotion (gait) patterns are specific to every individual, there are inherent characteristics observable in particular subject groups. For a normal subject, the stance phase is the first 60% period of the cycle when the foot is in contact with the ground. The cycle begins at right foot heel strike and ends with right foot toe off as illustrated in Figure 17. The remaining 40% of the cycle is termed swing phase and represents the foot moving in the air.

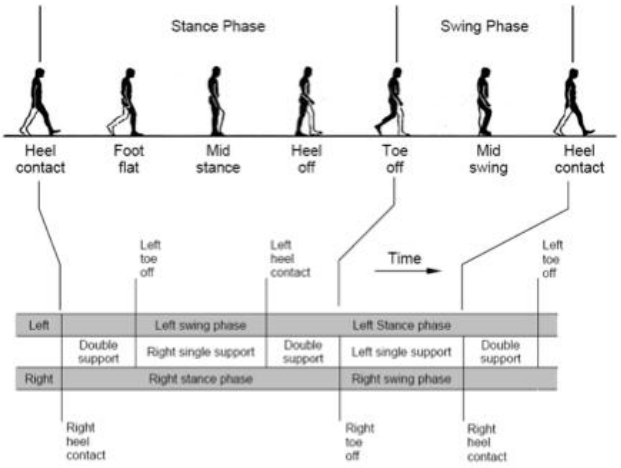


**Figure 17 - A typical gait cycle (Inman, 1981)**

Patients with OA are unlikely to exhibit normal gait due to limited range of motion and pain. Post-UKR patients are expected to regain gait patterns that are more normal, particularly compared to TKR patients.

The knee is the largest joint in the human body and one of the most complex. There are three articulating compartments of the knee (patellofemoral, medial tibiofemoral and lateral tibiofemoral compartments). It joins the femur to the tibia, with the patella articulating in the femoral trochlea and the fibula supporting the lateral tibia. As the knee flexes, the femur slides and rolls on the tibial plateau with surrounding muscles and ligaments constraining the

motion. The medial and lateral menisci of the tibiofemoral compartments provide load absorption and smooth articulation of the surfaces. The tibial plateau is flat, inclined at approximately 7 degrees (Hashemi et al., 2008, Matsuda et al., 1999) to the anatomical tibial axes, and it is steeper anteriorly (extension facet). The posterior parts of the femoral condyles (flexion facet) are spheres and the anterior parts are circular with a larger radius.

The muscles of the knee can be simplified and grouped into the hamstrings, gastrocnemius, and quadriceps (Morrison, 1968). The tensor fasciae latae, gluteus maximus, and popliteus do not fall naturally into these groups; however, the forces associated with them during walking and stair-climbing are small (Shelburne et al., 2006). The quadriceps tendon attaches the four quadriceps muscles to the patella and the patellar tendon attaches to the tibia.

The ACL consists of two bundles (anteromedial and posterolateral) adjoining the lateral femoral notch with the anterior of the tibia. The ACL restrains the tibia from anterior translation and medial rotation while the PCL restrains posterior translation. The LCL and MCL, adjoining the sides of the femur to the fibula and tibia, respectively, provide coronal stability, particularly during extension.

## 3.2 Literature Review

### *3.2.1 Overview*

Knee joint forces can be categorised as tibiofemoral and patellofemoral contact forces; muscle forces; and ligament forces. The tibiofemoral contact force is split between the medial and lateral condyles and includes normal and shear components. The muscles can be largely grouped into the quadriceps, hamstrings or gastrocnemius. The quadriceps force pulls on the patella which causes it to articulate against the femoral trochlea and pull on the patellar ligament to extend the knee. The hamstring muscles attach approximately at the level of the tibial tubercle to the medial tibia and lateral fibula and flex the knee. The gastrocnemius muscles attach to the posterior femur, just superior to the medial and lateral femoral condyles and also flex the knee. The ligaments of the knee can be simplified to the cruciate ligaments (anterior and posterior) and the collateral ligaments (medial and lateral).

Studies in the literature that predict/measure knee forces during specific activities have tended to be based on one or a combination of the following methods: (1) inversely resolving forces and moments measured from force plates and motion capture techniques; (2) optimisation solutions of indeterminate mathematical relationships of the lower limb; (3) telemetry from instrumented prostheses of arthroplasty patients.

Ideally, the most appropriate method for estimation of knee forces to model fixation of UKRs would be from an instrumented UKR; however, such a study does not exist. Results from instrumented TKRs and THRs are available in the literature. Telemetric data from instrumented prostheses (Bergmann et al., 2008) is the most reliable data set of in-vivo forces available; however, TKR and THR subjects tend to have antalgic gait patterns and are not representative of normal subjects with intact joints or UKR patients.

An important early contribution towards understanding knee forces was made by Morrison in the late 1960's (Morrison, 1968, Morrison, 1969, Morrison, 1970a, Morrison, 1970b). Morrison used force plates and photogrammetry to measure kinematics and calculate knee joint forces of subjects while walking and stair-climbing. He developed a mathematical model and made broad assumptions in order to reduce the problem so it could be solved.

If the broad assumptions that Morrison made are avoided, modelling the dynamic behaviour of the lower limb results in a complex multi-body system. The model requires non-linear mathematical relationships for skeletal force transmission, dynamic masses, and muscles and tendons as redundant actuators. Optimisation methods have been developed to find solutions to simulate these muscle groups associated with particular motions. Care must be taken with objective functions, as single objective functions, such as reducing energy or reducing peak load, are over simplistic and multiple objective functions require unsubstantiated weighting. These non-linear optimisation models are computationally expensive and often assumptions are required to simplify the problem. Using optimisation with a forward dynamics model is an alternative method and shown to reduce solution time by two orders of magnitude (Stelzer and von Stryk, 2006). The method involves finding a simplified inverse dynamics solution, based solely on the skeletal system, and inputting these into a forward dynamics model which is driven by kinematic and sometimes electromyographic data.

The studies using solely optimisation methods have been shown to be sensitive to input kinematic data (Fregly et al., 2008). The errors in the optimisation solutions can be reduced by using additional sources of data and/or using a combination of methods. Table 7 presents the most cited publications for knee force predictions/measurements in the literature categorised by the activity analysed and test method.

**Table 7 - Studies in the literature that predict/measure knee forces categorised by the activity analysed (walking, stair climbing and descent, and chair-rise) and test method.**

| Subject | Test Method | Activity | | | |
|---|---|---|---|---|---|
| | | Walking | Stair Climbing | Stair Descent | Chair-rise |
| Normal | Resolving Forces and Moments | Morrison (1968)<br>Morrison (1970) | Morrison (1969)<br>Andriacchi (1980)<br>Kowalk (1996)<br>Costigan (2002) | Morrison (1969)<br>Andriacchi (1980)<br>Kowalk (1996) | Rodoski (1989) |
| | Optimisation | Anderson (2001)<br>Shelburne (2006) | | | |
| Antalgic Gait (Post-THA and TKA) | Optimisation | Hurwitz (1998) | - | - | - |
| | Optimisation & Telemetry | Taylor (2004)<br>D'Lima (2006)<br>Zhao (2007) | Taylor (2004)<br>D'Lima (2006) | | D'Lima (2006) |
| | Telemetry | Taylor (2001)<br>Heinlein (2008) | Taylor (2001)<br>Heinlein (2008) | Taylor (1998)<br>Taylor (2001)<br>Heinlein (2008) | |

To illustrate the variability of the walking gait patterns reported in the literature, a comparison is presented in Figure 18. Zhao et al. (2007), Taylor and Walker (2001) and D'Lima et al. (2006) analysed post-TKR gait patterns; the four subjects reported by Taylor et al. (2004) are post-THR subjects and the analysis by Shelburne et al. (2006) is based on a normal subject. The differences are significant. Although, the distinct two-peak forces of the walking gait cycle are visible in all the gait patterns, they are least pronounced in TKR subjects.

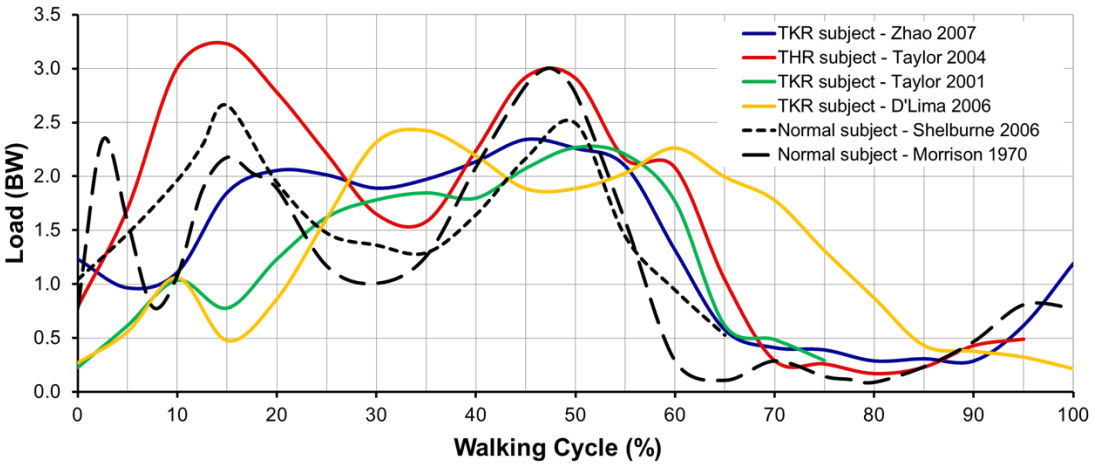


**Figure 18 - Knee joint load published in 6 studies of walking gait**

The differences in these gait patterns are due to characteristic changes made to the joints during arthroplasty. The ACL is resected in a TKA which disrupts tibiofemoral kinematics (depending on design the PCL may also be resected). ACL deficient subjects tend to exhibit quadriceps avoidance gait (Berchuck et al., 1990). The resurfacing of the tibial plateau and femoral condyles also disrupts the articulating surfaces; changes patellar tracking and therefore changes kinematics (Pandit et al., 2005) and magnitudes of resultant contact forces. Studies comparing UKR and TKR kinematics have found that the patellar tendon

length reduces following TKR (Weale et al., 1999) and the patellar tendon length is preserved for over ten years following UKR (Price et al., 2004). The kinematics of a hinged knee joint (used to derive knee forces by Taylor and Walker (2001)) is significantly different to that of normal subject; this is because the joint is artificially constrained.

Although THR patients exhibit antalgic gait, they may have normal functioning knees. As demonstrated by Taylor et al. (2004), the hip force from an instrumented THR can be used to derive knee forces and, as presented in Figure 18, the predicted forces are comparable to those of normal subjects. The subjects were 17 months post-operation and expected to have returned to normal gait (Andersson et al., 2001). For this reason this dataset has previously been used in a post-UKR bone adaptation study (Gillies et al., 2007).

UKR involves replacement of only a single compartment of the knee; the ACL and PCL remain intact; and the UKR is less constrained than TKR (particularly in the case of a mobile-bearing UKR). Therefore, the kinematics and loading of a UKR knee are expected to closer resemble those of a normal subject than those of a TKR patient. However, as presented in Figure 19, the differences are more pronounced for stair-climbing activities.

Another consideration is the effect of surgical trauma and post-arthroplasty recovery period on joint loads. Studies done on instrumented TKRs show that joint forces will stabilise within 6 weeks (D'Lima et al., 2006), increasing from 75% to 90% over the first few weeks and more gradually over the next 2 years (Taylor and Walker, 2001).

To be able to assess implant design for stress shielding and bone remodelling, the pre-arthroplasty knee forces must be known. Patients with medial osteoarthritis (OA) show adapted gait patterns. They tend to off-load the medial compartment (~70% of normal) and reduce total tibiofemoral knee force (~90% of normal) (Stauffer et al., 1977, Messier et al., 1992) using mechanisms such as lateral lean (Briem and Snyder-Mackler, 2009), shortening their stride and toeing-out (Wang et al., 1990). These mechanisms reduce external adduction moments at the knee (Briem and Snyder-Mackler, 2009). High external moments cause high medial contact forces (Zhao et al., 2007). However, these adaptive mechanisms exhibited by OA patients, do not mean that they exhibit lower than normal adduction moments. In fact studies have found that external adduction moments tend to be 30 percent higher than normal (Baliunas et al., 2002, Wada et al., 2001). OA patients also tend to exhibit quadriceps avoidance gait (26% of patients compared to 10% of normal subjects) where quadriceps force is half its normal amount (Stauffer et al., 1977, Baliunas et al., 2002, Wada et al., 2001) and tend to restrict their knee flexion (60% of normal) to avoid high patellofemoral forces particularly during activities such as stair climbing and chair-rise (Brinkmann and Perry, 1985, Messier et al., 1992, Briem and Snyder-Mackler, 2009).

### *3.2.1 Assessing Daily Activities*

The study by Morrison (1969) reported stair-climbing knee forces of two normal subjects. Unfortunately, subsequent studies investigating stair-climbing of normal subjects (Andriacchi et al., 1980, Kowalk et al., 1996, Costigan et al., 2002) did not report knee forces. However, there are published studies of post-THR and TKR subject knee forces obtained using instrumented implants. Taylor et al. (2004) reported stair-ascent and chair-rise knee forces of four post-THR subjects, and D'Lima et al. (2006) of a single post-TKR subject. Figure 19 illustrates the differences between two normal subjects and four post-THR subjects during stair-ascent. As presented in Figure 20, normal subjects tend to exhibit greater knee flexion and there are distinct differences of knee force magnitudes.

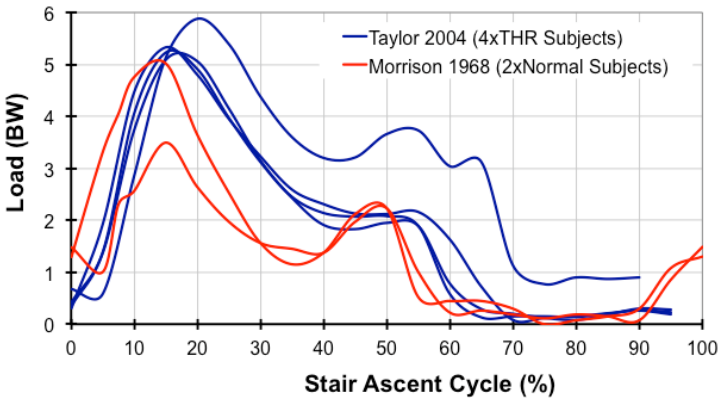


**Figure 19 - Comparison of stair-ascent forces between THR subjects (Taylor et al., 2004) and normal subjects (Morrison, 1968)**

As presented in Figure 20, the kinematic differences between walking, stair-climbing and chair-rise are significant. Although knee flexion is higher in chair-rise than stair climbing, the forces are less. Stair and chair-descent activities are reported to generate 10-12% higher knee loads than those for stair and chair-ascent activities (Taylor and Walker, 2001, D'Lima et al., 2005).

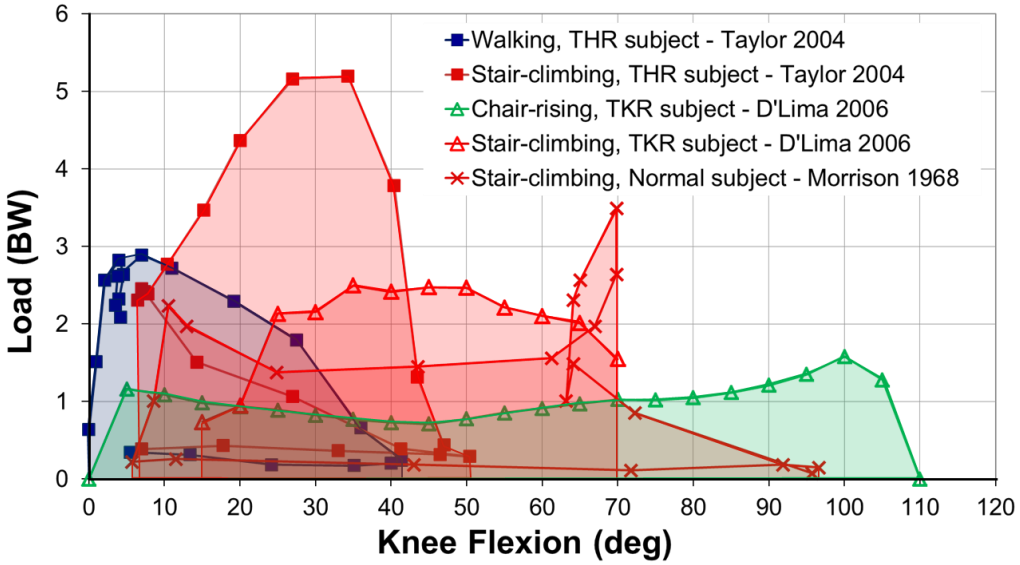


**Figure 20 - Comparison of knee joint loads verses knee flexion during various daily activities from two separate sources (Taylor et al., 2004, D'Lima et al., 2006).**

At a minimum, it is necessary to include walking, and stair-climbing activity knee forces when designing and assessing knee replacements.

### *3.2.2 Tibiofemoral Medial-Lateral Load-split*

Early studies by Morrison (1970b), Johnson et al. (1980) and Harrington (1976) revealed that the medial compartment is more loaded that the lateral compartment and that varus/valgus deformity is a major factor (Johnson et al., 1980, Harrington, 1983).

Using statically determinate muscle models, adduction moment was shown to be a major factor in the medial-lateral load-split (Andriacchi et al., 1986, Schipplein and Andriacchi, 1991) and a positive clinical correlation was demonstrated later by Zhao et al. (2007). It is widely known that 70% of the total knee load typically passes through the medial compartment (Hurwitz et al., 1998); however this is an average and the medial-lateral load-split as not constant.

The adduction moment varies during gait and this affects the medial-lateral load-split. In the walking cycle, at toe-off and swing phase the medial-lateral load split is roughly the same. The external knee adduction moment peaks just before contralateral toe off, causing higher medial forces. During single leg stance the contact force is mainly on the medial side whilst the muscles provide most of the resistance against adduction.

Based on optimisation solutions of walking gait (Anderson and Pandy, 2001), the medial compartment is predicted to take up the full joint load during the walking cycle (Shelburne et al., 2006). This is also evident from analysis of published results in the early work of

Morrison (1970b) : The knee joint forces and centre of pressures were analysed to deduce medial compartment forces and Figure 21 compares these to those published by Shelburne et al. (2006) (refer to Sub-section 3.3 for calculations method).

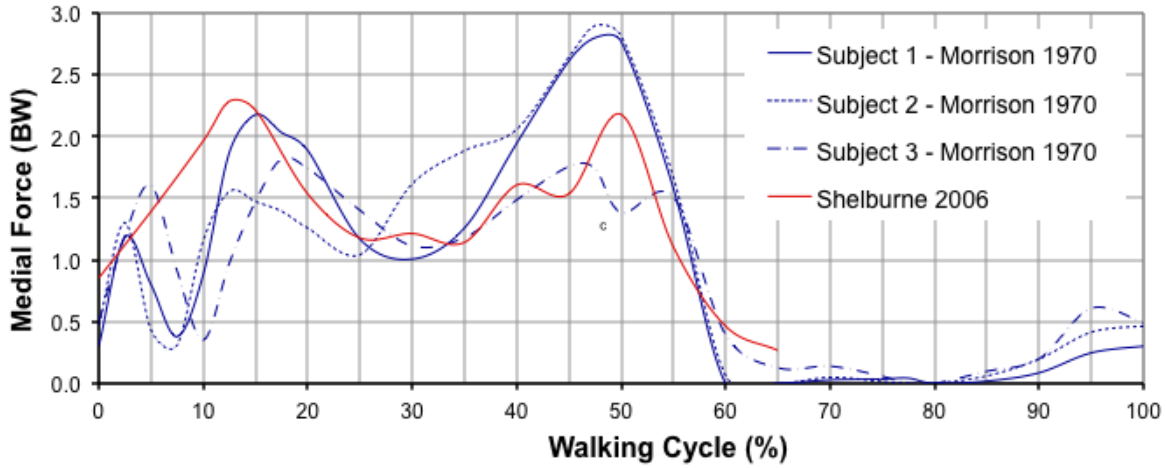


**Figure 21 - Estimated knee medial loads, based on results published in (Morrison, 1970b), compared with results published in (Shelburne et al., 2006).**

Based on studies by Shelburne et al. (2006), Hurwitz et al. (1998) and Schipplein and Andriacchi (1991) the peak force in the medial compartment is 2.3-2.4 BW while in the lateral compartment it is 0.8 BW. Note that, although Fregly et al. (2008) reported that optimisation solutions are sensitive to kinematic measurement and prone to error, the results of Morrison (1970b), which are based on traditional mathematical relationships, are in agreement with these results.

Studies of post-arthroplasty patients were also considered: Zhao et al. (2007) used telemetric data, from 15 post-TKR patients with instrumented prosthetics, alongside gait optimisation solutions to predict maximum medial loads of 70% of the total joint load. The peak total knee force was 2.06-2.74 BW and the medial force was 1.73-2.06 BW. A study by Hurwitz et al. (1998) assessing 26 subjects found a large variability of load-split. The average peak medial force to peak lateral force was 2.2 with a large standard deviation of 0.9 and range of 0.7 to 4.5. Varus deformity, a common symptom of OA, tends to increase adduction moment and medial compartment load, while valgus deformity will have the opposite effect. At the time of writing this thesis, it was common practice for surgeons to under-correct varus deformity to 1-3 degrees during UKR arthroplasty. Adduction moment is also dependent on the strength of the quadriceps, iliotibial band and gait pattern.

There are currently no published studies on medial-lateral knee load-split for stair-climbing activities in the literature; however, there are three published studies of knee adduction moments during stair-climbing: Andriacchi et al. (1980), Kowalk et al. (1996), and Costigan

et al. (2002). Unfortunately, there is disagreement between these data sets as presented by Kowalk et al. (1996) below:

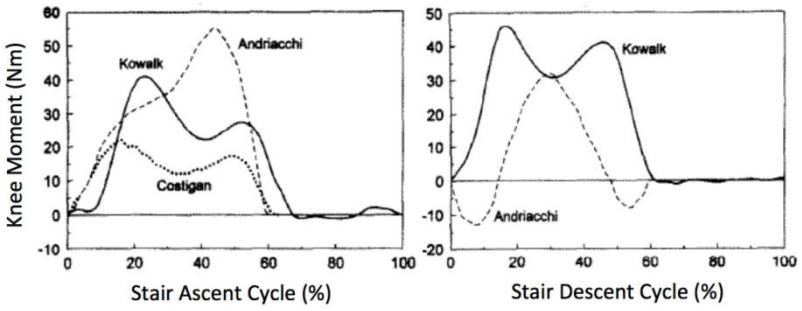


**Figure 22 - Comparison of the adduction knee moment data during stair climbing in the literature, published in (Kowalk et al., 1996)**

When making conclusions on the validity of these studies, it must be considered that the study by Andriacchi et al. (1980) is based on a single subject while those of Kowalk et al. (1996) and Costigan et al. (2002) are based on an ensemble of average of multiple subjects. For this reason, the medial-lateral load-split and the MCL and LCL ligament contributions calculated in Sub-section 3.3 are derived from Kowalk et al. (1996). Sensitivity assessments showed that the loads were sensitive to the chosen study results.

### *3.2.3 Tibiofemoral Kinematics and Contact*

The geometry and kinematics of the tibia, femur and patellar are complex; however, geometry simplifications can aid visualisation and understanding. Early influential studies of Goodfellow and O'Connor (1978) describe the femoral condyles as 2 spheres translating on a flat tibial surface constrained by a four-bar linkage formed mainly by the cruciate ligaments but also in part by the collateral ligaments. The medial tibial plateau is concave while the lateral tibial plateau is convex. The extension facet at the anterior of the medial tibial plateau rests against the femoral condyle during full extension. As the knee flexes, the femoral condyles rotate and slide over the tibia; the femur rotates externally causing the lateral condyle to move posteriorly while the medial condyle stays relatively in the same position. In deep flexion (greater than 120 degrees) both condyles move posteriorly, with the posterior horn of the lateral meniscus dropping over the posterior tibia. Knee kinematics is subject-specific and are influenced by the level of joint weight bearing, muscle activation (passive or active flexion) and internal/external torque (Hill et al., 2000).

The tibiofemoral kinematics of a normal knee has been well described in the literature. Early studies used in-vitro cadaveric specimens (Andriacchi et al., 1986, Butler et al., 1980, Fukubayashi and Kurosawa, 1980) to measure kinematics under simulated loads. Recent technologies using fluoroscopy, RSA (radiostereometry) and computational simulation

based on geometrical interpretation from CT and MRI imaging techniques have improved the accuracy of kinematic measurement (Martelli et al., 2002);Asano, 2001 #1821;Komistek, 2003 #1823}. Continuation of the work by Freeman and Pinskerova (2003) , Hill et al. (2000) and Johal et al. (2005) assessed ten male subject's knees in-vivo doing squats at ten degree increments under load bearing and non-load bearing activities.

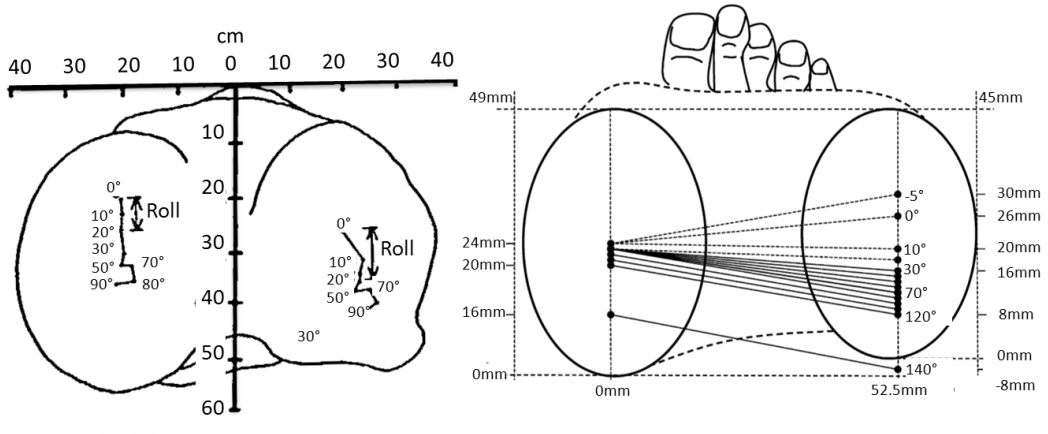


**Figure 23 - Weight bearing tibiofemoral contact kinematics as predicted by (Andriacchi et al., 1986) (left) and (Johal et al., 2005) (right).**

Figure 23 illustrates the difference in published medial condyle contact positions from two separate studies. During knee flexion, under no external joint torque, the medial compartment moves only 4-8 mm in the anterior-posterior direction while the lateral compartment moves over 10 mm for 60 degrees of flexion. The addition of internal/external joint torque mainly affects the position of the lateral condyle (Hill et al., 2000).

The UKR patient will not have the kinematics of a normal subject; however, it will be very different to a TKR patient (refer to Sub-section 3.2.1). A 16-patient radiographic study done on the early Oxford UKR design (Bradley et al., 1987), showed that the medial mobile-bearing moved posteriorly with 90 degrees of flexion, an average 4.4 mm (range of 0-13.5) from the implant midline. O'Connor and Imran (2007) computationally modelled the Oxford UKR and predicted similar bearing motion of 5 mm. Both studies concluded that the motion of the bearing was similar to the tibiofemoral contact movement of a normal subject.

Pandit et al. (2008) conducted a fluoroscopic analysis of ten medial Oxford UKR patients, with and without ACL reconstruction for a step-up (knee extension) activity. As presented in Figure 24, at 90 degrees flexion, the bearing was 2 mm posterior to the tibial component midline, it moved to the midline at 70 degrees and back posteriorly ending at 7 mm posterior to the midline at 0 degrees flexion. The ACL reconstructed UKR knees were shifted posteriorly by 2 mm. The average bearing movement was 7 mm ranging from 0.7 mm anterior to 9.1 mm posterior to the midline.

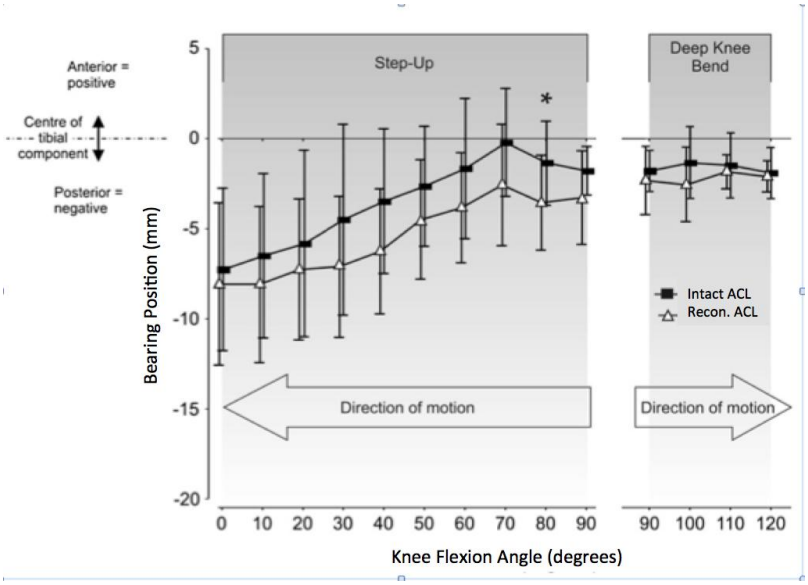


**Figure 24 - In-vivo translation of mobile-bearing position (relative to the tibial component) for intact and ACL reconstructed Oxford UKR patients during weight bearing knee flexion (Pandit et al., 2008).**

Li et al. (2006) conducted an in-vivo RSA study comparing kinematics of 28 Miller-Galante UKR knees with 28 Oxford UKR knees at two-year follow-up. As presented in Figure 25, the tibiofemoral contact point of the Miller-Galante UKR moved anteriorly 4.0 mm (1.2 - 6.6 mm) while the Oxford UKR moved posteriorly 2.1 mm (mean of 0.4 - 3.6 mm), from the full extension position. The tibial internal rotations of the Oxford UKR knees were larger than the Miller-Galante UKR knees (4.3°, 7.6°, 9.5° vs. 3.0°, 3.0°, 4.2°, respectively, at 30°, 60°, 90° of knee flexion). The mobile-bearing displacements reported by Li et al. (2006) were smaller than those reported by Pandit et al. (2008); however, this may be because the studies were done at two-years and one-year, respectively; and may be evidence that mobile-bearings seize-up over time. Both studies concluded that the Oxford UKR closer resembled normal knee kinematics compared to the TKR.

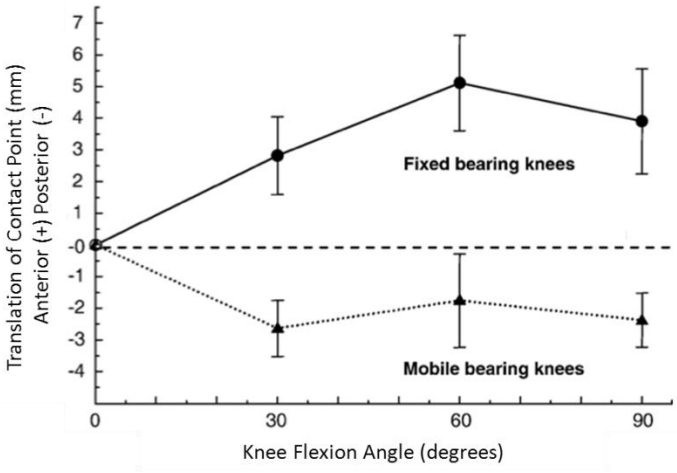


**Figure 25 - In-vivo translation of contact point of Oxford UKR during weight bearing knee flexion (Li et al., 2006).**

The tibiofemoral contact areas of the medial and lateral condyles are approximately both 1.2-2.0 $cm^2$ (Huberti and Hayes, 1984, Walker and Hajek, 1972). In the normal knee, the meniscus and cartilage spread the load over the tibial condyles. The contact area is halved if the menisci are removed (Scuderi et al., 2005). The contact area of the of UKRs depend on design, with congruent mobile-bearings having higher contact areas compared to fixed bearing designs (Bartley et al., 1994).

The literature described above relates tibiofemoral contact position to knee flexion angle. Fortunately the knee flexion is easy to measure for daily activities: Andriacchi et al. (1980) and Anderson and Pandy (2001) have published knee flexion angles during stair climbing and walking activities respectively. Stauffer et al. (1977) assessed 95 subjects for knee flexion during walking gait; comparing normal knees with those with OA knees (refer to Figure 26). The study highlighted the reduced flexion apparent in OA subjects.

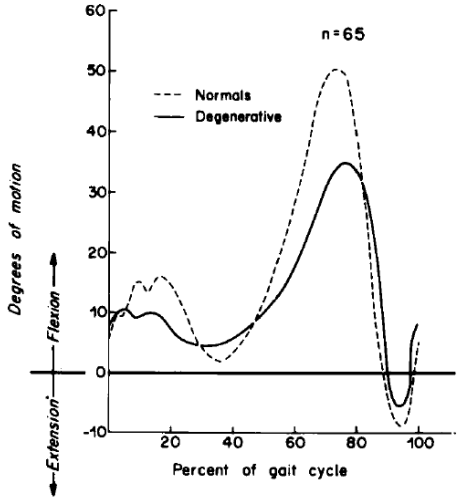


**Figure 26 - Comparison of flexion angle between normal and diseased knee (Stauffer et al., 1977)**

### *3.2.4 Patellar kinematics; Tendon Force and Patellofemoral Contact Force*

During knee flexion, the quadriceps muscles pull on the patella; the patella articulates over the femoral trochlea and pulls on the patellar tendon that is attached the tibial tubicle. The Q-angle is defined as the angle between the quadriceps and patellar tendon; it is approximately 10 degrees in normal subjects (Livingston and Mandigo, 1999) and ranges up to 16 degrees. The articulating surfaces of the patella contact the lateral and medial femoral condyles at approximately 61 and 68 degrees from the patella centreline (Ahmed et al., 1987). The patellar rotates (flexes) about the posterior femoral axis (defined by line joining two most posterior points on the femoral condyles) at 0.66 times the knee flexion angle (Amis et al., 2006b). During weight-bearing knee flexion, the forces imparted on the femur and tibia are substantial (greater than 2 BW) and the load-split of the quadriceps muscles to

these bones vary as a function of flexion angle (Ahmed et al., 1987), as presented in Figure 27.

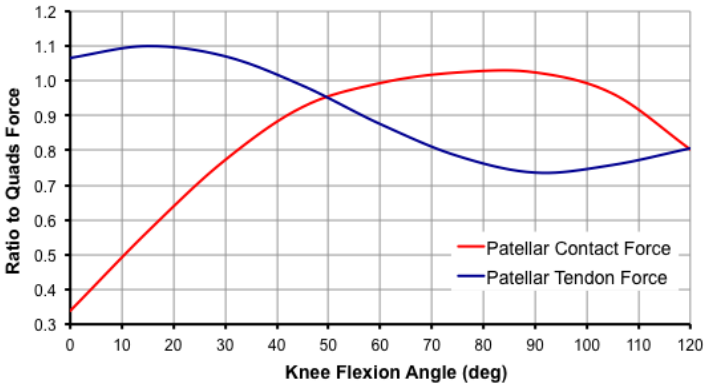


**Figure 27 - Proportion of quadriceps muscle force imparted on femoral trochlea and tibial tubicle (Ahmed et al., 1987)**

Using fluoroscopy and magnetic resonance imaging, patellar tracking (relative to the tibia and femur) has been documented in the literature (Li et al., 2007) and has been used to predict patellar tendon angle (direction of patellar tendon force on the tibial tubicle, refer to Sub-section 3.3). At full extension, the patellar tendon angle is 20 degrees anterior to the tibial anatomical axis and reduces relatively linearly to 5 degrees at 60 degrees flexion (Gill and O'Connor, 1996). Patellofemoral contact area increases from approximately 2.5 to 4 $cm^2$ from full extension to 60 degrees knee flexion (Matthews et al., 1977, Huberti and Hayes, 1984) and the contact points vary with flexion (Cohen et al., 2001, Goodfellow et al., 1976a, Goodfellow et al., 1976b, Goudakos et al., 2009), as presented in Figure 28.

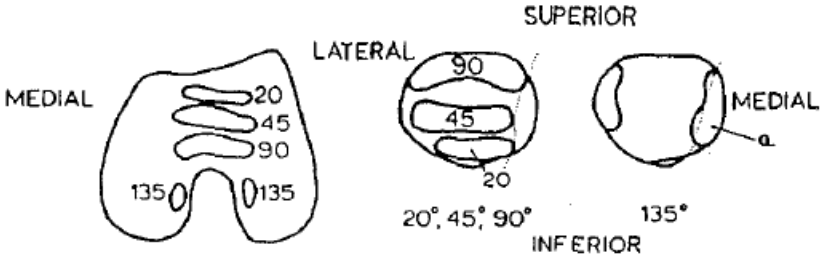


**Figure 28 - Progression of patellofemoral contact areas with knee flexion, starting at full extension, leading to two separate contact areas in deep flexion (Goodfellow et al., 1976b).**

## 3.3 Method: Walking, Stair Ascent & Descent Database of Knee Forces

A database of tibiofemoral joint contact forces for walking and stair ascent, with muscle and ligament forces, was determined from analysis of the literature. The full walking gait dataset was obtained from Shelburne et al (2004,2006). The stair climbing dataset was calculated from a combination of sources, as described herein.

The medial and lateral components of the total tibiofemoral load (Morrison, 1969) were calculated from abduction-adduction moments reported by Kowalk et al. (1996). The quadriceps, gastrocnemius and hamstring muscle forces, and medial and lateral contact forces contribute to resisting the abduction-adduction moments of the knee. The gastrocnemius muscles were given equal apportionment between the medial and lateral heads (since the muscles are of equal size). The hamstring muscles were also given equal apportionment; however, they contribute little to the adduction moment. The quadriceps muscles (via the patellar tendon) contribute most of the muscular moment needed to resist knee adduction (Shelburne et al., 2006). The medial and lateral condylar forces were assumed to be 20 mm from the knee centre (Wretenberg et al., 2002). The MCL and LCL were assumed to act only to provide additional moment when the load from medial-lateral apportionment was insufficient to resist the adduction moment (Morrison, 1970b). The dynamic effects were assumed to be negligible (Shelburne et al., 2004).

The ACL and PCL forces were estimated by resolving forces and moments for static equilibrium at every point of the stair-climbing cycle. The tibial slope was assumed to be 7 degrees. The positions and directions of the muscles and ligaments were determined from literature and from analysis of CT scans of pre-UKR patients. The ACL and PCL attachment locations were determined from literature (Amis et al., 2006a, Edwards et al., 2007a, Edwards et al., 2008, Edwards et al., 2007b). The force directions of the MCL, LCL and hamstring muscles were assumed to be constant with flexion, while the ACL, PCL and patellar tendon force directions varied with knee flexion.

These methods for predicting medial-lateral contact, MCL, LCL, ACL and PCL forces were verified by performing them on the total joint forces published for the walking cycle by Morrison (1970b) and Shelburne et al. (2006) and comparing the predictions against the published forces.

Using published patellar tendon load-split ratios (as a function of flexion angle) for walking and stair-climbing (Ahmed et al., 1987), the patellar tendon force was calculated from quadriceps muscle force predictions. Knee flexion angles for stair-ascent and stair-descent were obtained from (Andriacchi et al., 1980).

To verify the reliability of predictions of patellar tendon angle calculated from a simplified model of the knee (Gill and O'Connor, 1996), our own predictions were made from a recent reliable patellar tracking dataset published by Li et al. (2007). The patellar tendon geometry relative to the centre of the tibia was predicted from literature (Basso et al., 2001) and CT scans of pre-UKR patients.

All the knee forces were converted to multiples of body weight (BW) with a one unit of BW equal to 700N. For the purposes of understanding the joint forces with position, Figure 29 presents the peak medial condylar forces during these basic activities against flexion angle. The predicted knee forces (tibiofemoral and patellofemoral contact, muscles and ligaments) for walking, stair-ascent and descent activities are displayed in Figure 30.

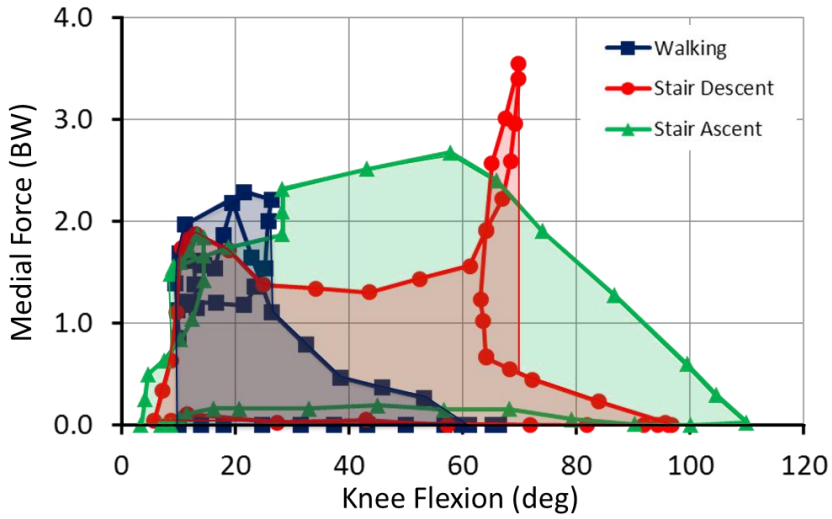


**Figure 29 - Summary of medial compartmental knee forces with flexion angle for daily activities. The plot highlights the loading of the femoral condyle.**

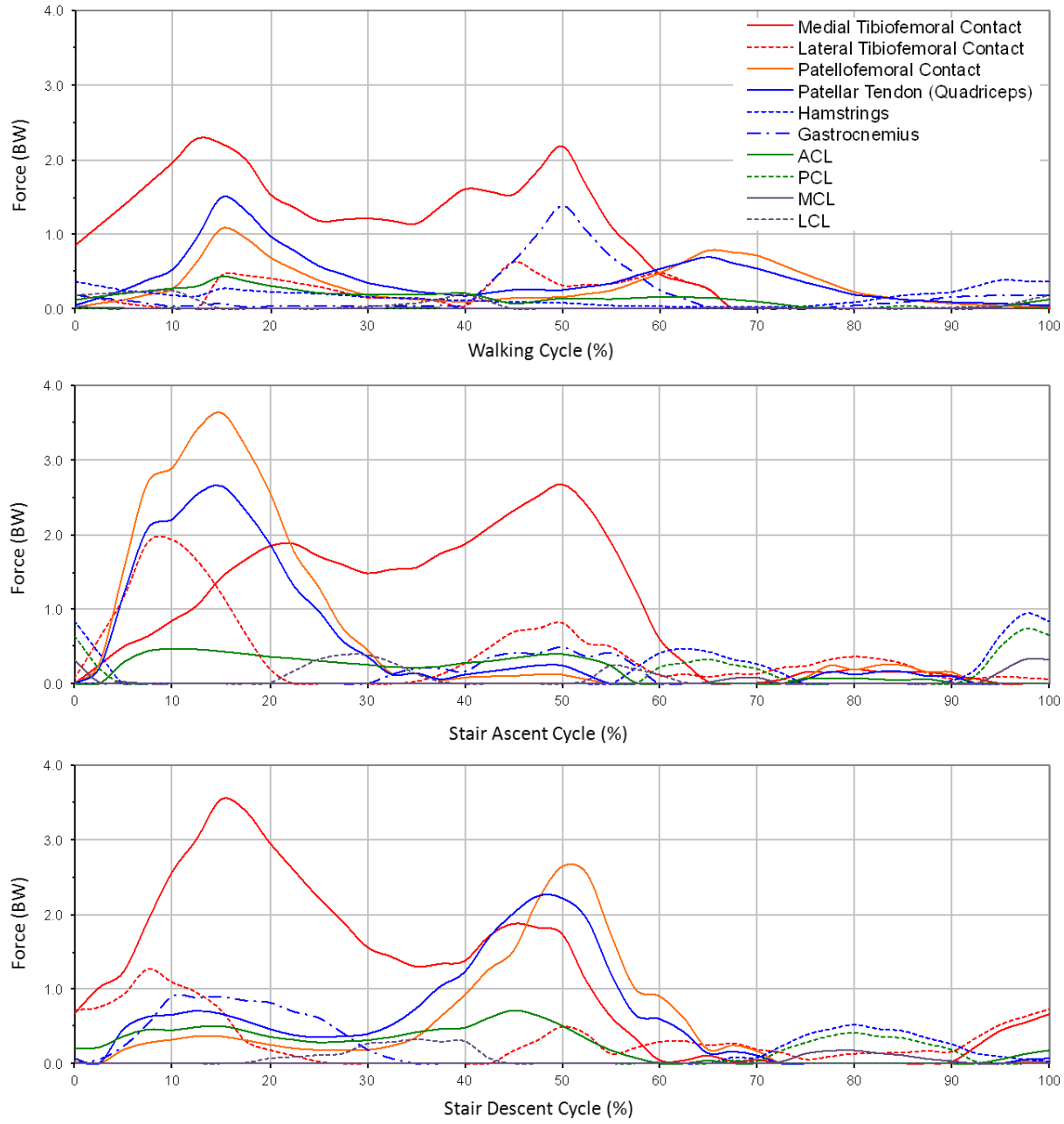


**Figure 30 - Plots of the knee forces (joint contact, muscles and ligaments) for daily activities of Walking, Stair Ascent and Stair Descent.**

## 3.4 Discussion and Limitations

The medial tibiofemoral and patellofemoral contact forces are the dominant knee forces during walking and stair-climbing activities. The peaks occur at approximately 15% and 50% of the cycles, which corresponds to contralateral toe-off and contralateral heel-strike, respectively. The largest medial tibiofemoral force is 3.5 BW and occurs at 15% stair descent. The largest patellofemoral force is also 3.5 BW and occurs at 15% stair ascent. The largest ligament and muscle contributors during peak walking and stair ascent loads are the ACL and patellar tendon. The FE models are relatively insensitive to the other ligaments and muscles, as demonstrated in Sub-section 4.2. The methods used to predict ACL and patellar tendon forces for stair-climbing were verified and the predictions compared against other literature sources where possible. As demonstrated in Sub-section 2.6, the dataset produces realistic bone strains for both the femur and tibia.

It is important to consider the limitations of this database. Although antalgic post-arthroplasty knee forces and kinematics have been reviewed, the database assumes that the kinematics and forces of UKR patients are not dissimilar to those of normal subjects. The database is generic, and has been amalgamated from multiple subjects and sources. A thorough literature review was undertaken to understand the reliability and uncertainty of the data; however, the sensitivity of these knee forces to subject specific variations of anatomy are unknown. The valgus-varus knee alignment is one such parameter that may be prevalent in pre and post-arthroplasty. Due to damage of the medial tibiofemoral cartilage, pre-arthroplasty patients tend to show slight varus alignment. The patient will regain some of her original knee alignment (with ligament balancing procedure); however, often the ligaments are imperfect and may have adapted with the arthritic knee.

Since the literature does not contain a full set of stair-climbing knee forces, they were calculated based on data from a number of sources. The forces and moments were resolved at each time frame and broad assumptions and simplifications were made. Dynamic effects were ignored, muscle groups and force directions were simplified, and the effect of patellar Q-angle on adduction moment excluded.

Chair-rise is another daily activity that produces large knee forces; however, there was insufficient data in the literature to derive a full set of knee forces for this activity. The database developed was deemed onerous because results from instrumented TKRs have shown that chair-rise total tibiofemoral loads (1.9-2.2 BW) are less than those of stair-climbing (D'Lima et al., 2006).

The knee forces database developed is complete, sufficiently robust, and appropriate for the assessment of UKR tibiae and femora using FE modelling.

# 4 Development of FE Models for UKR Fixation Analysis

## 4.1 Introduction

Structural modelling of bone and the interaction at the interface with engineered prosthetic materials is complex and has numerous challenges. Bone is difficult to model accurately because it is a living non-uniform structure that is continually adapting to its mechanobiological environment. Structural Finite Element (FE) models have traditionally been used to design manmade engineering structures. The potential benefits to implant design are significant when compared to how much it has reshaped other industries such as the civil and aerospace in the last few decades. Traditional FE techniques have to be adapted and assumptions have to be made in order to bridge the gap to modelling in the biological environment. This section discusses the FE modelling approach used in this thesis and presents findings of studies used to investigate the uncertainties associated with modelling of the UKR, and how these challenges were overcome.

## 4.2 Simplification of Knee Forces

A full database of knee forces was developed, as described in Section 3. The methods used to ascribe these forces to the FE models are described in this section.

### *4.2.1 Inclusion of ACL and Patellar Tendon Force*

The ACL force is nearly 50% of Body Weight (BW) at peak loads during walking, and stair-climbing. The patellar tendon force is over 250% BW during stair-climbing activity and the hamstring muscle reaches 30% BW at peak tibio-femoral loads during walking. Assessments were conducted investigating the sensitivity of excluding these forces on (1) bone strain (in the vicinity of the implant), and (2) bone-implant micromotion. A baseline FE model of the tibia with a cementless Oxford UKR implant was developed and the full database of knee forces (ACL, PCL, MCL, LCL, patellar tendon, quadriceps, hamstrings, tibiofemoral contact) from Section 3 were applied. Six variants of the baseline model were created, each with one of the force components omitted. The bone strains in the vicinity of the implant were qualitatively compared. The results demonstrated that at peak knee loads (at 15% and 50% of walking, stair-ascent and stair-descent activities) the PCL, MCL, LCL and Hamstrings had negligible effect on the local strains and interface micromotions. However, the impact of excluding the patellar tendon and ACL forces was significant. It is therefore concluded that they should be included in computer models for comprehensive analysis of UKR fixation.

### *4.2.2 Load Application*

The three basic methods of applying a force to an FE model are: (1) to nodes as individual forces; (2) to elements as pressure; (3) as contact between two defined bodies. Defining contact is very computationally expensive; therefore, it is only beneficial if the conditions of the contact are well defined (geometry and material) and the region-of-interest is near the force application point. Stresses tend to disperse from the force application surface and differences become less apparent with depth. In the defence and aerospace industries, a rule-of-thumb of 3 elements deep is often used as a precursor for taking readings to ensure these errors are minimal. For the lateral compartment, since we are not interested in strains near the region of force application, nodal forces are adequate. The same applies for all ligament and muscle forces at the knee.

For the medial compartment of intact bone models, the regions-of-interest are at depths 6 mm and greater (2-3 elements deep); therefore, the validity of the force application methods were considered. Although the geometry and the material properties of the tibia and femur bones are defined, the CT scans of the knee are too coarse to define cartilage accurately. Modelling contact may therefore be considered inaccurate. A less computationally expensive method is to simulate the tibiofemoral interface by using low elastic modulus boundary elements between a rigid femur and CT-mapped tibia or vice-versa. The latter method was used where computational expense could be spared.

For the implanted bones, strains immediately under the implant are of interest. The implant is over 50 times stiffer than the underlying bone; therefore, the nodal forces applied to the implant will spread rapidly with depth. An assessment was conducted comparing 4 different load application methods: (1) single nodal force to implant surface; (2) 5 nodal forces to implant surface; (3) nodal force to a simulated femoral component and PE bearing; (4) nodal force to a simulated femoral component and PE bearing with contact defined at the bearing-implant interface. The friction coefficient at the implant-bearing interface was assumed to be 0.1 (Cobalt Chrome against UHMWPE surface - estimate based on unpublished in-house assessments and Smith and Nephew “Oxinium” documentation).

As presented in Figure 31, the load application technique considerably influenced the cement stresses (in cemented implant models). The strain differences in the bone dissipated away within three elements, as presented in Figure 32. For the strain validation study (described in Section 6), the nodal force application method was adequate because the strain gauges were located far from the implant. For assessment of interface fixation (Sections 8 and 9), modelling the bearing was considered important.

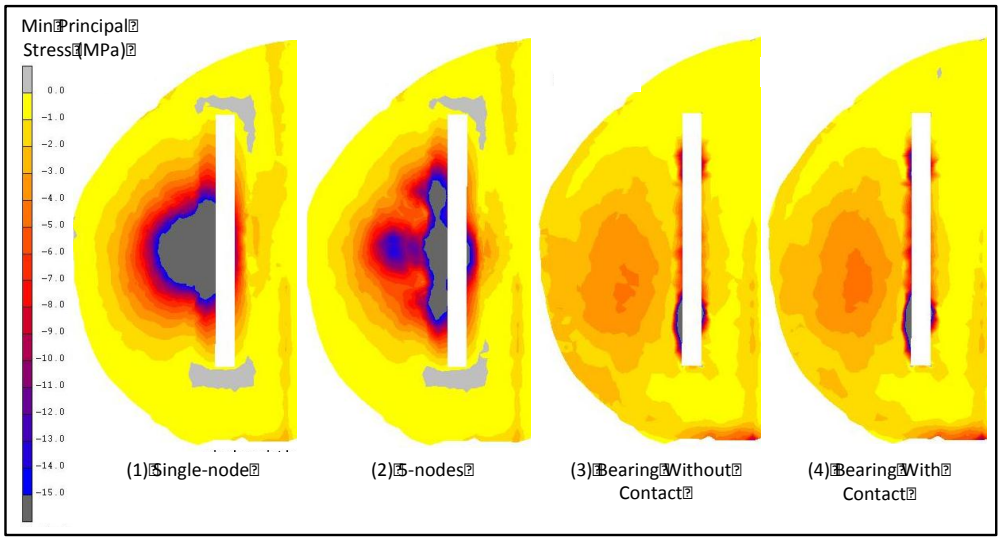


**Figure 31 - Plots of minimum principal stress in the cement-mantle (1mm under implant) in 4 progressively more detailed models under knee loads at 15% stair descent: (1) all medial condylar load applied at a single node; (2) at 5 nodes; (3) a PE bearing with nodes fixed at the bearing-implant interface; (4) a PE bearing with contact modelled at bearing-implant interface.**

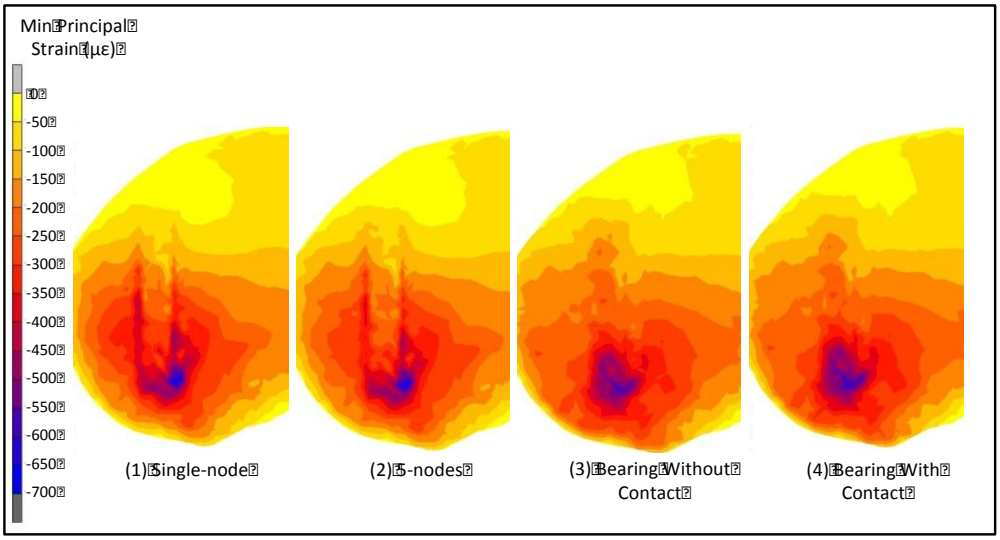


**Figure 32 - Plots of minimum principal strain at 9 mm under the implant, in 4 progressively more detailed models under knee loads at 15% stair descent: (1) all medial condylar load applied at a single node; (2) at 5 nodes; (3) a PE bearing with nodes fixed at the bearing-implant interface; (4) a PE bearing with contact modelled at bearing-implant interface.**

The curved femoral implant is much stiffer than the flat tibial tray (higher second moment of area and less bending); therefore, as presented in Figure 33 a single nodal force applied to the femoral implant produced representative stress distribution and the bearing was not required.

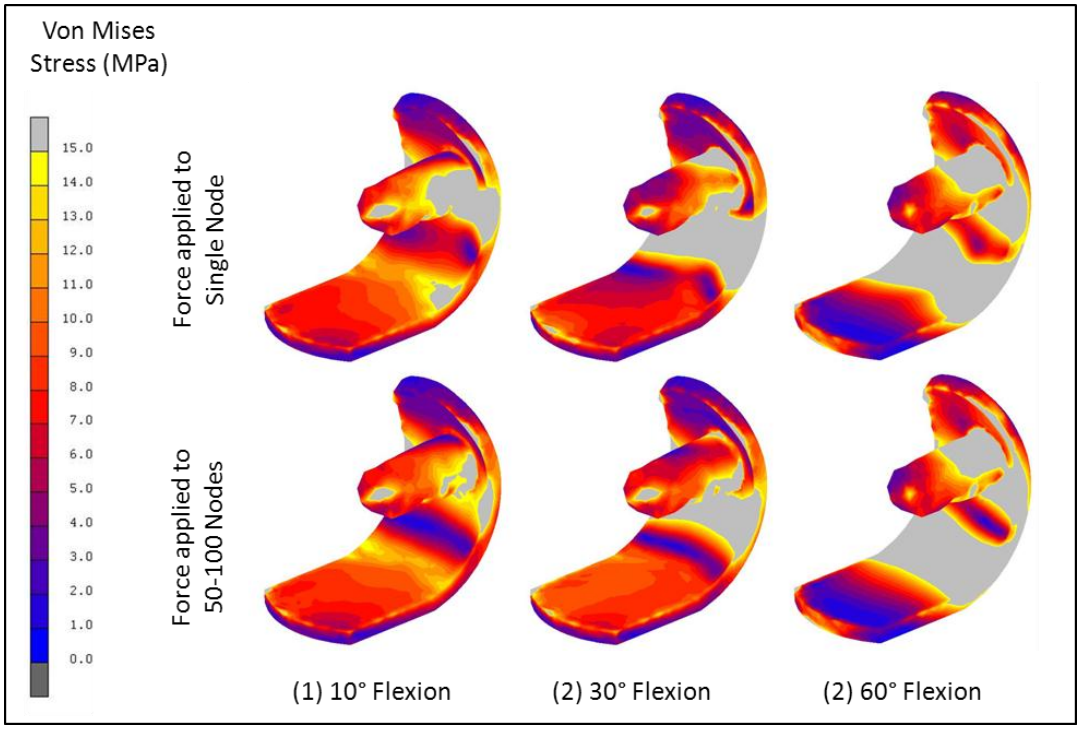


**Figure 33 - Plots of Von Mises stress in the femoral cement mantle. The plots show that applying a single nodal force to the femoral implant is acceptable.**

## 4.3 Geometry Generation

The surface topology of the tibia and femur is complex and varies considerably between subjects. It is important that subject-variation is considered and modelled accurately. This section describes the methods employed to generate accurate geometry for FE analysis of UKR fixation.

There are distinct geometrical features of a normal tibia. The medial plateau is concave and the lateral tibial plateau is convex, each of radius of approximately 70 mm (Goodfellow, 2006). The tibial plateau slopes posteriorly at approximately 6-7 degrees in females and 4-5 degrees in males (3 degrees of standard deviation) and the lateral condylar slope is 1-2 degrees steeper than the medial (Hashemi et al., 2008). The coronal tibia slope is approximately 3 degrees to the anatomical axis. The attachment of the ACL is usually identifiable with a tubercle just lateral to the anterior portion of the medial condyle. The tibial tubercle attachment for the patellar tendon is located anteriorly just medial to the centre of the tibial shaft (Cobb et al., 2008).

The medial and lateral condyles of the distal femur can be represented in the sagittal plane by three circular surfaces: (1) the anterior femoral condyles (articulating with the patella from 10-100 degrees), (2) the posterior femoral condyles (articulating with the tibia from 10-150 degrees), and (3) the distal condyles (articulating with the tibia from 0-10 degrees) (Elias et

al., 1990). The lateral condyle is less prominent than the medial condyle and they are separated at the distal end by the intercondylar notch. At the anterior, the patellar groove extends from the intercondylar notch and runs between the condyles.

### *4.3.1 Computed Tomography Scans*

All patient and cadaveric knees included in this thesis were CT scanned using a “Definition AS+” Computed Tomography (CT) scanner (Siemens Healthcare, Germany). The coronal voxel sizes were in the range 0.5-0.7 mm and slice thickness’ were 0.5-1.0 mm. Assurances were provided by the radiographers that all the quality assurance protocols of the scanner were up to date as specified in the operator manual. The scans were phantom-calibrated against air and water within 12 hours of performing the scans. The grey scale values calibrated as Hounsfield Units (HU) such that water corresponds to ± 4 HU and air to -1000 .

### *4.3.2 Segmentation*

Segmentation is the process of partitioning complex digital images into simplified representations of entities. In the context of this thesis, it is the partitioning of CT scans of the knee into tibia and femur bone geometries. CT scans are compiled of multiple stacks (or slices) of data, each stack consisting of a grid of voxels and each voxel assigned a grey-scale value. The grid is usually square with 512 by 512 divisions (262144 voxels) and a human knee typically requires 300-600 slices.

AVIZO 6.1 software (Visualization Sciences Group, USA) allows individual voxels to be selected and labelled as an entity. The femoral and tibial cortical and cancellous bones were manually partitioned into separate entities, slice-by-slice, using thresholding tools and judgement gained from cadaver dissections (refer to Sub-section 5.2). Triangular surface meshes were then automatically generated and smoothened using multiple-point averaging. Triangular surface meshes were chosen because they were shown to represent smooth surfaces better than quadrilateral surface meshes in the femur (Ulrich et al., 1999). Approximately 3-6 smoothing operations were made for each segmented entity. By continually comparing against the CT data, accurate surface geometry was preserved. Surface triangular meshes were exported to MARC Mentat 2010 where the cortical and cancellous bone segments were merged together.

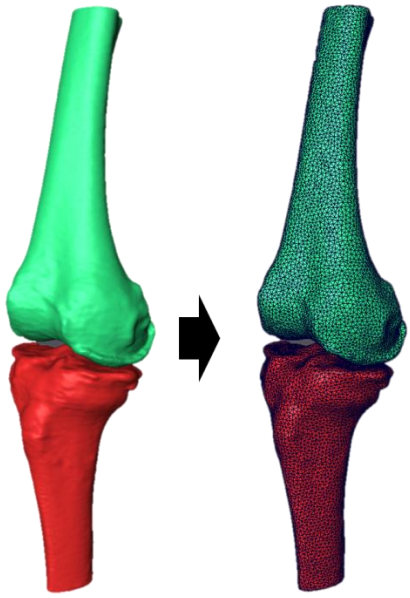

**Figure 34 - Segmentation from CT Scans and surface smoothed into a triangular surface mesh.**

The ‘manual thresholding’ segmentation technique employed herein is the traditional method adopted in the literature. Although automated segmentation algorithms can save considerable process time, generally they have not been adopted due to concerns of (1) accuracy; (2) high complexity of output surface; (3) algorithm errors (Viceconti et al., 1999). Viceconti et al. (1999) showed that the algorithms generated mesh geometries of the femur to within 0.9-1.6 mm accuracy; however, there were minor errors in the computation and the output meshes were incompatible for FE modelling unless smoothing and mesh simplification algorithms were used. A recent study by Varghese et al. (2011) validated 36 bones generated from an automatic segmentation algorithm (‘active contouring’ method’), claiming that the geometry was accurate to approximately a third of a voxel. Although the benefits of an automated segmentation algorithm are evident, the accuracy achieved using “manual thresholding” is adequate, it allows intelligent decisions around low density regions and it is highly credible in the field. Therefore, the FE models in this thesis were developed using the “manual thresholding” method.

### *4.3.3 Geometry and Axes*

The geometries and relationships between the tibia, femur and patella (including directions of ligament and muscle forces) are complex. Including these complex relationships in computer models is computationally expensive and time intensive; therefore, simplifications were made to the knee models. The tibia and femur were modelled separately, and instances of daily activities were simulated in quasi-static implicit FE models. To implement these simplifications and enable accurate allocation of boundary conditions, a robust set of tibial and femoral axes were defined.

The literature contains three main axis systems for the femur: 1) Epicondylar Axis (defined by two prominent points on the medial and lateral epicondyles); 2) Posterior Condylar Axis (based on a line touching the most posterior points of the femoral condyles); and 3) perpendicular to the Anteroposterior Axis. Since the posterior condylar axis is considered most reliable (Nagamine et al., 1998), it was used in this thesis.

A consistent and reliable tibial axis is more difficult to attain because there is no universally accepted tibial frame of reference. Three axes used in the literature include: (1) Anatomical Tibial axis (a line from the mid-point between the tibial spines, passing 1 mm medial to the medial border of the tubercle); (2) Posterior Condylar axis (a transverse line touching the most posterior points of the tibial plateau, with coronal plane defined to be perpendicular passing through the medial third of the tibial tubercle); and, (3) Sagittal Tubercle axis (a line passing through the middle of the posterior cruciate ligament and perpendicular to the projected femoral trans-epicondylar axis). Based on analysis of 19 knees, the Anatomical Tibial axis was shown to be the most reliable (Cobb et al., 2008) and this axis has been demonstrated to be the most applicable for modelling UKR (Fitzpatrick et al., 2007). Therefore, the Anatomical Tibial axis was used in this thesis.

### *4.3.4 Implant Geometry*

Implants of all sizes of the cemented and cementless versions of the Oxford UKR were obtained from Biomet Ltd (Swindon, UK) and the Uniglide UKR were obtained from Corin Group Plc (Cirencester, UK). The implant geometries were reverse engineered from templates made from the samples. To ensure compatibility with FEA capabilities, chamfers and rounded edges were excluded. Nurbs surfaces were used to regenerate implant geometries in MARC Mentat and the surfaces simplified to triangular meshes of size 1-1.4 mm. Figure 35 shows reverse engineered geometry of the Biomet Oxford and Corin Uniglide implants.

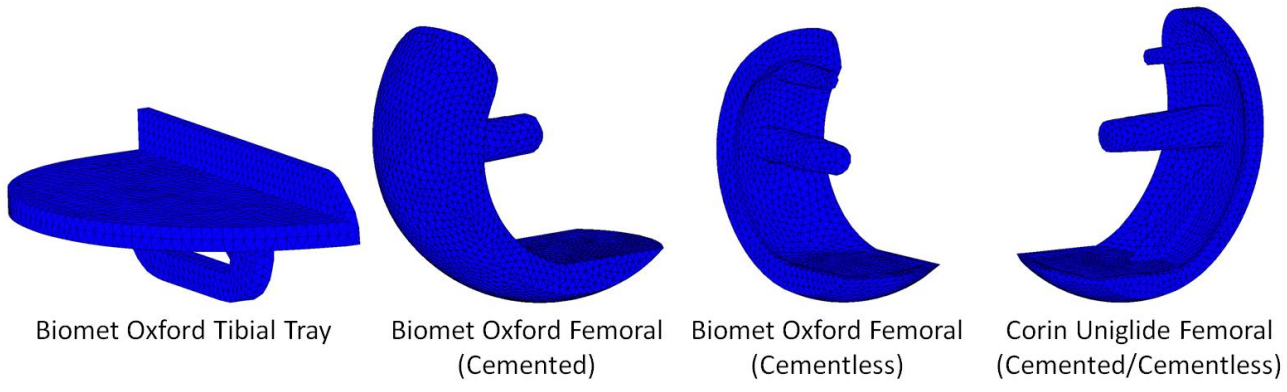


**Figure 35 - Biomet Oxford and Corin Uniglide implants reverse engineered and regenerated as triangular surface meshes.**

The Oxford tibial tray is 3 mm thick; the keel is 9 mm deep, 2.5 mm thick and contains a hole 3 mm wide; the side plate is 5 mm high and 1 mm thick. The UKRs come in 6 sizes (ranging from A-F) and vary in AP and ML dimensions only, as tabulated in Table 8.

**Table 8 - Biomet Oxford tibial tray UKR sizes.**

| Size | AP length (mm) | ML length (mm) |
|---|---|---|
| A | 45 | 26 |
| B | 48 | 26 |
| C | 51 | 28 |
| D | 55 | 30 |
| E | 58 | 32 |
| F | 60 | 33 |

The Oxford femoral component is 2-3 mm thick and has a single radius spanning from hyper-extension to deep flexion. The implant comes in 4 sizes Small, Medium, Large and Extra Large and the radii are 22.0, 23.5, 25.0, 26.5 mm, respectively. It is 20 mm wide with the same radius forming a spherical surface. The cemented implant has a single cylindrical fixation peg of 7 mm diameter that extends to the centre. The cementless implant has an additional cylindrical keel 3.5 mm diameter located at the anterior of the implant that extends approximately 13 mm. The anterior of the cementless implant protrudes round further than the cemented version to accommodate the additional keel.

The Corin Uniglide is based on similar principles as the Oxford UKR with minor variations to the geometry. The transverse profile of the Uniglide tibial tray is symmetrical and only 2 mm thick compared to the asymmetrical 3 mm thick Oxford implant. The seven standard sizes range from Gr2 to Gr8. The underside of the cementless implant is coated in Hydroxyapatite (HA) all over providing a flat recess-free surface. The keel has two 3 mm diameter round holes at the anterior and posterior aspects, compared to the single milled hole of the Oxford implant. The keel is also 2.5 mm thick but it extends further by 1 mm.

The Uniglide femoral component has a triple radius bearing surface that is claimed to conform to the femur more closely. It comes in 3 standard sizes Gr2, Gr3 and Gr4 with radii tabulated in Table 9. The frontal plane radius is the same as the sagittal plane radius corresponding to full knee extension (R2). The cemented and cementless implants both have two cylindrical stems similar to the Oxford cementless implant. A ridge connects the main stem to the posterior end which provides additional rotational support. Although the whole of the implant underside is HA coated, it also contains a rim similar to the Oxford implant.

**Table 9 - Corin Uniglide femoral component UKR sizes.**

| Size | R1 (mm) | R2 (mm) | R3 (mm) |
|---|---|---|---|
| Gr2 | 20.0 | 24.0 | 26.0 |
| Gr3 | 22.5 | 28.0 | 30.5 |
| Gr4 | 25.0 | 32.0 | 35.0 |

Care was taken to accurately model the under-surface of all cementless implants (Oxford and Uniglide tibial and femoral components). The HA coating covered the entire surface apart from a 3 mm thick rim. This rim sits up to 0.2 mm proud of the HA coating. The ledge was modelled by translating the nodes inside of the rim inwards away from the resected bone surface, such that only the rim was contacting the bone. To ensure accurate results, the mesh density was made finer at the contact interfaces (1-1.4mm), as recommended in the literature (Perillo-Marcone et al., 2003).

### *4.3.5 Virtual Implantation Tool*

Arthroplasty of the UKR tibia involves a resection formed with two bone cuts: (1) 7 mm under the medial tibial plateau, sloping 7-degrees posteriorly to the transverse plane; and (2) just medial to the anterior cruciate ligament, in the sagittal plane.

The surgeon uses a tibial saw guide which is clamped to the distal tibia to align the transverse cut. The surgeon then uses the same guide for the sagittal cut by aligning the saw direction with the femoral head. These virtual resections of computer models are difficult to perform accurately without whole-bone and soft tissue landmarks. The UKR patient CT scans used in this thesis include the hip, knee and ankles; however mid-shafts were excluded to minimise radiation dose to the patient. The knee cadavers were resected at the tibia and femur mid shafts before they were delivered to our laboratory.

The tibial axis, defined in Sub-section 4.3.3, was used to align the resections. The mechanical axis of the tibia was defined as a line joining the centre of the distal-shaft and mid-shaft/tibial plateau of the tibia. The centres of the medial and lateral condyles were found using the method of least squares to fit a circle the surface nodes. The cross product of the line adjoining the condylar centres and the mechanical axis was defined as the frontal plane normal. The sagittal plane normal was calculated by the cross product of the frontal plane normal and the mechanical axis. The plane of the medial tibial plateau was defined by selecting three nodes on the anterior, posterior and medial aspects. Marc Mentat was configured to automatically translate selected nodes to the resection surfaces.

A Microsoft Excel based tool was developed to automate this procedure. The tool calculated the tibial axis as defined above and based on user defined parameters it generated MARC Mentat procedure scripts to align the implant accurately.

Once the resection was completed, the models were moved to a common axis in order to be compatible with the full set of knee forces (tibiofemoral contact, ligament and muscle), described in Sub-section 3.3. However, the model needed to be able to move back to its original axis easily so that it was compatible with the material allocation program (to relate to

the CT scans). The virtual implantation tool generated procedure scripts to conduct these operations efficiently. The tibia models were aligned such that the transverse resection surface normal was the z axis.

The tool was also adapted for femoral implantations. The bone anatomical axis was calculated similarly from the centres of the base and mid-shaft. The epicondylar axis was calculated from the sagittal centres of the condyles. The frontal plane normal was defined as the cross product of the epicondylar and anatomical axis. The mechanical axis was defined as 7 degrees from the anatomical axis rotated about the frontal plane normal. The z axis was defined as the mechanical axis.

## 4.4 Implant & Cement Mantle

The Biomet Oxford tibial and femoral UKR components are made from cobalt chrome with the bearing-implant surfaces coated in titanium nitride, ceramic, Oxinium™ or titanium niobium. The Corin Uniglide UKR is also made of cobalt chrome but only comes coated in titanium nitride. The undersides of the cemented implants are uncoated while the cementless versions are coated in HA. The mobile-bearings are made of compression moulded polyethylene (PE).

The bone is cut to accommodate the keel of the tibial tray using a reciprocating saw. While Biomet also make available a special keel resection which provides greater accuracy, its use is not widespread due to additional expense to the surgeon. The transverse cut is made using an oscillating saw while the sagittal cut is made using a reciprocating blade. The resected corner forms a square edge and is sometimes over-cut (Clarius et al., 2009a). The transverse cuts are assumed to be flat – although our in-vitro experiments revealed that this was not always the case (refer to Section 5). The cementless implants are placed on the bone and hammered in place to ensure full contact. For the cemented implants, bone cement is placed under the keel and tray and the implant is hammered into place. The cement is consequently extruded into the trabecular pores while the cement extruded from the sides is removed. The cement-mantle consists of cement inter-digitised within trabecular bone. Implant companies tend to recommend 3-4 mm of cement penetration. However, based on visual assessment of Oxford UKR of cadaveric specimens (refer to Section 5), the cement-mantle was approximately 2 mm thick. This is also supported by cementation studies that have reported UKR cement mantles that were thinner than recommended (Clarius et al., 2010).

Studies have shown that mechanical properties are influenced by cement mixing techniques (Lewis et al., 1997). Elastic moduli range from 1.8-2.9 GPa (Lewis, 1997). Bone cement fails

in compression at approximately 25 MPa (Saha and Pal, 1984). The inter-digitised nature of the cement-mantle is such that it contains micro stress raisers and begins to fail under lower loads (Harrigan and Harris, 1991).

Failure of the cement-bone interface is dependent on the degree of inter-digitisation and the strength reduces with time (Waanders et al., 2010). Analysis of post-mortem retrieved THR implants showed tensile strengths of up to 2 MPa and shear strengths of up to 5 MPa (Waanders et al., 2010).

Fractographic assessments of retrieved THR femoral and acetabular explants have shown fatigue failure and fatigue crack propagation as factors that contributed aseptic loosening (Zant et al., 2007). Inspection of 3 composite bone femoral TKRs cyclic loaded on knee simulators to 1 million cycles showed hidden cracks of up to 10 mm (Cristofolini et al., 2008). Jasty et al. (1991) observed fatigue striations in retrieved THR implants, which were otherwise satisfactory, suggesting that fatigue may be an undiagnosed initiator of loosening. Mann et al. (2001) demonstrated that this inter-digitised region was the most common location of failure in femoral THRs. Negligible work has been conducted on the cement mantles of UKRs.

Damage accumulation in the cement-mantle is linear in low stress levels (Murphy and Prendergast, 2002); therefore Minor's rule is applicable. It becomes highly non-linear with increasing stress. Studies of S-N curves for bone cement reported in the literature (Davies et al., 1987, Burke et al., 1984, Murphy and Prendergast, 2002) were generated from tensile-compression load cycles of THRs. Fatigue damage should be considered when stresses exceed 10 MPa or 2000 με.

After bone cement has been applied to the bone-implant interface, it cures and exudes high exothermic temperatures that reach 40-110 degrees (Berman et al., 1984), depending on the cement-mantle thickness. Experiments conducted on rabbits show that temperature above 70 degrees can cause bone thermal necrosis. Reaming and cutting of the bone also generates heat at the bone interface, rising to temperatures of 36-52 degrees (Giannoudis et al., 2002) and higher (Frolke and Reeling Brouwer, 2004). The effects these processes have on bone properties are unknown and tend to be neglected in the FE models.

Another implication of bone cement curing is shrinkage. This can generate residual tensile stresses in the cement and can influence fatigue (Lennon and Prendergast, 2002). Although, residual stress in bone cement will relax over time due to its viscoelastic properties, the immediate effect may be significant. The preloaded structure may initiate crack formation and lead to a damage accumulation failure scenario, as described by Huiskes and Stolk (2005).

The initial stability of the implant-cement and cement-bone interfaces is good. From a FEA perspective, as demonstrated from the results of Section 5, it can be assumed that the cement nodes are fully bonded with the adjacent bone and implant. However, with time the interface will tend to degrade, with widening gaps at the interfaces. In a recent study, where retrieved femoral TKRs were physiologically loaded and micromotions were measured at the implant-cement and cement-bone interfaces (Mann et al., 2010) reported average micromotions of 131 μm, ranging from 0.6 to 830 μm. These values are much larger than would be expected at a bonded interface. Another retrieval study of successful TKRs (Miller et al., 2010) demonstrated that changes at the interface post-arthroplasty cause the interface to “soften” and lose rigidity. This may be due to reduction of interdigitisation at the boundary over time. The complex loading patterns of the THR involving compressive, tensile and torsional loads, combined with the effects of this complex interface, influence the mechanical response of the underlying bone. However, the loading of UKRs (particularly tibial trays) are mainly compressive and distinctly simpler than THRs. Therefore for UKRs, the effect of the complex interface is expected to have negligible effect on the mechanical response of bone. In all FE models that contained cement, the implant-cement and cement-bone interface nodes were fully bonded.

## 4.5 Mesh Convergence Study

Mesh convergence studies are used to find a satisfactory balance between the mesh size and computational expense: Typically, a finer mesh produces more accurate solutions but it takes longer to create them and solve them. However, the traditional method of modelling bone involves material allocation to individual elements which is also influenced by element size. A finer mesh does not necessarily produce more accurate solutions (limited by the CT voxel size). The overall mesh convergence problem is therefore complicated and has been split into two parts: (A) effect of element geometry; and (B) effect of material allocation.

Hexahedral elements were ruled from the outset for modelling bone in this thesis. This is because the methods for generating solid meshes are manual and extremely time consuming; therefore, they were deemed unsatisfactory for this thesis. The automeshers that are available for tetrahedral elements are well established (this is the preferred method for modelling bone in the literature); they produce good quality meshes with controllable mesh sizes and follow the complex three-dimensional surface contours of bone more closely than hexahedral elements.

### *4.5.1 Method*

A 33-year right male tibia was CT scanned. The long axis of the bone was aligned with the scanner axis, the slice thickness was 0.7 mm and the transverse voxels were 0.7 by 0.7 mm. The CT scans were segmented slice-by-slice; the surface meshed and smoothed with a fine (1 mm element size) triangular mesh using AVIZO software. The geometry was then imported into MARC 2010 and 11 different meshes (element size ranging from 1.3 to 6mm) were generated. Each new model was created by remeshing the surface elements using the "Patran Surface Mesher", specifying the required element size, and then solid meshed using the "Patran Tet Mesher" with a coarsening factor of 1.0. Twenty FE models were created: eleven 4-node linear tetrahedral element models and nine 10-node quadratic tetrahedral element models. Table 10 presents details of all the models assessed. Note that converged solutions were not obtained for models (2) and (16); therefore, they were excluded from the analysis

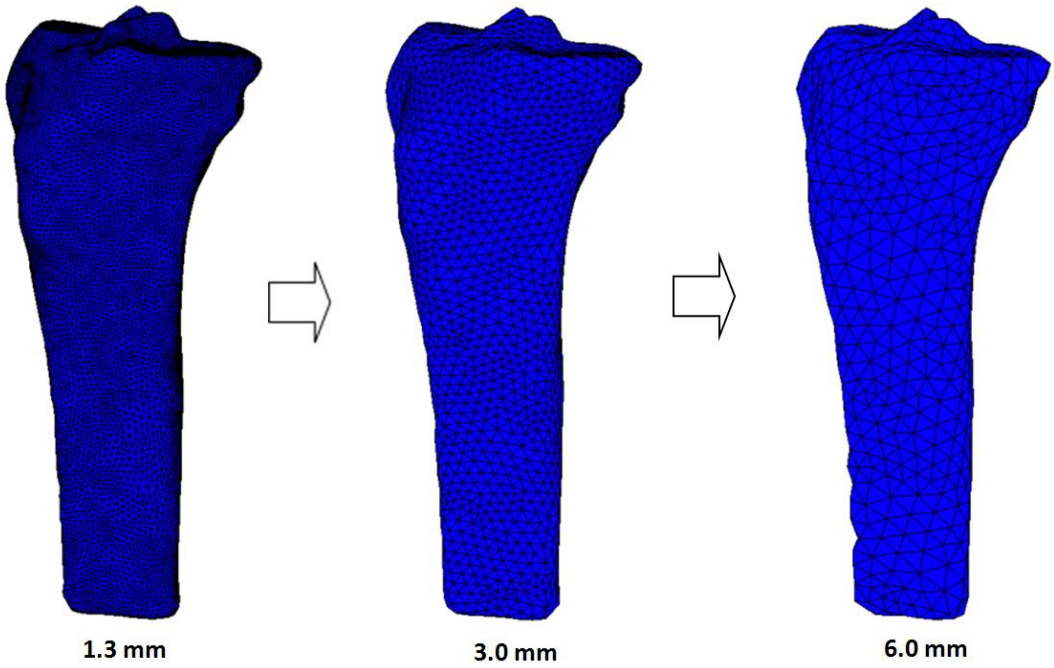


**Figure 36 - Range of mesh density of tibia models for mesh convergence study.**

The overall mesh convergence problem was split into two parts: (A) effect of element geometry (element size and type); and (B) effect of material allocation. To investigate (A) effect of element geometry (excluding the effect of material property allocation), all 20 models were assigned a uniform isotropic elastic modulus of 1 GPa and a Poisson's ratio of 0.3. To investigate (B) effect of material allocation, another 20 models were developed by assigning element-by-element isotropic elastic moduli derived from the CT data using an in-house program (material allocation program, Sub-Section 4.6.6). Poisson's ratio was

assumed to be 0.3 (Van Rietbergen et al., 1996) for all elements. Note that the results of part (B) models included effects of element geometry and material allocation combined; therefore, they were normalised based on the results of part (A), to determine material allocation effects alone.

Peak knee forces (medial and lateral joint contact, ACL and Patella tendon forces) during walking activity, as described in Sub-section 3, were applied to surface nodes. The surface nodes of all the 11 meshes were modified such that the loaded nodes (three for each force) were always in the same position. The transverse section of the base of the tibial shaft was globally restrained in space.

Three Regions of Interest (ROI), represented with 3 nodes each, were defined at the medial cortex, 10 mm below the tibial plateau, located at the (ROI-1) anterior, (ROI-2) medial, and (ROI-3) posterior extent. These were exactly the same positions in all 11 meshes.

All the models were solved using the MARC 2010 “multifrontal direct sparse” solver. The minimum principal strains, minimum principal stresses and vertical displacements at each ROI were output and analysed in Microsoft Excel.

**Table 10 - Details of FE models used in convergence study**

| Model Number | Element Type | Element Size | Number of Elements | Number of Nodes | Degrees of Freedom |
|---|---|---|---|---|---|
| 1[a] | Linear | 1.3 | 471315 | 84588 | 251226 |
| 2[b] | Linear | 1.5 | 352152 | 63158 | 187521 |
| 3 | Linear | 2 | 166537 | 30527 | 90330 |
| 4 | Linear | 2.5 | 106729 | 19773 | 58428 |
| 5 | Linear | 2.8 | 65299 | 12428 | 36663 |
| 6 | Linear | 3 | 53214 | 10226 | 30201 |
| 7 | Linear | 3.5 | 46884 | 8977 | 26517 |
| 8 | Linear | 4 | 30516 | 5992 | 17598 |
| 9 | Linear | 4.5 | 20695 | 4119 | 11979 |
| 10 | Linear | 5 | 16956 | 3412 | 9948 |
| 11 | Linear | 6 | 10989 | 2290 | 6636 |
| 12 | Quadratic | 2 | 166537 | 233324 | 698721 |
| 13 | Quadratic | 2.5 | 106729 | 150319 | 450066 |
| 14 | Quadratic | 2.8 | 65299 | 93250 | 279129 |
| 15 | Quadratic | 3 | 53214 | 76367 | 228624 |
| 16 | Quadratic | 3.5 | 46884 | 67148 | 201030 |
| 17 | Quadratic | 4 | 30516 | 44248 | 132366 |
| 18 | Quadratic | 4.5 | 20695 | 30219 | 90279 |
| 19 | Quadratic | 5 | 16956 | 24894 | 74394 |
| 20 | Quadratic | 6 | 10989 | 16418 | 49020 |

[a] unable to obtain a converged solution.

[b] unable to obtain solution for model with method (B) (element-by-element material allocation).

The converged solution was assumed to be the average of the two models which had the highest degrees-of-freedom (quadratic element models (12) and (13)). Error was defined as

the average of the percentage differences of the nodal solution values from the converged solution values:

$$\text{error}(\%) = \sum_{n=1}^{N} \left\{ \frac{x_n}{0.5(a_n + b_n)} - 1 \right\}$$

where, $x_n$ is the value at node n; $a_n$ is the value at node n of the model with the highest degrees-of-freedom; $b_n$ is the value at node n of the model with the second highest degrees of freedom; and N is the total number of nodes for each model. Note that N was 9 nodes for each of the 20 models.

### *4.5.2 Results – Effect of Element Geometry*

The displacements and minimum principal strain errors were calculated for all models and the convergence plots are displayed in Figure 37. Although axial displacement and minimum principal strain convergence is achieved with fewer degrees of freedom for the linear element models, the converged solution is less than that of the quadratic element converged solution. This implies that linear elements are 5-10% stiffer.

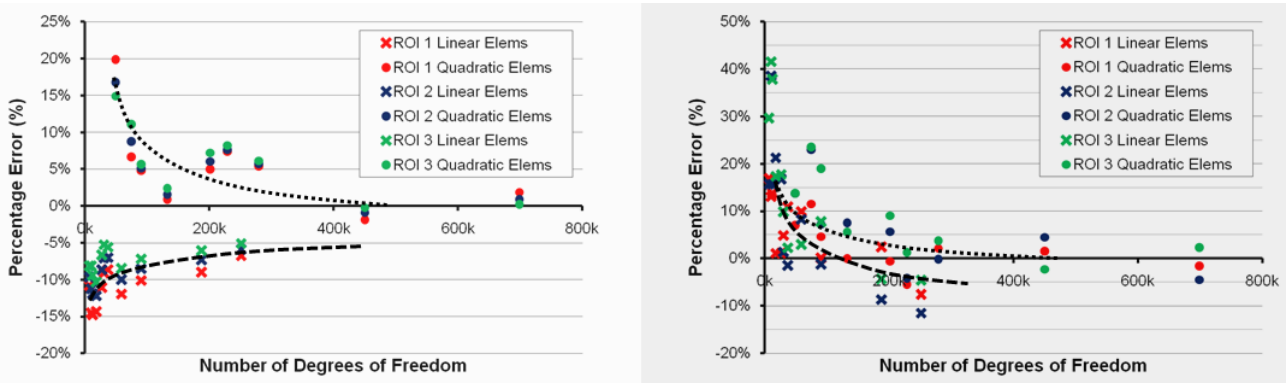


**Figure 37 - Element geometry convergence plots of (i) axial displacement error (left); and (ii) minimum principal strain error (right), comparing ROIs 1-3.**

Element sizes of 2.0 mm (for linear elements) and 3.5 mm (for quadratic elements) produced solutions that were within 10% of the converged value.

### *4.5.3 Results – Effect of Material Allocation*

The displacement and minimum principal strain error was calculated for all models based on method (B) and the convergence plots are displayed in Figure 38. Note that these models included effects of element geometry and material allocation

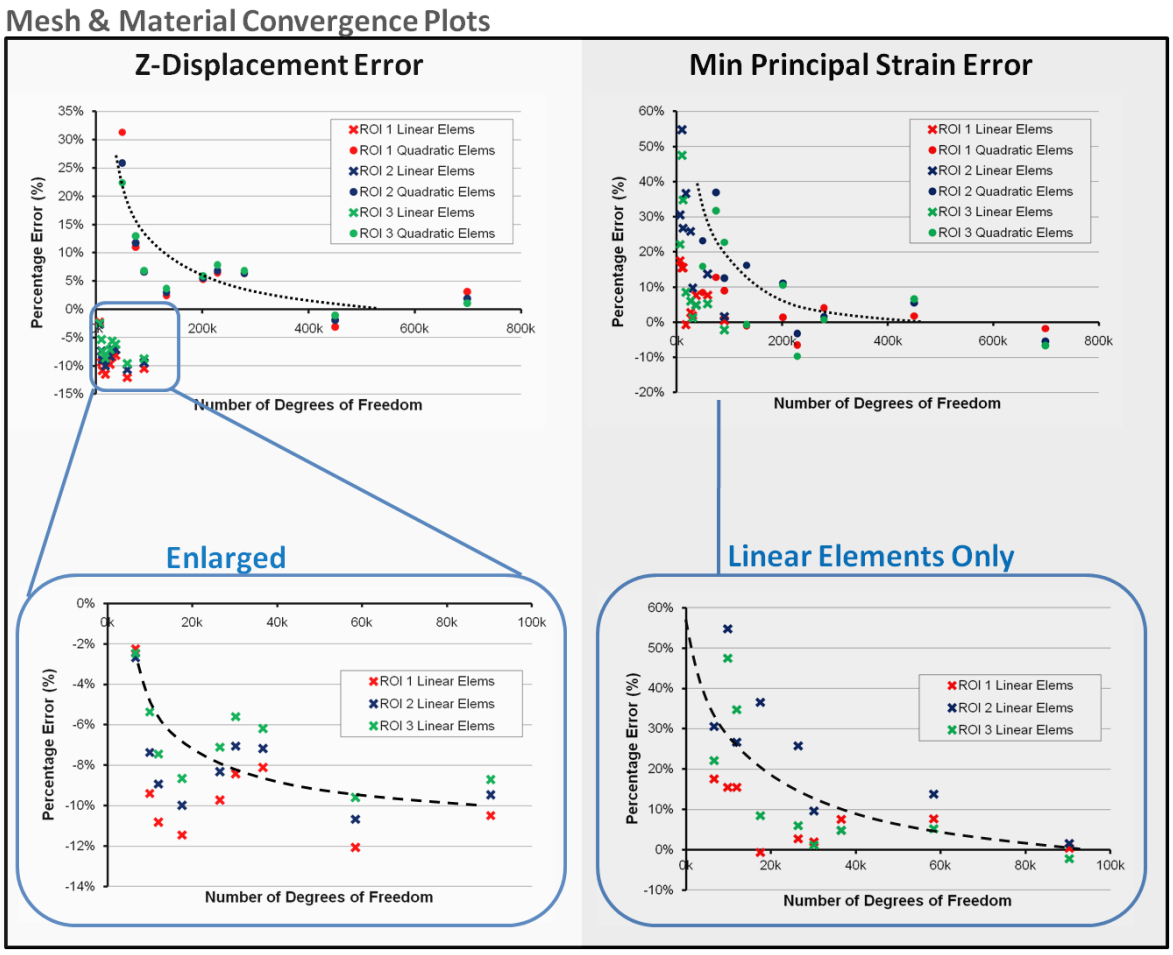


**Figure 38 - Material allocation and element geometry convergence plots of (i) axial displacement error (left); and (ii) minimum principal strain error (right), comparing ROIs 1-3. Error was defined as the average of the percentage differences of the nodal solution values from the converged solution values. The converged solution was assumed to be the average of the two models which had the highest degrees-of-freedom (quadratic element models (12) and (13)).**

Since a solution could not be obtained for model (1) (element size of 1.3 mm) and model (2) (element size of 1.5 mm), the maximum attainable degrees of freedom for a linear element model was 90k. A model with higher degrees of freedom was attainable if quadratic elements were used; and these models provided more stable convergence when the number of elements was more than 50k.

With element sizes of 2 mm, adequate convergence was achieved with linear elements.

Figure 39 displays the convergence of displacement errors that were normalised against errors generated from element geometry alone (from Sub-section 4.5.2) – i.e. the plots display effect of material allocation alone. Elements of size 2-4mm provide adequate accuracy to within 2% of the converged solution.

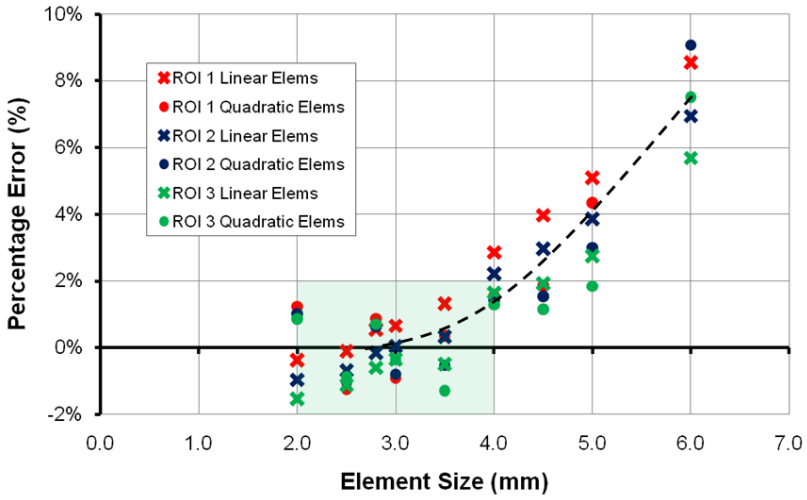


**Figure 39 - Plot showing convergence of displacement errors that were normalised against errors generated from element geometry alone (from Sub-section 4.5.2). The plots display the convergence of material allocation method with element size alone. Error was defined as the average of the percentage differences of the nodal solution values from the converged solution values. The converged solution was assumed to be the average of the two models which had the highest degrees-of-freedom (quadratic element models (12) and (13)).**

### *4.5.4 Discussion*

The concept of mesh convergence has traditionally been a topic of “little discussion” due to complexity and difficulty of achieving convergence in whole bone level FE models. In this study, in order to disaggregate the problem, it was broken down into two components: (A) element geometry; and (B) material allocation.

Although the convergence plots were more scattered than typical convergence plots seen for homogenous isotropic materials, convergence was achieved. The study by Polgar et al. (2001) also reported unconventional convergence plots when assessing principal stress in the femur. It is anticipated that this scatter arises from the material allocation procedure. CT scans exhibit ‘patchwork’ values, particularly as voxel sizes approach the size of trabeculae. For example an adjacent CT voxel may have an artificially low grey value because it may correspond to porosity within trabeculae. Although the average of a few voxels may yield accurate grey values, the single grey value corresponding to that artificially low voxel will not. With CT scan voxels of 0.7 mm elements of 2 mm or greater span more than 3 voxels. Element sizes that are less than 2 mm may yield results with decreasing accuracy. In this study, converged solutions were obtained with elements of 2 mm or greater.

Based on the element geometry convergence study (A), 2 mm linear elements and 3.5 mm quadratic elements produced converged solutions (within 10% accuracy). Based on the material allocation convergence study (B), elements sizes of 2-4mm produced adequate solutions (within 2% accuracy).

The results showed that linear and quadratic element models converged to different solutions. This may be due to the formulation of the linear tetrahedral element being 'stiffer' than the quadratic element – this effect has been reported elsewhere in the literature (Polgar et al., 2001).

Based on the conclusions of this study, the computer models in this thesis were developed with elements of 2-3 mm size (where possible), with preference for quadratic rather than linear elements. There were a few exceptions to the rule:

- For models where there was contact between two bodies (typically implant and bone for cementless implants), a finer element mesh size (typically 1.4 mm) was incorporated at the contact surfaces. Not only is modelling contact computationally expensive, but the micromotion analysis subroutines (described in Sub-section 4.6.7) are not optimised for quadratic elements. For these 'micromotion' models, equivalent quadratic element models were simultaneously developed (without the micromotion subroutines) to check that that errors were small and consistent with conclusions.
- For simulations of bone remodelling linear elements were used. This is due to computational limitations of the bone remodelling subroutine (Sub-section 4.6.8) being incompatible with quadratic elements. With linear elements the solution time was as much as 12 hours for some simulations. Using quadratic elements would have yielded even longer solution times; therefore, they were considered to be unsatisfactory for this purpose.

## 4.6 Optimising the Model

### *4.6.1 Modelling Cancellous Bone*

The convergence study, as described in Sub-section 4.5, revealed that 2-3 mm quadratic 10-node tetrahedral elements were best for modelling of tibial and femoral cancellous bone. The linear 4-node tetrahedral elements were adequate, with solutions within 10% of the converged value if they were 2 mm.

For cemented implant models, quadratic elements were used to model the cancellous bone. For cementless implant models, two sets of models were created: for the first set, quadratic elements were used for the cancellous bone; and for the second set, linear elements were used in order that micromotion subroutines could be effectively incorporated.

### *4.6.2 Modelling Cortex*

The surfaces of the proximal tibia and distal femur are covered by a thin layer of cortical bone. The cortical thickness is unreported in the literature and it is subject and site-specific. Based on laboratory experience (refer to Section 5) and experience of orthopaedic surgeons, the thickness is less than 0.5 mm and estimated to average 0.1 to 0.2 mm thick. The materials modelling method described in Section 2 is unable to represent this thin cortex. Firstly, the CT scans of minimum voxel size 0.5 mm are too large to detect the cortex; and secondly, the FE tetrahedral elements, of minimum achievable size of 1 mm, are too large to represent them accurately in the models.

Shell elements have been used in the literature to model the thin cortex in vertebrae (Imai et al., 2006) and pelvis (Anderson et al., 2005, Dalstra and Huiskes, 1995); however, the author is not aware of any studies that have modelled the cortex of the proximal tibia or distal femur in this way.

Sensitivity assessments were conducted to identify the implications of inclusion of the tibial cortex in FE models of tibial UKR. Figure 40 presents minimum principal strain plots of three slices through a proximal tibia. It demonstrates the local reduction of strain at the cortical boundary by including the shell elements. Modifying the cortical thickness and elastic modulus within the range of uncertainty had a very small effect on the local strains but it did slightly change the strains immediately under the implant.

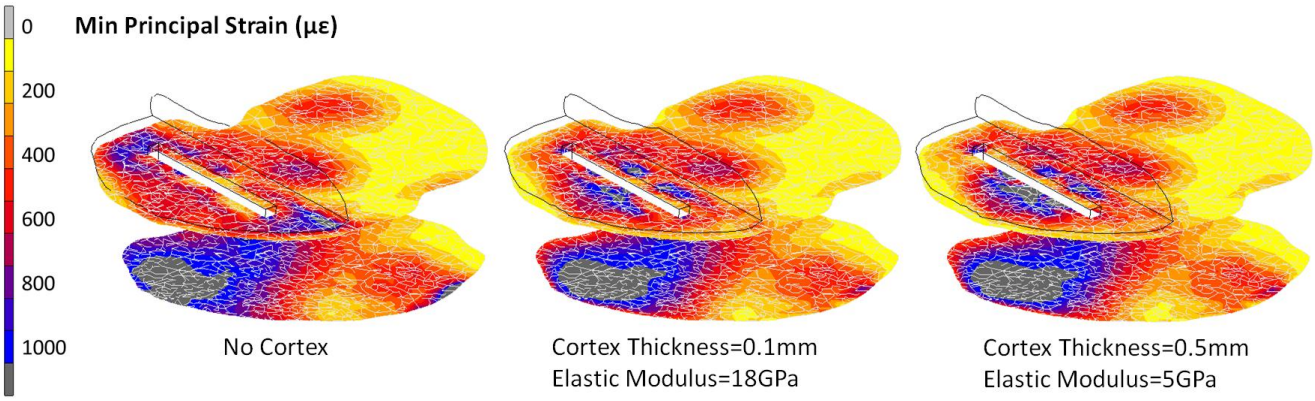


**Figure 40 - Sensitivity of bone strain by inclusion of proximal tibial cortex shell elements.**

Figure 41 presents the effect of adjusting cortical parameters on plots of the micromotion at the bone-implant interfaces. The inclusion of the cortex reduced the micromotions at the lateral edge and increased those towards the medial edge, but had negligible effect on the average magnitudes. Modifying the cortical thickness and elastic modulus within the range of uncertainty has a very small effect on micromotions, with the greatest change at the centre of the implant. A stiffer cortex reduced the micromotions at the implant centre.

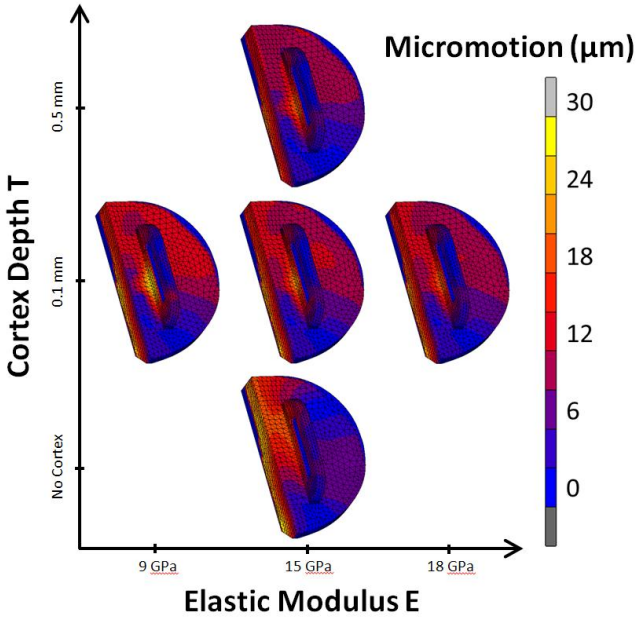


**Figure 41 - Sensitivity of implant-bone micromotions by inclusion of proximal tibial cortex shell elements.**

To assess the suitability of the elements, the inner, middle and outer layers of the shell elements were analysed to show that through-thickness strains were similar. This is indicative that the shells are deforming under compression not bending; hence, the error introduced from incompatibility of midside deformations should be minimal.

Based on these results, the inclusion of a cortex is important for local strains at the cortex and strains immediately under the implant. It has a negligible effect on the magnitudes of bone-implant micromotions but it does alter their distribution. In comparison, the uncertainty of the cortex parameters (thickness = 0.1-0.5 mm, elastic modulus = 9-18 GPa) have a minor effect on the strains and micromotions. Cortical shell elements were included in the UKR FE models and adapted depending on the model type: bilinear 3-node thin-triangular shell elements were used against linear cancellous bone elements; and quadratic 8-node one-side collapsed quadrilateral shell elements were used against quadratic cancellous bone elements.

### *4.6.3 Osseointegration*

The long-term success of cementless implants is dependent on achievement of initial stability (Hungerford and Kenna, 1983, Landon et al., 1986, Waugh, 1985). Stable fixation is a prerequisite for osseointegration to occur between the bone and implant; otherwise, a fibrous tissue layer forms at the boundary. The precise behaviour of the tissue formation at the interface is complex and has been linked to the level of interface motion (micromotion). Tangential micromotion is defined as the motion that is tangential to the surface normal (i.e.

measure of surface shear strain), while normal micromotion is defined as that which is normal to the surface.

The implant surface coating affects fixation. Carlsson et al. (1988) found that minor gaps of 0.35mm around stable smooth titanium implants in rabbits were not bridged by bone and the critical gap was close to zero. Porous-coated and hydroxyapatite coated implants improve fixation (Soballe et al., 1990). Since most modern implants are porous and hydroxyapatite coated, press-fit is no longer an important factor for consideration of osseointegration.

In the search for a threshold for bone ingrowth, a general micro-mechanics point of view yields the conclusion that micromotion must be less than the pore size of the porous coatings (approximately 150 μm for most porous coatings). In support of this theory, in-vivo canine bone-implant dental studies have demonstrated that bone ingrowth is less likely in smooth surfaces compared to porous surfaces (Maniatopoulos et al., 1986). However, the reality is further complicated by biological response such that a simple pore-size related threshold is inaccurate.

The biological response is similar to a healing fracture (Kuzyk and Schemitsch, 2011). Immediately post-arthroplasty, the implant-bone gap is filled with a blood clot. In the next few weeks, the gaps are filled with new trabecular bone with bone fragments (from surgical preparation) enveloped. Ossification of fully contacting bone and implant does not occur until later. In a stable implant, at 6-12 weeks all trabecular bone and most bone fragments are substituted by mature lamellar bone with few marrow spaces (Franchi et al., 2005). In animal studies osseointegration occurs by 6 weeks (Jasty et al., 1997a, Soballe et al., 1992, Prendergast et al., 1997); however, in humans this may be as long as 16 weeks (Cameron et al., 1973).

Based on an in-vivo canine study of femoral implants at 1-year, Pilliar et al. (1986) observed that tangential micromotions in bone-ingrown samples were less than 28 μm, while micromotions in samples with interface fibrous tissue were 50-310 μm. Another in-vivo canine study (Jasty et al., 1997a, Jasty et al., 1997b), in which daily in-vivo tangential micromotions of 0, 20, 40 and 150 μm were induced for six weeks on separate specimens, showed distinct histological differences at the bone-implant interfaces. Micromotions of 0 and 20 μm produced intimate contact between the bone and implant, without intervening layers of fibrous tissue. The implants subjected to 40 μm were surrounded by a mixture of trabecular bone, fibrocartilage, and fibrous tissue; in some areas the ingrown bone was in continuity with the surrounding bone, whereas in other areas it was separated by fibrocartilage or fibrous tissue. For implants subjected to 150 μm, the interface was made up of a 1-2 mm thick layer of dense fibrous tissue. Jasty et al. (1997b) found that up to 56 μm of

micromotion allowed full osseointegration at the bone-implant interface. A review of dental implants in animals (Szmukler-Moncler et al., 1998) concluded that a threshold for full osseointegration was in the range of 50 to 150 μm.

The quantitative analysis from animal studies provides a foundation to predict human response to implant micromotion, and these have been indirectly verified against human studies: A retrieval study of human THR femoral cementless implants found indications that micromotions less than 40 μm resulted in osseointegration, while 150 μm resulted in fibrous tissue (Engh et al., 1992b).

In implant fixation studies published in the literature, bone-ingrowth thresholds of 50-150 μm have been suggested (Chong et al., 2010, Abdul-Kadir et al., 2008, Gotze et al., 2002, Viceconti et al., 2000, Burke et al., 1991). The cementless implants analysed in this thesis are porous HA coated, similar to those in the literature. Interfaces with tangential micromotions less than 50 μm were defined as firmly-integrated; between 50 and 100 μm as semi-integrated; and 100 to 150 μm as poorly integrated.

### *4.6.4 Bone-implant Friction*

To successfully model the response of bone to cementless implants, the FE contact conditions must be clearly defined with appropriate friction coefficients and computational parameters.

The contact parameters developed by Abdul-Kadir et al. (2008) and Chong et al. (2010), during their PhD research at Imperial College London, were adapted to model implant-bone contact in UKRs and validated. The Coulomb friction model was used, which is implemented in MARC 2010 with a continuous differentiable “arctangent” function. The Coulomb friction parameters were adapted to mimic the non-linear response of bone-implant friction resistance to displacement (Shirazi-Adl et al., 1993) (‘RVCNST’ = 0.1 and ‘BIAS’ =0.95 (Abdul-Kadir et al., 2008). Nodes were defined as touching if their relative distance was less than 0.01 mm (assessments revealed relative insensitivity for tolerances less than 0.1 mm). To ensure that inaccuracies in geometry definition did not create pre-stressed contact, an additional parameter available with MARC 2010 was enabled. During the initialisation step, overlapping nodes are moved to stress-free contact positions.

The friction coefficient between tibial cancellous bone cubes and porous-surfaced metal plates were measured by Rancourt et al. (1990) and an average of 0.28 was found for smooth surfaces. For fibre mesh and beads, the average values were between 0.44 and 0.63. In published micromotion FE studies, friction coefficients used tended to be 0.0 to 0.42 for smooth surfaces and 0.20-1.73 for rough surfaces. Kuiper and Huiskes (1996) used zero

for smooth surfaces, 0.15 for lubricated surfaces and 0.4 for coated surfaces. Keaveny and Bartel (1993) used zero for smooth surfaces and 1.73 for coated surfaces. Two other studies (Ando et al., 1999, Biegler et al., 1995) used 0.42 for smooth surfaces and 0.61 for coated surfaces. Viceconti et al. (2001) used a much lower friction coefficient of 0.20 for a coated implant.

The Oxford UKR is coated with HA and a friction coefficient of 0.4 is assumed most relevant. Five FE models of the implanted UKR tibia were developed with the implant-bone friction coefficients ranging from 0.0 to 0.8. The results showed that micromotion predictions were insensitive to friction coefficient with variations of up to 5%.

THRs have been demonstrated to be sensitive to friction coefficient (Abdul-Kadir et al., 2008); however, the mechanism responsible for inducing micromotion in tibial UKRs is very different: In UKRs, the primary load is perpendicular to the bone-implant interface, particularly in mobile-bearing UKRs, if the bearing-tray friction force is assumed to be low. In THRs, the primary load is parallel to the bone-implant interface; therefore, friction force is the primary mechanism resisting the load.

### *4.6.5 Press-fit*

UKR patients tend to have a narrow gap between the side-plate of the tibial tray and bone. A sensitivity assessment with and without side-plate bone contact revealed that micromotions were slightly reduced when side-plate contact was omitted. At first this seemed counter-intuitive; however, at closer inspection, the removal of the side-plate constraint allowed a more stable bed of bone as the implant was no longer influenced by bone deformation at the side-plate. Since the existence of a narrow gap (or highly elastic fibrous tissue) is also evident in radiographs of UKR patients (radiolucencies), it was deemed most appropriate to exclude contact between the side-plate and bone in the FE models.

As described in Sub-section 5.5.4, the keel resection can be accidentally over-cut, thereby removing the 3 mm width of base support. A sensitivity assessment with and without the bottom of the keel contacting the bone revealed that the effect on micromotions was negligible.

The keel of the tibial tray tends to be press-fitted with the surgeon hammering the implant into place. Pandit et al. (2009) reported that the keel incisions of Oxford cementless UKRs were intentionally made smaller than the actual size of the keel.

Interference fit is a significant factor on initial stability in THRs (Abdul-Kadir et al., 2008); however, the effect on the UKR tibial tray is unreported. Due to the viscoelastic nature of bone, residual stresses are expected to relax by 50% (Shultz et al., 2006), and remodel

depending on the level of bone strain. Five FE models with keel interference fits of 0 to 50 µm were developed and analysed. Figure 42 shows that micromotions reduce with press-fits up to 10 µm and increase thereafter. Bone strains approach and exceed its yield limit for press-fits greater than 50 µm.

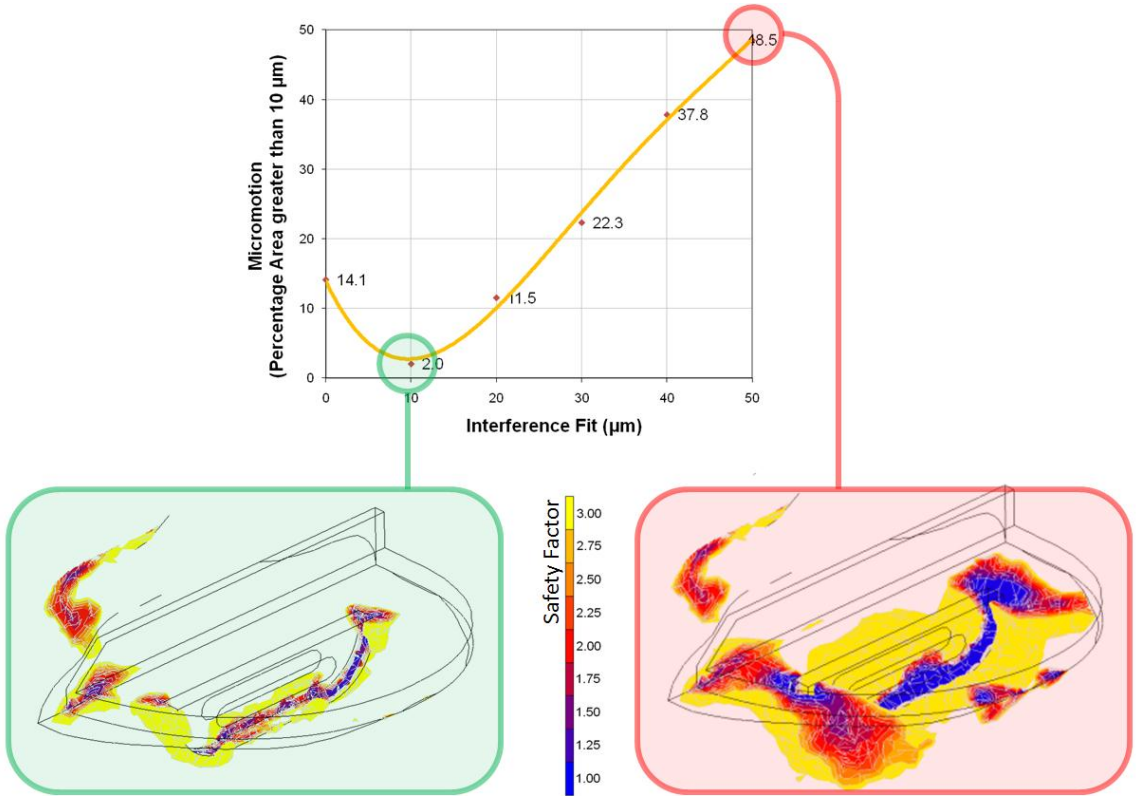


**Figure 42 - Effect of keel press-fit on UKR tibial tray micromotion and bone strain.**

With press-fits of greater than 10 µm the implant-bone interface micromotions increased. This is because the press-fit is causing the surface of the resected bone (that comes in contact with the surface of the implant) to warp, with the region surrounding the keel slot to rise superiorly (Figure 43). This distortion of the bone interface enables the implant to be able to rock and slide more easily against the bone surface under compressive load. This increases the interface micromotions. Bone-implant interface warping is an important factor in UKR micromotion. It should be noted that the models assume linear-elastic behaviour and do not simulate the viscoelastic behaviour of bone. Viscoelasticity could render this residual strain around the keel to become negligible within a period of a few days.

The benefits of having a small press-fit are outweighed by the detrimental repercussions of over doing the press-fit that could lead to fracture initiation, patient pain and implant migration. Modelling UKR press-fit is complex, it has a small effect on micromotions, and the press-fit predictions are uncertain and unable to be substantiated. That said, the effect on bone strain is large and should be kept in mind in the analysis of intra-operative scenarios and peri-prosthetic fractures that occasionally occur in patients (Vardi and Strover, 2004).

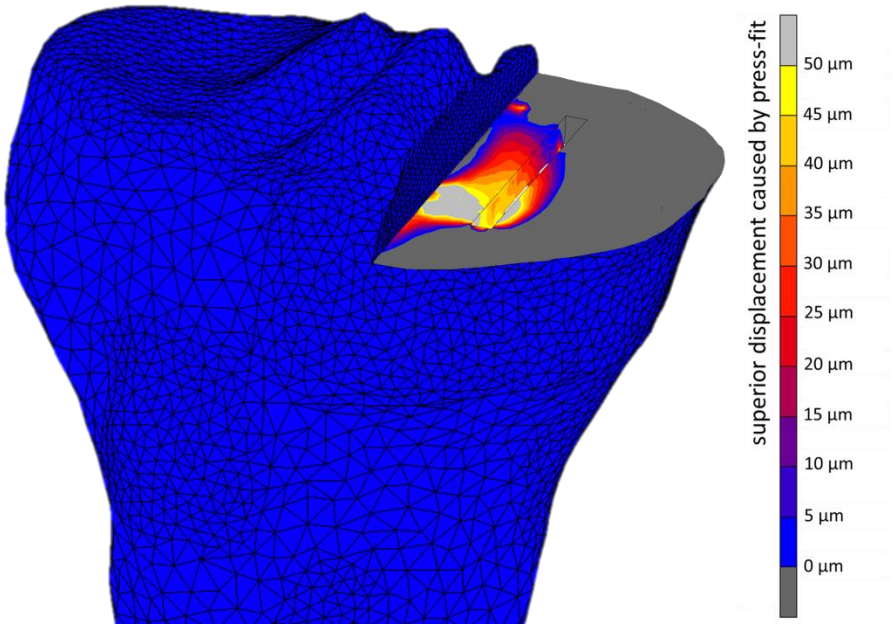


**Figure 43 - Plot of superior displacement on the surface of the resected tibia (the interface in contact with the implant) caused by a press-fit interference of 50 µm at the keel. There are no knee forces acting on the tibia. The top surface has warped superiorly due to the lateral expansion at the keel slot.**

### *4.6.6 Materials Allocation Program*

A bone material allocation program was developed by Dr Hopkins as part of post-doctoral research (2007) at Imperial College London. For the purposes of this thesis, the program was adapted to generate elastic moduli from alternative material property relationships (refer to Sub-section 2.6). The program defines 9 sampling points at the interior inner two-thirds of each tetrahedral element and determines corresponding grey scale values at each location from corresponding AVIZO format CT data. The program calculates the average for each element, from which it calculates apparent bone densities and elastic moduli, based on the material property relationships described in Sub-sections 2.3 and 2.4.

### *4.6.7 Micromotion Subroutine*

To compute micromotions at the bone-implant interface, a subroutine initially written by Abdul-Kadir et al. (2008) was further developed to output micromotion at the bone-implant interface. The algorithm tracks two initially coincident nodes and calculates the relative displacement as the model deforms under prescribed loads. For the purposes of this thesis, the subroutine was developed to calculate the surface normal at the nodes and resolve the relative displacements into tangential and normal components. The output solutions were then able to be post-processed both visually and numerically in MARC Mentat.

### *4.6.8 Remodelling Subroutine*

The biological process of bone remodelling plays an important role in understanding long-term implant fixation. A bone remodelling algorithm called 'REM3D', based on the theory of Huiskes et al. (1987) as described in Sub-section 8.1, was developed by Chong (2009), during his PhD research at Imperial College London. The model was developed for MARC 2005 based on the apparent bone density to elastic modulus material property relationship proposed by Carter and Hayes (1977)(refer to Sub-section 2.4). In order to comply with the conclusions of Sub-section 2.6, the subroutine was developed to include capability to model the three-part elastic-modulus relationships outlined in Table 5 (Section 2).

The model was updated to be compatible with MARC 2010 and verified by comparing an old model solved on both systems. The code was also updated in order to be able to handle models with up to 300,000 elements (previously confined to 100,000).

### *4.6.9 Bone Failure Subroutine*

To assess implant fixation effectively, it was deemed important to consider the failure limit of bone. Based on the strain failure criterion described in Sub-section 2.5, a MARC subroutine was developed to visually and numerically post-process bone safety-factor. The subroutine calculates the maximum and minimum principal strains from the six isotropic strain components and computes the minimum safety factor by dividing with the corresponding strain failure limits, as described in Sub-section 2.5 and defined below:

For Tibia, $Y_{Tensile} = 6500\mu\varepsilon$, $Y_{Compression} = 7300\mu\varepsilon$

For Femur, $Y_{Tensile} = 6100\mu\varepsilon$ $Y_{Compression} = 8500\mu\varepsilon$

The principal strains are determined by calculating the eigen values of the strain matrix using Cardano's analytical algorithm. Cardano's analytical algorithm and the corresponding Fortran code were validated by comparing against the maximum and minimum engineering strain outputs from MARC 2008.

### *4.6.10 Simulated DXA Program*

To compare patient Dual X-Ray Absorptiometry (DXA) scans with those predicted from FE models, a Fortran program called "SimDXA" was developed. The program simulates two-dimensional DXA scan images from three dimensional FE model output files. The program outputs both MARC Mentat files and text-files (in matrix form) that can be post-processed with alternative software. The SimDXA output files were used to calculate the change of

bone mass in user-defined regions. Figure 44 presents the program method in the form of a flow diagram.

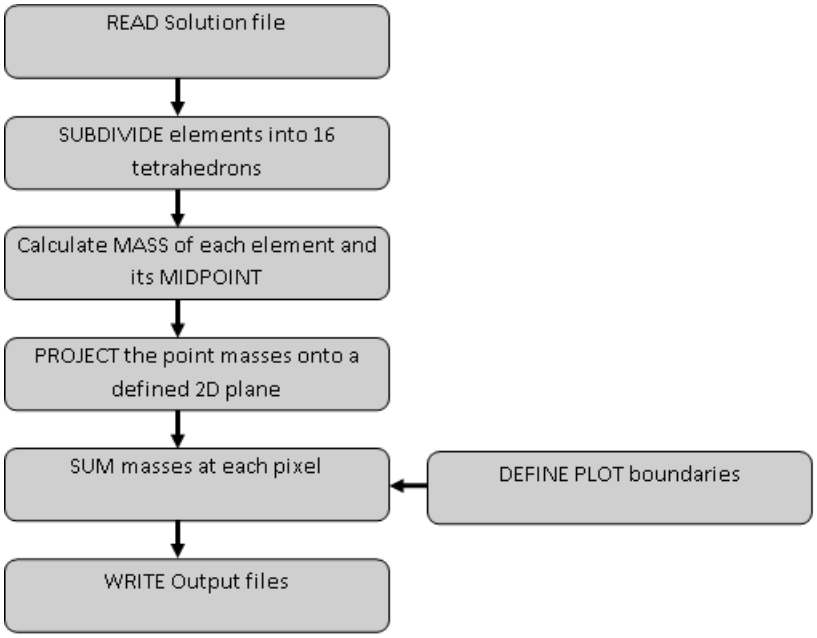


**Figure 44 - Flow diagram of SimDXA program method.**

SimDEXA was validated using a dummy model which contained known regional apparent densities.

## 4.7 Conclusion

The FE modelling approach used in this thesis to model fixation of UKR implants has been presented and discussed in detail in this section. The traditional techniques used for modelling bone in the literature have been reviewed, and adapted where necessary. The uncertainties of the modelling parameters have been discussed, reviewed and the risks reduced as low as reasonably practicable. A robust foundation of modelling techniques and tools has been developed by reviewing literature, conducting sensitivity studies and verification and validation processes. The strain validation (presented in Section 6) and remodelling validation (presented in Section 8) confirm the FE modelling approach used in this thesis.

# 5 In-vitro Mechanical Tests

## 5.1 Introduction

The response of biological bone tissue to mechanical stimulus is difficult to predict. In-vitro experiments of cadaveric specimens in the laboratory provide a controlled environment to test out primary fixation of implants by measuring bone strain and bone-implant displacement. The drawback of using only a laboratory test environment is inefficiency, high cost and inability to replicate biological processes such as remodelling. However, if the in-vitro assessments are conducted alongside computer models, then upon validation of the computer models, virtual assessments can be performed to improve implant designs. The validation process also helps to understand modelling accuracy so that uncertainty can be responsibly managed.

Since UKR arthroplasty is a minimally invasive technique, it is difficult to identify the precise physical state of the tibia and femur post-arthroplasty. The in-vitro experiments were designed to understand and identify practical considerations of modelling UKRs accurately.

UKRs are often available in cemented and cementless versions; however, minimal research has been done about how these design features affect fixation. Surgeons often use personal experience to decide whether to use cemented or cementless UKRs; experienced surgeons tend to use cementless implants on “strong active patients” while cemented implants are used in 96 percent of the cases (Schindler et al., 2010). It is postulated that the reason for this may be because cementless implants create higher bone strain so only the stiffest and strongest bones can respond well. It is also postulated that bone-implant displacements are lower in stiffer bone; hence, osseointegration would occur more readily.

Radiolucencies occur in both cemented and cementless tibial UKR implants and they are linked to micromotion at the bone-implant interface (Kwong et al., 1992). The cemented Oxford UKR tends to develop radiolucencies in 60-75% of arthroplasties (Gulati et al., 2009a) while for the cementless it is as low as 7% (Pandit et al., 2009). The author is not aware of any studies that have measured or predicted bone-implant micromotion of tibial UKRs.

A new UKR cementation technique has been developed at Charing Cross Hospital, London UK. Suction-cementation involves using a suction unit to apply, a vacuum under the tibial tray. It is postulated that the technique aids cement penetration, providing a more stable fixation (lower bone-implant displacement and lower bone surface strains). There are no

studies in the literature that have investigated whether suction-cementation aids fixation, particularly in UKRs.

The objectives of the in-vitro mechanical tests were as follows:

- To obtain in-vitro UKR implanted tibia and femur strains for FE model validation;
- To obtain in-vitro UKR implanted tibia bone-implant displacements for FE model validation;
- To replicate UKR arthroplasty in the laboratory in order to identify practical surgical considerations for modelling UKR implants accurately.
- To compare fixation (bone strains and bone-implant displacement) of cemented and cementless UKR implants;
- To compare fixation of normal-cemented and suction-cemented UKR tibial implants.

Ethical approval was obtained in August 2009 for in-vitro mechanical testing of 10 cadaveric specimens.

## 5.2 Materials & Method – Mechanical Tests

Cadaveric bones were instrumented and loaded in order to attain the objectives listed above. Bone strains were measured by using strain gauges and bone-implant interface micromotion was measured using Linear Variable Displacement Transducers (LVDTs).

Ten (five pairs) of fully intact fresh frozen human knees of donors from the Unites States were obtained and kept frozen at -18 °C until use. Table 11 presents the details of the cadavers including age, gender, specimen reference and (where available) the weight and height. The cadaveric knees were left to thaw naturally for 36 hours before computed tomography (CT) scans were taken (refer to Sub-section 6.2.1 for details of image parameters). Table 11 includes average bone densities, volume and mass (only distal 100 mm of femur and proximal 100 mm of tibia). The bone volume and average densities were calculated from the individual segmented specimen CT scans (segmented using AVIZO 6.1 software (Visualization Sciences Group, USA)).

**Table 11 - Details of cadaveric knee specimens including bone volume, mass and average density.**

| Spec. Ref. | Bone | Age | Gender | Weight (Kg) | Height (cm) | Leg | Mean ρ ($g/cm^3$) | ρ Std Dev | Vol. ($cm^3$) | Bone Mass(g) | Max. CT |
|---|---|---|---|---|---|---|---|---|---|---|---|
| CAD1 | Tibia | 65 | M | 64 | 183 | R | 0.344 | 0.458 | 199.0 | 68.5 | 2619 |
| CAD2 | Tibia | 65 | M | 64 | 183 | L | 0.333 | 0.441 | 191.8 | 63.9 | 2134 |
| CAD3 | Tibia | 81 | F | 91 | 152 | R | 0.296 | 0.443 | 154.1 | 45.7 | 2233 |
| CAD4 | Tibia | 81 | F | 91 | 152 | L | 0.292 | 0.438 | 149.3 | 43.6 | 2169 |
| CAD5 | Tibia | 74 | M | 82 | 175 | R | 0.302 | 0.391 | 184.9 | 55.9 | 2205 |
| CAD6 | Tibia | 74 | M | 82 | 175 | L | 0.286 | 0.392 | 194.4 | 55.6 | 2325 |
| CAD7 | Tibia | 96 | M | - | - | R | 0.334 | 0.429 | 191.0 | 63.9 | 22343 |
| CAD8 | Tibia | 96 | M | - | - | L | 0.342 | 0.437 | 191.5 | 65.4 | 2271 |
| CAD9 | Tibia | 64 | F | - | - | R | 0.342 | 0.486 | 121.0 | 41.4 | 2353 |
| CAD10 | Tibia | 64 | F | - | - | L | 0.325 | 0.485 | 125.5 | 40.9 | 2330 |
| CAD1 | Femur | 65 | M | 64 | 183 | R | 0.334 | 0.394 | 255.7 | 85.3 | 2218 |
| CAD2 | Femur | 65 | M | 64 | 183 | L | 0.320 | 0.374 | 246.1 | 78.8 | 2171 |
| CAD3 | Femur | 81 | F | 91 | 152 | R | 0.296 | 0.407 | 212.6 | 63.0 | 2114 |
| CAD4 | Femur | 81 | F | 91 | 152 | L | 0.290 | 0.394 | 199.3 | 57.8 | 2180 |
| CAD6 | Femur | 74 | M | 82 | 175 | L | 0.301 | 0.356 | 238.8 | 72.0 | 2138 |
| CAD7 | Femur | 96 | M | - | - | R | 0.354 | 0.387 | 239.7 | 84.9 | 2370 |
| CAD8 | Femur | 96 | M | - | - | L | 0.360 | 0.389 | 232.0 | 83.6 | 2351 |
| CAD9 | Femur | 64 | F | - | - | R | 0.392 | 0.456 | 150.6 | 59.1 | 2296 |
| CAD10 | Femur | 64 | F | - | - | L | 0.380 | 0.446 | 149.1 | 56.7 | 2291 |

The knees were paired as follows: CAD1-2, CAD3-4, CAD5-6, CAD 7-8, and CAD9-10. As detailed in Table 11, bone density, volume and mass were similar within the pairs but there was a higher density in the right leg ($T(8)=2.40$, $P=0.04$). An orthopaedic surgical registrar (Amgad Nakhla, Charing Cross Hospital), with experience of performing 50-100 UKR arthroplasties using the Oxford UKR (Biomet UK Ltd, Swindon, UK), performed all surgical procedures, as outlined in the Oxford UKR surgical procedure manual. Ten surgeries were performed on ten knees in two separate sessions (five at a time) with each surgery lasting approximately 40 minutes. Surgeries of the first five cadaveric specimens (CAD6-10) were done in the first session with the remaining (CAD1-6) in the second session. A full set of UKR equipment for performing the surgeries was leased from Biomet UK Ltd, UK. The transverse surgical bone cuts (on the tibia and femur) were made using an electric cordless Stryker (Stryker Plc., Michigan, USA) oscillating saw with a 12 mm wide oscillating saw blade and the sagittal cuts (including the tibial keel cuts) were made using a Stryker reciprocating saw. For the second batch of cadavers an alternative Bosch oscillating saw was used.

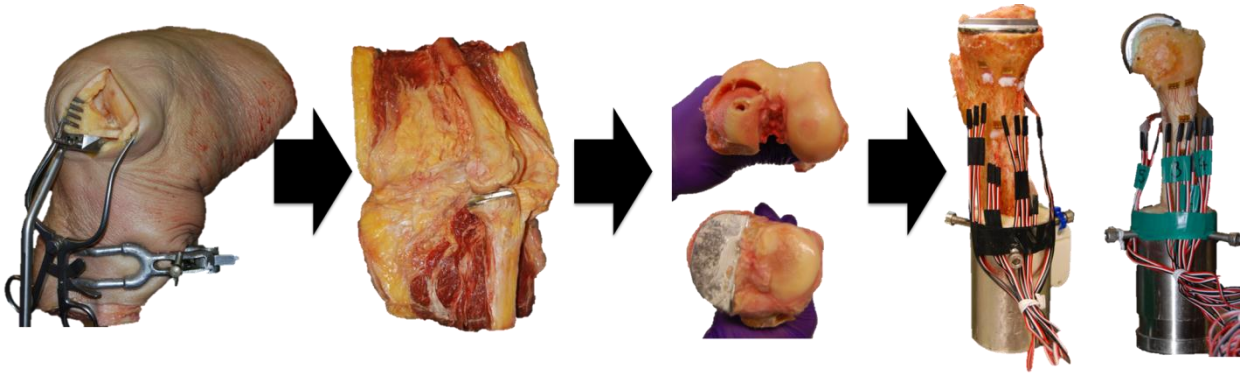

**Figure 45 - Photographs demonstrating the preparation of the bone constructs.**

All the UKR arthroplasties were medial. The cadaveric knees were mounted on a jig at approximately 90 degrees flexion and the implantations were made through a minimally invasive medial incision. A full set of cemented and cementless implants were donated by Biomet UK Ltd; therefore, as would be performed in the operating theatre, the implant sizes were determined during surgery. The correctly sized cementless tibial trays were hammered into place. Cementless femoral components were hammered into femoral specimens CAD7 and CAD10 and cemented femoral components were used in specimens CAD1-4, CAD6 and CAD8-9. The details of the cementations are described below. Prior to UKR implantation, specimen CAD6 had been used in a patellofemoral resurfacing arthroplasty trial; therefore the femur was excluded from the study. The anterior facets of the resected femoral condyles were trimmed (part of surgical procedure so impingement does not occur). Post-surgery the specimens were disarticulated and all soft tissues were removed. The bones were re-frozen to -18°C and stored away until bone-construct assembly and testing.

The bone constructs were prepared as pairs, commencing with the tibiae. Approximately 40 mm of the distal tibial and proximal femoral shafts were cemented into stainless steel pots, using Simplex Polymethyl Methacrylate (PMMA) bone cement (Simplex Rapid, Austenal Dental Products Ltd, UK). Three screws, around the rim of the pot, were tightened to ensure that the specimens were centralised and fully anchored. The tibiae were aligned such that the transverse resections were aligned parallel to the horizontal base of the pots. The femora were aligned such that the two most distal points of the medial and lateral condyles formed a horizontal line parallel with the base of the pots.

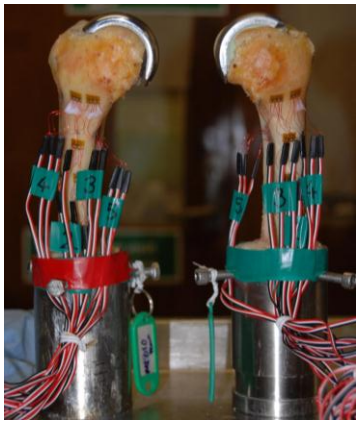

**Figure 46 - A paired set of femoral bone constructs (from the same donor) with strain gauges carefully positioned in similar locations.**

The intended positions of the strain gauge rosettes were marked on the bone using a marker pen. Using a scalpel, a half-round hand file, and medium grade sand paper, the soft tissues and periosteum were removed until the cortical bone was fully exposed. The bone was lightly sanded down to ensure an uninterrupted flat surface. Note that the exact positions of the strain gauges were chosen primarily on the quality of the underlying surface: Bone surfaces were required to be flat and continuous without porosities. The bone surfaces were degreased using CSM degreaser (Vishay Precision Group) and neutralised using MN5A-1 M-Prep Neutralizer 5 (Vishay Precision Group). Once the bone surfaces were dry, they were coated in a layer of M-Bond Catalyst (Vishay Precision Group). The topsides of the rosettes were attached temporarily to sellotape while a drop of M-Bond 200 (Vishay Precision Group) was placed on the rosettes' underside. The rosettes were immediately placed on the bone and thumb pressure maintained for 2 minutes. The rosettes were 45-degree planar 350 Ohm type C2A-06-062LR strain gauge rosettes (Vishay Precision Group Ltd, USA), prewired on a matrix measuring 2.8x4.1 mm. They were chosen for their thermal stability and versatility for ease of mounting. Although stacked rosettes are smaller than planar rosettes, they are stiffer; therefore, they were avoided based on the relatively low stiffness of bone.

The approximate positions of the five rosettes are illustrated in Figures 47 and 48. Since all the implants were medial UKRs, the rosettes were positioned to measure strains at the medial regions of both the proximal tibia and distal femur. For the tibiae, three rosettes were placed just beneath the implant tray (at medial, central and posterior positions) and the remaining two rosettes were placed one beneath each other on the stiff cortical bone of the medial tibial shaft. For the femur, a similar approach was adopted; however, the rosettes were located further away from the implant because the bone surfaces were not flat enough to ensure good gauge attachment. Due to similar surface morphologies, the rosettes could be positioned at similar positions for each pair of specimens; however, they were slightly different between donors.

The LVDTs (Solartron Metrology Ltd, Sussex, UK) were mounted in the configurations illustrated in Figure 47. Two different mounting techniques have been used in the literature: (1) mounted on to the implant with the pointer resting on the bone surface; and (2) mounted to the bone and the pointer resting on the implant. Both techniques were used to measure surface-tangent motion, with method (1) used at the implant anterior and posterior and method (2) used at the implant medial. Method (2) was used to measure the surface-normal motion at the implant anterior and posterior. Figure 49 shows the three LVDT assemblies with distances of 2-4 mm between the bone-implant interface and LVDT reference point.

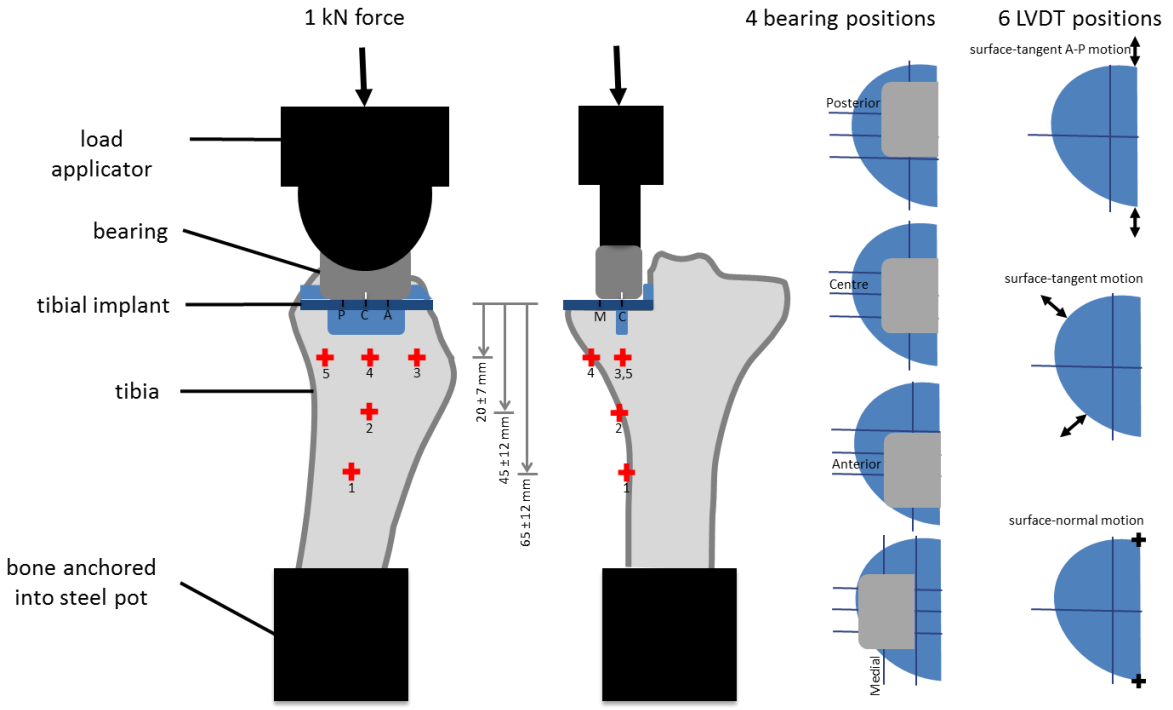


**Figure 47 - Experimental set-up of tibial bone-constructs, with idealised positions of strain gauge rosettes (labelled in red), bearing loads and LDVTs.**

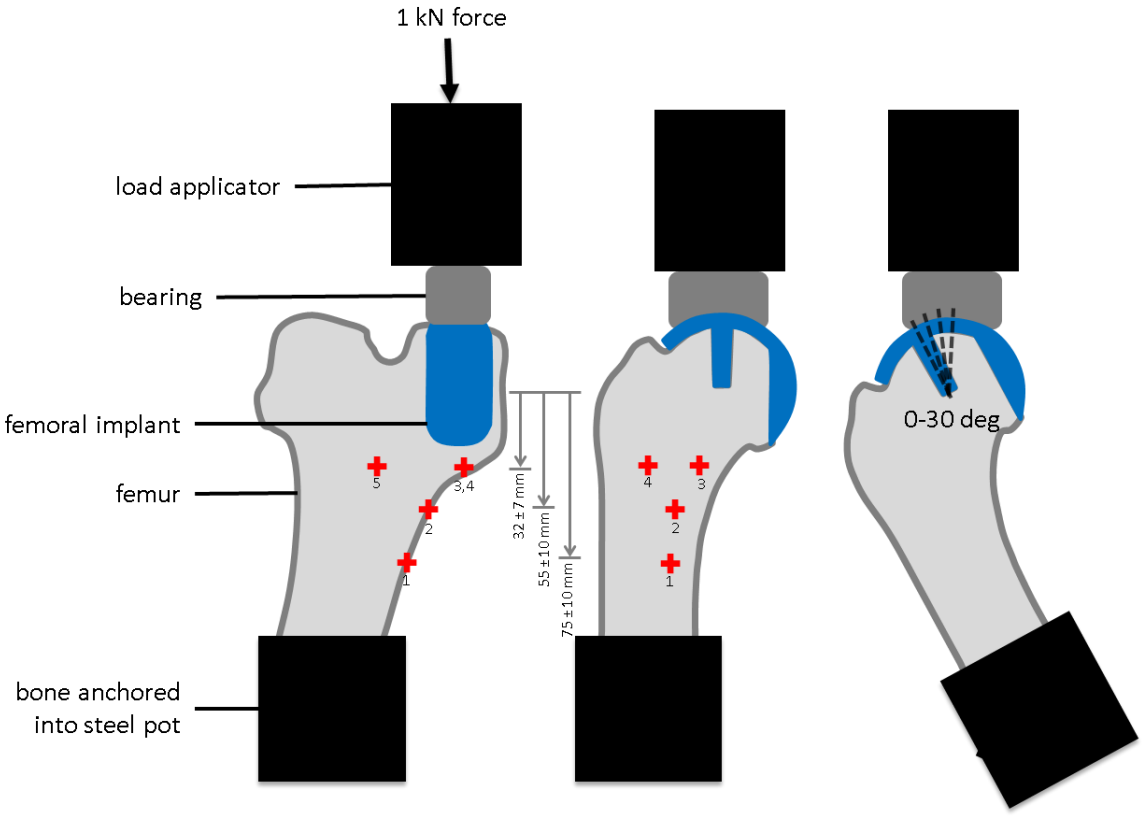


**Figure 48 - Experimental set-up of femoral bone-constructs, with idealised positions of strain gauge rosettes (labelled in red) and bearing orientations.**

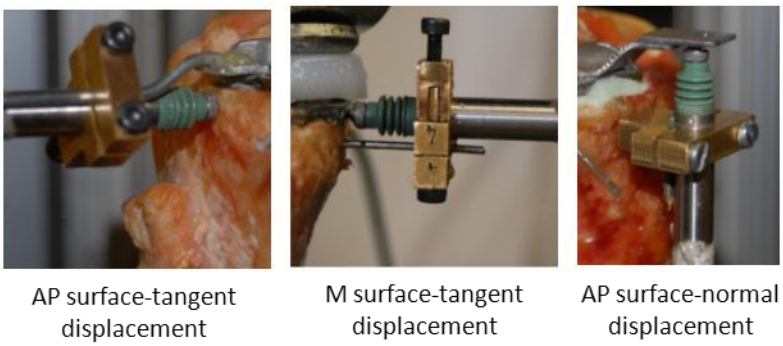


**Figure 49 - Assembly of LVDTs on tibia bone-constructs.**

Once the bone-constructs were assembled, the positions of the rosettes, bone resections and LVDT anchor points were registered relative to bony landmarks and the steel pot, using a Polaris Optical Tracking System (Northern Digital Inc., Canada). The system calculates the position of a pointer based on visual tracking of two markers (on the pointer) by two cameras. The positions were recorded relative to a steel block placed beside the bone-constructs that defined the vertical and horizontal.

The bone-constructs were mounted on a screw-driven Linear Instron 5565 materials testing machine (Instron Ltd, High Wycombe, UK) with a 5 kN load cell. A jig, bolted to the Instron bed, was used to position the bone-constructs accurately; the jig allowed transverse plane positioning and dual axis rotation.

For loading the tibia specimens, a specialised component was manufactured to hold a medium sized femoral component to the Instron cross head. A 4 mm polyethylene bearing was placed between the tibial tray and femoral component. The centre of the tibial tray side plate was marked and extended to the lateral edge of the tray. Two more markers were added at 5 mm anterior and posterior to the centre. The centre of the lateral side of the bearing was marked to position it accurately on the tibial tray. As presented by Figure 47, four bearing positions were tested: (1) 5 mm anterior to centre; (2) centre; (3) 5 mm posterior to centre; and (4) 5 mm medial to centre.

For the femoral specimens, a flat-end load applicator was attached to the Instron crosshead and a 4 mm bearing was placed between it and the femoral component. The femur bone-construct was clamped to the jig such that it could be rotated in the sagittal plane (flexed). The jig was manufactured with predrilled slots to clamp the construct at 10 degrees increments from the nominal position (0 degree knee flexion).

Each of the 15 strain gauges (five rosettes) was connected to a quarter Wheatstone bridge circuit configured with a 350 Ohm resistor using an FE-MM16 16-channel strain gauge amplifier (Fylde Electronic Laboratories Ltd, Preston, UK). The gauges were connected with

three wires for increased thermal stability. The quarter Wheatstone bridge circuits were balanced at the start of each set of experiments. The voltage across the bridge was 2.5 Volts and the gauge factor for all gauges was 2.1. The equipment was connected to a computer and MADAQ data acquisition software (Fylde Electronic Laboratories Ltd, Preston, UK) was used to record the voltage across the bridge at a sampling rate of 10 Hz.

The LVDTs were connected a computer. Orbit Digital System software (Solartron Metrology Ltd, Sussex, UK) plugin for Microsoft Excel 2007 was used to record the displacements at 200 Hz. The LVDT readings were reset at the start of each experiment.

Ten cycles of 1 kN force were applied to all loading configurations, at a linear rate of 100 N per second and held for 2 seconds at the extremes. The first two cycles were excluded from the analysis of the results. The experiments were repeated three times with a different LVDT configuration for each experiment repetition. Therefore, there were three sets of 10-cycle strain gauges readings and one set of 10-cycle LVDT displacements for each loading configuration.

Once the testing was complete, the cementless implants on the tibia bone-constructs were removed and replaced with cemented versions of the same size. Two-part Palacos radiopaque bone cement (Heraeus Holding GmbH, Hanau, Germany) was vacuum mixed for 40 seconds using a Stryker Mixevac III (Stryker Plc., Michigan, USA) before applying to the bone and implants. The cement was applied all over the implants including the keels. The implants were hammered into position and a strong pressure was maintained for 10 minutes (from the start of cement mixing). Excess cement was removed.

The same cementation technique was used for the femora. If the resection surface was slightly sclerotic, the bone surface was perforated with a 2 mm drill to allow cement penetration. Note that only femora CAD07 and CAD10 required second stage cementation as all the others were cemented at stage one.

Half of the tibia bone-constructs were randomly chosen (CAD1, CAD4, CAD6, CAD7, CAD10) for a suction cementation: As presented in Figure 50, a suction tube was placed approximately 10 mm under the transverse resection, through the predrilled hole at the anteromedial aspect (part of the arthroplasty procedure). The position of the tube was confirmed by pouring water over the resection to check that it was displaced into the suction tube. The vacuum was maintained for 8 minutes after cement application.

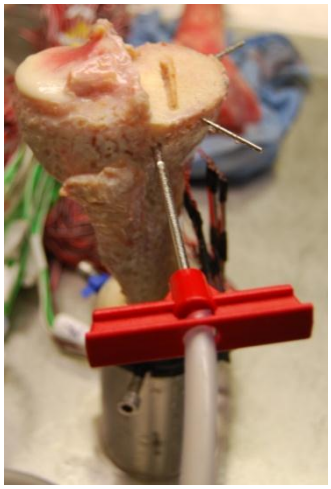

**Figure 50 - Photo showing insertion of suction tube during suction-cementation of a UKR tibial tray.**

After cementation, the same test procedure was repeated on the bone-constructs. Throughout the testing, the bones were regularly hydrated and all the tests were performed within 5 days of thawing.

## 5.3 Method – Data Processing

The mechanical testing generated 67,500 cycles of strain gauge data and 9,000 cycles of LVDT displacements. Matlab software (Mathworks Ltd, Massachusetts, USA) was used to process the data.

The gauge data files were imported into Matlab and saved as a data structure (class structure in Matlab) identified by specimen (1-10), fixation type (cemented/cementless), version (1-3), load position (tibia: central, anterior, posterior, medial; and femur: 0 to 30 degrees) and gauge number (1-15).

Although the gauges were balanced before every set of experiments (0 Volts at 0 kN force), the voltages drifted between experiments. Note that the effects of drift were minimised with the data processing conducted to analyse the results. The drift occurred because the bone exhibited viscoelastic behaviour and the strain gauge was sensitive to heat and moisture. With progression of the experiments, slight warping of the bone was visually evident and some of the implants migrated with repeated loading. It was therefore deemed important to calculate the amplitude of the cycles to calculate the strains accurately.

Although considerable care was taken when handling strain gauges, some were damaged during the mechanical tests; sometimes only temporarily but most damage was permanent due to debonding. Each strain gauge dataset (of 6750 datasets) was plotted with time and individually checked for reliability. The gauge was considered unreliable if it was unresponsive, lagged, or exhibited irregular behaviour against the load profile. Eighty-seven

percent of the tibia and 99 percent of the femur rosettes were considered reliable. Of those rosettes considered unreliable, sometimes only one of the gauges had stopped working; therefore, the working gauges were analysed and if deemed appropriate results extracted.

For each experiment (set of 15 gauge data), the most prominent response was selected and analysed to determine the times at which the peaks and troughs occurred. For all the remaining 14 gauges in the experiment, the peak and trough values were determined from these times. This was repeated for all 450 experiments. The amplitudes of each cycle were determined and the averages and standard deviations calculated with the first two cycles excluded.

A Matlab program was written to find the peaks and troughs in a dataset. The data was smoothened with a moving average algorithm of 5 data points (0.5 seconds). The gradient of the data series was calculated (difference between consecutive data points). A peak or trough was identified when the gradient was zero. The algorithm determined whether the first turning point was a peak or a trough and it searched looking for the alternate. Other search parameters (such as cycle time of 24 seconds) were included to exclude intermediate local peaks and troughs. If all ten cycles were not identified in the first iteration, the algorithm automatically modified the search parameters until the correct solution was found.

The voltage readings were converted to microstrains using the following equation (Vishay Measurements Group, Tech Note TN-507-1):

$$\mu\varepsilon = \frac{4000 \times V_{out}}{GF \times V_{in}}$$

where, GF = 2.1 gauge factor, $V_{in}$ = 2.5 V, and $V_{out}$ = gauge readings in mV.

All the rosettes were oriented with gauge 2 aligned along the bone shaft. The maximum and minimum principal strains and principal strain directions were calculated using the following


equations:

$$\varepsilon_{min,max} = \frac{\varepsilon_1 + \varepsilon_3}{2} \pm \frac{1}{\sqrt{2}}\sqrt{(\varepsilon_1 - \varepsilon_2)^2 + (\varepsilon_2 - \varepsilon_3)^2}$$

$$\theta = \frac{1}{2}\tan^{-1}\left(\frac{\varepsilon_1 - 2\varepsilon_2\varepsilon_3}{\varepsilon_1 - \varepsilon_3}\right)$$

If gauges 1 or 3 were identified as unreliable, the principal strain directions in previous measurements were checked and if they were aligned within 5 degrees of gauge 2, then the minimum principal strain was calculated from gauge 2. If gauge 2 was identified as

unreliable, and checks revealed that the principal direction was aligned with the rosette and the assumption of uniaxial strain was considered valid, then the minimum principal strain was calculated from the mean of gauges 1 and 3:

$$\varepsilon_{min} = \left(\frac{2}{1-\nu}\right)\left(\frac{\varepsilon_{45} + \varepsilon_{-45}}{2}\right)$$

The LVDT displacements were also processed using Matlab. The datasets were imported into Matlab and saved as a data structure (class structure in Matlab) identified by specimen (1-10), fixation type (cemented/cementless), load position (tibia: central, anterior, posterior, medial; femur flexion: 0 to 30 degrees), and LVDT position (tibia: MM1-MM6). The datasets were resampled at a rate of 10 Hz and the cycle amplitudes calculated using the algorithm described above. The average and standard deviations were calculated with the first two cycles excluded.

## 5.4 Method - Statistical Analysis

The Kolmogorov-Smirnov non-parametric test was used to test all variables for normality using SPSS software (IBM Software Group, New York, USA). The test confirmed that all bone-implant displacement and bone strain variables were normally distributed and that a two sample student t-test was suitable for testing statistical difference of the following parameters:

- Minimum principal strains between cemented and cementless implanted tibia;
- Minimum principal strains between cemented and cementless implanted femur;
- Bone-implant displacements between cemented and cementless implanted tibia;
- Minimum principal strains between normal-cemented and suction-cemented implanted tibia;
- Bone-implant displacements between normal-cemented and suction-cemented implanted tibia.

## 5.5 Results

The strain readings were repeatable with an average standard deviation of 43 με ranging from 16 με (for tibia CAD1) to 122 με (for the tibia CAD3). The average standard deviation within each set of 10 load cycles was 24 με. The average minimum principal strains at each rosette under each loading condition are presented in Figure 51 and Figure 52 for the tibia and femur, respectively. There was a statistically significant decrease in bone strains when tibia implants were cemented ($T(164)=-4.30$, $P=0.00003$). With the Bonferronni post-hoc

correction used to account for multiple comparisons, this result remained statistically significant. A statistical difference was not found between cementless and cemented implanted femora.

Figure 53 and Figure 54 present average minimum principal strains at each rosette location for each pair of tibiae and femora, respectively. Assessing a range of bone specimens was found to be necessary because the bone strains were different between donors, as demonstrated with an ANalyis Of VAriation (ANOVA) test: Performed on the tibia and femur pairs, a statistically significant difference in means was observed (tibia: $F(4,36)=6.136$, $P=0.001$; and femur: $F(4,16)=6.952$, $P=0.001$).

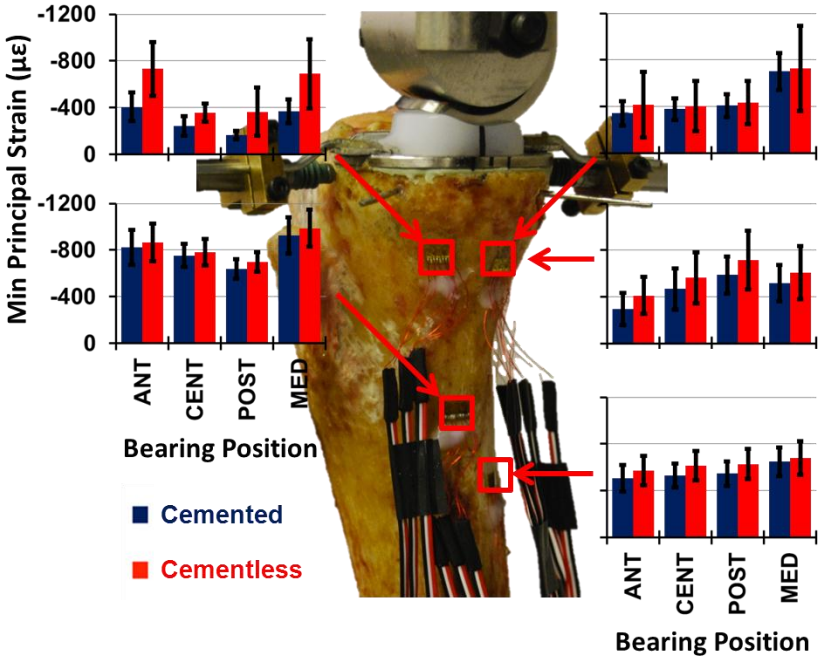


**Figure 51 - Comparison of average measured Min Principal Strains between cemented and cementless tibial implants. The full error bar is one standard deviation. Cemented implant bone strains were lower (statistically significant).**

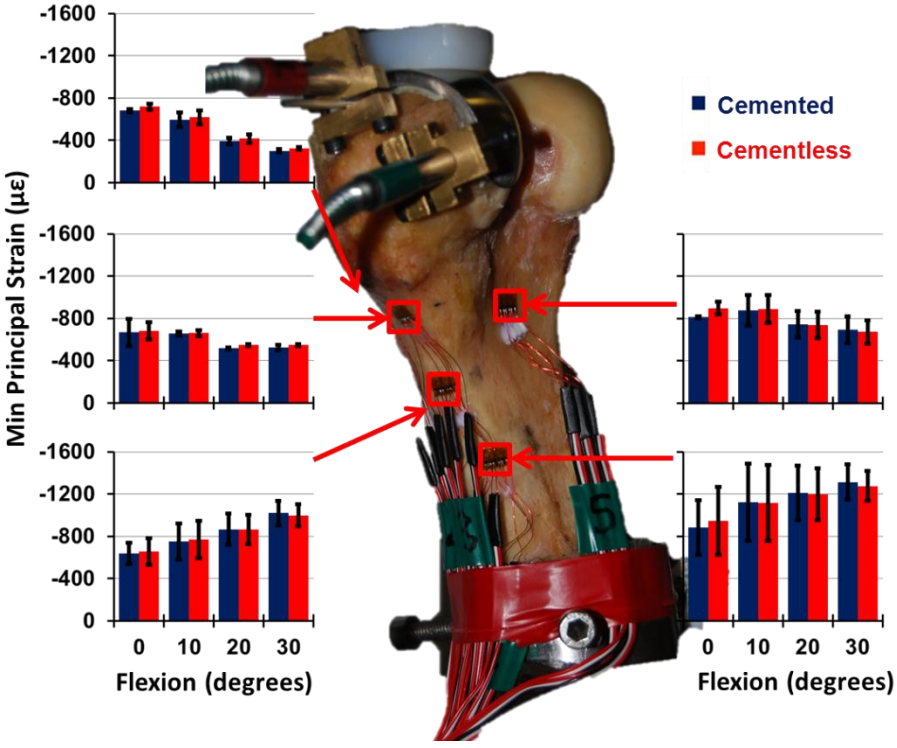


**Figure 52 - Comparison of average measured Min Principal Strains between cemented and cementless femoral implants. The full error bar is one standard deviation. No statistical difference.**

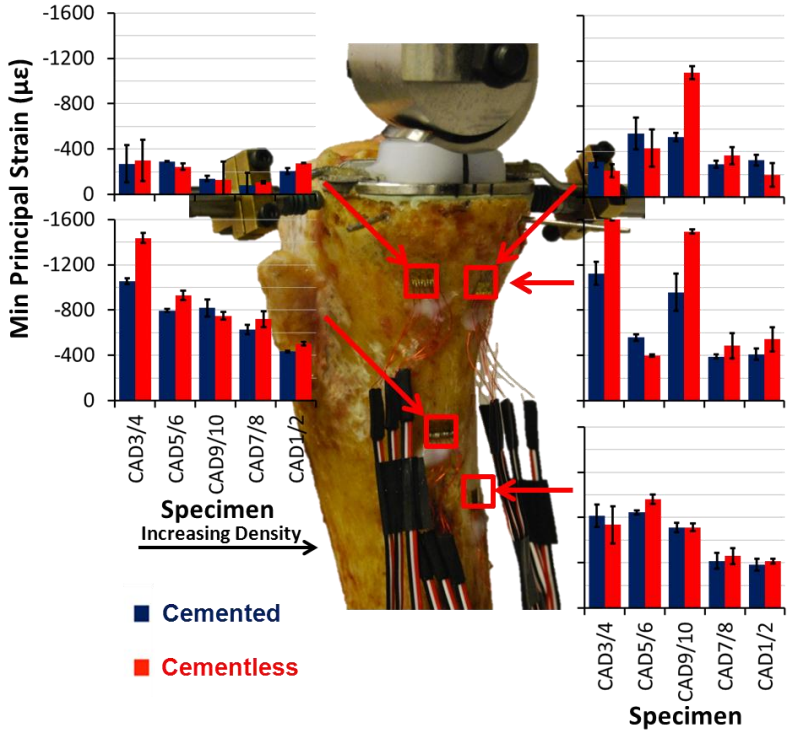


**Figure 53 - Average minimum principal strain when the bearing is 5 mm posterior from the centre of the tibial tray. Both cemented and cementless bone strains are presented showing the variation amongst the specimens. The specimens are in order of increasing density. The error bars represent one standard deviation. The results of the pair of specimens from each donor were averaged.**

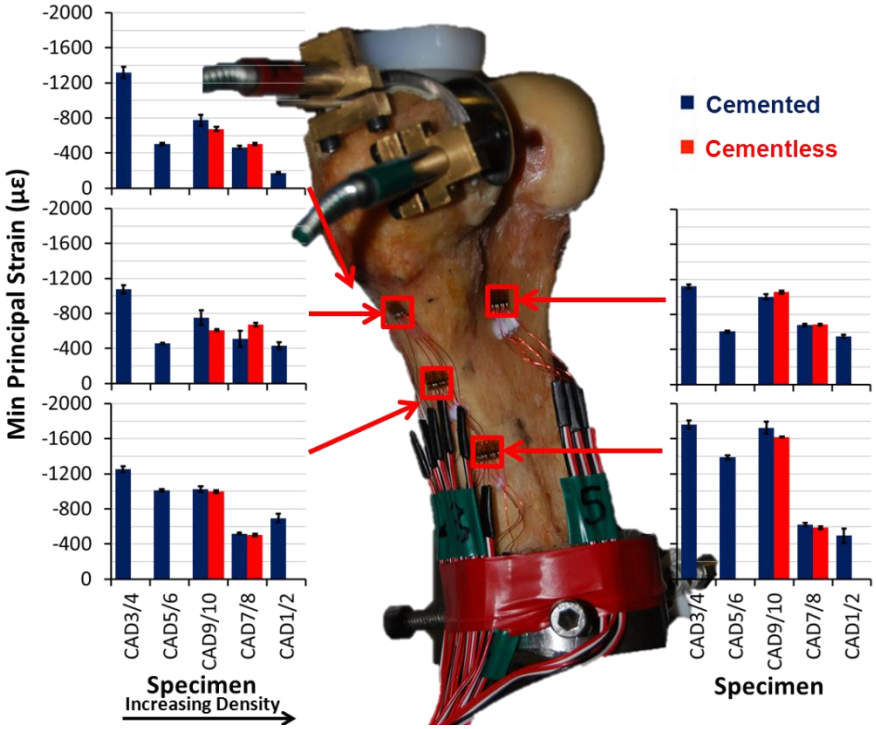


**Figure 54 - Average minimum principal strain when the femur is at full extension. Both cemented and cementless bone strains are presented showing the variation amongst the specimens. The specimens are in order of increasing density. The error bars represent one standard deviation. The results of the pair of specimens from each donor were averaged.**

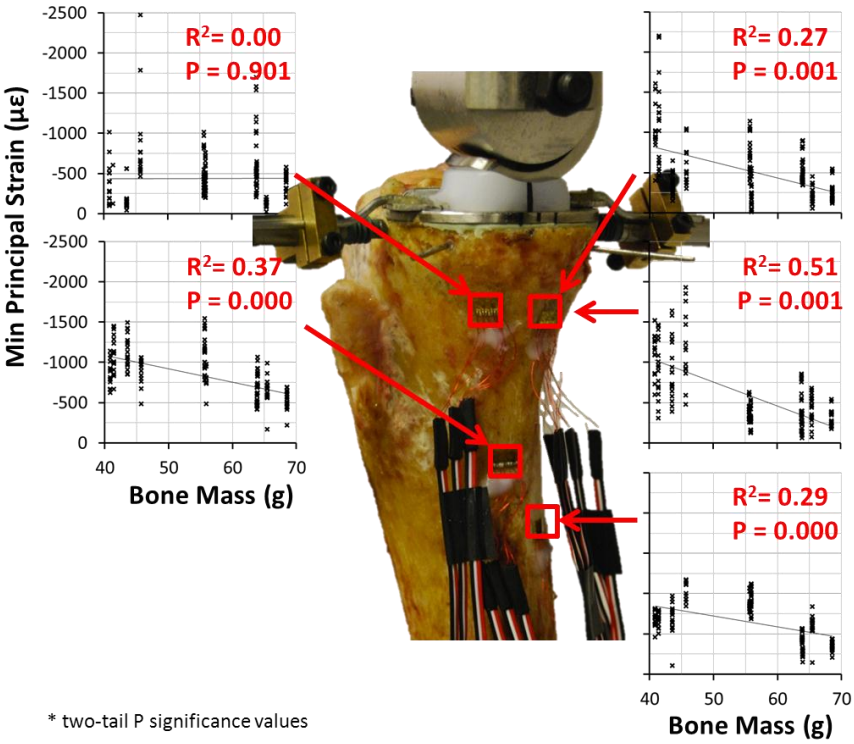


**Figure 55 - Plot of minimum principal strain against bone mass for all tibia specimens. Bone strains reduce with bone mass particularly at the proximal posterior. The anterior medial strains were not correlated to bone mass.**

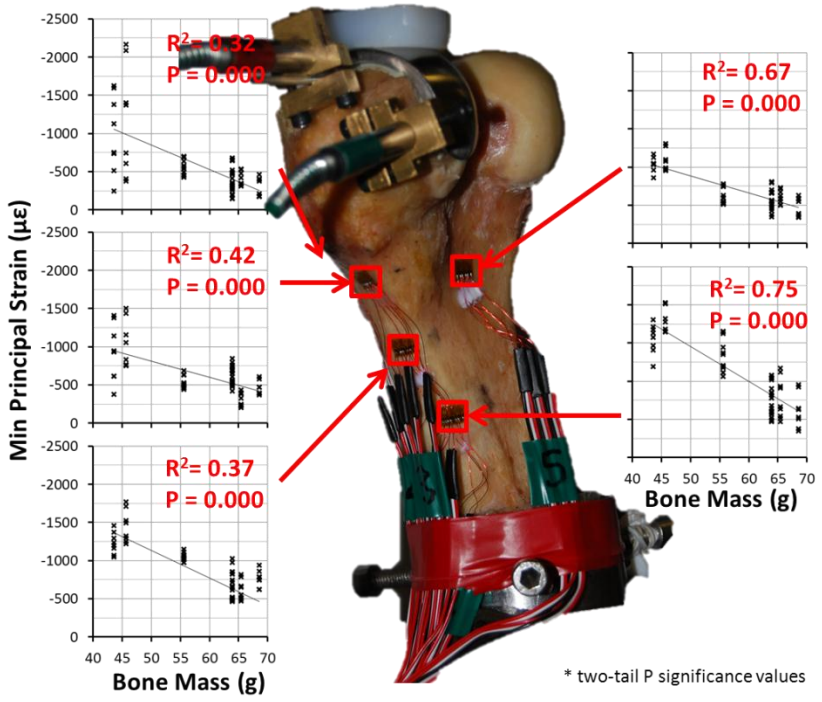


**Figure 56 - Plot of minimum principal strain against bone mass for all femur specimens. The anterior medial strains were not correlated to bone mass.**

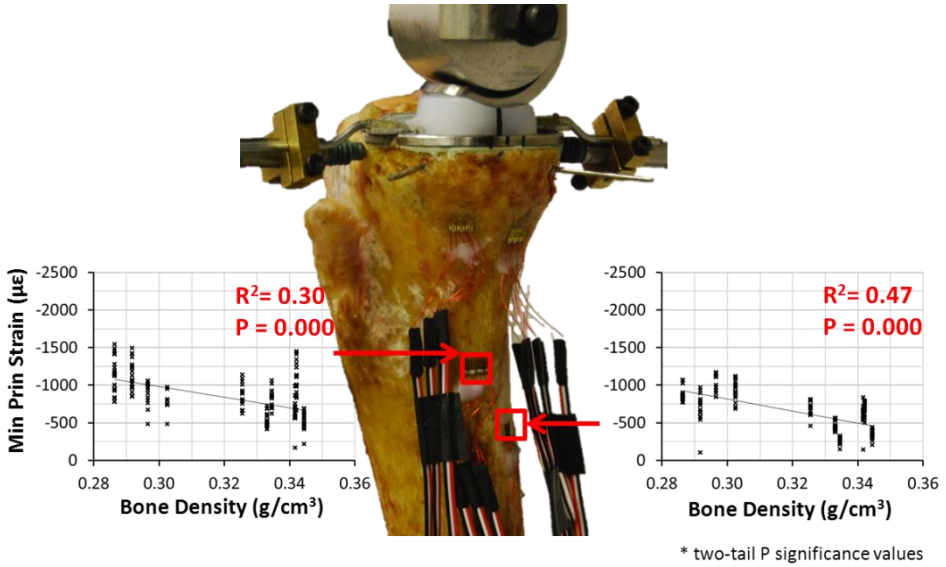


**Figure 57 - Plot of minimum principal strain against bone density for all specimens at rosette positions located on the cortical bone. There was no correlation between density and strain for other gauges.**

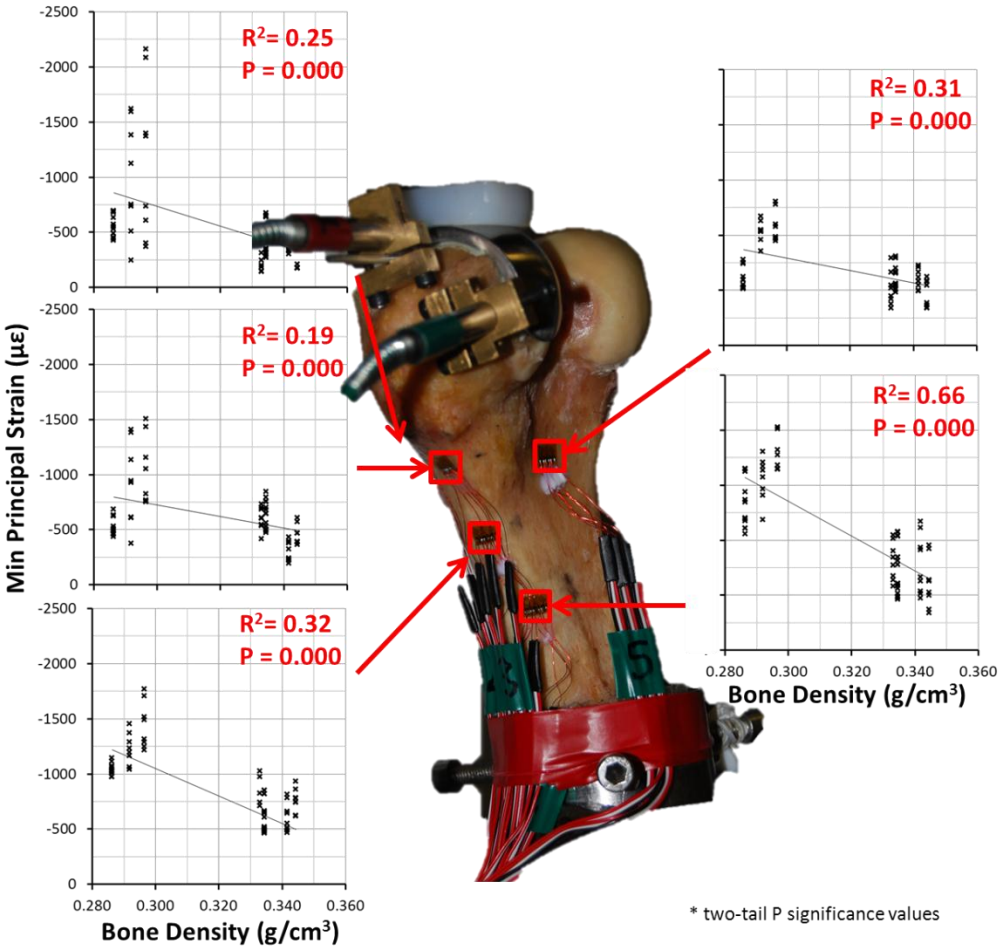


**Figure 58 - Plot of minimum principal strain against bone density for all femur specimens.**

The minimum principal strains were tested for correlation against bone density, bone volume and bone mass. The highest pooled correlation was achieved with bone mass ($R^2$ =0.21 for

tibia $R^2$=0.40 for femur) and bone volume ($R^2$ =0.18 for tibia and $R^2$ =0.34 for femur) and the correlation with bone density was smaller ($R^2$ =0.04 for tibia and $R^2$ =0.27 for femur). When individual locations were analysed, bone density was correlated with cortical bone strain, as illustrated in Figures 57 and 58. Figures 55 and 56 present correlation coefficients of minimum principal strain against bone mass at each strain gauge location.

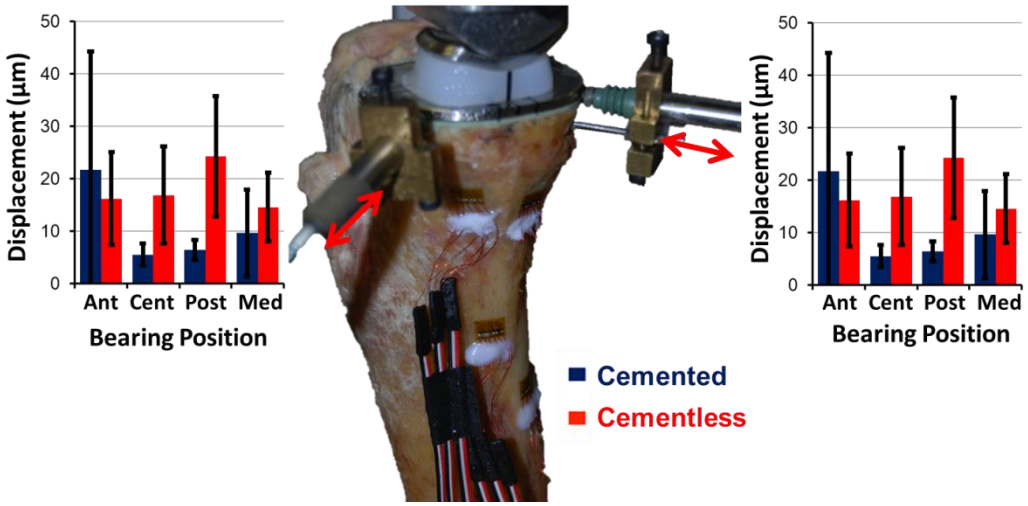


**Figure 59 - Average transverse interface displacement at medial aspects of the implant. The error bars show one standard deviation from average.**

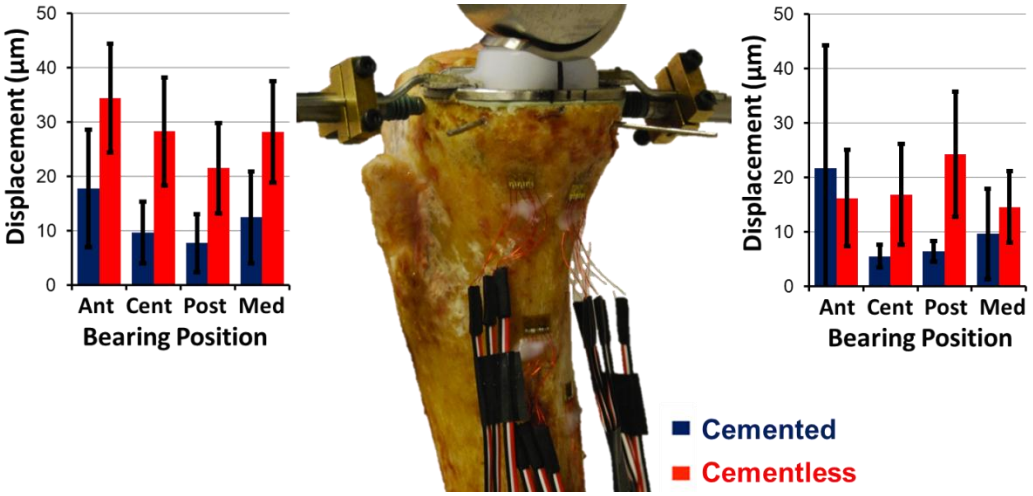


**Figure 60 - Average transverse interface displacement at anterior and posterior aspects of the implant. The error bars show one standard deviation from average.**

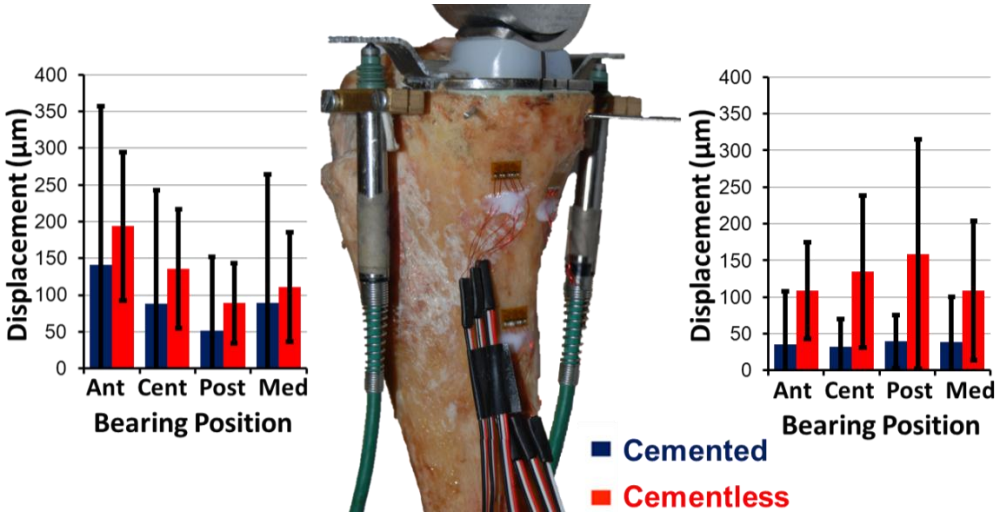


**Figure 61 - Average surface-normal interface displacement at anterior and posterior aspects of the implant. The error bars show one standard deviation from average.**

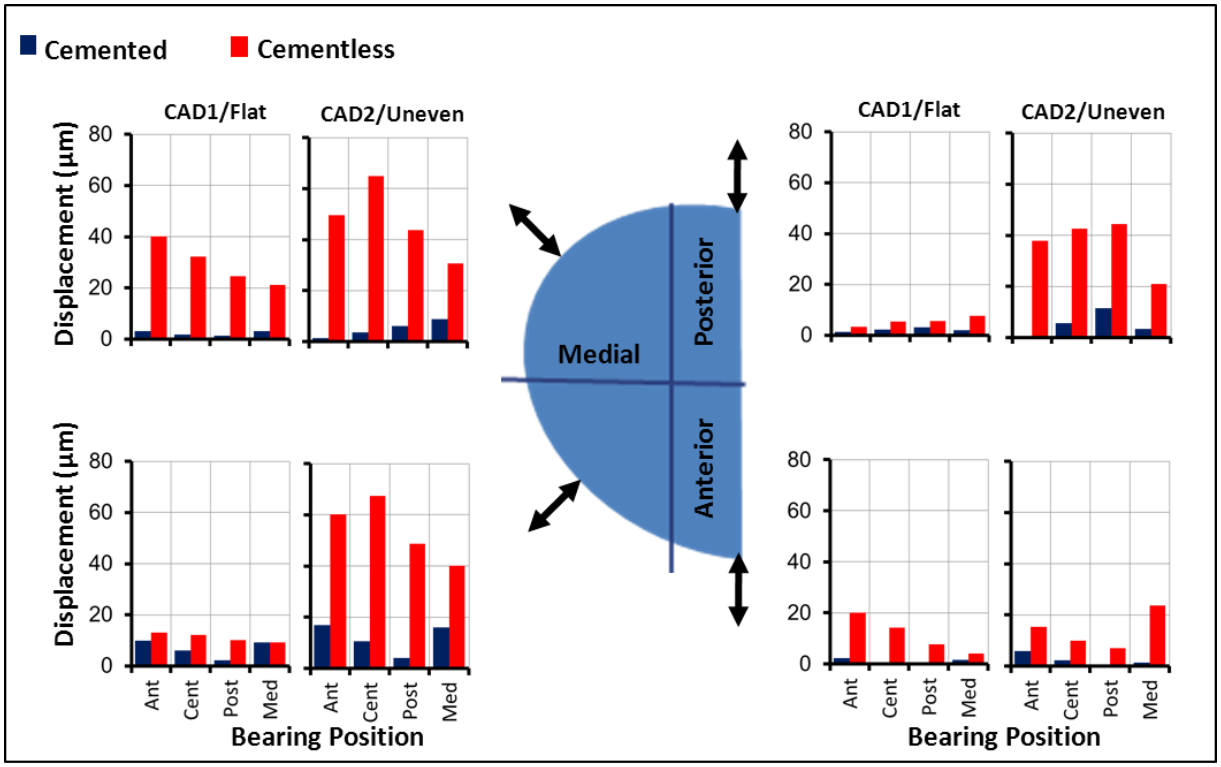


**Figure 62 - Comparison of surface-tangent interface displacements of a flat (specimen CAD1) and uneven (specimen CAD2) UKR resections.**

The measured bone-implant displacements are presented in Figures 59 to 61. They demonstrate that cemented displacements 16.8 ± 35.8 µm (mean ± SD) were less than cementless displacements 67.3 ± 80.9 µm (T(177)=-9.23, P=0.0001). With the Bonferronni post-hoc correction used to account for multiple comparisons, this result remained statistically significant.

There were inter-specimen differences in bone-implant displacement. The quality of the bone resection effected displacement, with higher interface motion for uneven resections. Figure 62 presents a comparison of two specimens (of the same donor) and demonstrates that the difference in means (flat: 14.4 ± 10.6 µm; uneven: 37.9 ± 18.8 µm) was significant (T(15)=-5.07, P=0.0001). No correlations were found between bone density/mass and bone-implant displacements. For specimens CAD3/4 surface-tangent displacements were 33 ± 24 µm and surface-normal displacements 247 ± 190 µm; these were markedly higher than for the other specimens (surface-tangent displacement 15 ± 9 µm and surface-normal 72 ± 49 µm).

Bone-implant displacement is indicative of lack of osseointegration (Jasty et al., 1997a) and has been linked with radiolucencies (Kwong et al., 1992). The measured results were analysed to understand the distribution of the bone-implant displacements. Figure 63 presents the distribution of surface-tangent and surface-normal displacements between

cemented and cementless implanted tibiae. The cemented surface-tangent displacements were less than 20 µm while 75% of the cementless displacements were less than 50 µm. The surface-normal displacements were significantly higher with 60% greater than 100 µm.

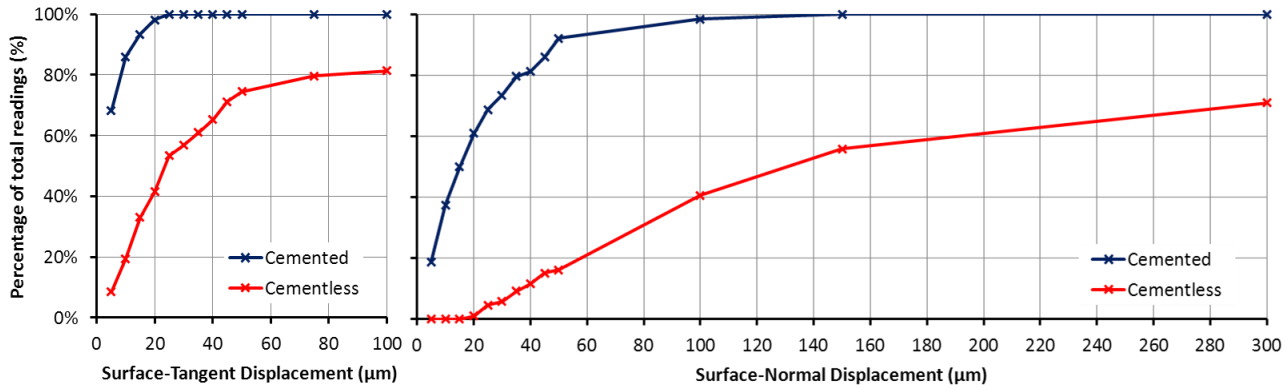


**Figure 63 - Percentage distribution of measured interface displacements on cemented and cementless implant specimens. Surface-normal displacements are significantly higher and spread out.**

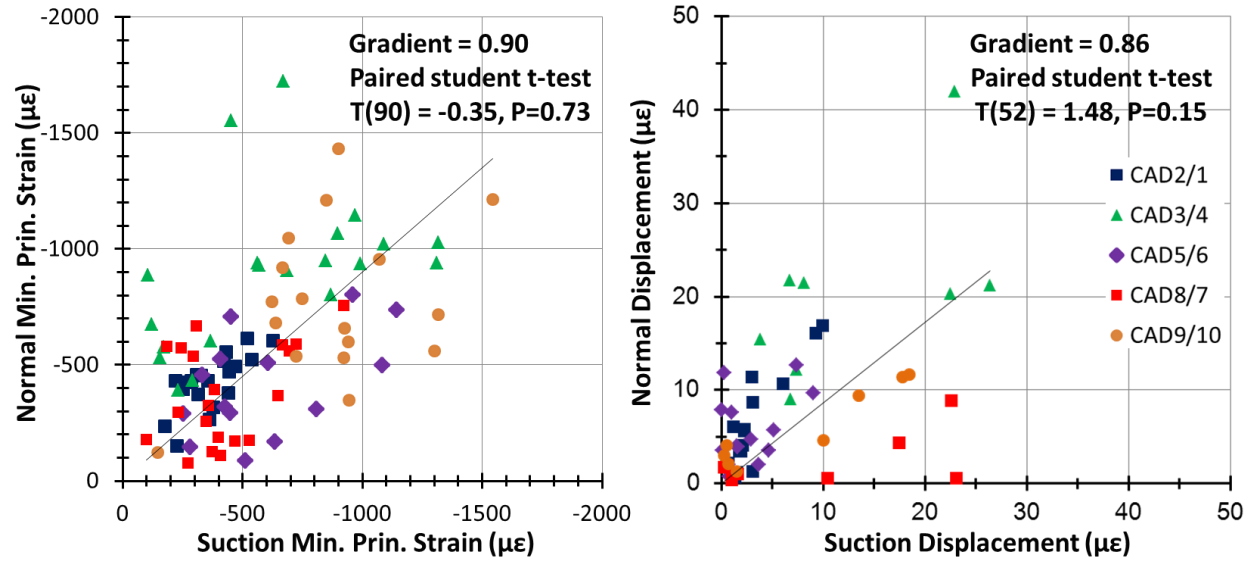


**Figure 64 - Comparison of pooled results of normal cementation and suction cementation. Minimum principal strains and bone-implant displacements have been compared. Student t-test results showed that a difference could not be proved.**

The effect of cementation method on bone strain and bone-implant displacement was compared by pooling the results, as illustrated in Figure 64. Comparison of pooled data strains and pooled data bone implant displacements revealed no statistical difference; however, there were statistically significant differences when specific parameters were compared. A comparison of cortical bone strains (rosettes 1 and 2) showed that suction-

cemented cortical bone strains were lower than normal cemented strains (T(33)=-2.22, P=0.03). A comparison of bone-implant displacements revealed that three pairs had statistical significance showing displacements were less when suction-cementation was used CAD1/2 T(14)=4.15, P=0.001, CAD3/4 T(7)=2.39, P=0.048, CAD5/6 T(12)=2.59, P=0.024. The other two tibia pairs showed an opposite trend ( suction-cementation displacements higher than normal-cementation) but they were not statistically significant.

### *5.5.1 Comparison to Literature*

The measurement techniques used in this study are well established and have been adopted in numerous in-vitro cadaveric studies in the literature. Strain gauges on cadaveric bone have been shown to accurately measure surface bone strains (Milgrom et al., 2004). Strain gauges have even been mounted on living human subjects (Burr et al., 1996, Lanyon et al., 1975). Bone-implant micromotion is difficult to measure physically, due to the small motions involved and the difficulty in taking measurements at the bone-implant interface. Using LVDTs to measure the relative displacement of implant and bone is an established technique (Cristofolini et al., 2007, Chong et al., 2010). Assuming that surface deformations of adjacent measurement points are small, it is implied that the measured displacements are representative of the micromotion at the interface (refer to Sub-section 6.4 for details of an in-silico reference study).

Studies investigating cadaveric tibial bone strains are common in the literature: Gray et al. (2008) tested a single UKR implanted cadaveric tibia and Varghese et al. (2011) tested multiple intact tibiae. However, this is the first study that has measured multiple UKR implanted tibiae. For the femur, studies of multiple cadaveric specimens have been published (Schileo et al., 2007); however, none have investigated the distal femur or investigated UKR implanted strains. In addition, none have investigated bone strains and bone-implant displacements of cemented and cementless UKR implants.

The bone strains measured are within the large range of strains reported in the literature for both in-vivo (Al Nazer et al., 2012) and in-vitro studies. For a comparable in-vitro study, Gray et al. (2008) reported tibia strains of up to 500 με (cortical bone) under 0.5 kN which compares to our maximum strains of 1200 με (most distal tibia rosette) under 1 kN. The average standard deviation of 43 με (24 με within each set of 10 load cycles) is higher than that reported by Gray et al. (2008) (maximum 28 με) because: (1) final loads were held for only 2 seconds (not over 30 seconds as was done in previous studies); (3) final loads were greater; (4) multiple specimens were assessed (repeatability was specimen dependent); and (5) the experiments were repeated only after all load configurations were tested (specimens prone to damage accumulation).

Bone is viscoelastic, so to ensure repeatable strains, previous studies have applied a single specimen load (non-cyclic) and maintained it for at least 30 seconds before taking readings. The drawback of this technique is that it is unrepresentative of in-vivo conditions where high loads are usually applied in multiple cycles with short periods e.g. walking, stair climbing, jogging etc. It was postulated that if repeated cycles were applied, it would provide some repeatability and would also help to understand the uncertainty of predicting such bone strains. In this respect the methodology employed in this study was unorthodox compared to the literature but more realistic for assessing in-vivo strains.

### *5.5.2 Viscoelasticity and Implant Migration*

Bone exhibits viscoelasticity, which is the behaviour of a material to exhibit the mechanical characteristics of viscous flow and elastic deformation. It deforms very slowly and progressively under constant stress (creep). Bone strain is made up of both recoverable (temporary deformation) and permanent deformation. The viscoelastic nature of bone was evident from the strain response measured on the strain gauges; two cycles of load were usually required for the bone to reach a stable and consistent lower strain value, as presented in Figure 65.

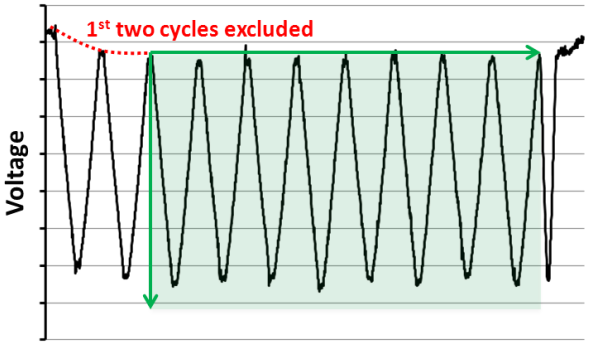


**Figure 65 - Typical strain gauge reading, showing two cycles to reach a stable repetitive cyclic bone strain response.**

The permanent deformation of bone was not observed in the strain measurements, because the measurement period was too short, but was noted visually when comparing photographs of the shape at the start and end of the set of experiments. The implants migrated as displayed by the photographs of specimen CAD4 in Figure 66. A similar pattern of implant migration is commonly seen in UKR patients (Ryd et al., 1983). Although implant migration was clearly apparent in tibia specimens CAD3/4, it was not apparent in all the specimens. The femoral components of the same donor CAD3/4 did not migrate enough to be visually apparent. Tibial trays may be more prone to migration than femoral components and particularly in subjects with low quality bone.

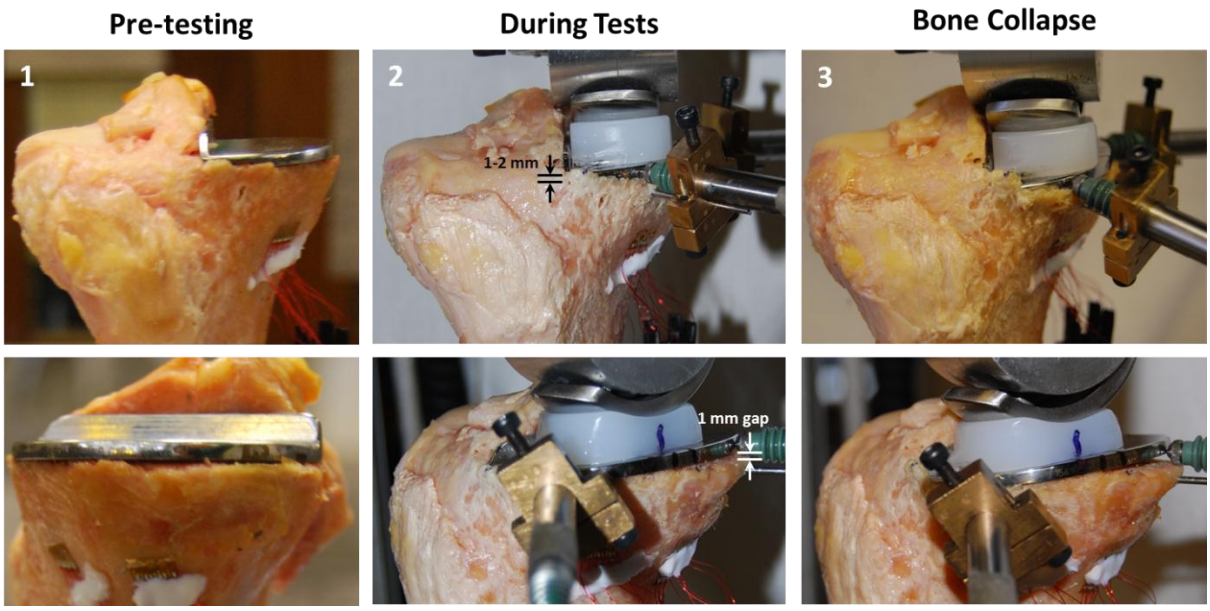


**Figure 66 - Migration of tibial implant under cyclic loading leading to bone collapse at the anterior-lateral resection corner.**

The displacement of the load applicator gradually increased at a declining rate with consecutive cycles. For cementless implants, during the first ten cycles, the displacement increase ranged from 0.005 to 0.02 mm per cycle depending on bone density. This gradually reduced with progression of the experiment. Unfortunately, it could not be ascertained what portion of this displacement was migration and viscoelasticity and whether migration settled (the recoverable and permanent components of deformation could not be differentiated).

The permanent deformation of bone (under reasonable but not excessive strains) is partly due to accumulation of fatigue damage under repeated cycles. The resected bone immediately under the implant is weaker than the surrounding bone because it is primarily composed of half cut open trabeculae. As a result, this is the first region to fail and collapse, exhibiting what appears to be implant migration (Figure 67). The resected corner is the region of highest bone strain (refer to Section 9); therefore, this is where tibia specimens are most likely to fail next (Figure 67).

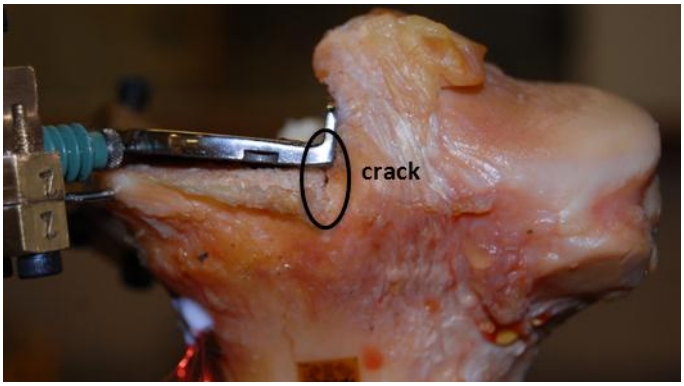


**Figure 67 - Posterior of tibial specimen CAD4, showing emergence of a crack at the resection corner.**

### *5.5.3 Bone Failure*

Micro-cracks develop during cyclic loading of bone (Donahue et al., 2000, Fazzalari et al., 1998); however, in living tissue the rate at which they develop is usually less than the rate of repair of the damage by bone remodelling (the osteoblasts counterbalance the damage). How these micro-cracks develop is unclear; however, studies have shown that they can develop under low strains (900 με) (Donahue et al., 2000) and are significant above 4000 με (Pattin et al., 1996). A low load of 1 kN was chosen to minimise damage accumulation; however, due to the wide inter-specimen variation highlighted in this study, the weaker specimens may have suffered accumulated damage. The effects of accumulated damage would be: the measured strains would alter as micro-fractures coalesced forming cracks that spanned across whole trabeculae; measurements would be less repeatable with higher standard deviations; these damaged specimens would also exhibit principal strain direction change (deviating from axial alignment); and near the implant surface this would manifest as higher bone-implant micromotions. Tibia specimens CAD3/4 exhibited these characteristics and part-failed during cementless implant testing, as displayed in Figure 67. This was probably due to rapid damage accumulation as bone strains in the vicinity of the implant were higher than average.

Retrospective analysis of CT measured parameters (bone mass and density) did not identify CAD3/4 to be at increased risk of premature fracture compared to the other specimens: Specimen CAD5 had the lowest bone density and CAD10 had the lowest bone mass and neither failed prematurely. Bone architecture may have an important role to play (Lee et al., 1991). It was apparent when handling CAD3/4 that trabecular pore sizes were larger than other specimens; a property that isn't identifiable from standard CT scanners.

As discussed in Sub-section 5.5.5 and supported by computer models (Sub-section 0), cementless implants may be more susceptible to migration and bone failure. The results

reveal a statistically significant increase in strains in cementless implants (T(164)=-4.30, P=0.00003) and this is supported in the literature (Seeger et al.).

### *5.5.4 Clinical Considerations*

The UKR arthroplasties were performed in the laboratory and dissected to remove all soft tissues. Examination of the tibia resection surfaces revealed that they were not perfectly flat. Specimen CAD2 had a dip in the posterior-middle that extended up to 3 mm deep, and this had a degrading effect on fixation performance (refer to Section 6). This occurred because under minimally invasive surgery (51.5% of surgeries (Schindler et al., 2010)) the posterior part of the resection is visually hidden from the surgeon. In the clinic the surgeon may have been more careful with the preparation and the final state may not have been so poor. However, the flatness of the resection is clearly an important factor to consider for UKR fixation.

The keel resection is usually performed using a reciprocating saw followed by press-fit implant template. Upon dissection it was found that one of the tibiae had been over-cut, penetrating through the posterior cortex, as illustrated in Figure 68. Although the tibia did not fail here, the observation is crucial for improving future implant designs and operating procedures, and consideration for investigating fixation at the keel. This error can occur in clinical cases, when the tip of the saw passes down into softer bone (D.W. Murray, personal communication).

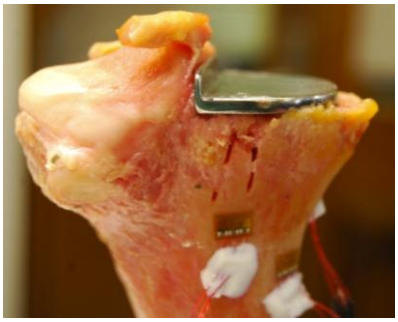

**Figure 68 - Overcut keel resection. The reciprocating saw penetrated through the proximal-posterior tibia and was unnoticed by the surgeon.**

The posterior resection of the femur is also visually hidden from the surgeon during minimally invasive arthroplasty. Figure 69 shows an overcut of one of the femora. The femoral bone is not in contact at the implant posteriorly which creates higher strains at the stem. If the surgeon is aware of the overcut, the surgeon may be able to repair with cement; however, it is difficult to get it perfect due to visual restrictions. As presented in Figure 69, the femoral posterior can be overcut. Even when the femoral posterior resection is performed parallel to the implant, the design does not encourage cement pressurisation

when the implant is inserted (Clarius et al., 2010). Note that the cementation of the femur in Figure 69 was done once all soft tissue was removed.

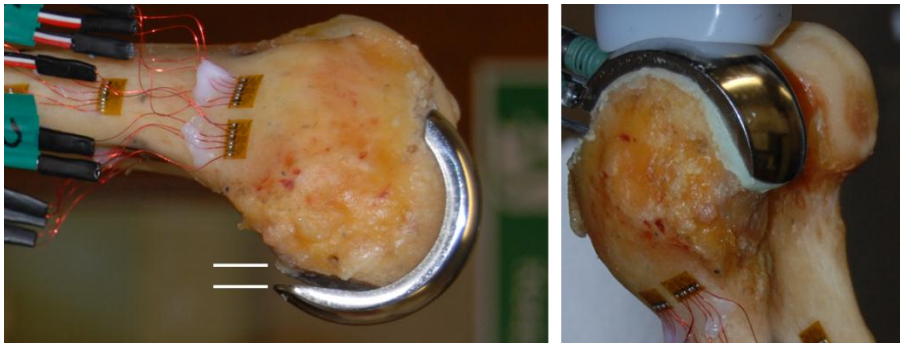

**Figure 69 - Overcut femur posterior (left) and cemented to fill the gap (right). Since the femur posterior is hidden from view during arthroplasty, it is difficult to achieve a perfect resection.**

The femoral spherical reamer penetrates deep into the anterior surface of the femoral condyle. Significant trimming of the sharp anterior rim is required to prevent impingement exposing a potential stress raiser.

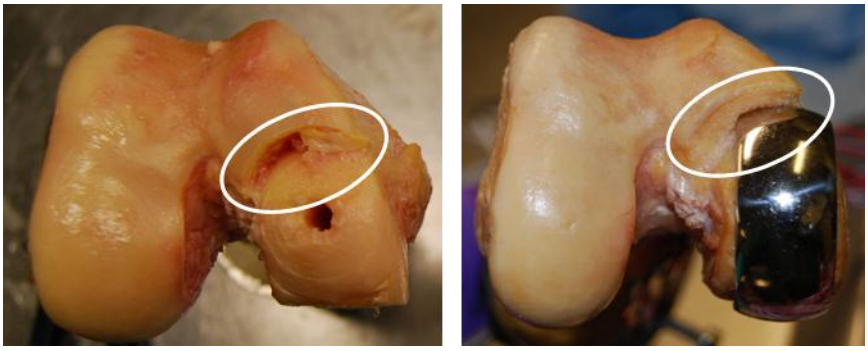

**Figure 70 - Femoral condyle after spherical milling. The cutter penetrates deep into the anterior surface and significant anterior trimming is required to prevent impingment.**

Once all testing was complete the specimens were loaded to fracture. The tibiae fractured at the resected corner (Figure 71) and the femora fractured at the reamed corner (Figure 72).

**Figure 71 - Implanted tibia which failed at the resection corner. The bone around the whole implant fractured at a depth of 2-8 mm from the cement-line.**

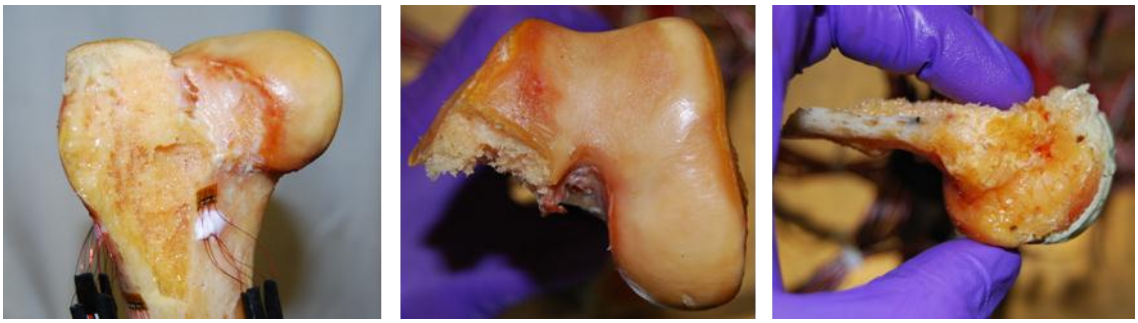

**Figure 72 - Implanted femur which failed at the anterior resection.**

The implications of the observations on fixation have been considered and discussed in the preceding chapters of this thesis.

### *5.5.5 Cemented Versus Cementless Fixation*

The cemented fixation of tibial implants produced lower bone strains compared to cementless fixation ($T(164)=-4.30$, $P=0.00003$). However, a statistically significant difference was not found between cemented and cementless femoral implants.

The reasons for this difference (for tibial trays) were two-fold: (1) due to load distribution of the cement-layer and mantle; and (2) due to slight differences in tibial tray design. The tibial implant included a recess around the rim which was approximately 0.2-1.0 mm proud of the under-surface. When cemented, the rim had no effect on load distribution because the cement filled the void. Although the cementless version of the implant was coated in HA, the rim was still proud. Therefore, the load path was through the outside rim of the implant, creating higher strains on the cortex of the proximal tibia. The implications for fixation are that cementless implants may be more prone to migration, particularly in weaker bone. The interior bone was shielded against strain. In the clinic, the interior bone would be shielded for the first few weeks post-arthroplasty until osseointegration occurred. Once osseointegration has occurred, it is anticipated that the load path may return towards the centre. The implications of stress-shielding on osseointegration are unclear; however, clinical observations show good osseointegration with this particular type of cementless implant (Pandit et al., 2009). It must be noted that since cementless implants are chosen for patients with good quality of bone, high migration would not be observed in retrospective patient studies unless a randomised trial was conducted.

The small bone strain differences between cemented and cementless femora may be because there is negligible difference to load distribution over the implant interface. Full bone-implant contact may be occurring for both implants. The effect of the following differences must be small: (1) inclusion of a cement-mantle; and (2) design differences

(underside rim thickness of cementless implant has negligible effect when placed on a spherical bone resected surface or the bone at the rim deforms sufficiently to enable load path through the whole implant under-surface).

The bone-implant displacements of the cemented implants were less than cementless implants (statistically significant T(177)=-9.23, P=0.0001). Therefore if no changes occurred to primary fixation, we would expect it would be most likely that radiolucencies would develop in the cementless cases rather than the cemented. Since current evidence for the Oxford UKR is on the contrary (Pandit et al., 2009), we must conclude that cemented radiolucencies must be occurring due to changes to the bone-implant interface post-arthroplasty. Miller et al. (2010) reported post-mortem-retrieved cement-bone interfaces of THRs to be more compliant compared to laboratory prepared specimens. Possible factors excluded in laboratory assessments that may influence interface micro-mechanics post-arthroplasty include: (1) bone resorption due to stress-shielding; (2) bone thermal necrosis from exothermic cement or cutting tools (3) fatigue-damage accumulation with inhibited bone regenerative response.

Excessive stress-shielding can lead to bone resorption and has been related to radiolucencies and implant loosening. As presented in Sections 7 and 8 and supported by the literature (Gillies et al., 2007, Dabirrahmani et al., 2008), bone resorption can occur under the UKR tibial tray. However, there is little evidence to suggest that bone resorption in UKR is catastrophic and is solely responsible for failures; this is supported by the studies presented in Sections 7 and 8, but it may well be a contributing factor.

Thermal necrosis of bone can occur from temperature elevation from exothermic cement or reciprocating surgical tools. A study of UKR and TKR arthroplasties showed that median maximum temperatures, 2 mm below the resection surface, were 47 °C during cutting and 37 °C during cement curing (Larsen and Ryd, 1989). A threshold temperature for bone necrosis is dependent on temperature and exposure time; estimates range from 44 °C (Eriksson and Albrektsson, 1984) to 70 °C (Berman et al., 1984). A study on rabbits (Eriksson and Albrektsson, 1984) showed that temperatures above 44 °C impaired bone regeneration.

As discussed above, bone accumulates fatigue damage and if bone regeneration is impaired, micro-fractures will coalesce and bone will fail. Figure 71 illustrates how one of the tibia bones failed just under the bone-cement interface. With inhibited bone regeneration, micromotion may increase, causing fibrous tissue to form or leaving a region of osteoporotic bone. These would appear as radiolucencies (Kwong et al., 1992) that are commonly seen in the clinic (Gulati et al., 2009a). If bone regeneration was impaired at isolated regions of

the bone-implant interface, then incomplete radiolucencies would be indicative that there was some fixation, sufficient to prevent complete failure.

### *5.5.6 Suction-Cementation*

Although there were no statistical differences between suction-cemented and normal-cemented UKR bone strains or bone-implant displacements with the pooled data, there were statistical differences when individual parameters were assessed. Comparing cortical bone strains (rosettes 1 and 2) showed that suction-cemented cortical bone strains were lower than normal cemented strains ($T(33)=-2.22$, $P=0.03$).

There were also statistical differences between individual pairs of knees: In all pairs, except CAD3/4, the higher density tibia pair (irrespective of cementation method) had lower strains - statistically significant for CAD1/2 ($T(19)=-2.69$, $P=0.015$) and CAD5/6 ($T(19)=-2.56$, $P=0.024$). For the exception CAD3/4, the lower density tibia pair (suction-cemented) had lower strains ($T(19)=-3.11$, $P=0.006$). Out of all the specimens, CAD3/4 had the smallest difference in average density (difference of 0.004 g/cm$^3$); however, CAD3/4 also fractured during cementless experiments and had to be repaired for the cemented experiments. Therefore these results may reflect the quality of the repair conducted and not suction-cementation. Note that there was no statistical difference in bone density between the randomly selected normal-cemented and suction-cemented knees ($T(4)=1.34$, $P=0.25$).

The results suggest that both higher bone density and suction-cementation cause bone strain to reduce. However, the effect of suction-cementation is minimal compared to the effect of small changes in bone density.

Bone-implant displacements of normal-cemented and suction-cemented tibiae were also individually tested for statistical significance. Of the three pairs that had statistical significance, they all showed that displacements were less when suction-cementation was used CAD1/2 $T(14)=4.15$, $P=0.001$, CAD3/4 $T(7)=2.39$, $P=0.048$, CAD5/6 $T(12)=2.59$, $P=0.024$. Although the other two tibia pairs did not demonstrate statistical significance, they showed an opposite trend with suction-cementation displacements higher than normal-cementation.

Only 5 cadaver pairs were compared for suction-cementation and based on the analysis described above, there was not enough statistical power in the experiments to prove overall statistical difference. It would be useful to test more specimens.

## 5.6 Conclusion

Ten tibiae and femora implanted with the Oxford mobile-bearing UKR were mechanically tested in-vitro and bone strains and bone-implant displacements were obtained for FE model validation. UKR arthroplasty was performed on all ten cadaveric specimens by a practicing surgeon. Practical considerations such as surgical technique, surgical error and qualitative observations of bone response, were noted. Effects of fixation type were assessed. Cementless fixation produced higher proximal tibia surface strains and bone-implant displacement than cemented fixation. A statistical difference between normal-cemented and suction-cemented UKR tibial implants was not demonstrated with the small number of specimens available.

Bone strains reduced with bone mass; however, no indications from CT scans were evident to identify premature failure of one of the donors. There were no observable correlations between bone mass/density and bone-implant displacements; however, the two specimens that failed prematurely exhibited elevated displacements compared to the others.

# 6 Validation of FEA Predictions of Bone Strain and Bone-Implant Motion

## 6.1 Introduction

Finite Element (FE) models require simplifications and assumptions regarding geometry, materials and boundary conditions. The impact of these simplifications and assumptions must be verified and understood in order to use the models effectively. Sensitivity assessments provide an initial verification (refer to Section 4) and physical validation provides a final check to confirm that results reflect reality.

This section describes the validation of the FE models of the tibia and femur post-UKR. Development of bone material property input parameters were described in Section 2, the boundary conditions for walking and stair-climbing were described in Section 3, and the FE techniques developed to model the UKR tibia and femur were described in Section 4. In light of the literature review and studies described in Sections 2 to 4, validation is important to prove credibility of the computer predictions of UKR bone strains and bone-implant micromotions.

In Section 5, the in-vitro mechanical experiments conducted on 10 human cadaveric knees were described, and the results presented and analysed. The measured bone strains and bone-implant displacements have been compared to FE model predictions in this section.

There are distinct challenges with modelling the proximal tibia and distal femur: (1) 2-4mm tetrahedral elements will not capture the thin 0.2 mm cortical bone (cortex) surrounding the proximal tibia or distal femur; (2) bone strains are sensitive to bone material property allocation; (3) there is uncertainty in the knee forces due to limitations of the literature. Most validation studies performed in the literature are of diaphyseal bone strains (of thick cortical bone). Validating metaphyseal bone strains (of the proximal tibia and distal femur) is distinctly more challenging: Not only is modelling difficult (thin cortex), but measurement of bone strains is difficult (due to difficulty of attaching strain rosettes to such regions).

There are numerous examples of the validation of predictions of bone strains in the literature. A basic form of validation (and by far the most economical) is validation against composite bones (Cristofolini et al., 1996). However, composite bones are simplistic, they do not accurately capture: (1) the inhomogeneous and anisotropic behaviour of bone; and (2) inter-specimen variation. In-vitro validation against cadaveric specimens is more challenging

due to the complexities associated with specimen preparation; bone cortices have to be carefully prepared for strain gauge attachment and the experiments have to be conducted within a few days to ensure that specimens do not decompose. Most cadaveric validation studies in the literature have used only one specimen (Barker et al., 2005, Bitsakos et al., 2005, Chong et al., 2010, Gray et al., 2008, Gupta et al., 2004). Recent studies have included multiple specimens (Schileo et al., 2007, Varghese et al., 2011).

The following study is the first to validate multiple UKR tibiae and femora for bone strain and bone-implant displacement. This section demonstrates the reliability of the method developed in Section 4 and the FE models developed herein.

## 6.2 Method

### *6.2.1 Geometry Generation*

Eight separate FE models (4 femora and 4 tibiae) were developed to represent cadaveric bone specimens tested in the laboratory. The models were developed in line with the conclusions of Section 4. Solid tetrahedral quadratic elements, of mesh size 2-4mm, were used. The bones were CT scanned using a “Definition AS+” Computed Tomography (CT) scanner (Siemens Healthcare, Germany) as described in Sub-section 4.3.1. The coronal voxel sizes were in the range 0.5-0.7 mm and slice thicknesses were 0.5-0.7 mm.

As described in Sub-section 4.3.2, the tibiae and femora were segmented manually using AVIZO 6.1 software (Visualization Sciences Group, USA) and the surfaces smoothed and meshed using triangular elements of 3 mm length. Separate meshes of the cortical bone geometries were generated. The surface geometries were imported into MARC Mentat 2010 software (MSC Software Corporation, USA) where the cortical and cancellous geometries were merged together while maintaining the cortical-cancellous boundary. The bones were transformed into a new axis (Anatomical Tibial axis for the tibia and Posterior Condylar axis for the femur, as described in Sub-section 4.3.2) based on identifiable bone landmarks.

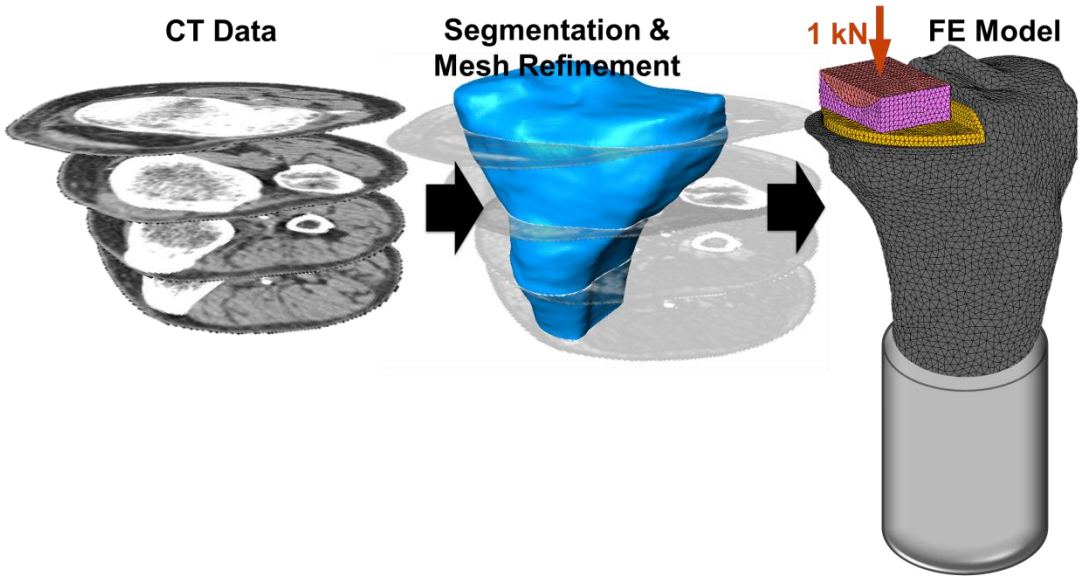


**Figure 73 - Development of FE models from CT scans.**

As described in Sub-section 5.2, the cadaveric specimens were registered using the Polaris Optical Tracking System (Northern Digital Inc., Ontari, Canada). The positions of the strain gauges, LVDT anchor points, implant resections, and steel base were measured relative to the surface profile of the specimen. The registered points were mapped onto the bone models. The virtual implantations were performed as described in Sub-section 4.3.5 so that the implants were aligned to the mapped points. The five 5x8 mm strain gauge rosettes were represented with eight elements forming a diamond around a central node, four corner nodes and 4 mid-side nodes. Single nodes were positioned at the LVDT anchor points. The surface nodes of the bone shafts that corresponded to the positions of the steel pots were fixed in x, y and z coordinates.

### *6.2.2 Mesh Parameters*

Both cemented and cementless implant models were developed for the tibiae. The cementless implant models included a contact interface between the implant and bone, with a friction coefficient of 0.4. The implant was in contact around the rim (four elements wide, 1.2 mm size elements), and the underside inner surface (hydroxyapatite coated region) recessed by 0.2 mm. The cementless models were formed of linear tetrahedral type 134 elements and the proximal tibial cortex modelled using 0.2 mm thick linear triangle shell type 138 elements (refer to Sub-section 4.5). The cemented implant models shared nodes at the bone-cement and cement-implant interfaces. A 2 mm deep cement-mantle was modelled (refer to Sub-section 4.4). The cemented models were formed of quadratic tetrahedral type 127 elements, with the proximal tibial cortex modelled using 0.2 mm thick quadratic one-side collapsed quadrilateral shell type 22 elements (refer to Sub-section 4.5). The shell and

tetrahedral element edge nodes were shared while the mid-side nodes were left coincident and independent (for algebraic compatibility).

The cemented implant models of the femur were similarly formed of quadratic tetrahedral type 127 elements. The models were fully fixed at the bone-cement and cement-implant interfaces with the 2 mm deep cement mantle. One of the femur models was also modelled with a cementless implant. Note that the cementless femoral implant has an additional fixation peg at the anterior portion and stretches slightly more anteriorly than the cemented version. The model was formed of linear tetrahedral type 134 elements with 1.2 mm size elements at the bone-implant interface. The implant underside inner surface (the hydroxy-apatite coated region) was recessed by 0.2 mm.

### *6.2.3 Material Parameters*

The implants were assigned with an isotropic elastic modulus of 210 GPa (corresponding to Cobalt Chrome) and the cement mantles were assigned with 1.8 GPa (refer to Sub-section 4.4).

For the baseline model, bone elastic moduli were assigned separately to the cancellous and cortical materials. The cancellous moduli were assigned on an element-by-element basis, assuming isotropy, using a linear relationship to calculate apparent density from CT grey scale values (as described in Sub-section 2.3) followed by a three-part relationship to calculate elastic moduli (as described in Sub-section 2.4). The cortical bone was represented with a single isotropic elastic modulus that was determined from an estimation of the average CT value of the cancellous bone. As illustrated by Figure 74, the elastic moduli predictions of cortical bone were lower than expected; the literature reports cortical bone moduli ranging from 14-20 GPa. The tibia showed the greatest inter-specimen variation of cancellous bone. Since the cortical bone elastic moduli predictions were unconvincing, a single cortical modulus was assigned based on the relative density of the cancellous bone.

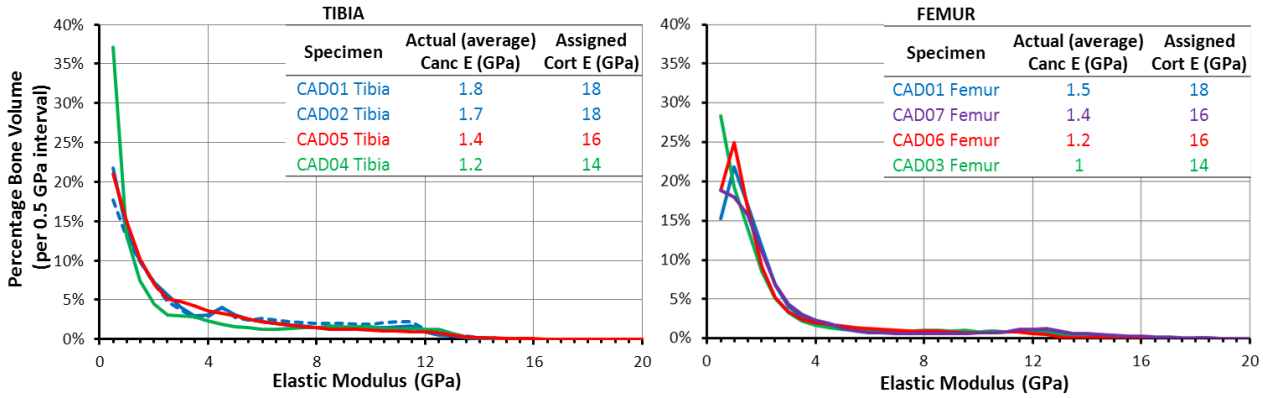


**Figure 74 - Distribution of bone volume per 0.5 GPa interval of elastic moduli in proximal 10 cm of tibia and distal 10 cm of femur specimens. The cortical bone elastic moduli were assigned based on the average of the actual cancellous bone elastic modulus (derived as described in Sub-section 2.4).**

To confirm that this material allocation technique was appropriate, variations of this baseline model were created for tibia specimen CAD1:

Baseline. Cancellous element moduli were derived from site-specific CT data. A single modulus of 18 GPa was assigned to all cortical solid elements and cortex shell elements.

Model 2. Cancellous element moduli were derived from site-specific CT data. The cortical element moduli were scaled from site-specific CT data such that average was 18 GPa (scaling factor of 1.3). A single modulus of 18 GPa was assigned to all cortex shell elements.

Model 3. Cancellous element moduli were derived from site-specific CT data. The cortical element densities were derived using an alternative linear relationship (gradient scaled by 1.2 of the original). The elastic moduli were derived as per normal from these new densities, using site-specific CT data. A single modulus of 18 GPa was assigned to all cortex shell elements.

Model 4. A single modulus of 1.8 GPa (based on average CT data) was assigned to all cancellous elements and 18 GPa to all cortical and cortex shell elements.

Model 5. Cancellous and cortical element moduli were derived from site-specific CT data. The cortical elements on the outside boundary were identified and a single modulus of 18 GPa was assigned to these solid elements and all cortex shell elements.

Model 6. Cancellous element moduli were derived from site-specific CT data. A single modulus of 18 GPa was assigned to all cortical solid elements. Cortex shell elements were omitted.

Model 7. All cancellous and cortical element moduli were derived from site-specific CT data. A single modulus of 18 GPa was assigned to cortex shell elements.

Figure 75 illustrates the adjustments made to the cortical bone elastic moduli based on the variations of models 2, 4, and 6 (described above) from baseline.

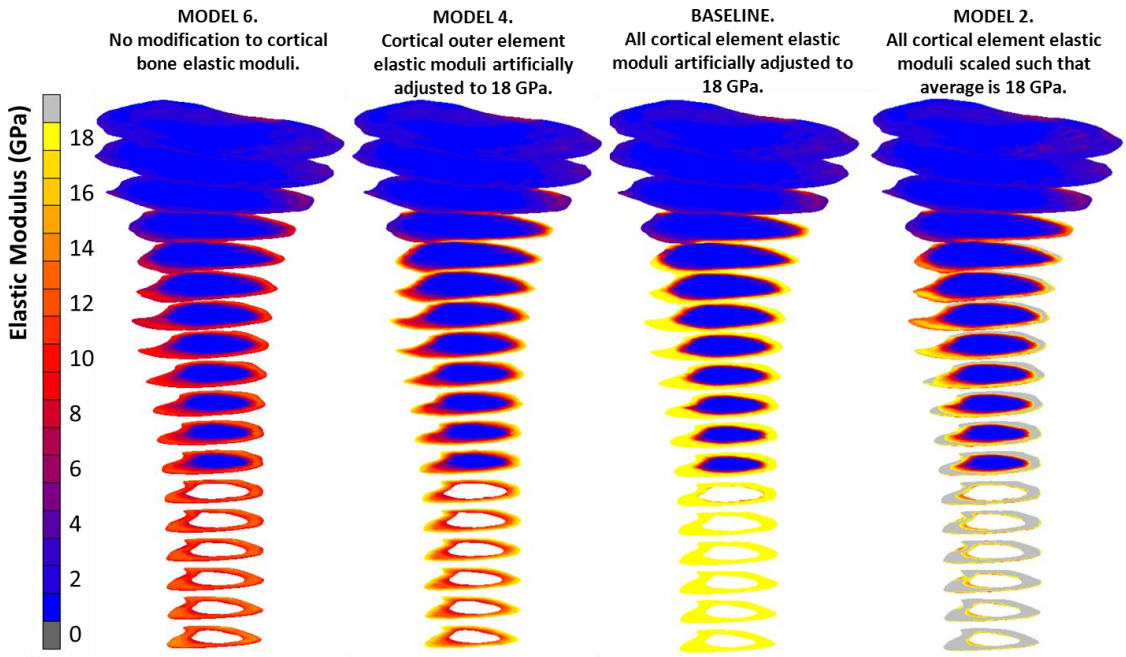


**Figure 75 - Transverse slices of FE models of specimen CAD1, illustrating the effect of adjustments made to cortical bone elastic moduli.**

### *6.2.4 Boundary Conditions*

The boundary conditions applied to the models represented the experiments performed in the laboratory. On the tibia models, a force of 1 kN was applied sequentially at 4 bearing positions: the bearing centre at (1) 5 mm anterior to the centre; (2) centre; (3) 5 mm posterior to the centre; and (4) 5 mm medial to the centre. The full 1 kN force was applied to a single node (since the implant stiffness was 50-200 fold greater than that of the bone, the force distribution is insensitive to how the force is applied to the implant). On the femur models, the force of 1 kN was applied sequentially from -10 degrees to 60 degrees knee flexion at increments of 10 degrees.

The forces were aligned to match the laboratory experiments. However, it was noticed that during the experimentation, the specimens deformed (unloaded state) with time and implants migrated under repeated forces. As the force on the bone construct was increased, the increased deformation caused small changes to the force direction. This accompanied with unavoidable misalignment errors generated friction at the implant-bearing interface. This effect was pronounced with tibial trays and was negligible in femoral components (due the

curved implant-bearing interface). In-house experiments estimated the friction coefficient of the Oxford UKR bearing-implant (of the tibial component) to be approximately 0.1; thereby imparting a potential friction force of 100 N in any direction (dependent on the deformed implant slope of the loaded bone construct). Additional micromotion FE models were developed to include bearing-implant interface friction. Four perturbations of the baseline model were assessed that included 100 N friction forces in four different directions (anterior, posterior, medial, and lateral).

One of the tibia specimens (CAD2) was imperfectly resected such that the surface was noticeably uneven. A mould was taken of the surface profile and replicated in the cementless tibia FE model in order to assess the impact on micromotion. The cemented version of model CAD2 was assumed to have a perfectly flat resection similar to all the other specimen models.

### *6.2.5 Post-processing*

The models were solved using the MARC 2010 CASI solver and post-processed in MARC Mentat 2010. The minimum principal strains at the rosette positions were calculated by averaging the values of nine nodes for each rosette (mid-side nodal values of quadratic elements were ignored). The simulated LVDT motions were calculated by outputting the x y z displacements at each anchor point and calculating the component of the relative motion in the direction of the LVDT. The post-processing was automated using MARC procedure files. The output text files were computed in Microsoft Excel and statistically analysed.

## 6.3 Results

### *6.3.1 Bone Strain*

The minimum principal strains at five rosettes, under 4 loading configurations, for eight FE models were post-processed and compared against measured values from the laboratory. The results of the cemented tibia and femur correlated more closely with laboratory values than those from cementless fixation.

Figures 76 and 77 present measured and predicted strains for all specimens of the cemented tibia and femur respectively. Although four load configurations were assessed, for clarity only one configuration has been presented (5 mm posterior to the tibial tray centre corresponds to approximately full extension of the knee (Pandit et al., 2008, Li et al., 2006)). Since sensitivity assessments of uncertainty in modelling parameters revealed that the greatest uncertainty in the modelling predictions was the position of the rosette, error bars based on a ± 2mm variation were included in the plots.

Figures 78 and 79 present measured and predicted strains at one load configuration for all specimens of the cementless implant tibia and femur respectively.

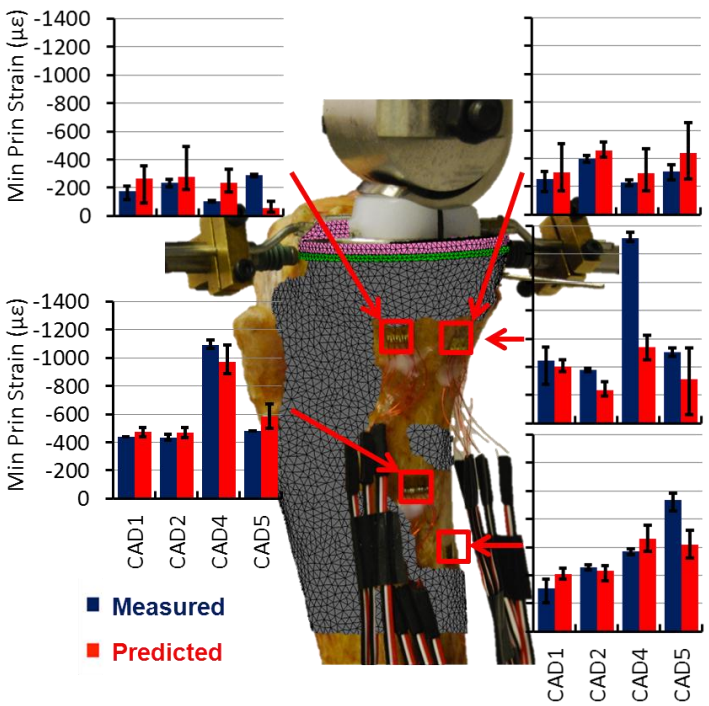


**Figure 76 - Comparison of predicted and measured minimum principal strains of the cemented UKR tibia. The tibial tray was cemented and the bearing was positioned 5 mm posterior from the centre of the tibial tray. The "measured strain" error bars represent measured range and the "predicted strain" error bars represent the sensitivity to gauge location (± 2 mm).**

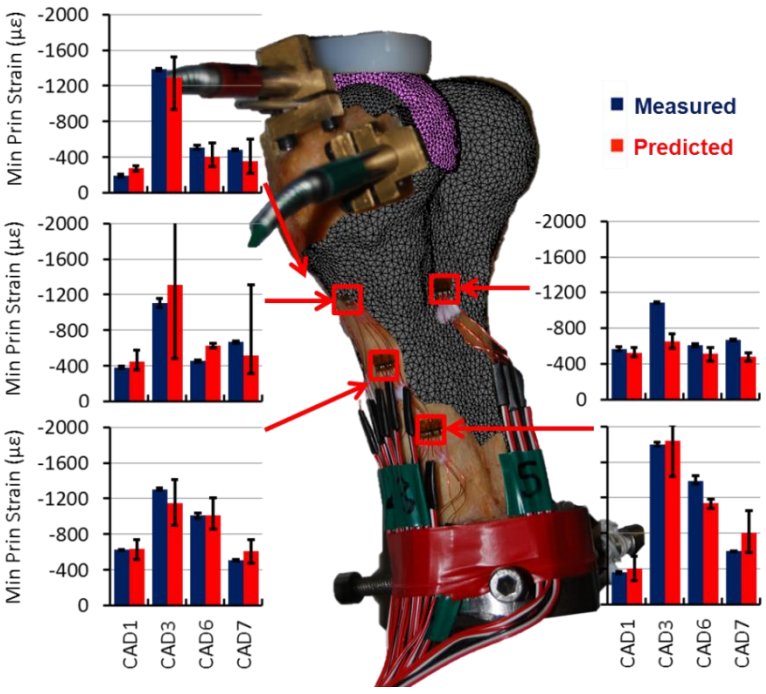


**Figure 77 - Comparison of predicted and measured minimum principal strains of the cemented UKR femur. The femur was positioned at full extension. The "measured strain" error bars represent measured range and the "predicted strain" error bars represent the sensitivity to gauge location (± 2 mm).**

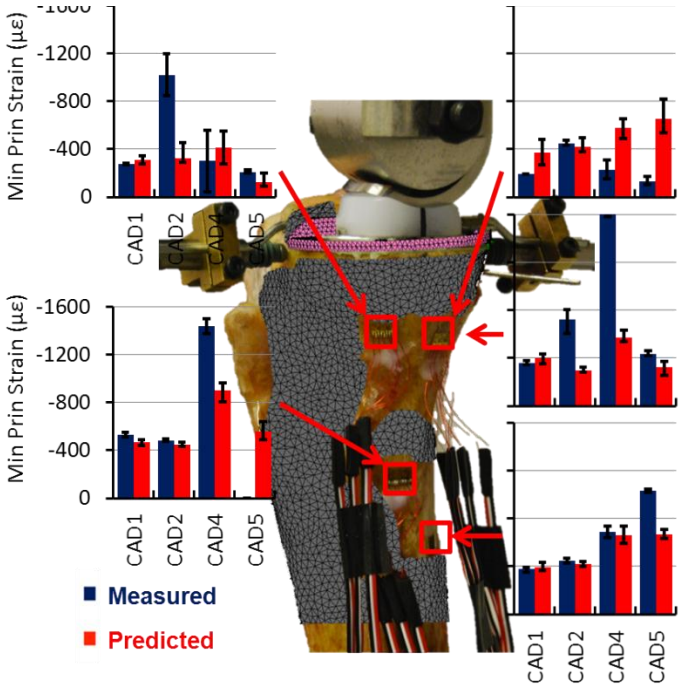


**Figure 78 - Comparison of predicted and measured minimum principal strains of the cementless UKR tibia. The bearing was positioned 5 mm posterior from the centre of the tibial tray. The "measured strain" error bars represent measured range and the "predicted strain" error bars represent the sensitivity to gauge location (± 2 mm).**

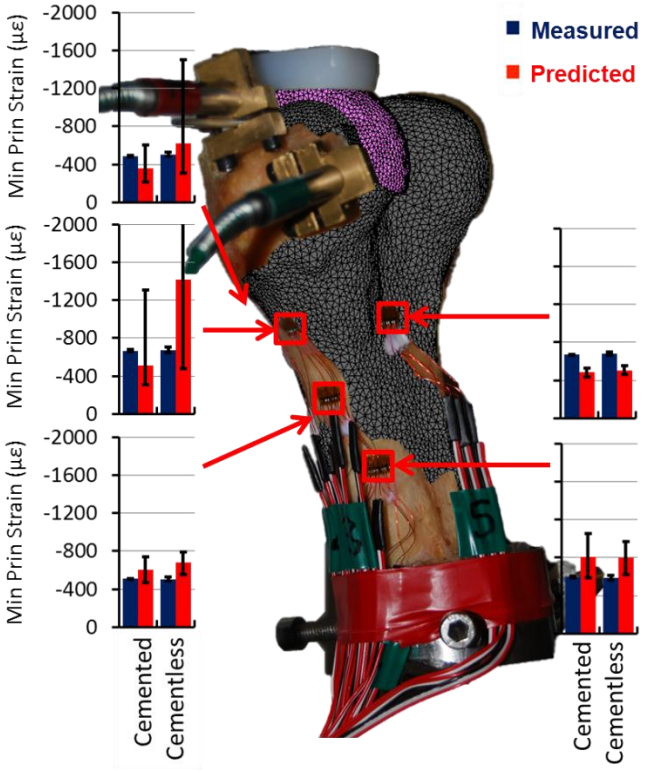


**Figure 79 - Comparison of predicted and measured minimum principal strains of the cementless UKR femur. The femur was positioned at full extension. The "measured strain" error bars represent measured range and the "predicted strain" error bars represent the sensitivity to gauge location (± 2 mm).**

The square of the Pearson product-moment correlation coefficient ($R^2$) was calculated for both cemented and cementless implant models. Pooled $R^2$ values were also calculated and those for the cemented tibia and femur are illustrated in Figure 80.

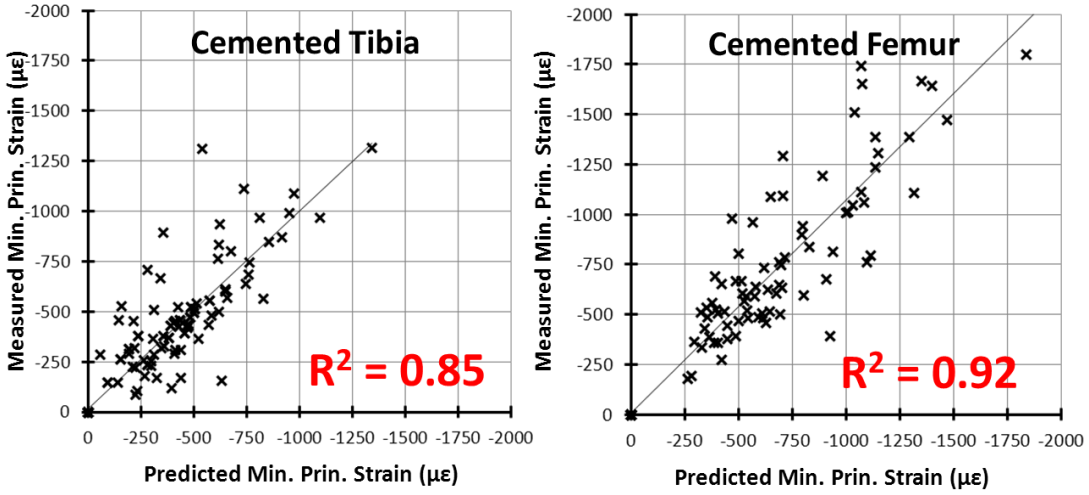


**Figure 80 - Correlation between predicted and measured strains of implanted tibia and femur of eight specimens. The plots show correlations for cemented tibial UKR (left) and cemented femoral UKR (right).**

The cemented $R^2$ values (0.85 and 0.92 for tibia and femur respectively) were significantly better than those of the cementless implants (0.62 and 0.73 for the tibia and femur, respectively).

A perfect correlation should yield a linear gradient of unity, with an under-unity gradient signifying over-predicted strains. A breakdown of correlation parameters is presented in Figure 81. The cemented femur correlation gradients were all higher than unity (for the tibia they were just below unity). This may suggest that the true femoral bone elastic moduli are slightly less than what was used in the models. Note that in Section 2, the most appropriate femoral bone density to elastic modulus relationship was found to be of the proximal femur (not distal femur).

The reason for the under-predicted strains of cementless tibia CAD2 may be due to errors introduced from imperfect resection. A mould of the resected surface showed that the cut varied as much as 3 mm from the ideal flat level (discussed below). The cementless femur correlation was skewed because of one over-predicted strain (close to the anterior cementless implant peg Figure 79). This is likely to be because there is a large strain gradient at this location for the cementless femur, (not present for the cemented femur).

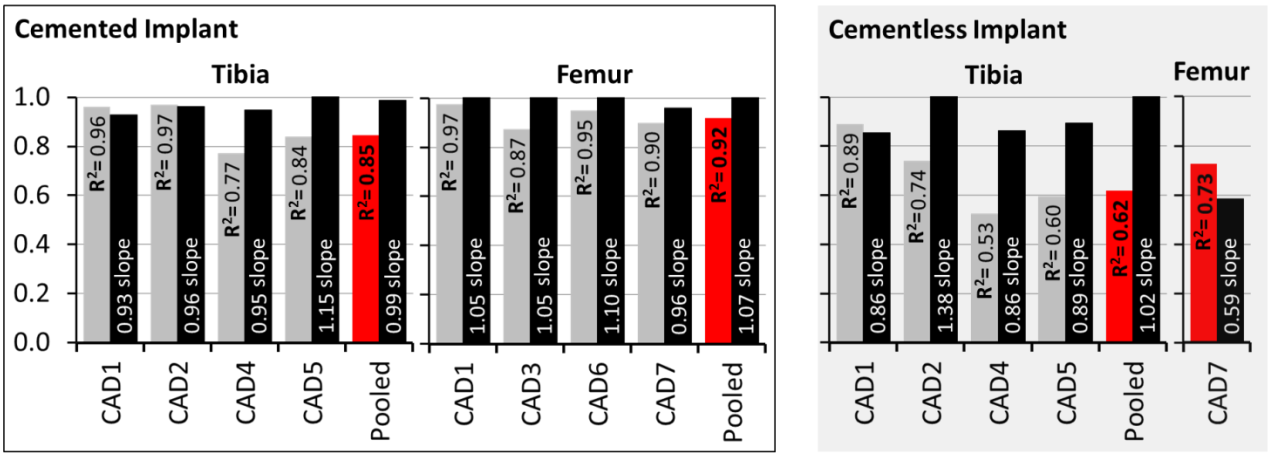


**Figure 81 - Pearson's Correlation $R^2$ values and regression slope for cemented and cementless UKR specimens of the tibia and femur. A regression slope less than unity is representative of over predicted strains i.e. elastic moduli are too low.**

### *6.3.2 Bone-Implant Displacement*

Surface-tangent (transverse) and surface-normal (superior-inferior) bone-implant displacements, under 4 loading configurations, for eight specimens were post-processed and compared against measured values from the laboratory. Since these displacements were close to the boundary of the bone-implant interface, they were considered to be representative of micromotion.

Sensitivity assessments of uncertainty in modelling parameters revealed that displacements were most sensitive to friction at the bearing-implant interface. Figure 82 compares measured and predicted transverse displacements of cementless tibial trays in specimens CAD1, CAD4 and CAD5. Predicted displacements were comparable with measured values. Specimen CAD2 is the corresponding pair to CAD1 and is presented separately in Figure 83. As demonstrated, the flatness of the resection has a significant effect on bone-implant displacement.

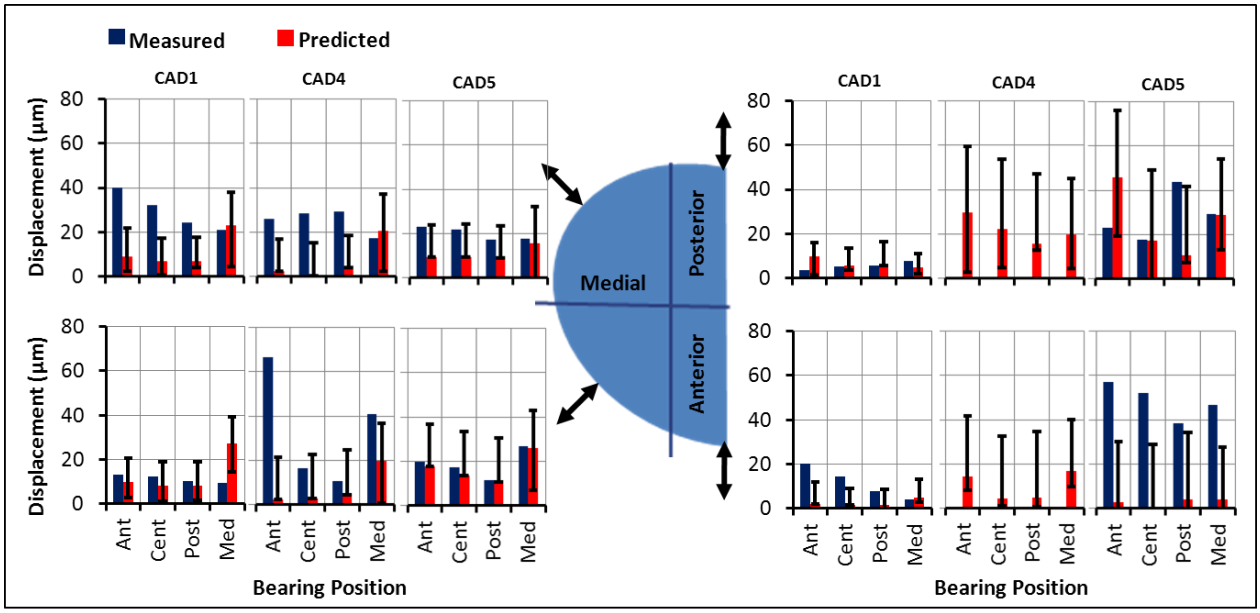


**Figure 82 - Comparison of measured and predicted transverse displacements of the cementless tibial implant. The error bars show the upper and lower bounds of displacement generated from implant-bearing friction (µ=0.1).**

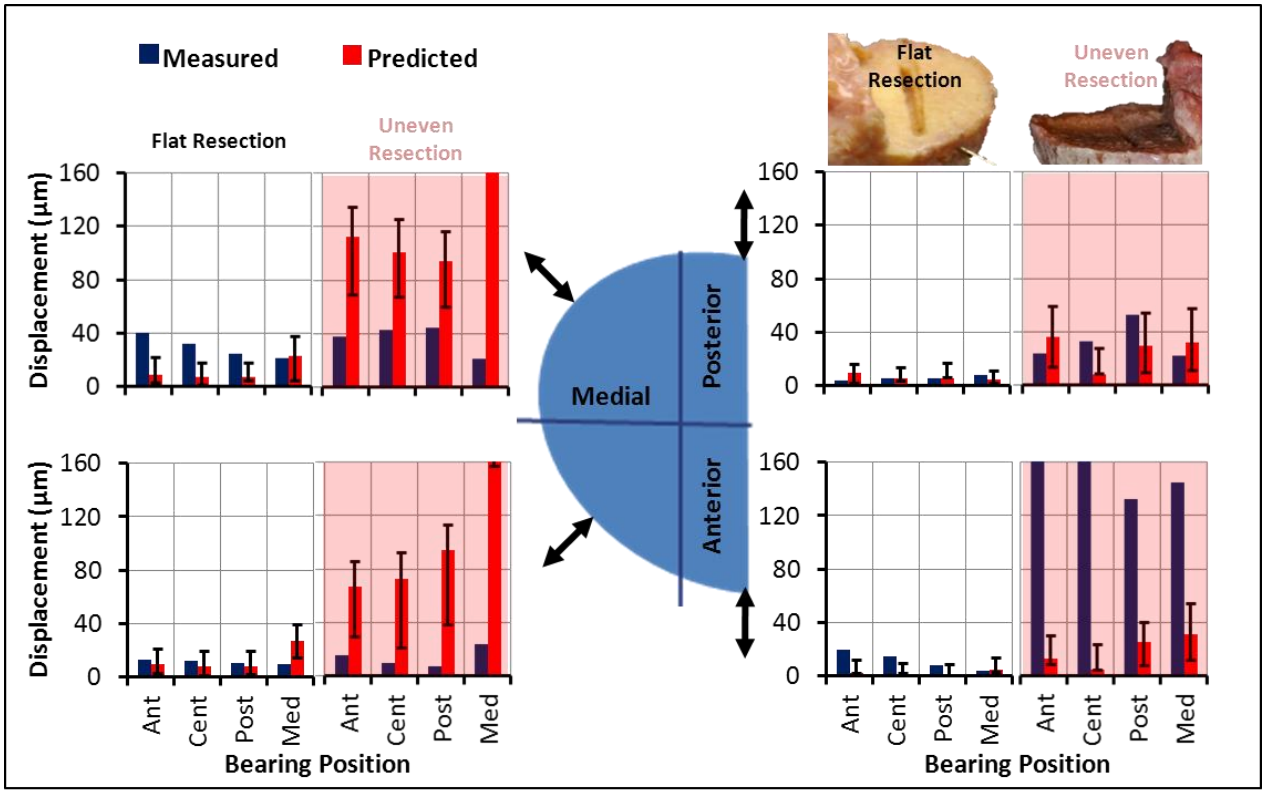


**Figure 83 - Transverse displacements at 4 points of the cementless bone-implant interface. The two specimens are a pair from the same cadaver. While FE predicted displacements were similar to those measured for the flat resection, the uneven resection predictions were less accurate. The error bars show the upper and lower bounds of displacement generated from implant-bearing friction (µ=0.1).**

The pooled Pearson correlation $R^2$ values (cemented and cementless implant specimens) are presented in Figure 84. The predicted displacements adjusted for inclusion of friction coefficient are also presented and produce $R^2$ values of 0.91 and 0.84 for cemented and cementless fixations, respectively.

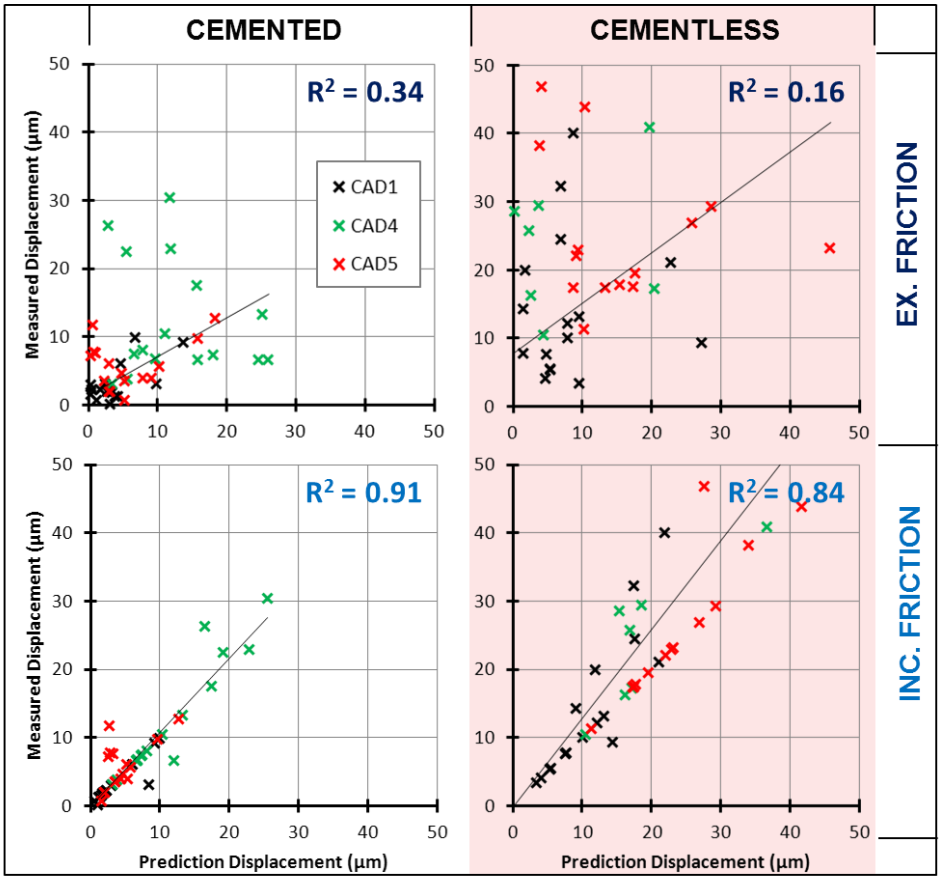


**Figure 84 - Correlation between predicted and measured tangential micromotions of the implanted tibia. The plots show correlations for cemented and cementless fixation. The bottom plots include the effect of implant-bearing friction (µ=0.1).**

There was a discrepancy between measured and predicted superior-inferior displacements which was particularly noticeable for cementless fixation as displayed by Figure 85. Interestingly, specimen CAD2, which had a dip in the middle of the resection, produced the closest displacements to those predicted. This may be because the centre dip inhibited rocking of the implant. Figure 85 shows that the superior-inferior displacements of the cemented tibial trays were small (excluding CAD4) and correlated more closely to the predicted values. The reason for the discrepancy in specimen CAD4 may be due to premature fracture of the CAD4 bone (refer to Section 5), that occurred in the vicinity of the strain rosettes.

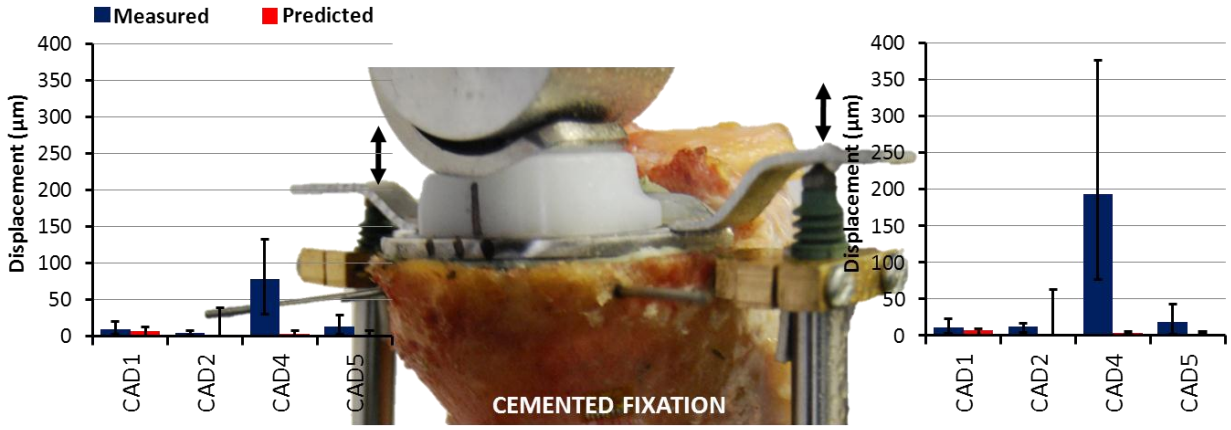


**Figure 85 - Average inter-specimen superior-inferior displacements at the anterior and posterior of the cemented tibial tray. The "measured displacement" error bars represent measured range and the "predicted displacement" error bars represent the effect of implant-bearing friction (µ=0.1).**

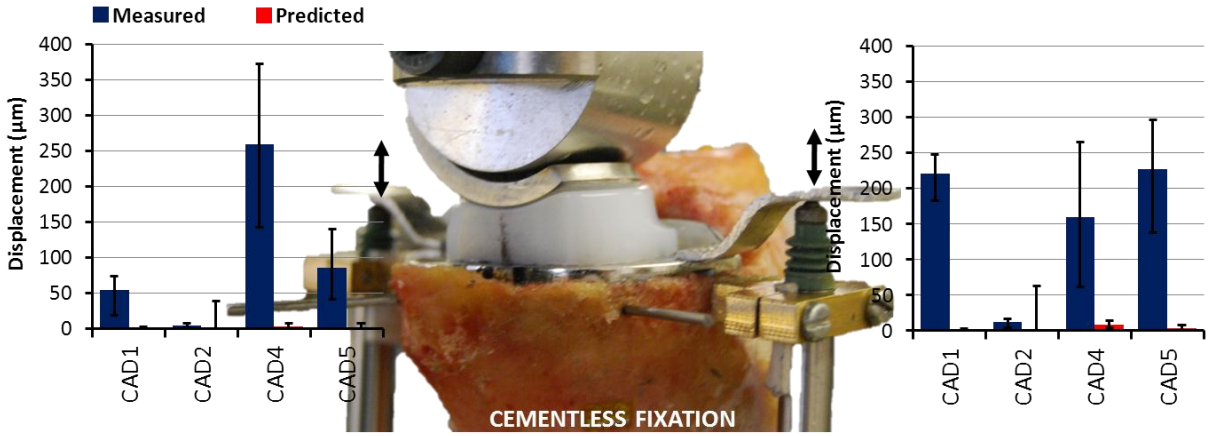


**Figure 86 - Average inter-specimen superior-inferior displacements at the anterior and posterior of the cementless tibial tray. The plots show the discrepancy between measured and predicted displacements. The "measured displacement" error bars represent measured range and the "predicted displacement" error bars represent the effect of implant-bearing friction (µ=0.1).**

## 6.4 Discussion

### *6.4.1 Bone Elastic Modulus*

The process of validation revealed the unexpectedly low predicted elastic moduli of cortical bone in all bones based on the relationship developed in Sub-section 2.4. Figure 87 presents a comparison of the correlations of different cortical bone modulus assignment strategies applied to model CAD1 (cemented implant). Sensitivity model 6 (traditional method employed in literature) produced inaccurate strain predictions; however, if the moduli were scaled up (sensitivity models 1-3), such that average modulus was 18 GPa, then the strains correlated well.

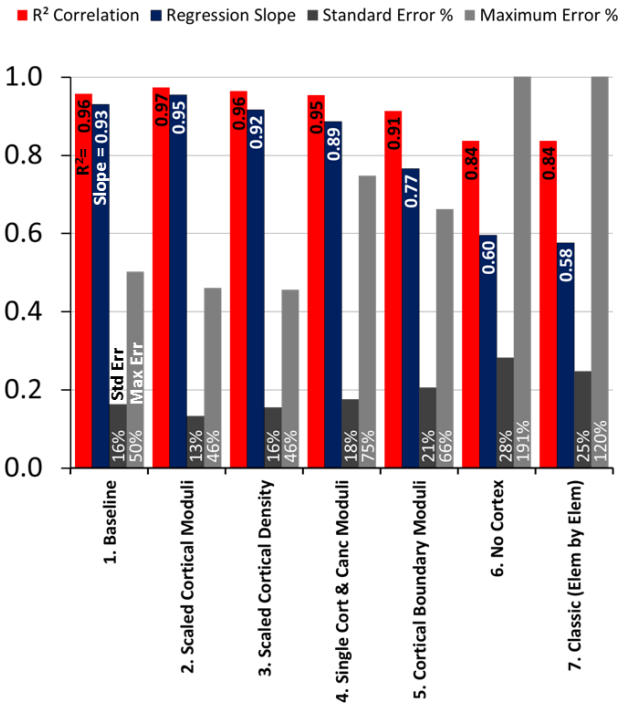


**MODEL DESCRIPTIONS**

Baseline. Cancellous element moduli were derived from site-specific CT data. A single modulus of 18 GPa was assigned to all cortical solid elements and cortex shell elements.

Model 2. Cancellous element moduli were derived from site-specific CT data. The cortical element moduli were scaled from site-specific CT data such that average was 18 GPa (scaling factor of 1.3). A single modulus of 18 GPa was assigned to all cortex shell elements.

Model 3. Cancellous element moduli were derived from site-specific CT data. The cortical element densities were derived using an alternative linear relationship (gradient scaled by 1.2 of the original). The elastic moduli were derived as per normal from these new densities, using site-specific CT data. A single modulus of 18 GPa was assigned to all cortex shell elements.

Model 4. A single modulus of 1.8 GPa (based on average CT data) was assigned to all cancellous elements and 18 GPa to all cortical and cortex shell elements.

Model 5. Cancellous and cortical element moduli were derived from site-specific CT data. The cortical elements on the outside boundary were identified and a single modulus of 18GPa was assigned to these solid elements and all cortex shell elements.

Model 6. Cancellous element moduli were derived from site-specific CT data. A single modulus of 18 GPa was assigned to all cortical solid elements. Cortex shell elements were omitted.

Model 7. All cancellous and cortical element moduli were derived from site-specific CT data. A single modulus of 18 GPa was assigned to cortex shell elements.

**Figure 87 - Sensitivity study assessing correlation of 6 different model predictions against measured minimum principal strains. Results are for tibia cemented specimen CAD1 only. A regression slope less than unity is representative of over-predicted strains i.e. elastic moduli are too low.**

There are two possible reasons for the cortical elastic modulus discrepancy: (1) cortical bone density-modulus relationship; and/or (2) partial volume effects at the cortical-cancellous boundary. The first reason may be due to errors in the cortical bone range of density-modulus relationship proposed by Snyder and Schneider (1991). Although the method was anatomic and species specific (human tibia), the accuracy of the clinical equipment used in the study was questioned in the conclusions. The gradient of the linear relationship between density and Hounsfield Unit was reported to be $4.45 \times 10^{-4}$ HU/(g/cm$^3$) which is less than half

the value used in this study ($9.2 \times 10^{-4}$ HU/(g/cm$^3$)). Although scaling the cortical densities linearly by a factor of 1.2 (Sensitivity Model 3 in Figure 87) improved the correlation, it is actually contrary to the study conclusions of Snyder and Schneider (1991). Note also that after scaling (sensitivity models 2 and 3), cortical elastic moduli values exceeded maximum known values of cortical bone (14-16 % of the elements had elastic moduli values greater than 22 GPa).That said, there is evidence in the literature that bone elastic moduli (of FE models) have been scaled to improve correlation but with no explanation given: In a previous validation study of the tibia conducted by Gray et al. (2008), separate CT-density relationships were used for the cancellous and cortical bone - unfortunately the precise relationship was not included in the article. Discrepancies regarding cortical bone densities have recently been highlighted (Schileo et al., 2008a) and this may extend to density to elastic moduli relationships. It is recommended that a detailed study, similar to that performed for cancellous bone by Morgan et al. (2003), is necessary for cortical bone, to ascertain an accurate and consistent relationship between density and elastic modulus. Without further detailed investigation of cortical bone elastic moduli relationships, the conservative approach is to use a single elastic modulus for all cortical bone. Since the UKR implant does not rest on the thick cortical bone region of the shaft, this assumption has no impact on the conclusions of Section 9.

The second reason for the low predicted cortical elastic moduli may be due to partial volume effects generated at the boundaries of cortical bone. Geometry errors from the segmentation process are in the region of 1-2 mm (1.6 mm reported by Viceconti et al. (1999)); therefore, FE elements can span across air and bone. This effect is exacerbated by the limited resolution of the CT scans - the pixels of width 0.5-0.7 mm also span across the boundary. The bone material allocation program (described in Sub-section 4.6.6) calculates the material properties based on 9 sampling points at the interior inner two-thirds of each tetrahedral element. Based on an element size of 3 mm, the program is tolerant to 0.5 mm of geometry error. Since this tolerance is insufficient, some of the outer boundary elements have artificially low moduli. The same effect occurs at the cortical-cancellous bone boundary; however, it is less pronounced - particularly in the diaphysis where the cortical bone is thicker. The improved correlation of sensitivity model 4 (compared to sensitivity model 6), as presented in Figure 87, demonstrates that the partial volume error may have some validity. However, it cannot be the sole reason for this discrepancy because the correlation is not as good as the baseline model.

It is clear that material allocation strategy has a large effect on the accuracy of the results and the literature supports this conclusion. Taddei et al. (2007) compared two material mapping strategies: (1) elastic modulus calculated from an average element density; and (2)

elastic modulus calculated from the average derived from each voxel Hounsfield Unit. The study showed that changing this simple strategy could improve correlation $R^2$ coefficient from 0.69 to 0.79. Schileo et al. (2007) compared three different material relationships against in-vitro laboratory measured strains and demonstrated $R^2$ coefficient improvements of 0.55 to 0.91. The author is unaware of any studies that have compared cortical bone material allocation strategies.

### *6.4.2 Strains: Comparison with Literature and Limitations*

The $R^2$ correlations reported in this study are comparable to FE models of the tibia and femur reported the literature. For the femur: Keyak et al. (1993) reported a $R^2 = 0.59$; Ota et al. (1999) reported 0.66; Gupta et al. (2004) reported $R^2 = 0.89$; Anderson et al. (2005) reported $R^2 = 0.82$; Taddei et al. (2006) reported a $R^2$ 0.89; and Schileo et al. (2007) reported 0.91. For the tibia: Gray et al. (2008) reported $R^2 = 0.97$ (regression gradient = 1.25); Varghese et al. (2011) report $R^2 = 0.98$ (with incomparable method using optimised material properties). Gray et al. (2008) found that the model was 25% less stiff than those measured on a cadaver. This study has improved on this by using more credible material relationships proposed by Morgan et al. (2003) (refer to Sub-section 2.6 for an explanation of why the model was 25% less stiff).

It is important to look at the literature carefully to understand the uncertainty in these types of models. Stresses and strains can give remarkably different correlations (Taddei et al., 2007) depending on the boundary conditions of the model. Lotz et al. (1991) showed that although strains did not match in-vitro experiments, femoral fractures did correlate well. The errors in these studies can be over 100% (Gupta et al., 2004) and can generate anomalies that can be omitted from the analysis (Keyak et al., 1993). It is also important to consider the magnitudes of bone strain since error increases with strain (Schileo et al., 2008a); with strains above 500 με showing exponentially increasing errors. Since the standard error for elastic modulus prediction alone (from material derivation studies), is at least 30% (for anatomic and site-specific as used in this study) (Morgan et al., 2003), these large strain errors are inevitable.

In addition to modelling errors, there are practical errors generated from correlating predicted strains with in-vitro measurements. The error from misalignment/misplacement of strain gauges can be large (Cristofolini et al., 1997); therefore, the rosette positions were determined using an optical tracking system and strain gauge rosettes were used instead of single gauges to remove the need for accurate alignment. Sensitivity assessments of uncertainty in modelling parameters revealed that misalignment of strain gauges generated the greatest uncertainty in strains. This was exacerbated if rosettes were located in regions

of steep strain gradient which tended to be towards the proximal tibia and distal femur regions (rosette locations 3-5). Since planar rosettes were used, the minimum principal strain was made up of strains from three gauges that were aligned transversely a distance of 2 mm from each other (maximum distance of 4 mm). There was also error in the accuracy of the optical markers used to locate the rosettes of maximum 1 mm. The possible errors from misalignment were included in plots of strain comparison (Figures 76 to 79). Despite not including the effects of these misalignment errors in the calculations of correlation coefficient $R^2$, the values were good. Other errors associated with the in-vitro experiments have not been included (refer to Sub-section 0).

Previous studies have applied tensile loads (as well as compressive) to specimens (Gray et al., 2008, Schileo et al., 2007) to improve the range of strain values and therefore improve the correlation coefficient. Due to the nature of the physiological knee loads and experimental set up of the implanted tibia and femur, tensile strains could not be applied to the bones. In order to produce representative linear regressions start strains of zero were included in the regression calculations. Figure 88 presents a typical strain rosette reading with strains consistently returning to the same state under repeated loading.

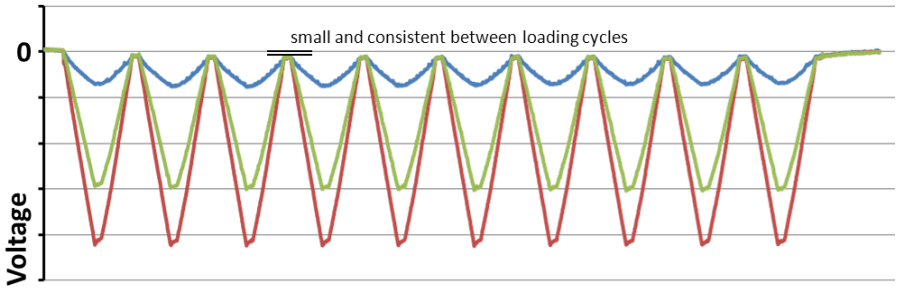


**Figure 88 - Typical strain rosette reading showing strains return to same state under repeated loading cycles.**

### *6.4.3 Bone-implant Micromotion: Comparison with Literature and Limitations*

Validation of bone-implant interface micromotion predictions is difficult due to the physical impracticalities of measuring bone-implant micromotion of cadavers in the laboratory. The in-vitro experimental set-up used in this study is the most common approach used in the literature (Cristofolini et al., 2007). Figure 89 compares bone-implant surface-tangent micromotion against transverse displacements (comparable to those measured in the laboratory) for one of the cementless tibia models. Although the displacements are indicative of interface micromotion, they are not directly related to the micromotion distributions. For example, high displacement at the medial extent does not mean high micromotion at the bone-implant medial extent. FE models must be analysed with caution.

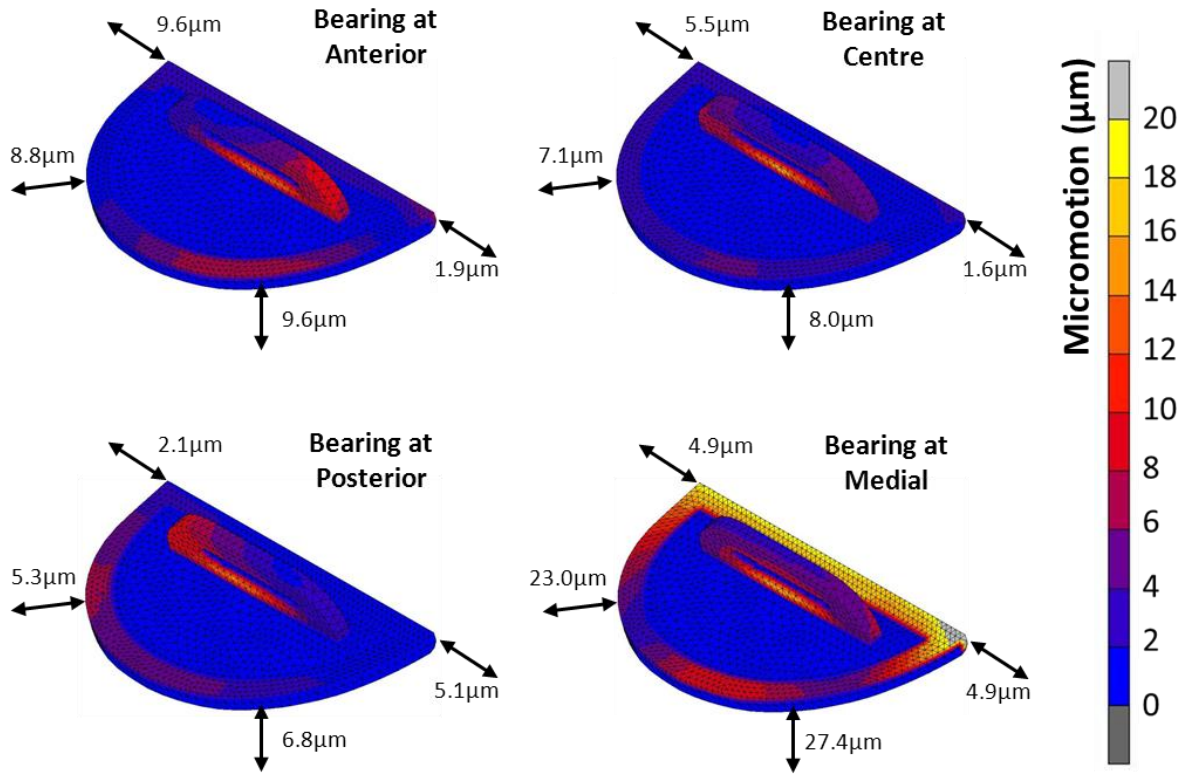


**Figure 89 - Comparison of bone-implant interface micromotion and interface displacements (representative of those measured in laboratory). Results represent model CAD1 with the cementless tibial tray.**

Implant-bone interface mechanics is complex and was greatly simplified in these FE models (a classical approach used in the literature). The laboratory measured surface-tangent (transverse) displacements were vastly different to the surface-normal (superior-inferior) displacements at the interface; therefore, they have been treated separately. As presented by Figure 84, the transverse displacements were comparable to measured values once frictional errors were taken into account. However, the superior-inferior displacements were orders of magnitude larger than predicted displacements. The largest differences were seen for the cementless implant, as presented in Figure 86. The reasons for this discrepancy are probably due to a combination of: (1) a simplistic interface model; and (2) non-flat implant resections.

The bone-implant interfaces were assumed to be perfectly flat with isotropic linear elastic properties and frictional response based on a modified Coulomb's model. The resected surface actually consists of open trabecular cells that are cut leaving thin pillar-like structures resting against the implant. The assumed elastic moduli are for interior bulk trabecular cellular structures (refer to Sub-section 2.1 for a detailed discussion of theory), i.e. for non-resected bone. The properties of open pillar-like structures are different because they are more prone to distortion, buckling and fracture. These interface structures are highly

deformable (in the direction of the loading); hence producing high superior-inferior displacements. Under repeated loading, without biological repair processes, these interface structures would fracture and collapse manifesting in implant migration. Implant migration was visually evident in the experiments. This phenomenon is documented in the literature; it created errors in pre-1990 measurements of bone elastic modulus that used the early version of the platen technique for resected specimens. Once this error was highlighted (Keaveny et al., 1997, Linde et al., 1992), the method was modernised to avoid end-effect errors by using extensometers to measure strain at the centre of resected specimens (refer to Sub-section 2.4).

Another reason for the high superior-inferior displacements may be due to non-flat bone resections causing implant rocking. Figure 83 shows how an uneven resection (dipping in the middle) produced higher transverse displacements. This uneven surface was included in the FE model (from a cast of the actual surface) and improved the correlation against measured values. This dip in the surface also reduced the magnitude of superior-inferior displacements (Figure 86) which may be because an implant can't rock on a concave surface. If the bone-implant interfaces of specimens CAD1, CAD4 and CAD5 were accidently resected to be convex (or became convex due to failure of outer bone edge), these high displacements could be explained.

The superior-inferior micromotion was also high in the cemented fixated implants. Studies of retrieved THR explants with micro-CT FE studies show that the cement-bone interfaces are compliant and not fully rigid (Waanders et al., 2011). Although the compliant nature of the cement-bone interface will affect strain distribution at a curved interface (acetabular-cup of THR)(Waanders et al., 2011), it should have a less pronounced effect on a flat cement-bone interface.

There is negligible literature about surface-normal micromotion and its impact on implant fixation. Surface-tangent micromotion is considered to be the more meaningful parameter in assessing osseointegration (refer to Sub-section 4.6.3 for discussion of osseointegration thresholds). Since the predicted surface-tangent micromotions were correlated with laboratory measured interface motions, this parameter is considered adequate for analysing implant fixation.

### *6.4.1 Multi-specimen Validation*

The most recent validation studies in the literature have included multi-specimens (Schileo et al., 2007, Varghese et al., 2011) and produced better correlations than older studies. Schileo et al. (2007) used an anatomy-specific material relationship that had not been previously used for femora (Morgan et al., 2003) and produced excellent correlations. Since there are

no credible cortical bone material relationships in the literature, they extrapolated the cancellous relationship into the cortical region without substantiation. Although the same source (Morgan et al., 2003) for material relationship was used in this study, the relationships weren't extrapolated into the cortical region due to unrealistic high predictions of elastic modulus. Varghese et al. (2011) got round this problem by optimising the material properties in order to improve the correlation; this supports our concern about cortical bone material property relationships being inadequate for the proximal tibia.

The value of a multi-specimen validation is important. As detailed in Section 5, there was high variation of bone strain between specimens. The specimens validated in this study were chosen based on their response to mechanical testing; they represent extremes of bone density (specimen CAD1/CAD2 most dense to CAD3/CAD4 least dense, and CAD5/CAD6/CAD7 representing the average). The denser bones produced better correlations because the strains were smaller under the same load (increased error with larger deformations (Schileo et al., 2008a)). The added complication of tibia specimen CAD4 was that it fractured during testing (refer to Section 5) and was repaired for cemented implantation. The fracture developed over repeated loading by coalescence of micro-fractures. The femur specimen CAD4 would have also developed these micro fractures, thereby modifying the effective bone moduli with repeated loads. The FE models are based on linear elastic material properties (exclude micro-fracture damage and accumulation of micro-fractures), and therefore become less accurate with increased strains and repeated loading.

## 6.5 Conclusions

Specimen-specific FE models of 4 cadaveric tibiae and 4 femora were developed. The predicted strains and bone-implant interface displacements were correlated against measured values from laboratory in-vitro experiments and the models were validated. The models are fit-for-purpose for analysis of implant fixation by predicting bone strains and bone-implant interface micromotions.

# 7 BMD Changes Post-UKR - Results of a Clinical DXA Study

## 7.1 Introduction

Bone adapts to the functional mechanical requirements to which it is exposed. Reduced activity causes bone loss whilst increased activity causes bone apposition. Trauma also causes bone to grow, and excessive forces can cause bone to migrate or deform. Functional adaptation of bone is described by Wolf's law.

After Unicompartmental Knee Replacement (UKR) arthroplasty, the bone in the vicinity of the implant will remodel to adapt to trauma and biomechanical changes. In Sections 5 and 6, primary fixation was assessed and was demonstrated to be good for both cemented and cementless Oxford UKRs. Long-term fixation is also important to assess success. Since biological processes are the driving factors for long-term implant fixation, and these are not able to be replicated with in-vitro tests, a prospective clinical study was undertaken to follow-up 12 UKR patients post-arthroplasty.

Most bone remodelling occurs within the first year post-arthroplasty (Seitz et al., 1987, Engh et al., 1987). The signs for good long-term fixation are minimal bone loss around the implant; which is usually due to minimal stress-shielding imposed by the implant. Dual X-Ray Absorptiometry (DXA) is commonly used to measure Bone Mineral Density (BMD) to quantify bone density changes of patients. Although numerous studies have been conducted on Total Knee Replacement (TKR) patients (Bohr and Lund, 1987, Petersen et al., 1995b, Trevisan et al., 1998, Li and Nilsson, 2000, Lonner et al., 2001) and Total Hip Replacement (THR) patients (McCarthy et al., 1991, Kiratli et al., 1992, Cohen and Rushton, 1995), no studies have been conducted or published on UKR patients.

The objectives of the study were:

- To identify which regions of the knee undergo BMD changes;
- To quantify BMD changes, in order to calibrate computer simulations of bone remodelling ;
- To identify whether there are any signs of stress-shielding of UKR tibial and femoral implants.

Although several studies have suggested that UKR femoral components are more likely to undergo loosening than their tibial counterparts (Saldanha et al., 2007, Goodfellow, 2006, Monk et al., 2009, Kalra et al., 2011), there are few studies in the literature that have

investigated femoral component fixation. This may be because radiographic studies are difficult to interpret (Monk et al., 2009, Kalra et al., 2011), because (particularly in TKRs) the underlying bone is hidden from view due to the curvature of the femoral implant. Since the UKR only involves a single condylar implant, the radiographs were easier to interpret. The clinical DXA study described herein (coupled with the computational analysis of Section 8) provided a new perspective on femoral component fixation.

## 7.2 Materials & Methods

### *7.2.1 Patient Recruitment*

The research ethics approval was agreed in August 2009 and patient recruitment commenced immediately thereafter.

All UKR arthroplasty patients of consultant surgeon Professor Justin Cobb (Charing Cross Hospital, London, UK and King Edward VII Hospital, London UK) were assessed for eligibility for the study and twelve patients were recruited over the course of a year. The first patient was recruited on 30$^{th}$ October 2009 and the final patient on 22$^{nd}$ October 2010. All surgeries were performed by consultant surgeon Prof. Justin Cobb and registrar Amgad Nahkla.

Patients were selected upon satisfying three conditions: (1) that they had a pre-operative knee CT scan; (2) that they would have the Oxford UKR (Biomet Ltd, Swindon, UK) on their medial condyle; (3) that they lived within 10 miles of Charing Cross Hospital. The patients were recruited regardless of whether cemented or cementless implants were used. Table 12 presents the details of all patients in the study. Patients were approached pre-surgery for initial consultation and consent was taken post-surgery. The first DXA scan was taken within 10 days from the date of surgery, with the remaining scans taken at 3, 6, and 12 months. Patients were scanned in both frontal and lateral knee orientations.

**Table 12 - Details of patients recruited for the UKR follow-up study.**

| Patient ID | Gender (M/F) | Age (Y) | Weight (Kg) | Height (cm) | Implant Type | Notes |
|---|---|---|---|---|---|---|
| 1 | M | 63 | 77 | 175 | CD | ACL deficient, significant pain in contralateral knee. Active (gardening). |
| 2 | M | 70 | 110 | 192 | CL | Happy with UKR. Active. |
| 3 | F | 68 | 64 | 161 | CD (S) | Lost patient at 1-Year. |
| 4 | F | 55 | 76 | 155 | CD (S) | Using walking stick due to contralateral knee pain. Being treated for spinal pain. Weight loss. Happy with UKR. |
| 5 | M | 67 | 91 | 176 | CL | Bilateral UKR. Happy with UKR. |
| 6 | M | 79 | 91 | 173 | CD | Intermittent pain with no correlation to activity, sometimes 'unbearable'. |
| 7 | X | X | X | X | X | Declined after 1st Scan |
| 8 | F | 50 | 81 | 150 | CD | 'Stiff' knee & low flexion at 3-months, happier at 6-months with more exercise. Ant. tibial pain during stair-descent. Post. tibial pain and ant. tibial pain at 1-year. |
| 9 | F | 63 | 75 | 152 | CD (S) | Using walking stick due to contralateral knee pain. Lateral tibial pain at 6 months. No pain at 1-year. |
| 10 | M | 79 | 95 | 185 | CL | Happy with UKR. Active (swimming). |
| 11 | F | 42 | 58 | 153 | CD (S) | Taking steroids for kidney problems, substantial weight gain. |
| 12 | F | 62 | 86 | 159 | CD | Resumed playing golf 3 times a week at 1-year. Happy with UKR. |
| 13 | M | 61 | 81 | 176 | CL | Limp and pain at 6-months. |

At 6-months, two sets of scans were taken with the patient repositioned between scans. The purpose of this was to assess the accuracy of patient positioning and repeatability of the scans.

### *7.2.2 Set-up & Equipment*

All DXA scans were performed using a GE Lunar Prodigy Scanner (GE Healthcare, Chalfont St Giles, UK). Frontal and lateral scans were performed, as illustrated in Figure 90, using equipment specifically designed and manufactured for the study. The frontal scan was taken with the tibia inclined at 7 degrees to the scanner bed (the Oxford UKR operative technique recommends a 7 degree posterior slope) while and lateral scan was taken at a knee flexion angle of 30 degrees.


**Figure 90 - Frontal and lateral scan patient alignment using specialised equipment.**

Since the scanner did not have a pre-defined setting for knee scans, the 'AP Spine' mode was selected with 'Smart Scan' mode setting deactivated. As is commonly used for knee scans (Trevisan et al., 1998), two rice bags were also used as a soft tissue substitute.

The reproducibility of the BMD measurements was calculated in each subject by making two consecutive scans at 6-months in both frontal and lateral projections, with the subject being repositioned after each scan.

### *7.2.3 Quality Assurance*

Due to organisational changes at Charing Cross Hospital, a second DXA scanner (identical type and same manufacturer, GE Lunar Prodigy) was used for scans taken from 1st January 2011 onwards. A crossover study was conducted using an aluminium spine phantom as displayed in Figure 91.

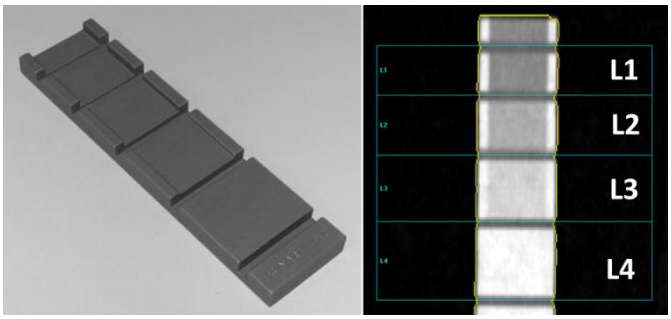


**Figure 91 - Lunar aluminium spine phantom used for the crossover study (left) with an image of the DXA scan showing the Regions-Of-Interests (right).**

Thirty-five scans were taken on each scanner over the course of four months. The average BMD and standard deviation for each spinal region L1-L4 was calculated for each group. The error was calculated based on a 95% confidence interval (2 standard deviations) from

the average. Figure 92 presents the results of the crossover study in tabular and graphical form. There was a good match between the scanners.

| | Region-Of-Interest | | | | |
|---|---|---|---|---|---|
| | Av L1-4 | L1 | L2 | L3 | L4 |
| | *Average BMD (g/cm²)* | | | | |
| Scanner 1 | 1.187 | 0.912 | 1.068 | 1.235 | 1.407 |
| Scanner 2 | 1.183 | 0.910 | 1.063 | 1.232 | 1.400 |
| | *Standard Deviation (g/cm²)* | | | | |
| Scanner 1 | 0.006 | 0.006 | 0.011 | 0.015 | 0.012 |
| Scanner 2 | 0.006 | 0.011 | 0.010 | 0.013 | 0.012 |
| | *Percentage Error (95% Confidence Interval)* | | | | |
| Scanner 1 | 1.0% | 1.4% | 2.1% | 2.4% | 1.7% |
| Scanner 2 | 1.0% | 2.3% | 1.8% | 2.1% | 1.7% |

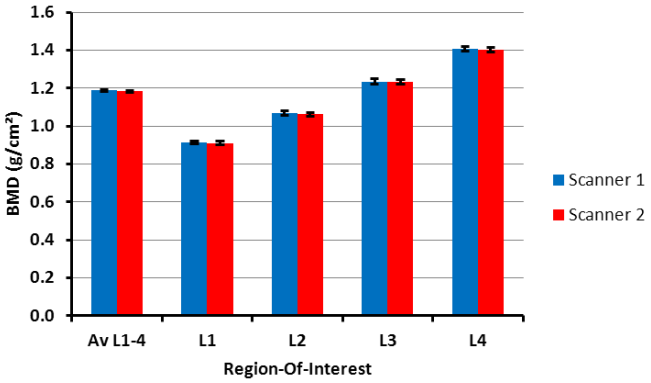


**Figure 92 - Summary of crossover study results demonstrating a good match between the two DXA scanners used in this study. The table (left) presents the average measurements of BMD and the associated percentage errors. The chart (right) compares the averages with the error bars indicating one standard deviation from average. There was an excellent match between the scanner measurements.**

Each time the scanner was used, it was calibrated with a standard Lunar Prodigy Quality Assurance (QA) Calibration Block to ensure that the measurements were consistent and comparable. All QA checks were passed. For scanner 1, between 1st July 2009 and 27th November 2010, the mean BMD medium (3.000 mA) was 0.993 g/cm$^2$ with a coefficient of variation of 0.08%. For scanner 2, between 27th November 2010 and 28th January 2012, the mean BMD medium (3.000 mA) was 0.995 g/cm$^2$ with a coefficient of variation of 0.09%. These were considered to be with satisfactory levels of accuracy (Faulkner and McClung, 1995).

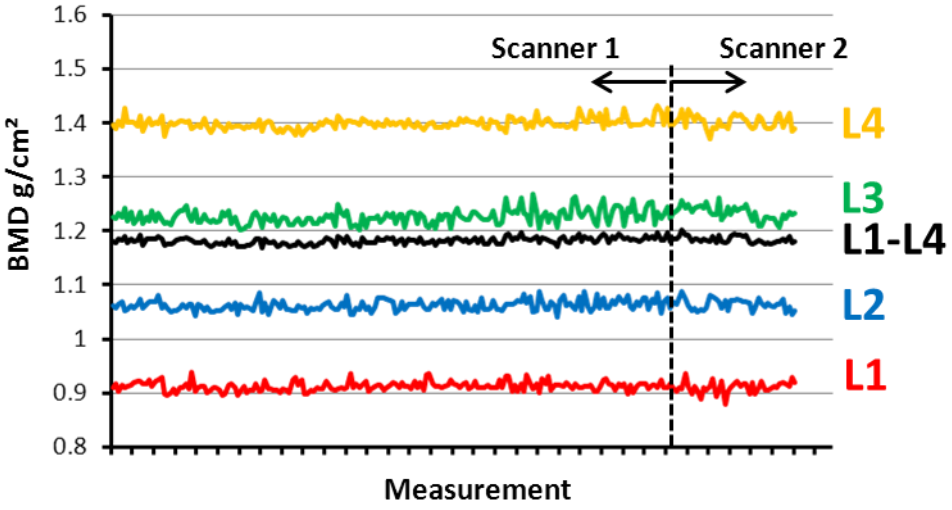


**Figure 93 - Plot of secondary calibration check results of aluminium spine phantom. The standard deviations were 0.52%, 0.96%, 0.91%, 1.09%, and 0.73% for regions L1-L4, L1, L2, L3, and L4 respectively.**

At regular intervals, a secondary calibration check was made using an aluminium spine phantom and these are plotted in Figure 93. The standard deviations were 0.52%, 0.96%, 0.91%, 1.09%, and 0.73% for regions L1-L4, L1, L2, L3, and L4 respectively. These were considered acceptable.

### *7.2.4 Analysis*

The patient data was anonymised and analysed using EnCore 2008 (GE Healthcare, Chalfont St Giles, UK). The scans were converted to 'knee' mode and ten Regions-Of-Interest (ROIs) were defined for the frontal and lateral scans as displayed in Figure 94. All the 1-year data was analysed at the same time to maintain consistency between scans.

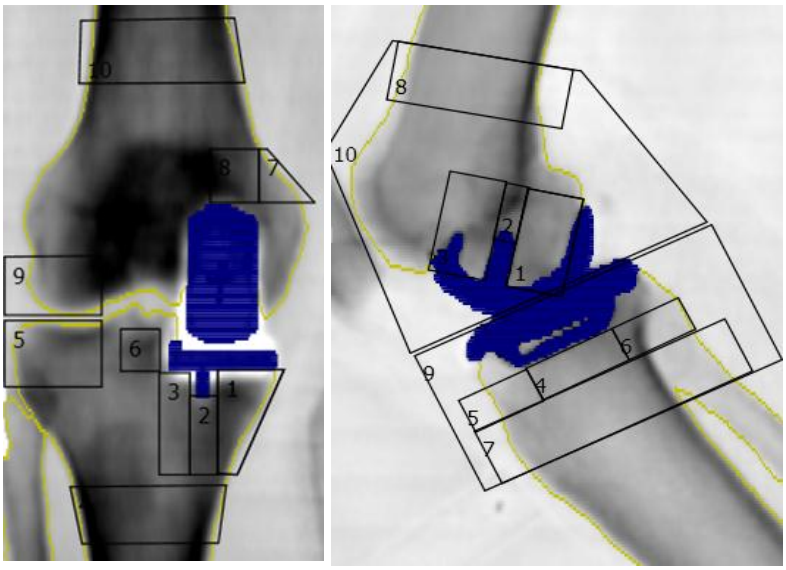


**Figure 94 - Positions of ROIs on the Frontal (left) and Lateral (right) DXA scans.**

The data was exported in to Microsoft Excel software (version 2011, Microsoft Corporation, USA) and analysed for trends and graphical output.

The Kolmogorov-Smirnov non-parametric test was used to test all variables for normality using SPSS software (IBM Software Group, New York, USA). The test confirmed that all BMD variables were normally distributed and that a paired student t-test was suitable for testing statistical difference.

## 7.3 Results

Figure 95 shows the error associated with patient repositioning. The error was calculated as follows:

$$error(\%) = \frac{1}{N}\sum_{n=1}^{N} \frac{\sqrt{(BMDi_n - BMDii_n)^2}}{\frac{1}{2}(BMDi_n + BMDii_n)}$$

where, BMDi is the first BMD reading of patient n, BMDii is the second reading of patient n, and N is the total number of patients.

The errors for ROIs F7 and F8 were large because the results were sensitive to the medial position of the patella (sensitive to the alignment of the knee). BMD was higher when the patella was medial (i.e. when it was overlapping ROIs F7 and F8). The high error of ROI L6 was for similar reasons (the BMD was sensitive to the position of the fibula).

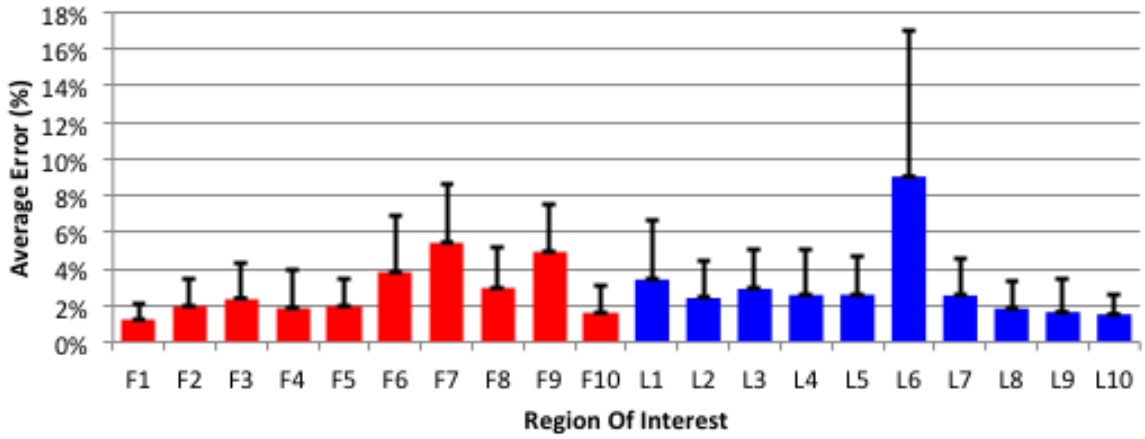


**Figure 95 - Average accuracy of the DXA BMD measurements for each ROI. ROIs F1-10 are frontal scan and L1-10 are lateral scan ROIs. The error bars display 1 standard deviation.**

### *7.3.1 Tibia*

Figure 96 presents 1-year post arthroplasty BMD change beneath the tibial intercondylar eminence; the BMD drop at 6-months was 17.9% ± 9.5% (mean ± standard deviation) and this decrease was statistically significant (T(10)=6.251, P=0.0001). At 1-year the mean BMD drop reduced to 15.1% ± 12.3% and this reduction was also statistically significant (T(10)=-4.071, P=0.0022).

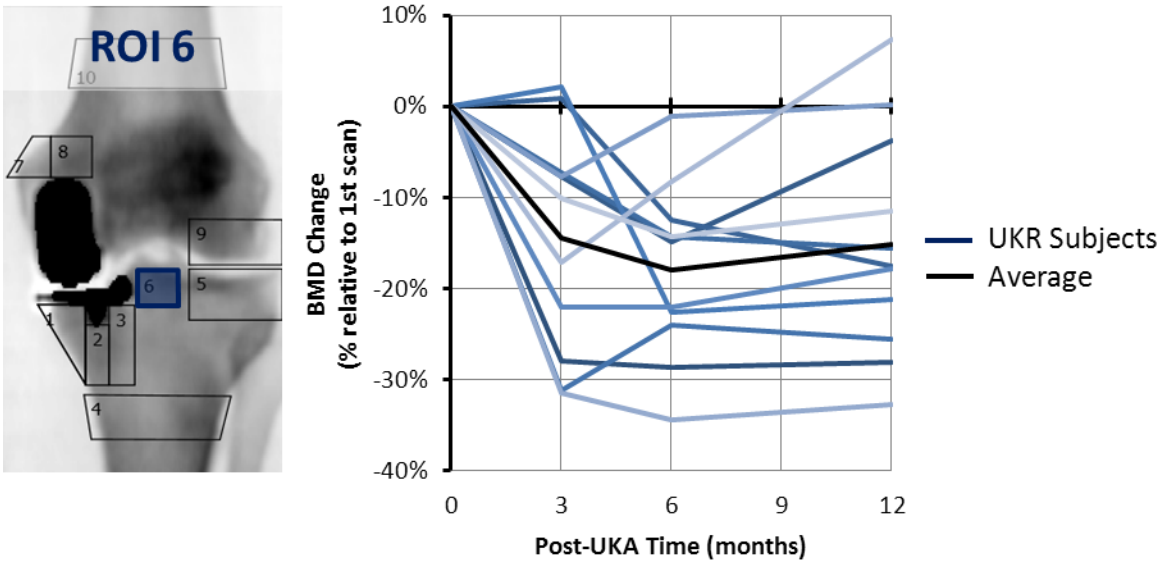


**Figure 96 - One year post-UKR arthroplasty BMD change at ROI F6 for all DXA subjects. A statistically significant drop of BMD was observed beneath the tibial intercondylar eminence at 6-months and 1-year.**

Figure 97 displays the BMD changes at three ROIs located beneath the UKR tibial tray of all subjects in the DXA study. The total average decrease in BMD under the tibial tray at 1-year was -4.0% ±16.6% (mean ± standard deviation). As presented in Figure 100, the average BMD increased under the keel (0.4%±18.2%) while it decreased in the medial region (-6.2% ± 17.6) and lateral region (-6.2% ± 14.5%). There was considerable variation between the subjects.

From the lateral view (Figure 98) it was clear that on average, the BMD under the keel was stable (-1.5%±16.4%) while it decreased significantly at the anterior region (13.7% ± 13.9%). The reduction of 13.7% at the anterior region was statistically significant ($T(9)=3.106$, $P=0.0126$).

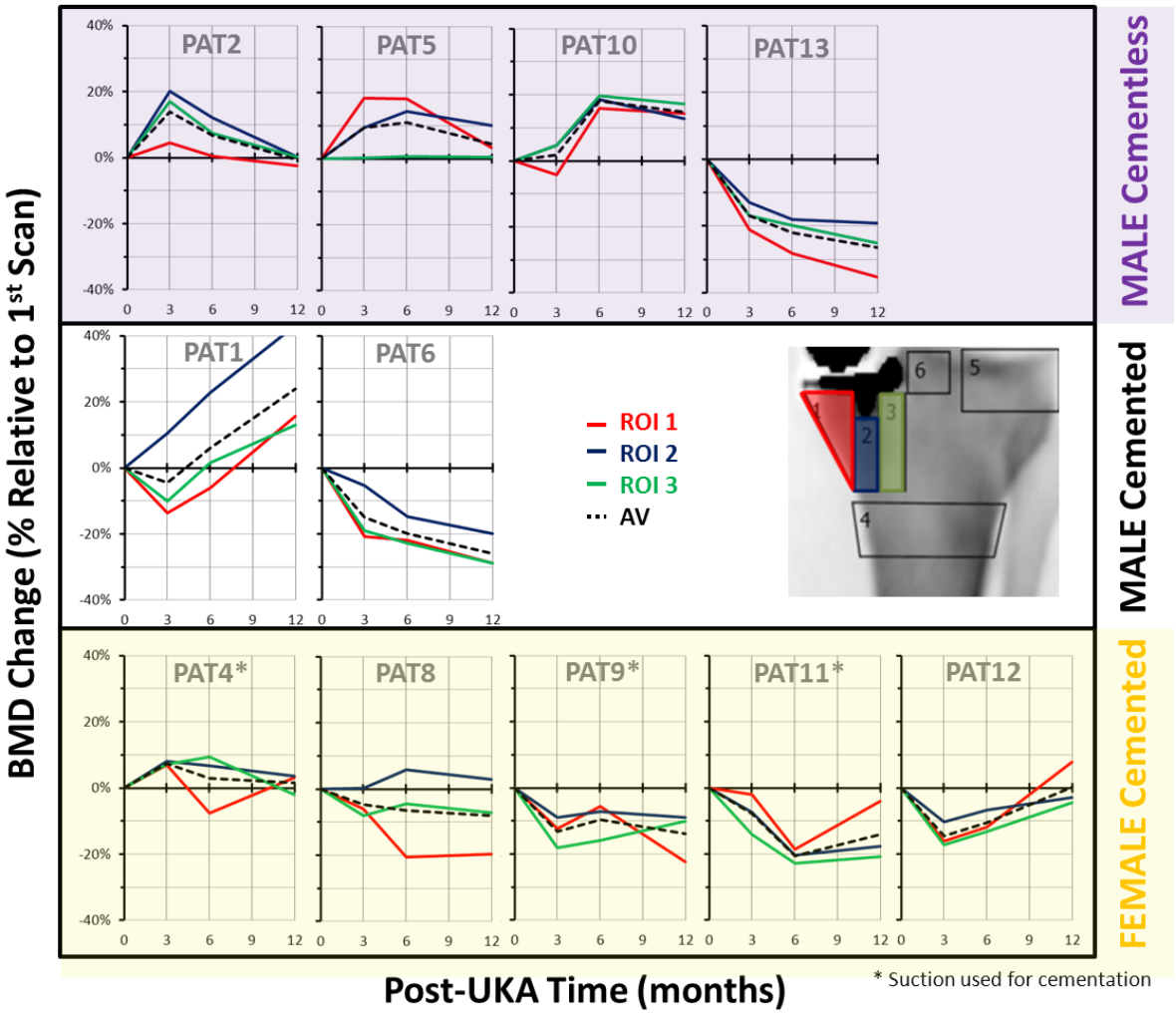


**Figure 97 - Frontal scan BMD changes under the tibial tray, of all subjects, for the course of one year following UKR arthroplasty.**

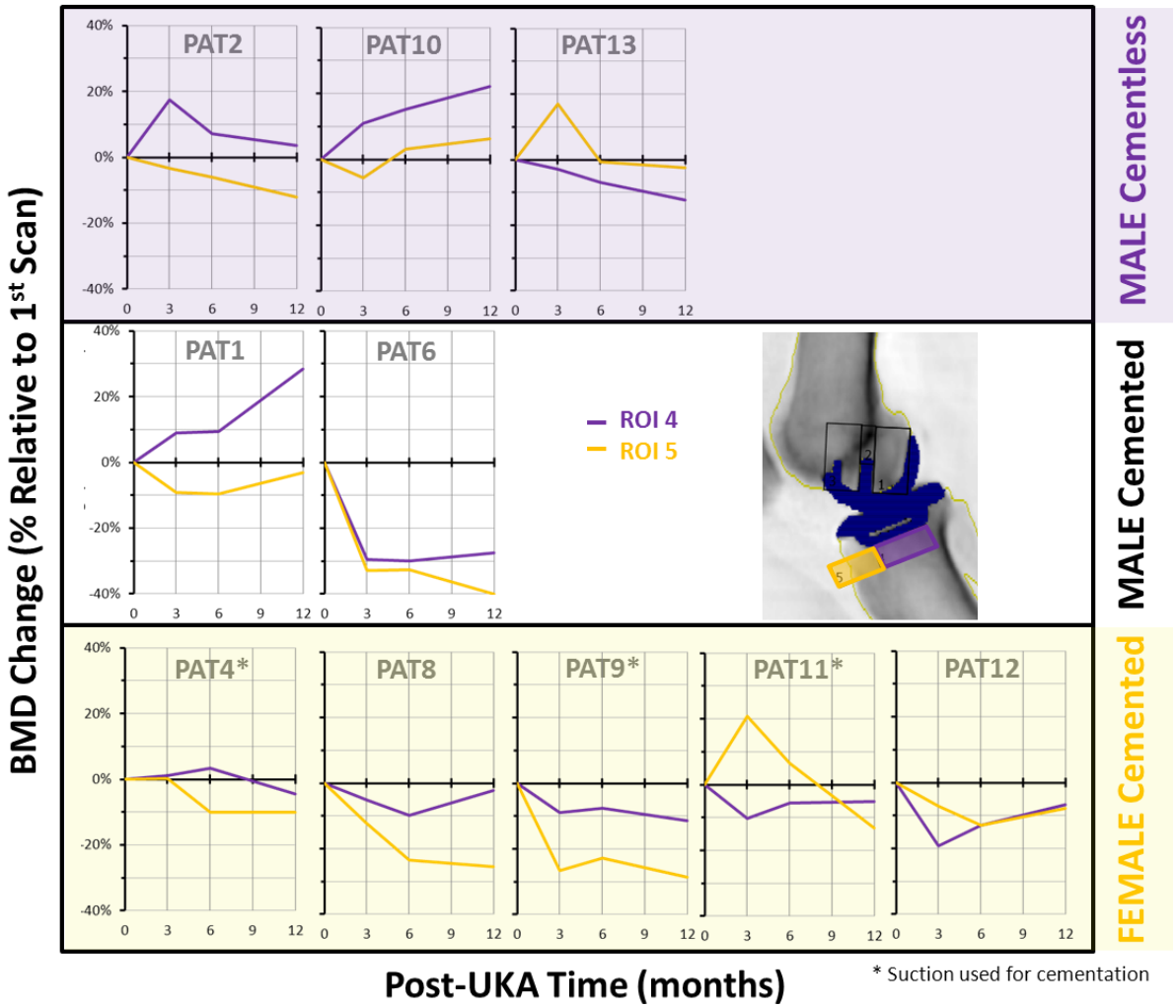


**Figure 98 - Lateral scan BMD changes under the tibial tray, of all subjects, for the course of one year following UKR arthroplasty.**

### *7.3.1 Femur*

Figure 99 displays the BMD changes at three ROIs located beneath the UKR femoral component of all subjects in the DXA study. As presented in Figure 100, the average BMD decreased under the femoral component by -12.9% ± 12.3%. The average BMD under the central peg decreased by -14.4% ± 17.5%, while under the posterior of the implant it was -11.0% ± 10.8%, and the anterior it was -13.5 ± 7.7%. These decreases were statistically significant (T(9)=3.226, P=0.0104, T(9)=5.525, P=0.0004, and T(9)=2.597, P=0.0289, respectively).

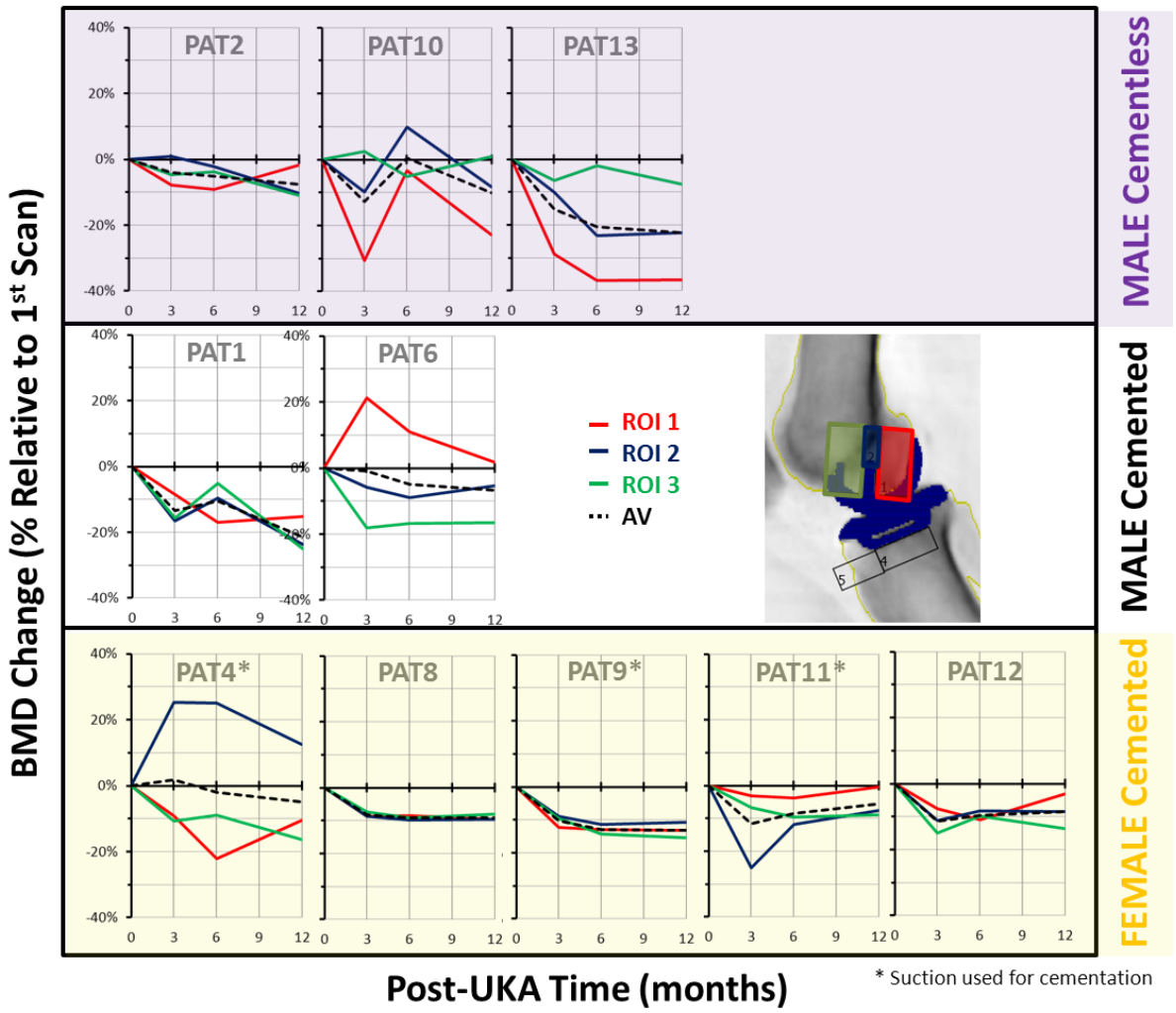


**Figure 99 - Lateral scan BMD changes under the femoral component, of all subjects, for the course of one year following UKR arthroplasty.**

### *7.3.2 Overall Observations*

Figure 100 summarises the BMD changes by plotting the average response of all patients during the course of one year following UKR arthroplasty. There was considerable difference of BMD change between the regions of the tibia while less difference was observed for the chosen regions of the femur.

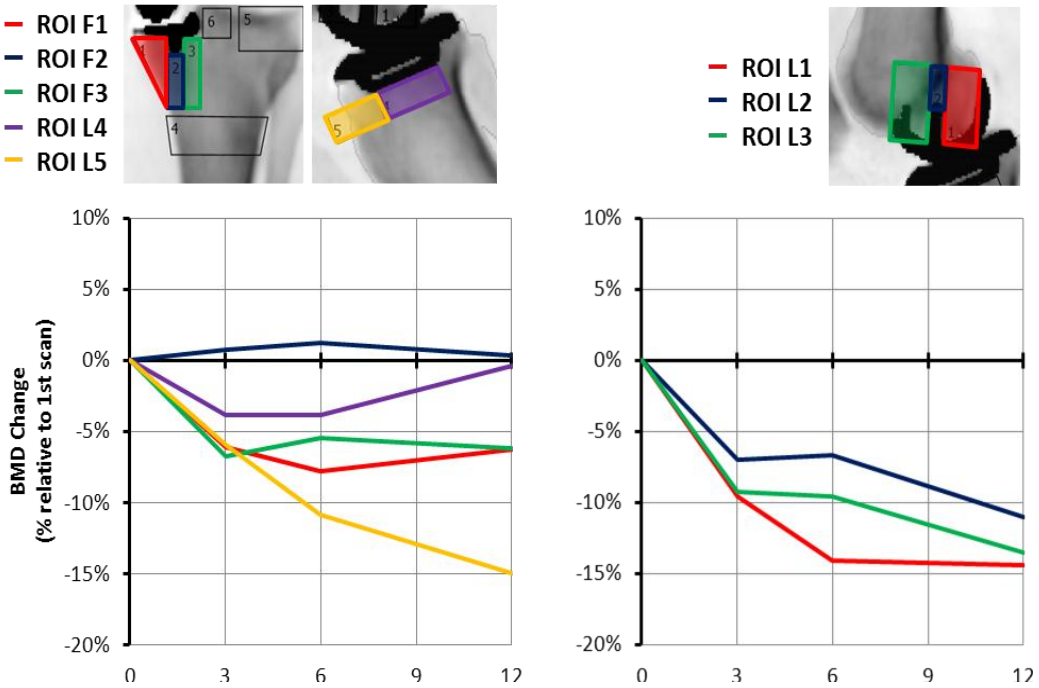


**Figure 100 - Summary of BMD changes under UKR tibial and femoral implants. The averages of all 11 subjects' BMD changes are presented for the course of one year following UKR arthroplasty.**

The overall BMD in the proximal tibia and distal femur declined by 2-5% over the course of the year, as displayed in Figure 101. There was good agreement between frontal and lateral scans of the femur. The spread and average BMD change was similar for ROIs F10 and L10/8. Although the spread of tibial BMD change was slightly different between the frontal and lateral scans (compare ROIs F4 and L7), the average BMD changes were similar.

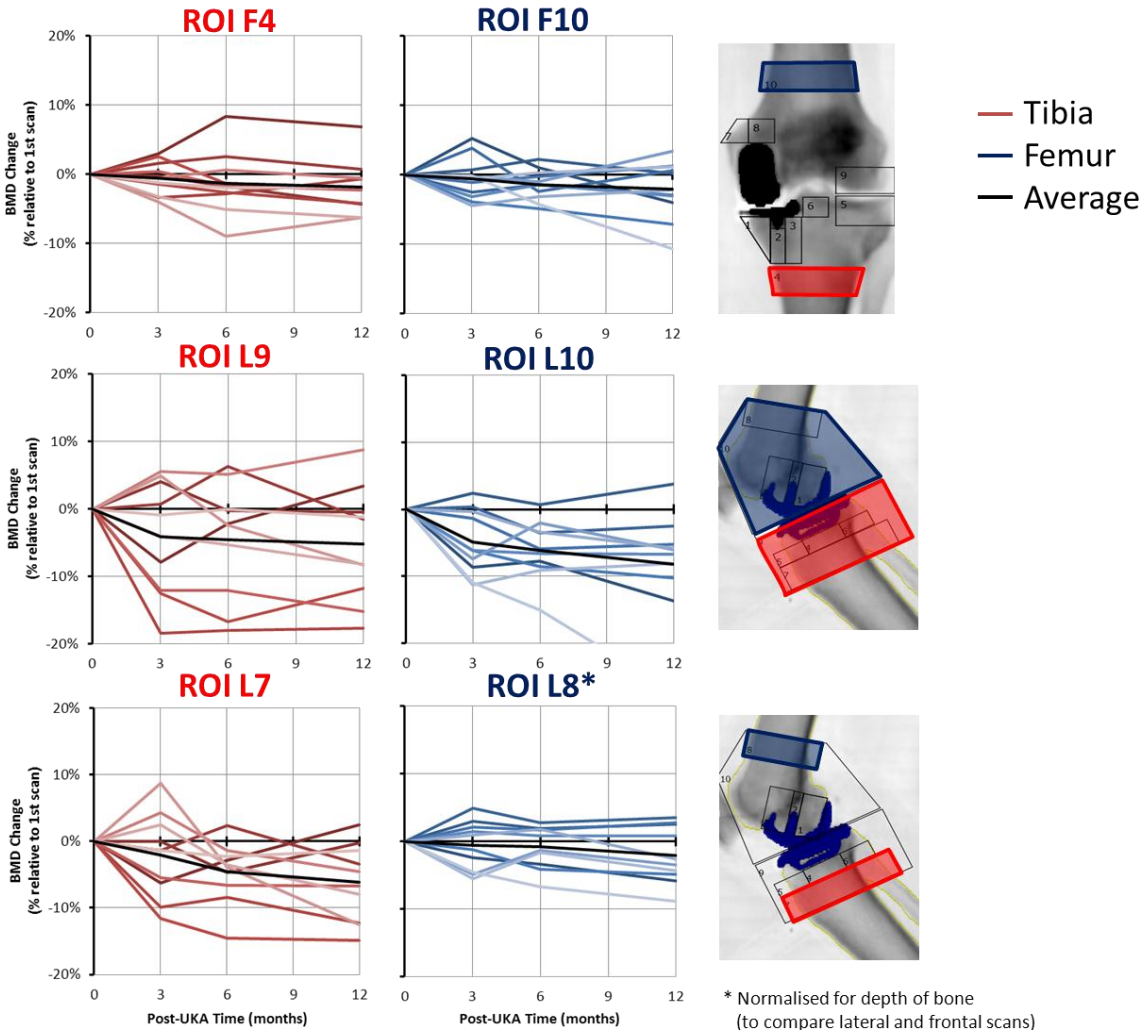


**Figure 101 - Comparison of proximal tibia and distal femur BMD change during the course of one year following UKR arthroplasty. The BMD units were normalised for bone depth for comparison of lateral and frontal scans.**

Figure 102 shows that there was an average drop of 5% BMD over the course of the year at the lateral compartment of the knee. Since the overall drop of BMD in the whole knee was similar, then this was suggestive that there was negligible change in adduction moments during daily activities. This is probably due to the combined effect of two counteractive factors: (1) varus-valgus correction (increase loading at lateral compartment), and (2) gait normalisation due to a pain-free medial compartment (reduce loading at lateral compartment).

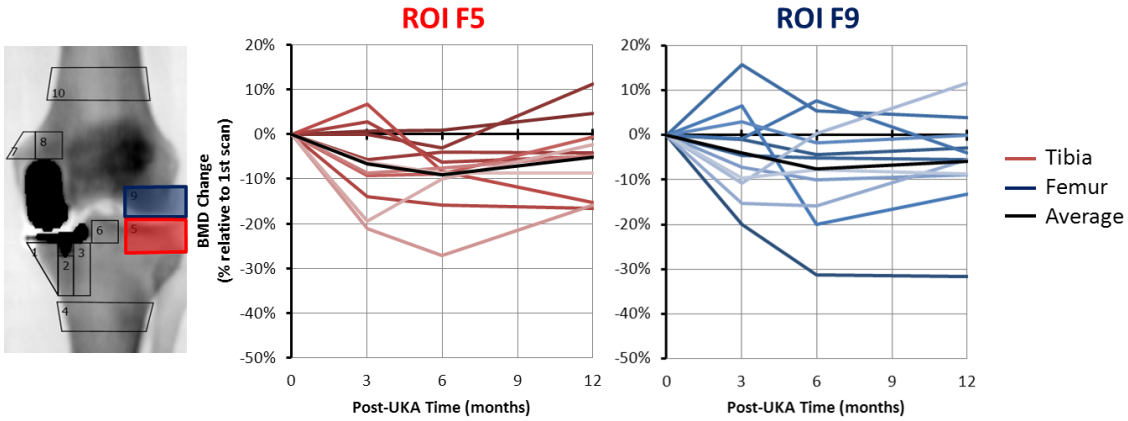


**Figure 102 - Post-operative BMD loss at the lateral condyle at 1-year.**

## 7.4 Discussion

### *7.4.1 Comparison with Literature*

This study demonstrates that there are post-arthroplasty bone density changes to the knees of UKR patients. The biggest change surprisingly occurred under the tibia intercondylar eminence which decreased steadily by an average of -17.9% at 6-months and which then reduced slightly to -15.1% at 1-year (statistically significant changes). This regional bone loss may have occurred due to (1) ACL inactivity or deficiency (Lonner et al., 2001); (2) reduced forces on the medial aspect of the intercondylar eminence post-arthroplasty; or (3) the sagittal resection may have reduced compressive strains dissipating from the medial condyle. FE analysis showed that the largest of these effects was (2). Refer to Section 8 for details of the FE modelling. The FE models showed that unless large pre-operative contact at the medial aspect of the tibial eminence was included in the model, there was bone apposition in region ROI F6, not bone resorption as seen in the radiographs.

The bone loss under the tibial tray was negligible; it was on average 1.8% which is equivalent to the overall bone loss that occurred in the whole knee (2-5%). However, the bone loss at the anterior portion was higher with an average decrease of -13.7% (statistically significant). This was balanced with 0.4% bone gain occurring under the tibial keel.

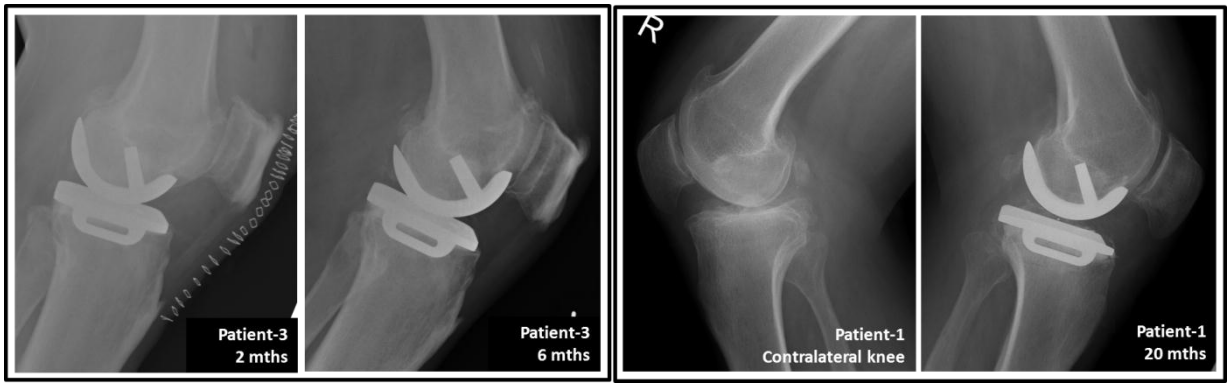


**Figure 103 - Available radiographs of study patients showing bone resorption at the anterior proximal tibia.**

The bone loss under the femoral component was more significant (-12.9% compared to 5% bone loss of the whole knee in the first year). The regions anterior and posterior to the central implant peg saw the largest bone loss (-13.5% and 14.4%, statistically significant).

Most subjects saw a large drop in BMD in the first 6 months following surgery, followed by a steady recovery. This trend is common following both THRs (Trevisan et al., 1997) and TKRs (Levitz et al., 1995). This is probably due to a metabolic reaction of the bone to operative trauma combined with the effect of the post-operative immobilization.

Although bone recovery is reported to stabilise after about one year post-TKR (Seitz et al., 1987) and THR (Engh et al., 1987)), longer-term reactions of TKRs have been reported in the literature. Seitz et al. (1987) reported a 1.5-7.5% decrease of bone mineral density at 6-12 months and Bohr and Lund (1987) found that TKR bone density recovered to pre-arthroplasty levels at 1.5-2 years. Hvid et al. (1988) found an 11% decrease in bone mineral density at 2 years and Petersen et al. (1995a) reported a statistically significant decrease of 22% at 3 years. Although Levitz et al. (1995) observed small changes in bone mineral density at 1 year, they found a statistically significant decrease (36.4%) at 8 years.

The reported regional BMD changes must be considered with respect to the overall 5% decline of bone density of the whole knee. This overall decline occurs in normal subjects with age (Khodadadyan-Klostermann et al., 2004) and has been similarly reported for TKR patients (Seitz et al., 1987, Levitz et al., 1995).

Although the patient sample sizes of cemented and cementless fixated implants were small, there were observational differences in bone density response. Figure 104 shows the average response of cemented and cementless fixation beneath both the tibial tray and femoral components. Bone loss was less for cementless tibial fixation (cementless -0.02±0.18) compared to cemented fixation (cemented -0.05±0.16) at 1-year post-arthroplasty. However, there was negligible difference for the femur (cementless -0.12±0.13

and cemented -0.11±0.06). For the tibia, the difference was most significant at 6 months (cementless fixation 0.03±0.18 compared to cemented fixation -0.08±0.10). This correlates with the conclusions of primary fixation presented in Sections 5 and 6, where it was demonstrated that tibial cementless fixation strains were higher than cemented strains (difference of femoral bone strains was small). The bone strains under the cementless tibial tray are initially high (first 6 months) and gradually reduce as osseointegration of the central tray region occurs. Similar behaviour has also been seen in TKR tibial trays, with bone loss in in the 1st 3 months for cemented fixation (Lonner et al., 2001, Li and Nilsson, 2000) and bone gain for cementless fixation (Bohr and Lund, 1987). It must noted that the decision to use a cemented or cementless implants was not randomised; surgeons tend to use cementless implants on denser ('stronger') bone which is a judgement made based on individual surgical experience. We would therefore expect that the cementless group would naturally respond better to UKR implants, particularly with evidence from the findings of Sections 5 and 6 and evidence from TKRs (Lee et al., 1991).

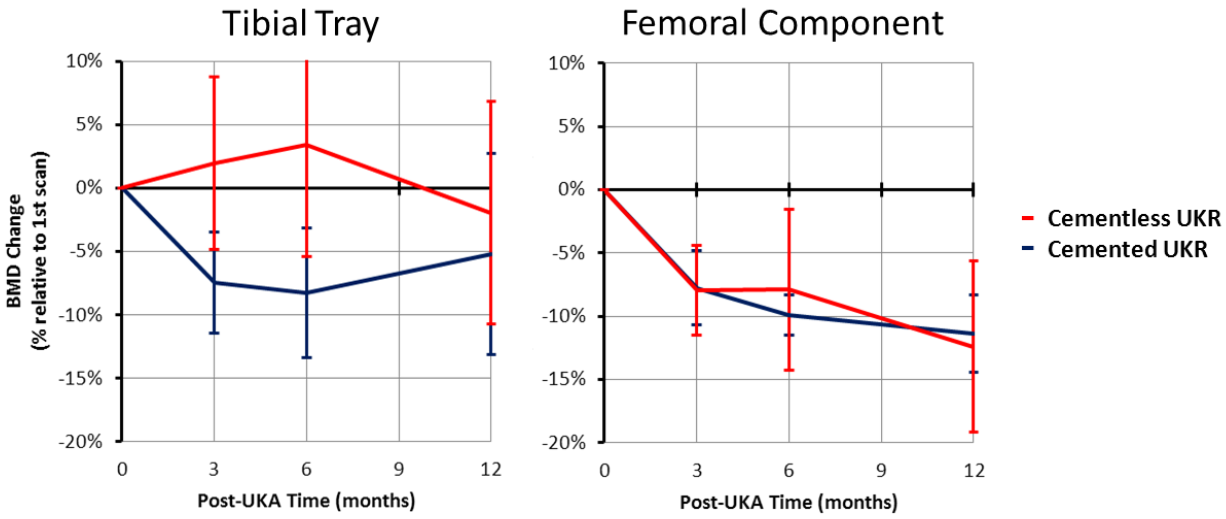


**Figure 104 - Comparison of Cemented and Cementless UKR implant average BMD changes over the course of one year post-arthroplasty, tibial tray (left) and femoral component (right). The error bars indicate one standard deviation.**

There were large differences in bone response between subjects, which is a common characteristic of post-arthroplasty DXA studies (Li and Nilsson, 2000, Bohr and Lund, 1987, Seitz et al., 1987, Lonner et al., 2001). With such a large variability between subjects, it is often difficult to ascertain the reasons for observed differences, without doing well-controlled studies with large cohorts of subjects. For example, investigations of TKR designs have revealed conflicting results: a statistical difference was found between cemented rotating and fixed bearing TKRs in a DXA follow-up study (Minoda et al., 2010) while no difference was found when a similar sample size was assessed using CT scans (Munro et al., 2010).

Another study found that a pegged tibial tray design produced less bone loss than a tibial tray with a cemented stem (Lonner et al., 2001).

### *7.4.2 Limitations*

The results of this study must be considered with regard to the limitations of the study. The sample size of 11 subjects is small and although general conclusions regarding UKR response is possible, conclusions comparing fixation (cemented verses cementless) are difficult and further complicated because choices were not randomised.

There are unavoidable confounding factors inherent in all clinical DXA trials based on individual subject characteristics that are difficult to monitor or measure. For gait characteristics, activity level, knee alignment are all factors that affect the level of knee loading: Petersen et al. (1995a) concluded that slight changes in knee loading resulted in changes in BMD under a TKR tibial tray within 3-6 months with some patients showing an increase of 2-7% and others showing a loss of 7-20%.

Although bone response is expected to stabilise after 1 year post-arthroplasty (TKR (Seitz et al., 1987) and THR (Engh et al., 1987)), individual subjects responses are variable and progressive late reactions have also been found (Brown and Ring, 1985). Year 2 data would add further confidence to the results.

The accuracy and precision of DXA for the evaluation of bone density in the proximity of metal implants has been thoroughly assessed in several studies of patients undergoing THR arthroplasty (McCarthy et al., 1991, Kiratli et al., 1992). Further evidence of the feasibility of DXA in this field comes from the studies of Robertson et al. (1994), who showed that DXA was better than the other considered methods at assessing bone mineral changes in the proximity of the TKR. DXA has a reported precision of 1.1- 7.5% when applied to THR (McCarthy et al., 1991, Kiratli et al., 1992, Cohen and Rushton, 1995) and 0.9-8.3% when applied to TKR (Petersen et al., 1996, Trevisan et al., 1998, Li and Nilsson, 2000). The precision of the present study is comparable with those reported in the literature.

The use of DXA has its shortcomings. The images are not three-dimensional so precise regional differences are difficult to assess and limited by accuracy of alignment. Repeatability between DXA scans was addressed by using the alignment features shown in Figure 90. Since images cannot be seen in real time (as is possible with fluoroscopy), the projections could not be accurately aligned parallel to the tibial tray – the rig ensured 7 degrees posterior slope as is outlined in the surgical manual.

## 7.5 Conclusions

The DXA study of the knees of 11 UKR patients showed that there were statistically significant post-arthroplasty bone density changes to the knees post-arthroplasty. Most subjects saw a large drop in BMD in the first 6 months following surgery, followed by a steady recovery. The biggest change occurred under the tibia intercondylar eminence which decreased steadily by an average of -17.9% at 6-months and which then recovered slightly to -15.1% at 1-year (statistically significant). The average bone loss under the tibial tray was low; however, the bone loss at the anterior portion was higher with an average decrease of -13.7% (statistically significant). There was a 0.4% bone gain occurring under the tibial keel. The bone loss under the femoral component was more significant (-12.9%). The anterior and posterior regions to the central implant peg saw greater bone loss (-13.5% and 14.4%, statistically significant)). The bone response of all patients was dissimilar and patient-specific. The study suggests that short-term stress-shielding of the Oxford UKR implant should not be a major concern but the study should be repeated with a larger cohort of patients to strengthen the evidence.

# 8 FEA Bone Remodelling Validation

## 8.1 Introduction

The ability to predict bone-adaptation following arthroplasty is of significant value for future development of orthopaedic implants. Numerous algorithms to model the bone-adaptation process have been proposed in the literature and some have been shown to produce realistic predictions when coupled with Finite Element Analysis (FEA) techniques. However, due to the difficulty in acquiring in-vivo bone-adaptation data there is a notable lack of clinical validation, particularly for human knee arthroplasty patients. The purpose of this section is to evaluate the algorithm developed by Huiskes et al. (1987), Kerner et al. (1999) and Chong et al. (2011) against in-vivo clinical data obtained from a one-year DXA follow-up study (presented in Section 7).

## 8.2 Background

The primary function of bone is to be stiff (resist deformation in response to both internal, and external forces) and to maintain stiffness it must be strong (resist breakage). Bone stiffness and strength can be increased by adding bone mass, by changing bone geometry, or by altering its microstructure. This process is called bone remodelling. It involves the continual replacement of old bone to maintain integrity and prevent micro-crack damage accumulation. Osteoblasts and osteoclasts are cells that are responsible for bone formation and bone resorption, respectively, and they closely collaborate in the bone remodelling process. In trabecular bone, remodelling occurs at the surface of the trabeculae and due to high surface area to volume ratios, remodelling rates are up to ten times higher than in cortical bone.

Bone adapts to the functional mechanical requirements to which it is exposed. Wolff's law describes the functional adaptation of bone, as self-optimising and able to control its mass and structure in direct relationship to its mechanical demands. Functional adaption of bone involves changes to bone architecture as well as to bone mass, which is why bone architecture is different between anatomical locations, species and levels of skeletal maturity.

The trigger for the bone remodelling process is uncertain (Pearson and Lieberman, 2004); however, it is generally assumed that micro-cracks and damage due to repeated mechanical deformation are an important factor. Since strain is a primary and directly measurable

physical quantity representing deformation, while stress is secondary (calculated indirectly), it is logical that the stimulus is a strain based variable (Cowin, 1984). The precise relationship between strain magnitude, number of cyclic deformations and strain rate with remodelling is unresolved. Animal studies have shown that bone remodelling has a non-linear dependence on strain and number of cycles (Ozcivici et al., 2010). Studies of cortical bone of rats have revealed that strain rates and magnitudes must be high (Mosley and Lanyon, 1998, Mosley et al., 1997) and strain rate affects the bone morphology (Turner et al., 1994). Studies investigating how the number of cycles affects bone remodelling have shown that temporary inactive episodes are required; increasing the number of cycles is not enough (Robling et al., 2000). Although these patterns may be similar for cancellous bone, this is unconfirmed due to the difficulties of conducting non-invasive tests for assessing cancellous bone in rats.

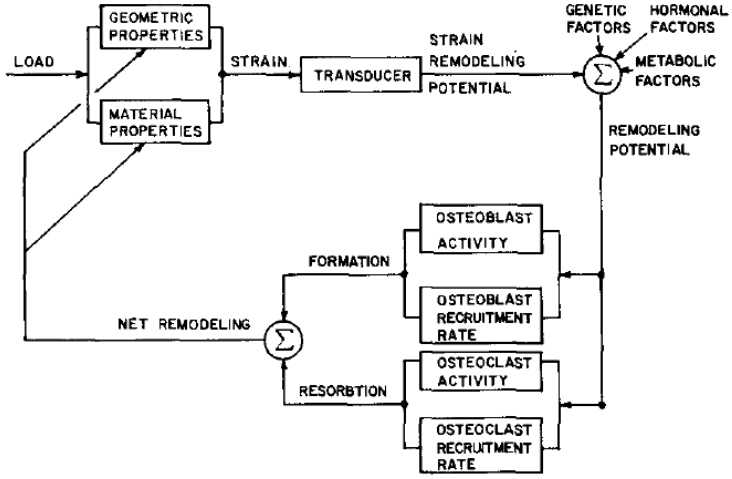


**Figure 105 - Schematic diagram for bone remodelling proposed by (Hart et al., 1984)**

Osteocytes that are distributed in the bone matrix have been suggested to be bone's mechanosensing cells (Cowin et al., 1995). Osteocytes are speculated to produce a signal proportional to mechanical loading by sensing strain on bone surfaces through stretch-activated ion channels (Duncan and Misler, 1989), flow of interstitial fluid (Cowin et al., 1995), electrical potentials (Harrigan and Hamilton, 1993) or cell deformation (as a result of fluid flow and matrix strain)(Nicolella and Lankford, 2002). It has also been suggested that they can sense fatigue micro-damage (Burr et al., 1985). The osteocytes send an inhibitory signal to osteoblasts that reduces their rate of bone formation (Marotti et al., 1992) and the osteoblasts control the osteoclasts (Rodan and Martin, 1981). The unified theory proposed by Martin (2000), proposes a system of cell-to-cell communication that is all based on inhibition of signals (including between osteoblasts to bone lining cells).

Strain energy density (U) (Fyhrie and Carter, 1986, Huiskes et al., 1987, Harrigan and Hamilton, 1992) is probably the most widely used mechanical stimulus for computer models in the literature (Ruimerman et al., 2005). Variations of a strain based stimulus include: principal strain (Gray et al., 2010), equivalent strain (Hart et al., 1984, Turner et al., 2005), strain energy density per unit bone density (Weinans et al., 1992b). Other stimuli investigated in the literature are von Mises stress (Herrera et al., 2007), strain rate (Lanyon and Rubin, 1984), damage-predictors (Prendergast and Taylor, 1994, Doblaré and García, 2001), and combinations of these (McNamara and Prendergast, 2007).

The bone remodelling response is influenced by anatomical site and time. For example the biological environments at different bone locations, such as the tibia and metatarsals or periosteal and endocortical surfaces of the same bone, may be different. No single bone remodelling response is applicable for all bones or in all regions of a single bone (Beaupre et al., 1990). The remodelling rate is also variable because it reduces with age (Sontag, 1992) and it is influenced by genetic predisposition (including gender) (Akhter et al., 1998) and environmental factors (such as metabolism and drug treatment).

Furthermore, the bone remodelling rate is suggested to be dependent on the free-surface available in the bone. This is because bone apposition and resorption can only occur at the free bone surfaces (Martin, 1972).

There are numerous bone remodelling theories reported in the literature with the common themes described above. The “Theory of Adaptive Elasticity” was developed by Cowin et al. (Cowin and Hegedus, 1976, Hegedus and Cowin, 1976, Cowin and Nachlinger, 1978, Cowin and Van Buskirk, 1978, Cowin and Firoozbakhsh, 1981). Constitutive remodelling rate equations relate the rate of bone tissue deposition and resorption to the mechanical stimulus (Cowin, 1993). External and internal remodelling are considered separately; the following equation is relevant for internal remodelling:

$$\frac{\partial \rho}{\partial t}(x) = A\big(S(x) - S_{ref}(x)\big)$$

where A is a remodelling constant, S is the stimulus, $S_{ref}$ is the reference stimulus at homeostatic equilibrium, and these are all functions of an anatomical site x.

The “Theory of Adaptive Elasticity” neglects (1) the influence of strain history on bone remodelling rate; and (2) trabecular alignment and material anisotropy.

Based on the principle of “self-optimisation”, the “Bone Maintenance Theory” was later developed by Carter et al. (Carter and Hayes, 1977, Fyhrie and Carter, 1986, Carter et al., 1987a, Carter et al., 1987b). Strain energy density was assumed to be the mechanical stimulus and the equations are derived assuming that bone optimises its stiffness to the

given loading with minimal material gain. The trabecular orientations align with the principal stress directions and the apparent density is proportional to an “effective stress”. The theory includes the daily load history (Carter et al. 1987a). The stimulus is a function of the strain energy density, loading cycles and apparent density:

$$\rho \propto \left(\sum n_i U_i^k\right)^{1/k}$$

where U is the strain energy density, i is the number of different loading conditions, n is the number of loading cycles, and k is a constant.

A credible combined comprehensive theory of “Adaptive Elasticity” and “Maintenance Theory” does not currently exist, although efforts have been made (Lekszycki,1999). Mathematical models of both theories have been developed and incorporated into FE programs to study bone remodelling post-arthroplasty. Studies by Kerner et al. (1999), Bitsakos et al. (2005) and Turner et al.(2005) compared FE predicted bone changes with measured bone changes of post-THR patients and found that the results had a similar order of magnitude.

In this study, the strain adaptive bone remodelling FE algorithm developed by Huiskes et al. (1987) has been used. This algorithm is based on an alternative formulation of the theory of “Adaptive Elasticity” and it uses strain energy density (U) as the mechanical stimulus:

$$U = \frac{1}{2}\varepsilon_{ij}\sigma_{ij}$$

where $\varepsilon_{ij}$ is the local strain tensor and $\sigma_{ij}$ is the local stress tensor.

The remodelling is stimulated when the difference between the actual U and a homeostatic equilibrium $U_{ref}$ is greater than a threshold which is defined by the lazy-zone, as illustrated in Figure 106. The remodelling response can be assumed to be linear (as originally formulated by Huiskes) or represented as a nonlinear response (Weinans et al., 1992a) with bone resorption faster (proportional to the cube of stimulus difference) than bone apposition (proportional to the square of stimulus difference).

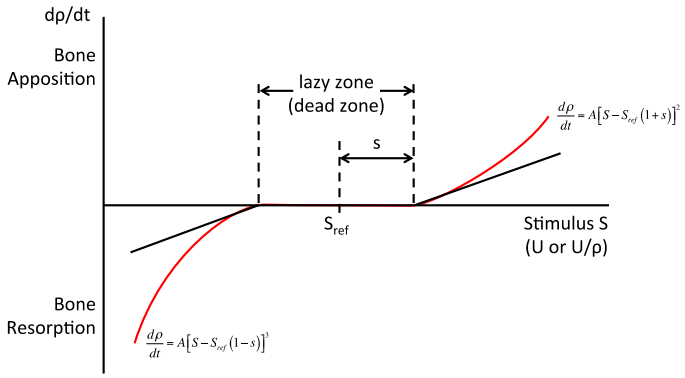


**Figure 106 - Strain adaptive bone remodelling relationship. The red line represents the nonlinear response purposed by Weinans et al. (1992a) and the linear response was proposed by Huiskes et al. (1987).**

To account for free-surface of bone on the rate of bone remodelling, the theory of Martin (1972) is incorporated into the algorithm. The internal free-surface area A(ρ) is estimated from bone apparent density, using the following empirical equation:

$$A(\rho) = 32.3\upsilon - 93.9\upsilon^2 + 134\upsilon^3 - 101\upsilon^4 + 28.8\upsilon^5$$

where: $$\upsilon = \frac{\rho}{\rho_{max}}$$

The 'Huiskes' algorithm was validated against canine experiments (Weinans et al., 1993) by comparing computer predictions against in-vivo response of animal bone to THR. Kerner et al. (1999) evaluated the computer predictions against human THR retrieval studies and Bitsakos et al. (2005) compared subject-specific THR patient computer predictions against DXA scans. The algorithm explained the qualitative changes that occurred but was less accurate for predicting regional and patient-specific quantitative changes. The algorithm parameters were optimised for the models and there was a distinct difference in lazy-zone parameter (animal s=35% compared to the human s=75-85%). Weinans et al. (1993) used U/ρ as the stimulus while Bitsakos et al. (2005) found U and principal strain produced better results. Although studies have used the algorithm for predicting stress shielding of Total Knee Replacements (TKRs) (Chong et al., 2011) and Unicompartmental Knee Replacements (UKRs) (Gillies et al., 2007), no study has yet comprehensively evaluated the algorithm against in-vivo DXA scans of knee arthroplasty patients.

## 8.3 Method

### *8.3.1 Patient Selection*

Two UKR patients from the Dual X-Ray Absorptiometry (DXA) clinical study (presented in Section 7) were chosen based on one having had cemented fixation (patient-9) and the other cementless fixation (patient-2). Figures 107 and 108 show the frontal and lateral scans of both patients assessed, highlighting the positions of the chosen Regions-Of-Interest (ROIs). Four separate Finite Element (FE) models were developed (two tibia and two femur) from pre-operative Computed Tomography (CT) scans. The models were developed in line with the conclusions of Chapter 6.

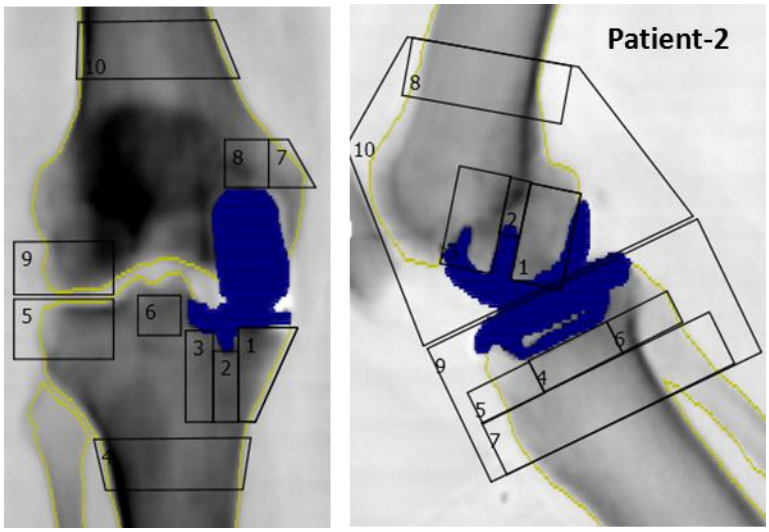


**Figure 107 - Frontal and lateral DXA scans of patient-2.**

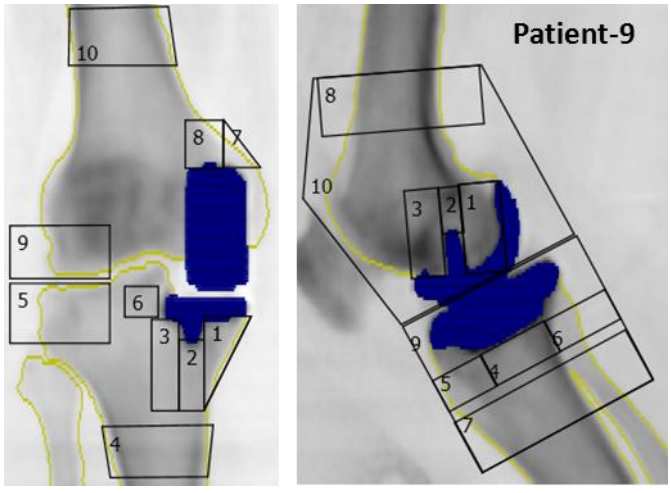


**Figure 108 - Frontal and lateral DXA scans of patient-9.**

### *8.3.2 Geometry and Materials*

The patients' knees were CT scanned using a "Definition AS+" Computed Tomography (CT) scanner (Siemens Healthcare, Germany). The coronal voxel sizes were in the range 0.5-0.7 mm and slice thickness' were 0.6-1.0 mm. Assurances were provided by the radiographers that all the quality assurance protocols of the scanner were up to date as specified in the operator manual. The scans were phantom-calibrated against air and water within 12 hours of performing the scans; the grey scale values were equivalent to Hounsfield Units (water corresponds to ± 4 HU and air to -1000 .

As described in Sub-section 4.3.2, the tibiae and femora were segmented manually using AVIZO 6.1 software (Visualization Sciences Group, USA) and the surfaces smoothed and meshed using triangular elements of 2-3 mm length. A separate mesh of the cortical bone geometry was generated. The surface geometries were imported into MARC Mentat 2010 software where the cortical and cancellous geometries were merged together while maintaining the cortical-cancellous boundary. The bones were transformed into a new axis (Anatomical Tibial axis for the tibia and Posterior Condylar axis for the femur, as described in Sub-section 4.3.2) based on identifiable bone landmarks.

Virtual implantations were performed, as described in Sub-section 4.3.5. The DXA scans were used to verify the final orientations of the implants. The femoral component of patient-9 was over-rotated posteriorly by no more than 5 degrees. Patient-2 had a 'Size F' tibial tray and 'Large' femoral component while patient-9 had a 'Size C' tibial tray and 'Medium' femoral component. Although the femoral reaming cutter creates a corner stress raiser at the anterior edge, usually the surgeon tends to chisel away to round off the corner. A single element chamfer was added to the models to remove the unrealistic stress raiser.

The cementless tibial and femoral implants of patient-2 included a contact interface between the implant and bone, with a friction coefficient of 0.4 (assuming no osseointegration). Once osseointegration had occurred (at three months), the implant-bone interface was fully bonded with shared nodes at the interface. The implant was in contact around the rim (four elements wide, 1.2 mm size elements), and the underside inner surface (hydroxy-apatite coated region) recessed by 0.2 mm. The cementless femoral component had 1.2 mm size elements at the bone-implant interface and the implant underside inner surface (the hydroxy-apatite coated region) was recessed by 0.2 mm.

For the cemented tibial and femoral implants of patient-9, shared nodes were modelled at the bone-cement and cement-implant interfaces. Note that the nodes at the tibial implant side-plate and sagittal bone resection were not shared and were modelled as non-contacting. This is because clinical evidence (radiolucencies) suggests that the side-plate is

often not bonded to the bone (Simpson et al., 2011). A 2 mm thick cement-mantle was modelled with an elastic modulus of 1.8 GPa (refer to Sub-section 4.4).

All the models were formed of linear tetrahedral type 134 elements of size 2-4 mm. A higher mesh density was assigned to the medial compartment to capture the bone remodelling changes more accurately. The proximal tibial and distal femoral cortices were not included as sensitivity assessments showed only local effects on bone strain (refer to Sub-section 4.5).

The bone elastic moduli were assigned separately to the cancellous and cortical materials. The cancellous moduli were assigned on an element-by-element basis, assuming isotropy, using a linear relationship to calculate apparent density from CT grey scale values (as described in Sub-section 2.3) followed by a three-part relationship to calculate elastic moduli (as described in Sub-section 2.4). The cortical bone was represented with a single isotropic elastic modulus of 17.9 GPa representing the maximum apparent bone density of 1.73g/cm$^3$.

In order to accurately determine the tibiofemoral contact conditions, the tibia and femur models were developed simultaneously. The bones were orientated to determine the contact points in both pre and post-arthroplasty conditions. The bone density was also taken into account: higher surface bone densities were considered to be indicative of highly loaded regions. In both patient knees, the medial aspects of the tibial intercondylar eminences were highly loaded compared to normal knees.

Figures 109 and 110 show the tibia and femur of patient-2 and patient-9 respectively, at pre and post-arthroplasty states. The bearings were 5 mm posterior of the tibial tray centre; and 4 mm from the side-plate for patient-2 and 0-1 mm for patient-9.

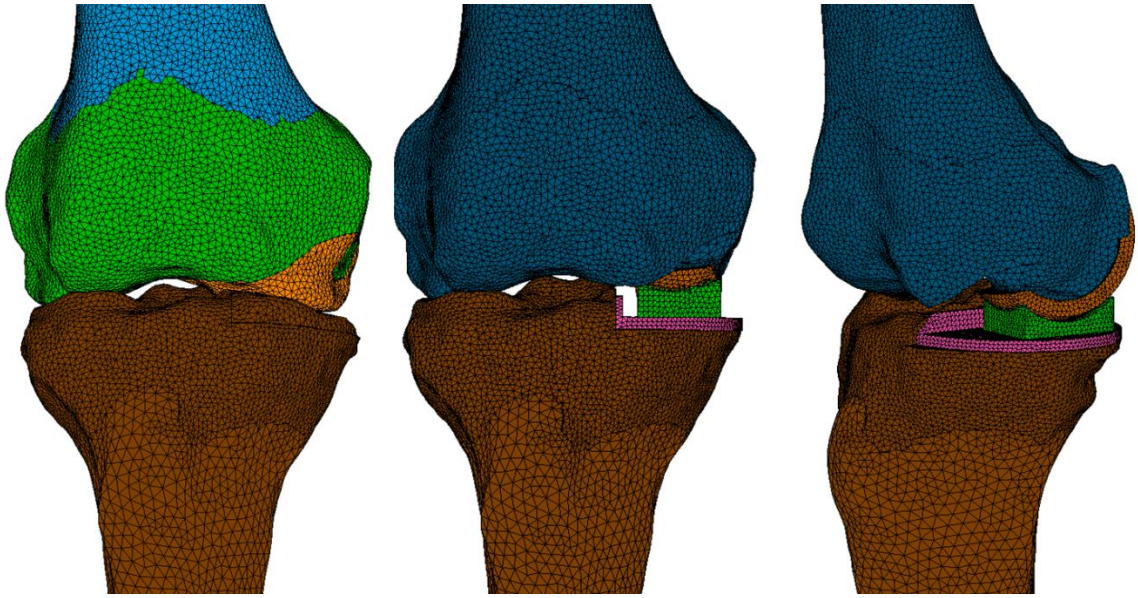

**Figure 109 - Determination of tibiofemoral contact conditions/positions/orientations at pre and post-arthroplasty states for patient-2.**

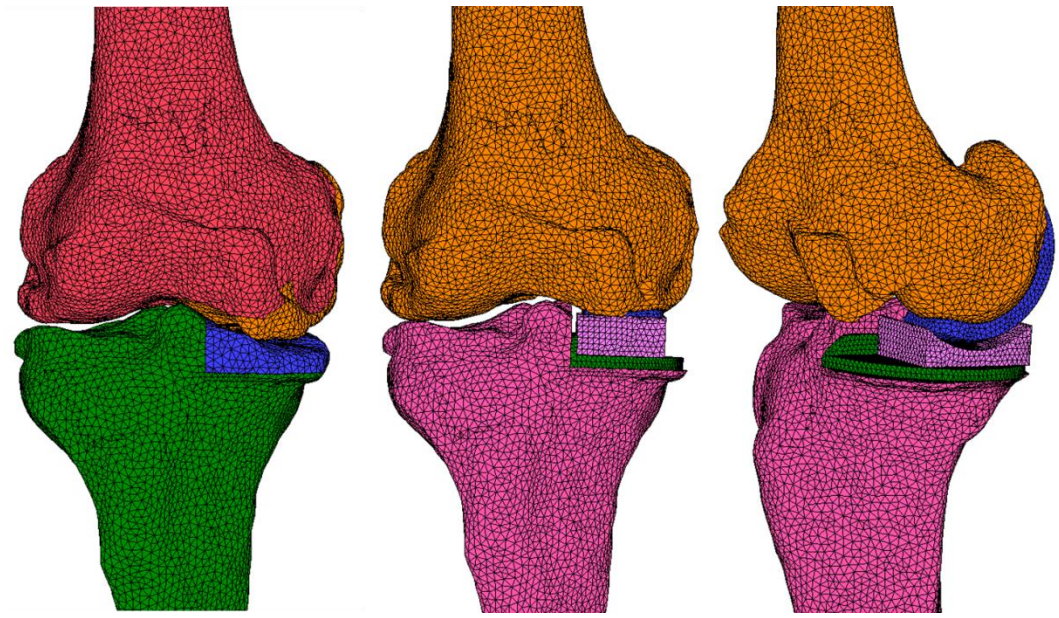

**Figure 110 - Determination of tibiofemoral contact conditions/positions/orientations at pre and post-arthroplasty states for patient-9.**

The first iteration of all post-arthroplasty models included basic representations of the polyethylene mobile-bearing. Since modelling contact is computationally expensive, the implant-bearing interfaces were simplified by assuming shared nodes. In the final models, the mobile-bearings were removed from the femoral models to optimise them for computational efficiency. Loads were applied directly to the implant surface nodes.

The reference model was developed to represent the pre-operative state of the knee. The mesh and element numbers were identical to the UKR models, with additional bone

elements added to represent the intact medial condyles. Although basic representations of the menisci were included in the first iterations of the models, they were later removed from all the models to improve computational efficiency. Although the elastic modulus of the meniscus is non-linear (at 20% strain elastic modulus is 20 MPa and increases to 300 MPa with increased strain (Leslie et al., 2000)), a single linear elastic modulus of 20 MPa was assigned because it produced strains of approximately 20%.

### *8.3.3 Remodelling Algorithm and Parameters*

The strain adaptive bone remodelling FE algorithm developed by Huiskes et al. (1987) was used. The objective of the remodelling process was defined as:

$$(1-s)S_{ref} \leq S \leq (1+s)S_{ref}$$

where: S is the stimulus; $S_{ref}$ is the Reference Stimulus (pre-operative state); and the interval between $(1\text{-}s)S_{ref}$ and $(1+s)S_{ref}$ represents the lazy-zone (bone is assumed to be unresponsive).

Bone remodelling was stimulated when the difference between the actual S and a homeostatic equilibrium $S_{ref}$ was greater than a threshold which was defined by the lazy-zone, as illustrated in Figure 106. The remodelling rate was assumed to be linear because (1) this was the original formulation by Huiskes and (2) for the algorithm to be compatible with the theory of Martin (1972). The nonlinear response proposed by Weinans et al. (1992a) was not considered. The bone remodelling rate (positive for apposition and negative for resorption) is illustrated in Figure 111.

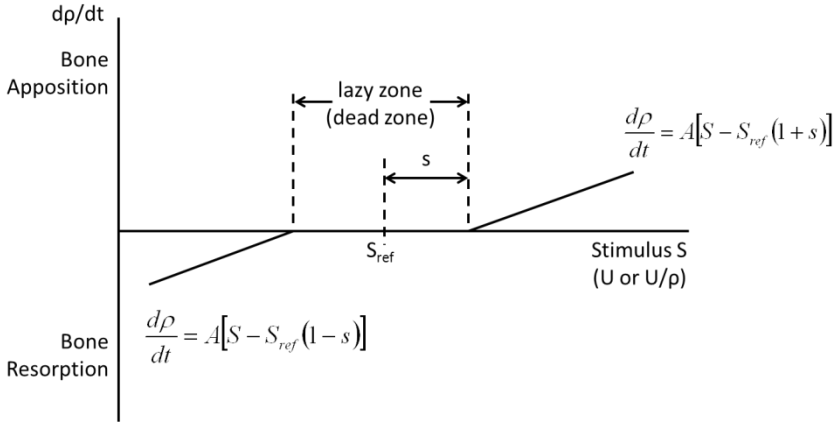


**Figure 111 - The strain adaptive algorithm developed by Huiskes et al. (1987) and used in the study.**

The remodelling rate was defined as:

$$\begin{cases} \frac{d\rho}{dt} = \frac{\tau A(\rho)}{V}\left(S - (1-s)S_{ref}\right) & if\ S < (1-s)S_{ref} \\ \frac{d\rho}{dt} = 0 & if\ S < (1-s)S_{ref} \leq S \leq (1+s)S_{ref} \\ \frac{d\rho}{dt} = \frac{\tau A(\rho)}{V}\left(S - (1+s)S_{ref}\right) & if\ S < (1+s)S_{ref} \end{cases}$$

where:

$\tau$ = time constant parameter, $s^{-1}$;

$A(\rho)$ = free-surface area of bone, $mm^2$;

V = volume of element, $mm^3$;

S = Stimulus, U (MPa) or U/ρ ($MPa/mm^3$);

$S_{ref}$ = Reference Stimulus, U (MPa) or U/ρ ($MPa/mm^3$);

s = lazy zone parameter.

The maximum apparent density was defined to be 1.73 $g/cm^3$ (in accordance with Martin (1972)) and the maximum change in apparent density defined as 0.437 $g/cm^3$.

The following parametric studies were conducted to optimise parameters to accurately predict bone remodelling following UKR arthroplasty:

- Two mechanical stimuli: (i) strain energy density (U); and (ii) strain energy density per unit mass (U/ρ).
- Four lazy-zone parameters: (i) 50%; (ii) 65%; (iii) 75%; and (iv) 90%.
- Six time-constant parameters: (i) 1; (ii) 12; (iii) 25; (iv) 50; (v) 75; (vi) 99.
- Theory of Martin: (i) include theory of Martin; (ii) exclude theory of Martin.

Since there are a number of different parameters to investigate, a starting point was required. A review of the literature demonstrated that the strain energy density (U) stimulus was the most widely adopted, lazy-zones of 75% and 90% were most accepted, and the theory of Martin was considered necessary. A total of 48 incremental FE analyses (four models, two lazy-zones, six time parameters) were developed with increasing time parameter $\tau$ = 1, 12, 25, 50, 99.

Once the optimal time-parameter was found, the remaining parametric studies were conducted.

### *8.3.4 Knee Loading*

As described in Section 3, walking, stair-ascent and stair-descent activities were represented by 120 load configurations (representing every 2.5% increment of each activity). For the tibia models, 6 load configurations were chosen (Table 13); two peaks for each activity.

**Table 13 - Loads applied to tibia models**

| Flexion (degree) | Activity | % Cycle | Force (% Body Weight) | | | | |
|---|---|---|---|---|---|---|---|
| | | | Medial Contact | Lateral Contact | Patella Tendon | ACL | PCL |
| 26º | Walking | 15% | 221% | 44% | 149% | 43% | 0% |
| 19º | Walking | 50% | 218% | 31% | 25% | 14% | 0% |
| 14º | Stair Ascent | 15% | 142% | 121% | 266% | 44% | 0% |
| 58º | Stair Ascent | 50% | 268% | 82% | 25% | 40% | 0% |
| 70º | Stair Descent | 15% | 354% | 72% | 67% | 50% | 0% |
| 11º | Stair Descent | 50% | 174% | 49% | 222% | 51% | 0% |

For the femur models, 8 load configurations were chosen (Table 14) based on the highest medial loads covering the full 0-70 degree flexion.

**Table 14 - Loads applied to femur models.**

| Flexion (degree) | Activity | % Cycle | Force (% Body Weight) | | | | |
|---|---|---|---|---|---|---|---|
| | | | Medial Contact | Lateral Contact | Patella Contact | ACL | PCL |
| 11º | Walking | 10% | 196% | 0% | 27% | 28% | 1% |
| 12º | Stair Descent | 48% | 182% | 31% | 219% | 64% | 0% |
| 22º | Walking | 13% | 229% | 0% | 64% | 30% | 0% |
| 26º | Walking | 15% | 221% | 44% | 108% | 43% | 0% |
| 28º | Stair Ascent | 45% | 232% | 69% | 11% | 35% | 0% |
| 43º | Stair Ascent | 48% | 251% | 74% | 12% | 39% | 0% |
| 65º | Stair Descent | 10% | 257% | 109% | 32% | 45% | 0% |
| 70º | Stair Descent | 15% | 354% | 72% | 37% | 50% | 0% |

The knee forces were adapted for each patient by taking into account their body-weight. Patient-2 weighed 110 kg while patient-9 weighed 75 kg.

It has been reported that joint forces can stabilise in the first 6 weeks (D'Lima et al., 2006) but can increase up to 2 years post-operative (D'Lima et al., 2005). In active patients, the joint forces are expected to reach nearly full loading after 3 months (Taylor and Walker, 2001, D'Lima et al., 2007). Unfortunately the activity levels of patients were not available, so assumptions were made based on conversations with the patients. Patient-2 was significantly more active than patient-9. For patient-2, it was assumed that the knee forces were 50% of those experienced pre-arthroplasty in the first 3-months and rose to 100% thereafter. Patient 9 was using a walking stick at 6-months due to pain in both operated and contralateral knee. At 12 months, she had no pain on the operated knee, but due to pain on the contralateral knee she was relatively inactive. For patient-9, it was assumed that the

knee forces were 50% of those experienced pre-arthroplasty for the first 3-months, rose to 75% at 6 months, 90% at 9 months and 100% at 1-year.

Based on analysis of the geometry of each patient's knee joint, a 'pinch' force was applied to the pre-arthroplasty reference tibia models and the opposite to the femur models. The pinching force was calculated based on approximation of the average surface contact normal; approximately 7 degrees in both patients.

The remodelling algorithm calculated the maximum stimulus for each bone element based on consideration of all load configurations. After each remodelling increment (8 FEA increments for femur and 6 FEA increments for tibia), the algorithm calculated the change in bone density of each bone element.

### *8.3.5 Modelling Osseointegration of Cementless Implants*

The immediate post-arthroplasty condition of the cementless UKR patient was modelled by defining contact at the bone-implant interface, as described in Sub-section 4.6.3. Once osseointegration had occurred, the bone-implant interface was modelled as a shared interface.

Since bone-implant micromotion was low at the entire interface of the cementless UKR (refer to Sub-section 6.4.3), full osseointegration at the bone-implant interface was assumed at 3 months. Therefore after running 3 months of simulated bone remodelling, the FE model was updated to include a fully fixed bone-implant interface (shared nodes at the interface). Note that the implant-side was not fixed to the bone. The model was then run for another 9 months of simulated bone remodelling.

For the first 3 months of the tibia simulation, the hole in the implant keel was assumed to be a void (no structural significance). At 3 months, this void was filled with bone with density of 0.1 g/cm$^3$ and allowed to remodel in the subsequent 9 months of simulation.

### *8.3.6 Post-processing*

The results were post-processed by simulating each analysis as a frontal and lateral DXA scan (refer to Sub-section 4.6.10) and calculating the total bone mass in each ROI (as presented in Figures 107 and 108). The results were exported into Microsoft Excel, and post-processed to calculate the percentage change ($\Delta$BMD) at 3, 6, 9, and 12 months and the percentage difference change against the actual measured DXA values.

## 8.4 Results

### *8.4.1 Parametric Study Results*

To determine the optimum time parameter, the difference between the predicted ΔBMD and measured ΔBMD were plotted against time-parameter as presented in Figures 112 and 113.

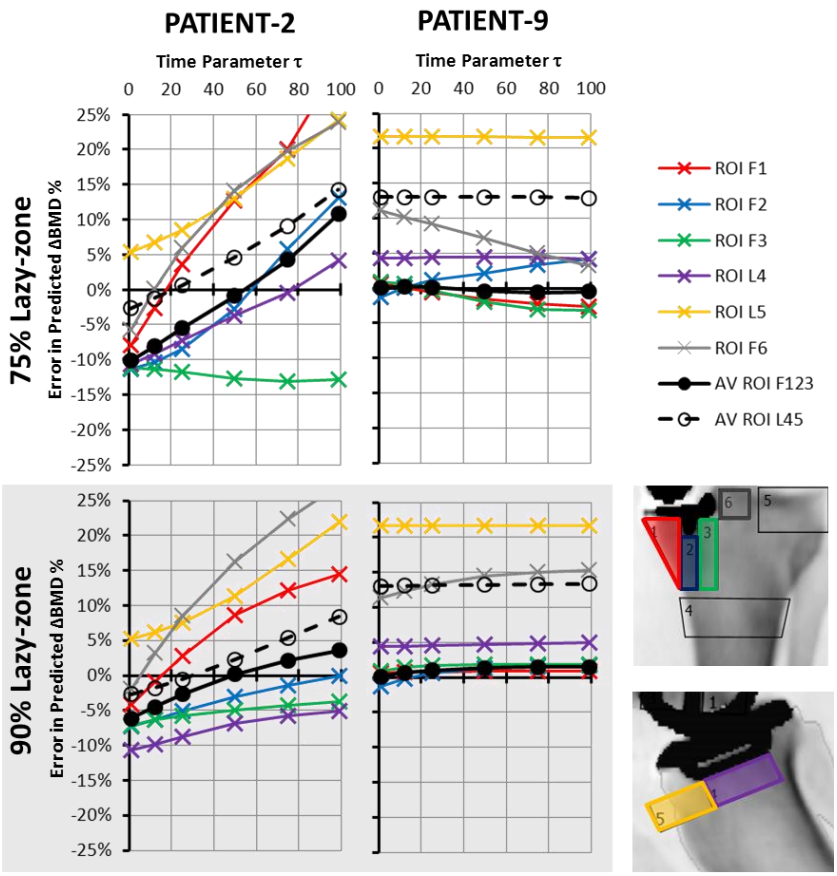


**Figure 112 - Plots display error of tibia BMD change predictions (ΔBMD Error = Predicted ΔBMD Error – Measured ΔBMD Error) against algorithm time parameter. A suitable time parameter is τ = 50.**

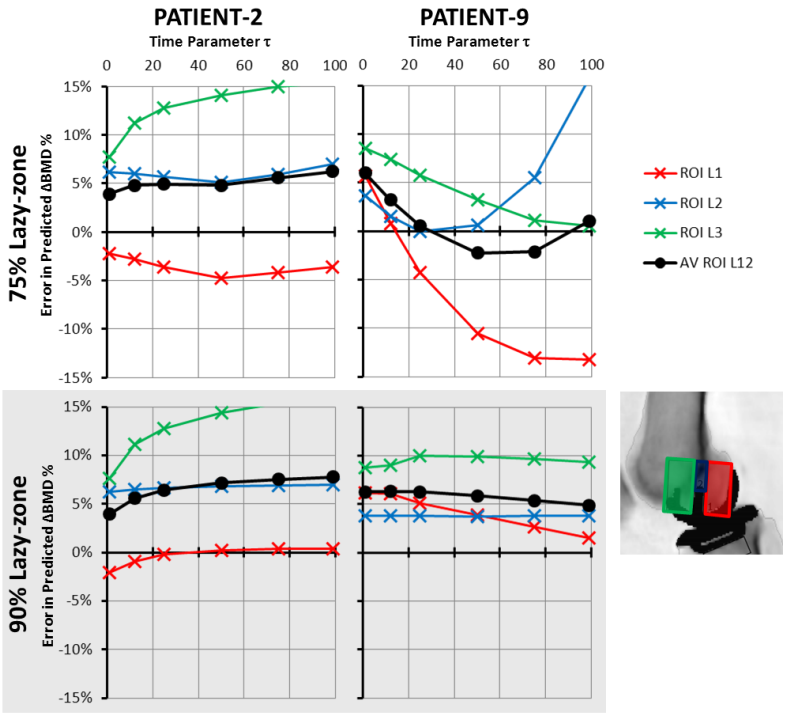


**Figure 113 - Plots display error of femur BMD change predictions (ΔBMD Error = Predicted ΔBMD Error – Measured ΔBMD Error) against algorithm time parameter.**

The optimal time parameter was difficult to determine from the results (Figures 112 and 113) because they were dependent on patient and on region of interest. However, after consideration of the results, and careful judgement based on a detailed review of the literature (refer to Sub-section 8.2) a time-parameter of $\tau = 50$ was judged to be most suitable. With the time-parameter set at $\tau = 50$, the remaining parametric studies were conducted. Figures 114 to 117 display changes to ΔBMD error due to variations of algorithm parameters: (1) Stimulus; (2) Lazy-zone; and (3) inclusion of Theory of Martin. Figures 114 to 115 display results for tibia models patient-2 and patient-9 respectively; and Figures 116 to 117 display results for femur models patient-2 and patient-9 respectively.

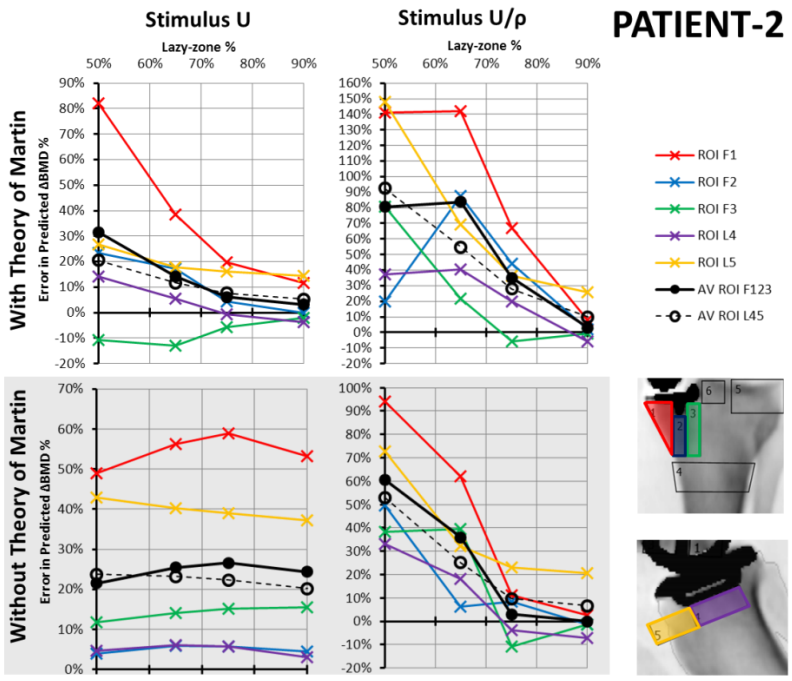


**Figure 114 - Comparison of bone remodelling algorithm parameters for the tibia of patient-2. Plots display error of BMD change predictions (ΔBMD Error = Predicted ΔBMD Error – Measured ΔBMD Error) against algorithm parameters: (1) Stimulus; (2) Lazy-zone; and (3) inclusion of Theory of Martin. A degradation of 4% (measured from neutral DXA scan ROIs) was included in the patient-2 predictions.**

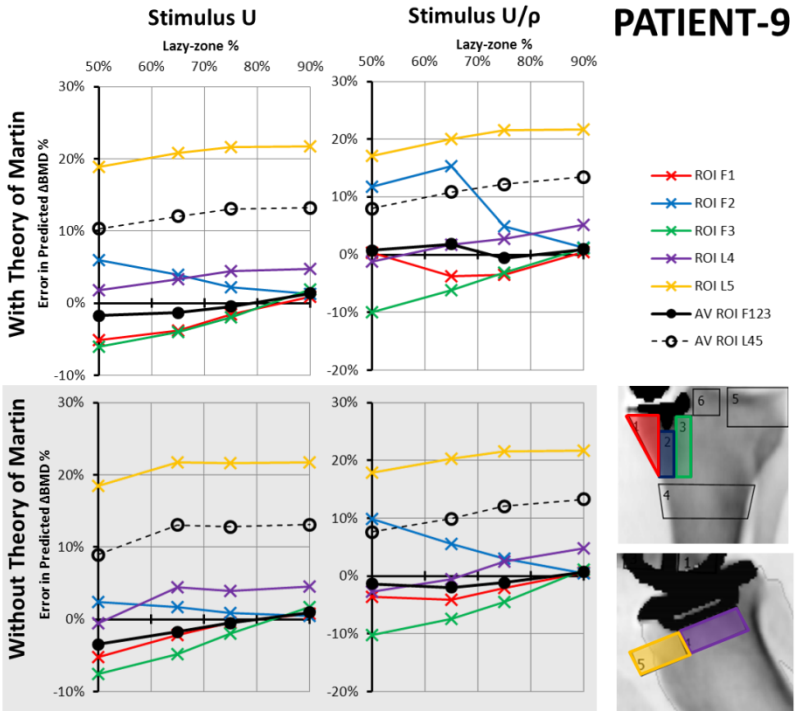


**Figure 115 - Comparison of bone remodelling algorithm parameters for the tibia of patient-9. Plots display error of BMD change predictions (ΔBMD Error = Predicted ΔBMD Error – Measured ΔBMD Error) against algorithm parameters: (1) Stimulus; (2) Lazy-zone; and (3) inclusion of Theory of Martin. A degradation of 7% (measured from neutral DXA scan ROIs) was included in the patient-9 predictions.**

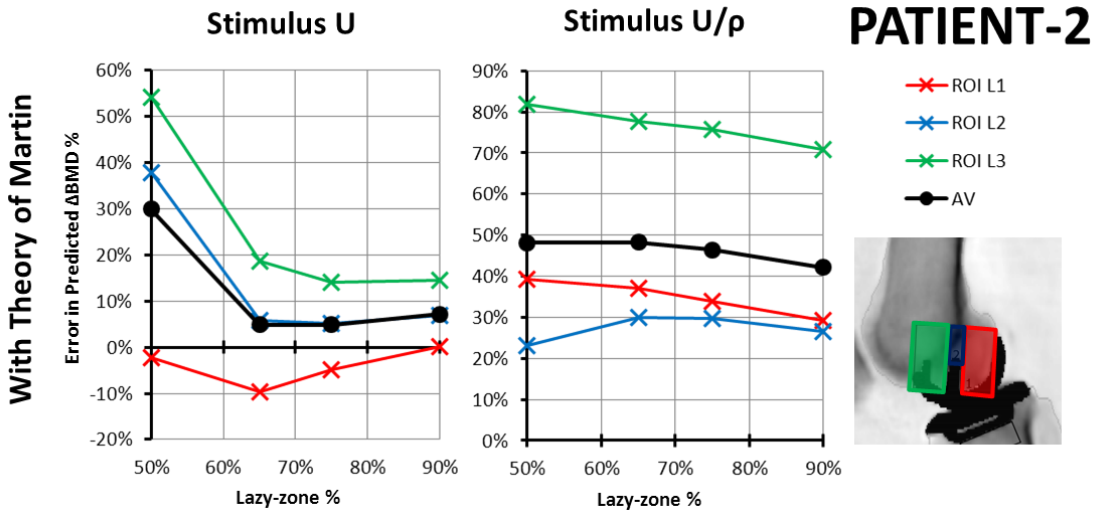


**Figure 116 - Comparison of bone remodelling algorithm parameters for the femur of patient-2. Plots display error of BMD change predictions (ΔBMD Error = Predicted ΔBMD Error – Measured ΔBMD Error) against algorithm parameters: (1) Stimulus; and (2) Lazy-zone. A degradation of 4% (measured from neutral DXA scan ROIs) was included in the patient-2 predictions.**

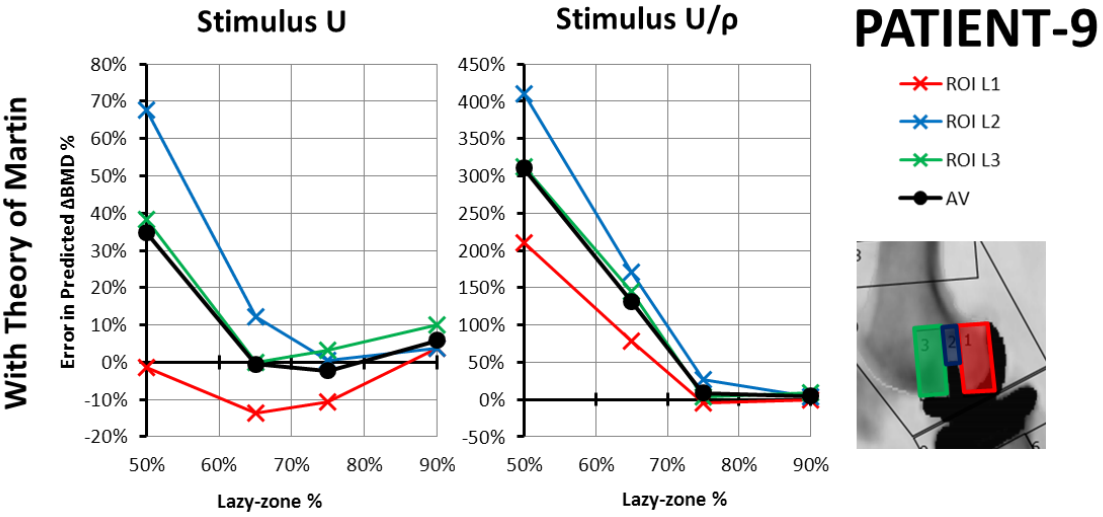


**Figure 117 - Comparison of bone remodelling algorithm parameters for the femur of patient-9. Plots display error of BMD change predictions (ΔBMD Error = Predicted ΔBMD Error – Measured ΔBMD Error) against algorithm parameters: (1) Stimulus; and (2) Lazy-zone. A degradation of 7% (measured from neutral DXA scan ROIs) was included in the patient-9 predictions.**

The results presented in Figures 114 to 117 are variable and inconclusive. In general the most realistic results were produced when stimulus U was used; however, there was no significant evidence to exclude the use of stimulus U/ρ. In general, the error reduced with increasing lazy-zone (except patient-2 femur with U/ρ as stimulus), and the most suitable lazy-zone was 75%. Using the Theory of Martin made little difference to bone remodelling in most of the models; however a large effect was observed for patient-2 tibia. This was because bone apposition was stimulated in a high density cortical region on the medial

proximal tibia, and the Theory of Martin significantly reduced the remodelling rate in this region when activated. Therefore, inclusion of the Theory of Martin was considered necessary.

### *8.4.2 Predicted BMD Changes in the Knee*

The parameters chosen to be most optimal for BMD change predictions were as follows:

- Stimulus = strain energy density (U);
- Lazy-zone = 75%;
- Time-parameter $\tau = 50$;
- Theory of Martin activated.

Figures 118 and 120 display simulated DXA scans of BMD of the tibia and femur, respectively. The figures highlight the BMD changes for both patients, with green circles indicating bone apposition and red indicating bone resorption. The arrows highlight the load path dissipating from the implant.

Figures 121 and 122 display how the BMD changes occur over the 12 month period for both patients and both tibia and femur.

Although the simulated 2D DXA scans are useful to clinicians who are familiar with using them, 3D images provide significant improvement. An advantage of developing computer models is that these can be analysed in 3D, adding further perspective to 2D clinical radiographs. Particularly for UKRs, 3D images can be used to separate BMD changes in the lateral compartment (which can distort the 2D radiographs). Figures 123 to 131 present 3D bone remodelling plots of the tibia and femur, respectively.

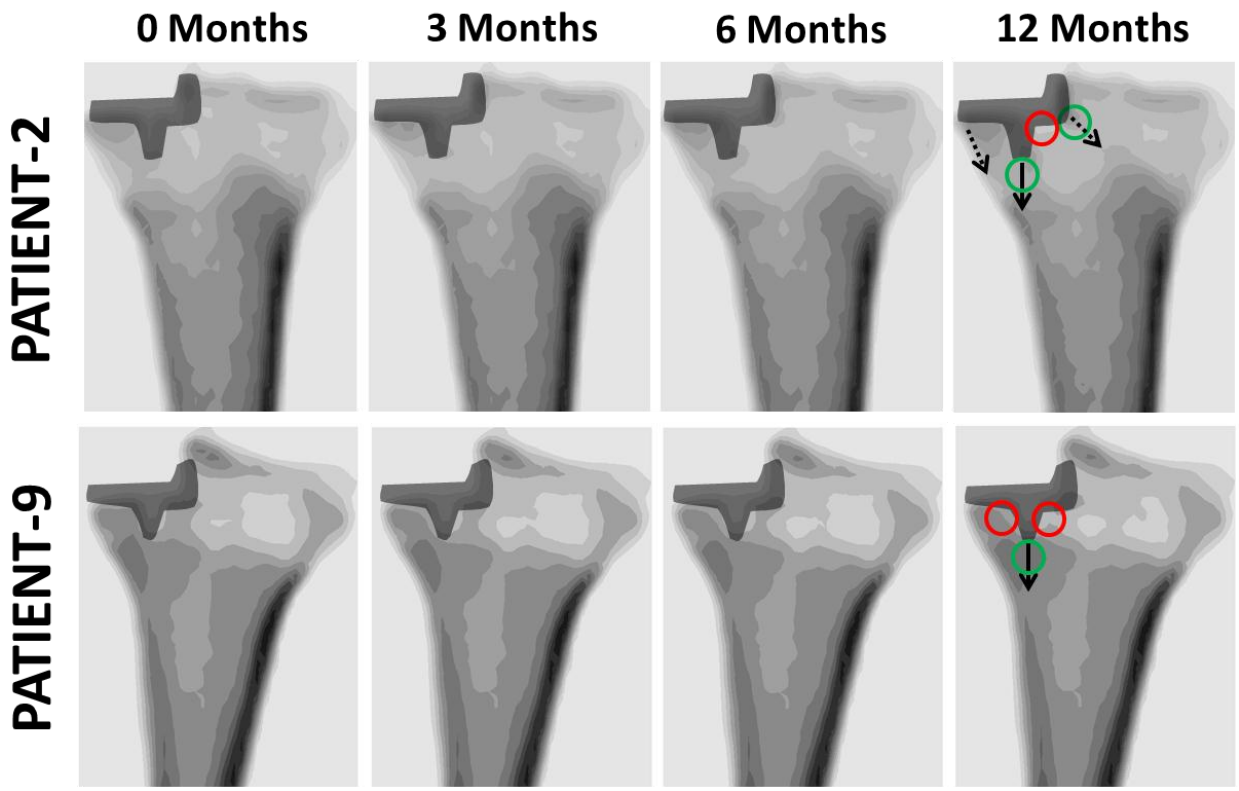


**Figure 118 - Simulated frontal tibia DXA scans of FEA bone remodelling predictions of patient-2 and patient-9.**

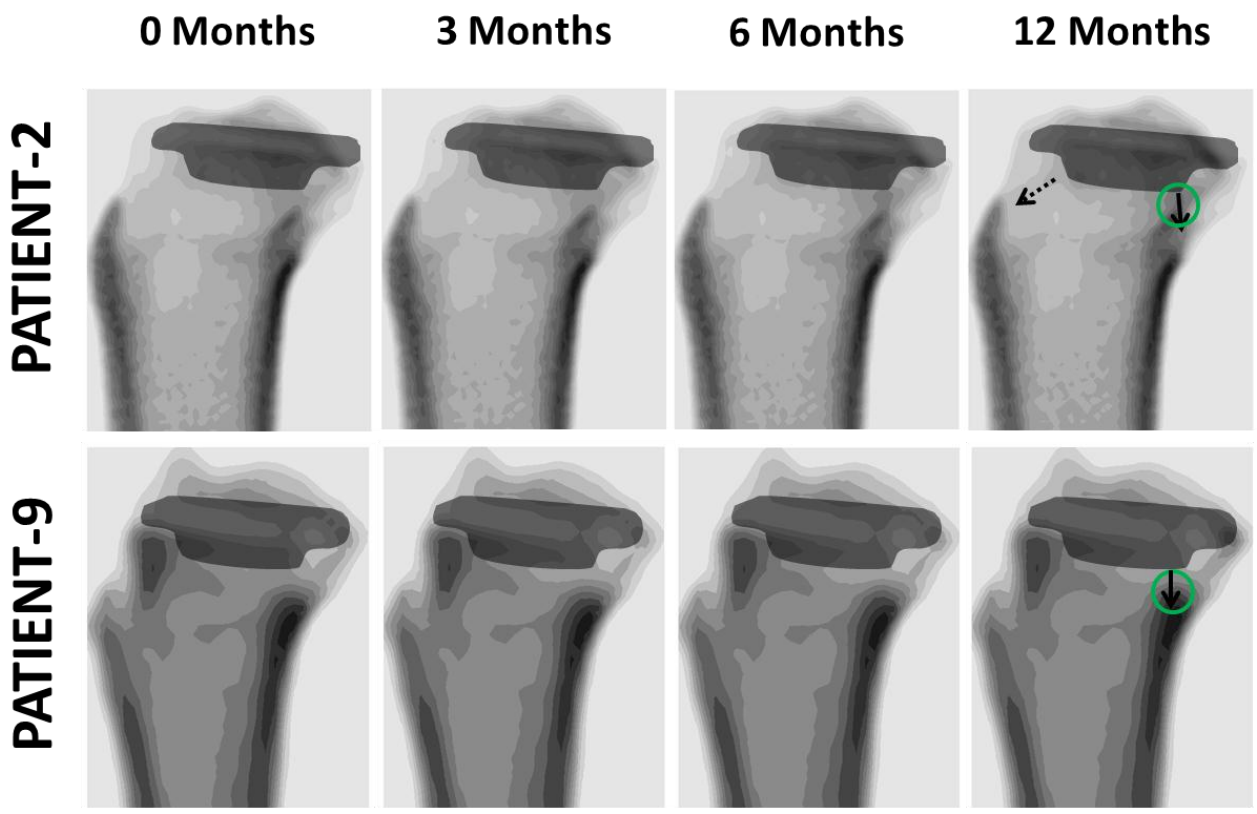


**Figure 119 - Simulated lateral tibia DXA scans of FEA bone remodelling predictions of patient-2 and patient-9.**

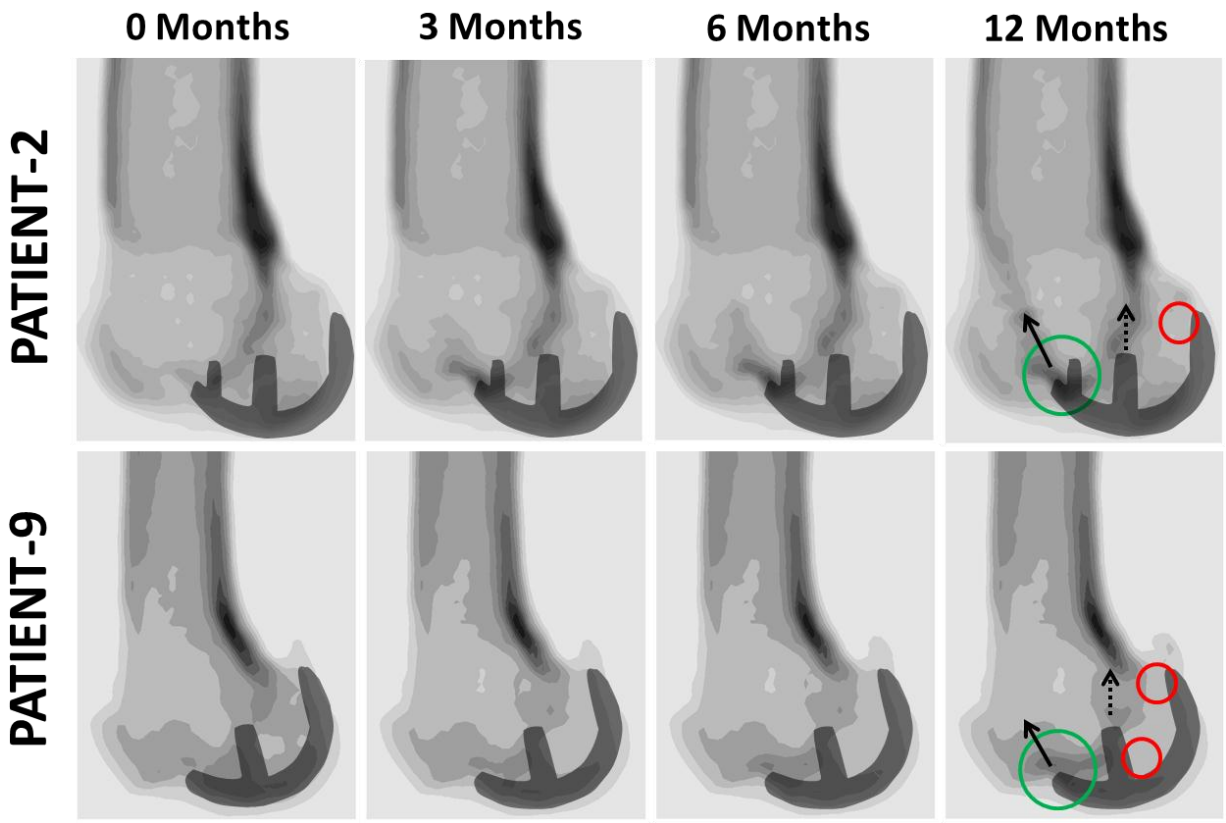


**Figure 120 - Simulated femur DXA scans of FEA bone remodelling predictions of patient-2 and patient-9.**

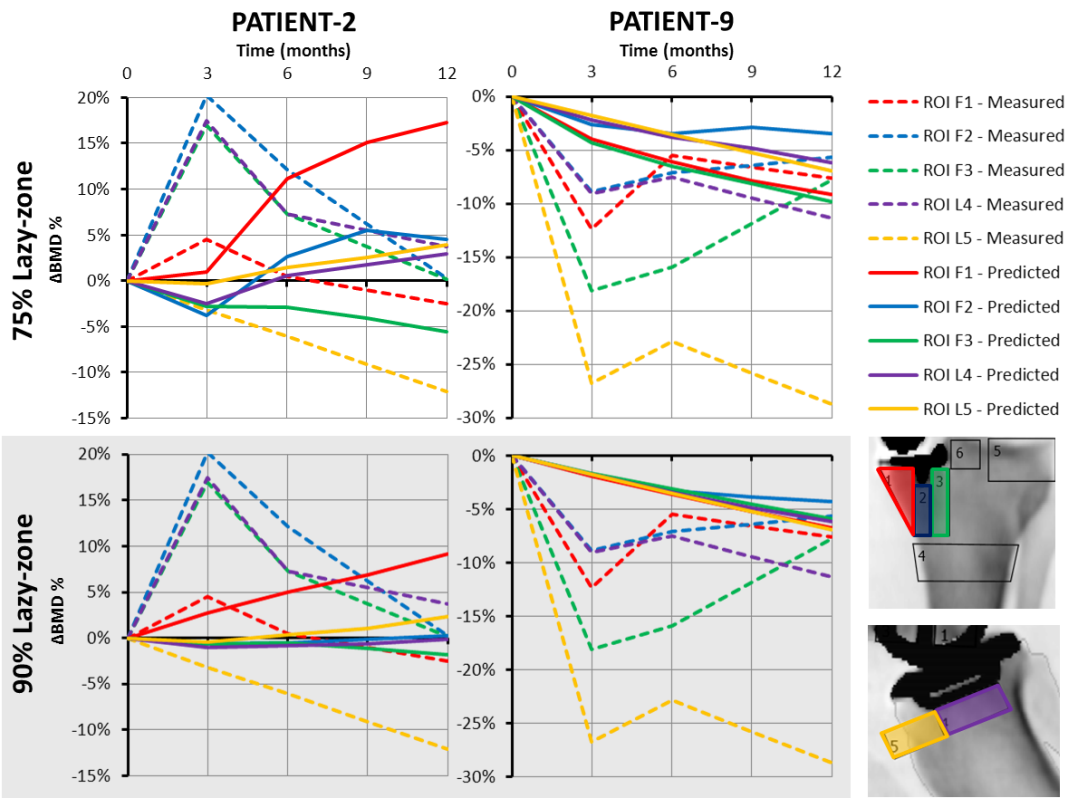


**Figure 121 - Plots of Tibia DXA BMD changes for the period of 1 year of patient-2 and patient-9. The predicted BMD changes are compared against the measured changes.**

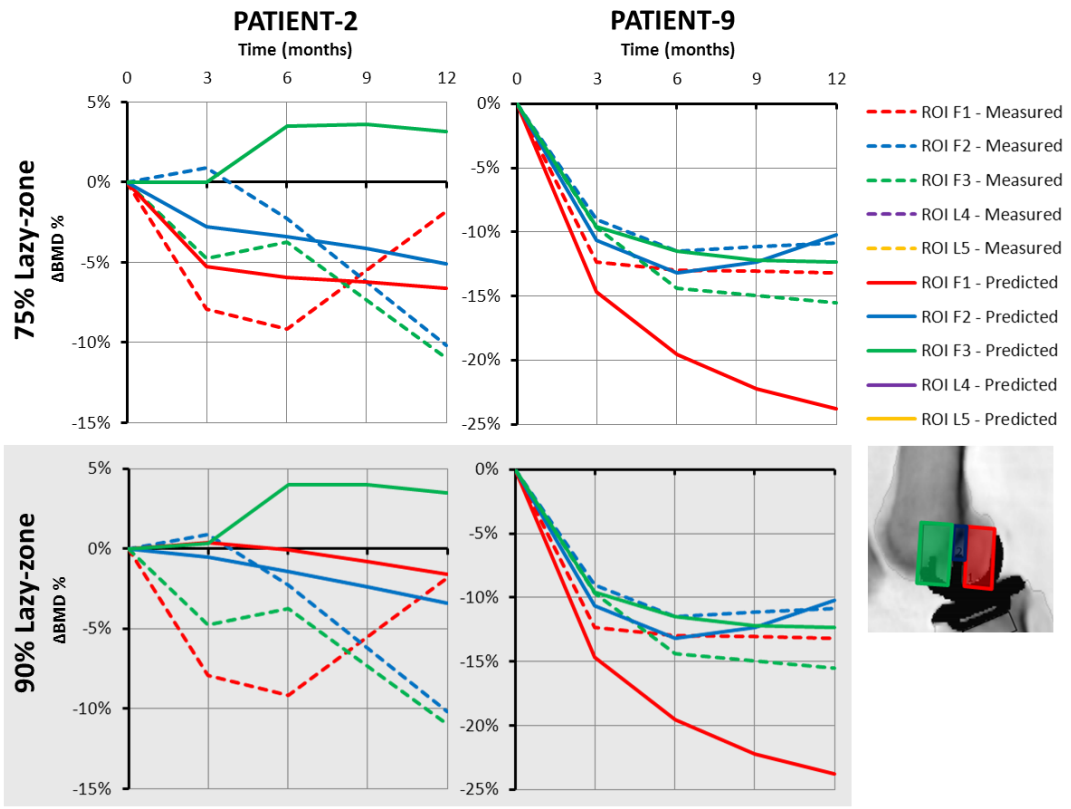


**Figure 122 - Plots of Femur DXA BMD changes for the period of 1 year of patient-2 and patient-9. The predicted BMD changes are compared against the measured changes.**

Figures 123 to 127 display the bone remodelling changes in patient-2 tibia and Figures 124 to 128 in patient-9. Figures 123 and 124 show slices of bone density with time and demonstrate that bone apposition occurs under the tibial tray keel. In both patients, the apposition forms a stiff load-path between the posterior keel and the cortical bone. In patient-9, the keel rests close to the cortical bone; therefore, bone apposition in this region is low. On the other hand, patient-2 has a wide proximal tibia and since the anterior of the keel is located in a region of low density bone, bone apposition has caused a second stiff load-path from the anterior keel to the cortical bone.

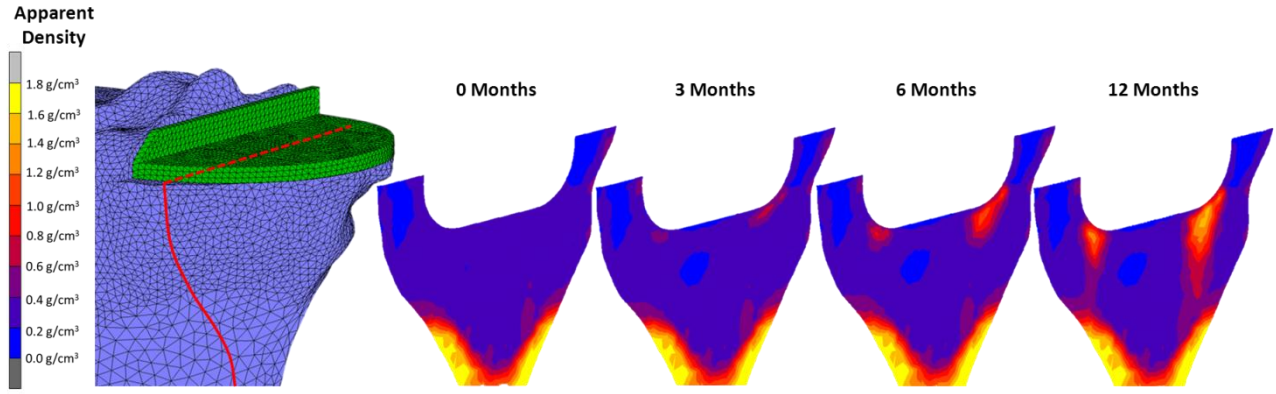


**Figure 123 - Bone remodelling under tibial keel of patient-2.**

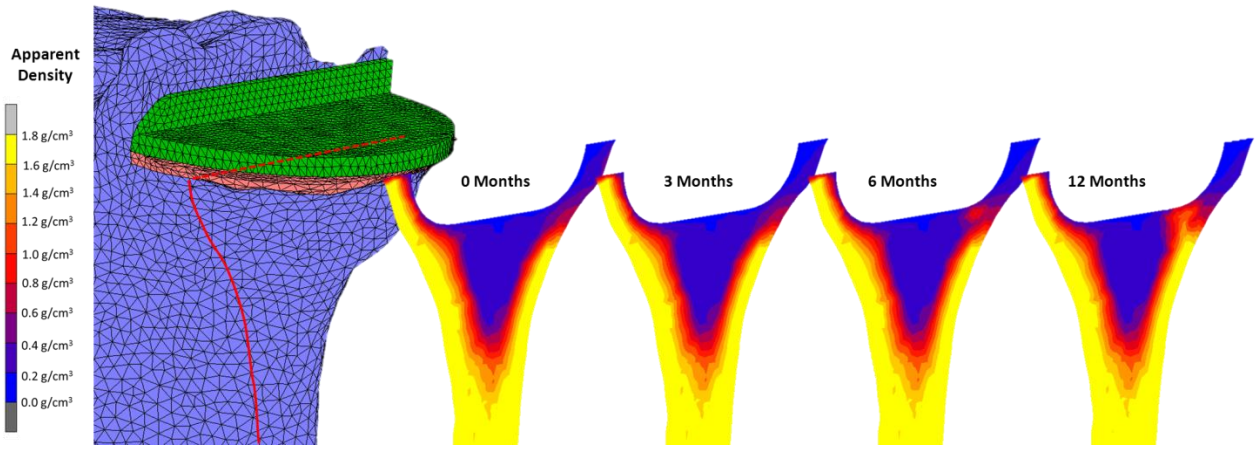


**Figure 124 - Bone remodelling under tibial keel of patient-9.**

Figures 125 and 126 show plots of bone apposition at the resected corner of the tibial implant. There was significant bone apposition at the anterior side-plate in both patients, and this corresponds to the sclerotic regions often seen in frontal radiographs. This highly strained region could be responsible for the pain that a large portion of Oxford UKR patients complain about. Note that the implant side-plate is not osseointegrated to the bone.

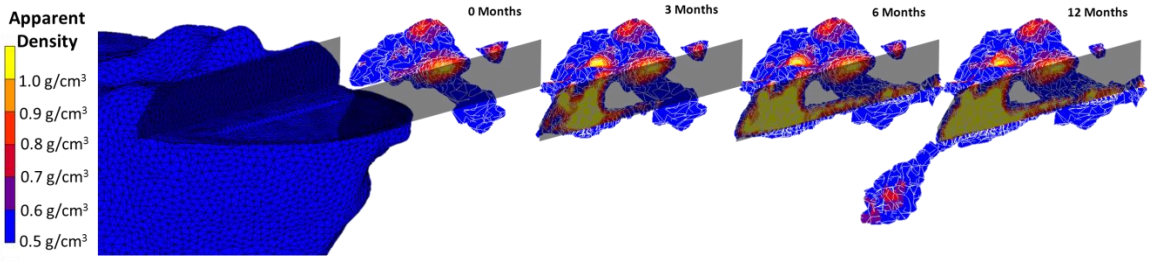


**Figure 125 - Bone apposition at the resected corner of the tibial tray of patient-2.**

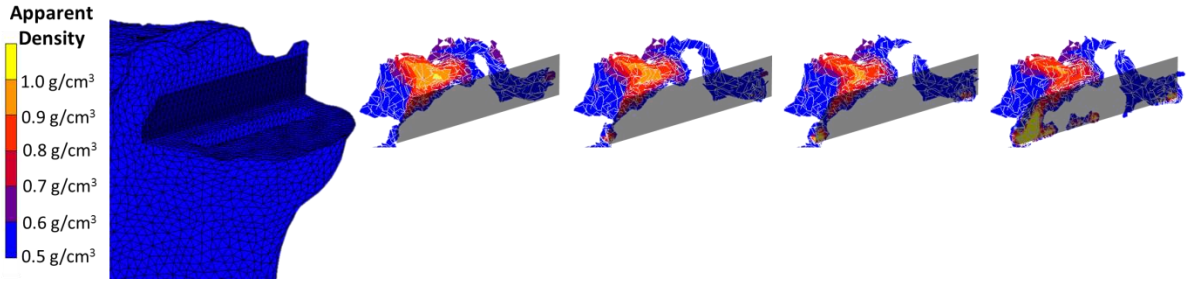


**Figure 126 - Bone apposition at the resected corner of the tibial tray of patient-9.**

Figures 127 and 128 display the bone remodelling changes at a slice 1 mm under the implant (for patient-2 cementless implant) and 1 mm under the cement-mantle (for patient-9 cemented implant), respectively. There was noticeable bone resorption on the lateral side of the cementless implant keel (Figure 127) while there was negligible change for the cemented implant (Figure 128).

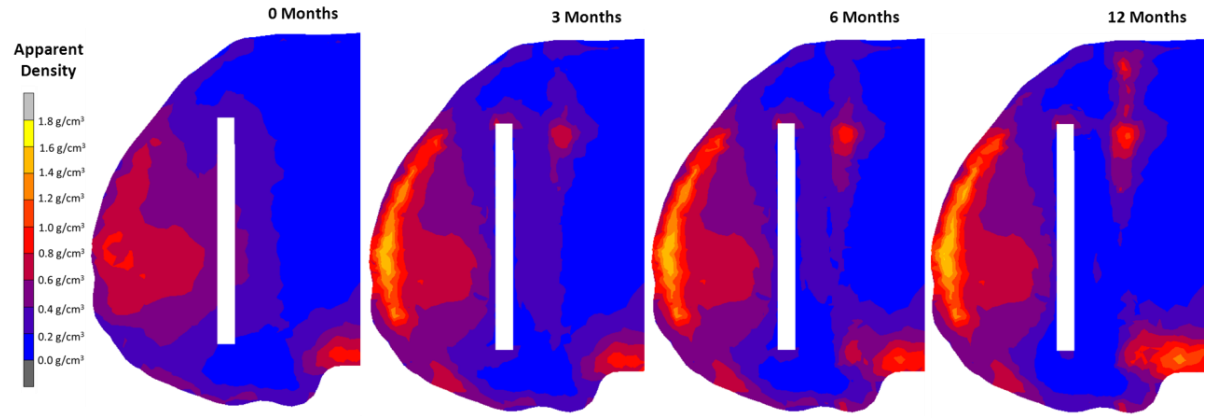


**Figure 127 - Bone remodelling of tibia bone 1 mm under the tibial tray of patient-2.**

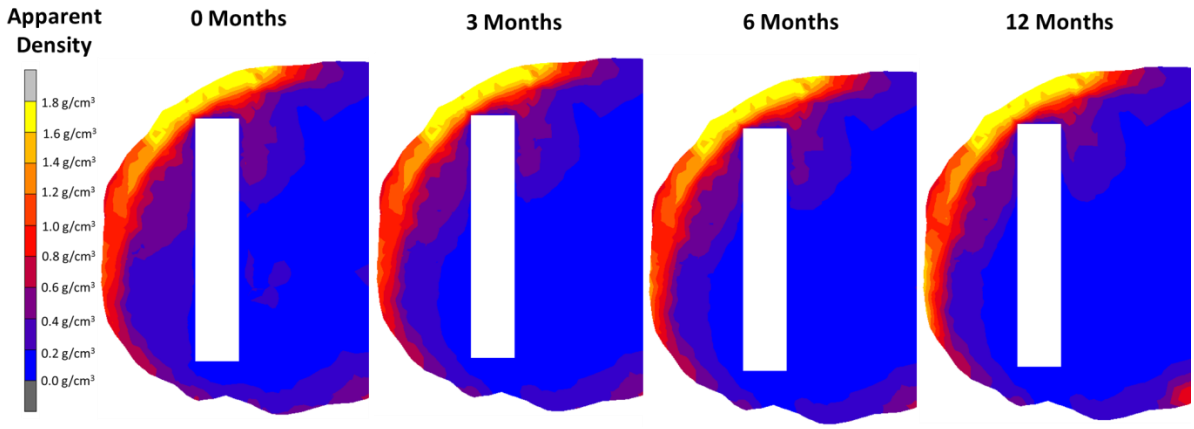


**Figure 128 - Bone remodelling of tibia bone 1 mm under the tibial tray of patient-9.**

Figures 129 and 130 show the bone apposition that takes place in the femur; leading from the anterior of the femoral implant to the anterior cortical bone. There was minimal bone apposition beneath the central peg, suggesting that this was not the main load-path. This is a distinct difference to what is commonly observed in TKRs. It was clear from these figures that the dense regions beneath the implant peg commonly seen in 2D radiographs (Figure 120) correspond to the intercondylar notch not the medial condyle. Since the load-path isn't through the implant stem, there was bone apposition beneath the central and anterior femoral implant.

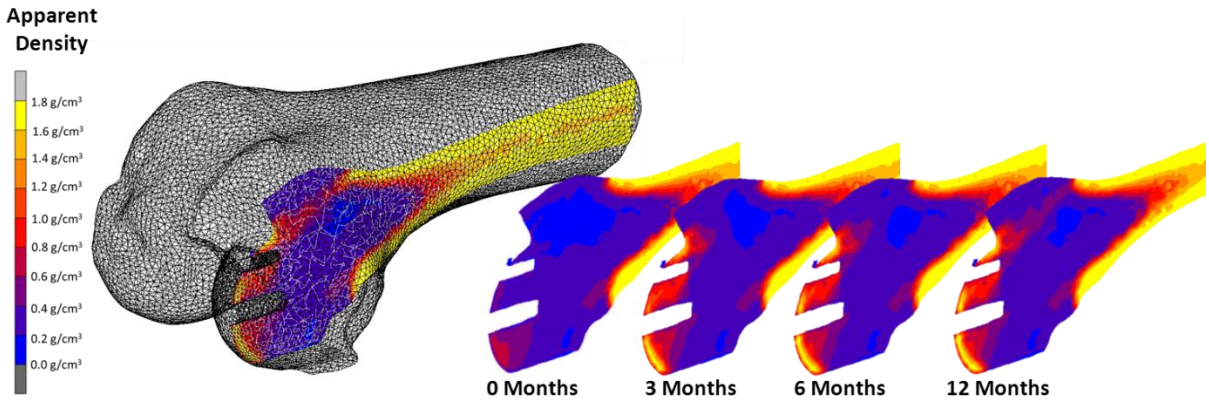


**Figure 129 - Bone remodelling at a slice through centre of femoral implant of patient-2.**

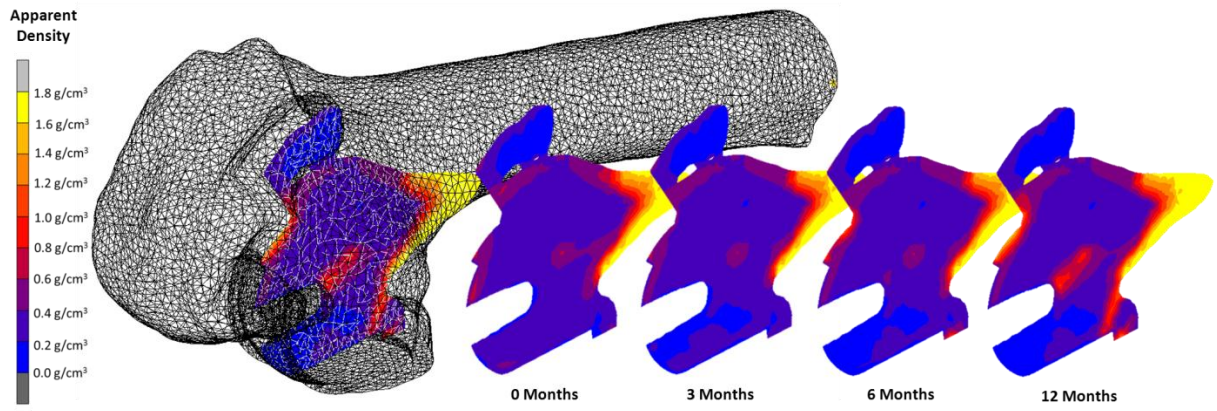


**Figure 130 - Bone remodelling at a slice through centre of femoral implant of patient-9.**

Figure 131 presents a slice 1 mm beneath the posterior femoral implant, with plots of bone density against time. There is bone resorption at the posterior of the implant in patient-9; this is also clear from Figure 130.

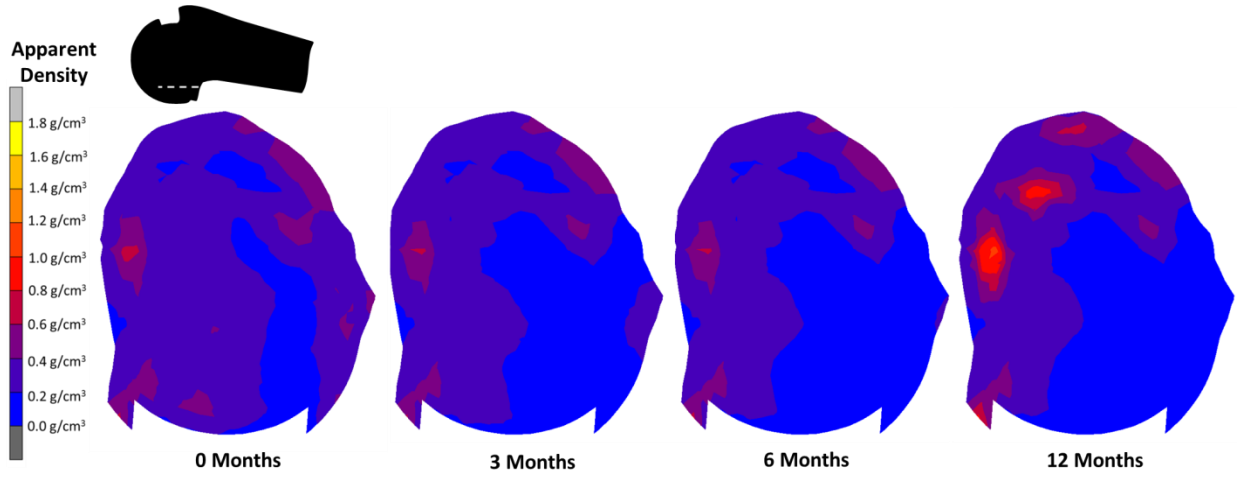


**Figure 131 - Bone resorption at a slice 1 mm beneath the posterior section of the femoral implant of patient-9.**

## 8.5 Discussion

### *8.5.1 Summary*

A study of bone remodelling parameters to model UKR human tibiae was completed. The following parameters were chosen to produce the most realistic predictions of the actual measured patient knees: a stimulus of strain energy density (U); lazy-zone of 75%; time-parameter of $\tau = 50$; and with the theory of Martin activated. The decision to use these parameters was based on judgement and qualitative analysis of quantitative assessment measures.

There was insufficient evidence to exclude the stimulus of strain energy density per unit mass (U/ρ) (used by Chong et al. (2011)). One of the reasons for rejecting stimulus U/ρ was that it was found to be more sensitive to the parameters, particularly the lazy-zone. The lazy-zones of 50% and 65% were excluded on the grounds that they stimulated too much bone-remodelling, and both lazy-zones of 75% and 90% produced realistic results. It is likely that the lazy-zone and time-parameters differ between patients and anatomy; however, for this study they were assumed to be the constant. The time parameter was chosen based on (1) clinical evidence that bone remodelling tends to stabilise at 1-2 years (Seitz et al., 1987, Engh et al., 1987), and (2) the model solutions were showing signs of convergence at 1 year with time parameter values of above 50.

The final models of post-UKR ΔBMD produced realistic DXA simulated radiographs that qualitatively matched with clinical results. The models followed the trends seen in the clinic, highlighting regions of bone loss and adding a further perspective to explain the clinical results. The quantitative ΔBMD predictions of ROIs were in general similar to those measured in the clinic; however, the error margins were high (as much as 20% compared to clinical measurement errors of up to 8%, refer to Section 7). The models could be useful tools for assessing how different design features may affect implant fixation. To improve the credibility of these tools, the sensitivity of the results to the input parameters was assessed. The following describes the main findings of the sensitivity assessments and discusses its implications.

### *8.5.2 Sensitivity to Activity and Load Configurations*

Bone remodelling predictions are sensitive to the magnitude, direction and position of knee forces. For the modelling algorithm used in this study, the following three knee force parameters were identified to be most uncertain:

- load configurations included in the analysis;
- rehabilitation and activity level of the patient before and after surgery;
- position of the tibiofemoral and patellofemoral contact locations.

Sensitivity of the remodelling predictions was assessed by making probable perturbations to these parameters.

Figure 132 shows the effect on BMD changes by using only three load configurations in the femur model, rather than the 8 used for the baseline model. The three loads assessed excluded any loads above 30 degrees of flexion. The reduced flexion model has more realistic results; this corroborates with discussions and observations of patient-9 who showed signs of likely low activity following arthroplasty and possibly reduced flexion. Note that although there were changes to the ROI ΔBMD predictions, the bone-apposition at the anterior reamed corner remained.

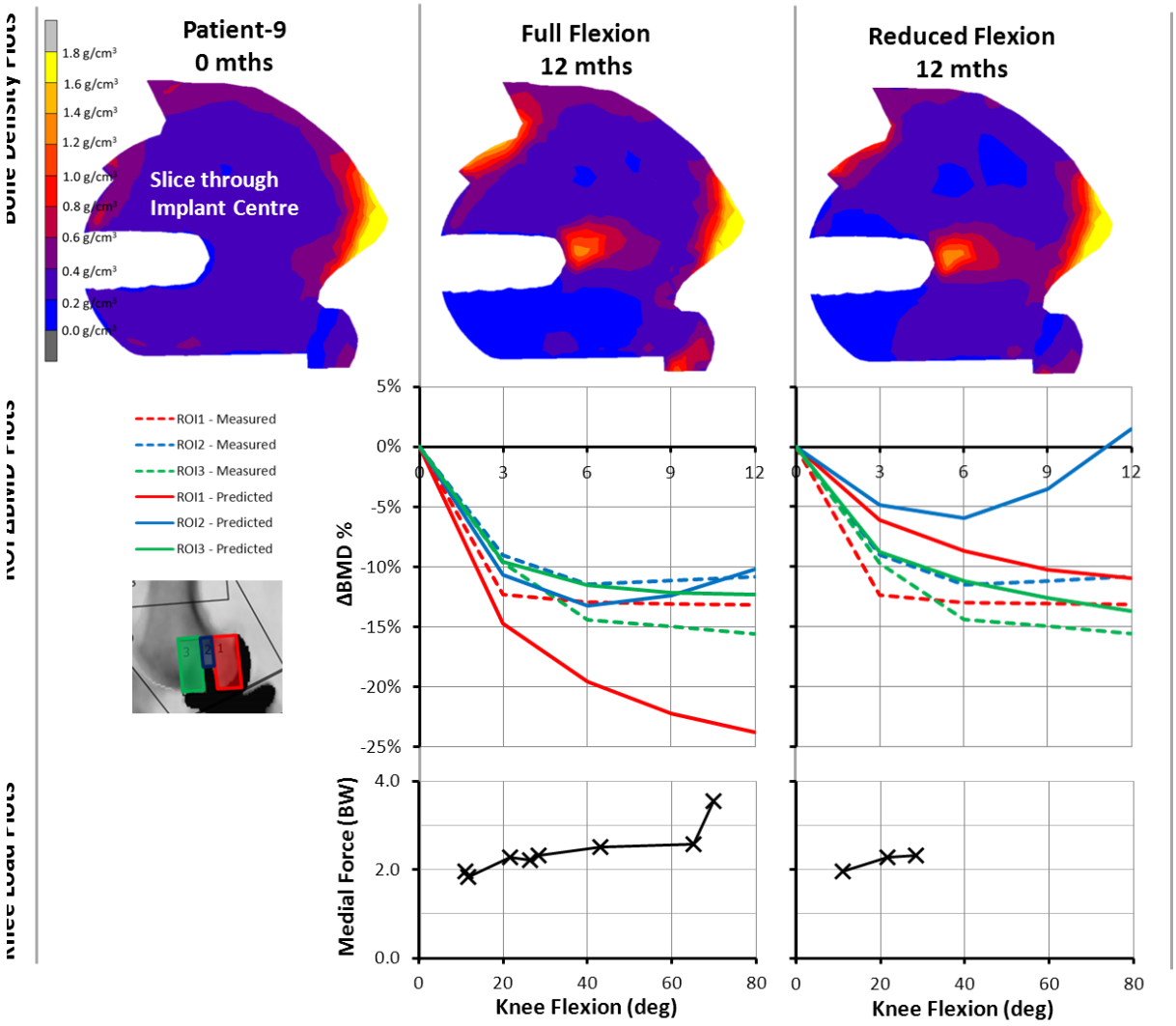


**Figure 132 - Comparison of measured and predicted BMD changes over one year. ROI BMD plots show how reducing the range of flexion angle loads improves predictions. The bone density contour plots of a slice through the centre of the implant show how, when flexion is reduced, there is increased BMD under the keel and less BMD at the anterior reamed corner.**

The sensitivity of the results to rehabilitation was simulated by varying how quickly the patient resumed full (pre-arthroplasty state) knee loads. Figure 133 plots BMD changes in the ROIs based on five progressively reducing recovery times. The quicker the patient resumes full activity, the less will be the bone resorption under the femoral implant.

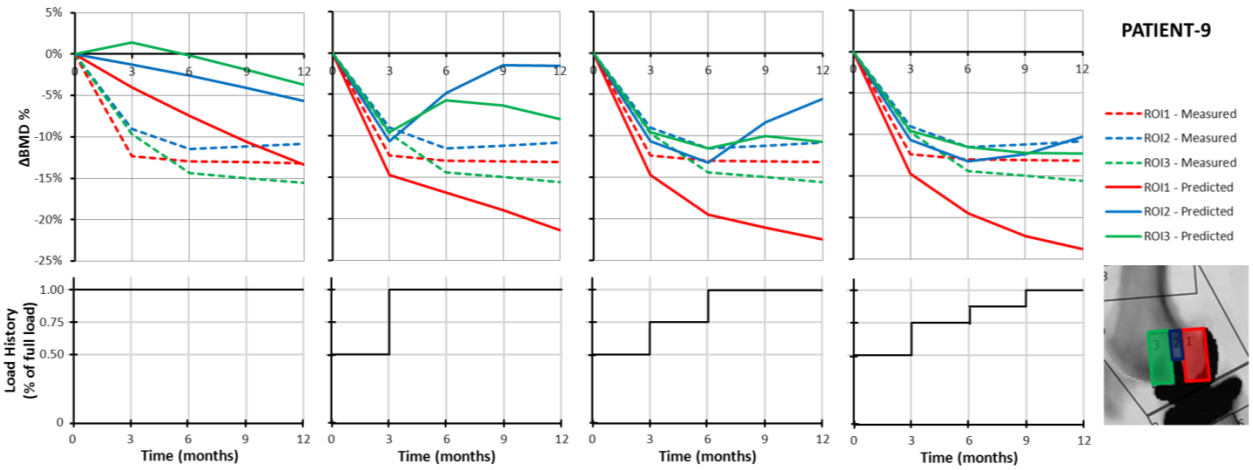


**Figure 133 - Comparison of measured and predicted BMD changes over one year. Plots show how reducing the ramping up of load significantly improves predictions.**

The contact locations of the pre-arthroplasty and post-arthroplasty state were modified to assess the sensitivity of the BMD predictions. The tibia models were found to be sensitive the mediolateral position of the medial condylar tibiofemoral contact forces in the reference (pre-arthroplasty state) model. Figure 134 shows the sensitivity of ROI 6 to changes to tibiofemoral contact at the intercondylar eminence in the pre-arthroplasty state. Figure 134 also demonstrates the effect of ACL function post-UKR. As discussed in Section 7.4, significant BMD drop was observed at ROI 6 in the UKR patient group and this analysis demonstrates that this may be due to some loss of ACL function.

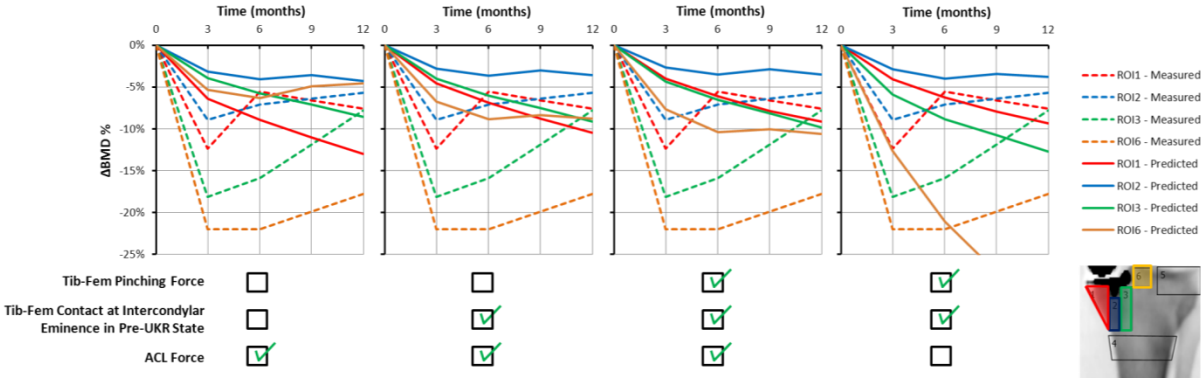


**Figure 134 - Plots showing the sensitivity of patient-9 ROI6 predictions to: (1) tibiofemoral contact at the intercondylar eminence in the pre-UKR state; and (2) ACL function post-arthroplasty.**

Figure 135 shows images of the model of patient-2 and demonstrates how UKR moves the centre of tibiofemoral medial condylar contact laterally and removes contact that may have existed at the tibial eminence. Since the tibiofemoral contact spans up the tibial eminence and this surface is sloping into the centre of the condyle, there is a ‘pinching force’ imparted on the tibia. Although the effect of this ‘pinching force’ is small (refer to Figure 134), it is not negligible.

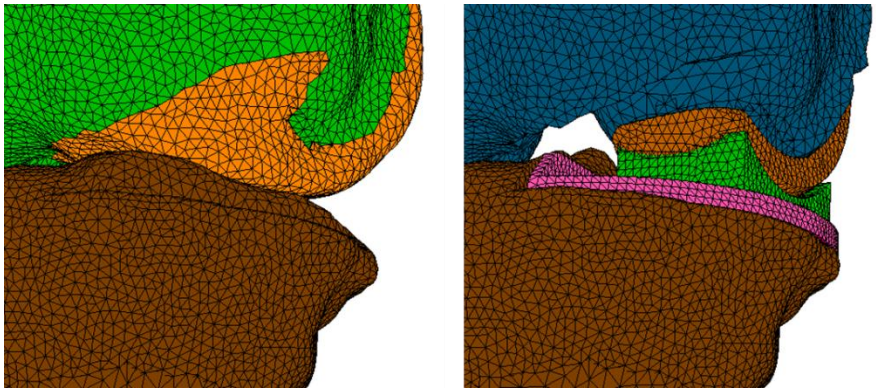

**Figure 135 - Plot showing how arthroplasty removes contact with tibial eminence.**

### *8.5.3 Sensitivity to Stress Raisers*

A stress raiser is a discontinuity in a structure which causes high localised stresses and strains. The arthroplasty creates two distinct stress raisers in the bone: at the resected corner of the tibia; and the anterior edge of the reamed area of the femur. The former is a real stress raiser that is produced by the arthroplasty technique and is often made worse by inexperienced surgeons who overcut the tibia (Clarius et al., 2009b). The strains at the tibia resection corner reach 3500 με (compared to tibia bone failure limit of 6500 με). As presented in Figures 125 and 126, this causes bone apposition lateral to the implant side-plate; this is representative of the typical sclerotic bone regions seen in such UKR patients as presented in Figure 141.

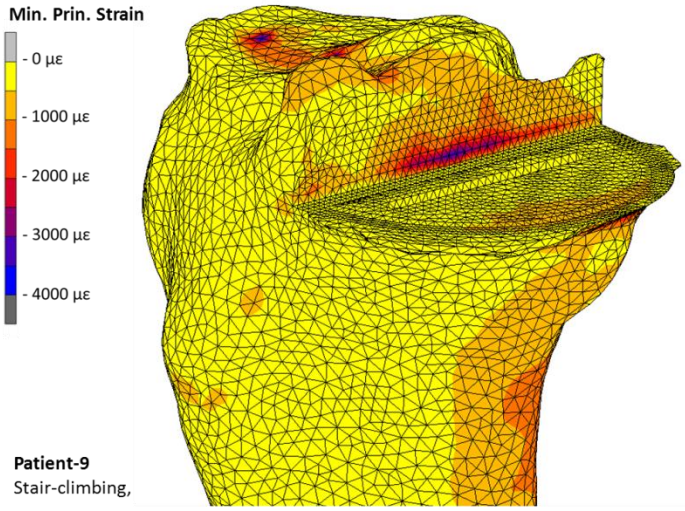


**Figure 136 - Bone strains at tibia resected corner approach bone failure limit of 6500 με during stair climbing activities.**

Simpson et al. (2011) also predicted high strains at the side wall of the UKR implant and these high strains may be conducive for development of fibrocartilage and lamellar bone around the tibial UKR (Gray et al., 2010).

The femoral anterior reamed corner stress raiser is produced because the femoral condyle does not conform to a single radius; the radius increases towards the anterior. The severity of the cut is dependent on patient anatomy and some patients are more prone to it than others. This was prominent in patient-9 as illustrated in Figure 137. Surgeons should chisel the bone away to round-off the corner; however a step is often evident. Note that in the femur model of patient-9 the osteophytes have not been removed; osteophytes are normal in osteoarthritis knees and the surgeon would usually remove these. A single element chamfer was added to the models to remove this stress raiser, as plotted in Figure 138.

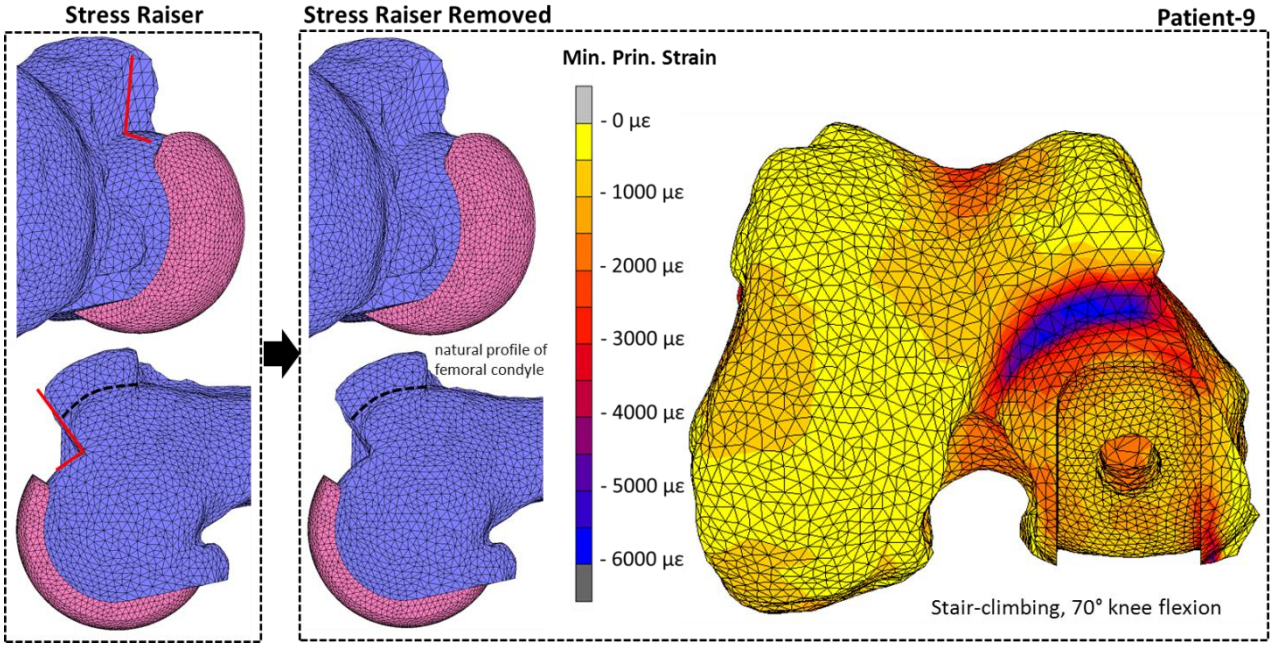


**Figure 137 - [Left] Removal of stress raiser at anterior reamed corner of the medial femoral condyle. [Right] Contour plots present bone strains at the anterior corner; strains approach the failure limit of femoral bone (6100 με) during stair climbing activities when forces act at 70 degrees flexion.**

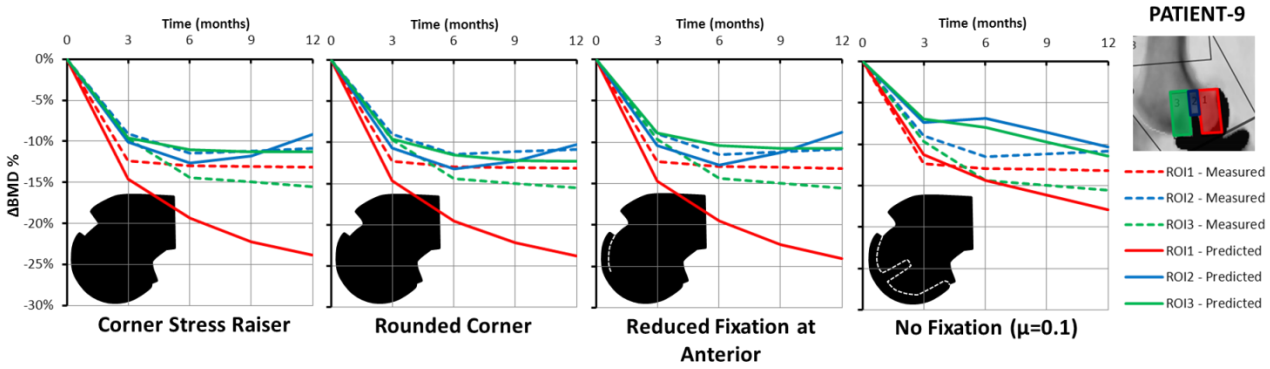


**Figure 138 - Sensitivity assessments conducted investigating how fixation and stress raisers effect BMD changes. Effect of removing corner stress raiser at the anterior reamed femur of patient-9 was negligible.**

Additional assessments were conducted investigating whether imperfect fixation at the anterior flange of the femoral component (reduction of shear force transfer due to tangential

micromotion) would reduce the high bone-apposition at this corner. Figure 138 shows that reducing fixation at the anterior bone-cement-implant interfaces had a negligible effect on the BMD predictions but reducing the shear fixation at the whole cement-implant interface did improve the BMD predictions. There is unfortunately insufficient evidence for reducing the shear fixation because the low interface micromotion (mainly less than 50 με with the posterior implant tip reaching 65 με during stair-climbing) should produce good fixation (refer to Sub-Section 4.6.3). Note, however, that the fixation modifications did not alter the high bone apposition seen at the anterior corner of the femur.

The bone apposition seen at the anterior corner is mainly stimulated from loads at 50-70 degree flexion angles (during stair-climbing activities). The minimum principal strain at this corner reaches close to its failure limit of 6100 με (Figure 137) and may be responsible for the discomfort felt by most patients immediately post-arthroplasty (patients tend to be very unaware of the precise location of the pain, personal discussion with Prof. Justin Cobb). The bone strains at this anterior corner may be too high for normal bone remodelling to take place; these limitations are discussed in Sub-Section 8.5.3 below.

### *8.5.4 Sensitivity to Osseointegration Parameters*

The models assume that osseointegration occurs at 3 months and this is a discontinuous change in boundary conditions. In reality, the process is gradual. The actual result lies in between the conditions that (1) osseointegration occurs immediately post-UKR; and (2) osseointegration occurs at 3 months. A sensitivity study was conducted to assess the impact of assuming condition (1) or (2), and the results are presented in Figure 139.

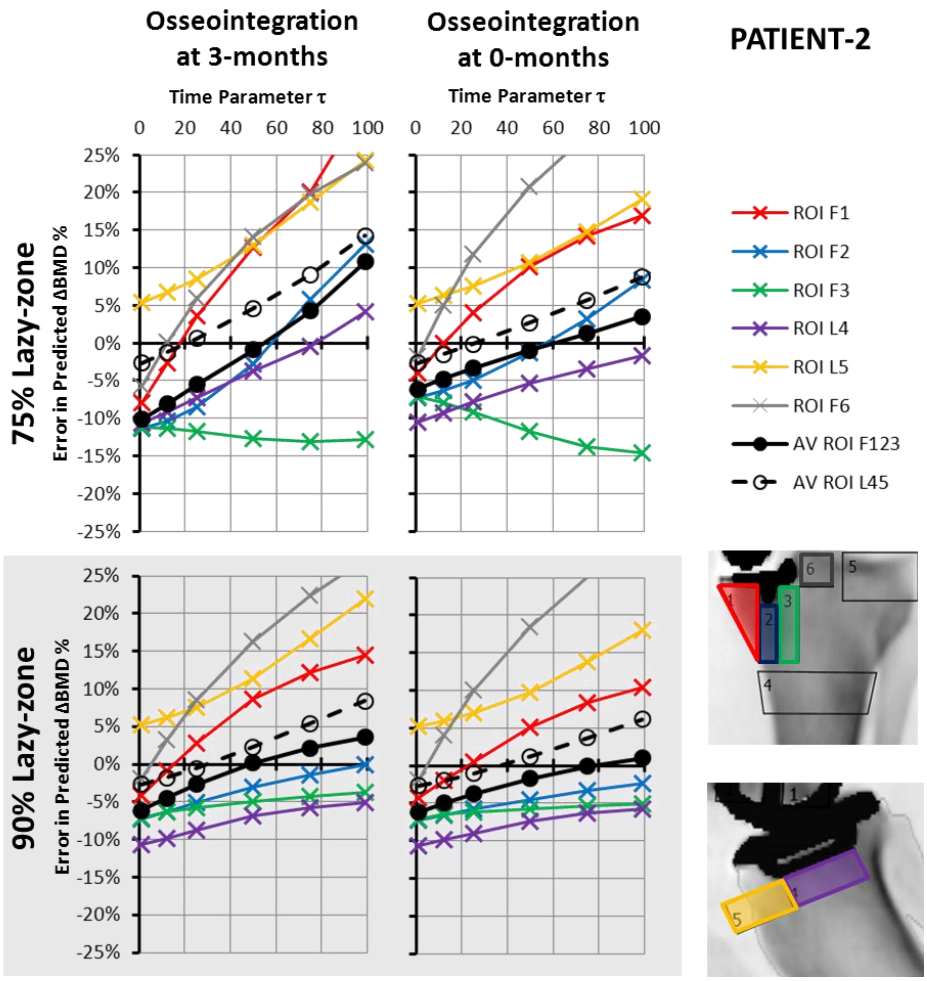


**Figure 139 - Effect of osseointegration parameter on remodelling predictions.**

The time at which full osseointegration is assumed has an effect on bone remodelling, with the largest difference occurring at ROI F6 (assuming $\tau$=50) of 7% error. The differences to ROIs F1-3 and L4-5 are less than 3% error. Noting the large inter-subject variations, this has a small effect. Overall, it was judged to be more accurate to assume osseointegration at 3-months.

### *8.5.1 Reduced ACL Function*

The significant bone loss under the tibial eminence (displayed by most patients in the clinical study of Section 7) has been shown to be due to a combination of lack of fixation on the implant side-wall, removal of lateral tibiofemoral 'pinch' forces at the medial condyle upon arthroplasty, and reduced ACL function. The former two reasons can explain up to 15% of the bone loss; higher bone loss is suggestive of reduced ACL function. Half of the clinical patients (Section 7) displayed bone loss greater than 15%. A possible explanation for the reduced ACL function could be because the femoral component of the Oxford UKR rests too posteriorly on the condyle. In vivo fluoroscopic analysis of UKR patients has shown that the

centre of pressure shifts posteriorly by an average of 5 mm post-arthroplasty (refer to Sub-Section 3.2.3). In this posterior position the implant bearing could be restricted from translating further posteriorly, which would in turn reduce the ACL force. This restriction could be caused by soft tissues, swelling, scar tissue, or fibrous tissue ingrowth. This would be more significant in small tibiae where the bearings are larger in comparison to the tibial tray. Although statistically insignificant (due to insufficient numbers), this trend exists in the clinical patient results (Figure 140).

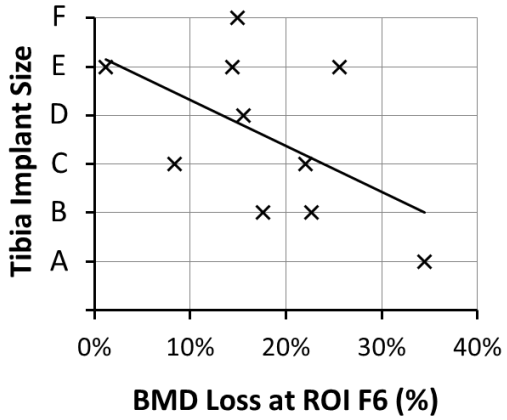


**Figure 140 - Plot of measured BMD loss at ROI F6 against tibia implant size.**

### *8.5.2 Comparison to Literature*

This is the first clinical follow-up DXA study conducted on UKR patients (none reported in the literature). Gillies et al. (2007) compared two fixed bearing polyethylene UKR designs (with and without keel), and concluded that the bone loss under a keeled tibial implant was approximately 5%. Unfortunately their models were never validated with clinical data. The present study found similar bone loss predictions for the mobile-bearing tibial implant and were based on validated patient specific models. This study also investigated the femoral implant, predicting bone-apposition at the anterior reamed corner and potential bone loss at the posterior of the condyle. While Gillies et al. (2007) only investigated cemented fixation, this study has compared both cemented and cementless implant patients. Although differences were observed between the cemented and cementless fixation patient models, they should not be compared because patient-specific anatomical differences can overshadow the effects due to the fixation. Section 9.1 compares predicted outcomes for both patients if alternative fixation was used.

This study is the first patient-specific bone-remodelling validation study conducted in-vivo on humans. Weinans et al. (1993) conducted the first bone-remodelling validation study on canine specimens and demonstrated that such models could predict bone loss in animals. Following on with this work, Kerner et al. (1999) repeated the study on human THR femora

from data produced earlier in a post-mortem retrieval study (Engh et al., 1992a). The pre-arthroplasty bone geometries (and reference stimuli) were generated from generic cases and the contralateral limbs. The study lacked detail on the time-course of the remodelling predictions; therefore, Bitsakos (2005) conducted another study on seven retrieved THR femora to find a time-parameter suitable for humans. The study used CT scans taken over the course of two-years which were previously published by Lengsfeld et al. (2002). Since pre-arthroplasty data was unavailable, the pre-arthroplasty bone geometries (and reference stimuli) were also generated from the contralateral limbs. During the same period, Turner et al. (2005) conducted a generic (non-patient-specific) validation study using 3 human cadaveric femora and compared the predictions against a generic data set of 56 DXA scanned THR patients over the course of two-years (data unpublished). Herrera et al. (2007) conducted a similar generic study looking at the long-term (12 year) effects of a THR implant. This study is unique because it was conducted prospectively on living patients using real DXA scans; all data was patient-specific including the pre-arthroplasty models, and the study was performed on both the tibia and femur.

The canine validation study by Weinans et al. (1993) found that a time-parameter of $\tau$=129 produced most optimal predictions of bone remodelling. With humans having a slower metabolism than canines, we would expect this time-parameter to be lower in humans. With addition of a fading memory function, Bitsakos (2005) found $\tau$=50 produced the most realistic results. Turner et al. (2005) did not publish their optimised time-parameter. In the current study, $\tau$=50 produced the most realistic BMD predictions.

In the literature, the lazy-zone threshold levels for stimulus vary from 60-90%, and this study found that the choice of stimulus affects the optimal lazy-zone. Weinans et al. (1993) found that on canines the most suitable lazy-zone was 35%.

In a study of human THR femora that were retrieved at autopsy, Maloney et al. (1989) found that cortical strain reduced by as much as 50% post-arthroplasty and did not reach pre-arthroplasty levels even at 17 years. This is suggestive that lazy-zones are higher in humans. In the study of humans, Bitsakos (2005) found 75% was more suitable and this has been used widely in the literature (Weinans et al., 1993, Huiskes and Rietbergen, 1995, Van Lenthe et al., 1997, Kerner et al., 1999, van Lenthe et al., 2002, Bitsakos, 2005). In studies utilising a stimulus other than strain energy density or strain energy density per unit mass, lower lazy zones have been used: Turner et al. (2005) used a stimulus of equivalent strain and found a lazy-zone of 60% to be most suitable, and a number of studies have followed suit (Gillies et al., 2007, Gray et al., 2010). In this study, it was found that lazy-zones of 75%

(and up to 90%) were more suitable. It has been speculated that these lazy-zones may be individual to each patient and to vary with age (Frost, 1988).

Studies of THR femora have tended to find that the algorithm over-estimated bone resorption (Weinans et al., 1993, Kerner et al., 1999, van Lenthe et al., 2002, Bitsakos, 2005), particularly if allowed to converge. Bitsakos (2005) showed that predictions improved if a 'memory loss' function was included in the algorithm. The present study did not find that the predictions were over-estimating bone loss, and bone-apposition predictions were higher than expected. To account for the gradual bone decline seen in older patients (Frost, 2001), a percentage of BMD reduction (determined from the average decline in DXA readings at regions that were unaffected by operative trauma and implant load distribution) was included. The reason for the difference (compared to the findings of Bitsakos (2005)) may be associated with the additional level of refinement in the present models: The present FE modelling method was validated for bone strain (as described in Section 6) and as a result of a material study (described in Sub-section 2.6), the method for assigning bone elastic moduli to the bone models was improved. The changes made a significant improvement to the accuracy of the bone strain predictions compared to previous elastic modulus estimations (Carter and Hayes, 1977) (used by Weinans et al. (1993), Kerner et al. (1999), Bitsakos (2005) and Chong et al. (2011)).

In this study, the results were sensitive to the simulated activities. Also, excluding the effects of activity, both patients' bones responded differently. This quantitative variability is common in patient-specific remodelling FE models in the literature (Bitsakos et al., 2005) and may be attributed to pre-arthroplasty bone density (Huiskes and Rietbergen, 1995) and anatomy differences. The qualitative bone changes can be better seen in X-Ray radiographs rather than DXA scans. Figure 141 shows frontal and lateral radiographs taken at 12 years of an Oxford UKR patient. The radiographs corroborate some of the findings of this study, showing bone apposition at (1) the tibia resected corner, (2) the tibia posterior under keel, (3) femur anterior reamed corner; and bone resorption at (1) anterior tibia, (2) base of femoral implant stem. The bone loss seen at the medial region under the tibial implant was not observed in the FE study of two patients. The bone loss here may be due to unloading of the medial compartment with tibiofemoral contact occurring at the medial tibial eminence. The present study highlighted that BMD changes were sensitive to this condition.

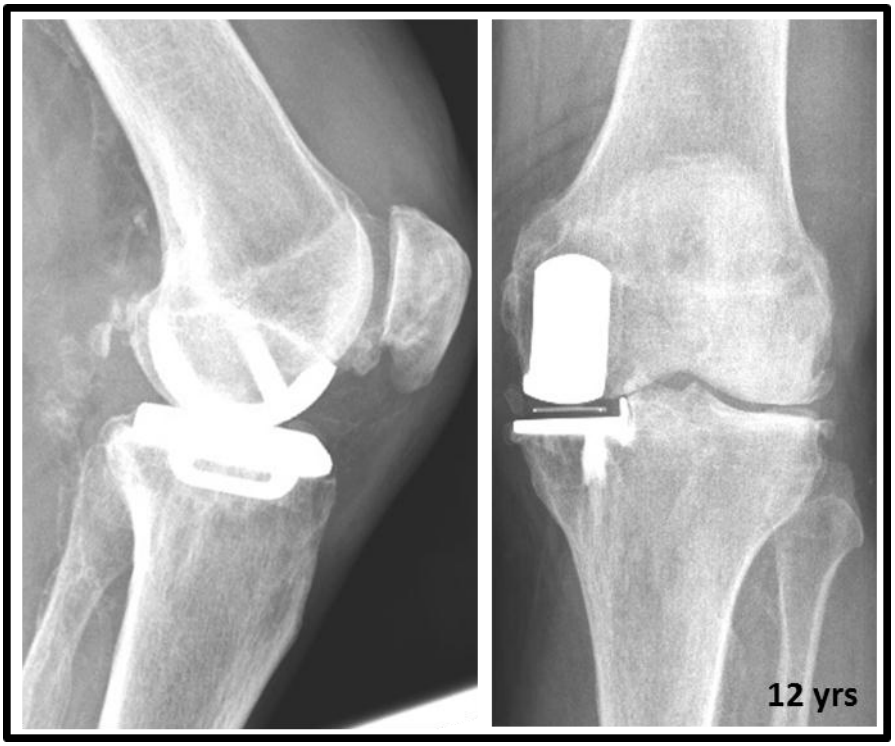


**Figure 141 - Radiograph of Oxford UKR patient knee at 12 years, showing bone apposition at (1) the tibia resected corner, (2) the tibia posterior under keel, (3) femur anterior reamed corner; and bone resorption at (1) anterior tibia, (2) base of femoral implant stem, (3) medial region under tibia implant.**

### *8.5.3 Limitations of the Bone Remodelling Algorithm*

Bone remodelling stimuli of U and U/ρ were both assessed in this study. The following discusses why $U/\rho^2$ would be a better stimulus for the bone remodelling algorithm than U/ρ. The original derivation of U/ρ (Huiskes et al., 1987) is discussed herein and it is argued that due to better understanding of bone since the publication of this work a better stimulus can be postulated.

Bone is assumed to be a self-optimizing material with the objective of aligning trabecular architecture with principal stress orientation and adapting its apparent density (Carter and Hayes, 1977) to an 'effective stress' $\sigma_{eff}$. Hence the following optimisation objective is defined:

$$\rho = constant \times \sigma_{eff}^{1/2}$$

where ρ is the average apparent density of bone. Using the definition of the strain energy density of a unit of mass, the following is expressed:

$$\sigma_{eff} = \sqrt{2UE}$$

where U is average strain energy density and E is average elastic modulus. It is assumed that cortical and cancellous bone can be defined with a single relationship proposed by Carter and Hayes (1977):

$$E = constant \times \rho^3$$

Based on these equations, the optimisation objective can be rearranged to demonstrate that bone remodels with time to try to maintain a steady-state constant U/ρ. Since we now know that elastic modulus is not proportional to $\rho^3$, and is in fact a better estimate would be to $\rho^2$ (for cancellous bone) then we can show that $U/\rho^2$ should prove to be a better remodelling stimulus. This has not been assessed in this study.

Bitsakos (2005) found that neither U nor U/ρ produced accurate converged solutions (that correlated with clinical results). He never considered $U/\rho^2$ as a stimulus but he did consider principal strain and found that the converged results were better. The BMD predictions, in the present study, showed signs of convergence which is as expected of patients at one-year post-arthroplasty. The most likely cause of the improvement of accuracy is the use of improved elastic modulus estimations in the FE models.

Bone resorption and apposition are assumed to occur at the same rate, but there is evidence to suggest that resorption occurs at a faster rate than bone-apposition (Lanyon, 1987, Frost, 2001). Faster resorption and slower apposition rates in the models could potentially improve the BMD predictions. However, a sensitivity study conducted by Bitsakos (2005) on THRs showed that altering bone remodelling rates had negligible effect to the BMD predictions.

The algorithm disregards bone ‘memory loss’. This theory is based on the assumption that recent loading events affect bone adaptation more than those in the past (Levenston et al., 1994). An histological study of the proximal femur showed that after 17 years cortical bone strain had still not stabilised to its pre-arthroplasty levels (Maloney et al., 1989). Petersen et al. (1995b) and Saari et al.(2007) concluded that the adaptive process stops after 5 years. A canine study (Jaworski et al., 1980) showed that full bone resorption did not occur after complete immobilisation of forelimbs, in fact it stabilised after 6 months post immobilisation. ‘Memory loss’ algorithms have been proposed by authors in the past (Bitsakos, 2005, Levenston et al., 1994, Kerner et al., 1999). Bitsakos (2005) considered a fading ‘memory loss’ function (proposed by Levenston et al. (1994)) with stimulus U and found this to reduce BMD change predictions and in some cases improve predictions. However optimal function parameters varied between subjects and it would be problematic to find a reasonable parameter in this study. Additionally, bone loss has only been investigated over a short period of one year, for which the effect of a ‘memory loss’ function would be minimal.

The algorithm assumes that lazy-zone is constant throughout the bone. Bitsakos (2005) speculated that lazy-zone may be site-specific and that this would explain differences between predicted and clinically observed results. Unfortunately with this assumption, the study becomes substantially complex; validation would not be possible with 2D scans and it would require optimisation algorithms to allocate site-specific lazy-zones from 3D post-arthroplasty scans.

The effect of age on bone-apposition rate is significant (Pearson and Lieberman, 2004) and has been neglected in the bone remodelling algorithm. An in-vivo animal study (Jaworski et al., 1980) showed that there was a reduction of 30% in bone apposition rate in older dogs. The age range of the UKR patients investigated in Section 7 was 42-79 years and the two patients used for the validation study were 70 and 63 years (patient-2 and 9 respectively). Although quantitative effects have been studied in animals (Sontag, 1992), the precise effects are unknown in humans and inclusion in our models would be unverified. The effects of age were considered in BMD predictions by inclusion of a patient-specific rate of decline of BMD.

In Sub-Section 8.5.3, it was highlighted that bone strains at the stress raisers may be too high for normal bone remodelling to take place. Figure 142 illustrates a tissue differentiation diagram proposed by Claes and Heigele (1999) and reproduced by Shefelbine et al. (2005) and demonstrates how high strains could form connective tissue rather than bone. The formation of low stiffness tissue (connective tissue) at this region could inhibit the anterior load path and instead distribute the load through the implant stem and posterior aspect of the femoral condyle.

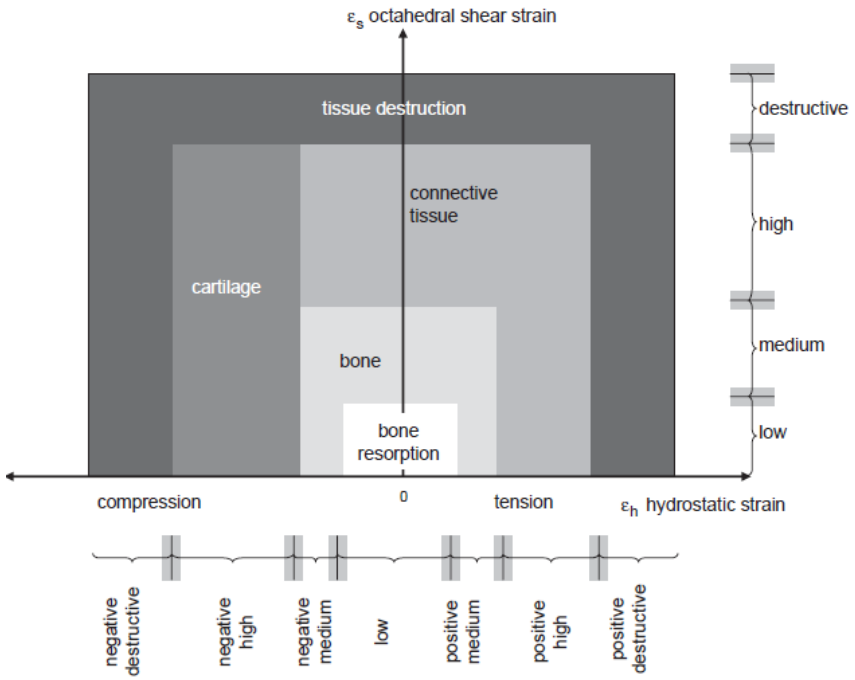


**Figure 142 - Tissue differentiation diagram based on Claes and Heigele (1999) and reproduced by Shefelbine et al. (2005).**

Traditionally, critical strain thresholds have not been included in remodelling algorithms; however, a recent 2D FEA feasibility study by McNamara and Prendergast (2007) implemented a simple critical strain threshold of 3500 με in their remodelling algorithm. A more sophisticated algorithm could also include tissue differentiation rules such that lower elastic modulus tissue is generated under particular mechanical conditions. Shefelbine et al. (2005) used a “Fuzzy Logic” algorithm, based on Claes and Heigele (1999), neglecting fluid flow and assuming linear elastic material properties to simulate fracture healing. Gray et al. (2010) implemented a similar tissue differentiation algorithm model at a predefined zone under an implant. Both studies assumed that tissue differentiation would be determined by mechanical stimuli alone. Although validation of these studies was not possible, the results of Gray et al. (2010) produced predictions that matched patient radiographs.

Another limitation of the algorithm is that it neglects surface bone modelling. This anterior corner is an exposed resected surface and it has propensity to accumulate micro-fractures (because it has been demonstrated to have very high strains). A callus could potentially grow from this corner altering the load distribution through this region. This ossified callus could potentially redistribute the load to reduce the strains at the corner and hence reduce bone-apposition.

The model assumes isotropic and heterogeneous elastic moduli so that the axial bone stiffness is the same as the transverse stiffness. This assumption is valid when the peak loads are in the direction of the assumed modulus; i.e. always valid for the tibia but with

decreasing validity at the femur with increasing knee flexion forces. The transverse elastic modulus of distal femoral bone is less than the axial modulus (Morgan et al., 2003); therefore, with anisotropic moduli the transverse loads may dissipate through the bone differently. Although recent studies have published new FE techniques for assigning anisotropic elastic moduli to bone (San Antonio et al., 2011), the remodelling algorithm in its current form is incapable of modelling anisotropic material properties.

Although improvements could be made to the bone remodelling algorithm, it is satisfactory in its current form to compare implant design features, particularly of UKRs for which the FE models have been validated. It is important that the users of the bone remodelling algorithm are aware of its limitations and that it is not used beyond the validated zone.

### *8.5.4 Limitations of Study*

The main limitation of this study is that only four patient-specific FE models (two patients) were validated and the patients had successful outcomes. As demonstrated by the high variability of patient outcomes in Section 7, the bone adaptation process is patient-specific. All patients included in the clinical study (Section 7) were happy with their outcomes and there were no revisions. An FE model assessing bone remodelling of a failed UKR would be beneficial for assessing the small portion of patients that have poor outcomes and using this as an additional case for comparing UKR designs in outlier patients. Although including more than two of the clinical patients would have improved confidence in the conclusions, the benefits were considered insufficient compared to the substantial work-effort required in developing the models. The two patients included in the study were representative of the cemented and cementless UKR patient population groups of the clinical study.

Due to computational and remodelling algorithm limitations, the FE models were developed using linear tetrahedral elements (4-node elements) and not quadratic elements (10-node elements) as recommended in Section 4. Therefore, there is potentially a 10% error in predicted bone strains (refer to Figure 37 of Section 4.5). Note that the error reported in Section 4.5 was consistent between models with 10% lower strains. Therefore, the difference in stimulus values (between the pre-arthroplasty (reference) model and the arthroplasty model) would be consistently 10% less and this error would be made negligible with the choice of optimum lazy-zone parameter.

Based on the conclusions of Section 4.5, the mesh density used in this study was deemed adequate. In comparison to previous implant studies employing this remodelling algorithm (Weinans et al., 1993, Kerner et al., 1999, Bitsakos, 2005, Chong et al., 2011), the models in this study were of finer mesh.

## 8.6 Conclusions

Four patient-specific FE models were developed to predict bone adaptation following UKR arthroplasty and validated against BMD DXA results of a clinical patient follow-up study. Using the bone remodelling algorithm developed by Huiskes et al. (1987), the following parameters were found to produce the most realistic predictions of the actual measured patient knees: a stimulus of strain energy density (U); lazy-zone of 75%; time-parameter of $\tau = 50$; and with the theory of Martin activated.

The rate at which the UKR patient resumed normal activity had a distinct effect on the BMD predictions and potentially on the future success of the implant. Maintaining activity levels following arthroplasty minimised bone loss in the high risk regions (posterior femoral condyle and proximal tibial tray keel). The quicker the adoption of normal activity levels the better the outcome was at one year, in relation to the preservation of bone mass.

The significant bone loss under the tibial eminence (displayed by most patients in the clinical study of Section 7) was shown to be due to a combination of lack of fixation on the side-wall of the implant, removal of lateral tibiofemoral forces at the medial condyle after arthroplasty and reduced ACL function. The former two reasons explained up to 15% of the bone loss. Greater bone loss was seen in half of the patients and was suggestive of reduced ACL function. A possible explanation for the reduced ACL function could be because the femoral component of the Oxford UKR lies too posteriorly on the condyle, inhibiting bearing movement (particularly in small size implants) and thus not being able to tense the ACL.

The developed FE models are a useful tool for comparing UKR implant designs; however, it is important that users are aware of the limitations of both the bone remodelling algorithm and the FE techniques employed.

# 9 Studies Investigating UKR Design

## 9.1 Introduction

This section compares Unicompartmental Knee Replacement (UKR) design features using the validated computer simulations developed in previous sections of this thesis. Bone strains in the vicinity of the implant were validated in 8 models (4 tibiae and 4 femora) in Section 6. High bone strain is an indicator of pain and should be maintained below the failure limit of bone for a successful outcome. Osseointegration of implant to bone is another factor for success; implant-bone micromotions of cementless implants should be maintained below 100 με for adequate fixation to develop. The 8 Finite Element (FE) models (4 tibiae and 4 femora) described in Section 6 were also validated for bone-implant micromotion. From the pool of in-vitro knee cadavers assessed (10 knees, 5 pairs from 5 cadavers as described in Section 5), three were chosen to represent a range of bone densities. Cadaver CAD1/2 had the densest bone while CAD3/4 had the least dense bone (fractured during testing), and CAD5/6 was considered to be average. A total of twelve FE models were used to assess fixation stresses, strains and bone-implant micromotions associated with cementless and cemented UKRs.

**Table 15 - FE models used to represent a range of bone densities for assessing UKR designs for fixation.**

| | **Weakest $CAD_{LOW}$** | **Average $CAD_{AV}$** | **Densest $CAD_{HIGH}$** |
|---|---|---|---|
| **Tibia** | CAD4 | CAD5 | CAD1 |
| **Femur** | CAD3 | CAD6 | CAD1 |

The long-term fixation of implants is governed partly by bone remodelling. Four FE models of two clinical UKR patients (PAT2 and PAT9) were validated in Section 8 against one-year Dual X-Ray Absorptiometry (DXA) scans of BMD change around the implants. The models were duplicated to include both cemented and cementless fixation; therefore, a total of eight FE models were used to compare UKR designs for bone remodelling.

**Table 16 - FE models used to represent two UKR patients for assessing UKR designs for fixation.**

| | **Active Patient $PAT_{CL}$** | **Less Active Patient $PAT_{CD}$** |
|---|---|---|
| **Tibia** | PAT2 | PAT9 |
| **Femur** | PAT2 | PAT9 |

A total of 20 validated models (cemented and cementless versions of ten specimens) were used as a baseline to compare UKR designs for initial and long-term fixation.

## 9.2 Cementless or Cemented Fixation?

### *9.2.1 Introduction*

UKR arthroplasty can be performed using either cemented or cementless implants. Recent studies have published good clinical results for cementless UKR implants (Pandit et al., 2009); however, 96% of surgeons prefer cemented fixation (Schindler et al., 2010). There is an increasing trend in Australia for using cementless fixation on UKR patients, particularly for the femur; however, cemented fixation still accounts for more than 75% (Australian National Joint Replacement Registry (2011)). Currently in the literature, there is no real clinical evidence specific to UKRs to suggest that cemented fixation is any better.

Only experienced surgeons tend to consider cementless UKRs. In addition they tend to make the decision of fixation method during surgery when they can actually see and feel the resected bone surface. It is speculated that surgeons inadvertently categorise patients into sub-groups and this categorisation differs from surgeon to surgeon based on their experience and training. This knowledge is mostly unrecorded for UKRs (and often unsupported by scientific evidence as it is based on knowledge accumulated from trial-and-error in part by the specific surgeon). It is therefore not possible to obtain retrospective clinical data from existing national registers to compare fixation method success rates with like-for-like patient sub-groups. Surgical experience tends to dominate UKR success rates, particularly from large multi-centre national registers and it is difficult to ascertain which fixation methods are most successful and to identify which are the best for particular patient sub-groups.

This study presents the findings of an in-silico study comparing identical bones with cemented and cementless fixation methods for the UKR. The computer models were used to simulate post-operative bone strains and bone-remodelling changes at 1 year. The performance of cementless and cemented fixation using the Oxford mobile-bearing UKR was compared for three specimen and two patient knees to identify the best fixation method.

### *9.2.2 Method*

The validated FE models (strain-validated $CAD_{LOW}$, $CAD_{AV}$ and $CAD_{HIGH}$; and remodelling-validated $PAT_{CD}$ and $PAT_{CL}$) were used to compare the fixation performance of cemented and cementless Oxford mobile-bearing UKRs.

The existing cemented and cementless versions of the strain-validated models were used with the only modification being that a full set of knee forces were applied (medial and lateral tibiofemoral contact, muscles and ligaments) to simulate walking and stair-climbing activities.

Two load cases were applied to each of the five tibia models to simulate peak walking (50% of the walking cycle) and stair-climbing (15% of stair-climbing cycle) knee forces. Eight load cases were applied to each femur model representing the peak knee forces at 10 degree increments of flexion angle taken from the pool of data for walking and stair-climbing activities. The knee forces applied to the models are tabulated in Sub-section 8.3.4. The polyethylene (PE) mobile-bearing and the femoral implant were included in the model to ensure that the medial condylar load onto the implant was represented as accurately as possible. Contact between the mobile-bearing and tibial tray was simulated using a Coulomb's friction model with coefficient of 0.1. No other changes were made to these strain-validated models. The development and validation of the FE models are detailed in Sections 4 and 6.

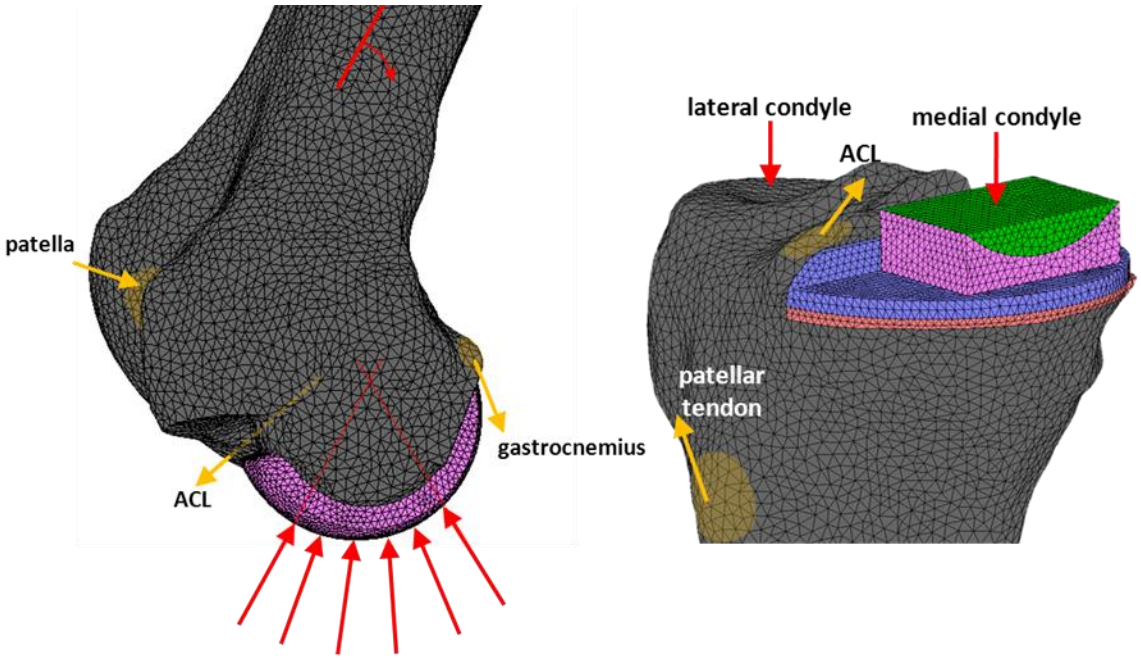


**Figure 143 - Forces applied to the UKR implanted tibia and femur models.**

Since the two remodelling-validated models only simulated the actual fixation used for the UKR patient, two additional models were developed to simulate what would have occurred if the alternative fixation was used (i.e. simulating a cemented implant for $PAT_{CL}$ and a cementless implant for $PAT_{CD}$). Note that the rehabilitation activity levels were different between the two patients, with a rapid rehabilitation to full activity taken by patient $PAT_{CL}$ and a gentle approach taken by $PAT_{CD}$. Eight additional FE models were developed from the remodelling models to assess initial bone strain and final bone strain at 1-year. No other changes were made to these strain-validated models. The validation of the FE models is detailed in Section 8.

Initial fixation is a measure of the immediate post-operative stability of the implant. Under daily activities, good initial fixation will exhibit low bone strains (less than 50% of the failure limit of bone). Good initial fixation also requires low micro-movements between the bone and implant at the interface (micromotion). Although micromotion is an important factor for cementless implants to ensure adequate osseointegration, it is not as important for cemented implants. For the purposes of direct comparison with cementless and cemented implants, micromotion was not considered in this section of the thesis.

To ensure long-term fixation is maintained, the integrity of the implant and bone must be kept intact. Bone-resorption caused by implant stress-shielding can degrade the integrity of the underlying bone. In this study, the bone density of two real UKR patients was assessed immediately after and at 1-year post-arthroplasty. The model of the UKR patient with the cemented implant was modified for a cementless implant to investigate what the effects would have been if she was to have had the alternative cementless fixation. Similarly, the model of the UKR patient with the cementless implant was modified for a cemented implant. It was assumed that all cementless implants developed fully osseointegrated bone-implant interfaces after three months (refer to Sub-section 4.6.3).

Initial fixation was assessed by comparing bone strains, simulated using all five tibiae and femora models. Long-term fixation was assessed by comparing bone density reduction at 1-year post-arthroplasty, simulated using the two remodelling-validated patient models.

### *9.2.1 Results: Initial Fixation*

Figures 144 to 146 , display bone strains plots at three cross-sections of the tibia. They demonstrate how bone strains increased with reduced bone density. The regions of highest bone strain are different for cemented and cementless implants, with higher strains produced with cementless fixation.

Under cemented fixation, the highest bone strains were produced beneath the keel, and these exceeded the failure limit of bone for the lowest density tibia ($CAD_{LOW}$). High bone strains can lead to progressive migration and tibial subsidence. Increased migration has been linked with higher probability of loosening (Ryd et al., 1995). It should be noted that only full activity loads were simulated in this study; with a more gentle rehabilitation programme the bone strains could be kept at sustainable levels. For the patient who had a cemented UKR ($PAT_{CD}$), the peak bone strains were as high as 85% of the failure limit of bone which could have caused some discomfort. However from clinical observation, it was deemed likely that she resumed full activity very gently (refer to Section 7), allowing time for the bone to adapt to these high strains.

With cementless fixation, the highest bone strains were produced around the rim of the tibial tray and at the anterior region of the resected corner. These bone strains exceeded the failure limit of bone for the average density ($CAD_{AV}$) and lowest density tibiae ($CAD_{LOW}$). For the patient who had a cementless UKR ($PAT_{CL}$), the peak bone strains under the tibial implant were within 60% of the failure limit of bone; however at the posterior of the keel, the strains approached the bone failure limit. From clinical observation, this patient's progress was very good: he resumed full activity immediately (with some pain initially) and he was very happy with his outcome. His initial pain may correspond to the high bone strains beneath the keel. Upon osseointegration of the cementless implants, the plots show that bone strains reduced by approximately 30%, particularly at the resected corner and posterior of the keel.

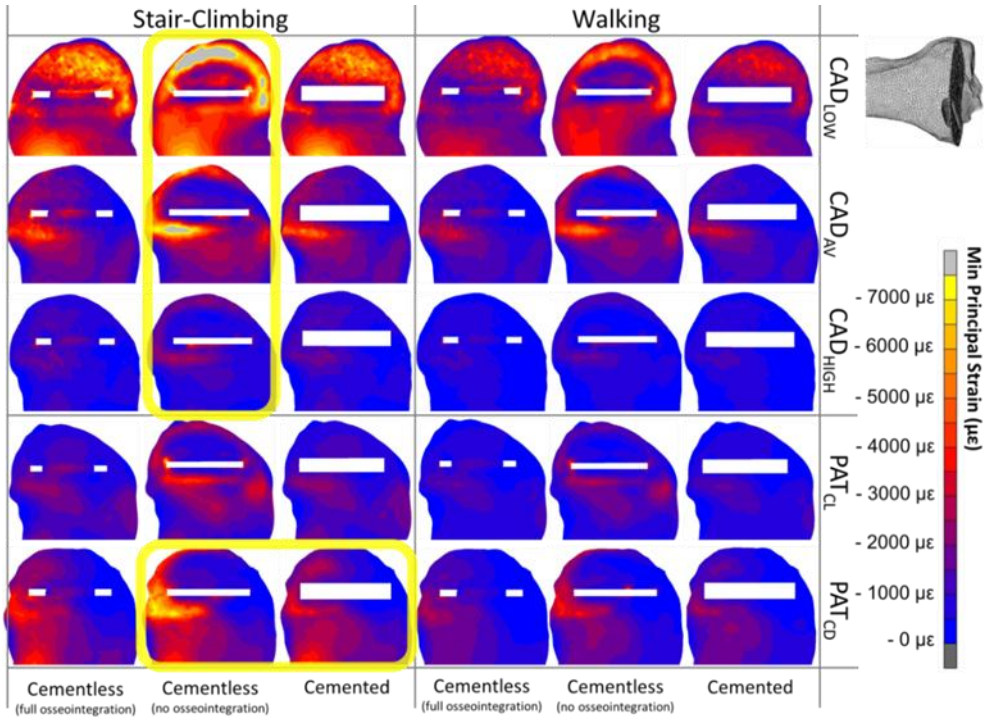


**Figure 144 - Initial fixation of cemented and cementless tibial implants. Minimum principal strain of tibia bone at transverse section 3 mm below the tibia-implant interface. The strain increased with reduced bone density, in particular for cementless implants (highlighted top). Cementation reduced peak bone strains, in particular for $PAT_{CD}$ (highlighted bottom).**

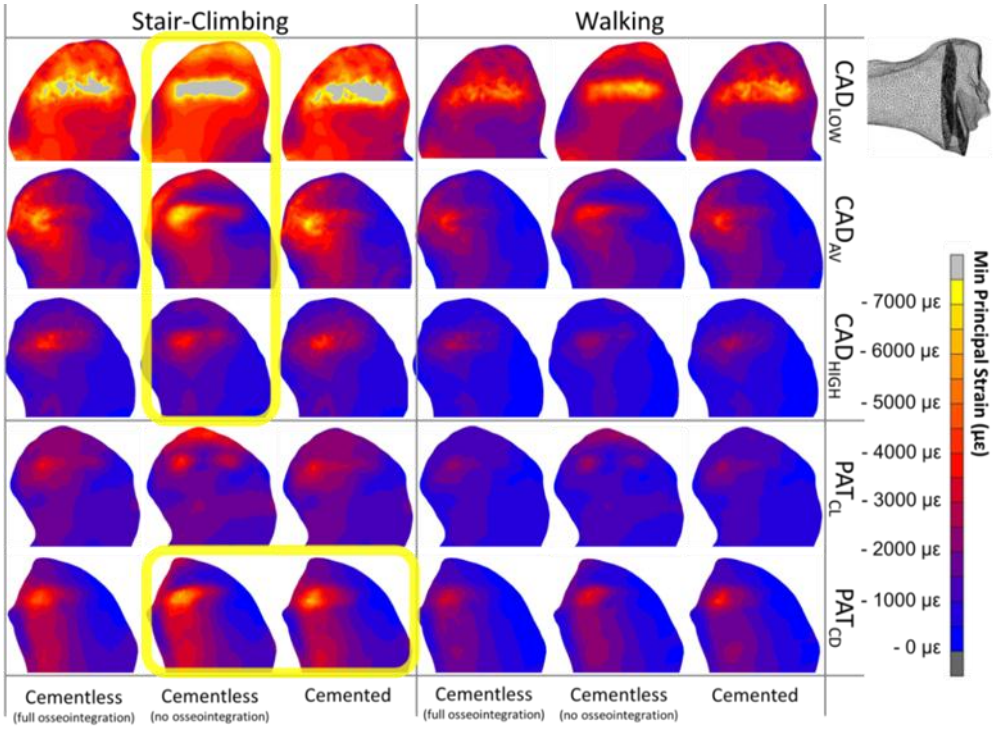


**Figure 145 - Initial fixation of cemented and cementless tibial implants. Minimum principal strain of tibia bone at transverse section 3 mm below the tibia-implant keel interface. The strain increased with reduced bone density, in particular for cementless implants (highlighted top). Cementation reduced peak bone strains, in particular for $PAT_{CD}$ (highlighted bottom).**

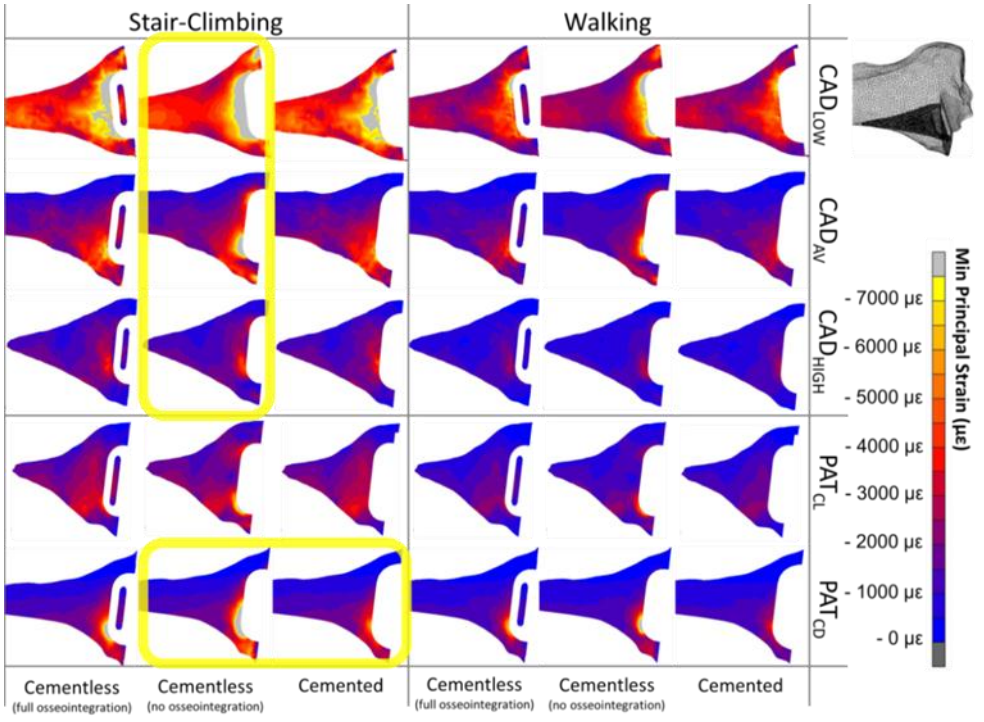


**Figure 146 - Initial fixation of cemented and cementless tibial implants. Minimum principal strain of tibia bone at sagittal section through centre of tibia implant keel. The strain increased with reduced bone density, in particular for cementless implants (highlighted top). Cementation reduced peak bone strains, in particular for $PAT_{CD}$ (highlighted bottom).**

Figures 147 to 149 display contour plots of bone strains at three cross-sections of the femur. The bone strains increased with reduced bone density and these support the results of the tibia simulations. A common feature of the strain plots is the high strains located at the anterior reamed edge. These strains approached the failure limit of bone. Note that for $PAT_{CD}$, the peak strains were located further anteriorly at the edge which is why they are not visible on the plots.

There were significant differences between the strain contour plots of the cemented and cementless femoral implants mainly due to the existence of a second peg for the cementless implant. In general, the second peg reduced the strains at the anterior reamed corner; however, this was not the case for all specimens. The results were variable because the bone density distributions and bone geometries were highly variable between specimens.

For the cemented implant, the load was more equally distributed (compared to the cementless implant). However the region posterior to the central peg was shielded from strain. There was also some initial stress-shielding beneath the posterior of the implant (Figure 149) with cementless fixation. This shielding occurred because the component of force in the anterior direction (this component increases with knee flexion) was reacted mostly by the bone surrounding the pegs (due to a stiff implant) and not the bone beneath the posterior shell.

For the cementless implant, the bone strains were sensitive to whether the base of the pegs rested against bone. In practice, the peg slot is longer than the peg itself so the peg base is “floating”. As a result, the main load-path is through the implant outer-shell. Once osseointegration has occurred the load-path through the keel increases depending on the relative density of the bone beneath it compared to that under the shell.

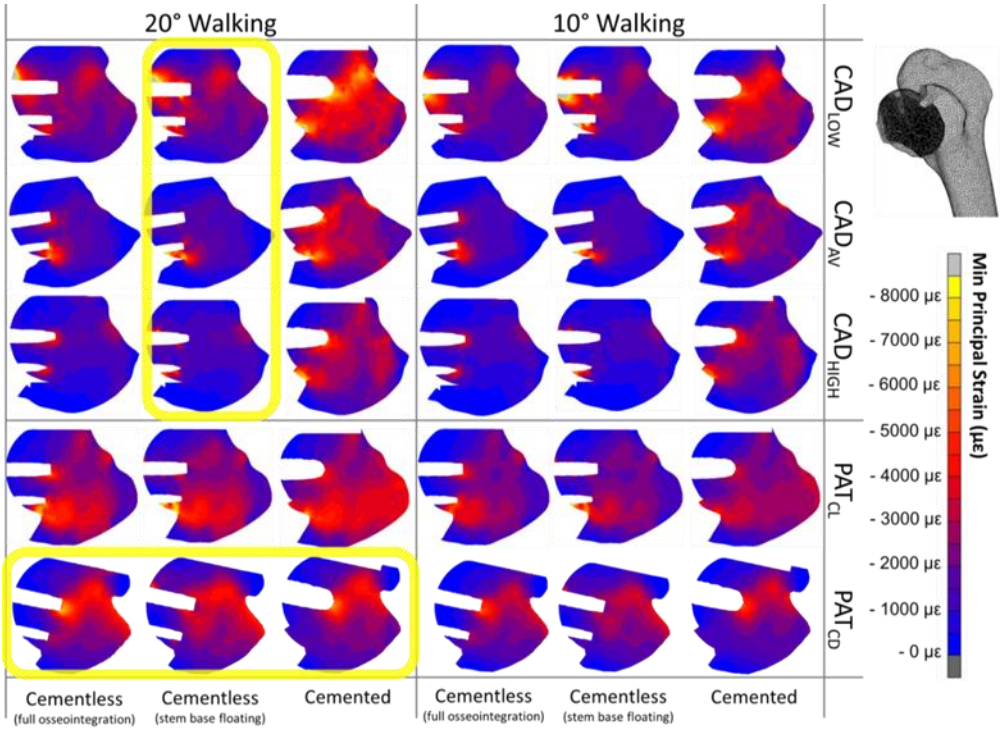


**Figure 147 - Initial fixation of cemented and cementless femoral implants. Minimum principal strain of femur bone at sagittal section through the centre of the implant stem. The strain increased with reduced bone density, in particular for cementless implants (highlighted top). Cementation had a negligible effect on peak bone strains (highlighted bottom).**

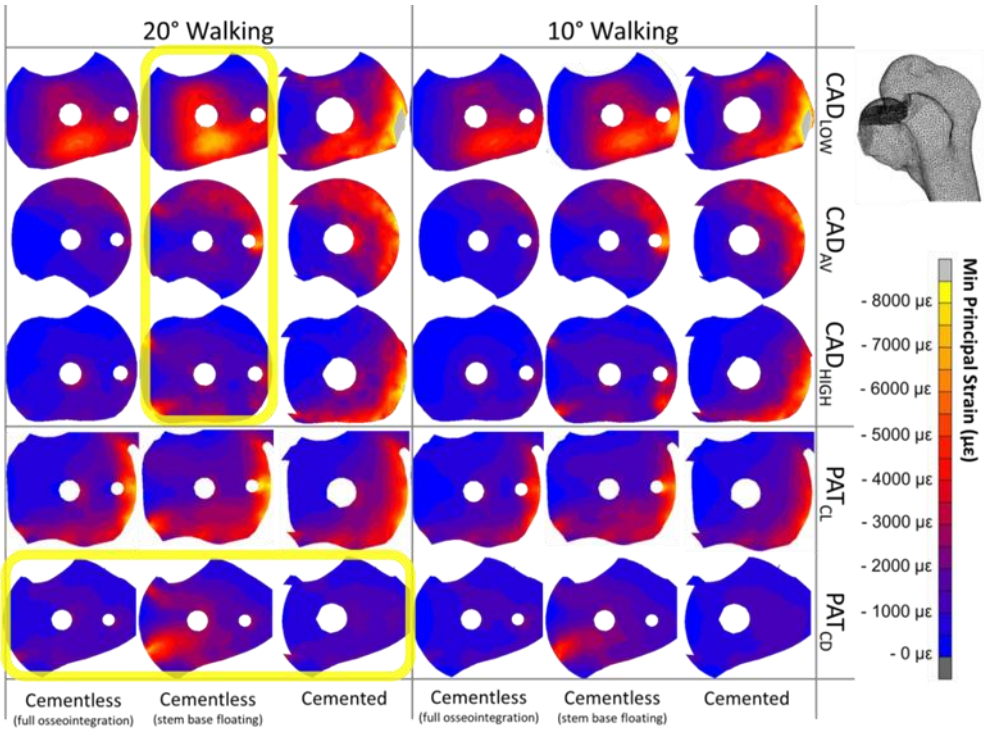


**Figure 148 - Initial fixation of cemented and cementless femoral implants. Minimum principal strain of femur bone at transverse section midway along implant stem. The strain increased with reduced bone density, in particular for cementless implants (highlighted top). Cementation reduced peak bone strains around the peg (highlighted bottom).**

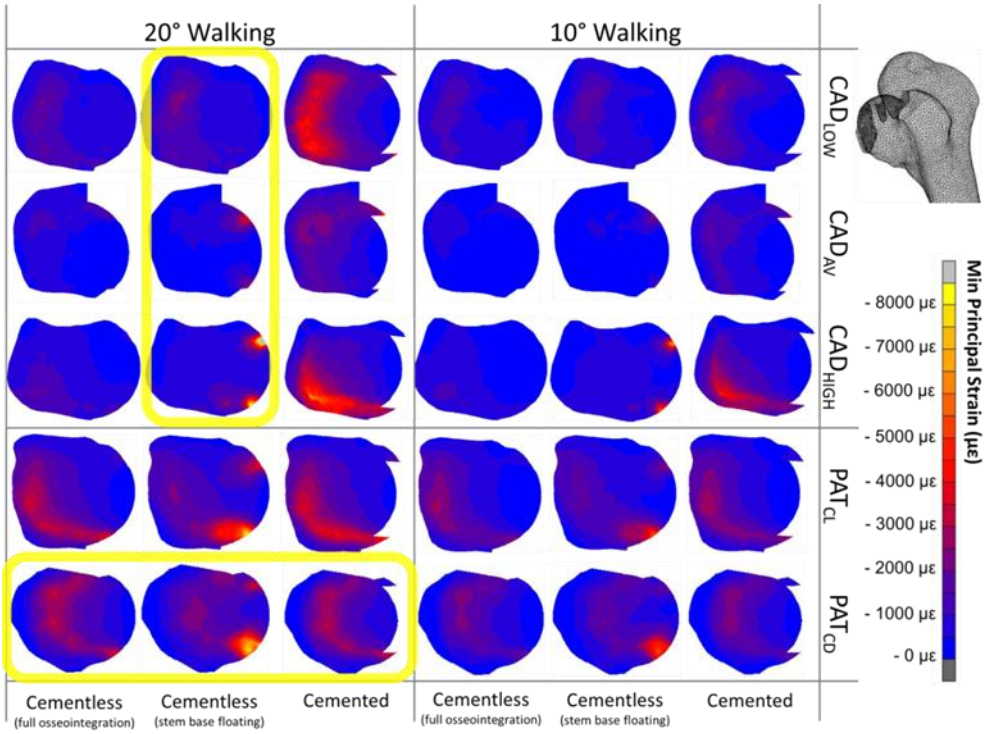


**Figure 149 - Initial fixation of cemented and cementless femoral implants. Minimum principal strain of femur bone at frontal section 3 mm beneath posterior femoral implant. The strain increased with reduced bone density, in particular for cementless implants (highlighted top). Cementation had a small effect on peak bone strains (highlighted bottom).**

### *9.2.2 Results: Long-term Fixation*

Figure 150 displays the bone density changes for the tibia under both cemented and cementless fixation. The average bone density beneath the cementless implant was higher than that of the cemented implant at 1-year. However, the regions of lowest density were also less for the cementless implant. This is because the cement acts as an intermediate layer that is significantly more flexible than the metal implant and spreads the pressure more equally than a simple metal-on-bone interface.

Figure 151 presents the bone density changes for the femur under both cemented and cementless fixation. The inclusion of the second peg for the cementless implant caused some bone densification anteriorly for patient $PAT_{CL}$. The difference in bone density at 1 year was generally insignificant.

Figures 152 to 157 present the changes to bone strain as the tibia and femur remodel in response to daily activities. The plots show that the bone strains reduced at 1 year, with the greatest reduction occurring for the cementless implant. The final bone strains were lower for the cementless implant than the cemented implant. This difference is because the higher strains produced by the cementless implant were enough to trigger bone remodelling while those of the cemented implants did not go above the threshold.

The bone strain changes that developed in the femora were more complex than those in the tibia. As the base of the peg osseointegrated with the bone, for patient $PAT_{CL}$, a greater proportion of the load transferred though it causing high bone strain at the distal region of the medial condyle (refer to Figure 155). This could potentially lead to pain for the patient.

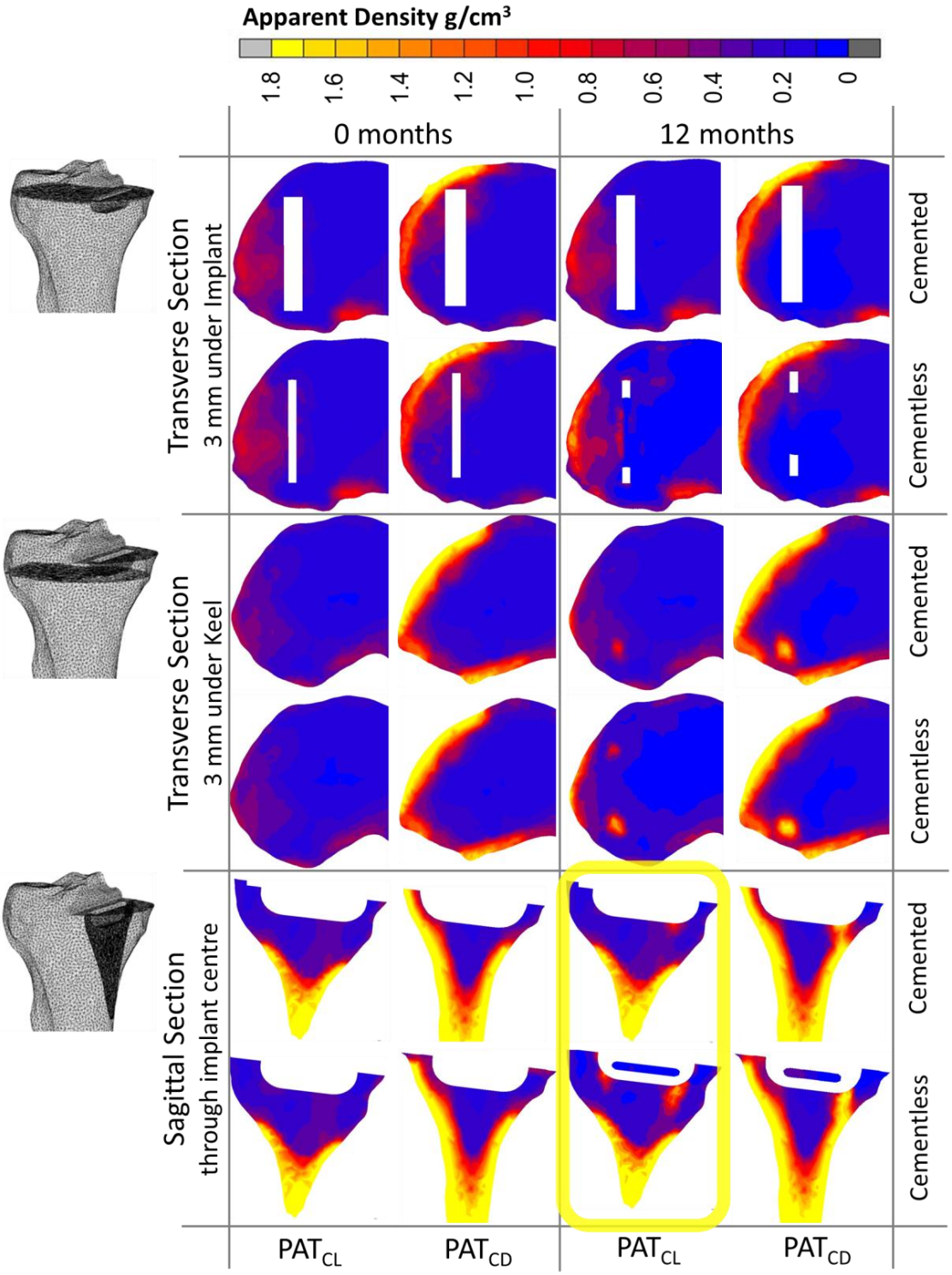


**Figure 150 - Bone remodelling comparison of cemented and cementless tibial implants. Both UKR patient bone models were implanted with both types of implants to compare the differences of bone densities at 1 year. Bone apposition was greater with cementless fixation (highlighted).**

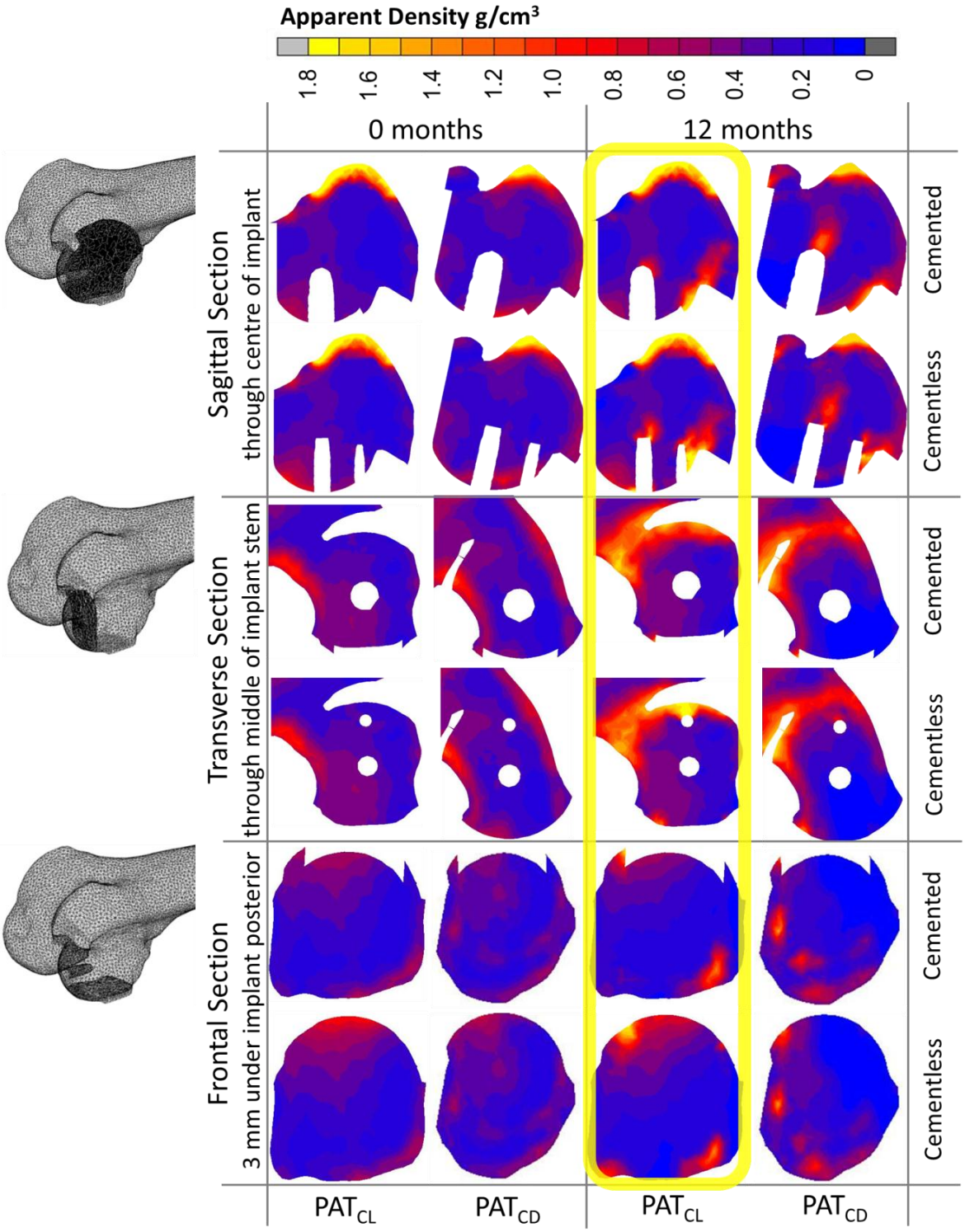


**Figure 151 - Bone remodelling comparison of cemented and cementless femoral implants. Both UKR patient bone models were implanted with both types of implants to compare the differences of bone densities at 1 year. Bone apposition was only slightly greater with cementless fixation (highlighted).**

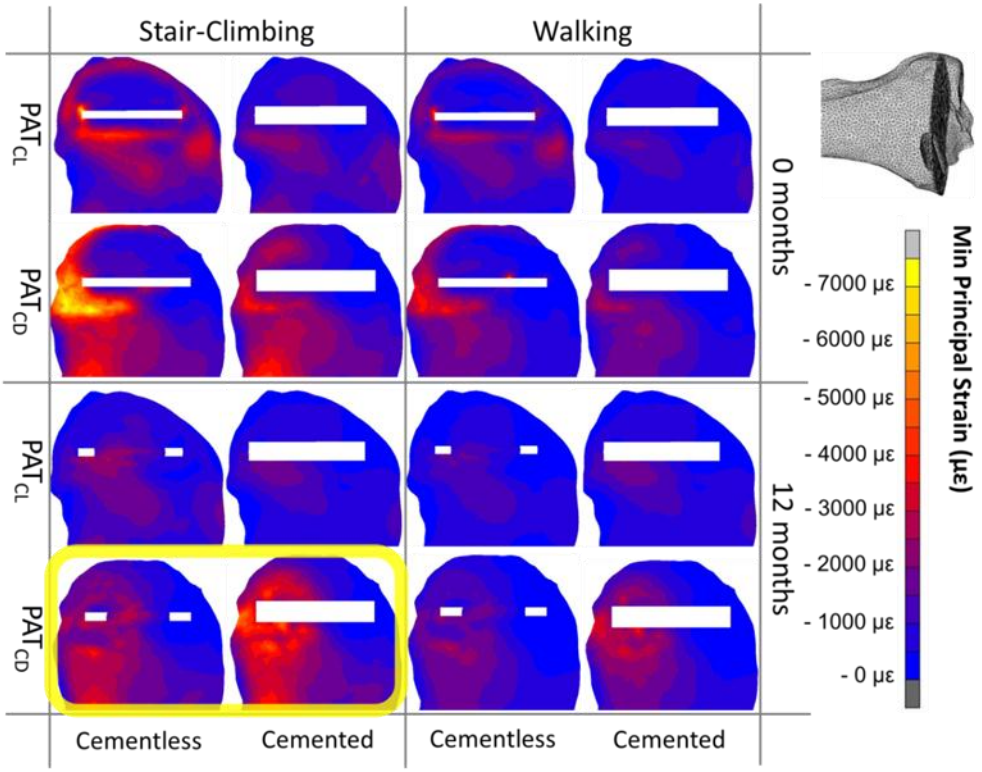


**Figure 152 - Fixation of cemented and cementless tibial implants at 1 year post-arthroplasty. Plots of minimum principal strain of tibia bone at transverse sections at 3 mm below the tibial implant. After one year, the cemented implant produced higher bone strains for $PAT_{CD}$ (highlighted), but not for $PAT_{CL}$.**

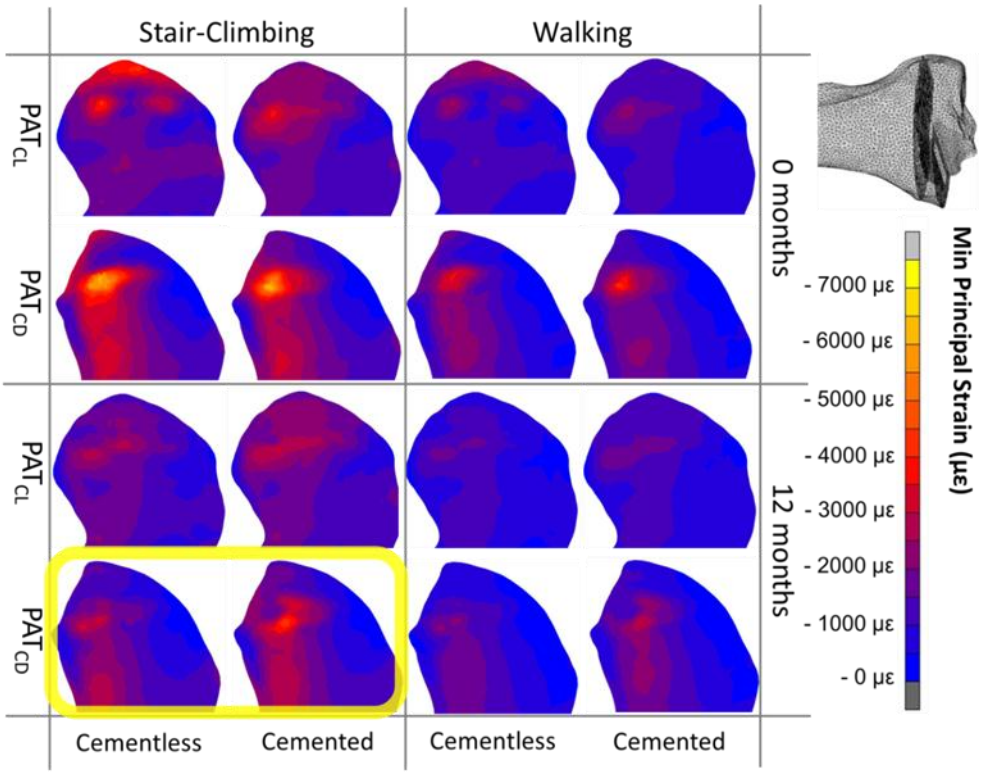


**Figure 153 - Fixation of cemented and cementless tibial implants at 1 year post-arthroplasty. Plots of minimum principal strain of tibia bone at transverse sections at 3 mm below the tibial keel. After one year, the cemented implant produced higher bone strains for $PAT_{CD}$ (highlighted).**

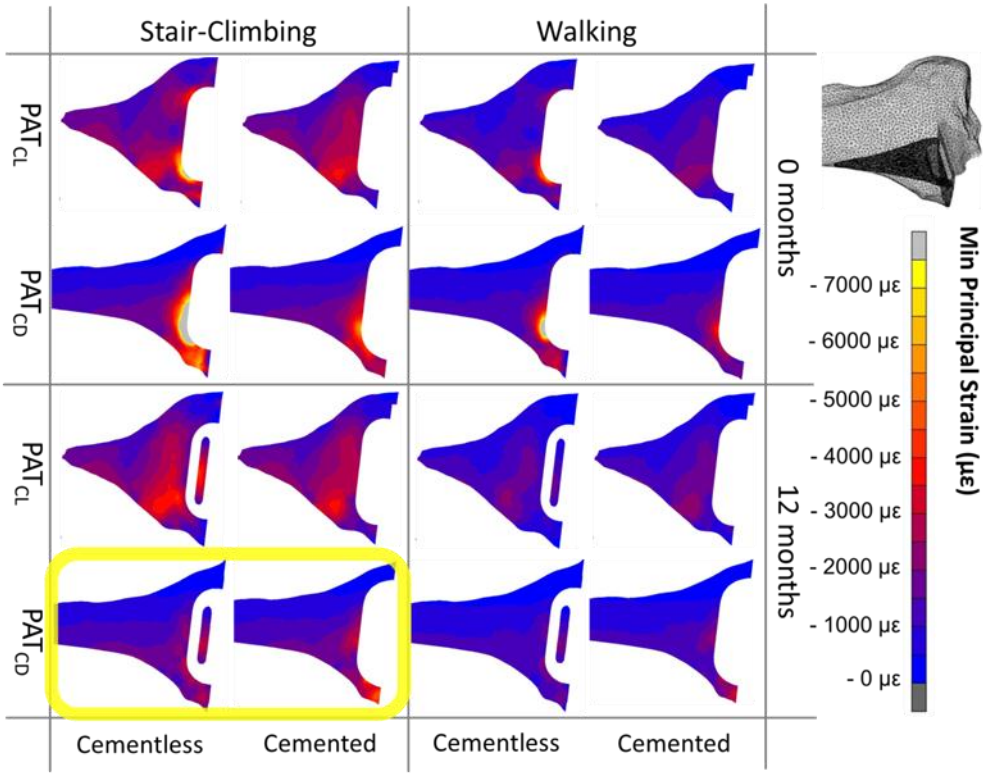


**Figure 154 - Fixation of cemented and cementless tibial implants at 1 year post-arthroplasty. Plots of minimum principal strain of tibia bone at sagittal sections through centre of the tibial keel. After one year, the cemented implant produced higher bone strains for $PAT_{CD}$ (highlighted), but not for $PAT_{CL}$.**

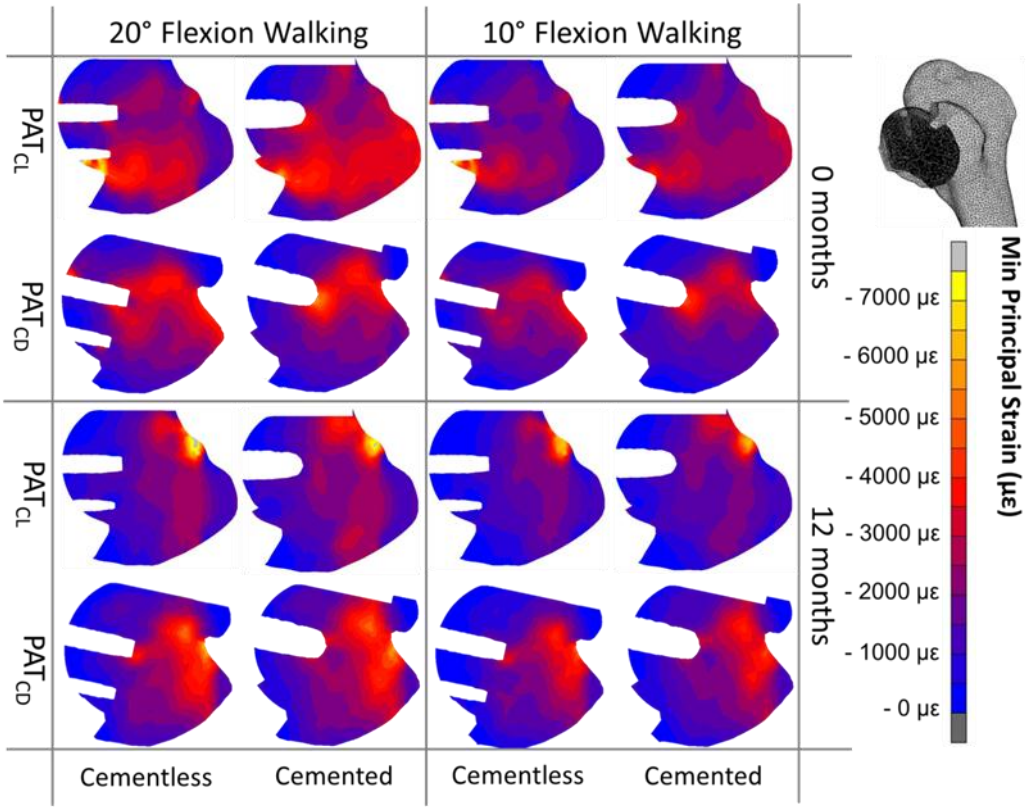


**Figure 155 - Fixation of cemented and cementless femoral implants at 1 year post-arthroplasty. Plots of minimum principal strain of femur bone at sagittal sections through the centre of the implant.**

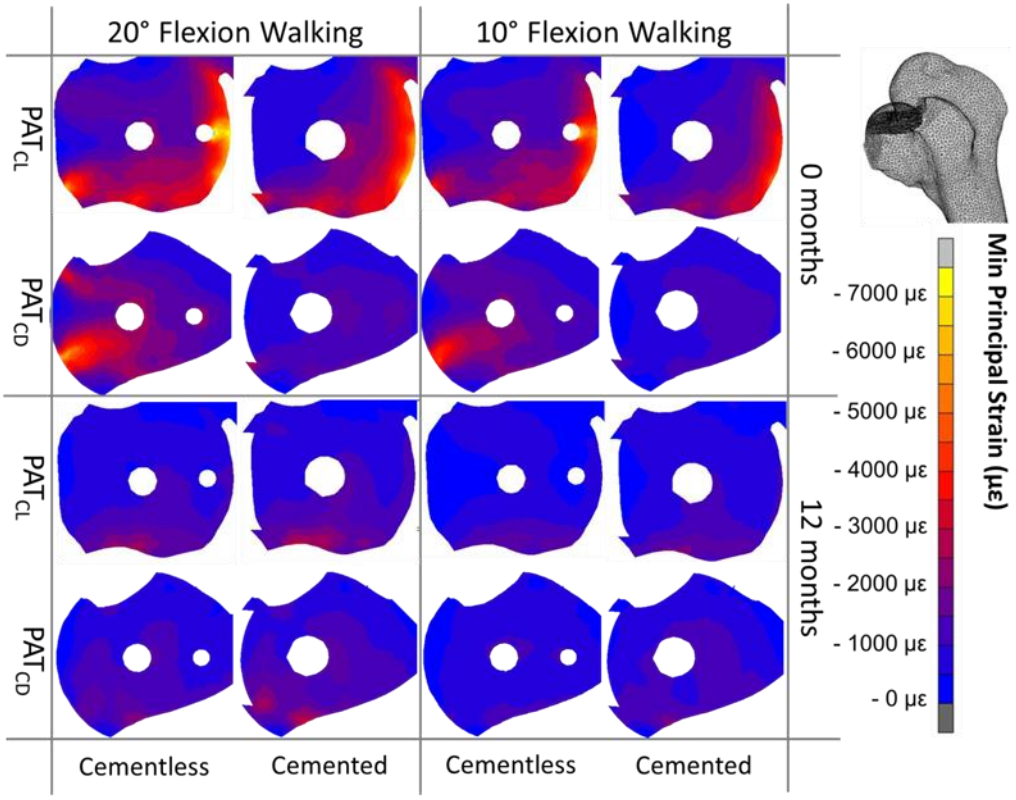


**Figure 156 - Fixation of cemented and cementless femoral implants at 1 year post-arthroplasty. Plots of minimum principal strain of femur bone at transverse sections through the middle of implant peg.**

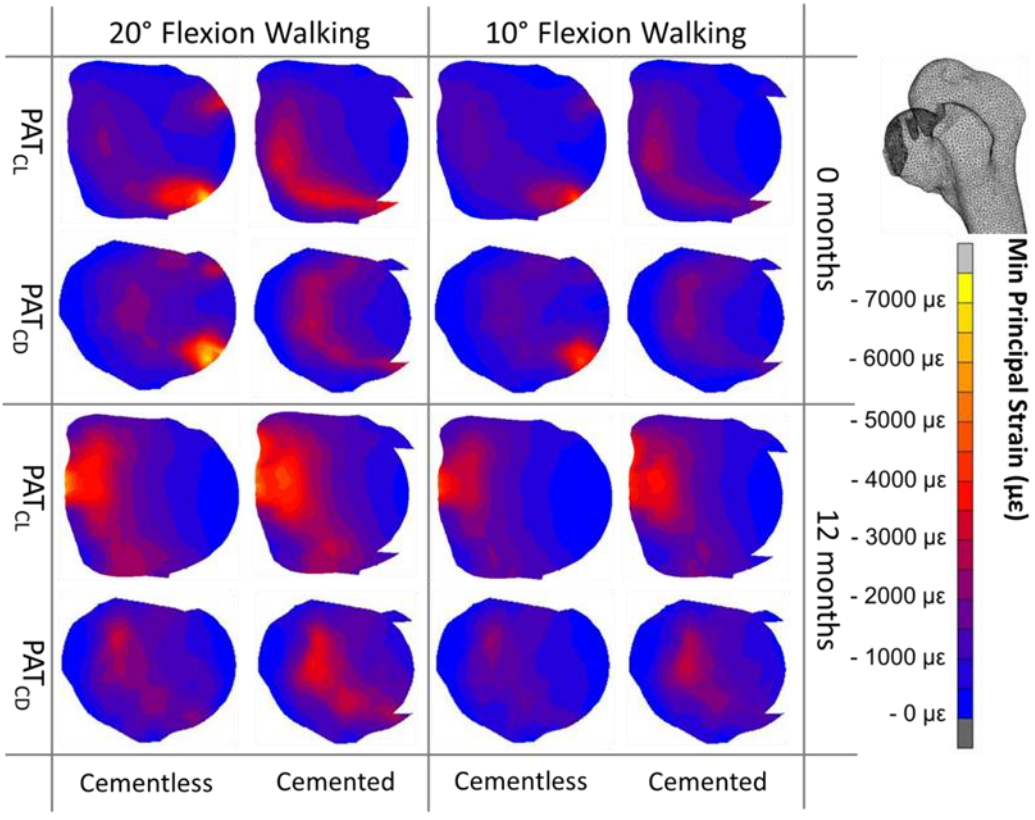


**Figure 157 - Fixation of cemented and cementless femoral implants at 1 year post-arthroplasty. Plots of minimum principal strain of femur bone at frontal sections at 3 mm beneath the posterior of the implant.**

### *9.2.3 Discussion*

This study highlights the differences in fixation of cemented and cementless UKR implants. Cemented implants provided best initial fixation independent of bone density. This was apparent because the bone strains were consistently lower. Cemented fixation was the preferred choice for the lowest density tibia because this reduced the bone strains as much as possible. For the tibia, the highest bone strains occurred at the resected corner and these approached the failure limit of bone for low density bone. Specifically for the cementless implant, there were high strains around the rim of the tray (before osseointegration occurred); once the implant had osseointegrated, these high rim-strains diminished. For the femur, the highest bone strains occurred at the anterior reamed-corner and these approached the failure limit of bone. Two of the strain-validated models showed a reduction in bone strain at the anterior reamed corner with inclusion of a secondary fixation peg. Although this reduction was not evident in the other three models, the inclusion of a secondary fixation peg may help to improve initial fixation and reduce these high bone strains. Bone strains tended to increase with knee flexion.

Cementless UKR implants provided the best long-term fixation for the tibia because stress-shielding was less, particularly at the anterior tibia. However, if initial bone strains are too high, this could cause migration, bone loss and could lead to early revision. These results may explain why four of the five cementless implant patients in the DXA study (presented in Section 7) maintained bone density beneath the tibial implant, while for one patient there was a significant decline.

The stress-shielding in the femur (posteromedial to the central peg) occurred irrespective of whether cemented or cementless fixation was used. This may explain why there was a negligible difference in bone density decline between cementless and cemented femoral implants in the DXA study. Therefore, the benefit of using cementless fixation over cemented fixation for the femur was found to be negligible.

### *9.2.4 Recommendations*

This study found that the Oxford mobile-bearing UKR provided adequate fixation irrespective of whether cemented or cementless fixation was used. Bone density was found to be an important factor in fixation performance, with low density bone being more susceptible to excessive bone strains that may exceed the failure limit of bone during daily activities. There was potential to improve the performance based on the decision to use cemented or cementless fixation from patient- specific characteristics of the knee.

The short-term fixation performance of the tibial components was best with cemented fixation; however, long-term success was compromised with patients of dense tibia who would benefit more with cementless fixation. The small rim around the Oxford mobile-bearing UKR cementless implant significantly reduced the contact area against the bone and increased bone strains. These high strains may be responsible for the increased pain that cementless UKR patients tend to feel (compared to cemented UKR patients) immediately post-arthroplasty (personal communication with Prof. Justin Cobb). This pain tends to diminish within a few months and these patients tend to have better radiographs at 1 year. Removing this rim would reduce these high bone strains and could improve success rates for patients with average bone density (provided this does not compromise osseointegration with the HA coating).

Analysis of multiple patient and cadaveric UKR knees highlighted stress-raisers at the resected corner of the tibia and at the reamed anterior edge of the femur. The bone strains approached the failure limit of bone; in particular for low density bone where it exceeded the failure threshold of bone. Although cementation reduced the bone strains, the UKR design and operative technique could be modified to reduce these stress-raisers.

The fixation of the femoral component was more complicated. Cemented fixation did not reduce bone strains. In fact, the omission of a secondary peg increased the bone strains at the anterior reamed corner of two of the five knees assessed. In order to benefit patients who have low density bone, cemented fixation used with an implant with a secondary peg may improve fixation. For patients with dense bone, for whom cementless fixation would reduce stress-shielding for the tibia and provide improved long-term success, the secondary peg of the cementless femoral implant could cause greater stress-shielding and the benefits over cemented fixation would be negligible. In this study, there was negligible long-term fixation benefit observed for using a cementless femoral implant; and since the accuracy of the resections involved in preparing cementless fixation is more critical to the success and the procedure is considered more difficult, this study suggests that only cemented fixation should be used for the femur.

## 9.3 Cementless Fixation: Is it good enough?

### *9.3.1 Introduction*

Of the orthopaedic surgeons that perform UKR in the UK, only 4% use cementless fixation (Schindler et al., 2010). This is very low given the benefits that cementless fixation could provide to selected UKR patients (those with high bone quality, who are active and have an average body mass index). This study presents micromotion predictions at the implant-bone interface and makes recommendations on how to obtain high success rates with cementless fixation.

In clinical practice, radiolucencies are often used as an indicator of bone-implant osseointegration. This technique is adequate for flat implant interfaces such as that of the tibial tray. There is clinical evidence to suggest that for selected patients that have had cementless UKRs, tibial osseointegration has occurred very successfully. There tends to be minimal radiolucencies beneath the tibial tray and in fact the clinical results tend to better than those of cemented UKRs (Pandit et al., 2009). This is also the experience of surgeons at Charing Cross Hospital (personal communication with Prof. Justin Cobb). However, the status of the osseointegration of the femoral implants is unknown due to the difficulty of identifying radiolucencies under the curved interfaces of the femoral UKR (Clarius et al., 2010). Some survival studies of the Oxford mobile-bearing UKR have reported higher rates of loosening for the femoral implants (compared to tibial implants) (Svard and Price, 2001, Murray et al., 1998). Investigation of femoral interface micromotion using computer models is valuable information that may help to identify the reasons for these failures.

The previous sections of this thesis have provided evidence to suggest that osseointegration of the implant and tibia should occur under normal knee forces for good quality bone (in-silico sensitivity assessments of Section 4, in-vitro studies of Section 5 and supporting validation studies of Section 6). Bone-implant micromotion is an indicator of the likelihood of osseointegration (refer to Sub-section 4.6.3). In this study, bone-implant interface micromotion plots, produced by the validated computer models, have been systematically presented and discussed. The three micromotion-validated models ($CAD_{LOW}$, $CAD_{AV}$ and $CAD_{HIGH}$) and the two remodelling-validated models ($PAT_{CL}$ and $PAT_{CD}$) have been adapted to simulate the extremes of bone-implant micromotion.

Bone-implant micromotions are difficult to measure particularly for curved interfaces such as the femoral implant. The tibial implant has a flat interface so it is easier to measure in-vitro (using displacement transducers) and easier to calculate from computer models (because the relative motions can be broken down into normal and tangential directions). Very little is

known about the bone-implant interface of UKR femur. This study is believed to be the first to investigate the bone-implant micromotions of the UKR femoral implant.

### *9.3.2 Method*

The validated FE models (micromotion-validated $CAD_{LOW}$, $CAD_{AV}$ and $CAD_{HIGH}$; and remodelling-validated $PAT_{CD}$ and $PAT_{CL}$) were used to generate bone-implant micromotion plots of cementless Oxford UKR implants. The development and validations of the FE models are detailed in Sections 4, 6 and 8.

As described in Section 4, the FE mesh was composed of linear elastic 4-node tetrahedral elements, with elements of size 1.4 mm at the bone-implant contact interface, 2 mm in the medial condyle and increasing to 3 mm towards the lateral condyle and shaft of the bones. Contact was modelled at the bone-implant interface assuming a friction coefficient of 0.4. Contact was also modelled at the bearing-implant interface with a Coulomb friction model of coefficient 0.1. Algorithms written into Marc software subroutines (refer to Sub-section 4.6.7) were used to calculate relative displacements between the bone and the implant. These displacements were broken down into surface-normal and surface-tangent direction components. The micromotion plots were generated for both the femur and tibia models in Marc Mentat 2010 (MSC Software Corporation, USA).

Peak walking and stair-climbing knee forces were applied to all models (at 50% walking and 15% stair-ascent activity cycles, refer to Section 3). Note that in practice, patients will probably not resume full activity immediately. However, since there is so much disagreement between surgeons regarding speed of rehabilitation, the most onerous scenario was simulated which assumed regaining full activity and full knee forces immediately post-surgery.

For the tibia models, frictional shear forces at the bone-implant interfaces were simulated by applying a “sticking” contact condition at the bearing-implant interface and applying 10% of the medial condylar contact force (corresponding to a friction coefficient of 0.1) in the anterior, posterior, medial and lateral surface-tangent directions in four subsequent separate load cases. It was speculated that the highest micromotions would occur under accidental over-twisting or lateral sliding of the knee, whereby the bearing may contact the side-plate and impose an external turning moment onto the tibial implant. Three additional load cases were developed, that applied a single lateral force to the bearing of 0.2 body-weight (BW), 0.4 BW and 0.6 BW. A spring of the stiffness 1 BW/mm was used to constrain the bearing from lifting in the superior direction. Note that the superior-inferior stiffness of the medial compartment is dependent on ligament stiffness, muscle activation, bodyweight and inertial body forces. The stiffness of 1 BW/mm was chosen based on consideration of ligament

stiffness. The medial collateral ligament is the greatest constraint to medial knee compartment separation laxity (Markolf et al., 1976), with a stiffness of 400-2000 N/mm (Reeves et al., 2003).

For the femur models, the whole database of walking and stair-climbing knee forces was analysed to retrieve the peak knee forces at knee flexion increments of ten degrees. Eight separate sets of knee forces were applied to each femur model (two load cases at 10 degree and 30 degree flexion angles, because it was not obvious which one of the two was more onerous, and single load cases at 20, 40, 60 and 70 degree flexion angles). Another sixteen load cases were included in the femur models to simulate frictional shear forces in the anterior and posterior directions (depending on whether the knee was flexing or extending). These friction forces were simulated by similarly adding a tangential force equivalent to 10% of the medial condylar contact force to the surface of the implants.

### *9.3.3 Results*

Figures 158 and 159 present implant-bone micromotion plots of the three cadaveric tibia specimen models ($CAD_{LOW}$, $CAD_{AV}$ and $CAD_{HIGH}$) and the patient models ($PAT_{CD}$ and $PAT_{CL}$). Figure 158 presents the relative micromotion which highlights the high micromotion at the centres of the implant, while Figure 159 presents the surface-tangent micromotion. The results demonstrate the degrading impact that low bone density has on micromotions. Micromotions greater than 100 µm were considered indicative of poor osseointegration and those less than 50 µm were considered to have very good osseointegration.

The tibial results of the cementless UKR patient ($PAT_{CL}$) displayed peak micromotions of less than 50 µm. This is indicative of good osseointegration and is supported by the clinical observations described in Section 7.

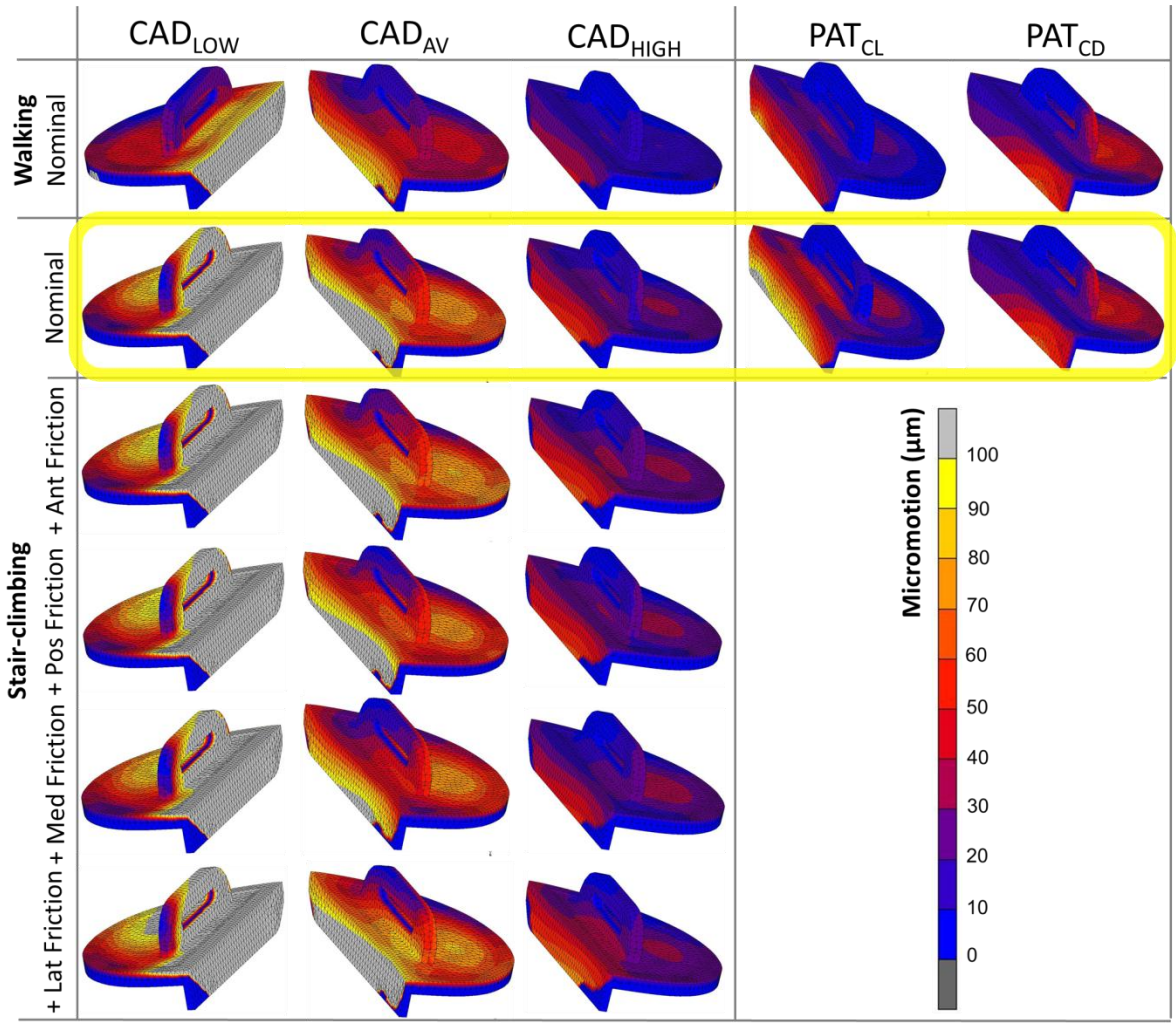


**Figure 158 - Relative micromotion plots at the bone-implant interfaces of cementless mobile bearing tibial UKRs. The plots show the most extreme micromotions under different directions of mobile bearing friction shear forces on the tibial tray under peak knee forces of stair-climbing.**

There was considerable variation in the locations of the tibial tray peak micromotions as this was dependent on the position of the bearing and on the stiffness of the underlying bone. The micromotions at the side-plate were consistently higher than the underside of the implant. This corroborates with typical radiographs of UKR patients that often show radiolucencies beside the side-plate (Figure 5 in Section 1).

The peak micromotions of the lowest and average density tibiae ($CAD_{LOW}$ and $CAD_{AV}$) were over 100 µm; therefore poor osseointegration would be expected at the lateral corners of these tibial components. In cementless UKR patients of lower than average bone density, full activity should not be resumed immediately. As displayed by Figure 160, under walking activity knee forces, peak micromotions were less than 100 µm beneath the implants of the least dense tibiae $CAD_{LOW}$ and $CAD_{AV}$. Although osseointegration would occur, there would

probably be some fibrous tissue allowing some interface movement lateral to the keel (Jasty et al., 1997a).

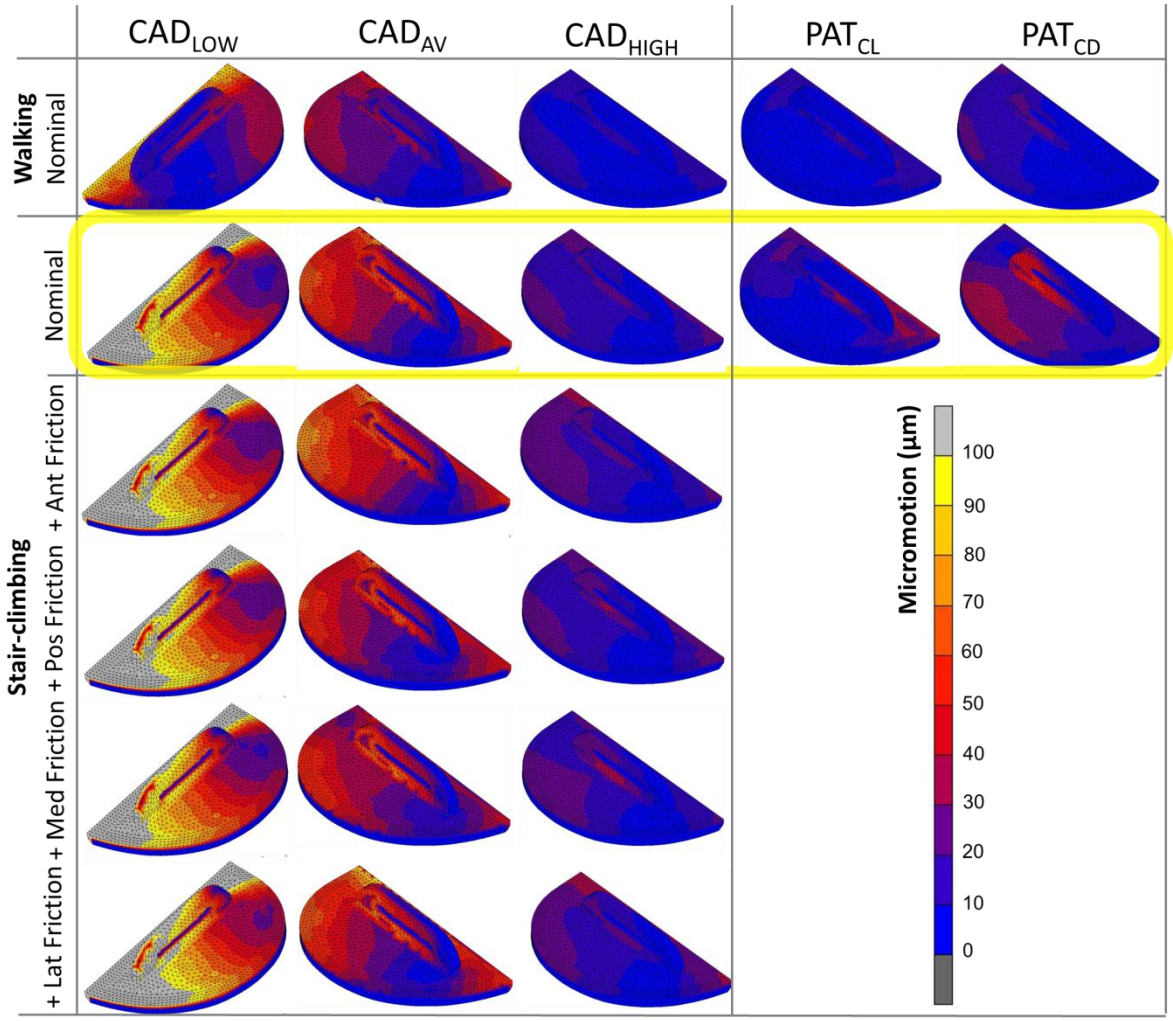


**Figure 159 - Surface-tangent micromotion plots at the bone-implant interfaces of cementless mobile bearing tibial UKRs. The plots show the most extreme micromotions under different directions of mobile bearing friction shear forces on the tibial tray under peak knee forces of stair-climbing.**

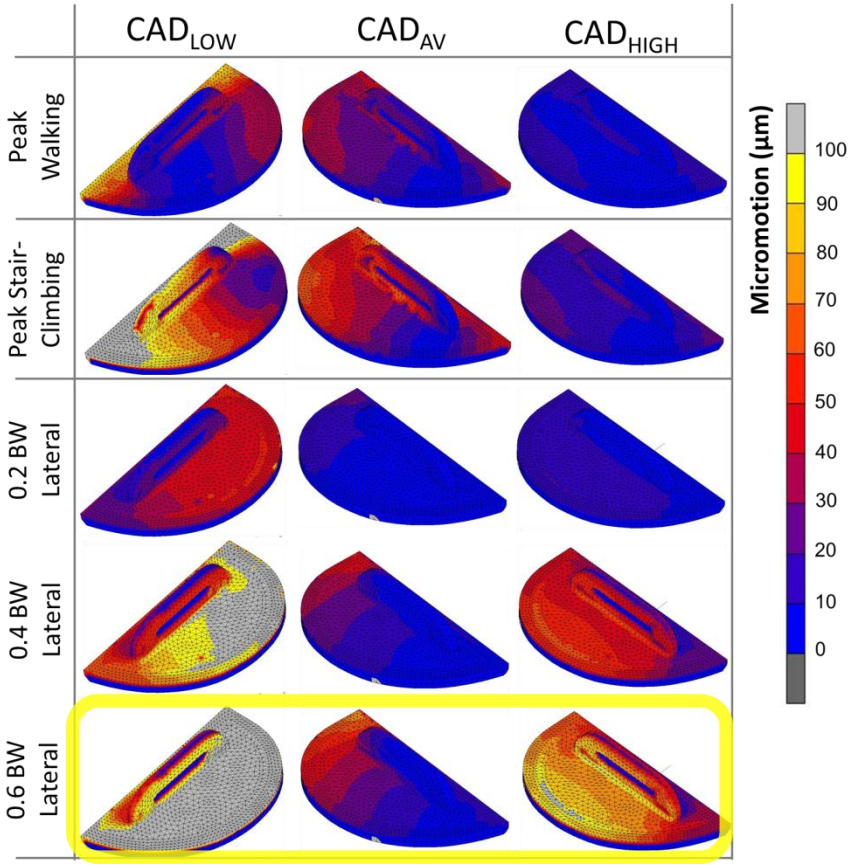


**Figure 160 - Surface-tangent micromotion plots at the bone-implant interfaces of cementless mobile bearing tibial UKRs. The plots show the extreme micromotions if the bearing was to knock the side-plate with increasing force.**

Figure 160 presents the results of the tibial implant micromotion simulations of the bearing contacting the tibial implant side-plate with a forces of 0.2 - 0.6 BW. Although 0.6 BW is a small force, the results demonstrate that it can generate micromotions significantly higher than 100 µm. Note that the implant does not actually lift off from the bone, so the surface-normal micromotions are maintained low. If the UKR was not aligned correctly such that the bearing contacted the side-plate during regular activity, the fixation would be significantly weakened. A one-off incident during the first few weeks post-arthroplasty could also impair fixation.

Figure 161 presents the peak bone-implant micromotions on the femoral UKR implant. Similarly to the tibia, the magnitudes of the micromotions are sensitive to the density of the bone. The micromotions significantly exceed 100 µm for the low density tibia ($CAD_{LOW}$). The magnitudes of the micromotions tended to increase with knee flexion, with the peaks occurring at the posterior of the implant, particularly at the posterior tip. The pegs consistently produced low micromotions. The cementless UKR patient showed low femoral micromotions indicating good osseointegration and corroborated with the clinical evidence in Section 7.

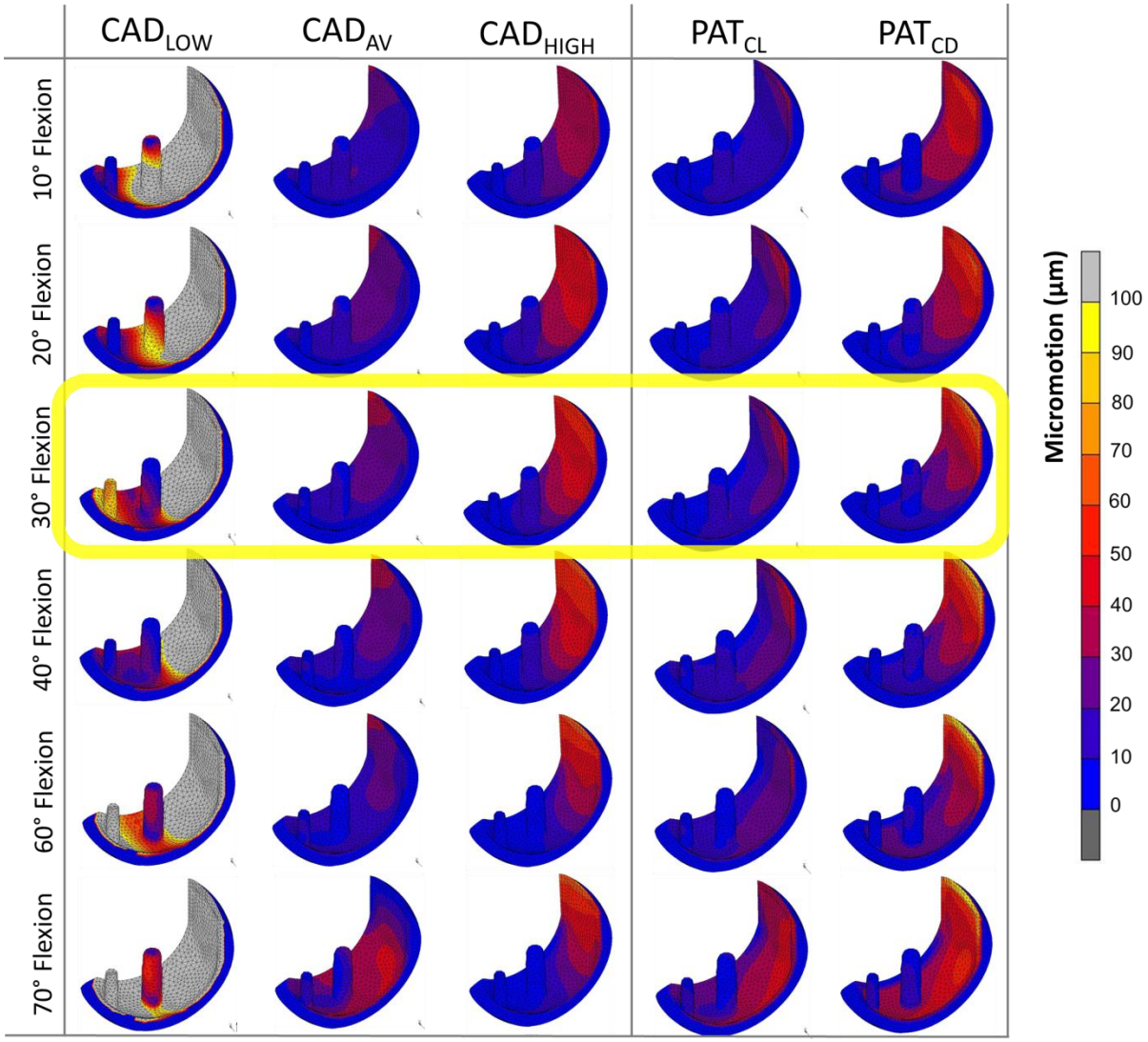


**Figure 161 - Surface-tangent micromotion plots at the bone-implant interfaces of cementless mobile bearing femoral UKRs. The plots show the most extreme micromotions at flexion angles up to 70 degrees under the peak knee forces of stair-climbing.**

### *9.3.4 Discussion and Recommendations*

The main finding of this study was that the UKR bone-implant micromotion was greater with lower bone densities of the tibia and femur. Since increased micromotion is indicative of weaker bone-implant osseointegration, the fixation performance of cementless fixation degraded with lower density tibiae and femora.

For the densest cadaveric specimen ($CAD_{HIGH}$) and the actual UKR patient who had a cementless UKR implanted ($PAT_{CL}$), the micromotions were below the threshold of 50 µm to allow firm osseointegration. The patient who had a cemented UKR ($PAT_{CD}$) showed low micromotions (less than 50 µm) at the tibia but moderate micromotions (approaching 100 µm) at the femur. The surgeon made a conservative choice with using a cemented implant

for this patient; however, a cementless implant may have osseointegrated well under gentle rehabilitation.

The average density cadaveric specimen ($CAD_{AV}$) produced moderate tibial micromotions and low femoral micromotions. Cementless fixation alongside a gentle rehabilitation programme could provide the average density knee with a good fixation outcome. The low density specimen ($CAD_{LOW}$) produced high micromotions in both the tibia and femur and based on this study, cementless fixation is not recommended for such bone. It should be appropriate for a clinical/biomechanical study to derive an evidence-based method which would guide the choice of implant.

A significant contributor to interface micromotions is considered to be shear forces on the implant. For the Preservation mobile-bearing UKR (DePuy Orthopaedics Inc., Warsaw, USA), the constrained bearing could have produced shear forces of 1-3 BW and this probably led to its poor success rates (Arastu et al., 2009). The mobile-bearing UKR is a good design to allow good osseointegration because the decoupled bearing minimises shear forces on the tibial and femoral implants. The shear forces are dependent on the friction at the implant-bearing interface. In-house experiments revealed that the Coulomb friction coefficient was approximately 0.1 for the Oxford mobile-bearing UKR. Over time bearing movement may seize, thereby increasing shear forces on the implant. However, since osseointegration would have already occurred, as long as the forces do not exceed the failure limit of the interface, good fixation should be preserved. The results also show that Impact onto the tibial implant side-plate has the potential to create excessive micromotions if the UKR is misaligned.

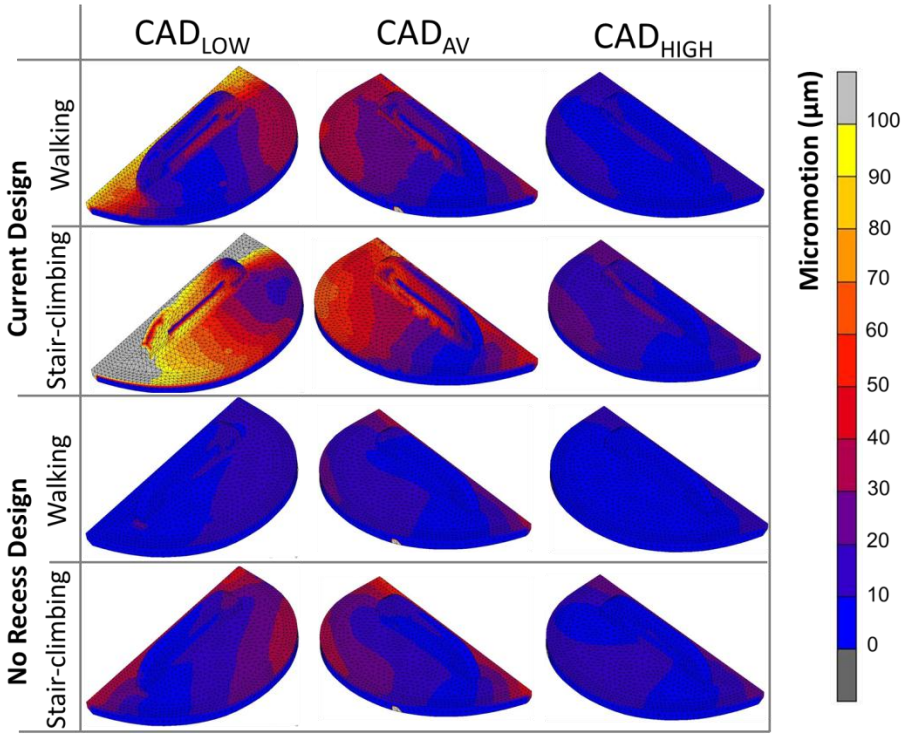


**Figure 162 - Surface-tangent micromotion plots at the bone-implant interfaces of cementless mobile bearing tibial UKRs. The plots show the reduction of micromotions with an improved flat tibial tray underside.**

In Sub-section 9.2, it was found that the rim around the tibial implant caused excessively high edge strains on the bone beneath. There would likely be inferior implant migration as the rim crushed bone and settled. A sensitivity study was conducted to investigate how removing this recess affected the interface micromotions. Figure 162 demonstrates that a flat tray underside would only reduce micromotions ensuring a more successful osseointegrated fixation.

In Sub-section 9.2, cementless fixation bone strains were identified to be high at the resected corner and around the rim of the tibial tray. The removal of the rim around the tibial tray will partly relieve these strains; however, the bone strains at the resected corner will still be higher than necessary. Possible solutions to reducing these strains have been investigated in preceding sections of this thesis.

## 9.4 Cemented Fixation: Are radiolucencies a problem?

### *9.4.1 Introduction*

Cemented Oxford UKR patients often display radiolucencies beneath the tibial implant (Gulati et al., 2009a, Pandit et al., 2009, Rea et al., 2007). Most are considered "physiological" and do not show any signs of progressive loosening (Gulati et al., 2009a).

A computer simulation study based on a single specimen (Gray et al., 2010), showed that soft tissue beneath the implant was responsible for the stiffening of underlying bone and the sclerotic margin often seen in patient radiographs. The following study aims to understand how the radiolucent lines affect fixation and how a range of specimens behave to such changes.

### *9.4.2 Method*

The validated FE models (strain-validated $CAD_{LOW}$, $CAD_{AV}$ and $CAD_{HIGH}$; and remodelling-validated $PAT_{CD}$ and $PAT_{CL}$) were used to compare the fixation performance of cemented Oxford UKRs taking into account potential degradation of the cement-bone interface and remodelling changes to the underlying bone.

The cemented versions of the strain-validated (Section 6 ) and remodelling-validated models (Section 8) were modified for this study. The elastic moduli of the regions 2 mm beneath the implants (simulated as a cement-mantle in the validated models) were reduced to 17% of their original value (Mann et al., 2008). This was to simulate the increased compliance that tends to occur at the cement-bone interface surrounding implants. The remodelling-validated models were used to simulate a rigid fixation from 0 to 12 months, followed by a simulation of compliant fixation for the period 12-24 months. No other changes were made to the models. The development and validation of the FE models are detailed in Sections 4, 6 and 8.

The bone strains of the strain-validated models and the bone densities at 0, 12 and 24 months of the remodelling-validated models were compared to identify the fixation effects of degradation of the cement-bone layer (compliant fixation).

### *9.4.3 Results*

Figures 163 and 164 show plots of minimum principal strain and the effect of a soft tissue layer on bone strains. The bone strains beneath the tibial tray increased with the compliant fixation (compared to the stiff fixation) for all the specimens. The increase was less

pronounced for the dense tibia suggesting that dense tibiae may be less likely to show radiolucencies. The bone strain differences under the keel were less pronounced.

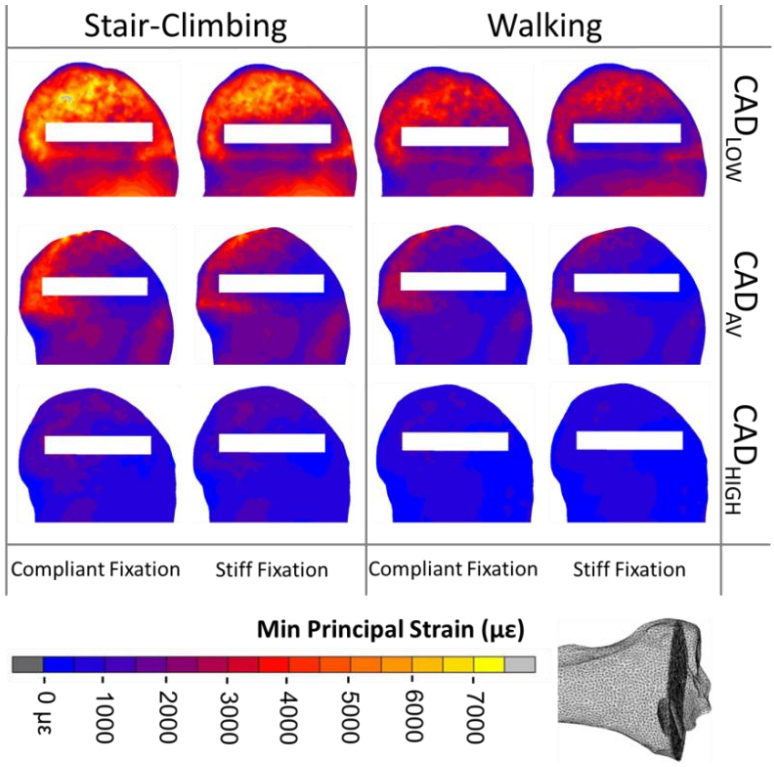


**Figure 163 - Minimum principal strain plots of strain-validated tibia models at transverse sections 3 mm below the implant interfaces. The plots compare the bone strains under (1) a solid cement-mantle (elastic modulus of 1.8 GPa) and (2) a degraded compliant cement-bone interface with reduced elastic modulus (0.3 GPa).**

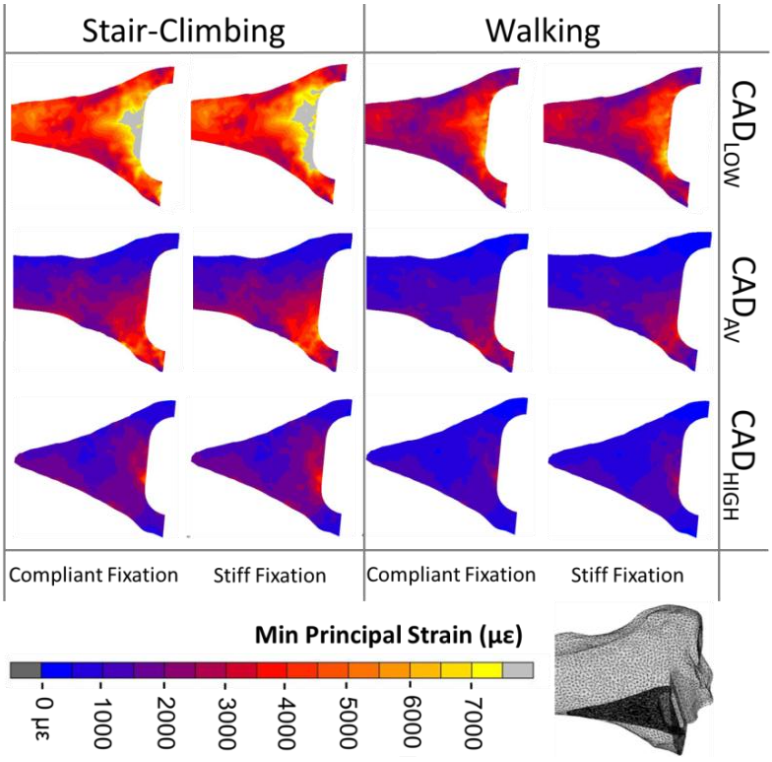


**Figure 164 - Minimum principal strain plots of strain-validated tibia models at sagittal sections through the centre of the keels. The plots compare the bone strains under (1) a solid cement-mantle (elastic modulus of 1.8 GPa) and (2) a degraded compliant cement-bone interface with reduced elastic modulus (0.3 GPa).**

Figures 165 to 167 show simulated apparent density plots at 0, 12 and 24 months based on the models of two UKR patients. The plots show that bone apposition occurs from 12-24 months if the cement-mantle layer becomes more compliant. This apposition occurred just beneath the tibial tray at the lateral region for both patients.

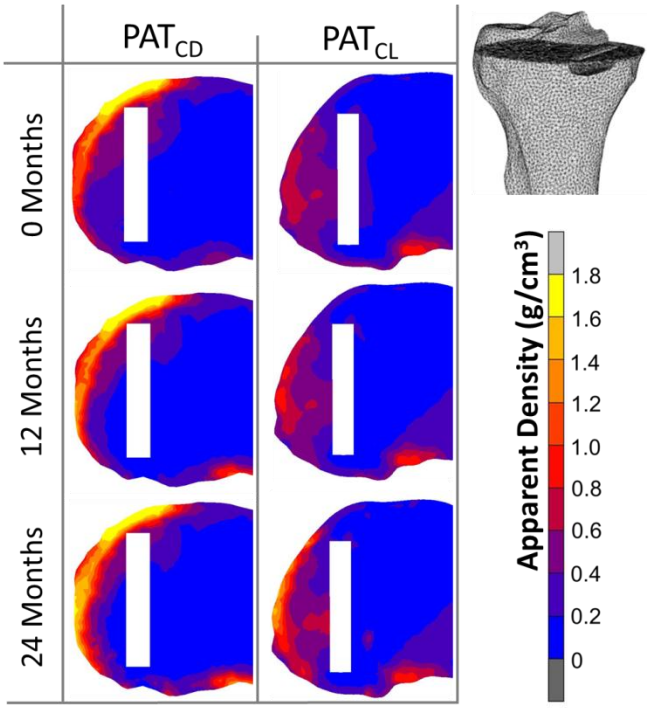


**Figure 165 - Apparent density plots of remodelling-validated tibia models at transverse sections 3 mm below the implant interface. The plots compare how the bone densities adapt under (1) a solid cement-mantle (elastic modulus of 1.8 GPa) during the first year, and (2) a degraded compliant cement-bone interface with reduced elastic modulus (0.3 GPa) from 1 to 2 years post-arthroplasty.**

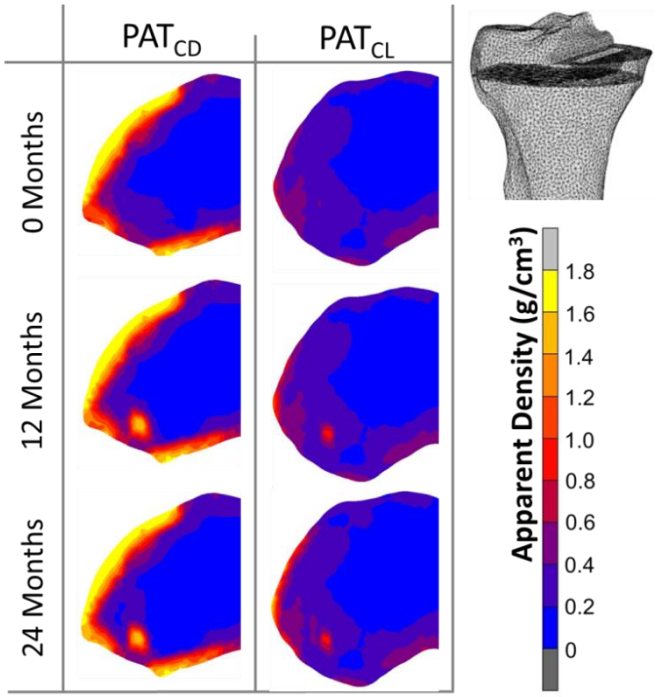


**Figure 166 - Apparent density plots of remodelling-validated tibia models at transverse sections 3 mm below the implant keel. The plots compare the how the bone densities adapt under (1) a solid cement-mantle (elastic modulus of 1.8 GPa) at 1-year and (2) a degraded compliant cement-bone interface with reduced elastic modulus (0.3 GPa) at 2-years post-arthroplasty.**

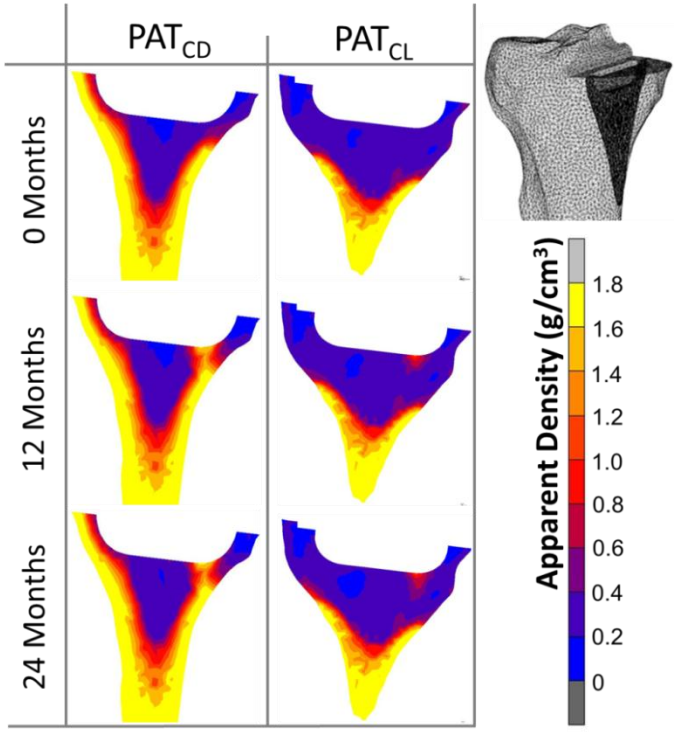


**Figure 167 - Apparent density plots of remodelling-validated tibia models at sagittal sections through the centres of the keels. The plots compare the how the bone densities adapt under (1) a solid cement-mantle (elastic modulus of 1.8 GPa) during the first year, and (2) a degraded compliant cement-bone interface with reduced elastic modulus (0.3 GPa) from 1 to 2 years post-arthroplasty.**

### *9.4.4 Conclusions and Recommendations*

The main finding of this study was that the reduction of stiffness of the cement-mantle layer (17% of its initial stiffness based on explants of THRs (Mann et al., 2008)) caused bone strains in the underlying bone to increase and bone apposition occurred. This may explain the sclerotic margin typically seen under radiolucencies of UKR tibiae (Gray et al., 2010). This study also concludes that a lower density tibia may be more susceptible to forming sclerotic margins following development of radiolucencies.

Reducing the elastic modulus of the cement-mantle of the tibial component caused small changes to the tibial strains. The load path changed such that a larger proportion was transmitted through the tibial tray rather than the keel. As a consequence the bone strains beneath the implant increased and the bone strain beneath the keel decreased.

Based on the analysis of bone strain and bone remodelling simulations, the development of a more compliant cement-mantle merely improved fixation and did not degrade it. Bone-implant and cement-bone micromotion was disregarded in this analysis due to the complexities in modelling these mechanisms upon fibrous tissue formation. It is expected that the micromotions would increase, but not to levels that would cause pain to the patient – there is no evidence that UKR patients who show physiological radiolucencies have additional pain (Gulati et al., 2009a).

## 9.5 Tibial Resection Depth: Does it affect fixation?

### *9.5.1 Introduction*

Post-arthroplasty, bone strains should be as close as possible to the pre-arthroplasty state to ensure good fixation. High strain increases will cause pain, migration or even bone collapse while large decreases will cause bone resorption. Based on the literature, researchers have speculated that shallower resections would provide better fixation (Goldstein et al., 1983). It was therefore hypothesised that shallower resections would reduce strain change and improve fixation of the Oxford mobile-bearing UKR.

The following multi-specimen computer simulation study is an investigation of bone strain in the vicinity of Oxford mobile-bearing tibial implants (both cemented and cementless versions) immediately post-arthroplasty. It is assumed that cementless implants have not yet osseointegrated and cemented implants are fully bonded all over (including the keel).

### *9.5.2 Method*

Six validated tibia models (cemented and cementless versions of $CAD_{LOW}$ $CAD_{AV}$ $CAD_{HIGH}$) were used for this study. Each validated model was taken to be resected at the nominal position and a further two versions of each model were developed based on resections 4 mm inferior and 4 mm superior relative to the nominal.

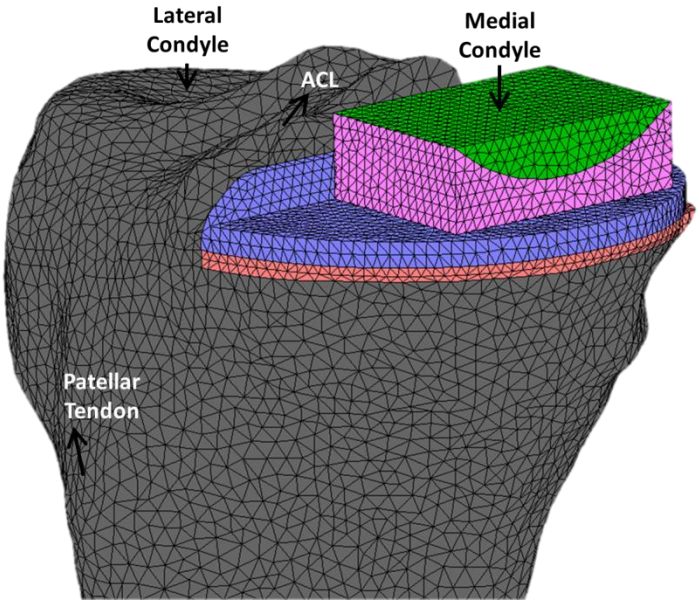


**Figure 168 - FE model of tibia $CAD_{HIGH}$ implanted with a mobile bearing UKR at nominal resection.**

Three intact tibia models of the specimens were also developed with the medial condylar forces applied to a simplified representation of the femur and meniscus. The implanted proximal tibiae were split into 30 zones (refer to Figure 169): each zone was 2 mm thick

(axial dimension); with nine zones in each of the first three layers (split into thirds); and three single-zone layers representing the region directly under the keel. The intact tibia models were defined with 93 zones corresponding to the same resection model locations (different for each resection depth).

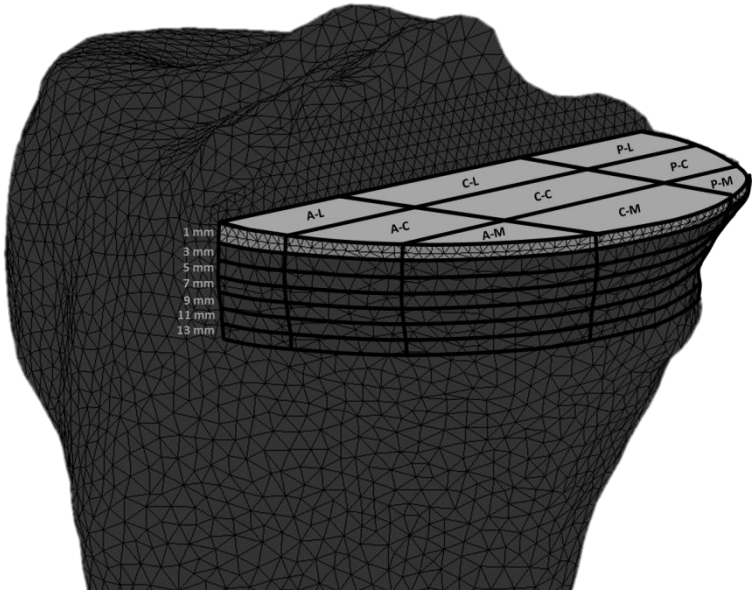


**Figure 169 - FE model of tibia $CAD_{HIGH}$ showing zones and the layers analysed.**

All 21 FE models were loaded with two loading conditions of peak walking and peak stair-climbing with the forces adjusted for body-weight. They were solved using the MARC Solver and the nodal minimum principal strains at each zone were output using Marc Mentat. Bone strain changes from the pre-arthroplasty to post-arthroplasty states were post-processed using Matlab software (Mathworks, USA). The model meshes were generated by a sponsored undergraduate student (Ryo Kashihara) under the instruction of the author.

### *9.5.3 Results*

The minimum principal bone strains were very different between specimens and varied depending on the bone density distribution in the vicinity of the implant. In the cementless cases, the overall peak bone strains correlated with the density of the bone immediately under the tray surface; i.e. strains were lower with reduced resection depth. The cemented cases were more complicated because peak bone strains depended on bone density both under the tray surface and under the keel. If the keel was close to the posterior cortical shell, peak bone strains reduced with deeper resection. This occurred with smaller tibiae ($CAD_{LOW}$ and $CAD_{AV}$). Figure 170 shows the apparent density distributions of all nine tibial resections (relative to the position of the implant) at a sagittal cross-section through the centre of the

keel. Figure 171 shows the apparent density distributions of the transverse sections and provides a comparison of relative tibia size.

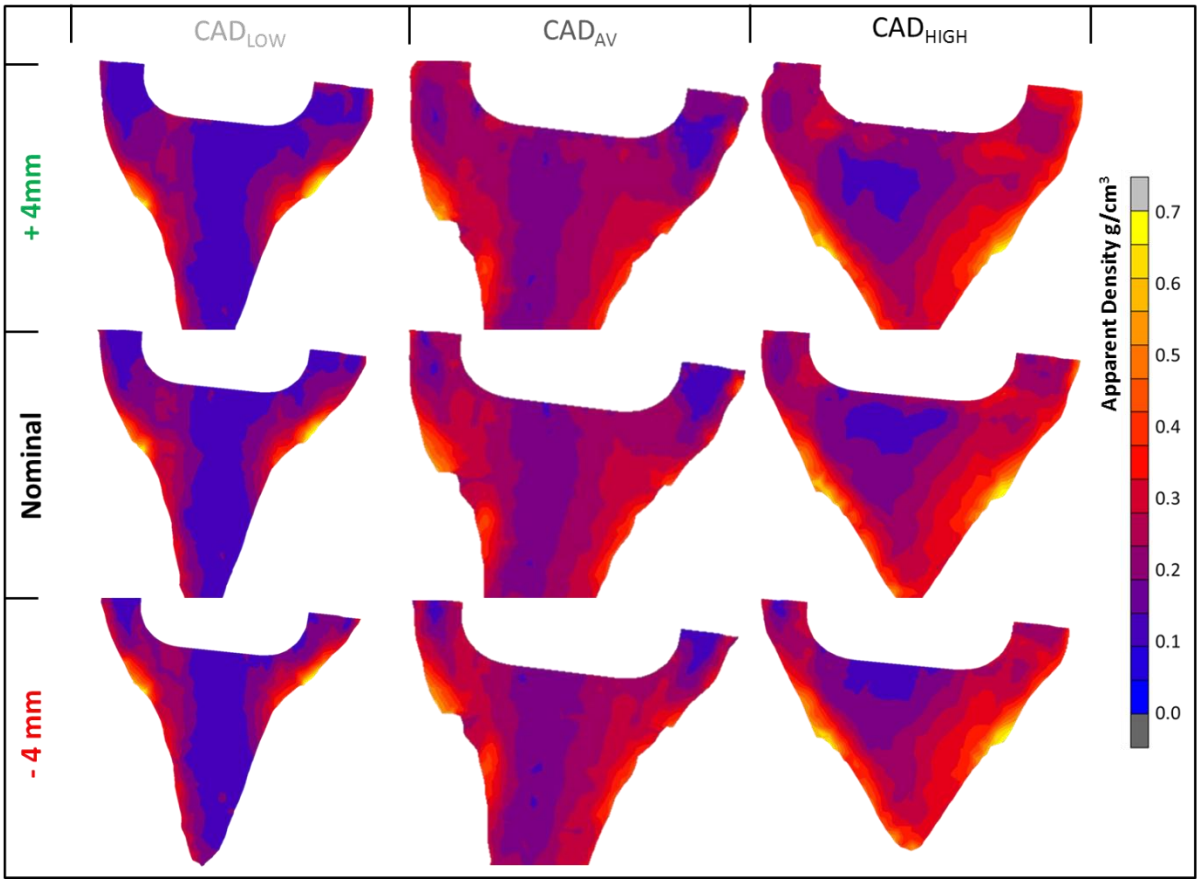


**Figure 170 - Apparent bone densities of all implant FE models assessed. Plots display cancellous bone density range at sagittal cross-section through centre of tibial tray keel.**

Post-arthroplasty, the average bone strains in the 30 zones immediately below the implant decreased by 18% for cemented UKRs and increased by 17% for cementless UKRs. For cementless fixation, bone strains under the tray increased with increased resection depth while for cemented fixation there was no consistent trend. This is because for the cemented cases, the load path depended on the bone density distribution in the vicinity of the implant keel. Figure 172 shows the inconsistent nature of the peak minimum principal bone strains with resection depth.

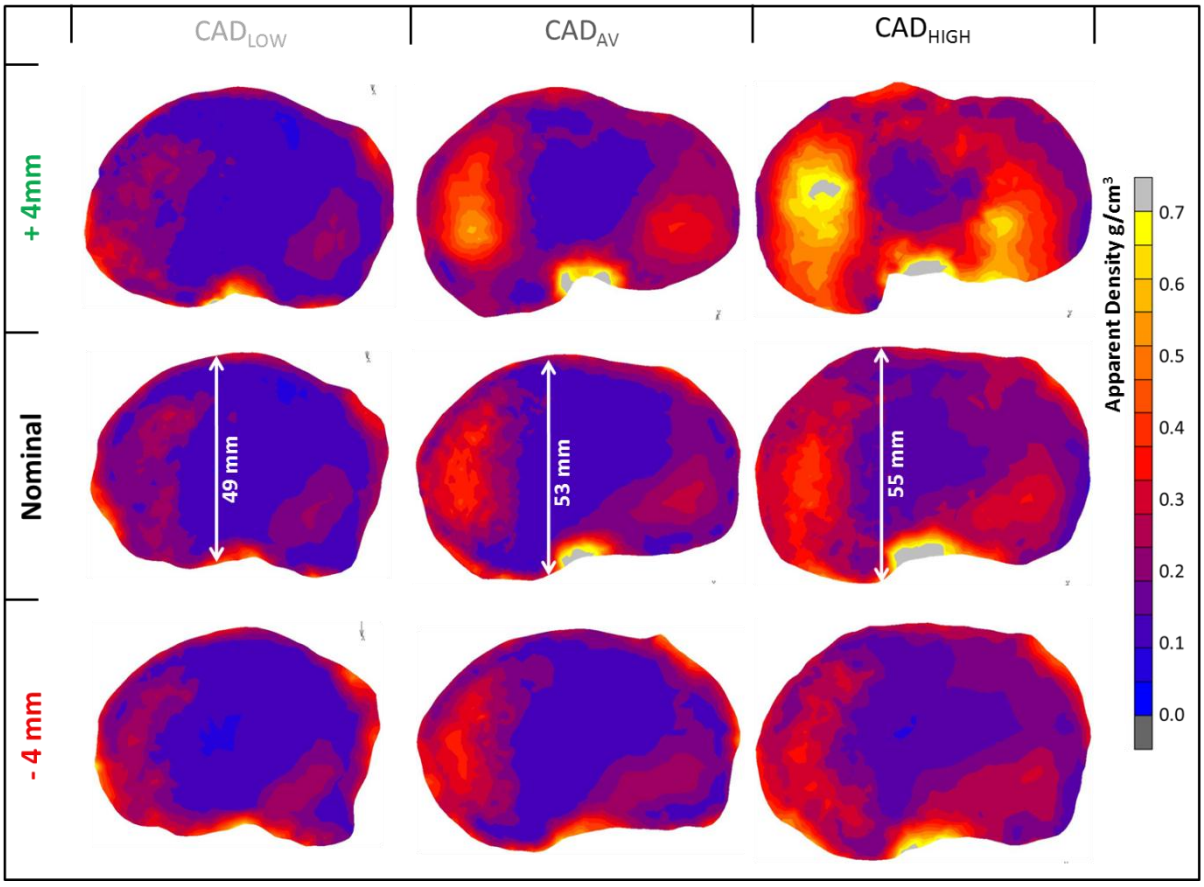


**Figure 171 - Apparent bone densities of all implant FE models assessed. Plots display cancellous bone density range at 1 mm below the transverse resection level of all resection models: (1) nominal, (2) 4 mm superior, and (3) 4 mm inferior.**

The specimen bone density (i.e. bone density difference between $CAD_{LOW}$, $CAD_{AV}$ and $CAD_{HIGH}$ specimens) proved to be a far more important factor on peak bone strains than resection depth. Peak minimum principal bone strains were larger for lower density tibiae and the differences (from intact condition) were also magnified (i.e. there was less variation of peak bone strain with depth below resection line for the dense tibia $CAD_{HIGH}$). The use of a cementless implant produced significant increases of bone strain under the tray surface (with less significant changes on strains under the keel).

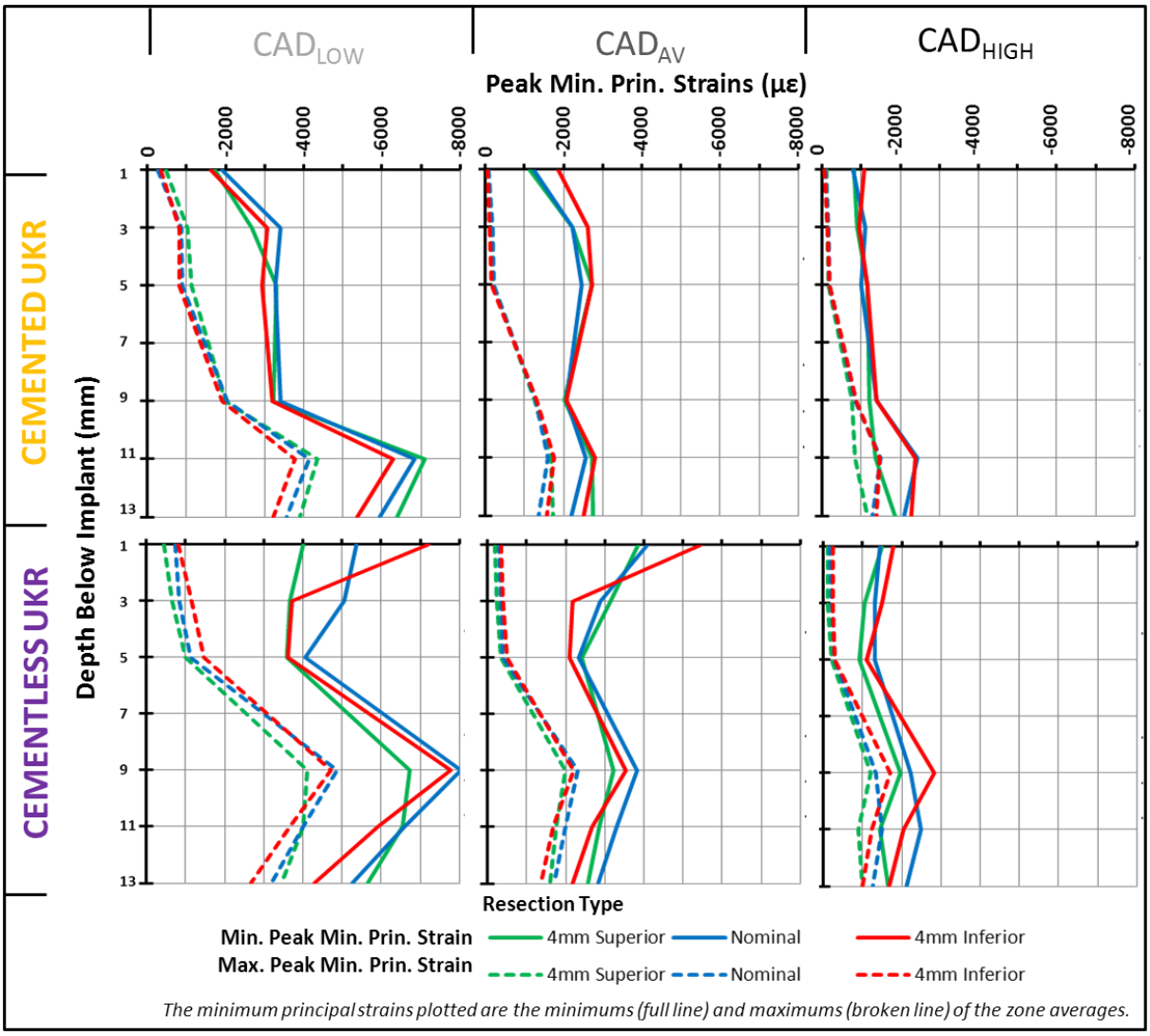


**Figure 172 - Plots of peak minimum principal bone strain with depth below the resection line for all 18 UKR models. At each depth, the minimum zone average of minimum principal strain was calculated and plotted. The tibial keel extended 9 mm the below implant tray and for cemented implants, the cement-mantle extended 2 mm below the implant.**

In general terms, the bone strain changes from pre- to post-arthroplasty decreased for cemented implants and increased for cementless implants (see Figure 173). Figure 174 shows how bone strains changed after arthroplasty by plotting the peak difference at each layer under the resection line.

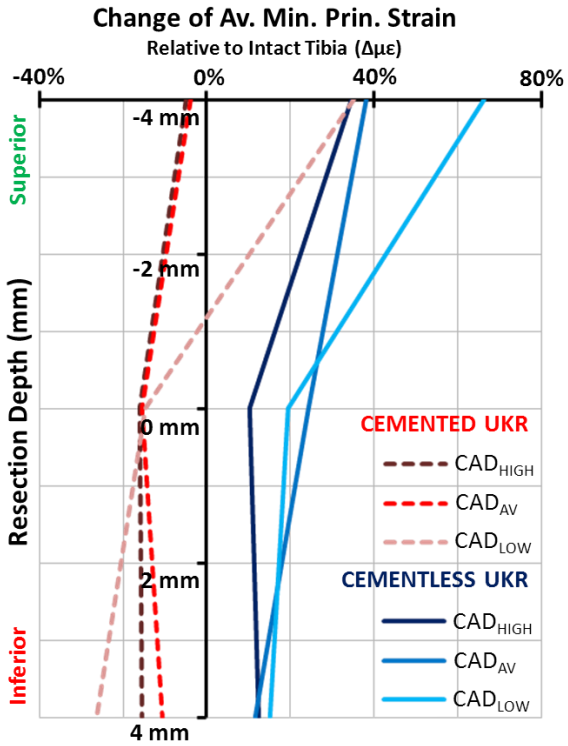


**Figure 173 - Effect of resection depth on change of average minimum principal bone strain (relative to pre-arthroplasty tibia).**

As illustrated by Figure 174, the dense tibia, with the cementless implant at nominal and inferior resections, produced average strains that most closely resembled the pre-arthroplasty state. Peak bone strain differences reduced with depth under the resection line with the largest differences occurring for the lowest density tibia and smallest differences for the densest tibia.

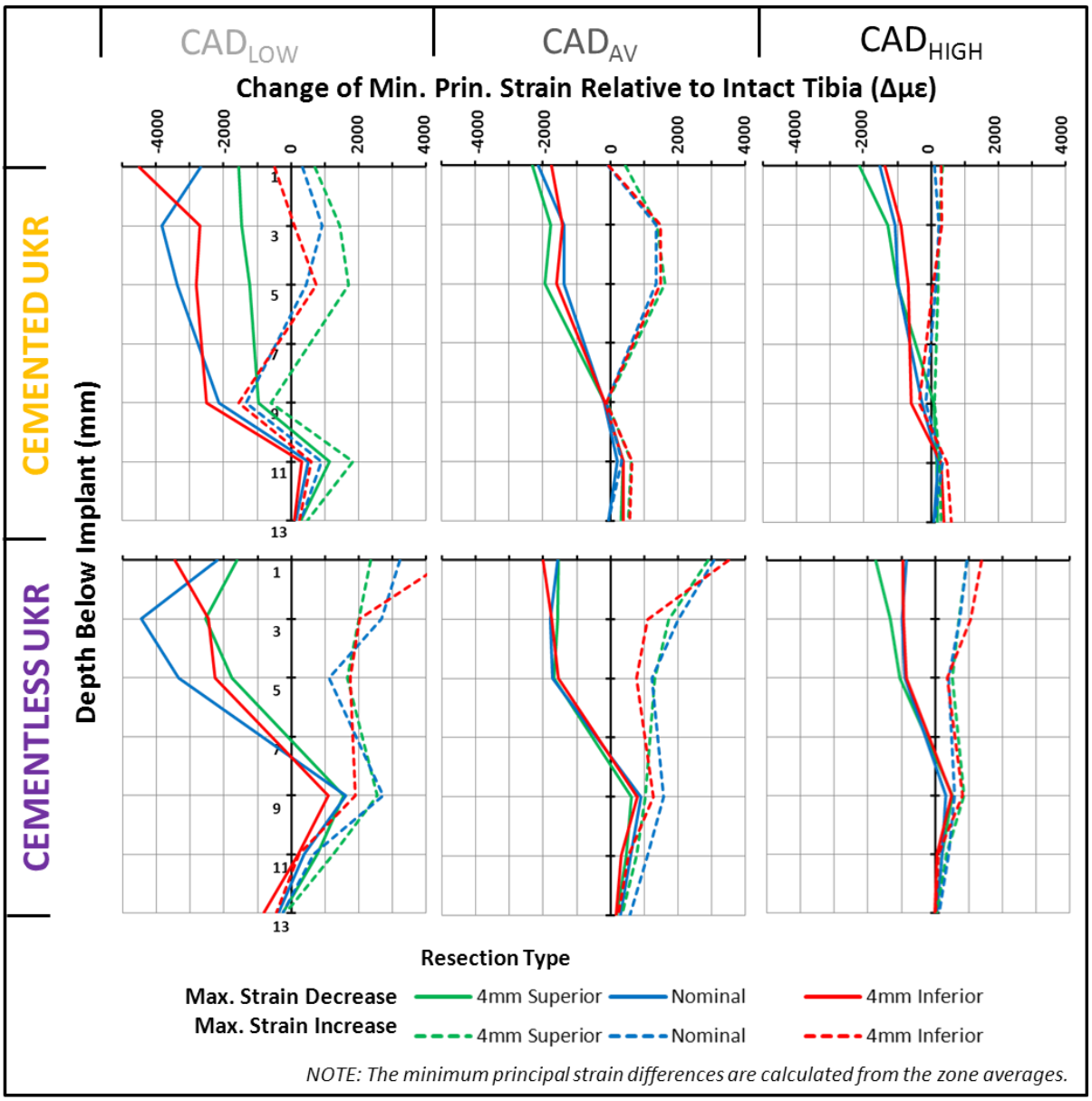


**Figure 174 - The peak increases and decreases of minimum principal strain relative to the intact tibia upon cemented and cementless implantation of a tibial UKR. The tibial keel extended 9 mm below the implant. For the cemented cases, the cement-mantle extended 2 mm below the implant.**

The studies of Sections 7 and 8 showed that the central region under the implant was most likely to experience stress-shielding and bone loss. For the central bone region (zone C-C), Figure 175 shows the average percentage change of bone strain relative to the intact tibia with bone depth. For the cemented case, the greatest decrease occurred in the cement-mantle under the tray (70% for tibia $CAD_{LOW}$ for inferior and nominal resections) and the anterior regions of the $CAD_{AV}$ and $CAD_{LOW}$ (60% and 80% respectively). This corroborates well with the DXA study results presented in Section 7. The reason for this decrease in bone strain may be because, for the smaller tibiae, the keel is very close to the dense cortical

bone of the posterior medial condyle, creating a direct load path. This stress-shielding was made worse with increased resection depth.

For the cementless UKR, strain decreased by up to 80% under the centre of the tray and increased by up to 80% under the keel. However, this does not imply bone loss at 1 year. This reduction of bone strain only occurs immediately post-arthroplasty. Within 3 months the bone strains increase, as the implant osseointegrates to the bone, and the tiny void under the tibial tray is filled or the rim crushes into the bone. Note that the Oxford cementless implant has a recess around the rim of the tray through which most of the load is transferred upon initial implantation.

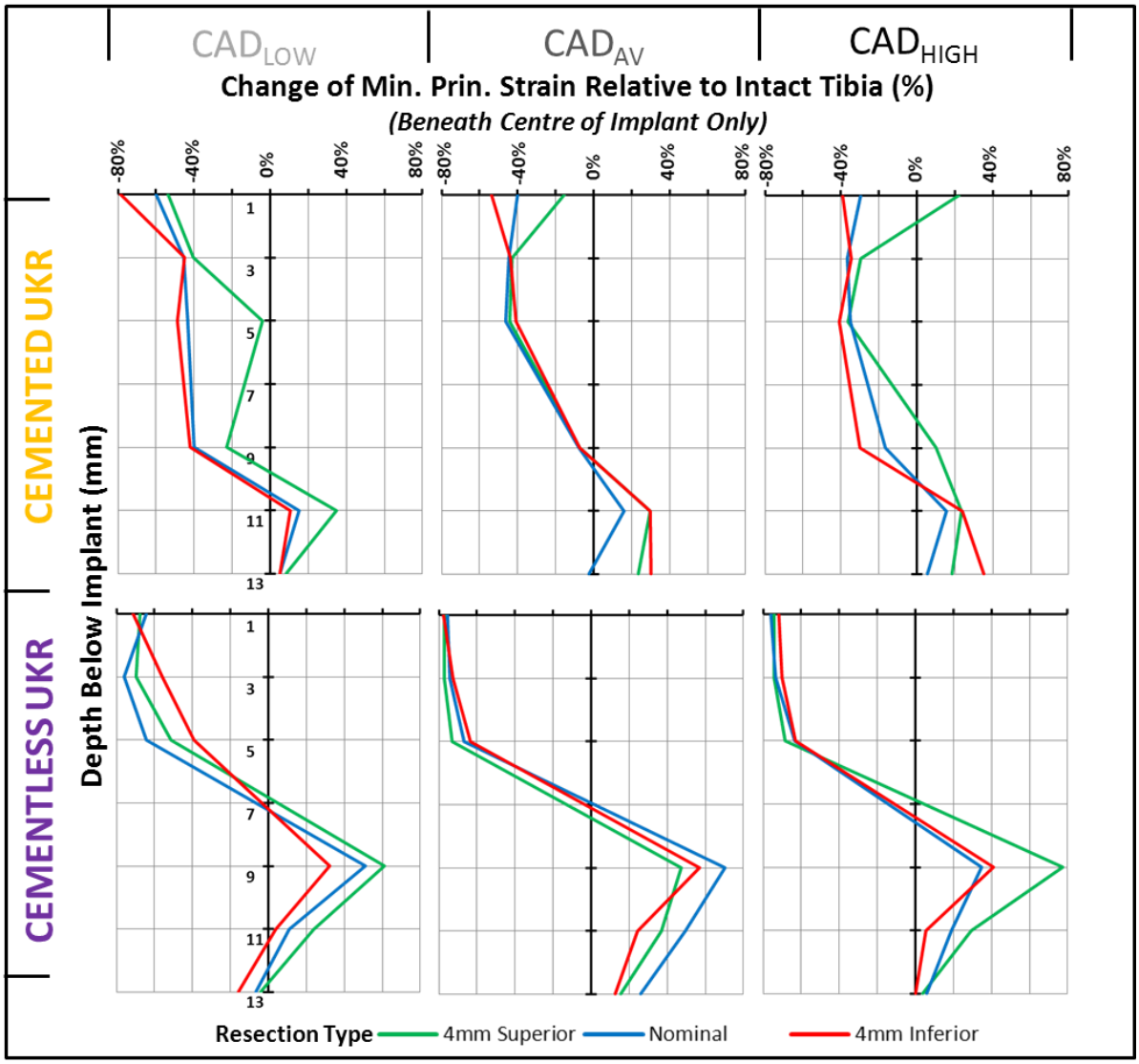


**Figure 175 - Percentage change in average minimum principal strain at centre of implant (zone C-C) relative to the intact tibia upon cemented and cementless implantation of the tibial UKR. The tibial keel extended 9 mm below the implant. For the cemented cases, the cement-mantle extended 2 mm below the implant.**

### *9.5.4 Discussion*

As presented in former sections of this thesis, there are distinct differences in bone strain for cementless and cemented UKRs. This is supported with in-vitro, in-vivo and in-silico studies. The effect of resection depth is also dependent on the fixation method. Cementation distributed the load over the entire tray and keel (with reduced peak strains in the vicinity of the implant), while cementless fixation loaded the edge of the tray.

Although some “stress shielding” under the centre of the tray was observed, it was not considerable: bone strain dropped by less than 70% for cemented implants which is at the threshold of whether bone loss would occur. More superior resections reduced the strain drop. Although bone strain dropped by 80% for cementless UKRs (under the tray centre), this would reduce with implant-bone osseointegration to become less than that of the cemented case. These results corroborated with results of the 1-year DXA follow-up study of 11 UKA patients described in Section 7.

The effect of the resection depth was dependent on how bone density differed due to location. Although superior resection preserved greater density under the tray, it moved the keel to an area of lower density (2 of 3 cases), the strains under the tibial tray were thus higher. The superior resection also changed the relative density between the medial and lateral aspects under the tibial tray; when loaded the implant rotated into the resected corner and this had the consequence of increasing the strains at the lateral resected corner.

These changes were tolerable for the normal and dense tibiae but caused bone yielding for the low density tibia. Two strategies for reducing the strains with superior resections may be: (1) increase the lateral-medial slope of the resection (to maintain an equal bone density distribution); and (2) shortening the keel with superior resections so that it is anchored in a region of high density bone. The effect of resection depth on strain changes under the centre of the cementless implant tray was small. However, around the rim of the implant tray it was more significant (particularly the anterior and posterior of the low density tibia) such that more superior resections reduced strain change.

The cementless implant produced on average 50% higher strains in the anterior region than the cemented (highest at the lateral side). Moving the cementless resection depth inferiorly caused the osteopenic tibia to yield in this region (it also failed here during in-vitro tests).

These assessments are relevant for the first few weeks post-arthroplasty because osseointegration and bone remodelling have not been considered. Knee forces were simplified such that the same loading states were applied to all tibiae adjusted for body-weight. The two common activities were assessed for which the bearing positions were

assumed to be similar (5 mm posterior from tray centre) – the effect of the bearing movements with different activities was neglected.

### *9.5.5 Recommendations*

One objective of the UKR implant fixation design is to minimise the bone strain changes from pre- to post-arthroplasty. If the bone strains increase significantly, they may cause pain, implant migration, bone collapse and lead to implant loosening. If the bone strains decrease significantly, they may cause bone resorption and lead to implant loosening. Although the resection depth makes a difference to bone strain changes, the effect was highly dependent on the patient (tibia density and geometry), whether cemented or cementless fixation was used, and the fit of the implant to the bone.

Based on the findings of this study, the hypothesis that “shallower resections would reduce strain change and improve fixation”, was found to be incorrect. The reason for this was two-fold: With superior resections (1) the keel was moved into a region of lower density, thus increasing the strains under the tray; and (2) the tray underside was moved into a region where the density under the lateral side was lower than the medial side, causing tilt when loaded, thus increasing the strains under the lateral side of the tray.

Cementless fixation produced higher bone strains (than cemented fixation) that less closely matched the pre-arthroplasty condition. Although the resection depth made little overall difference to the bone strains, the strains tended to increase with more superior resections. With osseointegration, these strains are expected to match the intact condition more closely than cemented fixation. The high bone strains could be reduced with (1) a shallower keel that was embedded in denser bone; and (2) the transverse resection made such that it is sloping to the medial aspect.

Cemented fixation produced lower bone strains (than cementless fixation), with some stress-shielding under the central region of the tibial tray. Stress shielding was higher with a lower density tibia. While superior resection reduced the magnitude of stress-shielding, it did not necessarily reduce the strain difference from the pre-arthroplasty state. With deeper resections, the keel moved closer towards the dense posterior cortex of the tibia – this was more obvious in the smaller tibiae. This created a load transmission pathway which was clear in the DXA results (Section 7). Reducing the posterior length of the keel in smaller implants would reduce this effect. Leaving the keel uncemented would also reduce stress-shielding.

Analysis of bone density plots of the transverse resections shows that the highest cancellous density is at the centre of the implant. This corresponds to the position of the centre of

pressure of the natural articulation, and also the implant keel; therefore the high stiffness of this region is not utilised in this design. If there was no keel at the centre of the implant, the fixation would be improved. A keel extending into the lateral side wall or anterior region might be a better option.

The biggest factor on bone strain and change of bone strain (from pre-arthroplasty state) was the bone density/size of the tibia. The highest density tibia produced strains that most closely matched the pre-arthroplasty state with stress-shielding under the tibial tray minimised. This was true for either cemented or cementless implants.

This study suggests that fixation of the tibial tray can be improved, by adapting the fixation design based on the patient's bone density. For low density bone, patient-specific fixation (for resection depth and keel depth) that utilises the regions of higher bone density may improve implant fixation. For high density bone, reduced keel length may improve fixation.

## 9.6 PE Tibial Trays: How do they compare?

### *9.6.1 Introduction*

The legacy of the failure of all-PE TKR tibial implants and the success of their metal-backed counterparts has influenced UKR implant designs. However, there is evidence that all-PE TKR tibial implants can be successful (Rodriguez et al., 2001, Adalberth et al., 2001, Rand, 1993, Apel et al., 1991) and it is therefore important not to infer conclusions to UKR designs.


**Figure 176 - Common all-PE UKR designs.**

Tibial subsidence has been clinically reported to be a cause of failure of UKRs with all-polyethylene (PE) tibial implants. (Aleto et al., 2008) reported that 87% of all UKR revisions that were caused by medial tibial collapse were all PE designs. Metal backing has been linked with improved success rates (Saenz et al., 2010) yet the role of metal backing on bone strains and cement stresses is not fully understood. Studies with composite tibiae have confirmed that bone strains are higher with all-PE implants (Small et al., 2010); however, it is not known how the bone strain distributions change and how PE thickness affects fixation (Lingaraj et al., 2010).

The early problems of all-PE implants were largely due to high wear rates and osteolysis. With recent developments of wear properties of PE materials (sterilized and highly cross-linked PE (Kurtz et al., 1999) and vitamin E infused PE (Kurtz et al., 2009a)), these are no longer significant barriers. The use of PE in implant design may once again become a viable option.

The following study compares bone strains and cement stresses of a mobile bearing (Oxford Biomet) tibial implant and a fixed bearing metal-backed (Oxford Biomet) implant with all-PE designs varying in thickness from 3 mm to 12 mm. The study also assesses the long-term implications on bone density and fixation with bone remodelling simulations.

### *9.6.2 Method*

Three strain-validated tibia models (cemented versions of $CAD_{LOW}$ $CAD_{AV}$ $CAD_{HIGH}$, refer to Section 6) and two remodelling-validated tibia models ($PAT_{CD}$ and $PAT_{CL}$, refer to Section 8) were used for this study. Fixation was assessed and compared between the Biomet Oxford mobile-bearing, Biomet Vanguard M PE metal-backed fixed-bearing, and a hypothetical all-PE fixed-bearing tibial tray UKR. FE geometry of the metal-backed tibial implant, as displayed in Figure 177, was developed and the validated FE models adapted to include these without disrupting the bone mesh. Only the implant mesh was changed, with the tibia and cement-mantle meshes kept exactly the same.

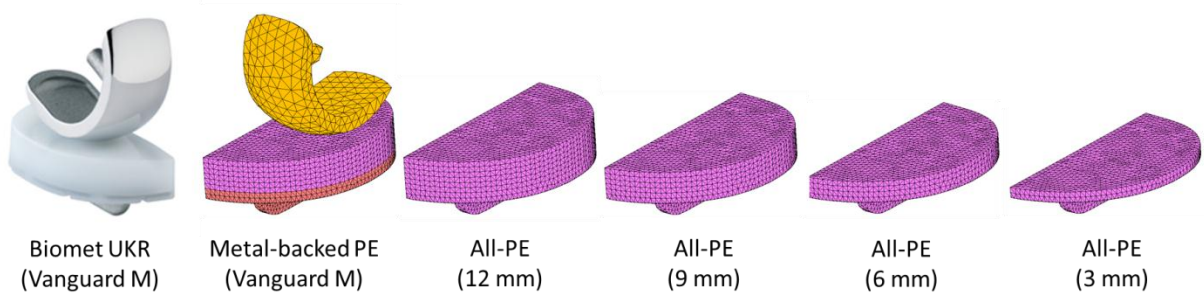


**Figure 177 - Development of metal-backed PE UKR (Oxford Vanguard M).**

The Vanguard M tibial implant consists of a 3 mm Cobalt Chrome base (assumed to be same geometry as the Oxford mobile bearing tibial tray but with the side plate removed) and a 9 mm PE upper insert. The 12 mm thick all-PE implant was assumed to have exactly the same geometry with only the material properties modified (i.e. the previous metal base was changed to be PE). The 9 mm all-PE implant had the same mesh as the 12 mm all-PE implant except the top 3 mm was removed. The 6 mm and 3 mm all-PE implant models were similarly generated. The PE was assumed to have an elastic modulus of 600 MPa (Kurtz et al., 1998). The base of the implants shared nodes with the 2 mm thick cement-mantle while the lateral side-wall nodes were not shared.

The strain-validated FE models ($CAD_{LOW}$ $CAD_{AV}$ $CAD_{HIGH}$ models) were loaded with two sets of peak walking and peak stair-climbing forces that were adjusted for body-weight. The remodelling-validated FE models ($PAT_{CD}$, $PAT_{CL}$) were loaded with exactly the same sets of forces used to validate them in Section 8. Note that a cemented version of the model $PAT_{CL}$ was developed because the validated version was for a cementless UKR. The loads were applied to the femoral implant, with the bearing centre positioned 5 mm posterior to the centre of the implant.

Contact was simulated between the cobalt chrome femoral implant and PE tibial implant upper surface. Sensitivity assessments showed that the all-PE implants results were

sensitive to whether contact was simulated or not. Therefore, since contact was considered mandatory, computational memory requirements had to be reduced by using linear elements (4-node tetrahedral and 3-node shell). The meshes at the regions of interest (tibial implant, cement and medial tibial condyle) were on average of 2 mm element size.

The models were solved using the MARC Solver and the nodal bone minimum principal strains and cement-mantle stresses at each zone were output using Marc Mentat. The average minimum principal strain was calculated for each zone; in addition the average minimum principal stress was calculated for each of the ten cement zones. The results were post-processed using Matlab software (Mathworks, USA) and Excel (Microsoft Corporation, USA).

The following comparisons were made: (1) compare bone strain and cement stresses of (i) mobile bearing (ii) metal backed and (iii) all PE; and (2) compare bone density at 12 months of (i) mobile bearing (ii) metal backed and (iii) all PE.

### *9.6.3 Results*

The tibial bone strains and cement stresses were similar between the Oxford mobile-bearing and metal-backed fixed bearing UKR designs. The all-PE implant produced larger peak minimum principal strains that increased with reduced PE thickness. Figure 178 plots the minimum principal bone strains at 4 levels under the tibial implant and compares all-PE, metal-backed and mobile bearing tibial trays. Bone strains above 7300 με have been highlighted in red and show that the all-PE produced strains which could cause subsidence in specimen $CAD_{LOW}$ (i.e. lowest density tibia). There was an approximately 10% increase in peak bone strains using a mobile-bearing (Oxford design) UKR compared to a metal-backed (Vanguard M design) UKR. A further 120% increase in peak bone strains occurred when using an all-PE UKR. The densest tibia $CAD_{HIGH}$ was the most resilient to these implant design changes and the lowest density tibia had bone strains in excess of 12000 με (below the plateau with thin all-PE components); this would probably lead to implant migration.

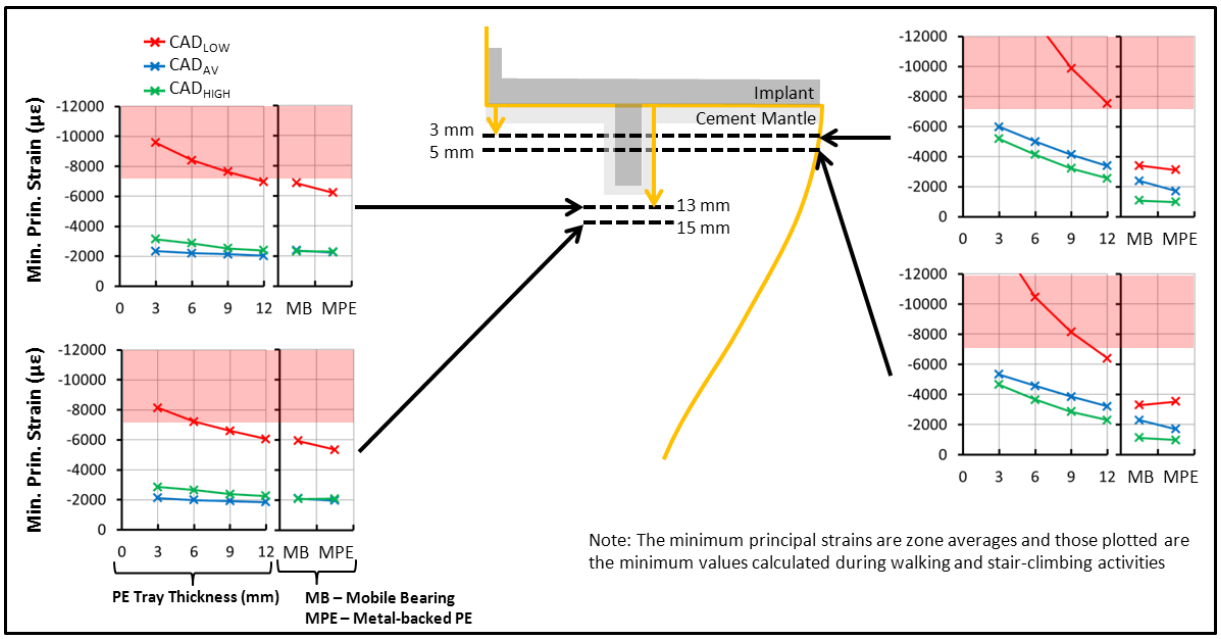


**Figure 178 - Plots of minimum principal bone strain at 4 levels under the tibial implant. The plots compare all-PE, metal-backed and mobile bearing tibial implant designs.**

Figures 179 and 180 display bone strains at a transverse section 3 mm below the implant (1 mm below the cement mantle) and a sagittal section through the centre of the keel. The all-PE implant increases compressive bone strains at the centre/posterior region of the tibia. For the low density tibia ($CAD_{LOW}$) fitted with any of the all-PE implants, tibial collapse would probably have occurred towards the medial/posterior region. For the normal density tibia ($CAD_{AV}$), tibial collapse would probably have occurred with PE thicknesses of 6 mm or less. Figure 179 shows that, for all three tibial bone densities (low, medium, high), the introduction of a metal baseplate reduced the tibial compressive bone strains below the implant.

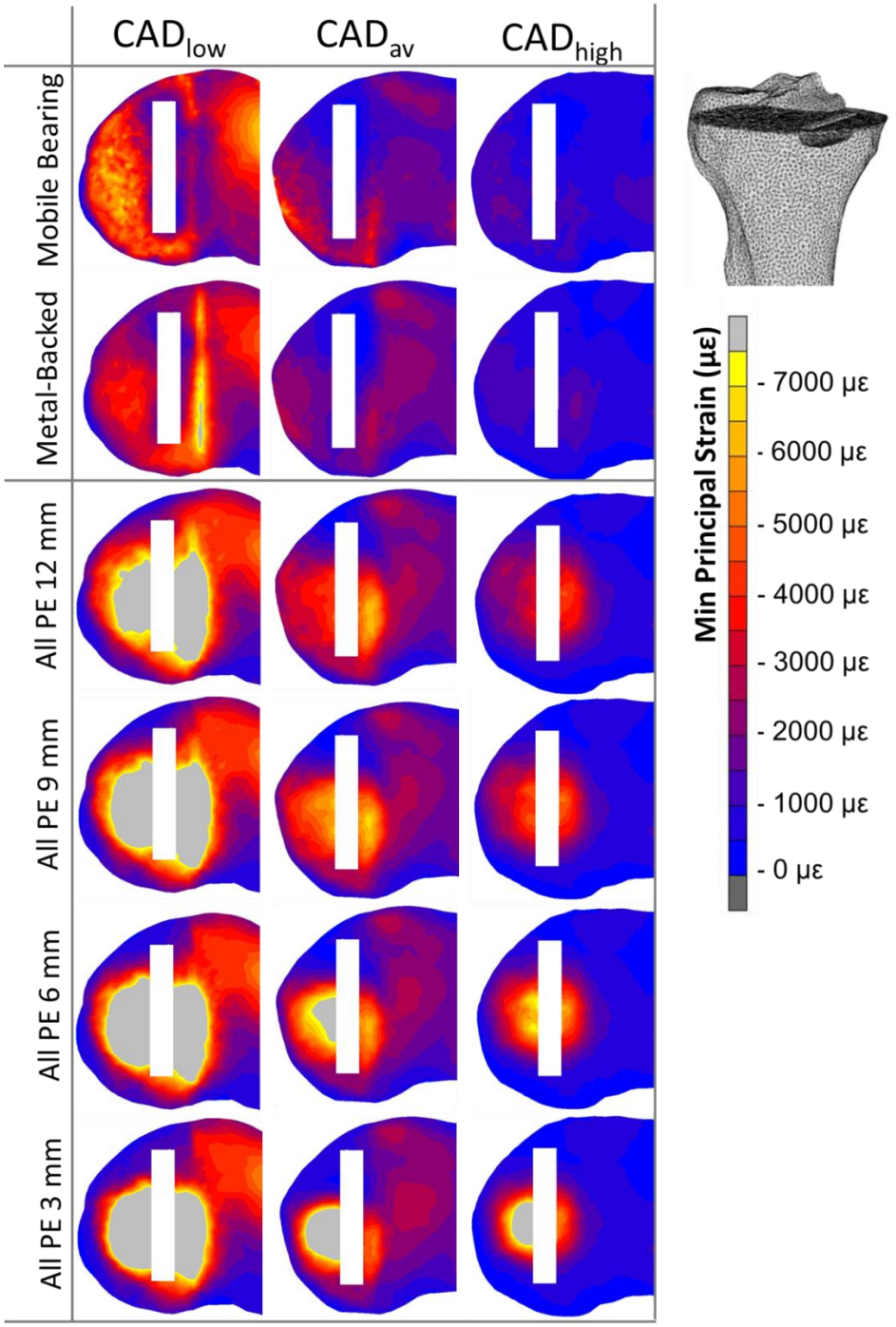


**Figure 179 - Plots of minimum principal bone strain at 1 mm beneath the cement-mantle (3 mm under implant). The plots show the high bone strains produced by the all-PE UKR, particularly for low density tibia.**

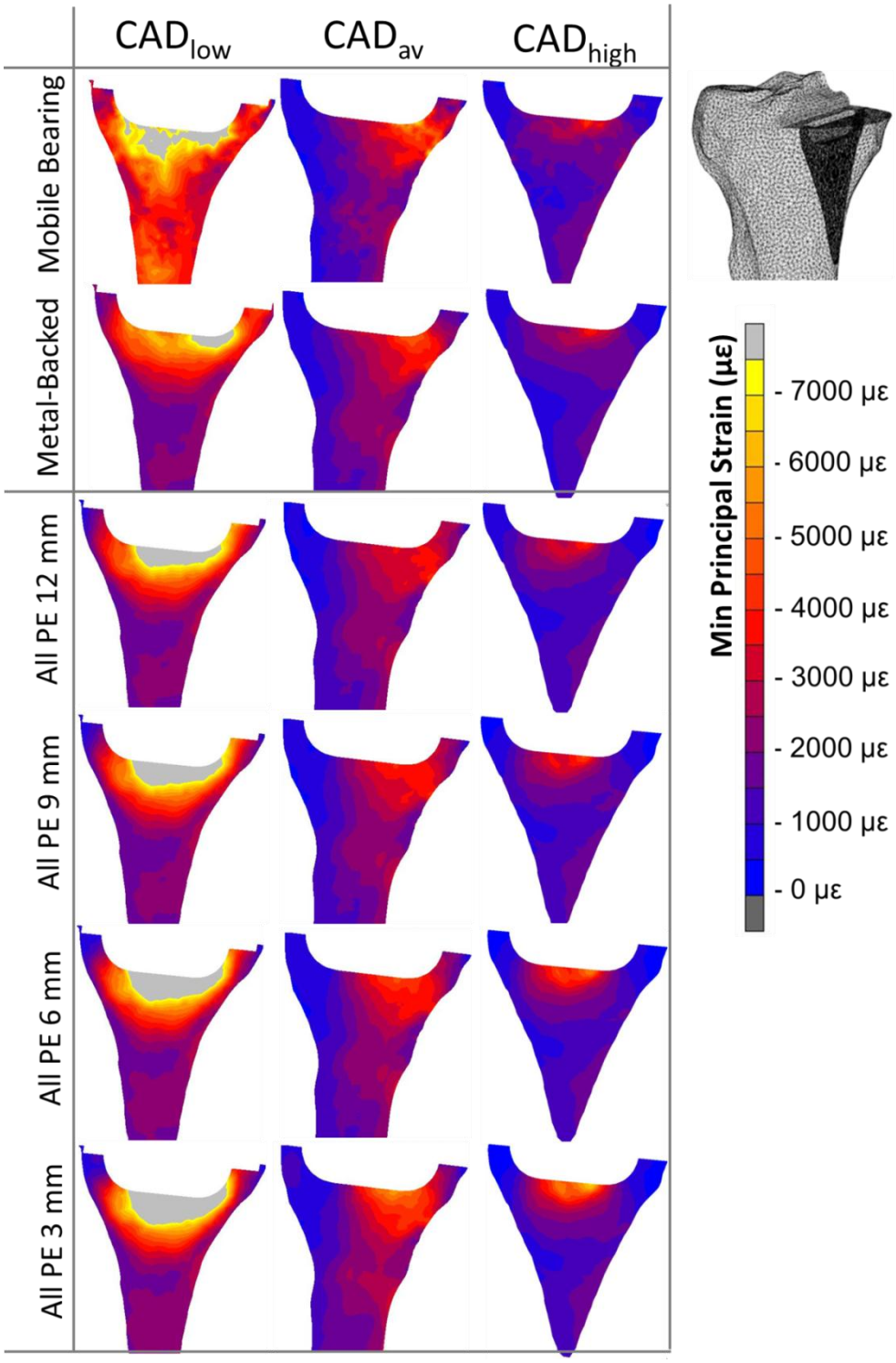


**Figure 180 - Plots of minimum principal bone strain at a sagittal section through centre of implant keel. The plots show the high bone strains produced by the all-PE UKR, particularly for low density tibia.**

The all-PE tibial implants produced the largest bone strains and these were located beneath the centre of the implant, followed by the centre of the resected corner. Note that an all-PE tibial implant with a deeper central keel may increase the stiffness of the implant (reduce bending of the implant) and provide better load transmission to the distal cortices; thereby

reducing peak bone strains. However, the location of the keel is important (refer to Sub-section 9.5), because bending strains may be higher if the distal tip of the keel rests in lower density bone. Since bone density reduces distally, an implant with no keel may also produce lower peak strains than one with a medium length keel.

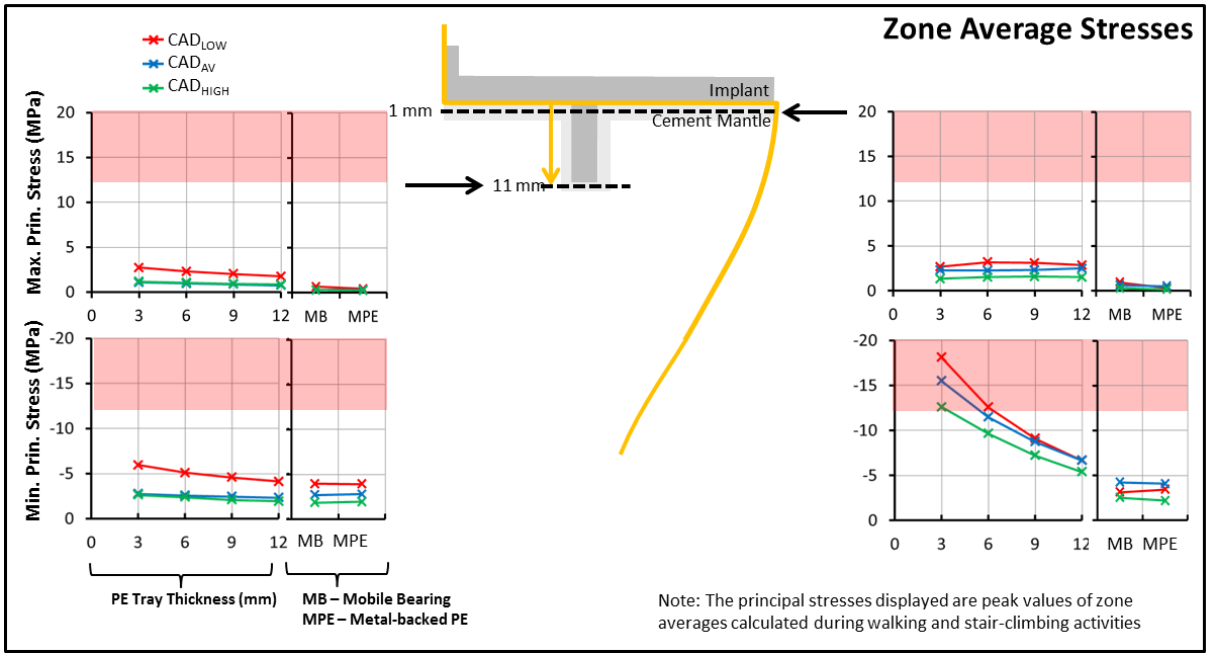


**Figure 181 - Plots of maximum and minimum principal cement stresses. The principal stresses displayed are peak values of zone averages calculated during walking and stair-climbing activities. The plots compare full PE with metal-backed and mobile bearing tibial trays.**

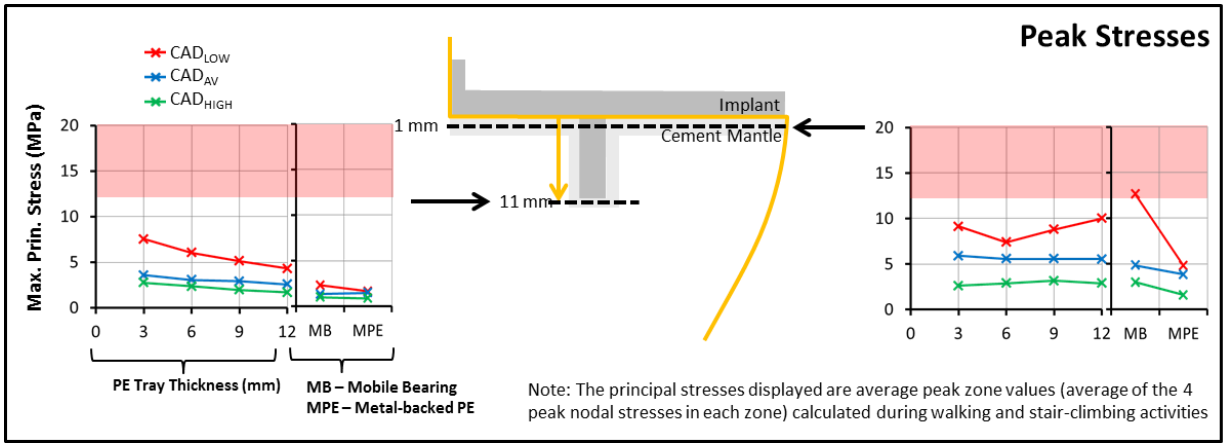


**Figure 182 - Plots of peak maximum principal cement stresses. The principal stresses displayed are average peak zone values (average of 4 peak nodal stresses in each zone) calculated during walking and stair-climbing activities. The plots compare full PE with metal-backed and mobile bearing tibial trays.**

The average maximum principal (tensile) cement stresses (average for each zone) were below the threshold limit that would cause fatigue failure of the cement (Figure 181). Stresses above 10 MPa were considered to be under moderate risk of fatigue damage, while stresses above 12 MPa were considered significant risk (Davies et al., 1987, Burke et al.,

1984, Murphy and Prendergast, 2002). There were, however, localised peak tensile stresses that could initiate fatigue cracking (Figure 182). The peak stresses were as high as 10 MPa for the all-PE UKR implanted in $CAD_{LOW}$. PE thickness had a small effect on peak stresses but the effect of bone density was significant (decreased to 3 MPa for the densest bone $CAD_{HIGH}$). The lowest cement peak stresses were for the metal-backed PE implant.

Figure 183 presents plots of tensile cement stresses through the middle of the cement-mantle. The peak stresses were higher for lower density bone and PE thickness made only a small difference to the magnitude of the stresses. The peak tensile stresses were located in two regions: (i) under loading point (mainly for lower density bone and thinner PE thickness), and (ii) at the lateral edge (just beneath the resected corner). Minimum principal (compressive) stresses in the cement-mantle are presented in Figure 184. The peak compressive stresses were in the same regions as the peak strains in the underlying bone.

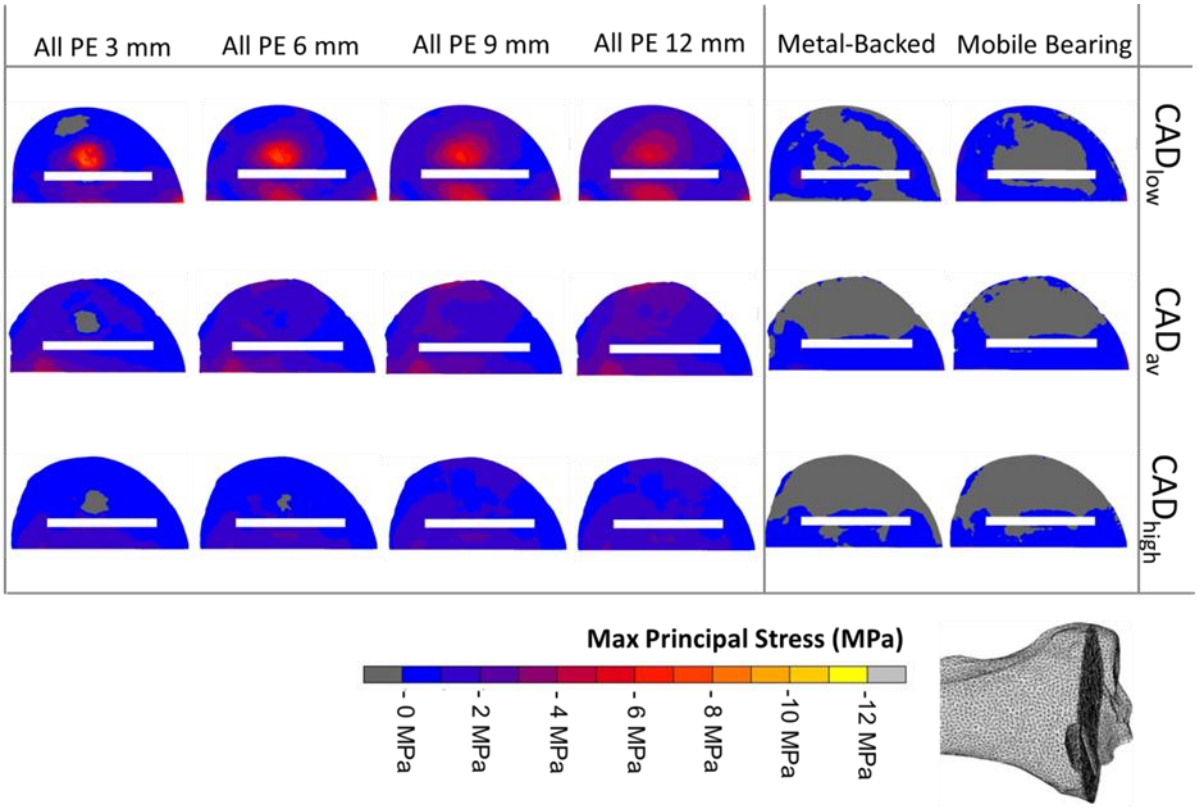


**Figure 183 - Maximum principal stresses at a transverse section through the middle of the cement-mantle.**

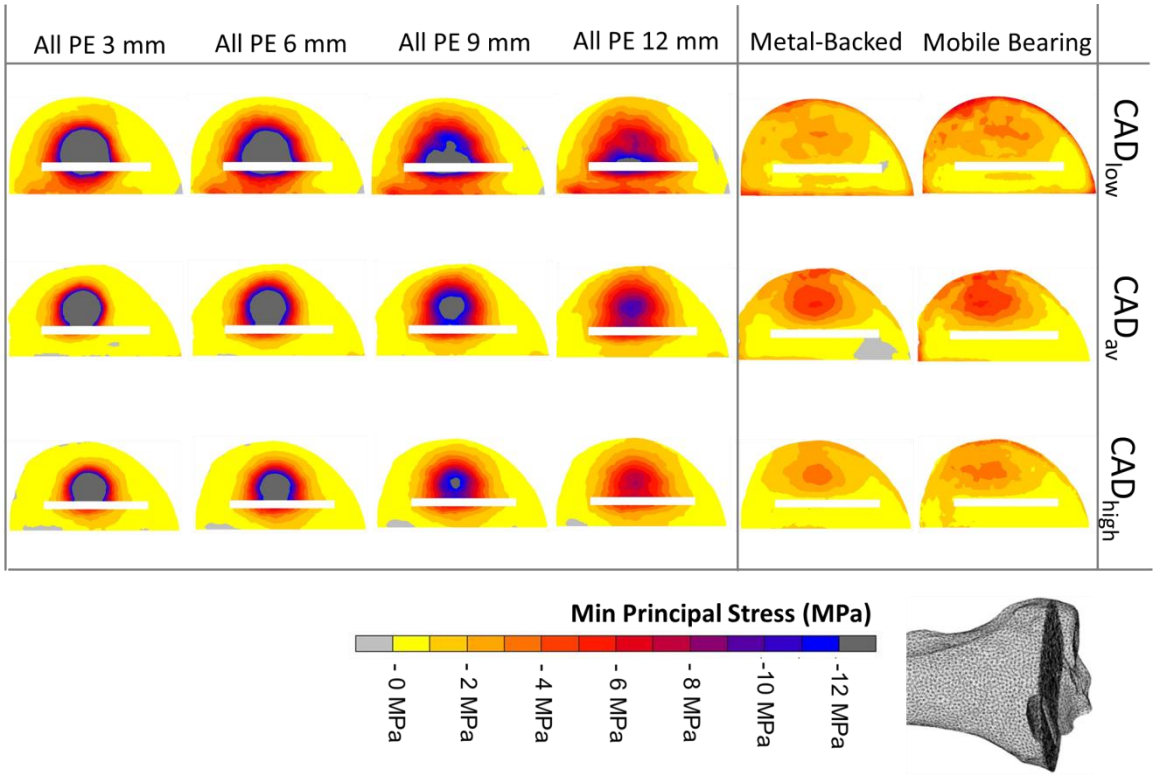


**Figure 184 - Minimum principal stresses at a transverse section through the middle of the cement-mantle.**

The cement-mantle stresses of the tibial implant were mostly compressive and bone cement fatigue usually occurs in tension. However, cement curing causes shrinkage and this can generate residual tensile stresses in the cement; hence generating tensile load cycles and can influence fatigue (Lennon and Prendergast, 2002). Although, residual stress in bone cement will relax over time due to its viscoelastic properties, the immediate effect may be significant. The preloaded structure may initiate crack formation and lead to a damage accumulation failure scenario, as described by Huiskes and Stolk (2005). The minimum principal (compressive) stresses should therefore be considered. The peak average cement minimum principal stresses of 3-5 MPa were similar between the metal-backed and mobile bearing UKRs. The peak stresses rose to 5-7 MPa with 12 mm thick all-PE implants and increased by 3 MPa with subsequent reductions of 3 mm in PE thickness (Figure 181). Figure 184 plots the minimum principal stresses in specimens $CAD_{LOW}$, $CAD_{AV}$ and $CAD_{HIGH}$ at the cement-mantle of all implant designs.

A 9 mm all-PE thick was considered to be adequate to maintain cement integrity, while 6 mm thick (or less) was conservatively considered under increased risk of cement fatigue and tibial subsidence. All the ten cement zones produced average stresses that were compressive; however, there were localised regions of tensile stress that could initiate cracking. Fatigue failure is most likely to occur at the central region for low density bone and may occur laterally for denser bone and stiffer implants. There are three subsequent scenarios with this type of failed cement mantle: (1) tibial subsidence; (2) increased interface micromotion and development of interface fibrous tissue; and (3) if the surrounding cement and bone were able to maintain integrity (under increased cement stresses at the periphery), bone loss could occur at the centre of the tray.

The bone remodelling simulations (remodelling-validated $PAT_{CD}$ and $PAT_{CL}$ models) correlated with the findings of the strain-validated models ($CAD_{LOW}$, $CAD_{AV}$ and $CAD_{HIGH}$). High strains were observed at the centre/posterior of the all-PE implants and subsequently bone apposition occurred in these regions. Figures 185 and 186 present plots of bone density at a transverse section 3 mm beneath the implant (1 mm beneath the cement mantle) and at a sagittal section through the centre of the keel, respectively.

There was some bone loss in patient $PAT_{CL}$ at the anteromedial region with both the mobile-bearing and metal-backed implants. Note that $PAT_{CL}$ had higher bone density and activity levels compared to $PAT_{CD}$ (refer to Section 7). With a 12 mm thick all-PE implant, patient $PAT_{CL}$ experienced no bone loss and instead bone apposition occurred at the anteromedial region. There was also a distinct difference in load path with the all-PE implant. The mobile-bearing and metal-backed implants caused bone apposition at the posterior region of the keel, whilst with the all-PE implants there was no change in bone density under the keel. A

higher proportion of the load transferred through the top bone-implant interface thereby reducing stress-shielding.

The less active (with less tibia bone density) patient tibia $PAT_{CD}$ behaved similarly but with notable differences to $PAT_{CL}$. For both mobile-bearing and metal-backed implants, whilst there was bone loss at the central region beneath the implant, there was slight bone apposition on the lateral side of the keel. The bone apposition was greater for the metal-backed implant, with some bone apposition occurring at the anterior resected corner. The all-PE implant had the effect of producing a significant amount of bone apposition beneath the centre of the implant, extending onto the lateral side of the keel. Since the centre of pressure of the femoral implant was above the keel, there was increased load transfer through the keel with reduced PE thickness. Although the load path changed (similarly to $PAT_{CL}$), bone apposition occurred under the keel because the centre of femoral implant pressure was location above it. Note that the centre of pressure on $PAT_{CL}$ was located medial to the keel due to the proportions of a larger tibia and implant.

A thick all-PE implant may provide reduced bone loss and improved long-term fixation provided that initial fixation is not compromised with the high bone strains immediately post-arthroplasty. Although a 12 mm thick all-PE implant produced the most suitable bone strains for patient $PAT_{CL}$, it produced significantly higher bone strains for patient $PAT_{CD}$. If an all-PE implant was used on patient $PAT_{CD}$ it would have to be thicker than 12 mm. This would be contrary to the philosophy of minimally invasive surgery, with deeper resection and could cause other complications. A possible alternative could be an implant with an elastic modulus between Cobalt Chrome and PE (i.e. the elastic modulus would be adapted to suit the patient rather than the implant thickness).

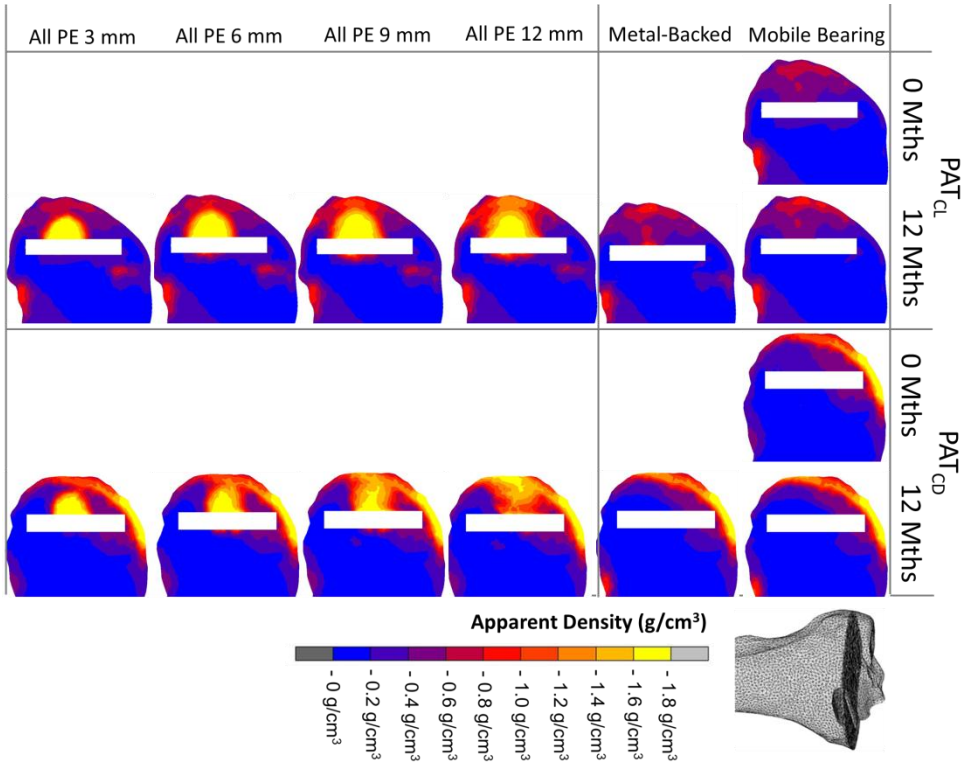


**Figure 185 - Bone remodelling at 1 mm under the tibial tray. The plots compare the mobile bearing Oxford UKR and the metal-backed Oxford UKR against all PE versions of reducing thicknesses for apparent density at 1 year.**

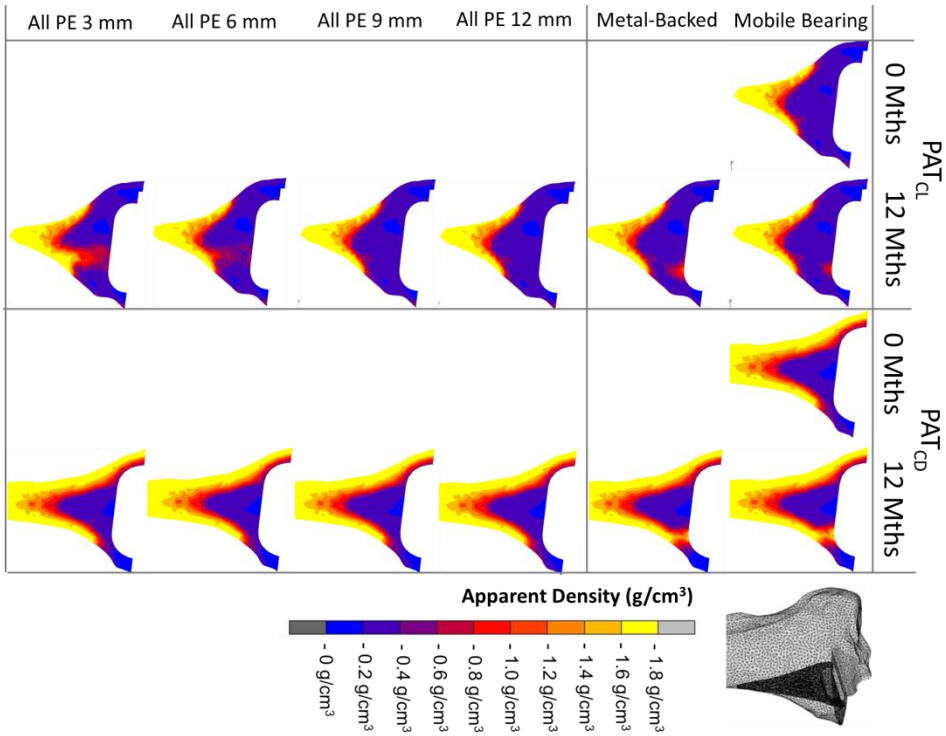


**Figure 186 - Bone remodelling at sagittal plane through the centre of the tibial tray. The plots compare the mobile bearing Oxford UKR and the metal-backed Oxford UKR against all PE versions of reducing thicknesses for apparent density at 1 year.**

### *9.6.4 Recommendations: What tibial tray PE thickness is required to have successful fixation?*

Based on the study of three cadaveric tibia specimens simulating low, medium and high density bone, the bone strains and cement stresses of all-PE tibial implants were compared to metal-backed and mobile-bearing implants. Since PE material has a lower stiffness than cobalt-chrome (or titanium), a thicker implant is required to provide comparable load distribution to that of a mobile-bearing or metal-backed tibial tray.

This study showed that a 12 mm thick all-PE tibial implant provided less rigidity compared to the mobile-bearing and metal-backed designs. There was up to a 120% increase in peak bone strains beneath the implant with a further 25% increase with every subsequent 3 mm reduced from the thickness. Bone strains were severe for the lowest density specimen with likely tibial collapse upon use of any all-PE implant up to 12 mm thickness. For the normal and highest density tibia specimens, the bone strains were within acceptable limits with all-PE implant thicknesses of 9 mm or greater.

The peak compressive cement stresses rose by 2 MPa to 5-7 MPa with a 12 mm all-PE implant and increased by 3 MPa with subsequent reductions of 3 mm in PE thickness. PE thickness had a small effect on the peak tensile cement stresses; however they were as high as 10 MPa for the lowest density tibia. They were within safe limits for the average and dense tibias. The tensile stresses were located either at the lateral edge or under the centre of the implant. PE thicknesses of 9 mm or greater were considered safe from cement fatigue failure.

Two actual UKR patient knees (an inactive patient with low density tibia and an active patient with high density tibia) were also simulated with all-PE implant of variable thicknesses. With the all-PE implant, both the simulated patient tibiae developed bone apposition at 1 year (regardless of PE thickness). The all-PE implants produced negligible bone loss. The bone apposition in the low density tibia patient was extreme while the 12 mm thickness all-PE implant produced the most optimum results for the high density tibia patient. In both cases, stress shielding was negligible. The trade-off was that the magnitudes of the bone strains were high and must be considered as they can cause tibial collapse and pain.

For the 9 mm and 12 mm all-PE implants, the highest bone strains occurred at 3 months Note that there was a gradual increase in activity levels which was different for both patients (50%, 75%, 90%, and 100% at 3, 6, 9, and 12 months for low density tibia patient and 50% at 3 months and 100% thereafter for high density tibia patient, refer to Section 8). With the 6 mm all-PE implant, both patients may have experienced significant pain with possible tibial subsidence as bone strains approached their failure limit (even under the very gradual

increase in activity levels for the low density tibia patient). The 3 mm all-PE implant would have caused tibial collapse for both patients (unless activity level increases were reduced significantly). The study shows that rehabilitation should be dependent on the patient tibia density, with activity levels resumed more slowly for lower density tibia.

The minimum thickness of PE required for fixation success is dependent on the bone density, patient weight and expected resumption of activity levels. For the active patient with high density bone, a 9 mm thick all-PE implant produced good results, while a 12 mm thick implant was required for normal bone density patients. Note that the three specimens and 2 patients assessed in this study did not consider the effect of obesity; the simulations assumed the actual body-weight of the donors and patients. Excess weight would require a thicker PE bearing to maintain the stresses and strains at safe levels. Based on this study, the all-PE implant performed poorly on the patient with low quality bone; therefore it is recommended that it is not used on patients that fall in this category.

This study demonstrates that the highest bone strains are located beneath the centre of pressure on the implant. If bone density is high in these regions, bone strains should be maintained below their failure limits. In was demonstrated in Sub-section 9.5 that with shallower resections, the bone density is higher particularly at the centre of the condyle. The performance of these all-PE implants would therefore be significantly enhanced with shallower resections where dense bone is in the regions where the highest bone strains are located.

There is clinical evidence to support the claims of this study. Failure of the UKR associated with tibial subsidence is more common with all-PE designs (Saenz et al., 2010, Aleto et al., 2008, Squire et al., 1999, Tabor Jr and Tabor, 1998). Poor performance has been linked with excess weight (Saenz et al., 2010) and younger more active patients (O'Rourke et al., 2005). Although, thinner PE bearings have been also associated with poorer outcomes, their failure has been associated with substantial wear (Argenson and Parratte, 2006, Hernigou et al., 2008). This is the first study (known to the author) that has investigated the effect of PE thickness on tibial subsidence. With improved PE wear properties, it is important to consider the implications of reduced PE thickness on tibial subsidence.

In general the performance of thin all-PE UKR implants have compared poorly with mobile bearing and metal-backed UKRs (Saenz et al., 2010), in particular UKRs with PE thicknesses less than 6 mm (Argenson and Parratte, 2006, Hernigou et al., 2008). These failures have been associated to high wear and osteolysis and studies have shown that thicker implants produced less wear (Argenson and Parratte, 2006, Hernigou et al., 2008). PE bearing stresses have been shown to be an important factor (Simpson et al., 2008). This

study demonstrates that for normal UKR patients, PE thicknesses greater than 9 mm are significantly less likely to produce tibial subsidence based on an assessment of bone strain, cement stress and bone remodelling. The Evolution UKR (Tornier Inc., France) is an example of a thick all-PE UKR that has demonstrated good results with specific patients (93.5% survival rate at 10 years (Lustig et al., 2009)).

In addition to understanding the failure mechanics, the study highlights the potential benefits using of all-PE tibial UKRs. If designed adequately, the benefits of reduced stress-shielding will improve long-term fixation. However, the study has demonstrated the sensitivity of the results to the quality of the bone and this may explain the current higher proportion of failures associated with all-PE implants compared to mobile-bearing and metal-backed designs. Potentially, the PE bearing could be customised based on a simple pre-assessment of the patient's bone density.

### *9.6.5 Recommendations: Are metal-backed tibial trays better than all-PE trays?*

The advantage of all-PE implants is that they could reduce stress-shielding (Hyldahl et al., 2001) in patients with high density bone. The drawback is that if the correct PE thickness is not used, they can produce high bone strains that can cause pain and tibial subsidence in patients with adverse bone quality.

This study adds further evidence to the body of clinical studies, for the recommendation of a minimum PE bearing thickness. However, this study recommends not to use a "one size fits all" philosophy and to determine the PE thickness from patient bone quality (assuming they are not obese, and have normal activity levels): PE bearings should not be used if the patient bone quality is poor; a minimum of 9 mm is used for patients of normal bone quality; and a minimum of 6 mm for patients of good bone quality. If the quality of the bone is unknown (this is particularly likely with surgeons of limited experience), the all-PE tibial UKR should not be used.

Despite the potential benefits of all-PE tibial UKRs, thick implants are not in-line with minimally invasive approach that is so strongly associated with the UKR philosophy. In this regard, mobile-bearing and metal-backed tibial trays may be a better solution for (1) patients of reduced bone quality, (2) obese patients, and (3) highly active patients (i.e. a stiffer implant with less thickness). Metal-backing reduces bone strains and cement stresses; therefore metal-backed PE implants have performed well (Small et al., 2010) and despite their bearing thicknesses being less than 6 mm (Lingaraj et al., 2010).

Mobile-bearing and metal-backed tibial UKRs have in general performed clinically better than all-PE UKRs (Saenz et al., 2010, Small et al., 2010). This may be because the "one

size (and design) fits all” philosophy is incompatible with the all-PE tibial UKR design. There is clinical evidence that with carefully selected patients, the all-PE implant improves long-term fixation compared to metal-backed designs; a Swedish randomised prospective trial showed reduced subsidence after 24 months compared to metal-backed designs (Hyldahl et al., 2001). For specific patients, all-PE UKRs may provide an improved outcome.

## 9.7 Tibial Tray Keel: Does it provide better fixation?

### *9.7.1 Introduction*

Initial fixation is important for the success of UKR implants, particularly for cementless implants. Initial fixation is usually provided using one or more of the following methods (1) cement, (2) keel, (3) pegs or (4) screws. The trade-off of using these initial fixation techniques is that they can compromise long-term fixation by stress-shielding; therefore they should be used carefully.


**Figure 187 - Different UKR cemented fixation designs.**

The cemented and cementless Oxford mobile-bearing tibial implants have identical keel geometries and this study investigates whether the cemented keel compromises long-term fixation.

### *9.7.2 Method*

Three strain-validated tibia models (cemented versions of $CAD_{LOW}$ $CAD_{AV}$ $CAD_{HIGH}$, refer to Section 6) and two remodelling-validated tibia models ($PAT_{CD}$ and $PAT_{CL}$, refer to Section 8) were adapted for this study. FE models of the metal-backed PE UKR tibial tray (Oxford Vanguard M) and a 12 mm thick all-PE UKR tibial tray were developed, as presented in Figure 188. The keels of all three of the different implants were adapted to simulate (1) standard large keel, (2) short keel and (3) no keel, as illustrated in Figure 189. Only the implant meshes were adapted, with the tibia and cement-mantle meshes maintained exactly the same as the original validated models.

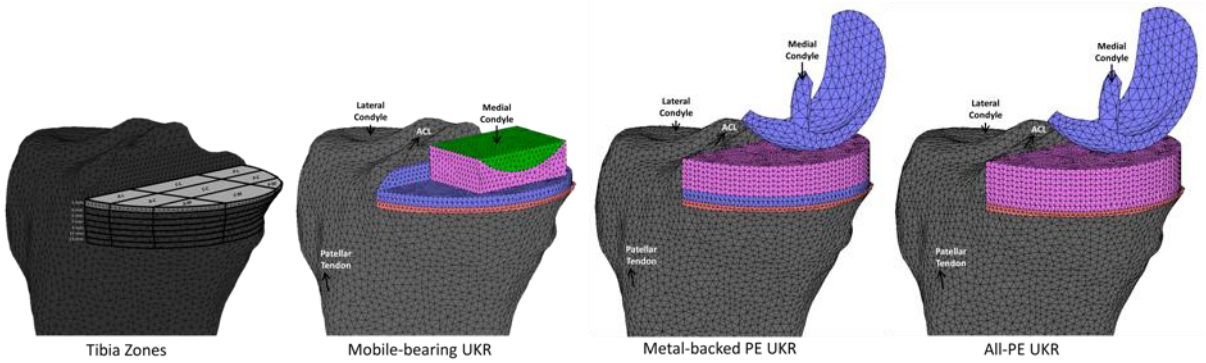


**Figure 188 - FE models of mobile-bearing, metal-backed PE and all-PE UKRs. The tibia bone was separated into zones as illustrated on the left.**

The strain-validated FE models ($CAD_{LOW}$ $CAD_{AV}$ $CAD_{HIGH}$ models) were loaded with two sets of peak walking and peak stair-climbing forces that were adjusted for body-weight. The remodelling-validated FE models ($PAT_{CD}$, $PAT_{CL}$) were loaded with exactly the same sets of forces used to validate them in Section 8. The loads were applied to a femoral implant that was positioned with the centre of pressure 5 mm posterior to the centre of the tibial implant.

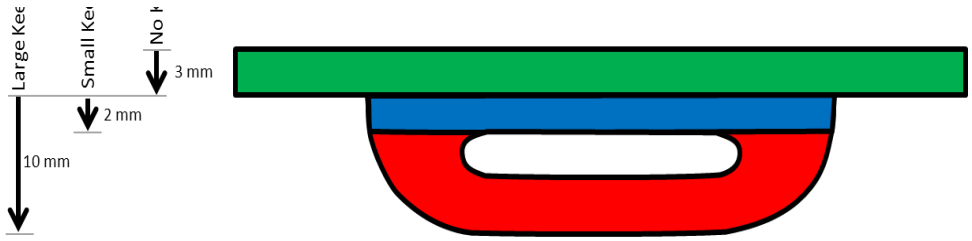


**Figure 189 - Schematic diagram presenting the geometries of the implant keel designs assessed.**

For the metal-backed and all-PE models, contact was simulated between the cobalt chrome femoral implant and PE tibial implant upper surface. Sensitivity assessments showed that the all-PE implants results were sensitive to whether contact was simulated or not. In order to compare accurately to the mobile-bearing designs, these models also incorporated contact (between the bearing and tibial implant). Since contact was considered mandatory, the computational memory requirements had to be reduced by using linear elements (4-node tetrahedral and 3-node shell). The meshes at the regions of interest (tibial implant, cement and medial tibial condyle) were on average of 1.5 - 2.0 mm element size.

The strain-validated tibia models were split into 30 zones (refer to Figure 188): each zone was 2 mm thick (axial dimension); with nine zones in each of the first three layers (split into thirds); and three single-zone layers representing the region directly under the large keel. Intact tibia models of each specimen were also developed, each defined with the same zones corresponding to the implanted tibia models.

The models were solved using the MARC Solver and the nodal bone minimum principal strains and cement-mantle stresses at each zone were output using Marc Mentat. The average minimum principal strain was calculated for each zone; in addition the average minimum and maximum principal stress was calculated for each of the ten cement zones. The results were post-processed using Matlab software (Mathworks, USA) and Excel (Microsoft Corporation, USA).

For each of the three implant designs (mobile-bearing, metal backed, and all-PE), the bone strains, cement stresses and bone-adaptation of the following keel designs were compared: (1) fully cemented 10 mm tibial keel; (2) uncemented 10 mm tibial keel; (3) uncemented 2 mm tibial keel; and (4) no tibial keel. A total of 60 simulations were developed and analysed.

### *9.7.3 Results*

Figures 190 and 191 present comparisons of bone strains beneath tibial UKRs of different keel designs. The bone strains were compared against those of the pre-arthroplasty state, and demonstrated increased stress-shielding with more bulky and stiffer keels, particularly for low density bone. Reduced keel size increased the bone strains immediately beneath the implant. For metal implants this bought the bone strains closer to the pre-arthroplasty strains. However for all-PE implants, the peak bone strains were closer to the pre-arthroplasty strains when a 10 mm keel was cemented, because the keel stiffened the PE tray.

The magnitude of stress shielding varied between specimens; this was most significant in the lowest density tibia. Figure 192 compares minimum principal bone strain plots at a transverse section 3 mm beneath the implant for the different keel designs of a mobile-bearing UKR. For the mobile-bearing UKR, cementing the keel made negligible difference to the strains, while for the metal-backed and all-PE UKRs it increased bone strains immediately beneath the implant. The difference in bone strains between the small uncemented keel and no keel designs was small.

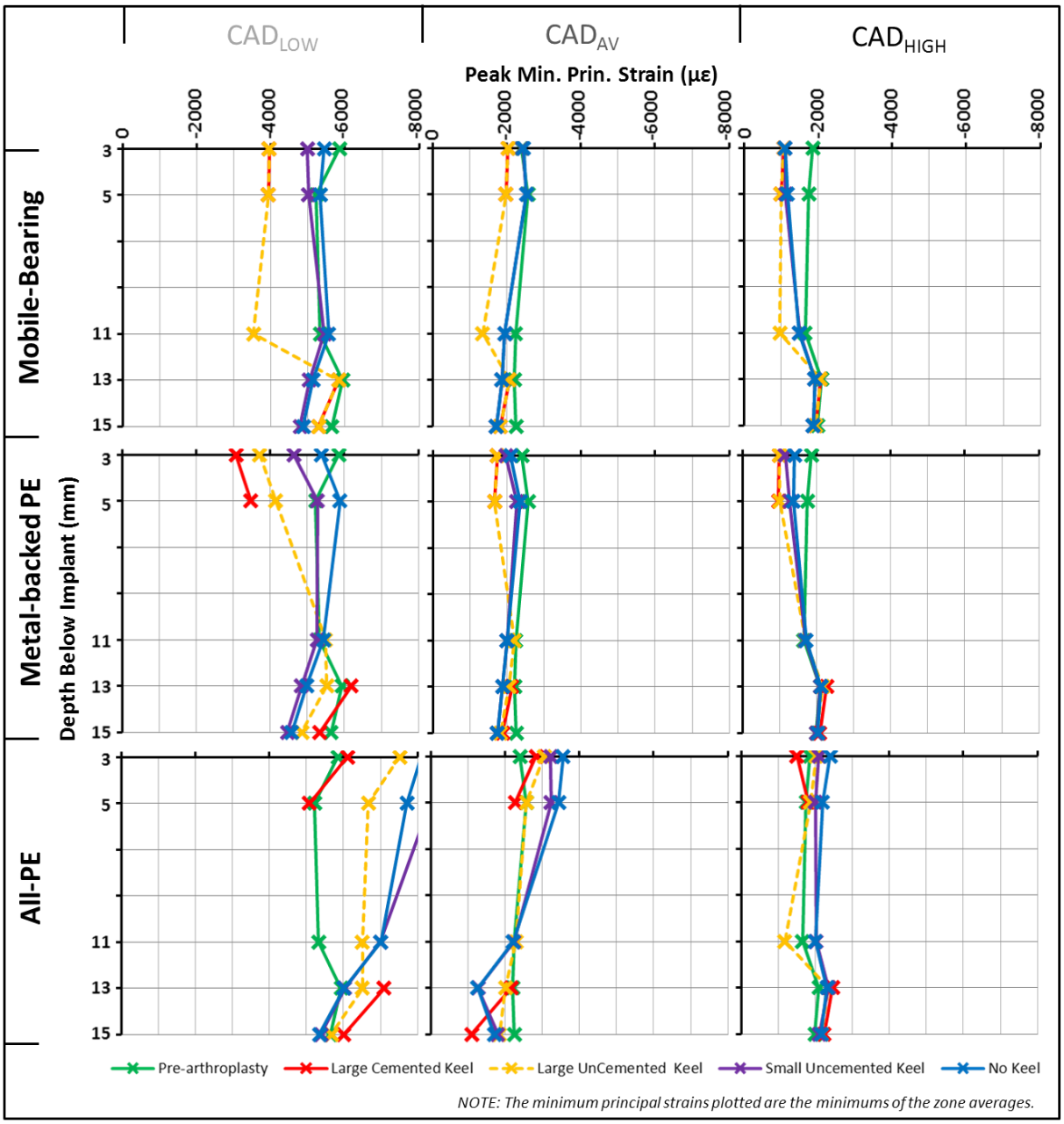


**Figure 190 - Comparison of UKR keel designs for peak bone strains beneath the implant. The bone strains are compared to those of the pre-arthroplasty state and the plots show that shortening the keel reduces stress-shielding.**

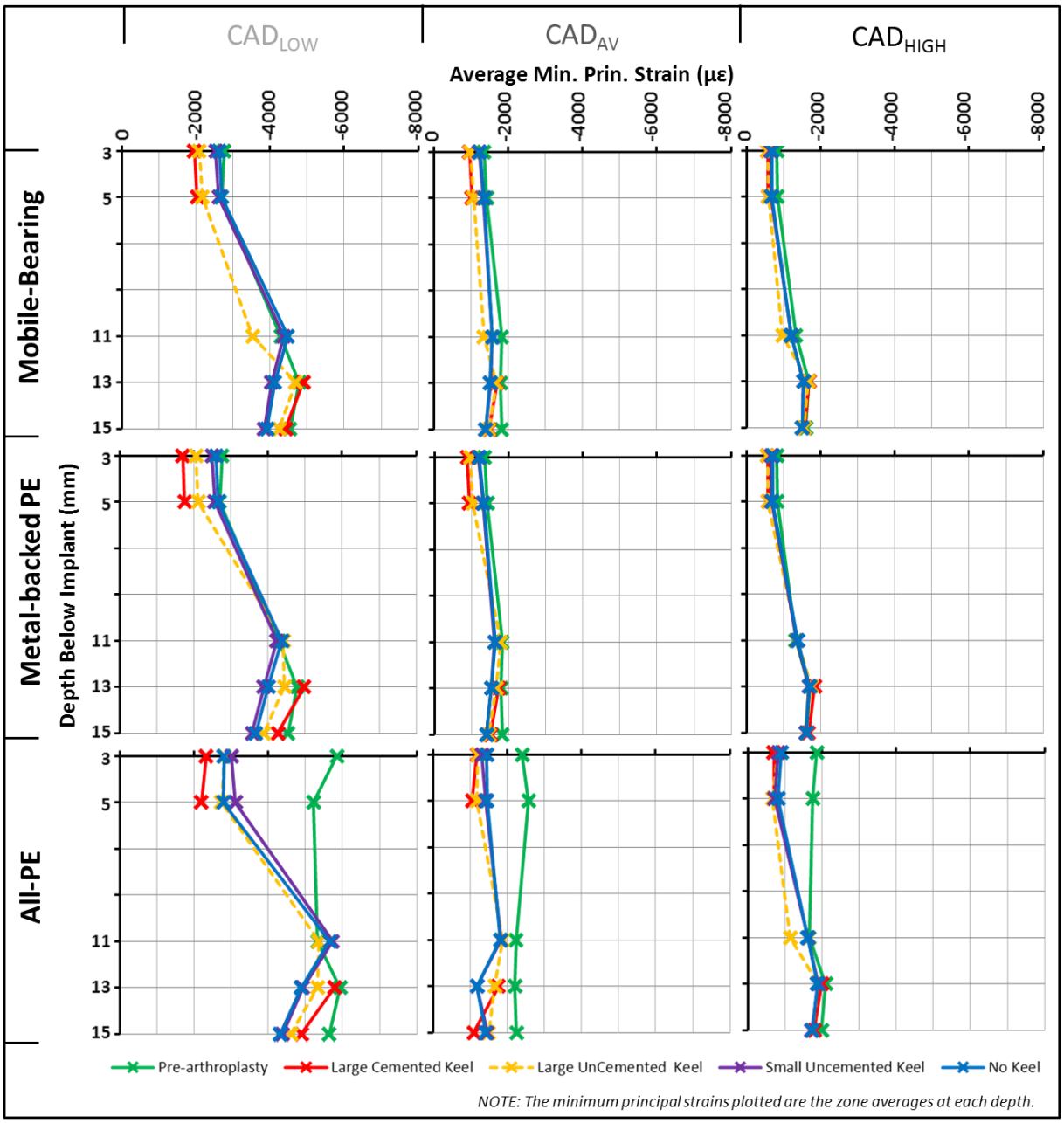


**Figure 191 - Comparison of UKR keel designs for average bone strains beneath the implant. The bone strains are compared to those of the pre-arthroplasty state and the plots show that shortening the keel reduces stress-shielding.**

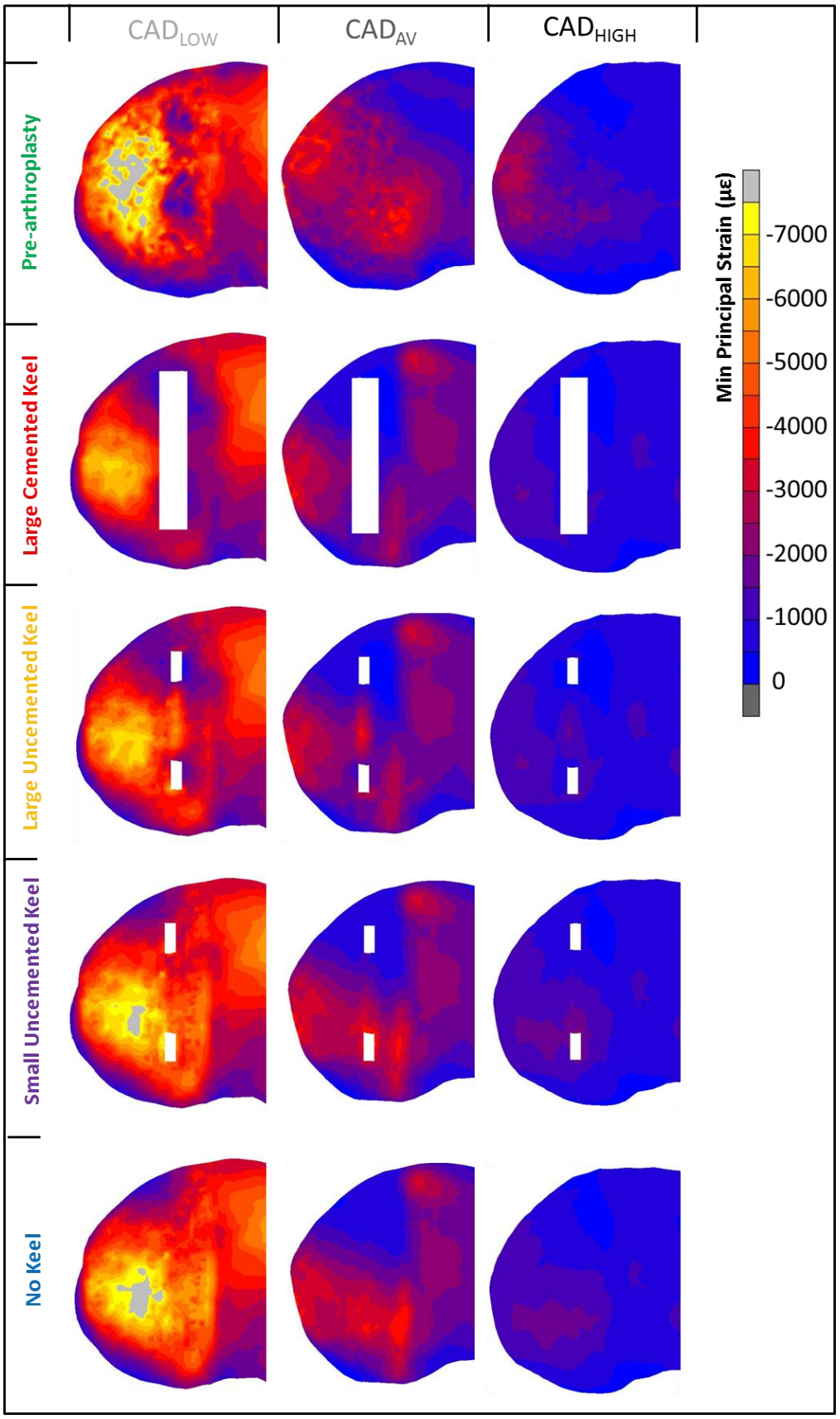


**Figure 192 - Plots of minimum principal bone strains of the mobile-bearing UKR of various keel designs and compared against pre-arthroplasty. The plots show strains at a transverse section 3 mm beneath the tibial implant, under peak stair-climbing knees forces.**

Figure 193 compares compressive and tensile cement stresses between three UKR designs and four keel designs. In general there were only small changes in cement stresses with reductions in keel sizes. For the lowest density tibia implanted with the all-PE UKR, the tensile stresses increased significantly because removal of the keel reduced bending stiffness.

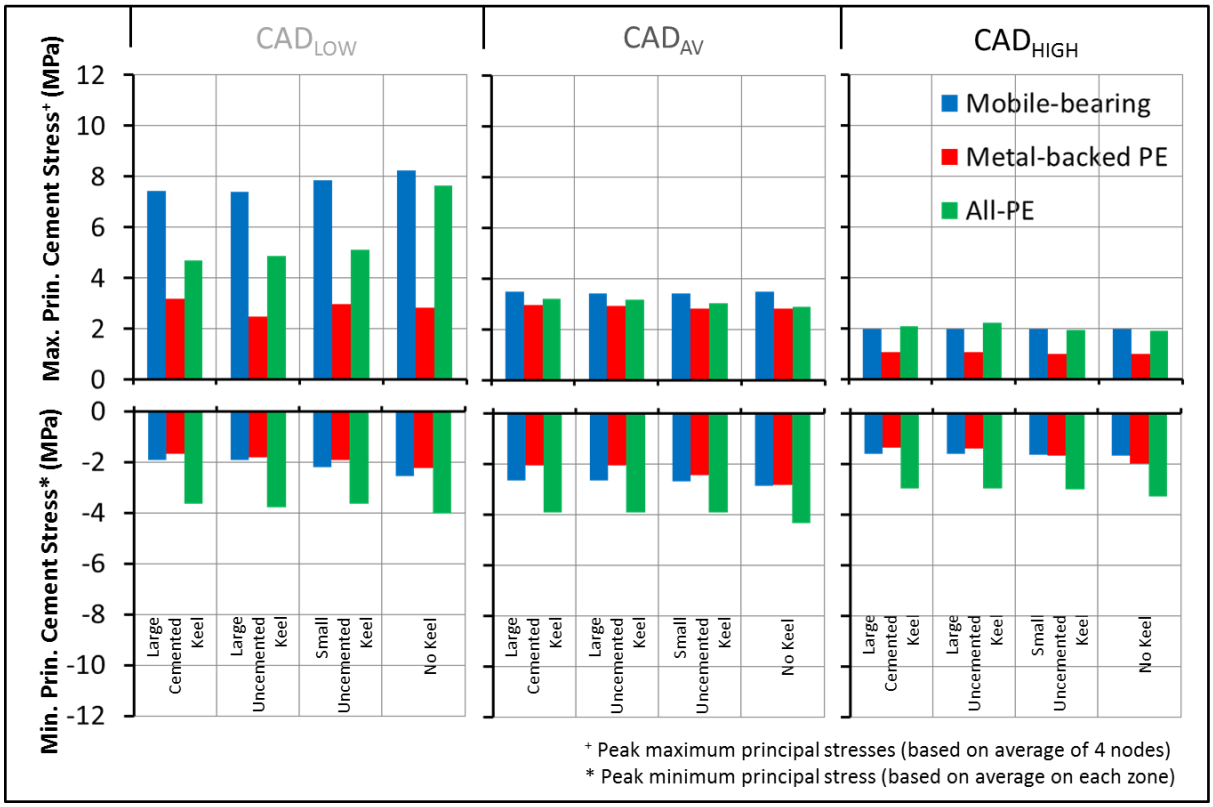


**Figure 193 - Effect of keel design on tensile and compressive cement stresses beneath the tibial tray in mobile-bearing and all-PE tibial UKRs. Keel design has a small effect on compressive cement stresses.**

Figures 194 and 195 show the effects of keel designs on bone-adaptation for both mobile-bearing and all-PE UKRs. The metal-backed UKR was omitted because the changes were similar to those of the mobile-bearing. The bone beneath the implant has better integrity than those with large keels. The uncemented keels produce better results than the cemented keels but the difference is small compared to the effect of reducing keel size.

The sagittal plots of Figure 195 show significant differences between the two patients. Patient $PAT_{CD}$ developed bone apposition at the posterior while patient $PAT_{CL}$ developed apposition at the anterior of the tibia because the load-paths were different. The shorter keel designs moved the load-path closer to the centre of the implant. Reduction of the keel size also tended to move the load-path medially. The significant bone apposition that occurred up to 5 mm beneath the centre of the all-PE implants was shallow because the load transferred medially through the medial cortex. The reduction in keel size for all-PE implants made a small difference to bone adaptation.

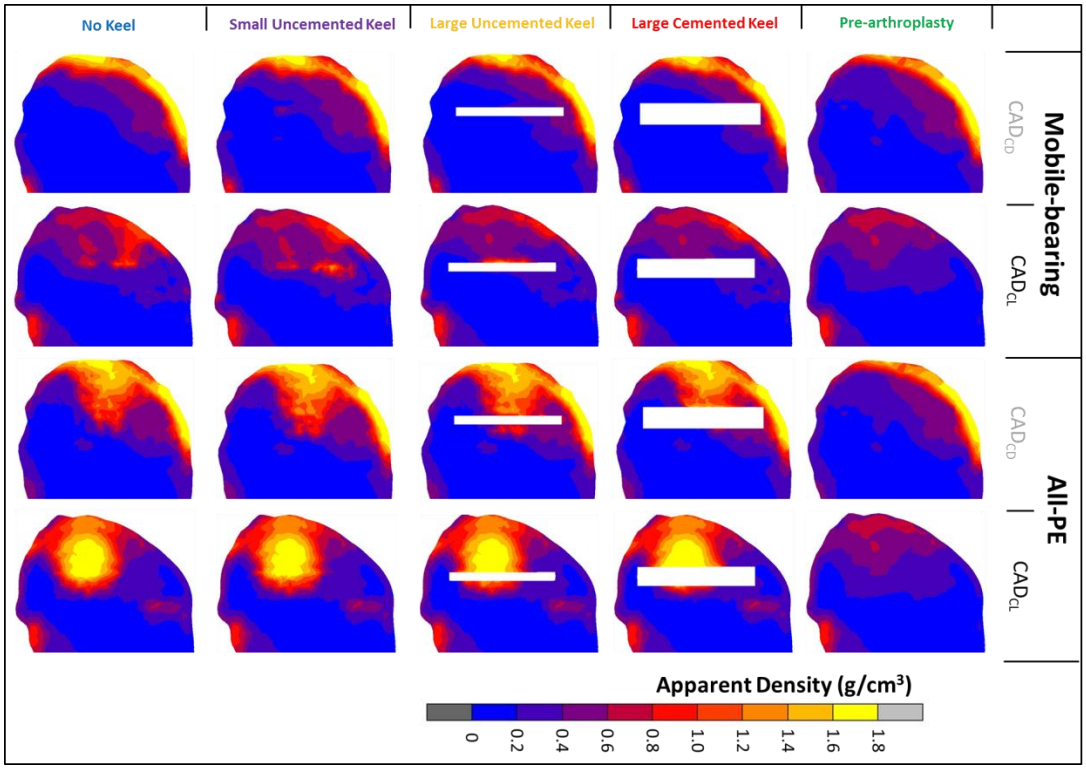


**Figure 194 - Effect of UKR keel design on bone adaptation. The plots are simulations of transverse sections of apparent density 3 mm beneath the implant at 1-year. The effect of keel design on the fixation performance of the mobile-bearing UKR is more significant compared to the all-PE design.**

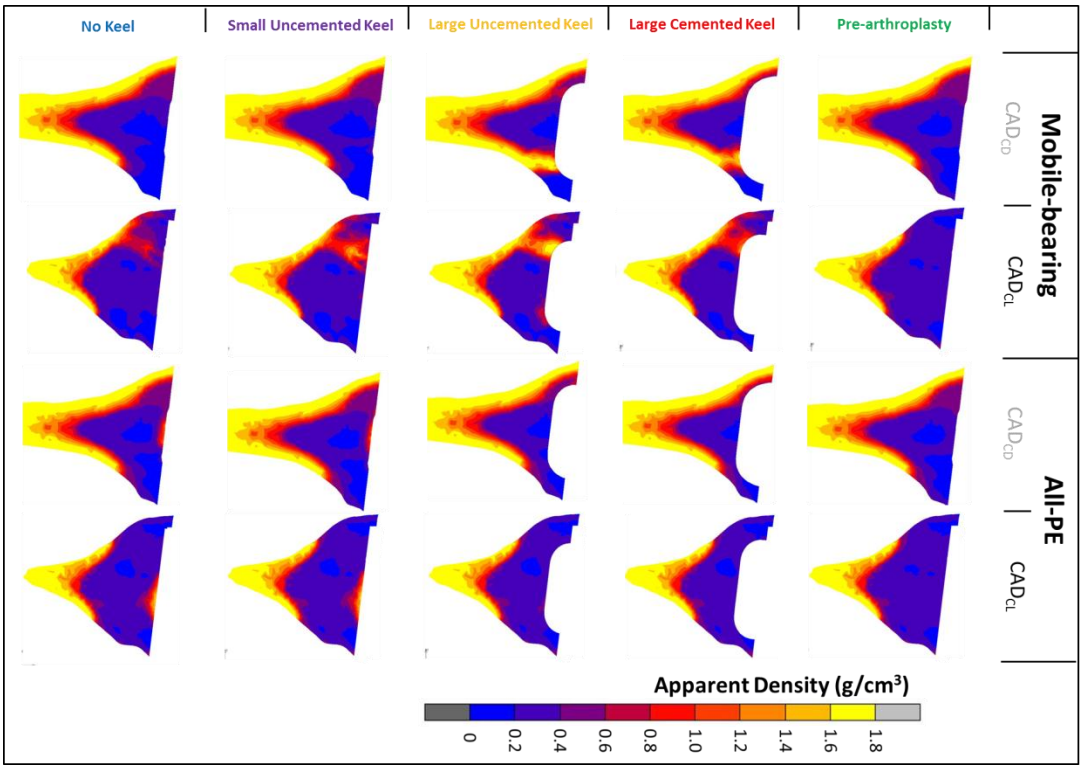


**Figure 195 - Effect of UKR keel design on bone adaptation. The plots are simulations of sagittal sections through the centre of the keel of apparent density at 1-year. The effect of keel design on the fixation performance of the mobile-bearing UKR is more significant compared to the all-PE design.**

### *9.7.4 Discussion and Recommendations*

The main finding of this study was that shorter keels increased bone strains beneath the implant and reduced stress-shielding, particularly for cemented mobile-bearing and metal-backed UKR tibial implants. The effect on all-PE UKRs was small.

For mobile-bearing and metal-backed UKRs, the reduction in keel size produced a negligible increase in cement stresses and these stresses were safely within failure limits. For normal and high density tibiae, the bone strains were also within safe limits; however, for the lowest density tibia the bone strains approached the failure limit of bone. Full cementation of the large keel helped to reduce the strains for this particular specimen.

For the all-PE UKR, the reduction in keel size produced increases of bone strains at the centre of pressure of the implant. If the tibia contained dense bone in this central region then bone strains were tolerable; however, for the low density tibiae (or deep resections) the keel-less all-PE UKR caused high bone strains that could potentially cause pain and tibial subsidence or even collapse.

This study has not investigated the possibility of bone fractures emanating from the keel and the impact of press-fit on the results. Peri-prosthetic tibial fractures from the keel do occur in some patients (Vardi and Strover, 2004). The in-vitro experiments, described in Section 5, also identified the potential risk of overcutting the keel resection. In Section 4, a sensitivity study of the effect of press- fit on bone strains revealed that 50 με interference fit caused high bone strains that approached the failure limit of bone. Reducing the keel size of UKR implants may also simplify the surgical procedure and reduce the likelihood of such fractures occurring.

Current mobile-bearing UKR designs have keels that extend 10 mm (Oxford Biomet and Uniglide Corin). The metal-backed UKR designs are variable; however the majority have keels. The all-PE UKR designs tend also to be variable with very short keels (Evolution Tornier, Accuris Smith & Nephew, and EIUS Stryker) and large keels (Uniglide Corin). In this study, the standard 10 mm cemented keel improved fixation of all-PE UKRs. However, for mobile-bearing and metal-backed UKRs they caused stress-shielding that could compromise long-term fixation. Therefore the keel size may be reduced for patients with good bone quality. Large cemented keels on metal implants provided good fixation for patients with low density bone.

## 9.8 Tibial Sagittal Overcutting: Is it a problem?

### *9.8.1 Introduction*

Recently in the literature, there has been increased attention on sagittal overcutting of the UKR tibial resection corner (Clarius et al., 2009b, Clarius et al., 2009a, Seeger et al., 2011). A study of 100 UKR bone composite preparations by experienced surgeons showed that 18% had posterior tibia cortex overcuts of greater than 4 mm (Clarius et al., 2009a). These tibial overcuts can lead to peri-prosthetic fractures (Clarius et al., 2009a) and cementless (compared to cemented) UKRs are more susceptible to these fractures (Seeger et al., 2011). This is because the overcuts tend to increase the bone strains at the stress-raiser (Simpson et al., 2011). Sourcing from clinical experience and relevant literature, it has been found that knee pain and tibial plateau fracture occur more commonly in the early postoperative period (Simpson et al., 2009, Pandit et al., 2007). Analysis of initial fixation of both cemented and cementless UKRs is therefore relevant.

A computer study by Chang et al. (2011), claimed that a radius at the resection corner would alleviate these high strains and reduce the likelihood of fracture. Unfortunately this study was based only on cemented tibia sawbones, and assumed a homogeneous elastic modulus throughout the tibia. This study neglected cementless fixated implants (which are probably more susceptible to peri-prosthetic fractures (Seeger et al., 2011)) and neglected the importance of the heterogeneous nature of bone (shown to be important in Section 2).

The number of peri-prosthetic fractures seen in the clinic is far less than the proportion of overcuts claimed to be the made by surgeons. This is probably because only a small group of patients are susceptible to such fractures. It is therefore important to understand clearly which group of patients are most susceptible so that surgeons can make better decisions.

The study presented in this section investigates how the heterogeneous nature of bone affects the bone strains when comparing cemented and cementless tibial fixation of: (1) a correct resection; (2) a posterior overcut of 10 degrees; and (3) a rounded corner.

### *9.8.2 Method*

The strain-validated FE models (specimens $CAD_{LOW}$, $CAD_{AV}$ and $CAD_{HIGH}$) were adapted to assess and compare bone strains generated from (1) a correctly resected tibia, (2) a 10 degree sagittal overcut tibia; and (3) rounded resected corner tibia (using a modified Oxford UKR tibial tray with a 3 mm radius). The development and validation of the FE models are detailed in Sections 4 and 6.

A full set of knee forces were applied (medial and lateral tibiofemoral contact, muscles and ligaments) to simulate walking and stair-climbing activities to the existing models. Two load cases were applied to each tibia and femur model (ten models) to simulate peak walking (50% of the walking cycle) and stair-climbing (15% of stair-climbing cycle) knee forces. The mobile bearing and femoral implant was modelled to ensure that the medial condylar load onto the implant was as accurate as possible. Contact between the mobile-bearing and tibial tray was simulated using a Coulomb friction model with coefficient of 0.1.

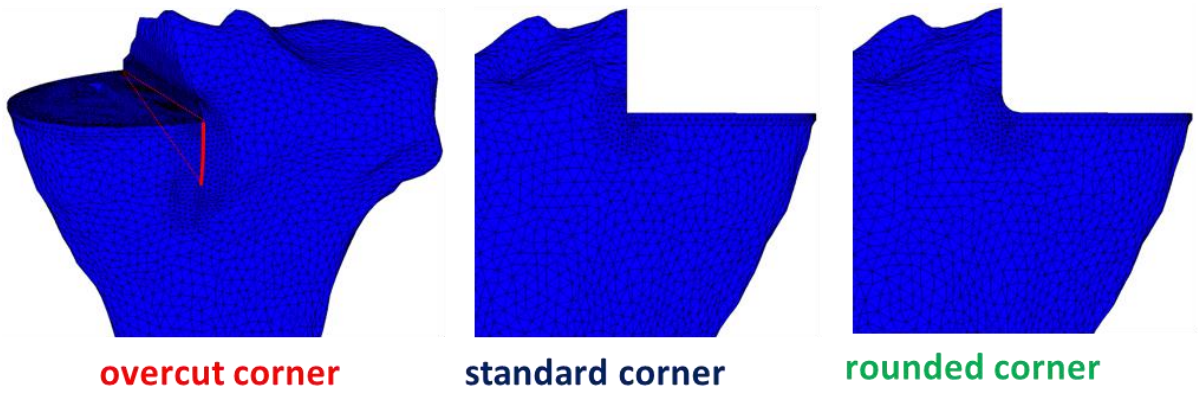


**Figure 196 - The tibia geometry for and (1) a 10 degree sagittal overcut corner; (2) a correct standard corner resection; (3) a rounded 3mm radius corner.**

The meshes surrounding the tibial resected corners were refined to improve bone strain predictions in these regions. The mesh size was reduced to 0.5 mm towards the corner with a gradual increase to 1.5 mm towards the implant-bone interface and 2-3 mm towards the body of the tibial cancellous bone. A 10-degree over-cut was simulated by separating elements by 0.1 mm down the sagittal plane from the resected corner. The rounded corner model was developed by adapting the cement-mantle to include a 3 mm radius fillet across the transverse-sagittal corner and a 3 mm radius fillet was added to the implant corner. Figure 196 presents a typical mesh and geometry of the three models developed. In all of the models, it was assumed that the tibial tray side-plate was not bonded to the adjacent bone. No other changes were made to the cemented and cementless models (six models in total) such that the same material and computational properties were used as the validated models.

A total of 9 simulations were developed based on three different specimens. The following scenarios were analysed for each specimen: (1) a correctly resected tibia, (2) a 10 degree sagittal overcut tibia; and (3) rounded resected corner tibia. Bone strains were compared against the failure limit of tibia bone (Morgan and Keaveny, 2001) as described in Section 2.

### *9.8.3 Results*

Figure 197 presents plots of the distribution of maximum principal (tensile) bone strain at the resection corner regions of all three specimens under peak knee load activity of stair-climbing. Figure 198 presents plots of the distribution of minimum principal (compressive) bone strain. The bone strains were higher with cementless fixation and in tibia of lower density. The lowest density tibia was most vulnerable to fracture with the red circle highlighting bone exceeding the failure limit of cancellous bone.

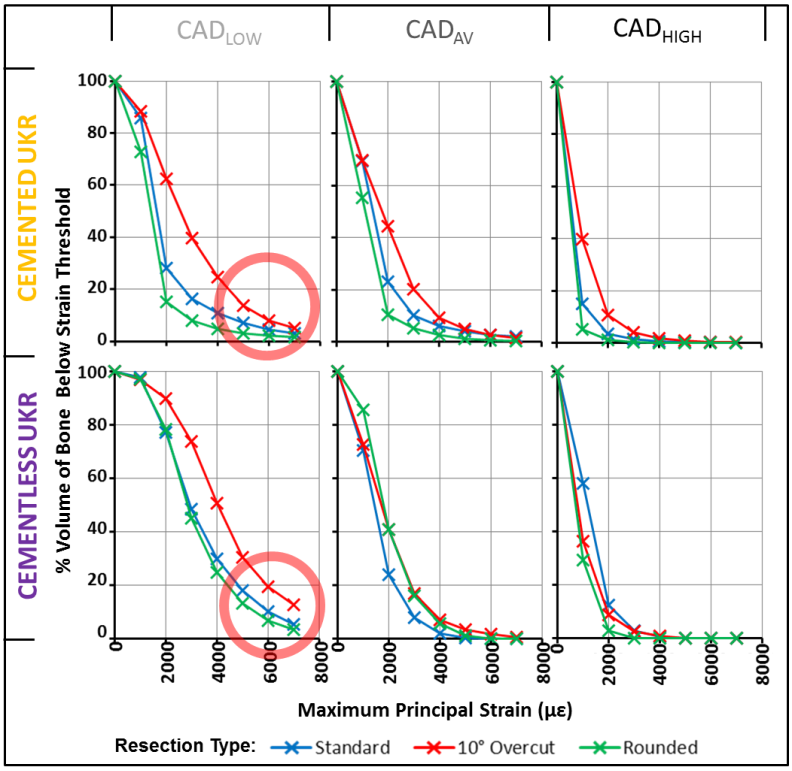


**Figure 197 - Distribution of maximum principal (tensile) bone strain at the resection corner region under peak knee load activity of stair-climbing. The red circles highlight bone exceeding the failure limit of cancellous bone in the lowest density tibia.**

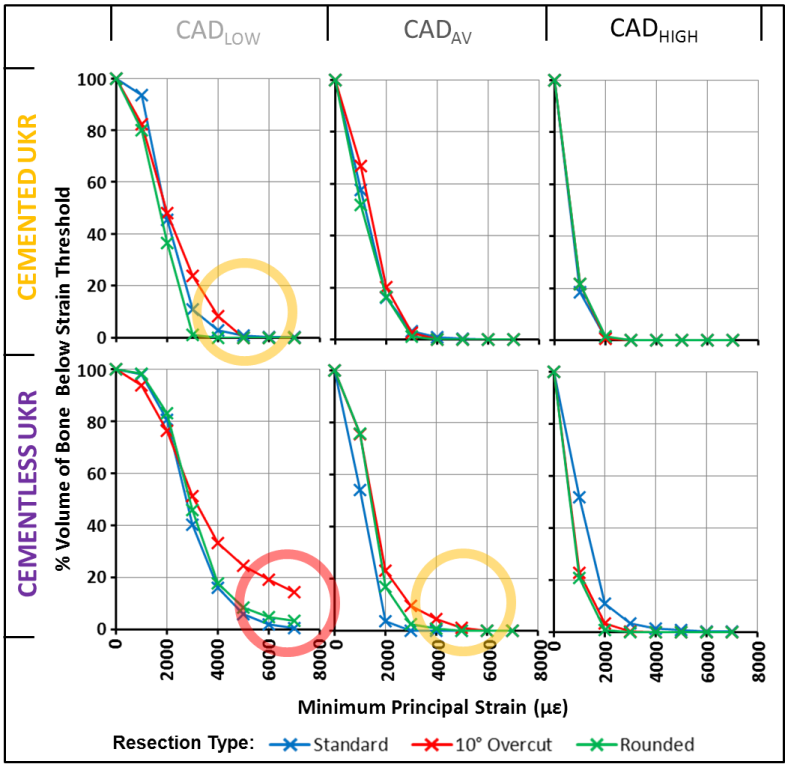


**Figure 198 - Distribution of minimum principal (compressive) bone strain at the resection corner region under peak knee load activity of stair-climbing. The red circle highlight bone exceeding and the amber circles highlight bone approaching the failure limit of bone.**

Since the lowest density tibia was identified to be the most susceptible to fracture, this specimen was analysed in more detail to understand how cementation and resection corner geometry affected bone strains: Figure 199 presents a bar chart illustrating the percentage of bone volume that exhibited tensile bone strains greater than 4000 με. Figure 200 includes compressive strains for the lowest density tibia only. The overcut doubled the volume of bone that exhibited bone strains approaching the failure limit of bone. The rounded corner produced the lowest bone strains.

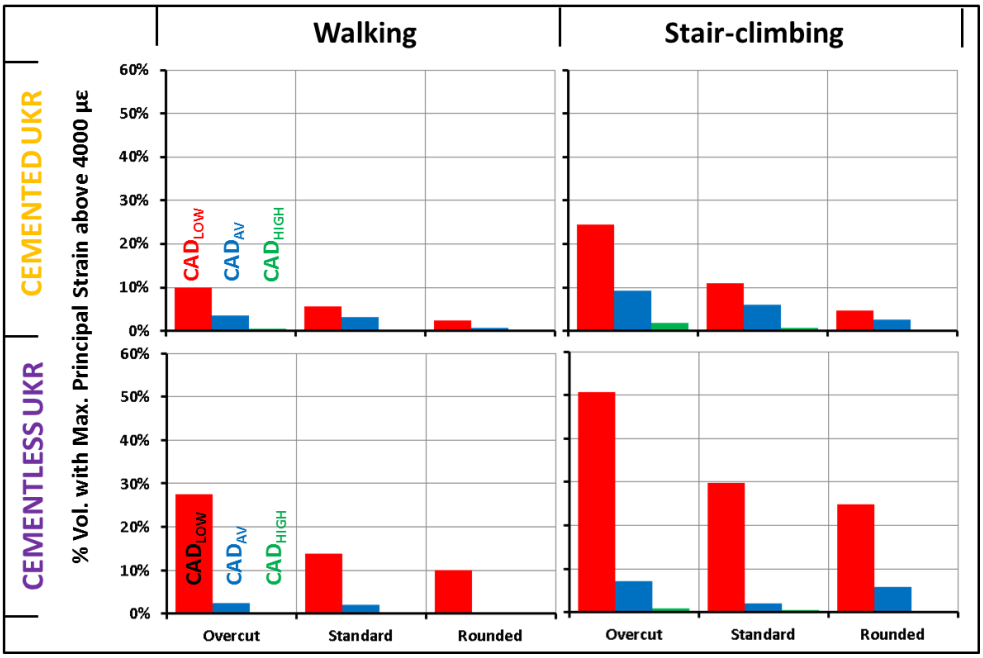


**Figure 199 - Bar charts illustrating the percentage of bone volume that exhibited maximum principal (tensile) strains greater than 4000 με under walking and stair-climbing knee forces. The tensile bone strains were highest for an overcut resection corner.**

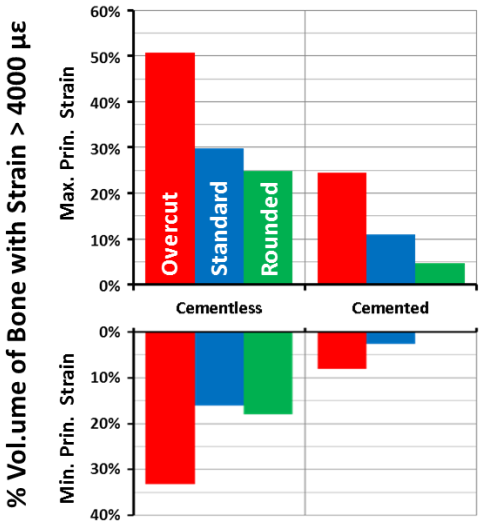


**Figure 200 - Bar chart illustrating the percentage of bone volume that exhibited principal (tensile and compressive) strains greater than 4000 με for the lowest density tibia under stair-climbing knee forces.**

Figure 201 shows plots of bone safety factor and tensile strain, comparing all three different resection corner geometries for cementless fixated simulations of the lowest density tibia ($CAD_{LOW}$). The overcut transferred the region of high bone strain distally towards the tip of the overcut. The bone density at the tip of the overcut was therefore important. It is difficult to appreciate the reduction of bone strain with a rounded corner resection because the surface contour plots do not show the internal bone strains beneath the surface.

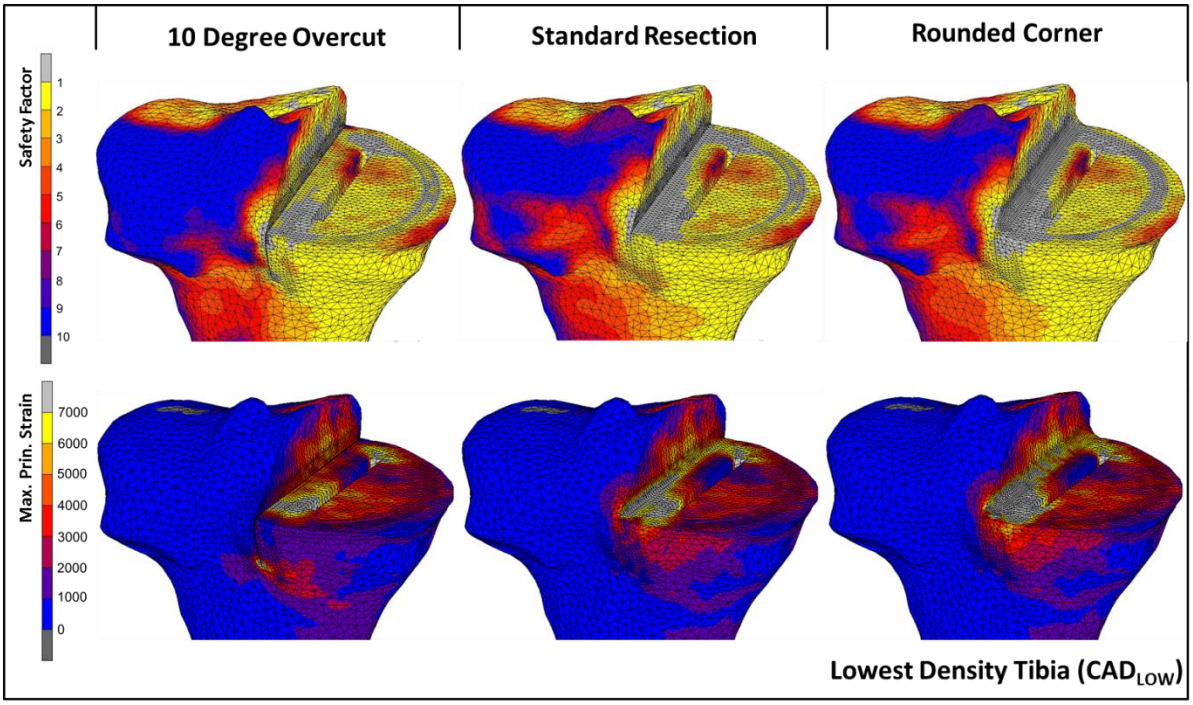


**Figure 201 - Plots of cementless fixated simulations of the lowest density tibia ($CAD_{LOW}$), showing bone safety factor (top) and tensile strain (bottom) comparing simulations of (1) a 10 degree overcut; (2) a standard resection; and (3) a rounded corner. The grey regions highlight bone that exceeded its failure strength.**

It should be noted that these simulations assumed elastic material properties of bone with no failure limit, so they did not simulate bone failure. In practice, when bone exceeds its failure strength, it separates or collapses causing the bone in the vicinity to take up the additional load. If the surrounding bone cannot sustain this additional load then the failure progresses and can become unstable causing fracture. Crack arrest can occur, when the surrounding bone is denser and can sustain lower bone strains with additional load. Figure 202 shows apparent density plots of the posterior of each tibia specimen and shows that the cracks opened more for lower density tibia.

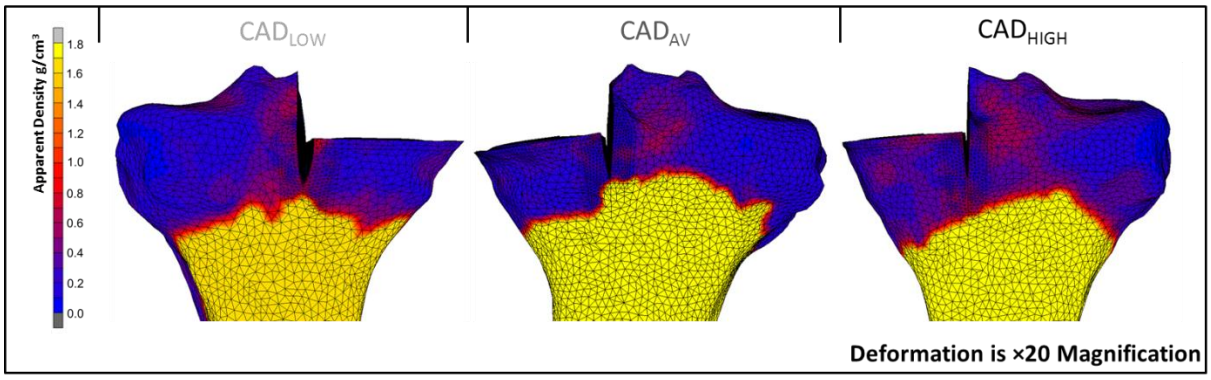


**Figure 202 - Apparent density plots with deformation of cementless UKR models with 10 degree posterior overcuts. The deformations have been magnified by a factor of 20 to illustrate crack opening.**

### *9.8.4 Conclusions and Recommendations*

This study supports the claim made in the literature that posterior tibial overcuts can cause fracture (Clarius et al., 2009b) and that cementless implanted UKR are more susceptible (Seeger et al., 2011). It is also supports the claim that bone strains are increased at the resected corner (Simpson et al., 2011) and that overcutting increases these strains (Chang et al., 2011). The important findings of this study were that tibiae of lower density were found to be more susceptible and the rounded corner produced the lowest bone strains at the resected corner. The heterogeneous nature of the bone seemed to add some inter-specimen differences depending on what the density of bone was at the tip of the resection.

It is recommended that surgeons are extra careful with patients with low density bone, not only because it is easier to make overcuts but because these tibiae are more susceptible to fracture. It is also recommended that inexperienced surgeons use UKR implants that have been redesigned with rounded corners.

## 9.9 Femoral Implant Conformity: Is tri-radius better than single-radius?

### *9.9.1 Introduction*

With a resurgence of interest in UKRs, implant companies have launched competitor designs to the original Oxford UKR. One of the perceived shortcomings of the Oxford UKR is that the single radius femoral implant produces a deep cut into the anterior region of the femur. This design feature was adopted due to the poor wear properties of PE in the early 1970s and that the single radius conformity with the mobile bearing would reduce wear.

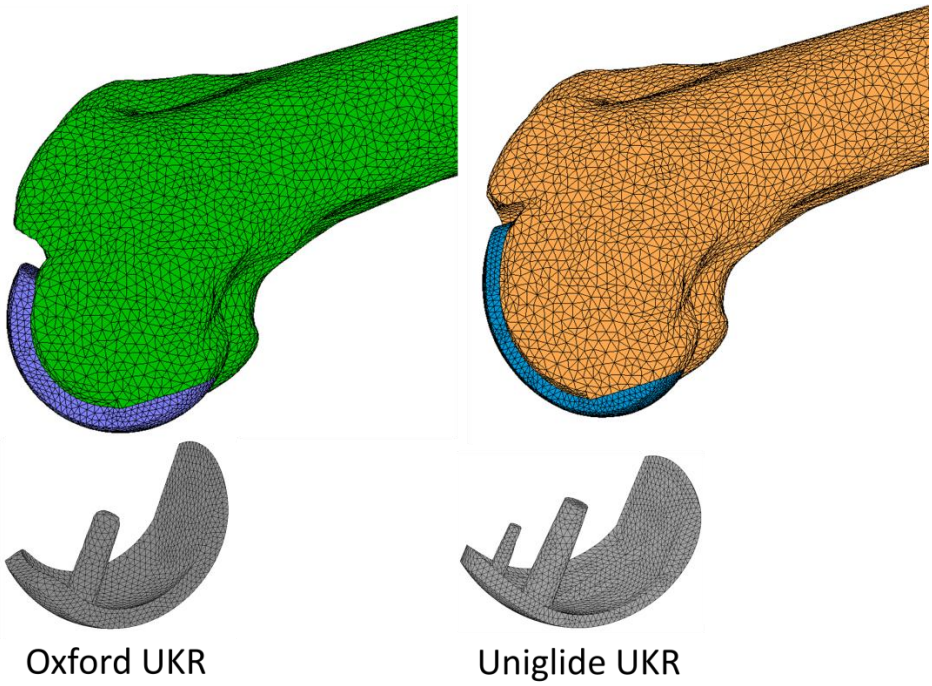


**Figure 203 - The Biomet Oxford and Corin Uniglide cemented femoral UKR implants.**

With improvements in PE wear resistance, the Corin Uniglide femoral implant has a tri-radius femoral implant claiming that it fits the profile of the femur more closely while maintaining low wear rates. The Uniglide also has a second smaller fixation peg similar to the cementless version of the Oxford UKR. Both implants are approximately the same thickness and the peg lengths are of similar length. Figure 203 illustrates the differences between the implants. The author is unaware of any studies in the literature that have attempted to answer the question of whether the improved conformity of the Uniglide femoral implant to the shape of the femur actually improves fixation compared to the Oxford UKR.

This section presents a comparative computer simulation study of the initial fixation of the Oxford and the Uniglide femoral UKR implants.

### *9.9.2 Method*

The fixation performance of the cemented Biomet Oxford single-radius femoral implant was compared to the Corin Uniglide tri-radius femoral implant.

The validated cemented versions of the Biomet Oxford implanted femur FE models (strain-validated $CAD_{LOW}$, $CAD_{AV}$ and $CAD_{HIGH}$; and remodelling-validated $PAT_{CD}$ and $PAT_{CL}$) were used to represent the single-radius femoral implant. The development and validation of the FE models are detailed in Sections 4 and 6.

Five additional FE models were built using the same method to represent the same specimens/patients with cemented Corin Uniglide implanted femora. The implants were positioned identically to the Oxford implant (the central pegs were aligned) and sized with the equivalent implant. The bone was resected such that the implant surface at 0-30° flexion was aligned with the Oxford implant. The mesh densities were similar for both sets of models. Both implants were made of cobalt chrome assuming identical material properties. The Uniglide implant had a second smaller anterior peg and a thin rib that stretched from the base of the large peg to the posterior of the implant. Refer to Sub-section 4.3.4 for details of the implant geometries.

A full set of knee forces were applied to all the models (medial and lateral tibiofemoral contact, muscles and ligaments) to simulate walking and stair-climbing activities. Eight load cases were applied to each strain-validated femur model representing the peak knee forces at 10 degree increments of flexion angle taken from the pool of data for walking and stair-climbing activities. The knee forces applied to the models are tabulated in Sub-section 8.3.4. Bone strains were compared at identical locations for the Oxford and Uniglide femoral implants.

The remodelling-validated FE models ($PAT_{CD}$, $PAT_{CL}$) were loaded with exactly the same sets of forces used to validate them in Section 8. Note that a cemented version of the model $PAT_{CL}$ was developed because the validated version was for a cementless UKR. Note that the rehabilitation activity levels were different between the two patients, with a rapid rehabilitation to full activity taken by patient $PAT_{CL}$ and a gentle approach taken by $PAT_{CD}$. Bone remodelling was simulated for a period of 12 months and bone density changes were predicted for both Oxford and Uniglide femoral implants.

### *9.9.3 Results*

Figures 204 and 205 present plots of femoral bone strain in all three specimens implanted with the Oxford and Uniglide femoral implants. The magnitudes and locations of the compressive bone strains were similar for both implants.

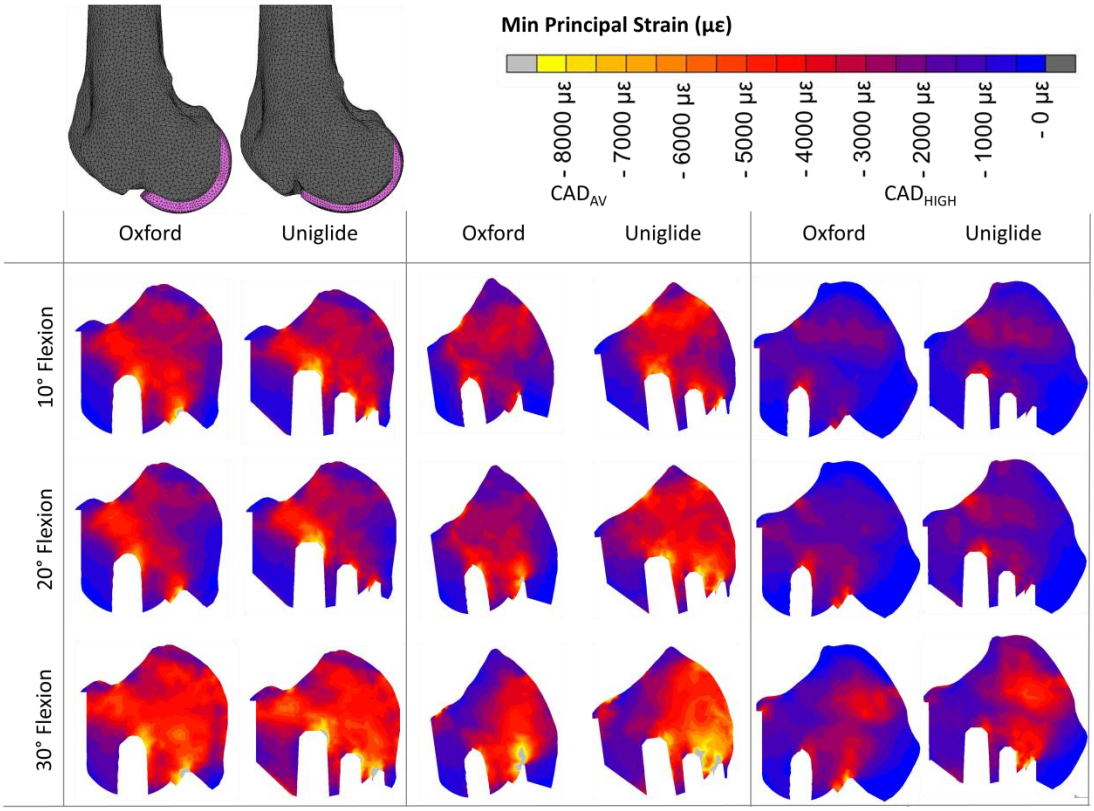


**Figure 204 - Comparison of minimum principal (compressive) bone strain plots of three femurs implanted with (i) Oxford and (ii) Uniglide mobile UKRs.**

When the femurs were loaded at knee flexions of 60 and 70° (during stair-climbing knee forces), the tensile strains were slightly higher for the Uniglide implant, particularly beneath the main peg. This may be because when loaded in flexion, (i) the wedge-shaped rib of the Uniglide implant may be generating a pull-out force; and (ii) the pull-out bending moments (about the anterior edge of the implant) are higher with the inclusion of a secondary anterior peg of the Uniglide implant (increased leverage).

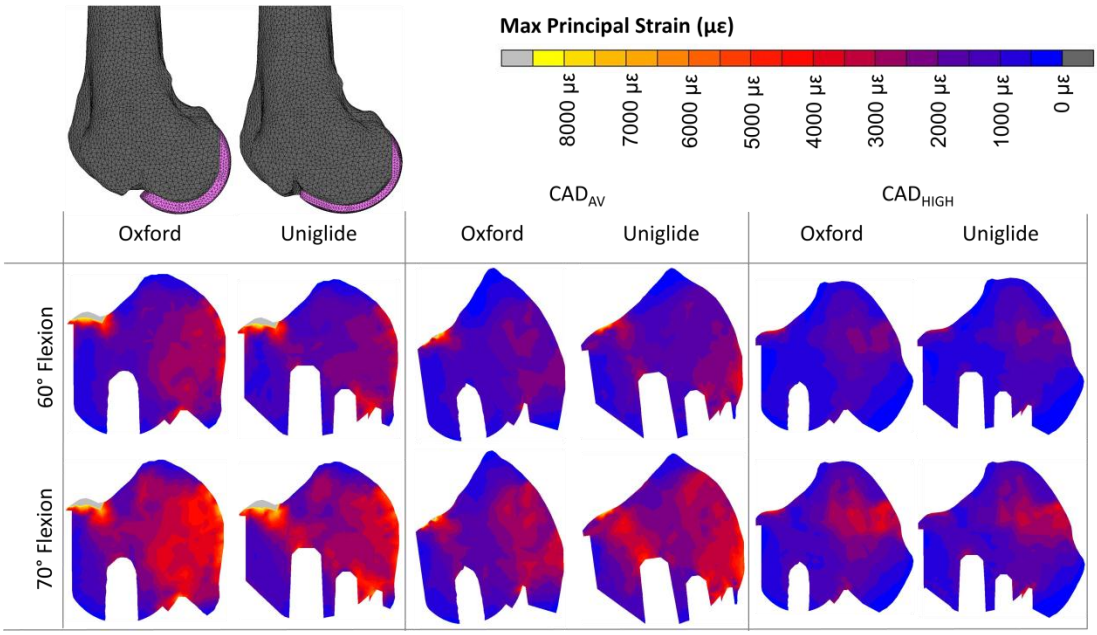


**Figure 205 - Comparison of maximum principal (tensile) bone strain plots of three femurs implanted with (i) Oxford and (ii) Uniglide mobile UKRs.**

Figures 206 and 207 present plots of minimum principal (compressive) and maximum principal (tensile) stress in the cement-mantle. The differences between the Oxford and Uniglide implants were insignificant.

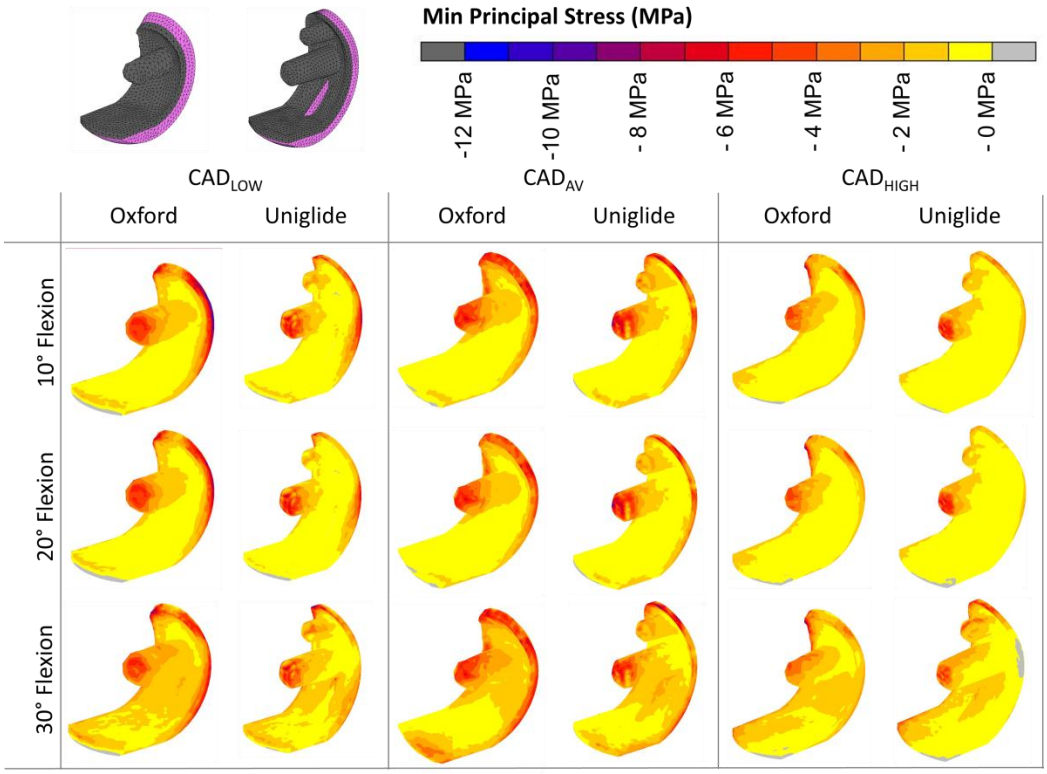


**Figure 206 - Femoral implant cement minimum principal (compressive) stress plots. Comparison of (1) Oxford and (2) Uniglide mobile UKRs.**

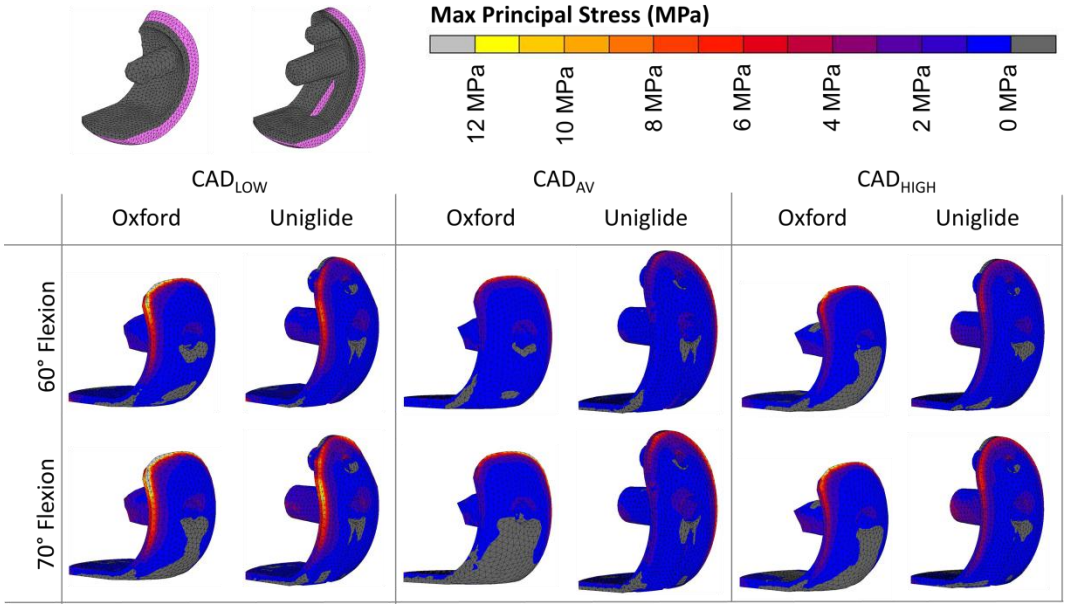


**Figure 207 - Femoral implant cement maximum principal (tensile) stress plots. Comparison of (1) Oxford and (2) Uniglide mobile UKRs. High tensile stresses anteriorly for both implant designs. Inclusion of a second keel reduced the tensile stresses at the posterior of the peg.**

### *9.9.4 Discussion and Recommendations*

The main finding of this study was that both the Oxford and Uniglide UKRs generated very similar bone strains with negligible differences. They both generated high strains at the anterior reamed corner. It was observed that the reamer cut very deep into the trochlear groove, potentially affecting the patellar tracking during deep flexion activities (angles greater than 60 degrees). Figure 208 presents images of the implanted Oxford and Uniglide UKRs, illustrating the extended cut towards the trochlea. There was negligible difference in fixation performance by using the Uniglide UKR instead of the Oxford UKR.

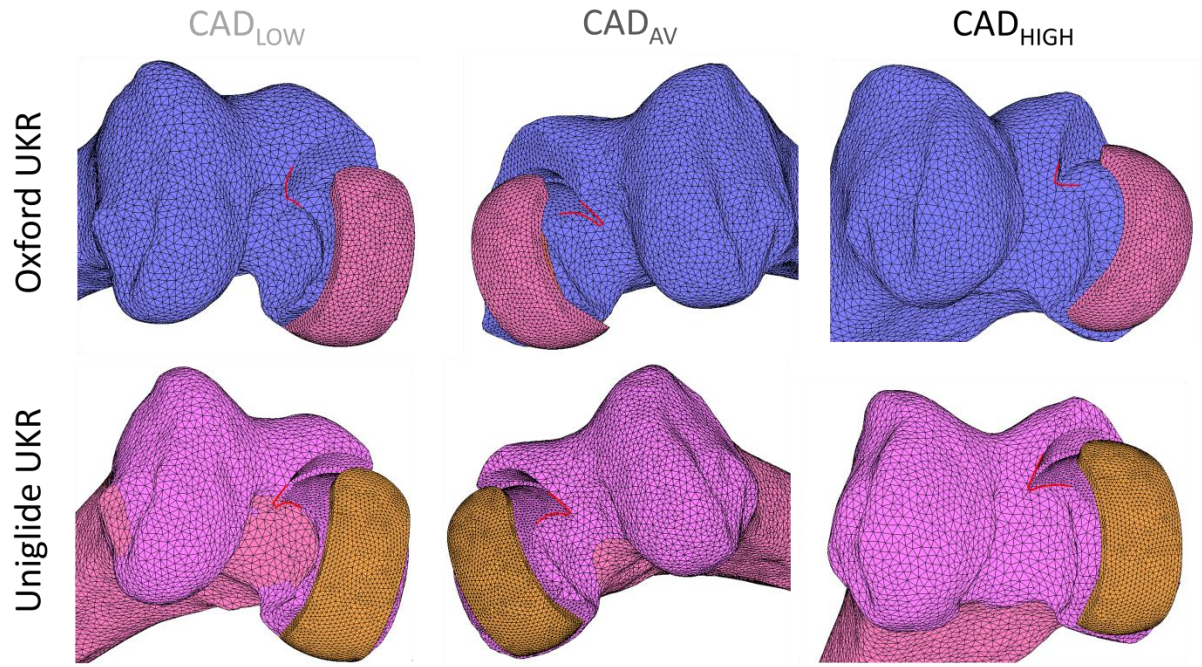


**Figure 208 - Images of femoral UKRs demonstrating the anterior reamed corner on both Oxford and Uniglide UKR designs. The Uniglide resection extends slightly further into the intercondylar notch whilst the Oxford resection is deeper and less conforming.**

The limitation of this study was that it did not consider the effects on tibiofemoral kinematics. It is likely that if the profile of the femur is not recreated in arthroplasty then the ligaments will not maintain their original laxity through the full range of flexion. The results of the DXA study in Section 7 found that there was significant bone loss under the tibial eminence following Oxford UKR and this could be due to reduced ACL function. With an improved femoral conformity, particularly at extension, the Uniglide UKR may enable better ACL function. A comparative DXA study of Oxford and Uniglide UKR patients may help to answer this question.

## 9.10 PE Femoral Implant: Is it an option?

### *9.10.1 Introduction*

The metal UKR femoral implant is stiff because it is constructed from a high elastic modulus material (cobalt chrome) and because of its rigid shape. Based on the results of the DXA study (presented in Section 7) and the computer simulations (presented in Section 6), stress shielding is more of a concern in the UKR femur than the tibia. It is hypothesised that using a material with a lower elastic modulus may reduce stress-shielding and improve the longevity of the UKR implant.

Due to traditionally high wear rates of PE implants prevalent in joint replacement, PE has not previously been a viable option for the femoral UKR implant. With recent improvements in PE wear properties, this option should be reviewed. It was hypothesised that PE would deform more under daily knee forces, transfer increased forces to the bone beneath the central region of the implant and reduce stress-shielding and bone resorption. Since PE is significantly less stiff than cobalt chrome, it should also be more forgiving towards irregular bone resections that do not fully conform against the implant under surface. The potential downsides, however, include the probability of increased wear rates and bone-implant micromotions.

This section presents the findings of a comparative computer simulation study assessing the differences between the Oxford UKR femoral implant and a hypothetical all-PE femoral implant with identical geometry.

### *9.10.2 Method*

The fixation performance of the cemented Oxford mobile-bearing single-radius femoral implant was compared to a hypothetical all-PE femoral implant with identical geometry.

The validated cemented versions of the implanted femur FE models (strain-validated $CAD_{LOW}$, $CAD_{AV}$ and $CAD_{HIGH}$; and remodelling-validated $PAT_{CD}$ and $PAT_{CL}$) were used in this study. The development and validation of the FE models are detailed in Sections 4 and 6.

The only change made to the Oxford UKR models was that a full set of knee forces (medial and lateral tibiofemoral contact, muscles and ligaments) were applied to simulate walking and stair-climbing activities. Eight load cases were applied to each strain-validated femur model representing the peak knee forces at 10 degree increments of flexion angle taken from the pool of data for walking and stair-climbing activities. The knee forces applied to the models are tabulated in Section 8.

The geometry and setup of the all-PE femoral implant models were identical to the validated models, with the only difference being the material properties of the implant. The all-PE implants were assumed to be isotropic and homogeneous with an elastic modulus of 600 MPa (Kurtz et al., 1998). For the purposes of direct comparison, the all-PE implant was loaded identically to the Oxford implant. Bone strains were compared at identical locations of the bone for the Oxford and all-PE implant models.

The remodelling-validated FE models ($PAT_{CD}$, $PAT_{CL}$) were loaded with exactly the same sets of forces used to validate them in Section 8. Note that a cemented version of the model $PAT_{CL}$ was developed because the validated version was for a cementless UKR. Note that the rehabilitation activity levels were different between the two patients, with a rapid rehabilitation to full activity taken by patient $PAT_{CL}$ and a gentle approach taken by $PAT_{CD}$. Bone remodelling was simulated for a period of 12 months and bone density changes were predicted for both Oxford and all-PE femoral implants.

### *9.10.3 Results*

Figures 209 to 211 present plots of minimum principal strain at particular sections of all three strain-validated specimens. The plots show that bone strains were higher in the regions posterior to the peg with the all-PE implant (compared to the current cobalt chrome implant). This region was previously reported to experience some stress-shielding (refer to Sections 7, 8 and Sub-section 10.2).

Figures 212 to 214 present plots of maximum and minimum principal (compressive and tensile) stress at the cement-mantle. The small increase of compressive stresses in the all-PE cement-mantles are within safe limits while the tensile stresses are reduced.

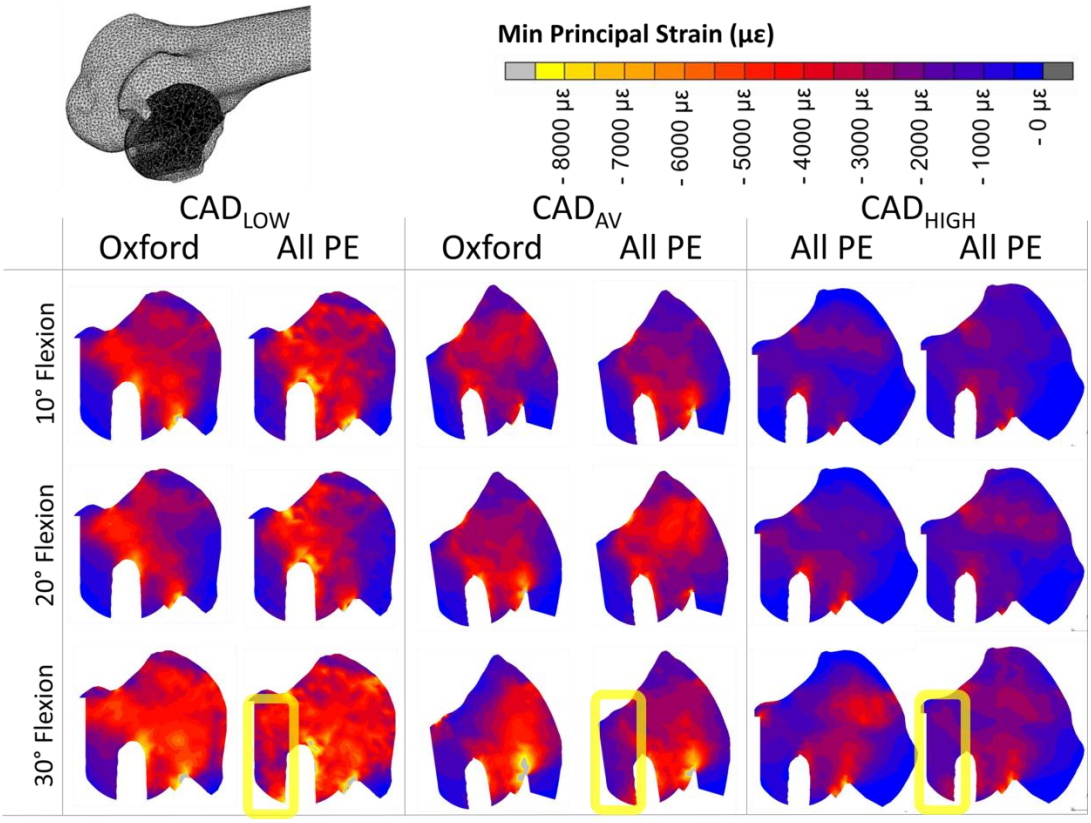


**Figure 209 - Plots of minimum principal (compressive) strain at the lateral section through the centre of the implant. Comparison of the Oxford UKR with the all-PE femoral implant.**

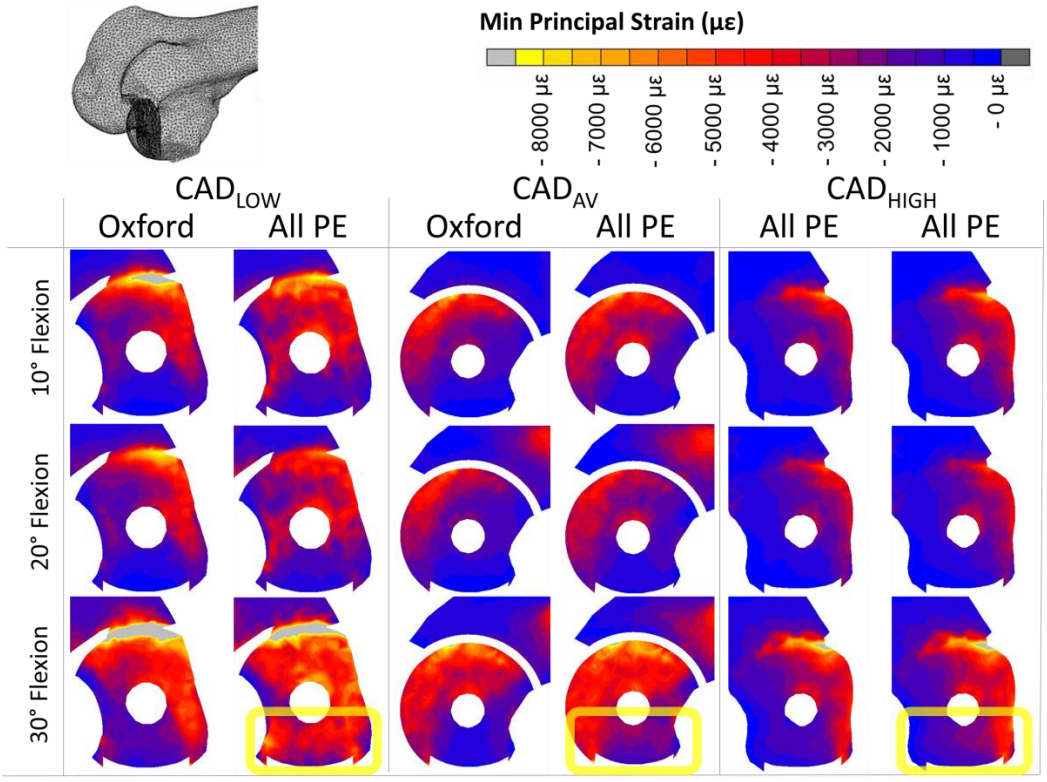


**Figure 210 - Plots of minimum principal (compressive) strain at the lateral section through the centre of the implant. Comparison of the Oxford UKR with the all-PE femoral implant.**

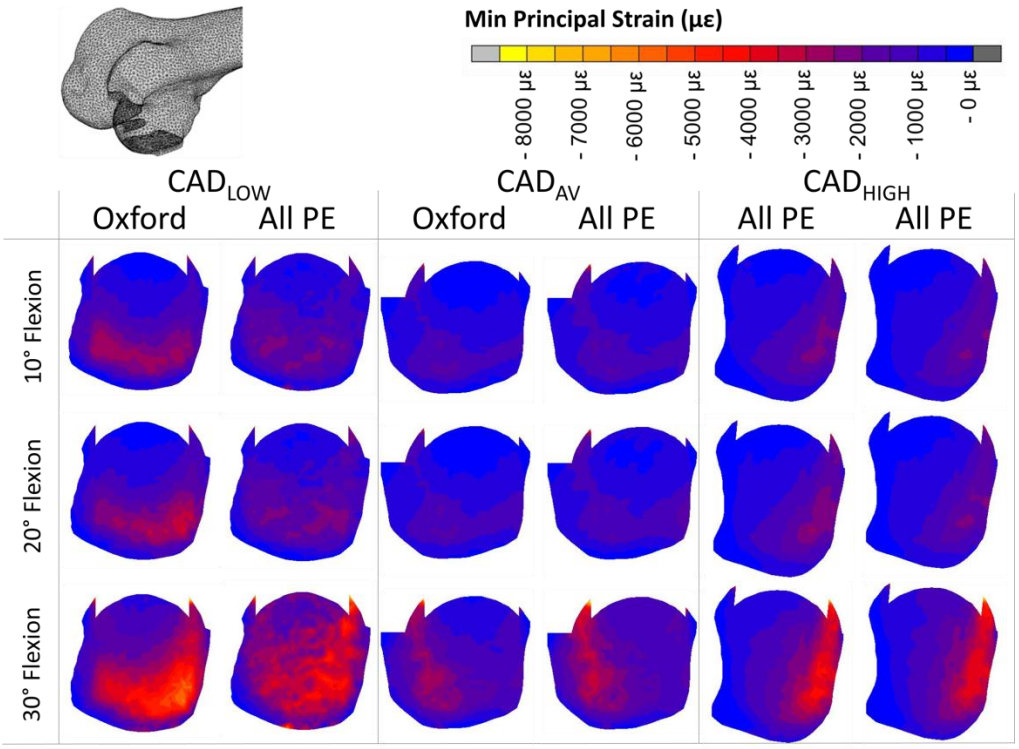


**Figure 211 - Plots of minimum principal (compressive) strain at a frontal section beneath the cement-mantle of the femoral implant. Comparison of the Oxford UKR with the all-PE femoral implant.**

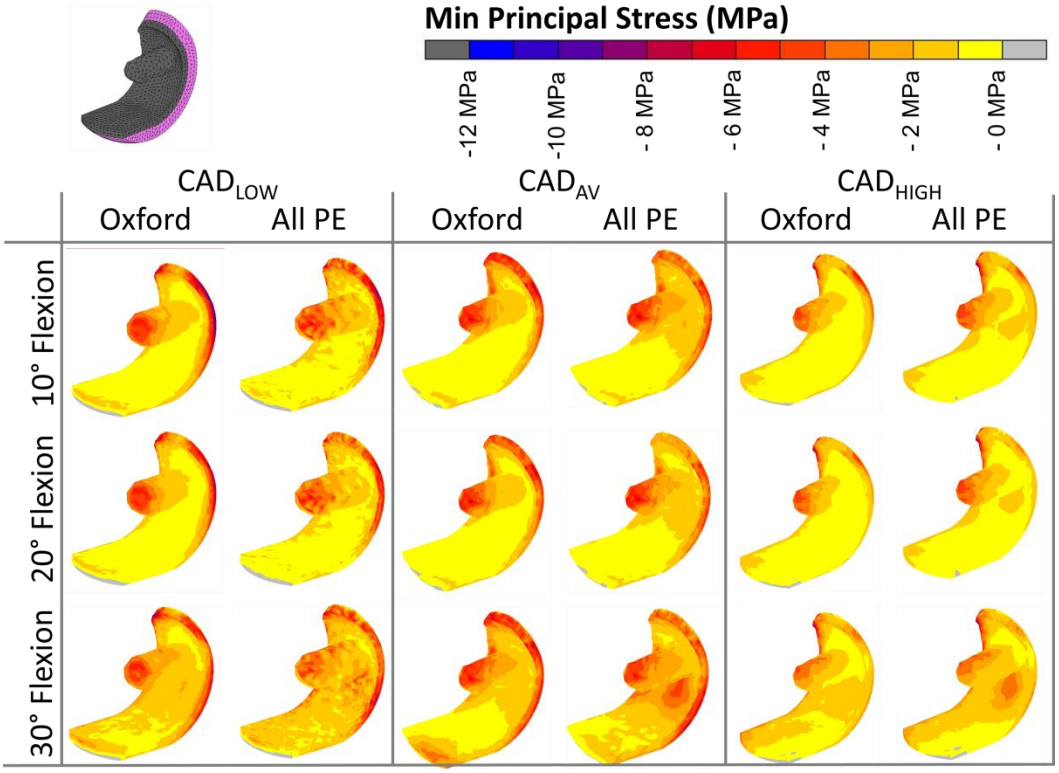


**Figure 212 - Plots of minimum principal (compressive) stress at the cement mantle. Comparison of the Oxford UKR with the all-PE femoral implant.**

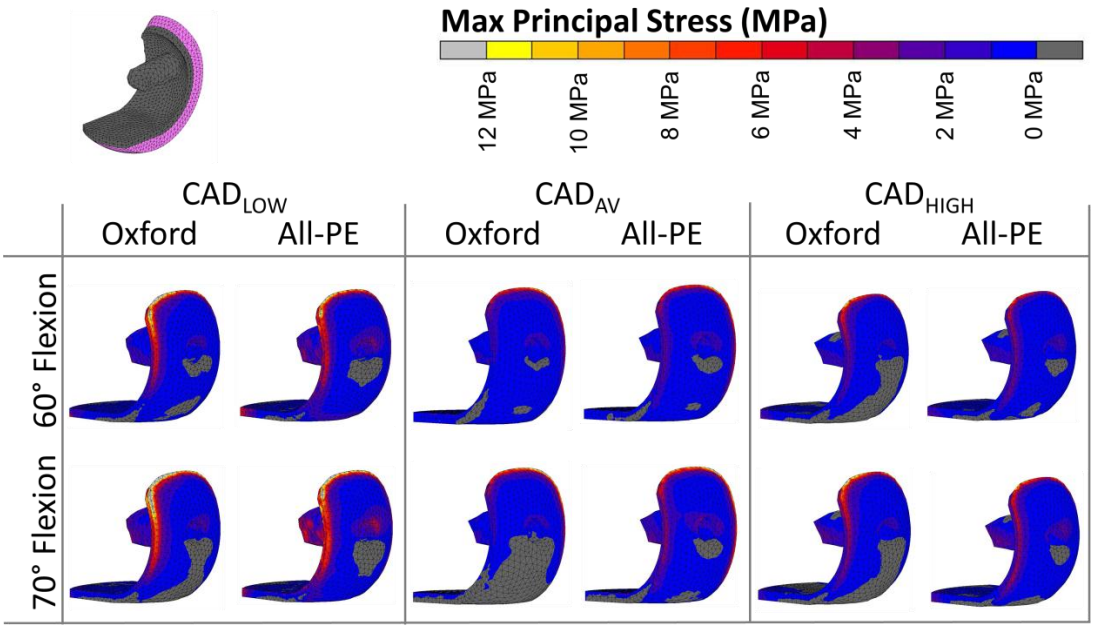


**Figure 213 - Plots of maximum principal (tensile) stress at the distal region of the cement-mantle. Comparison of the Oxford UKR with the all-PE femoral implant.**

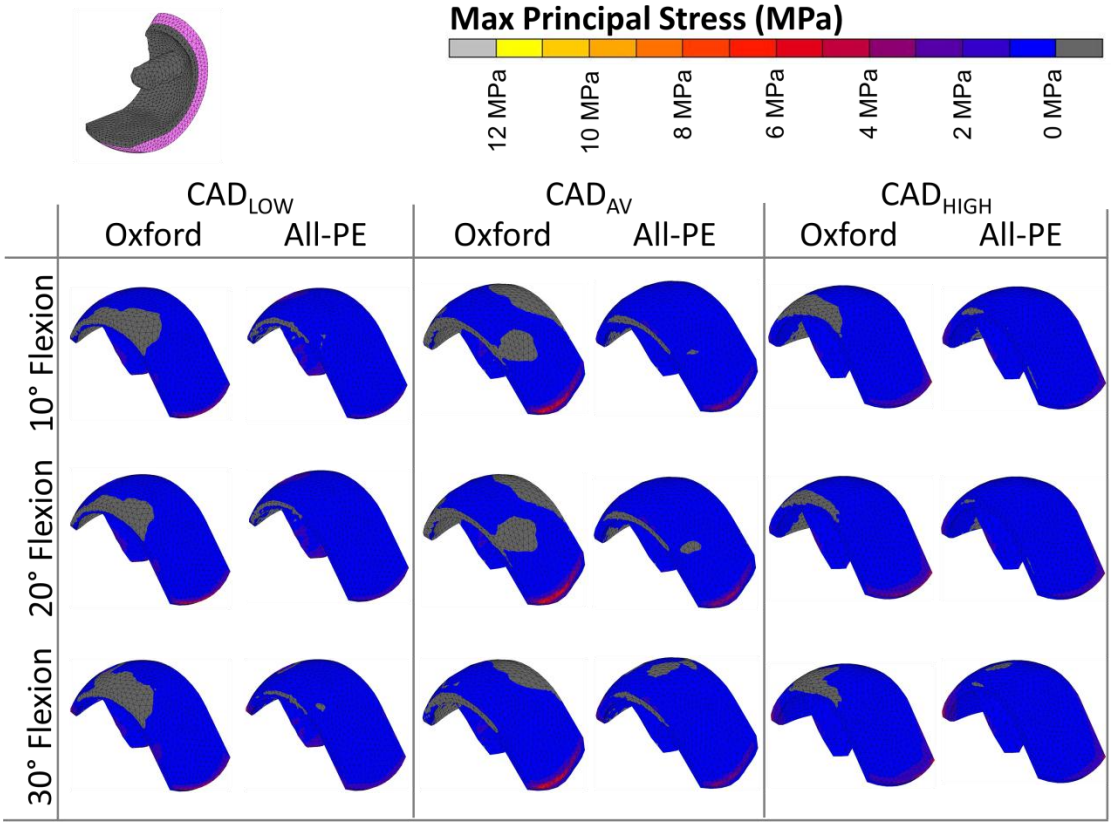


**Figure 214 - Plots of maximum principal (tensile) stress at the proximal region of the cement-mantle. Comparison of the Oxford UKR with the all-PE femoral implant.**

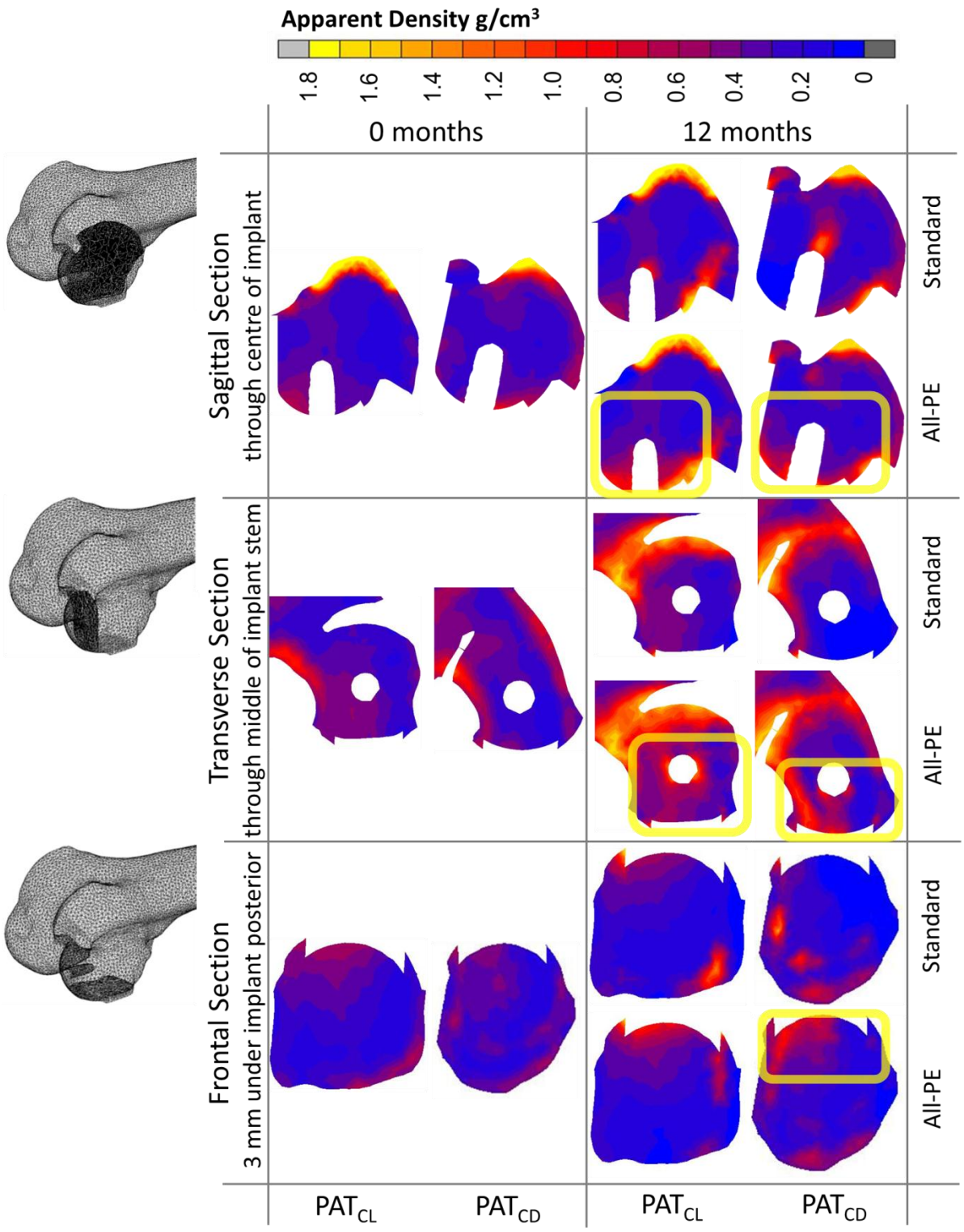


**Figure 215 - Bone remodelling comparison of the standard Oxford cobalt chrome femoral implant and the hypothetical all-PE UKR. The differences of bone densities at 1 year are compared.**

Figure 215 presents the results of the bone-remodelling simulations and compares the all-PE and cobalt chrome implants for bone density at 1 year post-arthroplasty. The all-PE implants stimulated bone apposition beneath the shell while there was bone resorption for the cobalt chrome implant.

### *9.10.4 Discussion*

The main finding of this study was that a hypothetical all-PE cemented femoral UKR implant reduced stress-shielding in the underlying bone when compared to the Oxford mobile-bearing femoral implant which is made of cobalt chrome. Using the all-PE implant, the increase in bone strains occurred in regions that were under-strained (posterior to the peg) and not in regions that were over-strained (the anterior reamed corner bone strains did not increase). The bone density under the all-PE implant was maintained; in fact it increased in some regions compared to the traditional design.

The long-term fixation performance of an all-polymer implant could therefore be better than the current cobalt-chrome implant provided that there are no deleterious effects such as (i) substantial wear rates; (ii) fatigue of the PE; (iii) development of high implant-cement or cement-bone micromotions with degradation of the cement-mantle.

Although this study neglected the effects of wear, there is evidence in the literature that wear of polymer materials used for femoral components could be low (Moore et al., 1998). Provided wear rates are low, the all-PE cemented UKR could improve longevity compared to metal femoral UKRs. With significant improvements in wear resistance of polymer based materials in recent years (Kurtz et al., 1999, Kurtz et al., 2009a), this may now be a viable option for femoral implants.

## 9.11 Femoral Implant Peg: Does it improve fixation?

### *9.11.1 Introduction*

It was demonstrated in Section 7 that stress-shielding was a more important consideration in the UKR femur than the tibia. It is widely speculated (based on experience of the TKR and THR designs) that shorter pegs reduce stress-shielding. The purpose of this study was to test this hypothesis by comparing the Oxford mobile bearing femoral UKR with hypothetical designs with decreasing peg lengths.

### *9.11.2 Method*

The cemented fixation performance of the Biomet Oxford UKR femoral implant was compared to modified versions of the implant with different peg configurations and lengths.

The validated cemented versions of the Biomet Oxford implanted femur FE models (strain-validated $CAD_{LOW}$, $CAD_{AV}$ and $CAD_{HIGH}$; and remodelling-validated $PAT_{CD}$ and $PAT_{CL}$) were used to represent the baseline Oxford UKR femoral implant. The development and validation of the FE models are detailed in Sections 4 and 6.

The validated models were modified to generate a refined mesh for the peg as illustrated in Figure 216. From each validated models, five simulations were developed, to simulate: (1) an uncemented full-length peg; (2) an uncemented half-length peg; (3) an uncemented 2 mm peg; and (4) no peg. A total of 25 simulations were generated. The fixation outcomes were compared against the cemented Oxford UKR.

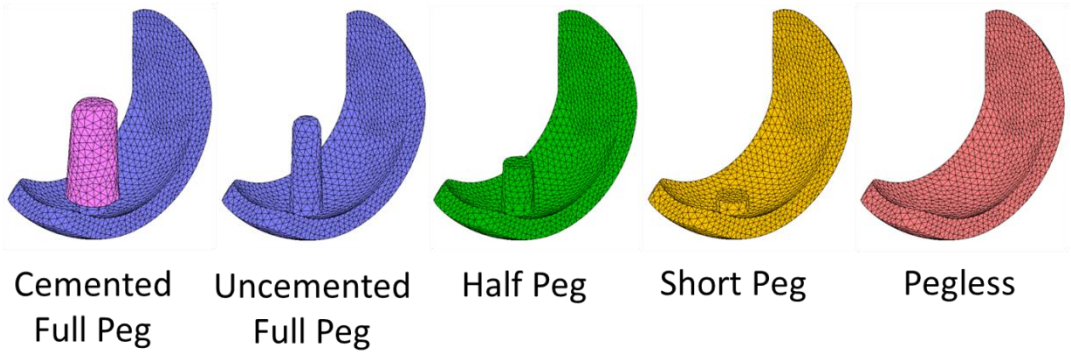


**Figure 216 - Different variations of peg designs investigated for fixation.**

A full set of knee forces were applied to all the models (medial and lateral tibiofemoral contact, muscles and ligaments) to simulate walking and stair-climbing activities. Eight load cases were applied to each strain-validated femur model representing the peak knee forces at 10 degree increments of flexion angle taken from the pool of data for walking and stair-

climbing activities. The knee forces applied to the models are tabulated in Sub-section 8.3.4. Bone strains were compared at identical locations for each peg design.

The remodelling-validated FE models ($PAT_{CD}$, $PAT_{CL}$) were loaded with exactly the same sets of forces used to validate them in Section 8. Note that a cemented version of the model $PAT_{CL}$ was developed although the validated version was for a cementless UKR. Note that the rehabilitation activity levels were different between the two patients, with a rapid rehabilitation to full activity taken by patient $PAT_{CL}$ and a gentle approach taken by $PAT_{CD}$. Bone remodelling was simulated for a period of 12 months and bone density changes were predicted for each peg design.

### *9.11.3 Results*

A total of 25 simulations were developed and the results analysed. Figures 217 and 218 present plots of minimum principal strain through sections of all three strain-validated specimen models. The plots show a small reduction in bone strain in the region posterior to the peg as peg length was increased. This was consistent amongst all specimens.

Figures 219 and 220 present equivalent plots for the remodelling-validated patient models at 0 and 12 months post-arthroplasty. The patient simulations showed that the difference in bone strain was negligible for the different peg configurations.

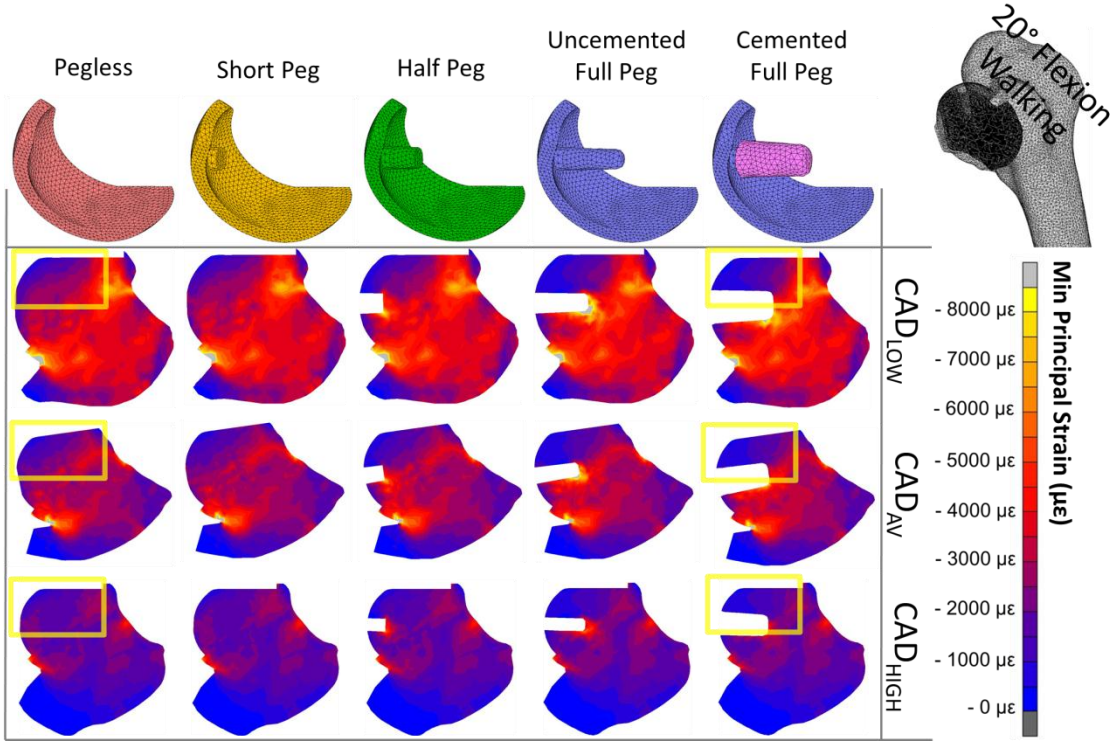


**Figure 217 - Plots of minimum principal bone strain through the lateral section of femoral implant. The plots show cemented femur specimens with different peg designs.**

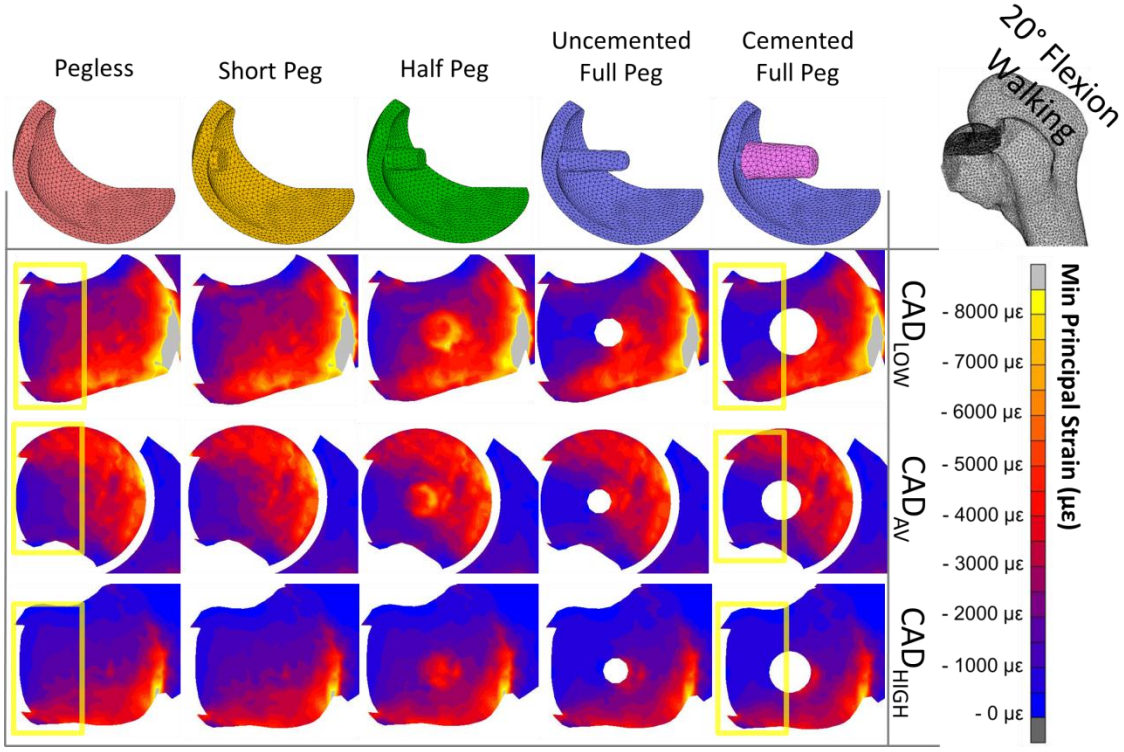


**Figure 218 - Plots of minimum principal bone strain at the coronal section midway through the standard femoral implant peg. The plots show cemented femur specimens with different peg designs.**

Figures 221 and 222 present plots of bone apparent density for the remodelling-validated patient models at 0 and 12 months. With the exception of changes to bone density under the base of the pegs, the differences in bone adaptation were insignificant between the different peg configurations.

The simulations did, however, show increased bone apposition under the base of the uncemented full-length peg compared to the cemented peg configuration. A sensitivity study was conducted to assess how the bone strains would be affected if the femoral peg base rested against bone as opposed to resting in a void. Figures 223 and 224 show how a higher portion of the load is transferred under the shell of the implant if the peg does not rest against bone. As the peg osseointegrates, this load transfers through the peg, therefore increasing the effect of stress-shielding on the underlying bone.

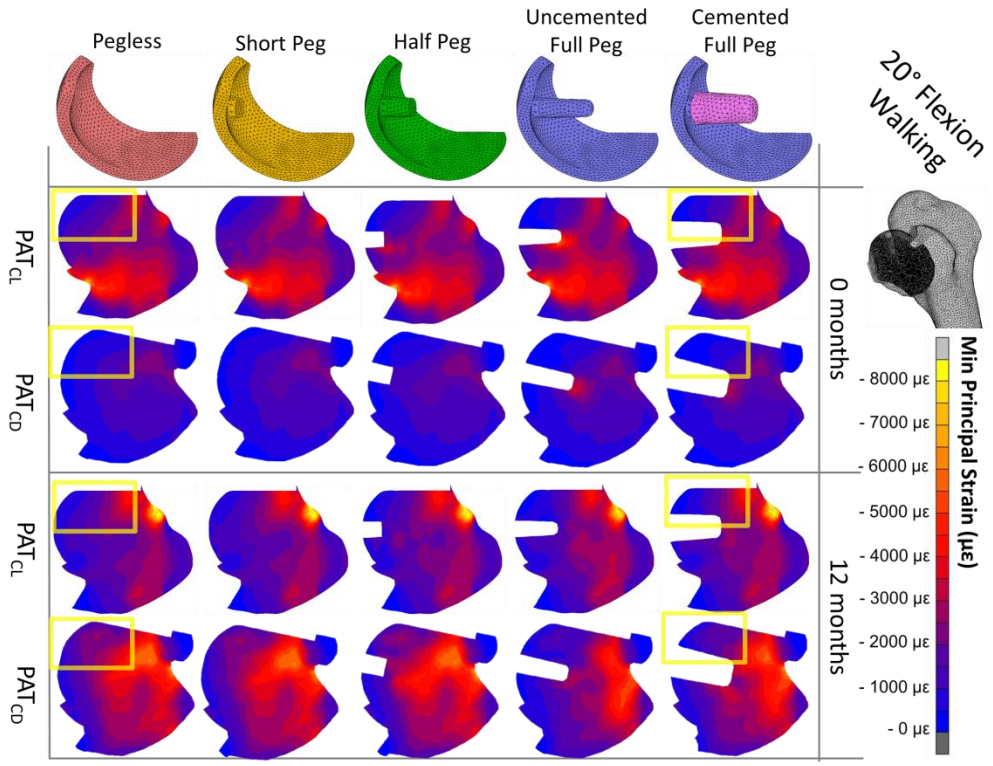


**Figure 219 - Plots of minimum principal bone strain through the lateral section of femoral implant. The plots show the effect of 12 months bone remodelling simulation on the cemented femora of patient models with different peg designs. Note that these are different knees to those shown in Figures 217-218.**

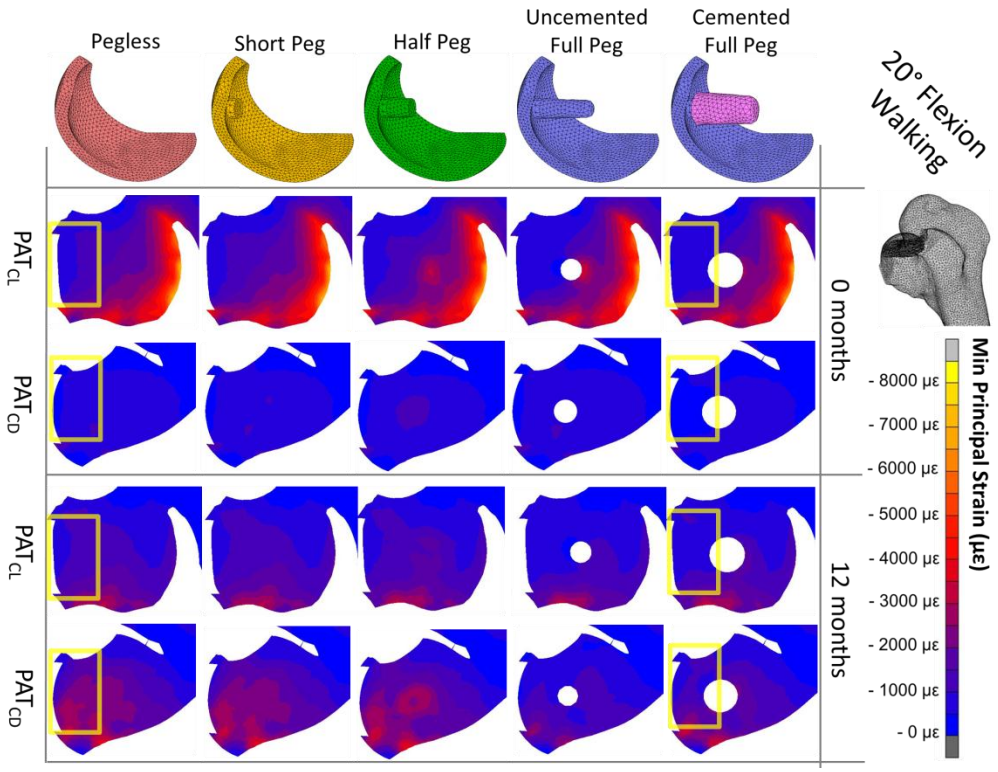


**Figure 220 - Plots of minimum principal bone strain at the coronal section midway through the standard femoral implant peg. The plots show the effect of 12 months bone remodelling simulation on the cemented femora of patient models with different peg designs.**

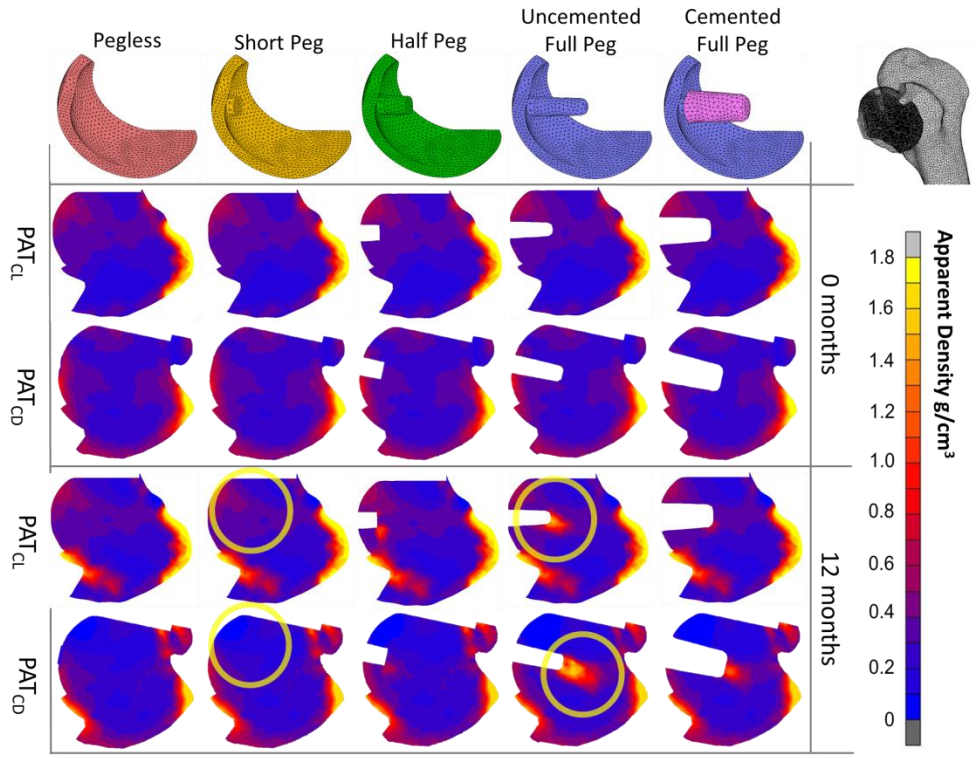


**Figure 221 - Plots of apparent density through the lateral section of femoral implant at 0 and 12 months post-arthroplasty. The plots show the effect of 12 months bone remodelling simulation on the cemented femora of patient models with different peg designs**

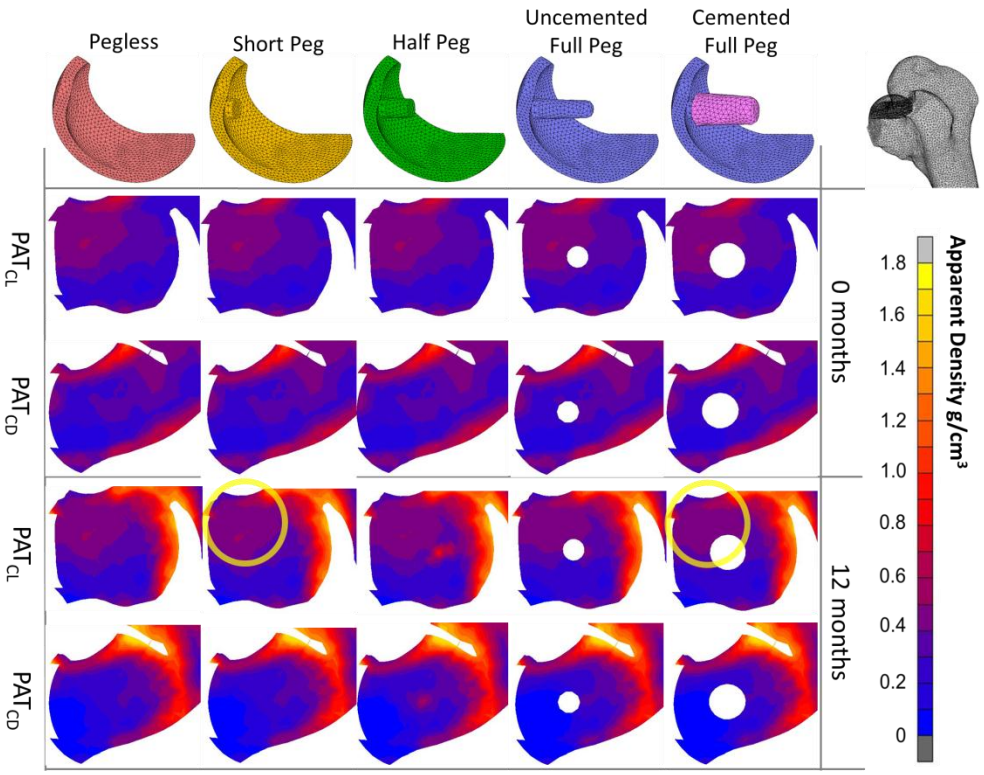


**Figure 222 - Plots of apparent density at the coronal section midway through the standard femoral implant peg at 0 and 12 months post-arthroplasty. The plots show the effect of 12 months bone remodelling simulation on the cemented femora of patient models with different peg designs**

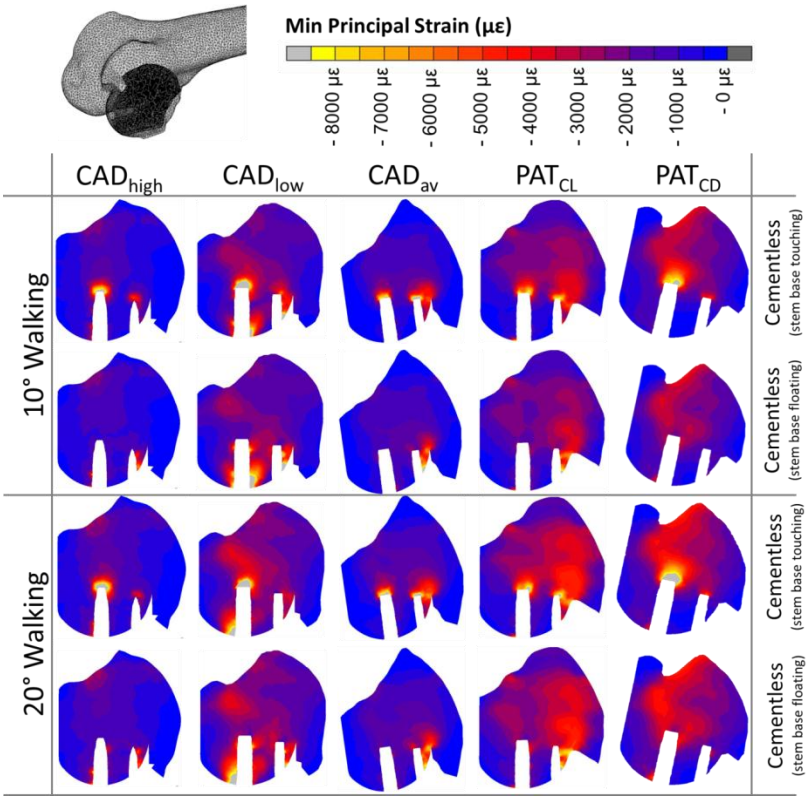


**Figure 223 - Initial fixation of cemented UKR, comparison of bone strain for (1) femoral stem resting against bone and (2) not resting against bone.**

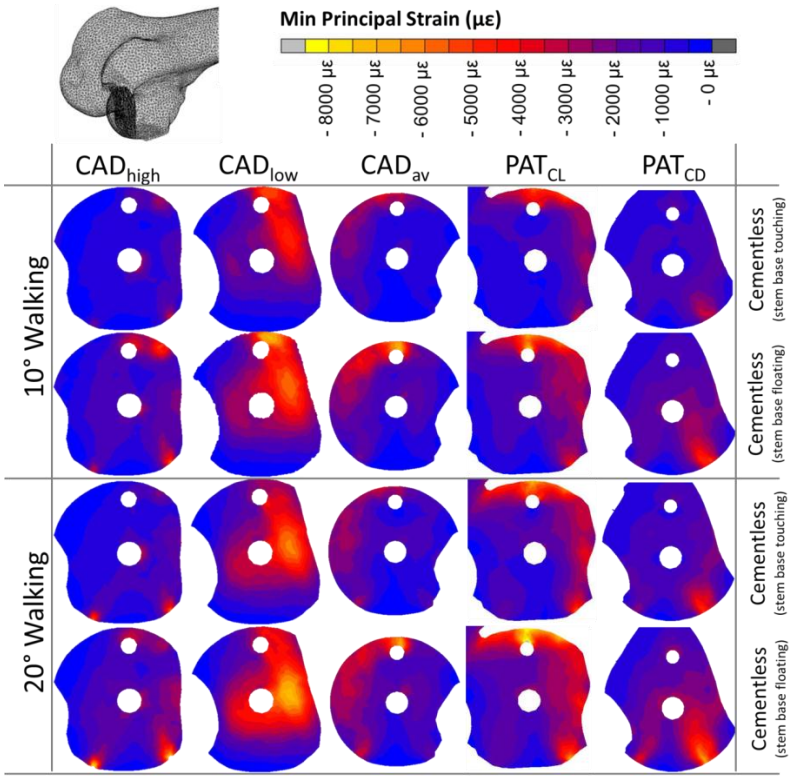


**Figure 224 - Initial fixation of cemented UKR, comparison of bone strain for (1) femoral stem resting against bone and (2) not resting against bone.**

### *9.11.4 Discussion and Recommendations*

The main finding of this study was that there was negligible improvement in fixation by using shorter pegs. Although some improvement was gained with a pegless design, more research is recommended to understand how such a design would perform under lateral knocks and whether a surgical method providing reliable positioning is possible.

The reason why reduced peg sizes did not reduce stress-shielding is because a significant portion of the simulated knee forces transferred through the thick cortices of the femoral trochlea and the posterior aspects of the femoral condyles. Reducing the peg length therefore, had a negligible effect on reducing stress-shielding. With a pegless design, the implant flexed significantly more under loading and the bone mass just beneath the implant surface was maintained. There was little improvement by reducing the peg length from full to half-length.

## 9.12 Femoral Implant Posterior Overcutting: Is it a problem?

### *9.12.1 Introduction*

While simulating UKR surgery in the laboratory on cadaveric knees, it was found that surgeons sometimes overcut the posterior of the femur. A study of 100 UKR bone composite preparations by experienced surgeons showed that the average posterior femur overcut was 1.3 mm (Clarius et al., 2009a). Since this region is difficult to reach and UKR implants are not designed to provide adequate cement compression, subsequent cementation is difficult.

There are no published studies about how this surgical error would affect fixation. The following study presents a multi-specimen comparative computer simulation study comparing validated simulations of the Oxford UKR to scenarios simulating these surgical errors.

### *9.12.2 Method*

The cemented fixation performance of the Oxford mobile bearing UKR was simulated with four scenarios of an overcut posterior condyle: (1) correct resection; (2) 0.2 mm overcut; (3) 1 degree overcut; and (4) 1 degree overcut with the anterior region cement bonded. Note that the reason for simulating a small overcut is for the purposes of having a near-identical mesh between the models such that potential errors due to imperfect mesh are removed. Contact between the overcut surface and the implant was ignored; therefore the depth of the overcut should be irrelevant.

The validated cemented versions of the Biomet Oxford implanted femur FE models (strain-validated $CAD_{LOW}$, $CAD_{AV}$ and $CAD_{HIGH}$; and remodelling-validated $PAT_{CD}$ and $PAT_{CL}$) were modified with small changes to mesh at the posterior condyle so that all four scenarios could be generated with the same mesh. Bone remodelling was only simulated for two of the scenarios (1) correct resection and (2) 1 degree overcut. The development and validation of the FE models are detailed in Sections 6 and 8.

The FE mesh geometry of the posterior condyles used to simulate all four scenarios are presented in Figure 225. A total of 12 simulations were generated for the strain-validated models and 4 for the remodelling-validated models.

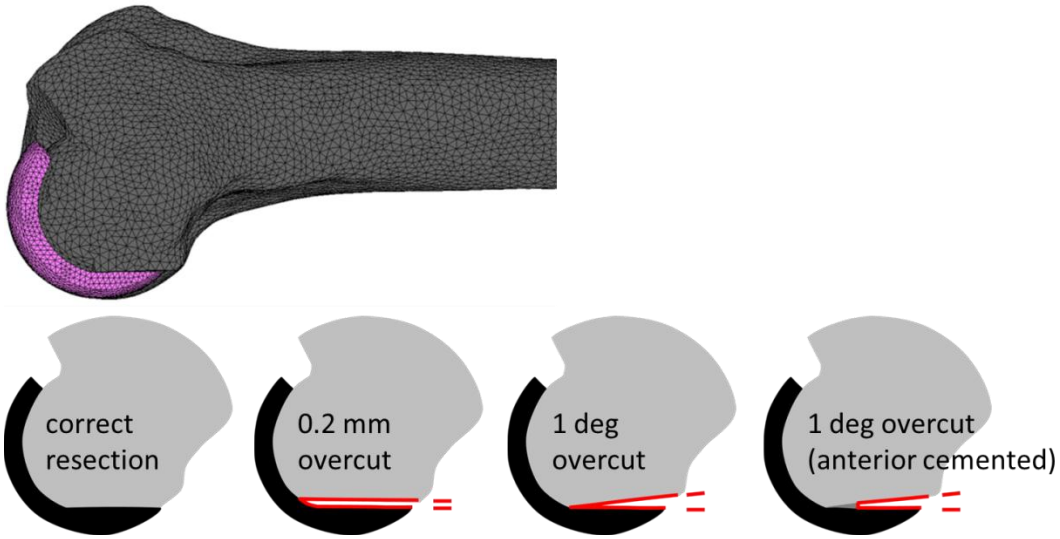


**Figure 225 - Illustration showing how the posterior cuts were represented.**

A full set of knee forces were applied to all the models (medial and lateral tibiofemoral contact, muscles and ligaments) to simulate walking and stair-climbing activities. Eight load cases were applied to each strain-validated femur model representing the peak knee forces at 10 degree increments of flexion angle taken from the pool of data for walking and stair-climbing activities. The knee forces applied to the models are tabulated in Section 8. Bone strains were compared at identical locations for each scenario.

The remodelling-validated FE models ($PAT_{CD}$ and $PAT_{CL}$) were loaded with exactly the same sets of forces used to validate them in Section 8. Note that a cemented version of the model $PAT_{CL}$ was developed (because the validated version was for a cementless UKR) and that the rehabilitation activity levels were different between the two patients (a rapid rehabilitation to full activity was taken by patient $PAT_{CL}$ and a gentle approach was taken by $PAT_{CD}$). Bone remodelling was simulated for a period of 12 months and bone density changes were predicted for each scenario.

### *9.12.3 Results*

Figures 226 to 233 present plots of minimum principal strain at sections of all three strain-validated specimen models under peak knee forces at 20 and 70 degrees of knee flexion. The differences of bone strains between the correct resection and the overcut scenario were small at knee flexion angles of under 30 degrees (Figures 226, 229 and 231).

Of the load cases assessed, the largest difference occurred at 70 degrees flexion with an increase in bone strain at the region posterior to the peg (Figures 227, 228 and 230). This increase may be enough to cause pain. However, this region was also shown to be associated with stress-shielding in Section 7; therefore, the overcut may act as a method of reducing these effects (provided the strains aren't too high).

There were also small increases in tensile bone strain at the anterior region of the implant (Figure 233). Figures 231 and 232 show that there were negligible differences in compressive bone strain to other regions of the knee.

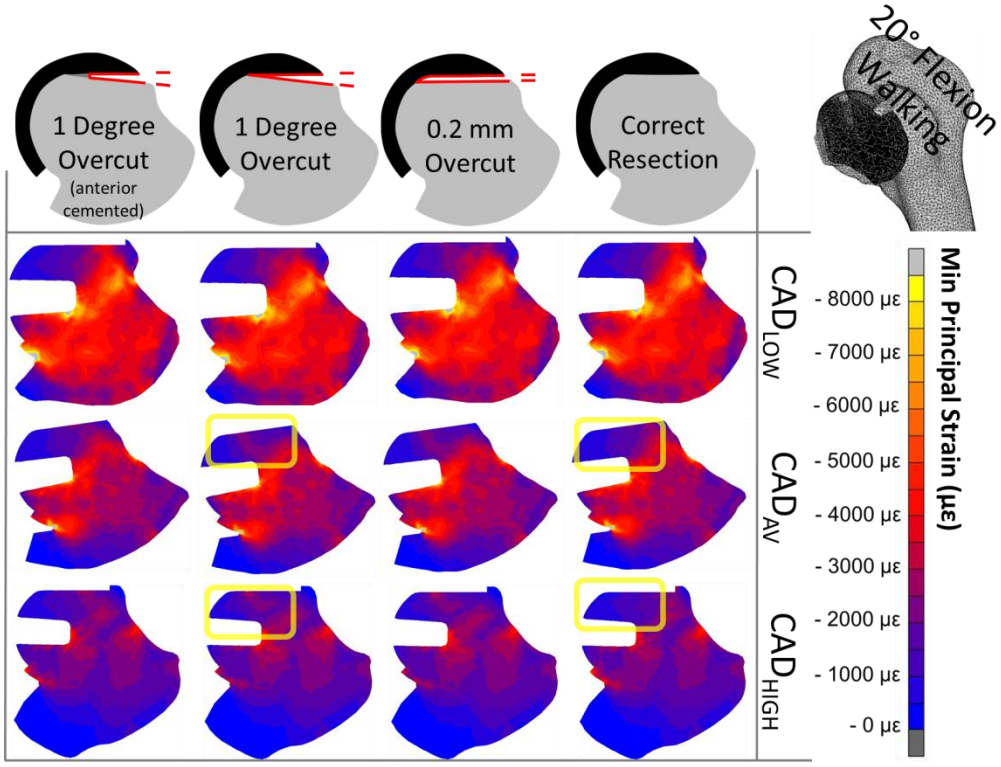


**Figure 226 - Plots of minimum principal strain through the lateral section of the femoral implant at 20 degrees flexion. The plots compare cemented femora of cadaveric specimen models that have posterior femoral overcuts.**

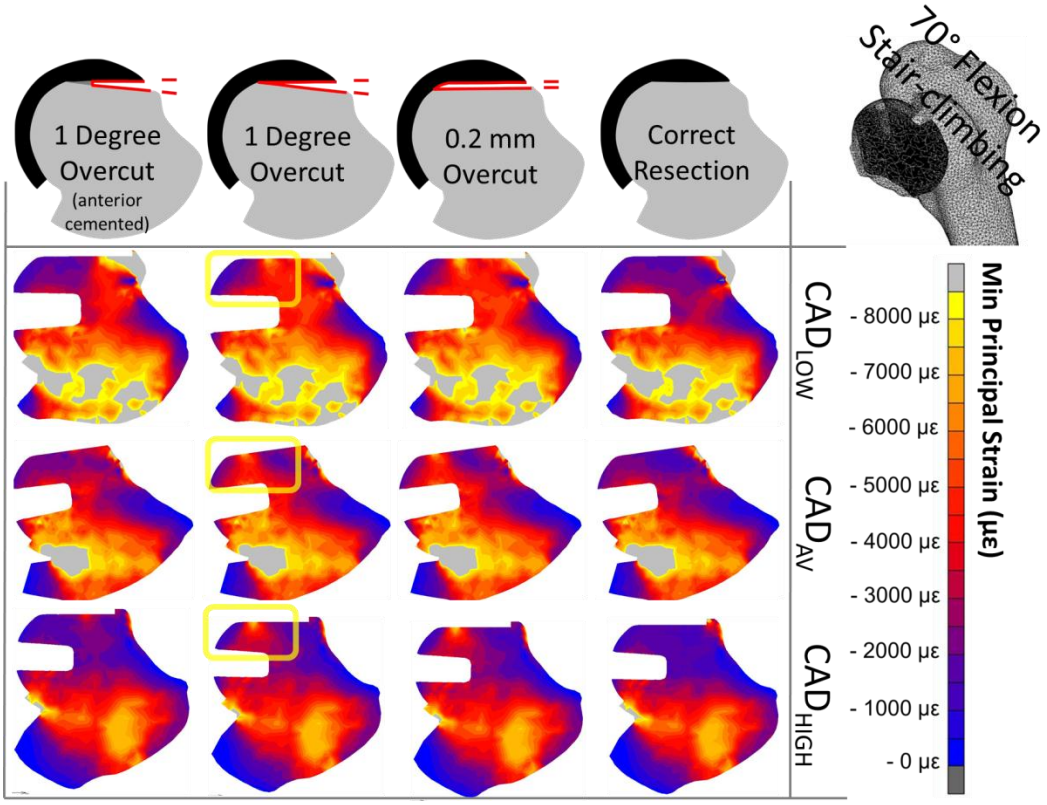


**Figure 227 - Plots of minimum principal strain through the lateral section of the femoral implant at 70 degrees flexion. The plots show an increase in compressive strains posterior to the peg with posterior femoral overcuts.**

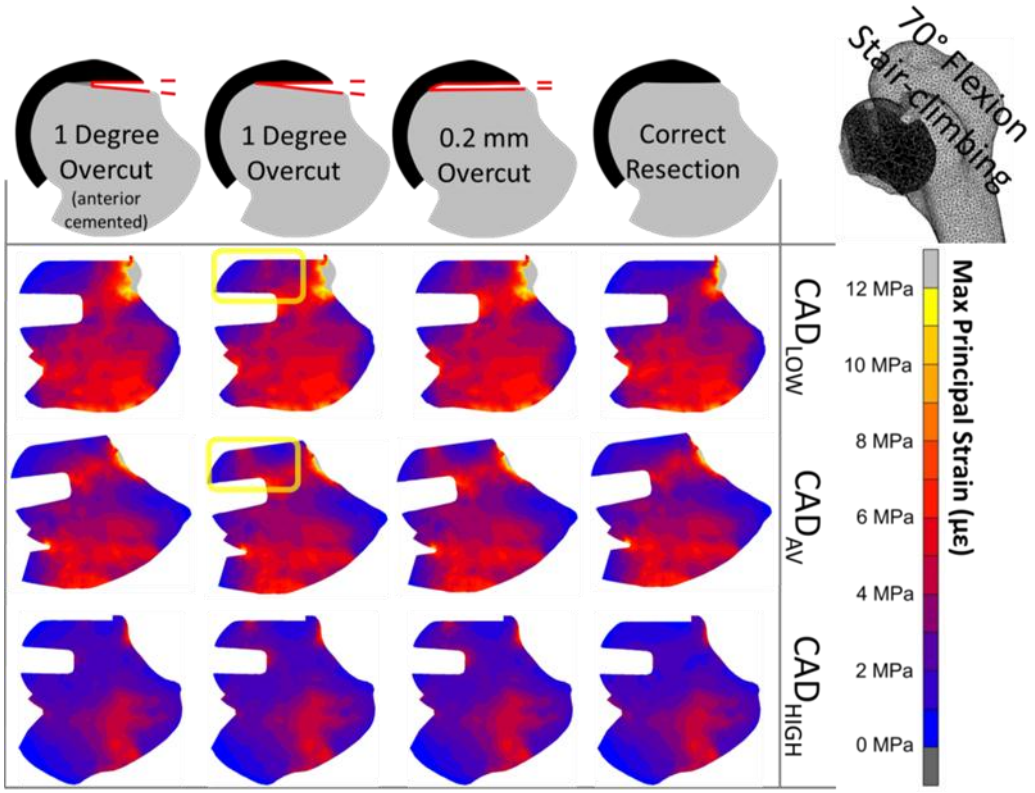


**Figure 228 - Plots of maximum principal strain through the lateral section of the femoral implant at 70 degrees flexion. The plots show an increase in tensile strains around the peg with posterior femoral overcuts.**

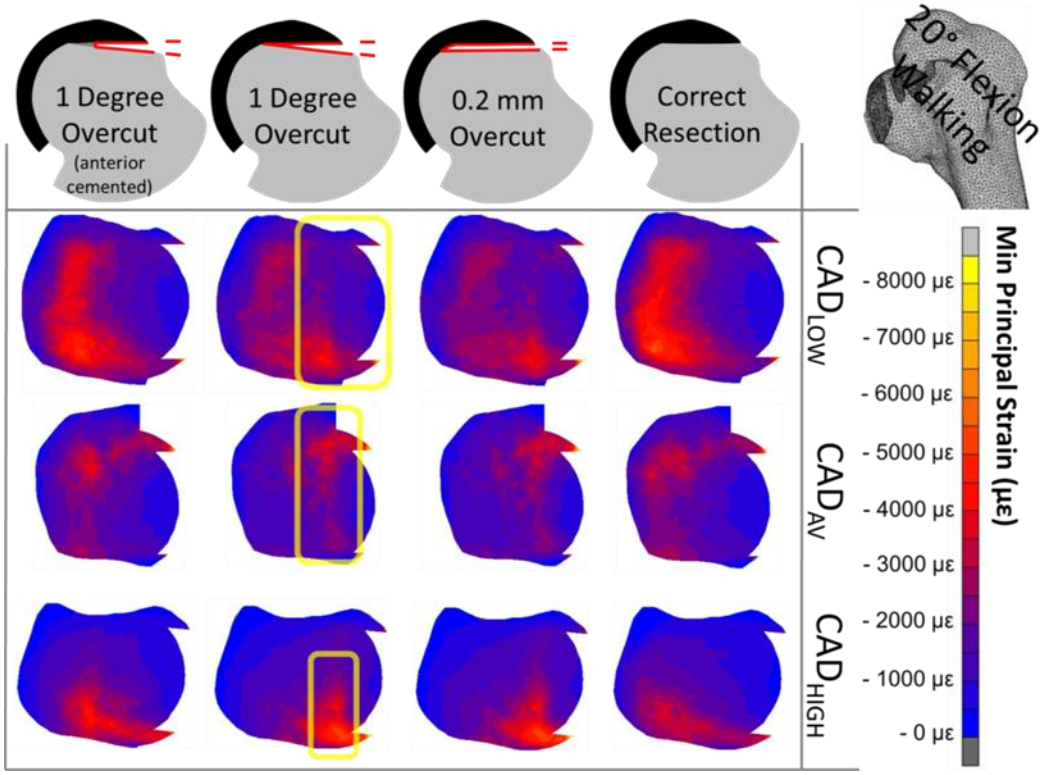


**Figure 229 - Plots of minimum principal strain at a frontal section 1 mm beneath the cement-mantle of femoral implant at 20 degrees flexion. The plots compare cemented femora of cadaveric specimen models that have posterior femoral overcuts.**

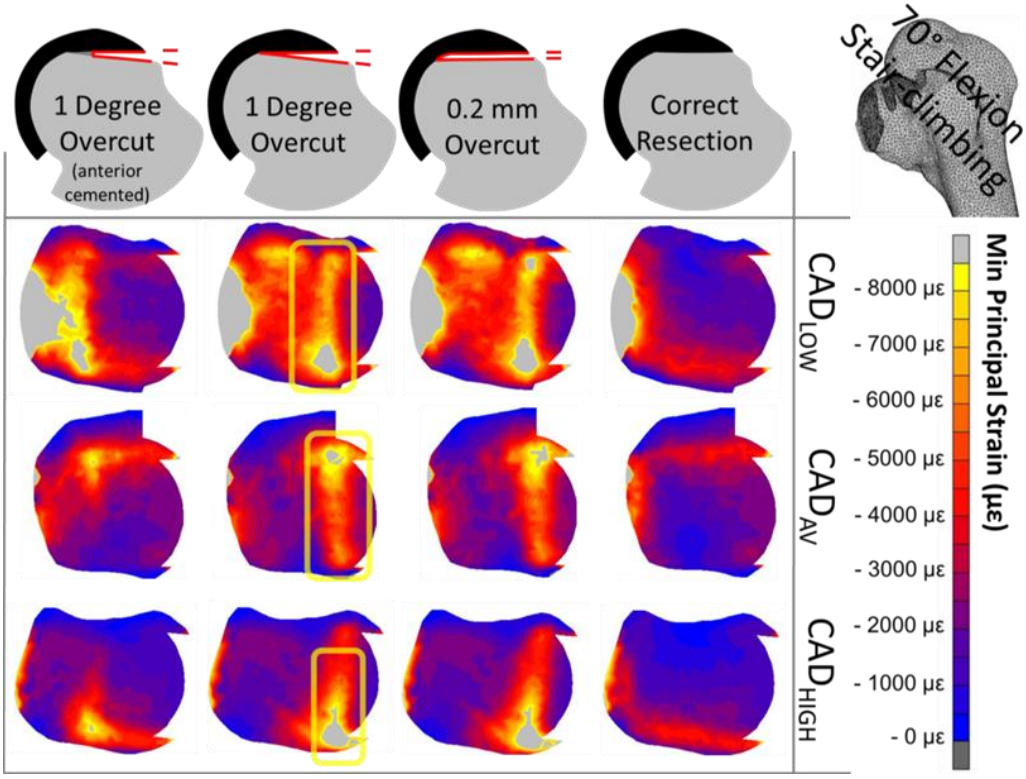


**Figure 230 - Plots of minimum principal strain at a frontal section 1 mm beneath the cement-mantle of femoral implant at 70 degrees flexion. The plots compare cemented femora of cadaveric specimen models that have posterior femoral overcuts.**

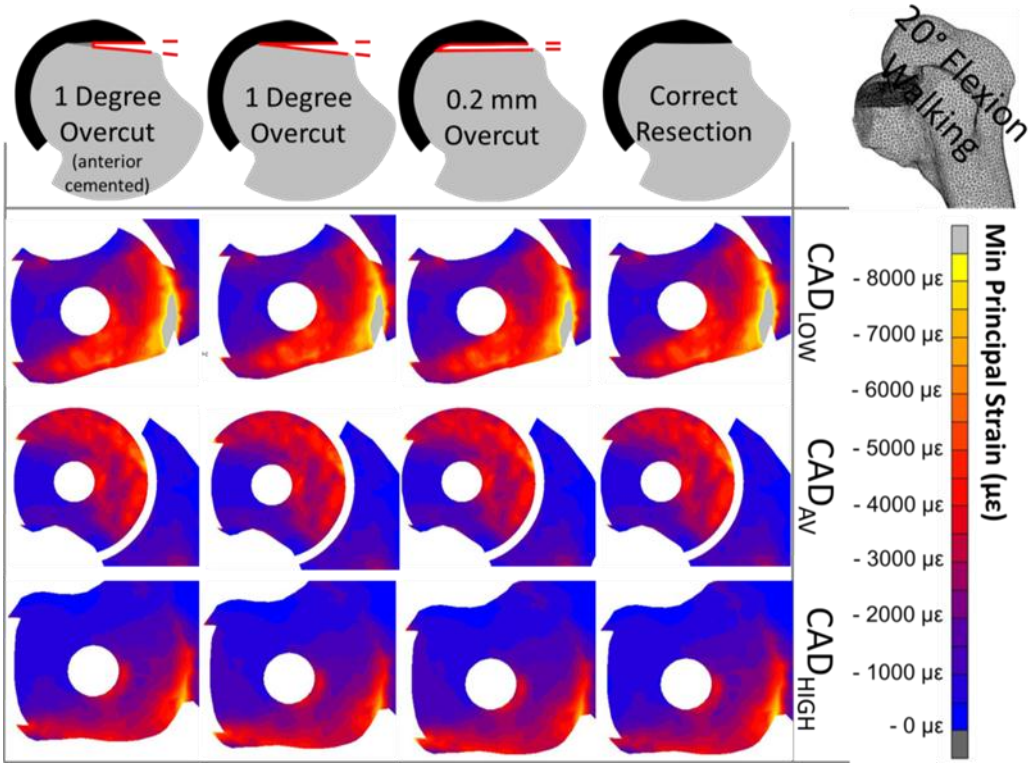


**Figure 231 - Plots of minimum principal strain at the coronal section midway through the standard femoral implant peg at 20 degrees flexion. The plots compare cemented femora of cadaveric specimen models that have posterior femoral overcuts.**

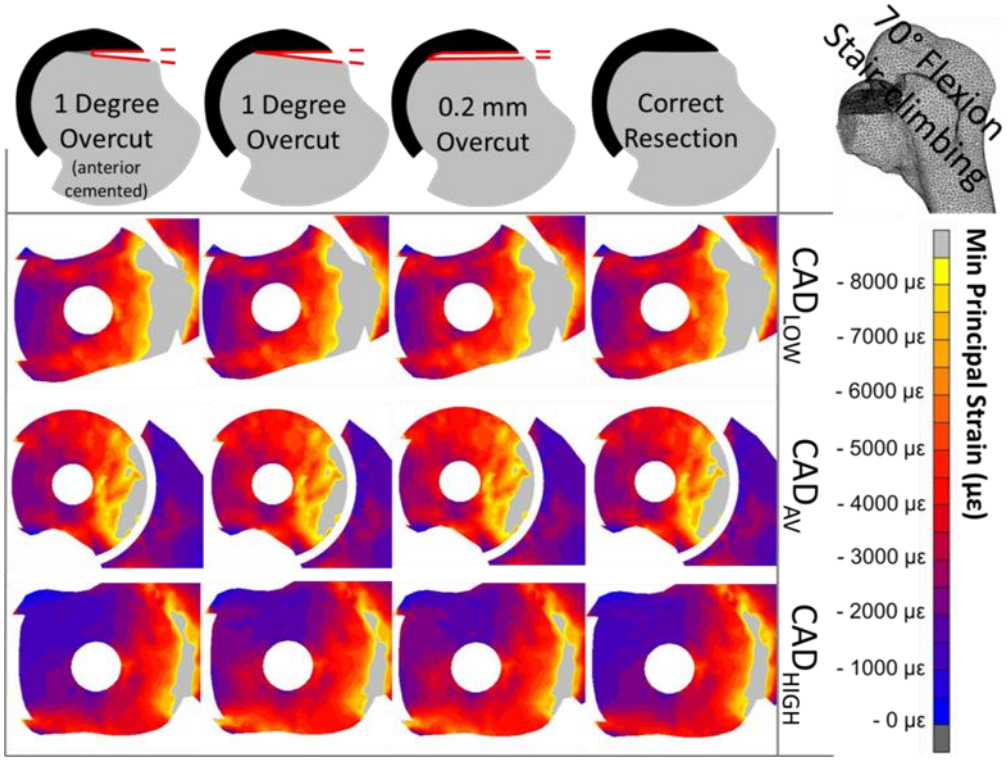


**Figure 232 - Plots of minimum principal strain at the coronal section midway through the standard femoral implant peg at 70 degrees flexion. The plots compare cemented femora of cadaveric specimen models that have posterior femoral overcuts.**

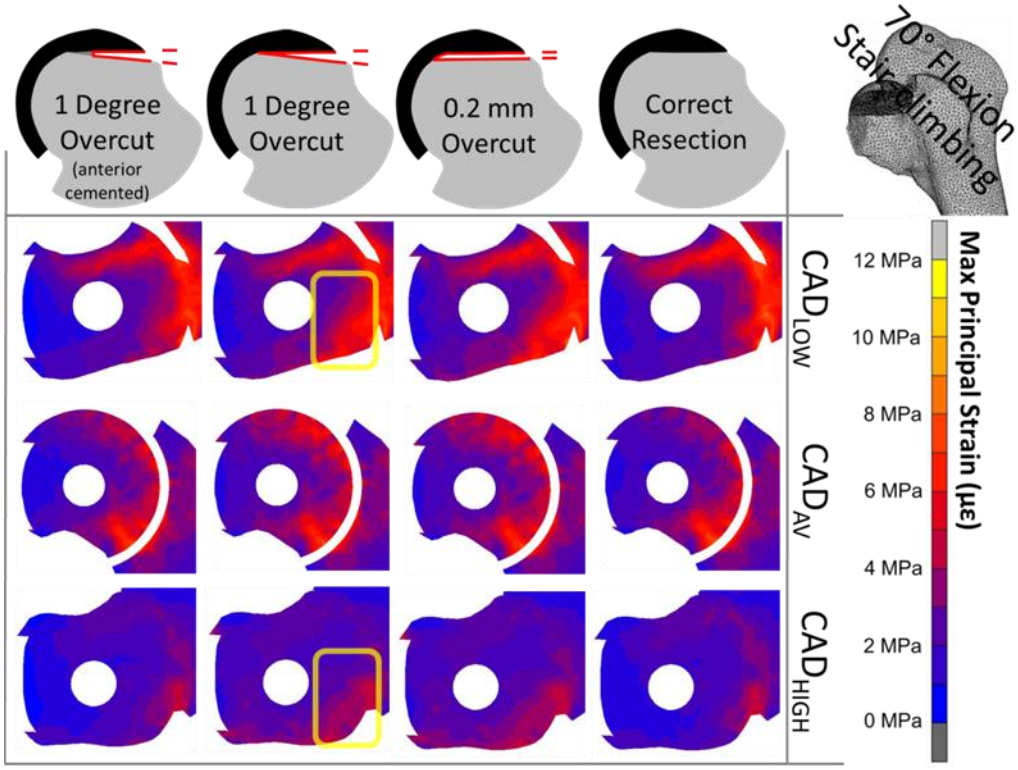


**Figure 233 - Plots of maximum principal strain at the coronal section midway through the standard femoral implant peg at 70 degrees flexion. The plots show an increase in anterior tensile strains with posterior femoral overcuts.**

Figure 234 presents plots of maximum principal (tensile) stress at the cement-mantle at 70° knee flexion under stair-climbing knee forces. There was negligible change in cement stresses with inclusion of a posterior femoral cut.

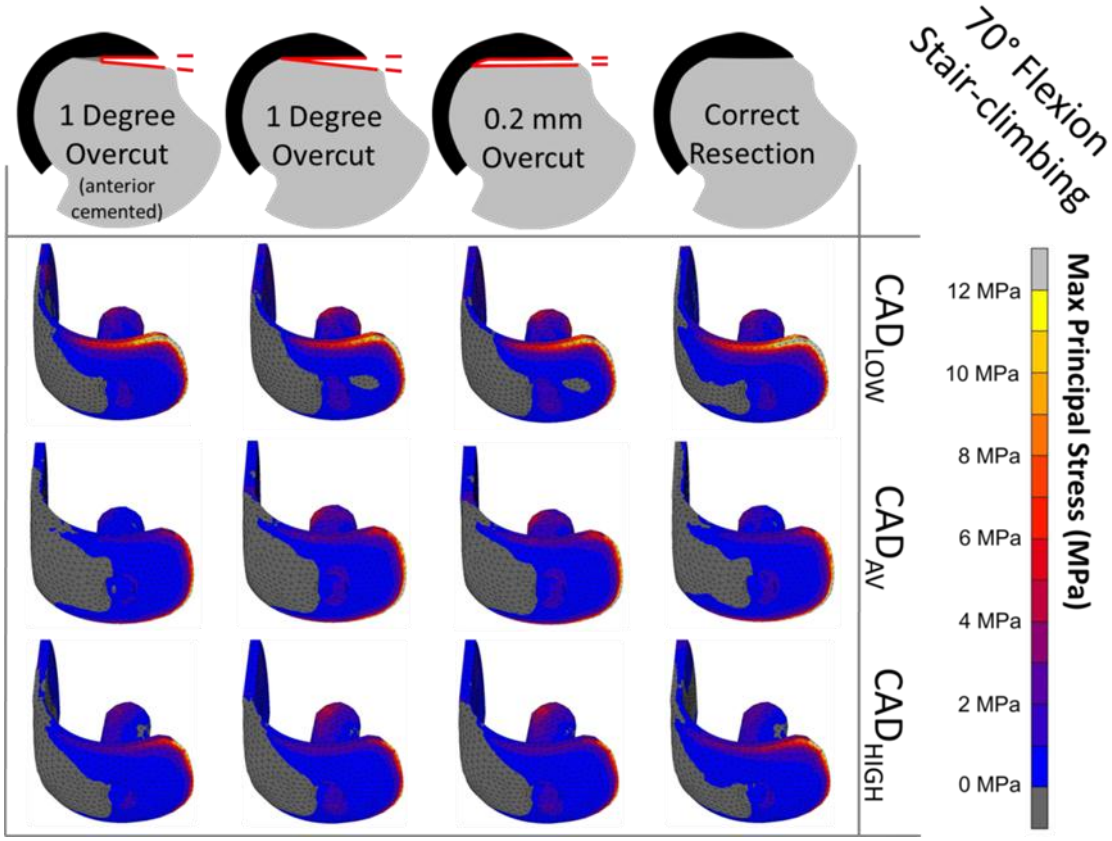


**Figure 234 - Plots of maximum principal (tensile) stress at the cement mantle.**

Figures 235 and 236 present plots of bone density at 0 and 12 months post-arthroplasty in the remodelling-validated patient simulations. The results show that the overcut actually increased bone apposition in the region posterior to the peg. This is in line with the results of the strain-validated models and demonstrates that an overcut may actually act as a method of relieving stress-shielding of this region.

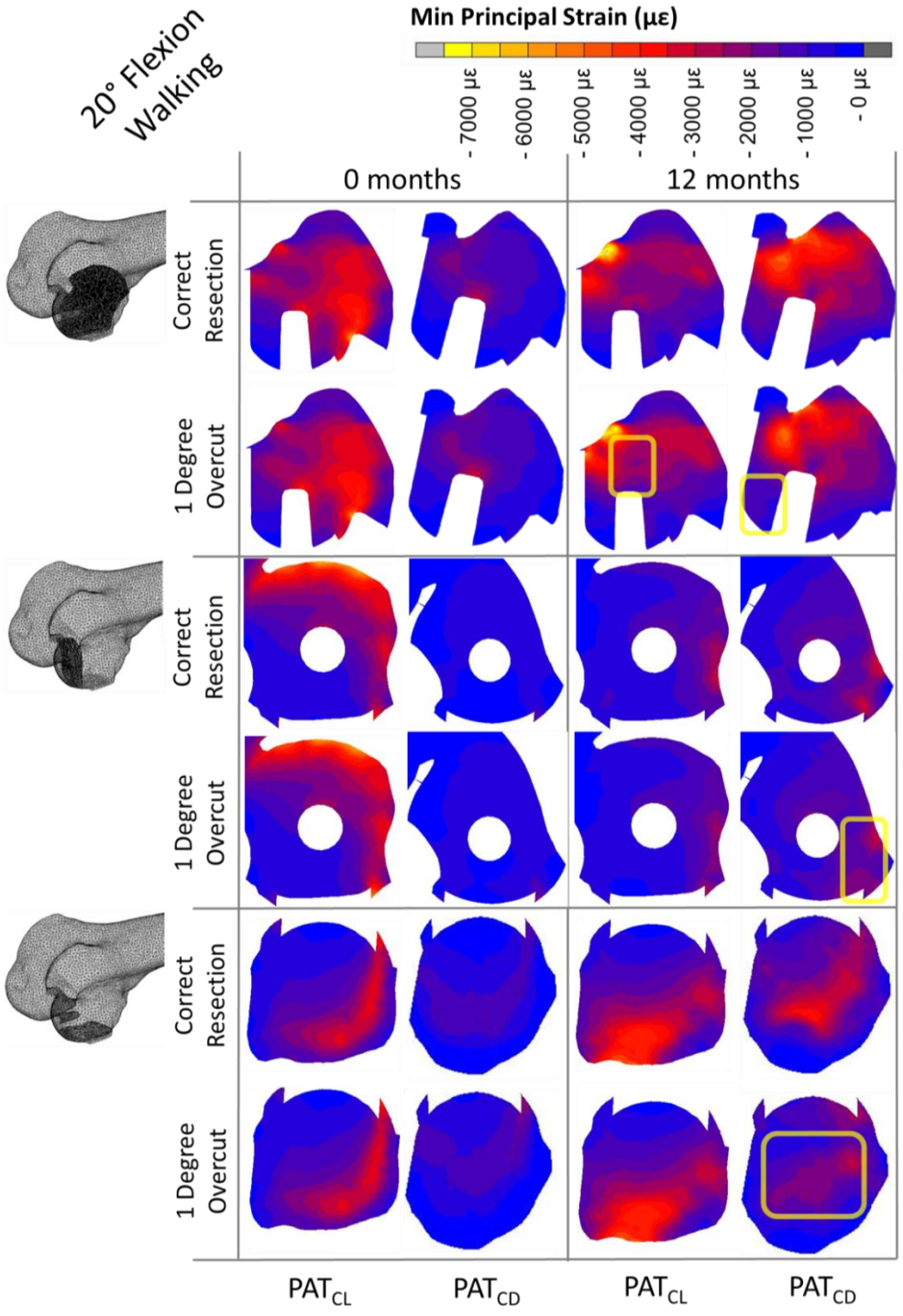


**Figure 235 - Plots of minimum principal strain of bone at three sections of the UKR implanted femur at 0 and 12 months post-arthroplasty. The plots compare the cemented femora of patient models with and without a femoral posterior overcut.**

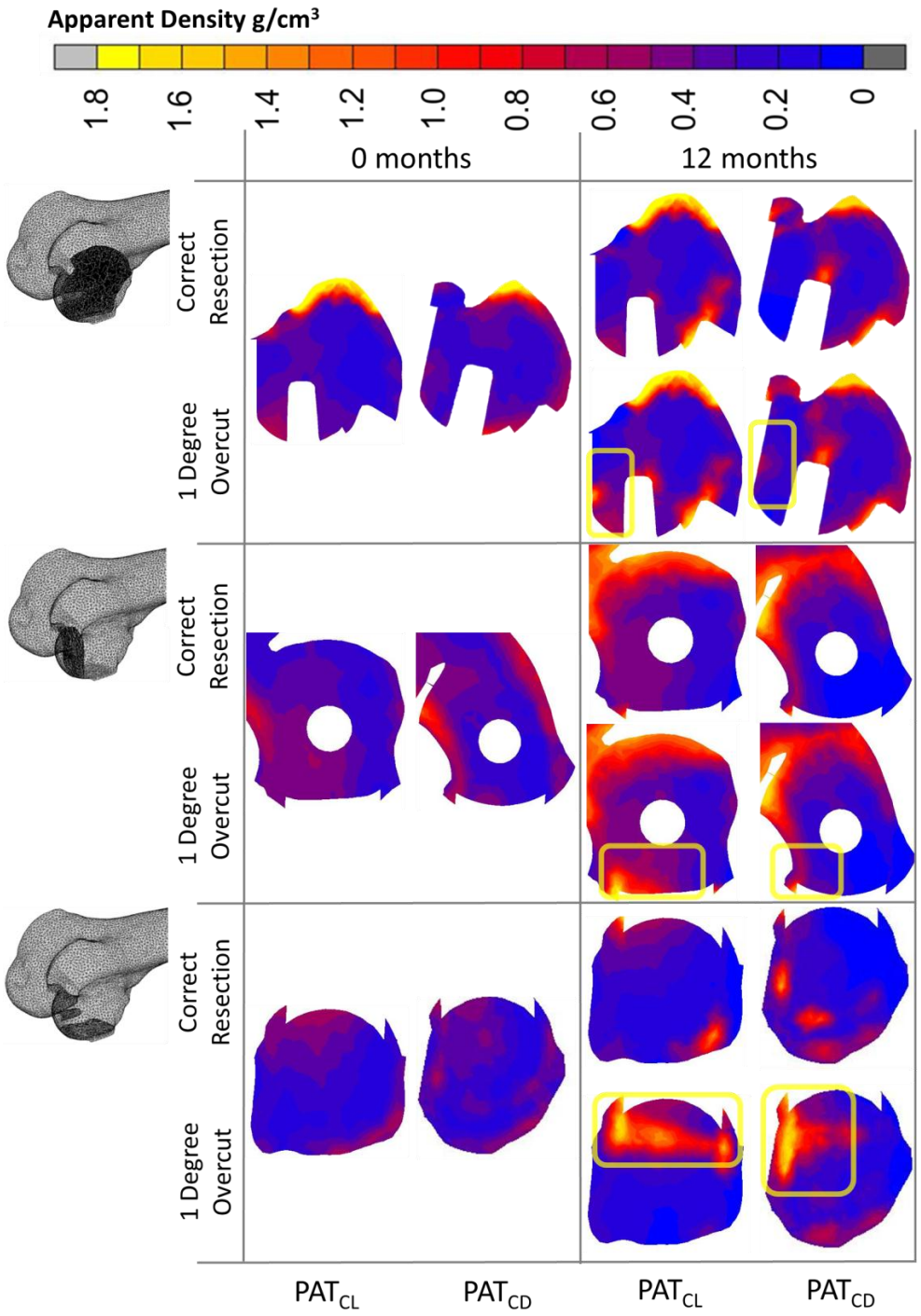


**Figure 236 - Plots of apparent density of bone at three sections of the UKR implanted femur at 0 and 12 months post-arthroplasty. The plots compare the cemented femora of patient models with and without a femoral posterior overcut.**

### *9.12.4 Discussion*

The main finding of this study was that the surgical error of overcutting the posterior condyle followed by inadequate cement fixation in this region created (i) elevated bone strains posterior to the peg that may cause pain to the patient, and (ii) bone resorption superoposteriorly beneath the posterior tip of the implant.

Due to inadequate fixation at the posterior, none of the load transferred through the posterior part of the implant. The load transferred through to a region located more anteriorly (the region just posterior to the peg) which is a region that experienced stress-shielding in the fully bonded scenario. Based on bone remodelling simulations, the results showed that an unbonded posterior region may reduce stress-shielding in the region posterior to the peg and may in fact stimulate bone apposition (or sclerotic bone).

However, the region superoposterior beneath the implant experienced stress-shielding (particularly when loaded under high knee flexions) and displayed some bone resorption. The bone remodelling simulations assumed that the posterior gap did not model into bone. In order to postulate whether this gap would develop into bone or fibrous tissue, a sensitivity study was conducted on specimen $CAD_{AV}$ to measure the micromotions between the implant and the bone. The simulations showed that the micromotions were less than 50 µm for knee flexions less than 30°, but they increased significantly exceeding 100 µm (relative motion) with increased flexions of up to 70°. This region would therefore probably develop into a highly compliant fibrous tissue that would prevent load transmission into this superoposterior region and cause bone resorption as predicted in the simulations.

With deeper flexion angles of 70 degrees, the high medial tibio-femoral contact force coupled with the inadequate fixation at this posterior generated a torque to rotate the implant about its peg, creating higher than normal bending moments in the implant. The implant is however stiff and of sufficient material strength to resist these increased loads. The simulations showed that the cemented peg provided sufficient anchorage to resist these high forces and there were only small differences in bone strain in other regions compared to the correctly resected cemented UKR knee.

The prevalence of posterior femur overcutting could be widespread amongst inexperienced surgeons; but there is no clinical evidence to substantiate this, therefore little research has been conducted on this subject. However, this study suggests that those patients who are more active and load their knees under higher flexions may be more susceptible to poor fixation outcomes. The study suggests that this problem would be more significant if there was insignificant peg anchorage in UKR femoral implants or the pegs were shorter. This should be a consideration in future UKR design alterations.

# 10 Conclusions and Proposed Future Work

## 10.1 Introduction

The overall aim of this research was to understand fixation of Unicondylar or Unicompartmental Knee Replacements (UKR) and make recommendations for improvement to designers and surgeons. Various medical research techniques were utilised for this project, including in-vivo, in-vitro and in-silico studies.

Following a detailed literature review of the current state of UKR, the project was structured around the Oxford mobile-bearing UKR because it is the most widely used implant in the UK (Schindler et al., 2010). A prospective UKR follow-up study of 11 Oxford UKR patients was developed and conducted for one-year, taking measurements of bone density through the course of a year using Dual X-Ray Absorptiometry (DXA) scanning. Detailed bone geometry and density distributions of the patients knees were gathered pre-operatively using computed tomography (CT) scanning.

The Oxford UKR surgical procedure was simulated in the laboratory on ten fresh frozen human cadavers by a surgeon of appreciable experience. The cadaveric soft tissues were then dissected to analyse the resections and the specimens prepared for in-vitro mechanical testing. The specimens were tested for bone strain and bone-implant interface motion with the implants fixed using first cementless and then cemented methods.

A detailed review of Finite Element (FE) computer models of implants was undertaken to utilise and develop current techniques to simulate the implanted UKR for investigation of bone strain, bone-implant interface micromotion and bone remodelling to assess initial and long-term fixation performance. Computer simulations of the tibiae and femora of 2 patients and 4 cadaveric specimens (obtained from the in-vivo and in-vitro studies) were developed and validated for bone strain, bone-implant interface micromotion and bone remodelling. Comparative multi-specimen computational studies were conducted to answer pertinent fixation questions and understand how particular design features affect fixation.

This thesis has numerous novel features including: (1) the first study to complete in-vivo validation of human bone remodelling simulations of knee arthroplasty patients; (2) the first study to validate multiple UKR tibiae and femora for bone strain and bone-implant displacement; and (3) the development of the most detailed multi-specimen FE models of UKR. This section outlines the conclusions of this thesis, the contributions to biomechanics research and recommendations for the future.

## 10.2 Conclusions and Contributions to Biomechanics Research

The evolving market of knee joint replacements is putting increased challenges on surgeons and implant designers to produce improved outcomes with greater efficiency. The younger demographics of patients with severe knee arthritis and their higher expected mobility outcomes have pushed surgeons and designers to consider alternative solutions. The UKR is considered a good option for younger patients with arthritis confined to a single condyle with the remaining knee fully functional. However there is remarkably little research on the fixation performance of the UKR and how it could be improved for primary fixation and longevity. A comprehensive analysis of the fixation performance of the UKR has been presented in this thesis and summarised below.

**Developments in computer simulations of the UKR knee**

Some published apparent bone density to elastic modulus relationships led to predictions of bone strains which exceeded published failure criteria under loads imposed by normal activities. Bone strains were found to be sensitive to the uncertainty of bone elastic modulus reported in the literature. The most reasonable moduli for the tibia and femur were found to be those which were anatomic site and human specific.

The traditional techniques for modelling bone were developed to reduce partial volume effects and reduce the uncertainty of bone strain predictions. The cortical and cancellous regions were meshed separately with local mesh refinement based on the results of convergence studies and the requirements of the specific simulations. The thin cortices of the proximal tibia and distal femur were modelled with shell elements.

Computer simulation sensitivity studies of the tibia and femur revealed that patella and ACL forces were important in modelling fixation performance of UKR knees. A comprehensive literature review was performed to understand and limit the uncertainty in knee force predictions reported in the literature. A full database of knee contact, muscle and ligament forces was generated to model the UKR knee.

**Bone strain validation**

In-vitro mechanical experiments were conducted on ten human cadaveric knees (Section 5) and the results of bone strain measurements used to validate four tibia and four femur models of the UKR implanted knee (Section 6). The cemented UKR pooled $R^2$ values were 0.85 and 0.92 for the tibia and femur respectively, while the cementless UKR pooled $R^2$ values were slightly lower at 0.62 and 0.73. This may have been due to the irregularity of bone resections. The validation results were shown to be comparable to those reported in the literature (for similar computer models) and the improved correlation was attributed to the

improved material property techniques used in this project. This study is the first to validate multiple UKR tibiae and femora for bone strain.

**Bone-implant interface micromotion validation**

The results of bone-implant displacements measured in the in-vitro mechanical experiments conducted on ten human cadaveric knees (Section 5), were used to validate four tibia and four femur models for micromotion. The predicted transverse displacements adjusted for inclusion of friction coefficient produced $R^2$ values of 0.91 and 0.84 for cemented and cementless UKR fixation, respectively. This study is the first to validate multiple UKR knee cadaveric specimens for bone-implant micromotion.

**Bone remodelling validation**

Due to the difficulty in acquiring in-vivo bone-adaptation data there is a notable lack of clinical validation of bone remodelling computer simulations of human joints. A DXA follow-up study was conducted on UKR patients and bone density changes were measured at the UKR tibia and femur at 0, 3, 6 and 12-months. Two of the patients were used to develop bone remodelling computer simulations of the cemented and cementless Oxford UKR tibia and femur and the results compared to the measured DXA results.

Using the bone remodelling algorithm developed by Huiskes et al. (1987), the following parameters were found to produce the most realistic predictions of the actual measured patient knees: a stimulus of strain energy density (U); lazy-zone of 75%; time-parameter of $\tau = 50$; and with the theory of Martin activated. The rate at which the UKR patient resumed normal activity had a distinct effect on the bone density changes and potentially on the future success of the implant.

This study was the first to attempt to validate bone remodelling changes following UKR arthroplasty to computer simulations.

**Stress-raisers in UKR resected tibia and femur**

Analysis of multiple patient and cadaveric UKR knees highlighted stress-raisers at the resected corner of the tibia and at the reamed anterior edge of the femur. The bone strains approached the failure limit of bone; in particular for low density bone where it exceeded the failure threshold of bone. Although cementation reduced the bone strains, the UKR design and operative technique could be modified to reduce these stress-raisers.

**Bone loss in Oxford UKR patients is manageable**

A DXA study was conducted on 11 UKR patients, for a follow-up period of one year, measuring bone density changes at 20 predetermined regions-of-interest on the tibia and

femur. There were statistically significant post-arthroplasty bone density changes to the knees of the UKR patients. Most subjects saw a large drop in BMD in the first 6 months following surgery, followed by a steady recovery. The biggest change surprisingly occurred under the tibia intercondylar eminence which decreased steadily by an average of -17.9% at 6-months and which then reduced slightly to -15.1% at 1-year (statistically significant). The average bone loss under the tibial tray was negligible; however, the bone loss at the anterior portion was higher with an average decrease of -13.7% (statistically significant). There was no change (0.4% mean bone gain) under the tibial keel. The bone loss under the femoral component was more significant (-12.9%). The regions anterior and posterior to the central implant peg saw greater bone loss (-13.5% and 14.4%, statistically significant)).

The results of the computer simulations demonstrated that maintaining activity levels following arthroplasty minimised bone loss in the high risk regions (posterior femoral condyle and proximal tibial tray keel). The quicker the adoption of normal activity levels the better the outcome was at one year. The significant bone loss under the tibial eminence was shown to be due to a combination of lack of fixation on implant side-wall, removal of lateral tibiofemoral forces at the medial condyle upon arthroplasty and reduced ACL function. The former two reasons explained up to 15% of the bone loss. Greater bone loss was seen in half of the patients and was suggestive of reduced ACL function. A possible explanation for the reduced ACL function could be because the femoral component of the Oxford UKR lies too posteriorly on the condyle, inhibiting bearing movement particularly in small size implants.

**Cementation reduces bone strain in the UKR implant tibia**

In-vitro mechanical experiments, conducted on ten human cadaveric knees (Section 5) comparing bone strains of cementless Oxford UKR knees, showed that cemented fixation produced a statistically significant reduction in bone strains at the proximal tibial cortices. The bone strain changes on the UKR implanted distal femur upon cementation were insignificant. Computer simulations (Section 6) showed that cementation distributed the knee force more evenly through the bone while the cementless implant created regions of high bone strain around the rim of the implant (Sub-Section 9.2). Upon osseointegration of the bone-implant interface, the simulations showed the bone strains reduced to similar levels experienced in the cemented UKR knee (Sub-Section 9.2). Further evidence for this difference were seen in the patient tibiae of the DXA study (Section 7), where the cemented fixation patients saw a larger drop in bone density compared to the cementless fixation patients.

These higher strains in cementless UKR patients may be responsible for the increased pain that these patients tend to feel (compared to cemented UKR patients) immediately post-arthroplasty (personal communication with Prof. Justin Cobb). This pain tends to diminish within a few months and these patients tend to have radiographs with no radiolucencies at 1 year (Pandit et al., 2009).

The cemented and cementless Oxford UKR were both shown to provide adequate fixation for most patients irrespective of whether cemented or cementless fixation is used; however, success rates could be improved with careful choice of fixation method. Cementless fixation in patients with a low density tibia generated bone strains that exceeded the failure strength of bone under normal peak daily activity knee loads. This could lead to tibial subsidence or even fracture. Therefore cementless fixation is not recommended for patients of low density bone.

Provided that there was no implant subsidence or fracture, the long-term fixation performance of cementless implants was slightly better than cemented implants because there was more bone gain and less bone loss (Sub-section 9.2). Although the short-term performance of the tibial components was best with cemented fixation, the long-term success may be compromised for patients with a dense tibia who would benefit more with cementless fixation.

**Cementless fixation of UKRs is good in dense bone**

Based on computer simulated predictions of bone-implant micromotion, the performance of the UKR cementless fixation osseointegration degraded for knees of decreasing bone density (Sub-Section 9.3). For dense bone, the micromotions were below the threshold of 50 μm to allow firm osseointegration. The average density knee produced moderate tibial and femoral micromotions (less than 100 μm) and although cementless fixation could be used in such patients, a gentle rehabilitation programme would be recommended. The low density knee produced high micromotions (greater than 100 μm) in both the tibia and femur; therefore cementless fixation is not recommended for such patients. Note also that cementless fixation was also shown to produce higher tibial bone strains (compared to cemented fixation) with potential tibial subsidence or fracture. This is further evidence to exclude patients with low density bone.

**Incomplete tibial UKR radiolucencies are not a problem**

Cemented Oxford UKR patients often display radiolucencies beneath the tibial implant (Gulati et al., 2009a, Pandit et al., 2009, Rea et al., 2007). Most are considered physiological and do not show any signs of loosening (Gulati et al., 2009a). A comparative study was

performed to assess the fixation performance based on increased compliance of the cement-mantle over time.

The reduction of stiffness of the cement-mantle layer (17% of its initial stiffness based on explants of THRs (Mann et al., 2008)) caused bone strains in the underlying bone to increase and bone apposition occurred. This may explain the sclerotic margin typically seen under radiolucencies of UKR tibiae (Gray et al., 2010). This study also concludes that lower density tibia may be more susceptible to forming sclerotic margins following development of radiolucencies.

Reducing the elastic modulus of the cement-mantle of the tibial component made small changes to the tibial strains. The load path changed such that a larger proportion was through the tibial tray rather than the keel. As a consequence the bone strains beneath the implant increased and the bone strain beneath the keel decreased.

**Shallower resections of keeled tibial UKRs do not improve fixation**

A multi-specimen comparative computer simulation study, of tibial implant UKR knees each resected at three depths (4 mm superior and 4 mm inferior to the nominal), demonstrated that the effect of the resection depth on bone strains was highly dependent on the geometry and density of the specimen.

The hypothesis that “shallower resections would reduce strain change and improve fixation”, was found to be incorrect. The reason for this was two-fold: With superior resections (1) the keel was moved into a region of lower density, thus increasing the strains under the tray; and (2) the tray underside was moved into a region where the density under the lateral side was lower than at the medial side, causing tilt when loaded, thus increasing the strains under the lateral side of the tray.

The highest density tibia produced bone strains that most closely matched the pre-arthroplasty state with stress-shielding under the tibial tray minimised. This was true for either cemented or cementless implants. Stress shielding was higher with a lower density tibia. While superior resections reduced the magnitude of stress-shielding, they did not necessarily reduce the strain difference from the pre-arthroplasty state.

Analysis of bone density plots of the transverse resections showed that the highest cancellous density was at the centre of the implant. This corresponded to the position of the implant keel; therefore the high stiffness of this region was not utilised in these Oxford UKR designs, particularly with more superior resections. If there was no keel at the centre of the implant, the fixation would be improved. Otherwise a keel extending into the lateral side wall (Simpson et al., 2011) or anterior region would be an improvement on the current design.

**All-PE tibial implants should not be less than 9 mm thick**

A multi-specimen comparative computer simulation study (Sub-Section 9.6), of tibial implant UKR knees implanted with various thicknesses of all-PE tibial implants, demonstrated that the bone strain distribution beneath all-PE UKR knees was significantly different to those of metal-backed and mobile-bearing UKR knees.

Bone strains were severe for the low density tibia with likely tibial collapse upon use of any all-PE implant less than 12 mm thickness. For the normal and highest density tibia specimens, the bone strains were within acceptable limits with all-PE implant thicknesses of 9 mm or greater.

**Metal-backed or All-Polyethylene UKR decision is patient dependent**

Based on the results of a multi-specimen comparative computer simulation study (Sub-Section 9.6), the fixation performances of the all-PE and metal-backed UKRs depended on the bone density of the tibia. The study recommends not to use a “one size fits all” philosophy and to determine the PE thickness from patient bone quality (assuming they are not obese, and have normal activity levels): PE bearings should not be used if the patient bone density is low; a minimum of 9 mm is used for patients of average bone density; and a minimum of 6 mm for patients of high bone density. If the quality of the bone is unknown (this is particularly likely with surgeons of limited experience), the all-PE tibial UKR should not be used as the all-PE implant was considered “unforgiving”.

**Shorter tibial UKR keels provide improved fixation for dense tibia**

Current mobile-bearing UKR designs have keels that extend 10 mm (Oxford Biomet and Uniglide Corin). The metal-backed UKR designs are variable; however the majority have keels. The all-PE UKR designs tend also to be variable with very short keels (Evolution Tornier, Accuris Smith & Nephew, EIUS Stryker) and large keels (Uniglide Corin).

Based on the results of multi-specimen comparative computer simulation study (Sub-Section 9.7), a large cemented keel improved fixation of all-PE UKRs. Although the large cemented keels of metal implants provided good fixation for patients with poor quality bone, they caused stress-shielding in the average and high density tibiae that could compromise long-term fixation. Tibia keels of 2 mm depth may improve fixation of average to high density tibiae of UKR patients.

**Tibial sagittal overcutting must be avoided**

A multi-specimen comparative computer simulation study (Sub-Section 9.8), comparing the standard UKR tibia to the 10 degree overcut tibia and a rounded resection corner tibia, was

conducted. The results showed that overcutting was not necessarily a problem for average and high density tibiae, but a significant hazard for low density tibiae.

If the knee is drilled at the resected corner before the transverse and lateral resections are made, that may help surgeons to reduce the over-resections which were shown to exacerbate bone strains in this study. The rounded corner also reduced the tensile bone strains at this region.

**The fixation of the tri-radius and the single-radius femoral UKR are similar**

It was hypothesised that the tri-radius femoral UKR would improve bone strains compared to the single-radius implant because it was better conforming and did not create a deep notch at the anterior of the femur. A multi-specimen comparative computer simulation study (Sub-Section 9.9), showed that the difference of bone strains was small because the major contributing factor was the impact of using a rotating reamer that cut into the trochlear groove.

Nevertheless, there were negligible differences in bone strains using the tri-radius femoral UKR compared to the Oxford UKR. The tri-radius UKR should perform equally as well with added potential improvements in kinematics, due to the implant shape conforming closer to the shape of the natural femur.

**The All-Polyethylene femoral UKR could provide better fixation**

The metal UKR femoral implant is very stiff because of its material and its shape and it has been demonstrated that stress shielding is more of a concern in the UKR femur than the tibia (Section 7). It was hypothesised that using a material with a lower elastic modulus may reduce stress shielding.

The results of a multi-specimen computer simulation study showed that an all-polymer femoral UKR reduced stress shielding and could improve longevity compared to metal femoral UKRs in relation to transmission of strains. This is provided that there are no deleterious effects such as (i) substantial wear rates; (ii) fatigue of the PE; (iii) development of high implant-cement or cement-bone micromotions with degradation of the cement-mantle. With significant improvements in wear resistance of polymers in recent years (Kurtz et al., 1999, Kurtz et al., 2009a), polymers may now be a viable option for femoral implants.

**The benefit of a shorter femoral UKR peg is small**

It has been demonstrated that stress shielding is more of a concern in the UKR femur than the tibia (Section 7). A comparative multi-specimen computer simulation study (Sub-Section 11) was conducted comparing bone strains and bone loss of femoral UKR knees of different

peg lengths. There was negligible improvement in using shorter pegs, but some improvement with no peg. The reason for this finding is because a significant portion of the UKR knee force transfers through the thick cortex of the femoral trochlea and the posterior aspect of the femoral condyle. With no peg the bone mass in this region was maintained; however there was little improvement by reducing the peg length from full to half-length.

**Femoral implant posterior overcutting may cause pain and stress-shielding**

While simulating UKR surgery in the laboratory on cadaveric knees, it was found that surgeons sometimes overcut the posterior of the femur. Since this region is difficult to reach and the implants are not designed to provide cement compression, subsequent cementation is difficult. In order to understand whether an unbounded posterior femoral implant would degrade the fixation performance of the femoral UKR, a multi-specimen comparative computer simulation study was conducted.

The main finding of this study was that the surgical error of overcutting the posterior condyle followed by inadequate cement fixation in this region created (i) elevated bone strains posterior to the peg that may cause pain to the patient, and (ii) bone resorption superoposteriorly beneath the posterior tip of the implant.

The prevalence of posterior femur overcutting could be widespread amongst inexperienced surgeons; but there is no clinical evidence to substantiate this, therefore little research has been conducted on this subject. However, this study suggests that those patients who are more active and load their knees under higher flexions may be more susceptible to poor fixation outcomes. The study suggests that this problem would be more significant if there was insignificant peg anchorage in UKR femoral implants or the pegs were shorter. This should be a consideration in future UKR design alterations.

**Overall Conclusions**

This thesis describes the most comprehensive study of UKR fixation. It includes the most thorough validation of computer models, using both imaging of patients in-vivo, and mechanical testing in-vitro. It has led onto a number of UKR design evaluations. A recurring theme has been the dependence of UKR fixation on overall bone density.

## 10.3 Future Work

The computer models developed and used in this research are capable of simulating the biomechanical and bone remodelling responses in the bone after implantation of UKRs. However the simulations are limited by the quality of the input data and the analysis capabilities and throughout this thesis the importance of understanding these limitations has

been emphasised. There are improvements that should be made in order to improve the capability and confidence of these simulations. These are outlined below:

**Understanding the UKR patient group**

The dependence of UKR fixation on overall bone density has been shown to be an important factor in fixation outcome; however, the bone density range of tibiae and femora of UKR patients is unknown. Although, human cadaveric knees were used to determine the range of bone densities analysed in this thesis, these knees were not real UKR patients. It is likely that UKR patients are more varus-aligned and have denser medial compartments compared to the normal population. Prospective or retrospective analysis of UKR patient computed-tomography scans could help to determine the range and distribution of bone density in this group of patients. The density range of the tibiae and femora assessed in this thesis could then be defined in relation to UKR patients.

Although bone density has been highlighted as an important factor in fixation outcome, body mass and the level of patient activity should also be important in determining fixation outcome. Body mass was factored into the knee forces used to assess UKR fixation, but due to the small number of specimens and patients assessed, the extremes of body mass in relation to bone density is unlikely to have been represented. Due to limitations in the literature, the effect of the difference in activity levels between patients was not assessed for determining fixation. With the availability of data, the effect of body mass and the level of activity within the UKR patient group should be investigated in more detail.

**Material properties of bone**

The results of Section 2 cast doubt on the use of some of the published density-modulus relationships for analysis of the human proximal tibia; it also highlighted the need for further experimental work to characterise the behaviour of bone with intermediate densities. Further work is recommended to increase the pool of bone property data for specific anatomy of human bone. This is particularly relevant for the distal femur where this data was not available. More data is also required to support and improve confidence in the range of human tibia and femur bone covering the cortical range. Although this data was available for human tibial cortical bone, there was some doubt over the experimental method used to obtain the data.

**Database of knee forces**

The open source dataset of knee forces provided by Prof. Bergmann (www.orthoload.com) is of substantial relevance and importance for simulating the knee. This is because this set of forces was generated from instrumented TKR prostheses so the post-TKR kinematics is

relevant. The kinematics of the UKR knee is different to those of the TKR. This thesis has also emphasised the importance of considering muscle and ligament forces, particularly for the UKR. Further research is required to improve the quality and confidence of knee forces data with the aim of obtaining patient-specific knee force datasets. Developing a minimally invasive instrumented UKR would be a good next step and would provide significant benefits for modelling both the intact knee and the UKR knee.

**Computational techniques**

With expected steady improvements in computational capability, larger and more complex simulations will be possible. The problem of simulating implant fixation is complex and fundamentally involves multi-scale modelling from tissue to whole bone-level. In this thesis, assumptions were made to define and develop relevant macro-scale models for the purposes of understanding UKR fixation. It is recommended that further studies are completed at the tissue-level with the aim of fully integrating multi-scale models.

This research highlighted some complex micro-mechanisms involved in simulating bone-implant micromotion that the macro-scale models could not accurately simulate. Although these assumptions proved to be valid for predicting surface-tangent micromotions, there were large discrepancies in predicted surface-normal micromotions. Tissue-level simulations of the bone-implant interface are required to understand and explain these differences and develop cohesive models that could be added to the macro-scale models used in this study. Based on tissue-level models developed from Total Hip Replacement (THR) explants, cohesive models have been developed for non-linear behaviour of the cement-bone interface (Mann et al., 2010). These have been included in macro-level simulations of THRs (Waanders et al., 2011). Similar research should be carried out for the implant-bone, implant-cement and cement-bone interfaces of UKRs and incorporated into macro-level models developed in this research.

The bone remodelling algorithm used to model long-term fixation assumes that all bone is remodelled as bone. Under specific biomechanical loads the bone could remodel as fibrous tissue. It is recommended that the remodelling algorithm is updated to account for these changes as implemented by Gray et al. (2010).

With very low wear rates of mobile-bearing UKRs, osteolysis is not a major concern for implant loosening; however, it can be for fixed bearing UKRs. Incorporating a parameter for osteolysis of adjacent bone would add value for assessing fixed bearing UKR designs. As a first step, this could be implemented using cohesive models developed from in-vivo studies of animals (Ren et al., 2004) in conjunction with FEA wear simulations to predict the volumes of PE particles.

# 11 References

ABDUL-KADIR, M. R., HANSEN, U., KLABUNDE, R., LUCAS, D. & AMIS, A. 2008. Finite element modelling of primary hip stem stability: the effect of interference fit. *J Biomech,* 41**,** 587-94.

ADALBERTH, G., NILSSON, K. G., BYSTROM, S., KOLSTAD, K. & MILBRINK, J. 2001. All-polyethylene versus metal-backed and stemmed tibial components in cemented total knee arthroplasty. A prospective, randomised RSA study. *J Bone Joint Surg Br,* 83**,** 825-31.

AHLBERG, A. & LINDEN, B. 1977. The radiolucent zone in arthroplasty of the knee. *Acta Orthop Scand,* 48**,** 687-90.

AHMED, A. M., BURKE, D. L. & HYDER, A. 1987. Force analysis of the patellar mechanism. *J Orthop Res,* 5**,** 69-85.

AKHTER, M. P., CULLEN, D. M., PEDERSEN, E. A., KIMMEL, D. B. & RECKER, R. R. 1998. Bone response to in vivo mechanical loading in two breeds of mice. *Calcified tissue international,* 63**,** 442-9.

AL NAZER, R., LANOVAZ, J., KAWALILAK, C., JOHNSTON, J. D. & KONTULAINEN, S. 2012. Direct in vivo strain measurements in human bone—A systematic literature review. *Journal of Biomechanics,* 45**,** 27-40.

ALETO, T. J., BEREND, M. E., RITTER, M. A., FARIS, P. M. & MENEGHINI, R. M. 2008. Early Failure of Unicompartmental Knee Arthroplasty Leading to Revision. *The Journal of Arthroplasty,* 23**,** 159-163.

AMIS, A. A., GUPTE, C. M., BULL, A. M. & EDWARDS, A. 2006a. Anatomy of the posterior cruciate ligament and the meniscofemoral ligaments. *Knee Surg Sports Traumatol Arthrosc,* 14**,** 257-63.

AMIS, A. A., SENAVONGSE, W. & BULL, A. M. 2006b. Patellofemoral kinematics during knee flexion-extension: an in vitro study. *Journal of orthopaedic research : official publication of the Orthopaedic Research Society,* 24**,** 2201-11.

ANDERSON, A. E., PETERS, C. L., TUTTLE, B. D. & WEISS, J. A. 2005. Subject-specific finite element model of the pelvis: development, validation and sensitivity studies. *J Biomech Eng,* 127**,** 364-73.

ANDERSON, F. C. & PANDY, M. G. 2001. Dynamic optimization of human walking. *J Biomech Eng,* 123**,** 381-90.

ANDERSSON, L., WESSLAU, A., BODEN, H. & DALEN, N. 2001. Immediate or late weight bearing after uncemented total hip arthroplasty: a study of functional recovery. *J Arthroplasty,* 16**,** 1063-5.

ANDO, M., IMURA, S., OMORI, H., OKUMURA, Y., BO, A. & BABA, H. 1999. Nonlinear three-dimensional finite element analysis of newly designed cementless total hip stems. *Artif Organs,* 23**,** 339-46.

ANDRIACCHI, T. P., ANDERSSON, G. B., FERMIER, R. W., STERN, D. & GALANTE, J. O. 1980. A study of lower-limb mechanics during stair-climbing. *The Journal of bone and joint surgery. American volume,* 62**,** 749-57.

ANDRIACCHI, T. P., STANWYCK, T. S. & GALANTE, J. O. 1986. Knee biomechanics and total knee replacement. *J Arthroplasty,* 1**,** 211-9.

ANSARI, S., NEWMAN, J. H. & ACKROYD, C. E. 1997. St. Georg sledge for medial compartment knee replacement. 461 arthroplasties followed for 4 (1-17) years. *Acta Orthop Scand,* 68**,** 430-4.

APEL, D. M., TOZZI, J. M. & DORR, L. D. 1991. Clinical comparison of all-polyethylene and metal-backed tibial components in total knee arthroplasty. *Clin Orthop Relat Res***,** 243-52.

ARASTU, M. H., VIJAYARAGHAVAN, J., CHISSELL, H., HULL, J. B., NEWMAN, J. H. & ROBINSON, J. R. 2009. Early failure of a mobile-bearing unicompartmental knee replacement. *Knee Surg Sports Traumatol Arthrosc,* 17**,** 1178-83.

ARGENSON, J. N., CHEVROL-BENKEDDACHE, Y. & AUBANIAC, J. M. 2002. Modern unicompartmental knee arthroplasty with cement: a three to ten-year follow-up study. *J Bone Joint Surg Am,* 84-A**,** 2235-9.

ARGENSON, J. N. & PARRATTE, S. 2006. The unicompartmental knee: design and technical considerations in minimizing wear. *Clin Orthop Relat Res,* 452**,** 137-42.

ASSOR, M. & AUBANIAC, J. M. 2006. [Influence of rotatory malposition of femoral implant in failure of unicompartimental medial knee prosthesis]. *Rev Chir Orthop Reparatrice Appar Mot,* 92**,** 473-84.

BALIUNAS, A. J., HURWITZ, D. E., RYALS, A. B., KARRAR, A., CASE, J. P., BLOCK, J. A. & ANDRIACCHI, T. P. 2002. Increased knee joint loads during walking are present in subjects with knee osteoarthritis. *Osteoarthritis Cartilage,* 10**,** 573-9.

BARÉ, J. V., GILL, H. S., BEARD, D. J. & MURRAY, D. W. 2006. A convex lateral tibial plateau for knee replacement. *The Knee,* 13**,** 122-126.

BARKER, D. S., NETHERWAY, D. J., KRISHNAN, J. & HEARN, T. C. 2005. Validation of a finite element model of the human metacarpal. *Medical engineering & physics,* 27**,** 103-13.

BARTLEY, R. E., STULBERG, S. D., ROBB, W. J., 3RD & SWEENEY, H. J. 1994. Polyethylene wear in unicompartmental knee arthroplasty. *Clin Orthop Relat Res***,** 18-24.

BASSO, O., JOHNSON, D. P. & AMIS, A. A. 2001. The anatomy of the patellar tendon. *Knee Surg Sports Traumatol Arthrosc,* 9**,** 2-5.

BAYRAKTAR, H. H., GUPTA, A., KWON, R. Y., PAPADOPOULOS, P. & KEAVENY, T. M. 2004a. The modified super-ellipsoid yield criterion for human trabecular bone. *J Biomech Eng,* 126**,** 677-84.

BAYRAKTAR, H. H. & KEAVENY, T. M. 2004. Mechanisms of uniformity of yield strains for trabecular bone. *J Biomech,* 37**,** 1671-8.

BAYRAKTAR, H. H., MORGAN, E. F., NIEBUR, G. L., MORRIS, G. E., WONG, E. K. & KEAVENY, T. M. 2004b. Comparison of the elastic and yield properties of human femoral trabecular and cortical bone tissue. *J Biomech,* 37**,** 27-35.

BEAUPRE, G. S., ORR, T. E. & CARTER, D. R. 1990. An approach for time-dependent bone modeling and remodeling-application: a preliminary remodeling simulation. *J Orthop Res,* 8**,** 662-70.

BECKER, R., JOHN, M. & NEUMANN, W. H. 2004. Clinical outcomes in the revision of unicondylar arthoplasties to bicondylar arthroplasties. A matched-pair study. *Arch Orthop Trauma Surg,* 124**,** 702-7.

BERCHUCK, M., ANDRIACCHI, T. P., BACH, B. R. & REIDER, B. 1990. Gait adaptations by patients who have a deficient anterior cruciate ligament. *J Bone Joint Surg Am,* 72**,** 871-7.

BERGER, R. A., MENEGHINI, R. M., SHEINKOP, M. B., DELLA VALLE, C. J., JACOBS, J. J., ROSENBERG, A. G. & GALANTE, J. O. 2004. The progression of patellofemoral arthrosis after medial unicompartmental replacement: results at 11 to 15 years. *Clin Orthop Relat Res***,** 92-9.

BERGER, R. A., NEDEFF, D. D., BARDEN, R. M., SHEINKOP, M. M., JACOBS, J. J., ROSENBERG, A. G. & GALANTE, J. O. 1999. Unicompartmental knee arthroplasty. Clinical experience at 6- to 10-year followup. *Clin Orthop Relat Res*, 50-60.

BERGMANN, G., GRAICHEN, F., ROHLMANN, A., WESTERHOFF, P., HEINLEIN, B., BENDER, A. & EHRIG, R. 2008. Design and calibration of load sensing orthopaedic implants. *J Biomech Eng,* 130, 021009.

BERMAN, A. T., REID, J. S., YANICKO, D. R., JR., SIH, G. C. & ZIMMERMAN, M. R. 1984. Thermally induced bone necrosis in rabbits. Relation to implant failure in humans. *Clin Orthop Relat Res*, 284-92.

BERT, J. M. 1998. 10-year survivorship of metal-backed, unicompartmental arthroplasty. *J Arthroplasty,* 13, 901-5.

BESSHO, M., OHNISHI, I., OKAZAKI, H., SATO, W., KOMINAMI, H., MATSUNAGA, S. & NAKAMURA, K. 2004. Prediction of the strength and fracture location of the femoral neck by CT-based finite-element method: a preliminary study on patients with hip fracture. *Journal of Orthopaedic Science,* 9, 545-550.

BIEGLER, F. B., REUBEN, J. D., HARRIGAN, T. P., HOU, F. J. & AKIN, J. E. 1995. Effect of porous coating and loading conditions on total hip femoral stem stability. *J Arthroplasty,* 10, 839-47.

BITSAKOS, C. 2005. *Computer Simulation of Periprosthetic Bone Remodelling after Total Hip Arthroplasty.* Imperial College London.

BITSAKOS, C., KERNER, J., FISHER, I. & AMIS, A. A. 2005. The effect of muscle loading on the simulation of bone remodelling in the proximal femur. *J Biomech,* 38, 133-9.

BOHL, J. R., BOHL, W. R., POSTAK, P. D. & GREENWALD, A. S. 1999. The Coventry Award. The effects of shelf life on clinical outcome for gamma sterilized polyethylene tibial components. *Clin Orthop Relat Res*, 28-38.

BOHM, I. & LANDSIEDL, F. 2000. Revision surgery after failed unicompartmental knee arthroplasty: a study of 35 cases. *J Arthroplasty,* 15, 982-9.

BOHR, H. H. & LUND, B. 1987. Bone mineral density of the proximal tibia following uncemented arthroplasty. *The Journal of arthroplasty,* 2, 309-12.

BOURNE, R. B. & FINLAY, J. B. 1986. The influence of tibial component intramedullary stems and implant-cortex contact on the strain distribution of the proximal tibia following total knee arthroplasty. An in vitro study. *Clin Orthop Relat Res*, 95-9.

BRADLEY, J., GOODFELLOW, J. W. & O'CONNOR, J. J. 1987. A radiographic study of bearing movement in unicompartmental Oxford knee replacements. *J Bone Joint Surg Br,* 69, 598-601.

BRIEM, K. & SNYDER-MACKLER, L. 2009. Proximal gait adaptations in medial knee OA. *J Orthop Res,* 27, 78-83.

BRINKMANN, J. R. & PERRY, J. 1985. Rate and range of knee motion during ambulation in healthy and arthritic subjects. *Phys Ther,* 65, 1055-60.

BROWN, I. W. & RING, P. A. 1985. Osteolytic changes in the upper femoral shaft following porous-coated hip replacement. *J Bone Joint Surg Br,* 67, 218-21.

BUCKWALTER, J. A., SALTZMAN, C. & BROWN, T. 2004. The Impact of Osteoarthritis: Implications for Research. *Clinical Orthopaedics and Related Research,* 427, S6-S15 10.1097/01.blo.0000143938.30681.9d.

BURKE, D. W., GATES, E. I. & HARRIS, W. H. 1984. Centrifugation as a method of improving tensile and fatigue properties of acrylic bone cement. *J Bone Joint Surg Am,* 66, 1265-73.

BURKE, D. W., O'CONNOR, D. O., ZALENSKI, E. B., JASTY, M. & HARRIS, W. H. 1991. Micromotion of cemented and uncemented femoral components. *J Bone Joint Surg Br,* 73**,** 33-7.

BURR, D. B., MARTIN, R. B., SCHAFFLER, M. B. & RADIN, E. L. 1985. Bone remodeling in response to in vivo fatigue microdamage. *Journal of Biomechanics,* 18**,** 189-200.

BURR, D. B., MILGROM, C., FYHRIE, D., FORWOOD, M., NYSKA, M., FINESTONE, A., HOSHAW, S., SAIAG, E. & SIMKIN, A. 1996. In vivo measurement of human tibial strains during vigorous activity. *Bone,* 18**,** 405-10.

BUTLER, D. L., NOYES, F. R. & GROOD, E. S. 1980. Ligamentous restraints to anterior-posterior drawer in the human knee. A biomechanical study. *J Bone Joint Surg Am,* 62**,** 259-70.

CAMERON, H. U. & JUNG, Y. B. 1988. A comparison of unicompartmental knee replacement with total knee replacement. *Orthop Rev,* 17**,** 983-8.

CAMERON, H. U., PILLIAR, R. M. & MACNAB, I. 1973. The effect of movement on the bonding of porous metal to bone. *J Biomed Mater Res,* 7**,** 301-11.

CARLSSON, L., RÖSTLUND, T., ALBREKTSSON, B. & ALBREKTSSON, T. 1988. Implant fixation improved by close fit Cylindrical implant – bone interface studied in rabbits. *Acta Orthopaedica,* 59**,** 272-275.

CARTER, D. H., ORR, T. E., FYHRIE, D. & SCHURMAN, D. J. 1987a. Influences of Mechanical Stress on Prenatal and Postnatal Skeletal Development. *Clinical Orthopaedics and Related Research,* 219**,** 237-250.

CARTER, D. R., CALER, W. E., SPENGLER, D. M. & FRANKEL, V. H. 1981. Fatigue behavior of adult cortical bone: the influence of mean strain and strain range. *Acta orthopaedica Scandinavica,* 52**,** 481-90.

CARTER, D. R., FYHRIE, D. P. & WHALEN, R. T. 1987b. Trabecular bone density and loading history: regulation of connective tissue biology by mechanical energy. *J Biomech,* 20**,** 785-94.

CARTER, D. R. & HAYES, W. C. 1977. The compressive behavior of bone as a two-phase porous structure. *J Bone Joint Surg Am,* 59**,** 954-62.

CARTIER, P., SANOUILLER, J. L. & GRELSAMER, R. P. 1996. Unicompartmental knee arthroplasty surgery. 10-year minimum follow-up period. *J Arthroplasty,* 11**,** 782-8.

CHAKRABARTY, G., NEWMAN, J. H. & ACKROYD, C. E. 1998. Revision of unicompartmental arthroplasty of the knee. Clinical and technical considerations. *J Arthroplasty,* 13**,** 191-6.

CHANG, T.-W., YANG, C.-T., LIU, Y.-L., CHEN, W.-C., LIN, K.-J., LAI, Y.-S., HUANG, C.-H., LU, Y.-C. & CHENG, C.-K. 2011. Biomechanical evaluation of proximal tibial behavior following unicondylar knee arthroplasty: Modified resected surface with corresponding surgical technique. *Medical Engineering & Physics,* 33**,** 1175-1182.

CHAU, R., GULATI, A., PANDIT, H., BEARD, D. J., PRICE, A. J., DODD, C. A., GILL, H. S. & MURRAY, D. W. 2009. Tibial component overhang following unicompartmental knee replacement--does it matter? *Knee,* 16**,** 310-3.

CHONG, D. Y., HANSEN, U. N. & AMIS, A. A. 2010. Analysis of bone-prosthesis interface micromotion for cementless tibial prosthesis fixation and the influence of loading conditions. *J Biomech,* 43**,** 1074-80.

CHONG, D. Y. R. 2009. *Biomechanical Analysis of Fixation and Bone Remodelling of Total Knee Replacement.* PhD, Imperial College London.

CHONG, D. Y. R., HANSEN, U. N., VAN DER VENNE, R., VERDONSCHOT, N. & AMIS, A. A. 2011. The influence of tibial component fixation techniques on resorption of supporting bone stock after total knee replacement. *Journal of Biomechanics,* 44**,** 948-954.

CIARELLI, M. J., GOLDSTEIN, S. A., KUHN, J. L., CODY, D. D. & BROWN, M. B. 1991. Evaluation of orthogonal mechanical properties and density of human trabecular bone from the major metaphyseal regions with materials testing and computed tomography. *J Orthop Res,* 9**,** 674-82.

CLAES, L. E. & HEIGELE, C. A. 1999. Magnitudes of local stress and strain along bony surfaces predict the course and type of fracture healing. *Journal of Biomechanics,* 32**,** 255-266.

CLARIUS, M., ALDINGER, P. R., BRUCKNER, T. & SEEGER, J. B. 2009a. Saw cuts in unicompartmental knee arthroplasty: an analysis of Sawbone preparations. *Knee,* 16**,** 314-6.

CLARIUS, M., HAAS, D., ALDINGER, P. R., JAEGER, S., JAKUBOWITZ, E. & SEEGER, J. B. 2009b. Periprosthetic tibial fractures in unicompartmental knee arthroplasty as a function of extended sagittal saw cuts: An experimental study. *Knee*.

CLARIUS, M., MOHR, G., JAEGER, S., SEEGER, J. B. & BITSCH, R. G. 2010. Femoral fixation pattern in cemented Oxford unicompartmental knee arthroplasty — An experimental cadaver study. *The Knee,* 17**,** 398-402.

COBB, J. P., DIXON, H., DANDACHLI, W. & IRANPOUR, F. 2008. The anatomical tibial axis: reliable rotational orientation in knee replacement. *J Bone Joint Surg Br,* 90**,** 1032-8.

CODY, D. D., GROSS, G. J., HOU, F. J., SPENCER, H. J., GOLDSTEIN, S. A. & FYHRIE, D. P. 1999. Femoral strength is better predicted by finite element models than QCT and DXA. *Journal of Biomechanics,* 32**,** 1013-20.

COHEN, B. & RUSHTON, N. 1995. Accuracy of DEXA measurement of bone mineral density after total hip arthroplasty. *The Journal of bone and joint surgery. British volume,* 77**,** 479-83.

COHEN, Z. A., ROGLIC, H., GRELSAMER, R. P., HENRY, J. H., LEVINE, W. N., MOW, V. C. & ATESHIAN, G. A. 2001. Patellofemoral stresses during open and closed kinetic chain exercises. An analysis using computer simulation. *Am J Sports Med,* 29**,** 480-7.

COSTIGAN, P. A., DELUZIO, K. J. & WYSS, U. P. 2002. Knee and hip kinetics during normal stair climbing. *Gait Posture,* 16**,** 31-7.

COURTNEY, A. C., HAYES, W. C. & GIBSON, L. J. 1996. Age-related differences in post-yield damage in human cortical bone. Experiment and model. *Journal of Biomechanics,* 29**,** 1463-71.

COWIN, S. 1984. Mechanical modeling of the stress adaptation process in bone. *Calcified Tissue International,* 36**,** S98-S103.

COWIN, S. C. 1993. Bone stress adaptation models. *J Biomech Eng,* 115**,** 528-33.

COWIN, S. C. & FIROOZBAKHSH, K. 1981. Bone remodeling of diaphysial surfaces under constant load: Theoretical predictions. *Journal of Biomechanics,* 14**,** 471-484.

COWIN, S. C. & HEGEDUS, D. H. 1976. Bone remodeling I: theory of adaptive elasticity. *Journal of Elasticity,* 6**,** 313-326.

COWIN, S. C. & NACHLINGER, R. R. 1978. Bone remodeling III: uniqueness and stability in adaptive elasticity theory. *Journal of Elasticity,* 8**,** 285-295.

COWIN, S. C. & VAN BUSKIRK, W. C. 1978. Internal bone remodeling induced by a medullary pin. *Journal of Biomechanics,* 11**,** 269-275.

COWIN, S. C., WEINBAUM, S. & ZENG, Y. 1995. A case for bone canaliculi as the anatomical site of strain generated potentials. *Journal of Biomechanics,* 28**,** 1281-1297.

CRISTOFOLINI, L., AFFATATO, S., ERANI, P., LEARDINI, W., TIGANI, D. & VICECONTI, M. 2008. Long-term implant-bone fixation of the femoral component in total knee replacement. *Proc Inst Mech Eng H,* 222**,** 319-31.

CRISTOFOLINI, L., MCNAMARA, B. P., FREDDI, A. & VICECONTI, M. 1997. In vitro measured strains in the loaded femur: quantification of experimental error. *The Journal of Strain Analysis for Engineering Design,* 32**,** 193-200.

CRISTOFOLINI, L., VARINI, E. & VICECONTI, M. 2007. In-vitro method for assessing femoral implant-bone micromotions in resurfacing hip implants under different loading conditions. *Proc Inst Mech Eng H,* 221**,** 943-50.

CRISTOFOLINI, L., VICECONTI, M., CAPPELLO, A. & TONI, A. 1996. Mechanical validation of whole bone composite femur models. *Journal of Biomechanics,* 29**,** 525-35.

CURREY, J. D. 1975. The effects of strain rate, reconstruction and mineral content on some mechanical properties of bovine bone. *Journal of Biomechanics,* 8**,** 81-6.

CURREY, J. D. 1988. Strain rate and mineral content in fracture models of bone. *J Orthop Res,* 6**,** 32-8.

D'LIMA, D. D., PATIL, S., STEKLOV, N., CHIEN, S. & COLWELL, C. W., JR. 2007. In vivo knee moments and shear after total knee arthroplasty. *J Biomech,* 40 Suppl 1**,** S11-7.

D'LIMA, D. D., PATIL, S., STEKLOV, N., SLAMIN, J. E. & COLWELL, C. W., JR. 2005. The Chitranjan Ranawat Award: in vivo knee forces after total knee arthroplasty. *Clin Orthop Relat Res,* 440**,** 45-9.

D'LIMA, D. D., PATIL, S., STEKLOV, N., SLAMIN, J. E. & COLWELL, C. W., JR. 2006. Tibial forces measured in vivo after total knee arthroplasty. *J Arthroplasty,* 21**,** 255-62.

DABIRRAHMANI, D., SAMUELS, L., HOGG, M., ROONEY, J., APPLEYARD, R. & GILLIES, R. M. 2008. *RE:* ***Adaptive Bone Remodelling Following Unicompartmental Knee Arthroplasty.***

DALSTRA, M. & HUISKES, R. 1995. Load transfer across the pelvic bone. *J Biomech,* 28**,** 715-24.

DALSTRA, M., HUISKES, R. & VAN ERNING, L. 1995. Development and validation of a three-dimensional finite element model of the pelvic bone. *Journal of Biomechanical Engineering,* 117**,** 272-8.

DAVIES, J. P., BURKE, D. W., O'CONNOR, D. O. & HARRIS, W. H. 1987. Comparison of the fatigue characteristics of centrifuged and uncentrifuged Simplex P bone cement. *J Orthop Res,* 5**,** 366-71.

DESHMUKH, R. V. & SCOTT, R. D. 2002. Unicompartmental Knee Arthroplasty for Younger Patients: An Alternative View. *Clinical Orthopaedics and Related Research,* 404**,** 108-112.

DOBLARÉ, M. & GARCÍA, J. M. 2001. Application of an anisotropic bone-remodelling model based on a damage-repair theory to the analysis of the proximal femur before and after total hip replacement. *Journal of Biomechanics,* 34**,** 1157-1170.

DONAHUE, S. W., SHARKEY, N. A., MODANLOU, K. A., SEQUEIRA, L. N. & MARTIN, R. B. 2000. Bone strain and microcracks at stress fracture sites in human metatarsals. *Bone,* 27**,** 827-833.

DUNCAN, R. & MISLER, S. 1989. Voltage-activated and stretch-activated Ba2+ conducting channels in an osteoblast-like cell line (UMR 106). *FEBS Letters,* 251**,** 17-21.

EDWARDS, A., BULL, A. M. & AMIS, A. A. 2007a. The attachments of the anteromedial and posterolateral fibre bundles of the anterior cruciate ligament: Part 1: tibial attachment. *Knee Surg Sports Traumatol Arthrosc,* 15**,** 1414-21.

EDWARDS, A., BULL, A. M. & AMIS, A. A. 2007b. The attachments of the fiber bundles of the posterior cruciate ligament: an anatomic study. *Arthroscopy,* 23**,** 284-90.

EDWARDS, A., BULL, A. M. & AMIS, A. A. 2008. The attachments of the anteromedial and posterolateral fibre bundles of the anterior cruciate ligament. Part 2: femoral attachment. *Knee Surg Sports Traumatol Arthrosc,* 16**,** 29-36.

ELIAS, S. G., FREEMAN, M. A. & GOKCAY, E. I. 1990. A correlative study of the geometry and anatomy of the distal femur. *Clinical orthopaedics and related research***,** 98-103.

EMERSON, R. H., JR. 2007. Preoperative and postoperative limb alignment after Oxford unicompartmental knee arthroplasty. *Orthopedics,* 30**,** 32-4.

EMERSON, R. H., JR., HANSBOROUGH, T., REITMAN, R. D., ROSENFELDT, W. & HIGGINS, L. L. 2002. Comparison of a mobile with a fixed-bearing unicompartmental knee implant. *Clin Orthop Relat Res***,** 62-70.

EMERSON, R. H., JR. & HIGGINS, L. L. 2008. Unicompartmental knee arthroplasty with the oxford prosthesis in patients with medial compartment arthritis. *J Bone Joint Surg Am,* 90**,** 118-22.

ENGH, C. A., BOBYN, J. D. & GLASSMAN, A. H. 1987. Porous-coated hip replacement. The factors governing bone ingrowth, stress shielding, and clinical results. *J Bone Joint Surg Br,* 69**,** 45-55.

ENGH, C. A., MCGOVERN, T. F., BOBYN, J. D. & HARRIS, W. H. 1992a. A quantitative evaluation of periprosthetic bone-remodeling after cementless total hip arthroplasty. *The Journal of bone and joint surgery. American volume,* 74**,** 1009-20.

ENGH, C. A., O'CONNOR, D., JASTY, M., MCGOVERN, T., BOBYN, J. D. & HARRIS, W. H. Year. Quantification of implant micromotion, strain shielding, and bone resorption with porous-coated anatomic medullary locking femoral prostheses. *In:* Clinical Orthopaedics and Related Research, 1992b. 13-29.

ENGH, G. A., DWYER, K. A. & HANES, C. K. 1992c. Polyethylene wear of metal-backed tibial components in total and unicompartmental knee prostheses. *J Bone Joint Surg Br,* 74**,** 9-17.

EPINETTE, J. A. & MANLEY, M. T. 2008. Is hydroxyapatite a reliable fixation option in unicompartmental knee arthroplasty? A 5- to 13-year experience with the hydroxyapatite-coated unix prosthesis. *J Knee Surg,* 21**,** 299-306.

ERHART, J. C., MUNDERMANN, A., ELSPAS, B., GIORI, N. J. & ANDRIACCHI, T. P. 2010. Changes in knee adduction moment, pain, and functionality with a variable-stiffness walking shoe after 6 months. *J Orthop Res,* 28**,** 873-9.

ERIKSSON, R. A. & ALBREKTSSON, T. 1984. The effect of heat on bone regeneration: an experimental study in the rabbit using the bone growth chamber. *J Oral Maxillofac Surg,* 42**,** 705-11.

FAULKNER, K. G. & MCCLUNG, M. R. 1995. Quality control of DXA instruments in multicenter trials. *Osteoporosis International,* 5**,** 218-227.

FAZZALARI, N. L., FORWOOD, M. R., MANTHEY, B. A., SMITH, K. & KOLESIK, P. 1998. Three-dimensional confocal images of microdamage in cancellous bone. *Bone,* 23**,** 373-378.

FISHER, D. A., WATTS, M. & DAVIS, K. E. 2003. Implant position in knee surgery: a comparison of minimally invasive, open unicompartmental, and total knee arthroplasty. *J Arthroplasty,* 18**,** 2-8.

FITZ, W. 2009. Unicompartmental knee arthroplasty with use of novel patient-specific resurfacing implants and personalized jigs. *J Bone Joint Surg Am,* 91 Suppl 1**,** 69-76.

FITZPATRICK, C., FITZPATRICK, D., LEE, J. & AUGER, D. 2007. Statistical design of unicompartmental tibial implants and comparison with current devices. *Knee,* 14**,** 138-44.

FLEMING, D., ELLIOT, A. J., MILES, J., BARLEY, M. A. & GRANT, S. G. 2006. Annual Prevalence Report. Royal College of General Practioners - Birmingham Research Unit.

FRANCHI, M., FINI, M., MARTINI, D., ORSINI, E., LEONARDI, L., RUGGERI, A., GIAVARESI, G. & OTTANI, V. 2005. Biological fixation of endosseous implants. *Micron,* 36**,** 665-71.

FREEMAN, M. A. & PINSKEROVA, V. 2003. The movement of the knee studied by magnetic resonance imaging. *Clinical orthopaedics and related research***,** 35-43.

FREGLY, B. J., BANKS, S. A., D'LIMA, D. D. & COLWELL, C. W., JR. 2008. Sensitivity of knee replacement contact calculations to kinematic measurement errors. *J Orthop Res,* 26**,** 1173-9.

FROIMSON, M. I., BLOOMFIELD, M. R. & SHERMAN, R. A. 2009. Revision of the Failed Unicompartmental Knee Arthroplasty. *Seminars in Arthroplasty,* 20**,** 23-28.

FROLKE, J. P. & REELING BROUWER, G. C. 2004. Friction burns within the tibia during reaming. *J Bone Joint Surg Br,* 86**,** 149; author reply 149-50.

FROST, H. 1988. Vital biomechanics: Proposed general concepts for skeletal adaptations to mechanical usage. *Calcified Tissue International,* 42**,** 145-156.

FROST, H. M. 2001. From Wolff's law to the Utah paradigm: Insights about bone physiology and its clinical applications. *The Anatomical Record,* 262**,** 398-419.

FUKUBAYASHI, T. & KUROSAWA, H. 1980. The contact area and pressure distribution pattern of the knee. A study of normal and osteoarthrotic knee joints. *Acta Orthop Scand,* 51**,** 871-9.

FURNES, O., ESPEHAUG, B., LIE, S. A., VOLLSET, S. E., ENGESAETER, L. B. & HAVELIN, L. I. 2007. Failure mechanisms after unicompartmental and tricompartmental primary knee replacement with cement. *J Bone Joint Surg Am,* 89**,** 519-25.

FYHRIE, D. P. & CARTER, D. R. 1986. A unifying principle relating stress to trabecular bone morphology. *J Orthop Res,* 4**,** 304-17.

GIANNOUDIS, P. V., SNOWDEN, S., MATTHEWS, S. J., SMYE, S. W. & SMITH, R. M. 2002. Friction burns within the tibia during reaming. Are they affected by the use of a tourniquet? *J Bone Joint Surg Br,* 84**,** 492-6.

GIBSON, L. J. 1985. The mechanical behaviour of cancellous bone. *Journal of Biomechanics,* 18**,** 317-28.

GIBSON, L. J. & ASHBY, M. F. 1982. The Mechanics of Three-Dimensional Cellular Materials. *Proceedings of the Royal Society of London. Series A, Mathematical and Physical Sciences,* 382**,** 43-59.

GILL, H. S. & O'CONNOR, J. J. 1996. Biarticulating two-dimensional computer model of the human patellofemoral joint. *Clin Biomech (Bristol, Avon),* 11**,** 81-89.

GILLIES, R. M., HOGG, M. C., KOHAN, L. & CORDINGLEY, R. L. 2007. Adaptive bone remodelling of all polyethylene unicompartmental tibial bearings. *ANZ J Surg,* 77**,** 69-72.

GIOE, T. J., KILLEEN, K. K., HOEFFEL, D. P., BERT, J. M., COMFORT, T. K., SCHELTEMA, K., MEHLE, S. & GRIMM, K. 2003. Analysis of unicompartmental knee arthroplasty in a community-based implant registry. *Clin Orthop Relat Res***,** 111-9.

GLEESON, R. E., EVANS, R., ACKROYD, C. E., WEBB, J. & NEWMAN, J. H. 2004. Fixed or mobile bearing unicompartmental knee replacement? A comparative cohort study. *Knee,* 11**,** 379-84.

GOLDSTEIN, S. A., WILSON, D. L., SONSTEGARD, D. A. & MATTHEWS, L. S. 1983. The mechanical properties of human tibial trabecular bone as a function of metaphyseal location. *J Biomech,* 16**,** 965-9.

GOODFELLOW, J. 2006. *Unicompartmental Arthroplasty with the Oxford Knee*, Oxford University Press.

GOODFELLOW, J., HUNGERFORD, D. S. & WOODS, C. 1976a. Patello-femoral joint mechanics and pathology. 2. Chondromalacia patellae. *J Bone Joint Surg Br,* 58**,** 291-9.

GOODFELLOW, J., HUNGERFORD, D. S. & ZINDEL, M. 1976b. Patello-femoral joint mechanics and pathology. 1. Functional anatomy of the patello-femoral joint. *J Bone Joint Surg Br,* 58**,** 287-90.

GOODFELLOW, J. & O'CONNOR, J. 1978. The mechanics of the knee and prosthesis design. *J Bone Joint Surg Br,* 60-B**,** 358-69.

GOODFELLOW, J. W., O'CONNOR, J. J. & MURRAY, D. W. 2010. A critique of revision rate as an outcome measure: RE-INTERPRETATION OF KNEE JOINT REGISTRY DATA. *J Bone Joint Surg Br,* 92-B**,** 1628-1631.

GOODFELLOW, J. W., TIBREWAL, S. B., SHERMAN, K. P. & O'CONNOR, J. J. 1987. Unicompartmental Oxford Meniscal knee arthroplasty. *J Arthroplasty,* 2**,** 1-9.

GOTZE, C., STEENS, W., VIETH, V., POREMBA, C., CLAES, L. & STEINBECK, J. 2002. Primary stability in cementless femoral stems: custom-made versus conventional femoral prosthesis. *Clin Biomech (Bristol, Avon),* 17**,** 267-73.

GOUDAKOS, I. G., KONIG, C., SCHOTTLE, P. B., TAYLOR, W. R., SINGH, N. B., ROBERTS, I., STREITPARTH, F., DUDA, G. N. & HELLER, M. O. 2009. Stair climbing results in more challenging patellofemoral contact mechanics and kinematics than walking at early knee flexion under physiological-like quadriceps loading. *J Biomech,* 42**,** 2590-6.

GRAY, H. A., TADDEI, F., ZAVATSKY, A. B., CRISTOFOLINI, L. & GILL, H. S. 2008. Experimental validation of a finite element model of a human cadaveric tibia. *J Biomech Eng,* 130**,** 031016.

GRAY, H. A., ZAVATSKY, A. B. & GILL, H. S. 2010. The sclerotic line: Why it appears under knee replacements (a study based on the Oxford Knee). *Clinical biomechanics (Bristol, Avon),* 25**,** 242-247.

GRIFFIN, T., ROWDEN, N., MORGAN, D., ATKINSON, R., WOODRUFF, P. & MADDERN, G. 2007. Unicompartmental knee arthroplasty for the treatment of unicompartmental osteoarthritis: a systematic study. *ANZ J Surg,* 77**,** 214-21.

GULATI, A., CHAU, R., PANDIT, H. G., GRAY, H., PRICE, A. J., DODD, C. A. & MURRAY, D. W. 2009a. The incidence of physiological radiolucency following Oxford unicompartmental knee replacement and its relationship to outcome. *J Bone Joint Surg Br,* 91**,** 896-902.

GULATI, A., PANDIT, H., JENKINS, C., CHAU, R., DODD, C. A. & MURRAY, D. W. 2009b. The effect of leg alignment on the outcome of unicompartmental knee replacement. *J Bone Joint Surg Br,* 91**,** 469-74.

GUPTA, S., VAN DER HELM, F. C., STERK, J. C., VAN KEULEN, F. & KAPTEIN, B. L. 2004. Development and experimental validation of a three-dimensional finite element model of the human scapula. *Proc Inst Mech Eng H,* 218**,** 127-42.

HANSEN, U., ZIOUPOS, P., SIMPSON, R., CURREY, J. D. & HYND, D. 2008. The effect of strain rate on the mechanical properties of human cortical bone. *Journal of Biomechanical Engineering,* 130**,** 011011.

HARRIGAN, T. P. & HAMILTON, J. J. 1992. An analytical and numerical study of the stability of bone remodelling theories: Dependence on microstructural stimulus. *Journal of Biomechanics,* 25**,** 477-488.

HARRIGAN, T. P. & HAMILTON, J. J. 1993. Bone strain sensation via transmembrane potential changes in surface osteoblasts: Loading rate and microstructural implications. *Journal of Biomechanics,* 26**,** 183-200.

HARRIGAN, T. P. & HARRIS, W. H. 1991. A three-dimensional non-linear finite element study of the effect of cement-prosthesis debonding in cemented femoral total hip components. *J Biomech,* 24**,** 1047-58.

HARRINGTON, I. J. 1976. A bioengineering analysis of force actions at the knee in normal and pathological gait. *Biomed Eng,* 11**,** 167-72.

HARRINGTON, I. J. 1983. Static and dynamic loading patterns in knee joints with deformities. *J Bone Joint Surg Am,* 65**,** 247-59.

HART, R. T., DAVY, D. T. & HEIPLE, K. G. 1984. Mathematical modeling and numerical solutions for functionally dependent bone remodeling. *Calcified tissue international,* 36 Suppl 1**,** S104-9.

HASEGAWA, Y., OOISHI, Y., SHIMIZU, T., SUGIURA, H., TAKAHASHI, S., ITO, H. & IWATA, H. 1998. Unicompartmental knee arthroplasty for medial gonarthrosis: 5 to 9 years follow-up evaluation of 77 knees. *Arch Orthop Trauma Surg,* 117**,** 183-7.

HASHEMI, J., CHANDRASHEKAR, N., GILL, B., BEYNNON, B. D., SLAUTERBECK, J. R., SCHUTT, R. C., JR., MANSOURI, H. & DABEZIES, E. 2008. The geometry of the tibial plateau and its influence on the biomechanics of the tibiofemoral joint. *J Bone Joint Surg Am,* 90**,** 2724-34.

HECK, D. A., MARMOR, L., GIBSON, A. & ROUGRAFF, B. T. 1993. Unicompartmental knee arthroplasty. A multicenter investigation with long-term follow-up evaluation. *Clin Orthop Relat Res***,** 154-9.

HEGEDUS, D. H. & COWIN, S. C. 1976. Bone remodeling II: small strain adaptive elasticity. *Journal of Elasticity,* 6**,** 337-352.

HELGASON, B., PERILLI, E., SCHILEO, E., TADDEI, F., BRYNJOLFSSON, S. & VICECONTI, M. 2008. Mathematical relationships between bone density and mechanical properties: a literature review. *Clin Biomech (Bristol, Avon),* 23**,** 135-46.

HELMICK, C. G., FELSON, D. T., LAWRENCE, R. C., GABRIEL, S., HIRSCH, R., KWOH, C. K., LIANG, M. H., KREMERS, H. M., MAYES, M. D., MERKEL, P. A., PILLEMER, S. R., REVEILLE, J. D., STONE, J. H. & NATIONAL ARTHRITIS DATA, W. 2008. Estimates of the prevalence of arthritis and other rheumatic conditions in the United States: Part I. *Arthritis & Rheumatism,* 58**,** 15-25.

HERNIGOU, P. & DESCHAMPS, G. 2004. Posterior slope of the tibial implant and the outcome of unicompartmental knee arthroplasty. *J Bone Joint Surg Am,* 86-A**,** 506-11.

HERNIGOU, P., POIGNARD, A., FILIPPINI, P. & ZILBER, S. 2008. Retrieved Unicompartmental Implants with Full PE Tibial Components: The Effects of Knee Alignment and Polyethylene Thickness on Creep and Wear. *The open orthopaedics journal,* 2**,** 51-6.

HERRERA, A., PANISELLO, J. J., IBARZ, E., CEGOÑINO, J., PUÉRTOLAS, J. A. & GRACIA, L. 2007. Long-term study of bone remodelling after femoral stem: A comparison between dexa and finite element simulation. *Journal of Biomechanics,* 40**,** 3615-3625.

HEYSE, T. & TIBESKU, C. 2010. Lateral unicompartmental knee arthroplasty: a review. *Archives of Orthopaedic and Trauma Surgery,* 130**,** 1539-1548.

HILL, P. F., VEDI, V., WILLIAMS, A., IWAKI, H., PINSKEROVA, V. & FREEMAN, M. A. 2000. Tibiofemoral movement 2: the loaded and unloaded living knee studied by MRI. *The Journal of bone and joint surgery. British volume,* 82**,** 1196-8.

HOPKINS, A. R., NEW, A. M., RODRIGUEZ, Y. B. F. & TAYLOR, M. 2009. Finite element analysis of unicompartmental knee arthroplasty. *Med Eng Phys*.

HUANG, C. H., HO, F. Y., MA, H. M., YANG, C. T., LIAU, J. J., KAO, H. C., YOUNG, T. H. & CHENG, C. K. 2002. Particle size and morphology of UHMWPE wear debris in failed total knee arthroplasties--a comparison between mobile bearing and fixed bearing knees. *J Orthop Res,* 20**,** 1038-41.

HUBERTI, H. H. & HAYES, W. C. 1984. Patellofemoral contact pressures. The influence of q-angle and tendofemoral contact. *J Bone Joint Surg Am,* 66**,** 715-24.

HUISKES, A. H. & STOLK, J. 2005. Biomechanics and Preclinical testing of Artificial Joints: The Hip. *In:* MOW, C. S. & HUISKES, A. H. (eds.) *Basic Orthopaedic Biomechanics And Mechano-Biology.* 3 ed.: Lippincott Williams and Wilkins.

HUISKES, R. & RIETBERGEN, B. V. 1995. Preclinical Testing of Total Hip Stems: The Effects of Coating Placement. *Clinical Orthopaedics and Related Research,* 319**,** 64-76.

HUISKES, R., WEINANS, H., GROOTENBOER, H. J., DALSTRA, M., FUDALA, B. & SLOOFF, T. J. 1987. Adaptive bone-remodeling theory applied to prosthetic-design analysis. *J Biomech,* 20**,** 1135-50.

HUNGERFORD, D. S. & KENNA, R. V. 1983. Preliminary experience with a total knee prosthesis with porous coating used without cement. *Clin Orthop Relat Res***,** 95-107.

HURWITZ, D. E., SUMNER, D. R., ANDRIACCHI, T. P. & SUGAR, D. A. 1998. Dynamic knee loads during gait predict proximal tibial bone distribution. *J Biomech,* 31**,** 423-30.

HVID, I., BENTZEN, S. M. & JORGENSEN, J. 1986. Remodeling of trabecular bone at the proximal tibia after total knee replacement. A CT-scan study. *Eng Med,* 15**,** 89-93.

HVID, I., BENTZEN, S. M. & JORGENSEN, J. 1988. Remodeling of the tibial plateau after knee replacement. CT bone densitometry. *Acta orthopaedica Scandinavica,* 59**,** 567-73.

HVID, I., BENTZEN, S. M., LINDE, F., MOSEKILDE, L. & PONGSOIPETCH, B. 1989. X-ray quantitative computed tomography: the relations to physical properties of proximal tibial trabecular bone specimens. *J Biomech,* 22**,** 837-44.

HVID, I. & NIELSEN, S. 1984. Total condylar knee arthroplasty. Prosthetic component positioning and radiolucent lines. *Acta Orthop Scand,* 55**,** 160-5.

HYLDAHL, H., REGNER, L., CARLSSON, L., KARRHOLM, J. & WEIDENHIELM, L. 2005. All-polyethylene vs. metal-backed tibial component in total knee arthroplasty-a randomized RSA study comparing early fixation of horizontally and completely cemented tibial components: part 2. Completely cemented components: MB not superior to AP components. *Acta Orthop,* 76**,** 778-84.

HYLDAHL, H. C., REGNER, L., CARLSSON, L., KARRHOLM, J. & WEIDENHIELM, L. 2001. Does metal backing improve fixation of tibial component in unicondylar knee arthroplasty? A randomized radiostereometric analysis. *J Arthroplasty,* 16**,** 174-9.

IMAI, K., OHNISHI, I., BESSHO, M. & NAKAMURA, K. 2006. Nonlinear finite element model predicts vertebral bone strength and fracture site. *Spine (Phila Pa 1976),* 31**,** 1789-94.

INMAN, V. T., ROLSTON, H.J., TODD, F. 1981. *Human Walking,* Baltimore, Williams & Wilkins Co.

INSALL, J. & AGLIETTI, P. 1980. A five to seven-year follow-up of unicondylar arthroplasty. *J Bone Joint Surg Am,* 62**,** 1329-37.

JASTY, M., BRAGDON, C., BURKE, D., O'CONNOR, D., LOWENSTEIN, J. & HARRIS, W. H. 1997a. In vivo skeletal responses to porous-surfaced implants subjected to small induced motions. *J Bone Joint Surg Am,* 79**,** 707-14.

JASTY, M., BRAGDON, C. R., ZALENSKI, E., O'CONNOR, D., PAGE, A. & HARRIS, W. H. 1997b. Enhanced stability of uncemented canine femoral components by bone ingrowth into the porous coatings. *J Arthroplasty,* 12**,** 106-13.

JASTY, M., MALONEY, W. J., BRAGDON, C. R., O'CONNOR, D. O., HAIRE, T. & HARRIS, W. H. 1991. The initiation of failure in cemented femoral components of hip arthroplasties. *J Bone Joint Surg Br,* 73**,** 551-8.

JAWORSKI, Z., LISKOVA-KIAR, M. & UHTHOFF, H. 1980. Effect of long-term immobilisation on the pattern of bone loss in older dogs. *J Bone Joint Surg Br,* 62-B**,** 104-110.

JOHAL, P., WILLIAMS, A., WRAGG, P., HUNT, D. & GEDROYC, W. 2005. Tibio-femoral movement in the living knee. A study of weight bearing and non-weight bearing knee kinematics using 'interventional' MRI. *Journal of Biomechanics,* 38**,** 269-76.

JOHNSON, F., LEITL, S. & WAUGH, W. 1980. The distribution of load across the knee. A comparison of static and dynamic measurements. *J Bone Joint Surg Br,* 62**,** 346-9.

KAISER, A. D. & WHITESIDE, L. A. 1990. The effect of screws and pegs on the initial fixation stability of an uncemented unicondylar knee replacement. *Clin Orthop Relat Res***,** 169-78.

KALRA, S., SMITH, T. O., BERKO, B. & WALTON, N. P. 2011. Assessment of radiolucent lines around the Oxford unicompartmental knee replacement: sensitivity and specificity for loosening. *J Bone Joint Surg Br,* 93**,** 777-81.

KANEKO, T. S., BELL, J. S., PEJCIC, M. R., TEHRANZADEH, J. & KEYAK, J. H. 2004. Mechanical properties, density and quantitative CT scan data of trabecular bone with and without metastases. *Journal of Biomechanics,* 37**,** 523-530.

KASODEKAR, V. B., YEO, S. J. & OTHMAN, S. 2006. Clinical outcome of unicompartmental knee arthroplasty and influence of alignment on prosthesis survival rate. *Singapore Med J,* 47**,** 796-802.

KEAVENY, T. M. & BARTEL, D. L. 1993. Effects of porous coating, with and without collar support, on early relative motion for a cementless hip prosthesis. *J Biomech,* 26**,** 1355-68.

KEAVENY, T. M. & HAYES, W. C. 1993. A 20-year perspective on the mechanical properties of trabecular bone. *J Biomech Eng,* 115**,** 534-42.

KEAVENY, T. M., MORGAN, E. F. & YEH, O. C. 2003. Bone Mechanics. *In:* KUTZ, M. (ed.) *Standard handbook of biomedical engineering and design*

1ed. New York: McGraw-Hill.

KEAVENY, T. M., PINILLA, T. P., CRAWFORD, R. P., KOPPERDAHL, D. L. & LOU, A. 1997. Systematic and random errors in compression testing of trabecular bone. *J Orthop Res,* 15**,** 101-10.

KEAVENY, T. M. & YEH, O. C. 2002. Architecture and trabecular bone - toward an improved understanding of the biomechanical effects of age, sex and osteoporosis. *J Musculoskelet Neuronal Interact,* 2**,** 205-8.

KEENE, G., SIMPSON, D. & KALAIRAJAH, Y. 2006. Limb alignment in computer-assisted minimally-invasive unicompartmental knee replacement. *J Bone Joint Surg Br,* 88**,** 44-8.

KENNEDY, W. R. & WHITE, R. P. 1987. Unicompartmental arthroplasty of the knee. Postoperative alignment and its influence on overall results. *Clin Orthop Relat Res*, 278-85.

KERNER, J., HUISKES, R., VAN LENTHE, G. H., WEINANS, H., VAN RIETBERGEN, B., ENGH, C. A. & AMIS, A. A. 1999. Correlation between pre-operative periprosthetic bone density and post-operative bone loss in THA can be explained by strain-adaptive remodelling. *J Biomech,* 32, 695-703.

KEYAK, J. H., FOURKAS, M. G., MEAGHER, J. M. & SKINNER, H. B. 1993. Validation of an automated method of three-dimensional finite element modelling of bone. *J Biomed Eng,* 15, 505-9.

KEYAK, J. H., KANEKO, T. S., TEHRANZADEH, J. & SKINNER, H. B. 2005. Predicting proximal femoral strength using structural engineering models. *Clinical orthopaedics and related research*, 219-28.

KEYAK, J. H., LEE, I. Y. & SKINNER, H. B. 1994. Correlations between orthogonal mechanical properties and density of trabecular bone: use of different densitometric measures. *J Biomed Mater Res,* 28, 1329-36.

KEYAK, J. H., ROSSI, S. A., JONES, K. A. & SKINNER, H. B. 1998. Prediction of femoral fracture load using automated finite element modeling. *Journal of Biomechanics,* 31, 125-33.

KEYS, G. W., UL-ABIDDIN, Z. & TOH, E. M. 2004. Analysis of first forty Oxford medial unicompartmental knee replacement from a small district hospital in UK. *Knee,* 11, 375-7.

KHODADADYAN-KLOSTERMANN, C., VON SEEBACH, M., TAYLOR, W. R., DUDA, G. N. & HAAS, N. P. 2004. Distribution of bone mineral density with age and gender in the proximal tibia. *Clin Biomech (Bristol, Avon),* 19, 370-6.

KIRATLI, B. J., HEINER, J. P., MCBEATH, A. A. & WILSON, M. A. 1992. Determination of bone mineral density by dual x-ray absorptiometry in patients with uncemented total hip arthroplasty. *Journal of orthopaedic research : official publication of the Orthopaedic Research Society,* 10, 836-44.

KNUTSON, K., LINDSTRAND, A. & LIDGREN, L. 1986. Survival of knee arthroplasties. A nation-wide multicentre investigation of 8000 cases. *J Bone Joint Surg Br,* 68, 795-803.

KOSKINEN, E., ESKELINEN, A., PAAVOLAINEN, P., PULKKINEN, P. & REMES, V. 2008. Comparison of survival and cost-effectiveness between unicondylar arthroplasty and total knee arthroplasty in patients with primary osteoarthritis: a follow-up study of 50,493 knee replacements from the Finnish Arthroplasty Register. *Acta Orthop,* 79, 499-507.

KOSKINEN, E., PAAVOLAINEN, P., ESKELINEN, A., PULKKINEN, P. & REMES, V. 2007. Unicondylar knee replacement for primary osteoarthritis: a prospective follow-up study of 1,819 patients from the Finnish Arthroplasty Register. *Acta Orthop,* 78, 128-35.

KOWALK, D. L., DUNCAN, J. A. & VAUGHAN, C. L. 1996. Abduction-adduction moments at the knee during stair ascent and descent. *J Biomech,* 29, 383-8.

KOZINN, S. C. & SCOTT, R. 1989. Unicondylar knee arthroplasty. *J Bone Joint Surg Am,* 71, 145-50.

KUIPER, J. H. & HUISKES, R. 1996. Friction and stem stiffness affect dynamic interface motion in total hip replacement. *J Orthop Res,* 14, 36-43.

KUMAR, A., CHAMBERS, I. & WONG, P. 2008. Periprosthetic fracture of the proximal tibia after lateral unicompartmental knee arthroplasty. *J Arthroplasty,* 23, 615-8.

KURTZ, S., ONG, K., LAU, E., WIDMER, M., MARAVIC, M., GÓMEZ-BARRENA, E., DE FÁTIMA DE PINA, M., MANNO, V., TORRE, M., WALTER, W., DE STEIGER, R., GEESINK, R., PELTOLA, M. & RÖDER, C. 2011. International survey of primary and revision total knee replacement. *International Orthopaedics,* 35, 1783-1789.

KURTZ, S. M., DUMBLETON, J., SISKEY, R. S., WANG, A. & MANLEY, M. 2009a. Trace concentrations of vitamin E protect radiation crosslinked UHMWPE from oxidative degradation. *Journal of Biomedical Materials Research Part A,* 90A**,** 549-563.

KURTZ, S. M., LAU, E., ONG, K., ZHAO, K., KELLY, M. & BOZIC, K. J. 2009b. Future young patient demand for primary and revision joint replacement: national projections from 2010 to 2030. *Clin Orthop Relat Res,* 467**,** 2606-12.

KURTZ, S. M., MURATOGLU, O. K., EVANS, M. & EDIDIN, A. A. 1999. Advances in the processing, sterilization, and crosslinking of ultra-high molecular weight polyethylene for total joint arthroplasty. *Biomaterials,* 20**,** 1659-1688.

KURTZ, S. M., ONG, K. L., SCHMIER, J., MOWAT, F., SALEH, K., DYBVIK, E., KARRHOLM, J., GARELLICK, G., HAVELIN, L. I., FURNES, O., MALCHAU, H. & LAU, E. 2007. Future clinical and economic impact of revision total hip and knee arthroplasty. *J Bone Joint Surg Am,* 89 Suppl 3**,** 144-51.

KURTZ, S. M., PRUITT, L., JEWETT, C. W., PAUL CRAWFORD, R., CRANE, D. J. & EDIDIN, A. A. 1998. The yielding, plastic flow, and fracture behavior of ultra-high molecular weight polyethylene used in total joint replacements. *Biomaterials,* 19**,** 1989-2003.

KUZYK, P. R. & SCHEMITSCH, E. H. 2011. The basic science of peri-implant bone healing. *Indian journal of orthopaedics,* 45**,** 108-15.

KWONG, L. M., JASTY, M., MULROY, R. D., MALONEY, W. J., BRAGDON, C. & HARRIS, W. H. 1992. The histology of the radiolucent line. *J Bone Joint Surg Br,* 74**,** 67-73.

LANDON, G. C., GALANTE, J. O. & MALEY, M. M. 1986. Noncemented total knee arthroplasty. *Clin Orthop Relat Res***,** 49-57.

LANYON, L. E. 1987. Functional strain in bone tissue as an objective, and controlling stimulus for adaptive bone remodelling. *Journal of Biomechanics,* 20**,** 1083-1093.

LANYON, L. E., HAMPSON, W. G., GOODSHIP, A. E. & SHAH, J. S. 1975. Bone deformation recorded in vivo from strain gauges attached to the human tibial shaft. *Acta Orthop Scand,* 46**,** 256-68.

LANYON, L. E. & RUBIN, C. T. 1984. Static vs dynamic loads as an influence on bone remodelling. *Journal of Biomechanics,* 17**,** 897-905.

LARSEN, S. T. & RYD, L. 1989. Temperature elevation during knee arthroplasty. *Acta Orthop Scand,* 60**,** 439-42.

LASKIN, R. S. 1978. Unicompartmental tibiofemoral resurfacing arthroplasty. *J Bone Joint Surg Am,* 60**,** 182-5.

LASKIN, R. S. 2001. Unicompartmental knee replacement: some unanswered questions. *Clin Orthop Relat Res***,** 267-71.

LAURENCIN, C. T., ZELICOF, S. B., SCOTT, R. D. & EWALD, F. C. 1991. Unicompartmental Versus Total Knee Arthroplasty in the Same Patient. *Clinical Orthopaedics and Related Research,* 273**,** 151-156.

LAZ, P. J., STOWE, J. Q., BALDWIN, M. A., PETRELLA, A. J. & RULLKOETTER, P. J. 2007. Incorporating uncertainty in mechanical properties for finite element-based evaluation of bone mechanics. *J Biomech,* 40**,** 2831-6.

LEE, R. W., VOLZ, R. G. & SHERIDAN, D. C. 1991. The role of fixation and bone quality on the mechanical stability of tibial knee components. *Clin Orthop Relat Res***,** 177-83.

LENGSFELD, M., GÜNTHER, D., PRESSEL, T., LEPPEK, R., SCHMITT, J. & GRISS, P. 2002. Validation data for periprosthetic bone remodelling theories. *Journal of Biomechanics,* 35**,** 1553-1564.

LENNON, A. B. & PRENDERGAST, P. J. 2002. Residual stress due to curing can initiate damage in porous bone cement: experimental and theoretical evidence. *J Biomech,* 35**,** 311-21.

LESLIE, B. W., GARDNER, D. L., MCGEOUGH, J. A. & MORAN, R. S. 2000. Anisotropic response of the human knee joint meniscus to unconfined compression. *Proc Inst Mech Eng H,* 214**,** 631-5.

LEVENSTON, M. E., BEAUPRÉ, G. S., JACOBS, C. R. & CARTER, D. R. 1994. The role of loading memory in bone adaptation simulations. *Bone,* 15**,** 177-186.

LEVITZ, C. L., LOTKE, P. A. & KARP, J. S. 1995. Long-term changes in bone mineral density following total knee replacement. *Clinical orthopaedics and related research***,** 68-72.

LEWIS, G. 1997. Properties of acrylic bone cement: state of the art review. *J Biomed Mater Res,* 38**,** 155-82.

LEWIS, G., NYMAN, J. S. & TRIEU, H. H. 1997. Effect of mixing method on selected properties of acrylic bone cement. *J Biomed Mater Res,* 38**,** 221-8.

LEWOLD, S., ROBERTSSON, O., KNUTSON, K. & LIDGREN, L. 1998. Revision of unicompartmental knee arthroplasty: outcome in 1,135 cases from the Swedish Knee Arthroplasty study. *Acta Orthop Scand,* 69**,** 469-74.

LI, G., PAPANNAGARI, R., NHA, K. W., DEFRATE, L. E., GILL, T. J. & RUBASH, H. E. 2007. The coupled motion of the femur and patella during in vivo weightbearing knee flexion. *J Biomech Eng,* 129**,** 937-43.

LI, M. G. & NILSSON, K. G. 2000. Changes in bone mineral density at the proximal tibia after total knee arthroplasty: a 2-year follow-up of 28 knees using dual energy X-ray absorptiometry. *Journal of orthopaedic research : official publication of the Orthopaedic Research Society,* 18**,** 40-7.

LI, M. G., YAO, F., JOSS, B., IOPPOLO, J., NIVBRANT, B. & WOOD, D. 2006. Mobile vs. fixed bearing unicondylar knee arthroplasty: A randomized study on short term clinical outcomes and knee kinematics. *Knee,* 13**,** 365-70.

LINDE, F., HVID, I. & MADSEN, F. 1992. The effect of specimen geometry on the mechanical behaviour of trabecular bone specimens. *J Biomech,* 25**,** 359-68.

LINDSTRAND, A. & STENSTROM, A. 1992. Polyethylene wear of the PCA unicompartmental knee. Prospective 5 (4-8) year study of 120 arthrosis knees. *Acta Orthop Scand,* 63**,** 260-2.

LINDSTRAND, A., STENSTROM, A. & EGUND, N. 1988. The PCA unicompartmental knee. A 1-4-year comparison of fixation with or without cement. *Acta Orthop Scand,* 59**,** 695-700.

LINGARAJ, K., MORRIS, H. & BARTLETT, J. 2010. Polyethylene thickness in unicompartmental knee arthroplasty. *Knee*.

LIVINGSTON, L. A. & MANDIGO, J. L. 1999. Bilateral Q angle asymmetry and anterior knee pain syndrome. *Clinical Biomechanics,* 14**,** 7-13.

LONNER, J. H., KLOTZ, M., LEVITZ, C. & LOTKE, P. A. 2001. Changes in bone density after cemented total knee arthroplasty: influence of stem design. *The Journal of arthroplasty,* 16**,** 107-11.

LOTZ, J. C., CHEAL, E. J. & HAYES, W. C. 1991. Fracture Prediction for the Proximal Femur Using Finite Element Models: Part I---Linear Analysis. *Journal of Biomechanical Engineering,* 113**,** 353-360.

LUND, B. 2011. Swedish Knee Arthroplasty Annual Report. *Dept. of Orthopedics, Skåne University Hospital* [Online].

LUSTIG, S., PAILLOT, J. L., SERVIEN, E., HENRY, J., AIT SI SELMI, T. & NEYRET, P. 2009. Cemented all polyethylene tibial insert unicompartimental knee arthroplasty: A long term follow-up study. *Orthopaedics & Traumatology: Surgery & Research,* 95**,** 12-21.

MACKINNON, J., YOUNG, S. & BAILY, R. A. 1988. The St Georg sledge for unicompartmental replacement of the knee. A prospective study of 115 cases. *J Bone Joint Surg Br,* 70**,** 217-23.

MALONEY, W. J., JASTY, M., BURKE, D. W., O'CONNOR, D. O., ZALENSKI, E. B., BRAGDON, C. & HARRIS, W. H. 1989. Biomechanical and histologic investigation of cemented total hip arthroplasties. A study of autopsy-retrieved femurs after in vivo cycling. *Clin Orthop Relat Res***,** 129-40.

MANIATOPOULOS, C., PILLIAR, R. M. & SMITH, D. C. 1986. Threaded versus porous-surfaced designs for implant stabilization in bone-endodontic implant model. *J Biomed Mater Res,* 20**,** 1309-33.

MANN, K. A., MILLER, M. A., CLEARY, R. J., JANSSEN, D. & VERDONSCHOT, N. 2008. Experimental micromechanics of the cement–bone interface. *Journal of Orthopaedic Research,* 26**,** 872-879.

MANN, K. A., MILLER, M. A., VERDONSCHOT, N., IZANT, T. H. & RACE, A. 2010. Functional interface micromechanics of 11 en-bloc retrieved cemented femoral hip replacements. *Acta orthopaedica,* 81**,** 308-17.

MANN, K. A., MOCARSKI, R., DAMRON, L. A., ALLEN, M. J. & AYERS, D. C. 2001. Mixed-mode failure response of the cement-bone interface. *J Orthop Res,* 19**,** 1153-61.

MARKOLF, K. L., MENSCH, J. S. & AMSTUTZ, H. C. 1976. Stiffness and laxity of the knee--the contributions of the supporting structures. A quantitative in vitro study. *The Journal of bone and joint surgery. American volume,* 58**,** 583-94.

MARMOR, L. 1976. The Modular (Marmor) knee: case report with a minimum follow-up of 2 years. *Clin Orthop Relat Res***,** 86-94.

MARMOR, L. 1988. Unicompartmental knee arthroplasty. Ten- to 13-year follow-up study. *Clin Orthop Relat Res***,** 14-20.

MAROTTI, G., FERRETTI, M., MUGLIA, M. A., PALUMBO, C. & PALAZZINI, S. 1992. A quantitative evaluation of osteoblast-osteocyte relationships on growing endosteal surface of rabbit tibiae. *Bone,* 13**,** 363-368.

MARTELLI, S., ZAFFAGNINI, S., FALCIONI, B. & MOTTA, M. 2002. Comparison of three kinematic analyses of the knee: determination of intrinsic features and applicability to intraoperative procedures. *Computer methods in biomechanics and biomedical engineering,* 5**,** 175-85.

MARTIN, B. R. 1972. The effects of geometric feedback in the development of osteoporosis. *Journal of Biomechanics,* 5**,** 447-455.

MARTIN, R. B. 2000. Toward a unifying theory of bone remodeling. *Bone,* 26**,** 1-6.

MATSUDA, S., MIURA, H., NAGAMINE, R., URABE, K., IKENOUE, T., OKAZAKI, K. & IWAMOTO, Y. 1999. Posterior tibial slope in the normal and varus knee. *Am J Knee Surg,* 12**,** 165-8.

MATTHEWS, L. S., SONSTEGARD, D. A. & HENKE, J. A. 1977. Load bearing characteristics of the patello-femoral joint. *Acta Orthop Scand,* 48**,** 511-6.

MCBROOM, R. J., HAYES, W. C., EDWARDS, W. T., GOLDBERG, R. P. & WHITE, A. A., 3RD 1985. Prediction of vertebral body compressive fracture using quantitative computed tomography. *J Bone Joint Surg Am,* 67**,** 1206-14.

MCCALDEN, R. W., MCGEOUGH, J. A., BARKER, M. B. & COURT-BROWN, C. M. 1993. Age-related changes in the tensile properties of cortical bone. The relative importance of changes in porosity, mineralization, and microstructure. *J Bone Joint Surg Am,* 75**,** 1193-205.

MCCARTHY, C. K., STEINBERG, G. G., AGREN, M., LEAHEY, D., WYMAN, E. & BARAN, D. T. 1991. Quantifying bone loss from the proximal femur after total hip arthroplasty. *The Journal of bone and joint surgery. British volume,* 73**,** 774-8.

MCNAMARA, L. M. & PRENDERGAST, P. J. 2007. Bone remodelling algorithms incorporating both strain and microdamage stimuli. *Journal of Biomechanics,* 40**,** 1381-1391.

MESSIER, S. P., LOESER, R. F., HOOVER, J. L., SEMBLE, E. L. & WISE, C. M. 1992. Osteoarthritis of the knee: effects on gait, strength, and flexibility. *Arch Phys Med Rehabil,* 73**,** 29-36.

MILGROM, C., FINESTONE, A., HAMEL, A., MANDES, V., BURR, D. & SHARKEY, N. 2004. A comparison of bone strain measurements at anatomically relevant sites using surface gauges versus strain gauged bone staples. *J Biomech,* 37**,** 947-52.

MILLER, M. A., EBERHARDT, A. W., CLEARY, R. J., VERDONSCHOT, N. & MANN, K. A. 2010. Micromechanics of postmortem-retrieved cement-bone interfaces. *J Orthop Res,* 28**,** 170-7.

MINODA, Y., IKEBUCHI, M., KOBAYASHI, A., IWAKI, H., INORI, F. & NAKAMURA, H. 2010. A cemented mobile-bearing total knee replacement prevents periprosthetic loss of bone mineral density around the femoral component: a matched cohort study. *J Bone Joint Surg Br,* 92**,** 794-8.

MISKOVSKY, C., WHITESIDE, L. A. & WHITE, S. E. 1992. The cemented unicondylar knee arthroplasty. An in vitro comparison of three cement techniques. *Clin Orthop Relat Res***,** 215-20.

MONK, A. P., KEYS, G. W. & MURRAY, D. W. 2009. Loosening of the femoral component after unicompartmental knee replacement. *J Bone Joint Surg Br,* 91**,** 405-7.

MOORE, D. J., FREEMAN, M. A., REVELL, P. A., BRADLEY, G. W. & TUKE, M. 1998. Can a total knee replacement prosthesis be made entirely of polymers? *J Arthroplasty,* 13**,** 388-95.

MORGAN, E. F., BAYRAKTAR, H. H. & KEAVENY, T. M. 2003. Trabecular bone modulus-density relationships depend on anatomic site. *J Biomech,* 36**,** 897-904.

MORGAN, E. F., BAYRAKTAR, H. H., YEH, O. C., MAJUMDAR, S., BURGHARDT, A. & KEAVENY, T. M. 2004. Contribution of inter-site variations in architecture to trabecular bone apparent yield strains. *J Biomech,* 37**,** 1413-20.

MORGAN, E. F. & KEAVENY, T. M. 2001. Dependence of yield strain of human trabecular bone on anatomic site. *J Biomech,* 34**,** 569-77.

MORRISON, J. B. 1968. Bioengineering analysis of force actions transmitted by the knee joint. *Biomed Eng*.

MORRISON, J. B. 1969. Function of the knee joint in various activities. *Biomed Eng,* 4**,** 573-80.

MORRISON, J. B. 1970a. The mechanics of muscle function in locomotion. *J Biomech,* 3**,** 431-51.

MORRISON, J. B. 1970b. The mechanics of the knee joint in relation to normal walking. *J Biomech,* 3**,** 51-61.

MOSLEY, J. R. & LANYON, L. E. 1998. Strain rate as a controlling influence on adaptive modeling in response to dynamic loading of the ulna in growing male rats. *Bone,* 23**,** 313-8.

MOSLEY, J. R., MARCH, B. M., LYNCH, J. & LANYON, L. E. 1997. Strain magnitude related changes in whole bone architecture in growing rats. *Bone,* 20**,** 191-8.

MUKHERJEE, K., PANDIT, H., DODD, C. A., OSTLERE, S. & MURRAY, D. W. 2008. The Oxford unicompartmental knee arthroplasty: a radiological perspective. *Clin Radiol,* 63**,** 1169-76.

MUNRO, J. T., PANDIT, S., WALKER, C. G., CLATWORTHY, M. & PITTO, R. P. 2010. Loss of tibial bone density in patients with rotating- or fixed-platform TKA. *Clin Orthop Relat Res,* 468**,** 775-81.

MURPHY, B. P. & PRENDERGAST, P. J. 2002. The relationship between stress, porosity, and nonlinear damage accumulation in acrylic bone cement. *J Biomed Mater Res,* 59**,** 646-54.

MURRAY, D. W., GOODFELLOW, J. W. & O'CONNOR, J. J. 1998. The Oxford medial unicompartmental arthroplasty: a ten-year survival study. *J Bone Joint Surg Br,* 80**,** 983-9.

NAGAMINE, R., MIURA, H., INOUE, Y., URABE, K., MATSUDA, S., OKAMOTO, Y., NISHIZAWA, M. & IWAMOTO, Y. 1998. Reliability of the anteroposterior axis and the posterior condylar axis for determining rotational alignment of the femoral component in total knee arthroplasty. *J Orthop Sci,* 3**,** 194-8.

NICOLELLA, D. P. & LANKFORD, J. 2002. Microstructural strain near osteocyte lacuna in cortical bone in vitro. *J Musculoskelet Neuronal Interact,* 2**,** 261-3.

NIEBUR, G. L., FELDSTEIN, M. J., YUEN, J. C., CHEN, T. J. & KEAVENY, T. M. 2000. High-resolution finite element models with tissue strength asymmetry accurately predict failure of trabecular bone. *Journal of Biomechanics,* 33**,** 1575-83.

O'CONNOR, J., GOODFELLOW, J. & PERRY, N. 1982. Fixation of the tibial components of the Oxford knee. *Orthop Clin North Am,* 13**,** 65-87.

O'CONNOR, J. & IMRAN, A. 2007. Bearing movement after Oxford unicompartmental knee arthroplasty: a mathematical model. *Orthopedics,* 30**,** 42-5.

O'ROURKE, M. R., GARDNER, J. J., CALLAGHAN, J. J., LIU, S. S., GOETZ, D. D., VITTETOE, D. A., SULLIVAN, P. M. & JOHNSTON, R. C. 2005. The John Insall Award: unicompartmental knee replacement: a minimum twenty-one-year followup, end-result study. *Clin Orthop Relat Res,* 440**,** 27-37.

ODDING, E., VALKENBURG, H. A., ALGRA, D., VANDENOUWELAND, F. A., GROBBEE, D. E. & HOFMAN, A. 1998. Associations of radiological osteoarthritis of the hip and knee with locomotor disability in the Rotterdam Study. *Ann Rheum Dis,* 57**,** 203-8.

ODGAARD, A. & LINDE, F. 1991. The underestimation of Young's modulus in compressive testing of cancellous bone specimens. *J Biomech,* 24**,** 691-8.

OTA, T., YAMAMOTO, I. & MORITA, R. 1999. Fracture simulation of the femoral bone using the finite-element method: how a fracture initiates and proceeds. *J Bone Miner Metab,* 17**,** 108-12.

OZCIVICI, E., LUU, Y. K., ADLER, B., QIN, Y.-X., RUBIN, J., JUDEX, S. & RUBIN, C. T. 2010. Mechanical signals as anabolic agents in bone. *Nat Rev Rheumatol,* 6**,** 50-59.

PANDIT, H., JENKINS, C., BARKER, K., DODD, C. A. & MURRAY, D. W. 2006. The Oxford medial unicompartmental knee replacement using a minimally-invasive approach. *J Bone Joint Surg Br,* 88**,** 54-60.

PANDIT, H., JENKINS, C., BEARD, D. J., GALLAGHER, J., PRICE, A. J., DODD, C. A., GOODFELLOW, J. W. & MURRAY, D. W. 2009. Cementless Oxford unicompartmental knee replacement shows reduced radiolucency at one year. *J Bone Joint Surg Br,* 91**,** 185-9.

PANDIT, H., MURRAY, D. W., DODD, C. A., DEO, S., WAITE, J., GOODFELLOW, J. & GIBBONS, C. L. 2007. Medial tibial plateau fracture and the Oxford unicompartmental knee. *Orthopedics,* 30**,** 28-31.

PANDIT, H., VAN DUREN, B. H., GALLAGHER, J. A., BEARD, D. J., DODD, C. A., GILL, H. S. & MURRAY, D. W. 2008. Combined anterior cruciate reconstruction and Oxford unicompartmental knee arthroplasty: in vivo kinematics. *Knee,* 15**,** 101-6.

PANDIT, H., WARD, T., HOLLINGHURST, D., BEARD, D. J., GILL, H. S., THOMAS, N. P. & MURRAY, D. W. 2005. Influence of surface geometry and the cam-post mechanism on the kinematics of total knee replacement. *The Journal of bone and joint surgery. British volume,* 87**,** 940-5.

PATTIN, C. A., CALER, W. E. & CARTER, D. R. 1996. Cyclic mechanical property degradation during fatigue loading of cortical bone. *Journal of Biomechanics,* 29**,** 69-79.

PEARSON, O. M. & LIEBERMAN, D. E. 2004. The aging of Wolff's “law”: Ontogeny and responses to mechanical loading in cortical bone. *American Journal of Physical Anthropology,* 125**,** 63-99.

PENG, L., BAI, J., ZENG, X. & ZHOU, Y. 2006. Comparison of isotropic and orthotropic material property assignments on femoral finite element models under two loading conditions. *Med Eng Phys,* 28**,** 227-33.

PERILLO-MARCONE, A., ALONSO-VAZQUEZ, A. & TAYLOR, M. 2003. Assessment of the effect of mesh density on the material property discretisation within QCT based FE models: a practical example using the implanted proximal tibia. *Comput Methods Biomech Biomed Engin,* 6**,** 17-26.

PETERSEN, M. M., JENSEN, N. C., GEHRCHEN, P. M., NIELSEN, P. K. & NIELSEN, P. T. 1996. The relation between trabecular bone strength and bone mineral density assessed by dual photon and dual energy X-ray absorptiometry in the proximal tibia. *Calcified tissue international,* 59**,** 311-4.

PETERSEN, M. M., NIELSEN, P. T., LAURITZEN, J. B. & LUND, B. 1995a. Changes in bone mineral density of the proximal tibia after uncemented total knee arthroplasty. A 3-year follow-up of 25 knees. *Acta Orthop Scand,* 66**,** 513-6.

PETERSEN, M. M., OLSEN, C., LAURITZEN, J. B. & LUND, B. 1995b. Changes in bone mineral density of the distal femur following uncemented total knee arthroplasty. *J Arthroplasty,* 10**,** 7-11.

PILLIAR, R. M., LEE, J. M. & MANIATOPOULOS, C. 1986. Observations on the effect of movement on bone ingrowth into porous-surfaced implants. *Clin Orthop Relat Res***,** 108-13.

POLGAR, K., VICECONTI, M. & O'CONNOR, J. J. 2001. A comparison between automatically generated linear and parabolic tetrahedra when used to mesh a human femur. *Proc Inst Mech Eng H,* 215**,** 85-94.

POPE, M. H. & OUTWATER, J. O. 1974. Mechanical properties of bone as a function of position and orientation. *J Biomech,* 7**,** 61-6.

PRENDERGAST, P. J., HUISKES, R. & SØBALLE, K. 1997. Biophysical stimuli on cells during tissue differentiation at implant interfaces. *Journal of Biomechanics,* 30**,** 539-548.

PRENDERGAST, P. J. & TAYLOR, D. 1994. Prediction of bone adaptation using damage accumulation. *Journal of Biomechanics,* 27**,** 1067-1076.

PRICE, A. & SVARD, U. 2011. A Second Decade Lifetable Survival Analysis of the Oxford Unicompartmental Knee Arthroplasty. *Clinical Orthopaedics and Related Research®,* 469**,** 174-179.

PRICE, A. J., DODD, C. A., SVARD, U. G. & MURRAY, D. W. 2005a. Oxford medial unicompartmental knee arthroplasty in patients younger and older than 60 years of age. *J Bone Joint Surg Br,* 87**,** 1488-92.

PRICE, A. J., REES, J. L., BEARD, D. J., GILL, R. H., DODD, C. A. & MURRAY, D. M. 2004. Sagittal plane kinematics of a mobile-bearing unicompartmental knee arthroplasty at 10 years: a comparative in vivo fluoroscopic analysis. *The Journal of arthroplasty,* 19**,** 590-7.

PRICE, A. J., WAITE, J. C. & SVARD, U. 2005b. Long-term clinical results of the medial Oxford unicompartmental knee arthroplasty. *Clin Orthop Relat Res***,** 171-80.

PRICE, C. P. 2000. Evidence-based laboratory medicine: supporting decision-making. *Clin Chem,* 46**,** 1041-50.

PSYCHOYIOS, V., CRAWFORD, R. W., O'CONNOR, J. J. & MURRAY, D. W. 1998. Wear of congruent meniscal bearings in unicompartmental knee arthroplasty: a retrieval study of 16 specimens. *J Bone Joint Surg Br,* 80**,** 976-82.

RAJASEKHAR, C., DAS, S. & SMITH, A. 2004. Unicompartmental knee arthroplasty. 2- to 12-year results in a community hospital. *J Bone Joint Surg Br,* 86**,** 983-5.

RANCOURT, D., SHIRAZIADL, A., DROUIN, G. & PAIEMENT, G. 1990. Friction Properties of the Interface between Porous-Surfaced Metals and Tibial Cancellous Bone. *Journal of Biomedical Materials Research,* 24**,** 1503-1519.

RAND, J. A. 1993. Comparison of metal-backed and all-polyethylene tibial components in cruciate condylar total knee arthroplasty. *J Arthroplasty,* 8**,** 307-13.

REA, P., SHORT, A., PANDIT, H., PRICE, A. J., KYBERD, P., BEARD, D. J., GILL, H. S. & MURRAY, D. W. 2007. Radiolucency and migration after Oxford unicompartmental knee arthroplasty. *Orthopedics,* 30**,** 24-7.

REEVES, N. D., MAGANARIS, C. N. & NARICI, M. V. 2003. Effect of strength training on human patella tendon mechanical properties of older individuals. *J Physiol,* 548**,** 971-81.

REGISTRY, A. N. J. R. 2011. Demographics of Knee Arthroplasty Australian Orthopaedic Association.

REN, W., YANG, S. Y. & WOOLEY, P. H. 2004. A novel murine model of orthopaedic wear-debris associated osteolysis. *Scand J Rheumatol,* 33**,** 349-57.

RHO, J. Y., ASHMAN, R. B. & TURNER, C. H. 1993. Young's modulus of trabecular and cortical bone material: ultrasonic and microtensile measurements. *J Biomech,* 26**,** 111-9.

RHO, J. Y., HOBATHO, M. C. & ASHMAN, R. B. 1995. Relations of mechanical properties to density and CT numbers in human bone. *Med Eng Phys,* 17**,** 347-55.

RHO, J. Y., TSUI, T. Y. & PHARR, G. M. 1997. Elastic properties of human cortical and trabecular lamellar bone measured by nanoindentation. *Biomaterials,* 18**,** 1325-30.

RICE, J. C., COWIN, S. C. & BOWMAN, J. A. 1988. On the dependence of the elasticity and strength of cancellous bone on apparent density. *J Biomech,* 21**,** 155-68.

RIDGEWAY, S. R., MCAULEY, J. P., AMMEEN, D. J. & ENGH, G. A. 2002. The effect of alignment of the knee on the outcome of unicompartmental knee replacement. *J Bone Joint Surg Br,* 84**,** 351-5.

RITTER, M. A., ZHOU, H., KEATING, C. M., KEATING, E. M., FARIS, P. M., MEDING, J. B. & BEREND, M. E. 1999. Radiological factors influencing femoral and acetabular failure in cemented Charnley total hip arthroplasties. *J Bone Joint Surg Br,* 81-B**,** 982-986.

ROBERTSON, D. D., MINTZER, C. M., WEISSMAN, B. N., EWALD, F. C., LEBOFF, M. & SPECTOR, M. 1994. Distal loss of femoral bone following total knee arthroplasty.

Measurement with visual and computer-processing of roentgenograms and dual-energy x-ray absorptiometry. *The Journal of bone and joint surgery. American volume,* 76**,** 66-76.

ROBERTSSON, O., KNUTSON, K., LEWOLD, S. & LIDGREN, L. 2001a. The routine of surgical management reduces failure after unicompartmental knee arthroplasty. *J Bone Joint Surg Br,* 83**,** 45-9.

ROBERTSSON, O., KNUTSON, K., LEWOLD, S. & LIDGREN, L. 2001b. The Swedish Knee Arthroplasty Register 1975-1997: An update with special emphasis on 41,223 knees operated on in 1988-1997. *Acta Orthopaedica,* 72**,** 503-513.

ROBINSON, E. J., MULLIKEN, B. D., BOURNE, R. B., RORABECK, C. H. & ALVAREZ, C. 1995. Catastrophic osteolysis in total knee replacement. A report of 17 cases. *Clinical Orthopaedics and Related Research***,** 98-105.

ROBLING, A. G., BURR, D. B. & TURNER, C. H. 2000. Partitioning a daily mechanical stimulus into discrete loading bouts improves the osteogenic response to loading. *Journal of bone and mineral research : the official journal of the American Society for Bone and Mineral Research,* 15**,** 1596-602.

RODAN, G. & MARTIN, T. 1981. Role of osteoblasts in hormonal control of bone resorption—A hypothesis. *Calcified Tissue International,* 33**,** 349-351.

RODRIGUEZ, J. A., BAEZ, N., RASQUINHA, V. & RANAWAT, C. S. 2001. Metal-backed and all-polyethylene tibial components in total knee replacement. *Clin Orthop Relat Res***,** 174-83.

ROSA, R. A., BERT, J. M., BRUCE, W., GROSS, M., CARROLL, M. & HARTDEGEN, V. 2002. An evaluation of all-ultra-high molecular weight polyethylene unicompartmental tibial component cement-fixation mechanisms. *J Bone Joint Surg Am,* 84-A Suppl 2**,** 102-4.

RUIMERMAN, R., VAN RIETBERGEN, B., HILBERS, P. & HUISKES, R. 2005. The effects of trabecular-bone loading variables on the surface signaling potential for bone remodeling and adaptation. *Ann Biomed Eng,* 33**,** 71-8.

RYD, L., ALBREKTSSON, B. E., CARLSSON, L., DANSGARD, F., HERBERTS, P., LINDSTRAND, A., REGNER, L. & TOKSVIG-LARSEN, S. 1995. Roentgen stereophotogrammetric analysis as a predictor of mechanical loosening of knee prostheses. *J Bone Joint Surg Br,* 77**,** 377-83.

RYD, L., BOEGARD, T., EGUND, N., LINDSTRAND, A., SELVIK, G. & THORNGREN, K. G. 1983. Migration of the tibial component in successful unicompartmental knee arthroplasty. A clinical, radiographic and roentgen stereophotogrammetric study. *Acta Orthop Scand,* 54**,** 408-16.

SAARI, T., UVEHAMMER, J., CARLSSON, L., REGNÉR, L. & KÄRRHOLM, J. 2007. Joint area constraint had no influence on bone loss in proximal tibia 5 years after total knee replacement. *Journal of Orthopaedic Research,* 25**,** 798-803.

SAENZ, C. L., MCGRATH, M. S., MARKER, D. R., SEYLER, T. M., MONT, M. A. & BONUTTI, P. M. 2010. Early failure of a unicompartmental knee arthroplasty design with an all-polyethylene tibial component. *Knee,* 17**,** 53-6.

SAHA, S. & PAL, S. 1984. Mechanical properties of bone cement: a review. *Journal of Biomedical Materials Research,* 18**,** 435-62.

SALDANHA, K. A., KEYS, G. W., SVARD, U. C., WHITE, S. H. & RAO, C. 2007. Revision of Oxford medial unicompartmental knee arthroplasty to total knee arthroplasty - results of a multicentre study. *Knee,* 14**,** 275-9.

SAN ANTONIO, T., CIACCIA, M., MÜLLER-KARGER, C. & CASANOVA, E. 2011. Orientation of orthotropic material properties in a femur FE model: A method based on the principal stresses directions. *Medical Engineering & Physics*.

SCHAFFLER, M. B. & BURR, D. B. 1988. Stiffness of compact bone: effects of porosity and density. *J Biomech,* 21**,** 13-6.

SCHILEO, E., DALL'ARA, E., TADDEI, F., MALANDRINO, A., SCHOTKAMP, T., BALEANI, M. & VICECONTI, M. 2008a. An accurate estimation of bone density improves the accuracy of subject-specific finite element models. *Journal of Biomechanics,* 41**,** 2483-91.

SCHILEO, E., TADDEI, F., CRISTOFOLINI, L. & VICECONTI, M. 2008b. Subject-specific finite element models implementing a maximum principal strain criterion are able to estimate failure risk and fracture location on human femurs tested in vitro. *J Biomech,* 41**,** 356-67.

SCHILEO, E., TADDEI, F., MALANDRINO, A., CRISTOFOLINI, L. & VICECONTI, M. 2007. Subject-specific finite element models can accurately predict strain levels in long bones. *J Biomech,* 40**,** 2982-9.

SCHINDLER, O. S., SCOTT, W. N. & SCUDERI, G. R. 2010. The practice of unicompartmental knee arthroplasty in the United Kingdom. *J Orthop Surg (Hong Kong),* 18**,** 312-9.

SCHIPPLEIN, O. D. & ANDRIACCHI, T. P. 1991. Interaction between active and passive knee stabilizers during level walking. *J Orthop Res,* 9**,** 113-9.

SCOTT, C. E., HOWIE, C. R., MACDONALD, D. & BIANT, L. C. 2010. Predicting dissatisfaction following total knee replacement: a prospective study of 1217 patients. *J Bone Joint Surg Br,* 92**,** 1253-8.

SCOTT, R. D., COBB, A. G., MCQUEARY, F. G. & THORNHILL, T. S. 1991. Unicompartmental knee arthroplasty. Eight- to 12-year follow-up evaluation with survivorship analysis. *Clin Orthop Relat Res***,** 96-100.

SCUDERI, R. G., TRIA, J. A. & BERGER, A. R. 2005. *MIS Techniques in Orthopedics*, Springer.

SEEGER, J., HAAS, D., JÄGER, S., RÖHNER, E., TOHTZ, S. & CLARIUS, M. 2011. Extended sagittal saw cut significantly reduces fracture load in cementless unicompartmental knee arthroplasty compared to cemented tibia plateaus: an experimental cadaver study. *Knee Surgery, Sports Traumatology, Arthroscopy***,** 1-5.

SEITZ, P., RUEGSEGGER, P., GSCHWEND, N. & DUBS, L. 1987. Changes in local bone density after knee arthroplasty. The use of quantitative computed tomography. *The Journal of bone and joint surgery. British volume,* 69**,** 407-11.

SEON, J. K., SONG, E. K., YOON, T. R., SEO, H. Y. & CHO, S. G. 2007. Tibial plateau stress fracture after unicondylar knee arthroplasty using a navigation system: two case reports. *Knee Surg Sports Traumatol Arthrosc,* 15**,** 67-70.

SHAKESPEARE, D. & JEFFCOTE, B. 2003. Unicondylar arthroplasty of the knee--cheap at half the price? *Knee,* 10**,** 357-61.

SHEFELBINE, S. J., AUGAT, P., CLAES, L. & SIMON, U. 2005. Trabecular bone fracture healing simulation with finite element analysis and fuzzy logic. *Journal of Biomechanics,* 38**,** 2440-2450.

SHELBURNE, K. B., PANDY, M. G., ANDERSON, F. C. & TORRY, M. R. 2004. Pattern of anterior cruciate ligament force in normal walking. *J Biomech,* 37**,** 797-805.

SHELBURNE, K. B., TORRY, M. R. & PANDY, M. G. 2006. Contributions of muscles, ligaments, and the ground-reaction force to tibiofemoral joint loading during normal gait. *J Orthop Res,* 24**,** 1983-90.

SHIRAZI-ADL, A., DAMMAK, M. & PAIEMENT, G. 1993. Experimental determination of friction characteristics at the trabecular bone/porous-coated metal interface in cementless implants. *J Biomed Mater Res,* 27**,** 167-75.

SHULTZ, T. R., BLAHA, J. D., GRUEN, T. A. & NORMAN, T. L. 2006. Cortical bone viscoelasticity and fixation strength of press-fit femoral stems: finite element model. *J Biomech Eng,* 128**,** 7-12.

SIMPSON, D. J., GRAY, H., D'LIMA, D., MURRAY, D. W. & GILL, H. S. 2008. The effect of bearing congruency, thickness and alignment on the stresses in unicompartmental knee replacements. *Clin Biomech (Bristol, Avon),* 23**,** 1148-57.

SIMPSON, D. J., KENDRICK, B. J., DODD, C. A., PRICE, A. J., GILL, H. S. & MURRAY, D. W. 2011. Load transfer in the proximal tibia following implantation with a unicompartmental knee replacement: a static snapshot. *Proc Inst Mech Eng H,* 225**,** 521-9.

SIMPSON, D. J., PRICE, A. J., GULATI, A., MURRAY, D. W. & GILL, H. S. 2009. Elevated proximal tibial strains following unicompartmental knee replacement-A possible cause of pain. *Med Eng Phys*.

SKOWRONSKI, J., JATSKEWYCH, J., DLUGOSZ, J., SKOWRONSKI, R. & BIELECKI, M. 2005. The Oxford II medial unicompartmental knee replacement. A minimum 10-year follow-up study. *Ortop Traumatol Rehabil,* 7**,** 620-5.

SKYRME, A. D., MENCIA, M. M. & SKINNER, P. W. 2002. Early failure of the porous-coated anatomic cemented unicompartmental knee arthroplasty: A 5- to 9-year follow-up study. *J Arthroplasty,* 17**,** 201-5.

SMALL, S. R., BEREND, M. E., RITTER, M. A., BUCKLEY, C. A. & ROGGE, R. D. 2010. Metal Backing Significantly Decreases Tibial Strains in a Medial Unicompartmental Knee Arthroplasty Model. *J Arthroplasty*.

SNYDER, S. M. & SCHNEIDER, E. 1991. Estimation of mechanical properties of cortical bone by computed tomography. *J Orthop Res,* 9**,** 422-31.

SOBALLE, K., HANSEN, E. S., BROCKSTEDT-RASMUSSEN, H., PEDERSEN, C. M. & BUNGER, C. 1990. Hydroxyapatite coating enhances fixation of porous coated implants. A comparison in dogs between press fit and noninterference fit. *Acta Orthop Scand,* 61**,** 299-306.

SOBALLE, K., HANSEN, E. S., H, B. R., JORGENSEN, P. H. & BUNGER, C. 1992. Tissue ingrowth into titanium and hydroxyapatite-coated implants during stable and unstable mechanical conditions. *J Orthop Res,* 10**,** 285-99.

SONTAG, W. 1992. Age-dependent morphometric alterations in the distal femora of male and female rats. *Bone,* 13**,** 297-310.

SQUIRE, M. W., CALLAGHAN, J. J., GOETZ, D. D., SULLIVAN, P. M. & JOHNSTON, R. C. 1999. Unicompartmental knee replacement. A minimum 15 year followup study. *Clin Orthop Relat Res***,** 61-72.

STAUFFER, R. N., CHAO, E. Y. & GYORY, A. N. 1977. Biomechanical gait analysis of the diseased knee joint. *Clin Orthop Relat Res***,** 246-55.

STEELE, R. G., HUTABARAT, S., EVANS, R. L., ACKROYD, C. E. & NEWMAN, J. H. 2006. Survivorship of the St Georg Sled medial unicompartmental knee replacement beyond ten years. *J Bone Joint Surg Br,* 88-B**,** 1164-1168.

STELZER, M. & VON STRYK, O. 2006. Efficient forward dynamics simulation and optimization of human body dynamics. *ZAMM - Journal of Applied Mathematics and Mechanics / Zeitschrift für Angewandte Mathematik und Mechanik,* 86**,** 828-840.

SVARD, U. C. & PRICE, A. J. 2001. Oxford medial unicompartmental knee arthroplasty. A survival analysis of an independent series. *J Bone Joint Surg Br,* 83**,** 191-4.

SZMUKLER-MONCLER, S., SALAMA, H., REINGEWIRTZ, Y. & DUBRUILLE, J. H. 1998. Timing of loading and effect of micromotion on bone-dental implant interface: review of experimental literature. *J Biomed Mater Res,* 43**,** 192-203.

TABOR JR, O. B. & TABOR, O. B. 1998. Unicompartmental arthroplasty: A long-term follow-up study. *The Journal of Arthroplasty,* 13**,** 373-379.

TADDEI, F., CRISTOFOLINI, L., MARTELLI, S., GILL, H. S. & VICECONTI, M. 2006. Subject-specific finite element models of long bones: An in vitro evaluation of the overall accuracy. *Journal of Biomechanics,* 39**,** 2457-67.

TADDEI, F., PANCANTI, A. & VICECONTI, M. 2004. An improved method for the automatic mapping of computed tomography numbers onto finite element models. *Medical engineering & physics,* 26**,** 61-9.

TADDEI, F., SCHILEO, E., HELGASON, B., CRISTOFOLINI, L. & VICECONTI, M. 2007. The material mapping strategy influences the accuracy of CT-based finite element models of bones: an evaluation against experimental measurements. *Med Eng Phys,* 29**,** 973-9.

TAKEDA, H., NAKAGAWA, T., NAKAMURA, K. & ENGEBRETSEN, L. 2011. Prevention and management of knee osteoarthritis and knee cartilage injury in sports. *British Journal of Sports Medicine,* 45**,** 304-309.

TAYLOR, M., TANNER, K. E. & FREEMAN, M. A. 1998. Finite element analysis of the implanted proximal tibia: a relationship between the initial cancellous bone stresses and implant migration. *J Biomech,* 31**,** 303-10.

TAYLOR, S. J. & WALKER, P. S. 2001. Forces and moments telemetered from two distal femoral replacements during various activities. *J Biomech,* 34**,** 839-48.

TAYLOR, W. R., HELLER, M. O., BERGMANN, G. & DUDA, G. N. 2004. Tibio-femoral loading during human gait and stair climbing. *J Orthop Res,* 22**,** 625-32.

TIBREWAL, S. B., GRANT, K. A. & GOODFELLOW, J. W. 1984. The radiolucent line beneath the tibial components of the Oxford meniscal knee. *J Bone Joint Surg Br,* 66**,** 523-8.

TREVISAN, C., BIGONI, M., DENTI, M., MARINONI, E. C. & ORTOLANI, S. 1998. Bone assessment after total knee arthroplasty by dual-energy X-ray absorptiometry: analysis protocol and reproducibility. *Calcified tissue international,* 62**,** 359-61.

TREVISAN, C., BIGONI, M., RANDELLI, G., MARINONI, E. C., PERETTI, G. & ORTOLANI, S. 1997. Periprosthetic bone density around fully hydroxyapatite coated femoral stem. *Clinical orthopaedics and related research***,** 109-17.

TURNER, A. W., GILLIES, R. M., SEKEL, R., MORRIS, P., BRUCE, W. & WALSH, W. R. 2005. Computational bone remodelling simulations and comparisons with DEXA results. *J Orthop Res,* 23**,** 705-12.

TURNER, C. H. & COWIN, S. C. 1988. Errors induced by off-axis measurement of the elastic properties of bone. *J Biomech Eng,* 110**,** 213-5.

TURNER, C. H., FORWOOD, M. R., RHO, J. Y. & YOSHIKAWA, T. 1994. Mechanical loading thresholds for lamellar and woven bone formation. *Journal of bone and mineral research : the official journal of the American Society for Bone and Mineral Research,* 9**,** 87-97.

TURNER, C. H., RHO, J., TAKANO, Y., TSUI, T. Y. & PHARR, G. M. 1999. The elastic properties of trabecular and cortical bone tissues are similar: results from two microscopic measurement techniques. *J Biomech,* 32**,** 437-41.

ULRICH, D., VAN RIETBERGEN, B., LAIB, A. & RUEGSEGGER, P. 1999. The ability of three-dimensional structural indices to reflect mechanical aspects of trabecular bone. *Bone,* 25**,** 55-60.

VAN LENTHE, G. H., DE WAAL MALEFIJT, M. C. & HUISKES, R. 1997. Stress shielding after total knee replacement may cause bone resorption in the distal femur. *J Bone Joint Surg Br,* 79**,** 117-22.

VAN LENTHE, G. H., WILLEMS, M. M., VERDONSCHOT, N., DE WAAL MALEFIJT, M. C. & HUISKES, R. 2002. Stemmed femoral knee prostheses: effects of prosthetic design and fixation on bone loss. *Acta Orthop Scand,* 73**,** 630-7.

VAN RIETBERGEN, B., WEINANS, H., HUISKES, R. & POLMAN, B. J. W. 1996. Computational strategies for iterative solutions of large FEM applications employing voxel data. *International Journal for Numerical Methods in Engineering,* 39**,** 2743-2767.

VARDI, G. & STROVER, A. E. 2004. Early complications of unicompartmental knee replacement: the Droitwich experience. *Knee,* 11**,** 389-94.

VARGHESE, B., SHORT, D., PENMETSA, R., GOSWAMI, T. & HANGARTNER, T. 2011. Computed-tomography-based finite-element models of long bones can accurately capture strain response to bending and torsion. *Journal of Biomechanics,* 44**,** 1374-1379.

VERHAVEN, E., HANDELBERG, F., CASTELEYN, P. P. & OPDECAM, P. 1991. Meniscal bearing dislocation in the Oxford knee. *Acta Orthop Belg,* 57**,** 430-2.

VICECONTI, M., MONTI, L., MUCCINI, R., BERNAKIEWICZ, M. & TONI, A. 2001. Even a thin layer of soft tissue may compromise the primary stability of cementless hip stems. *Clin Biomech (Bristol, Avon),* 16**,** 765-75.

VICECONTI, M., MUCCINI, R., BERNAKIEWICZ, M., BALEANI, M. & CRISTOFOLINI, L. 2000. Large-sliding contact elements accurately predict levels of bone-implant micromotion relevant to osseointegration. *J Biomech,* 33**,** 1611-8.

VICECONTI, M., ZANNONI, C., TESTI, D. & CAPPELLO, A. 1999. CT data sets surface extraction for biomechanical modeling of long bones. *Computer methods and programs in biomedicine,* 59**,** 159-66.

VORLAT, P., PUTZEYS, G., COTTENIE, D., VAN ISACKER, T., POULIART, N., HANDELBERG, F., CASTELEYN, P. P., GHEYSEN, F. & VERDONK, R. 2006. The Oxford unicompartmental knee prosthesis: an independent 10-year survival analysis. *Knee Surg Sports Traumatol Arthrosc,* 14**,** 40-5.

VORLAT, P., VERDONK, R. & SCHAUVLIEGHE, H. 2000. The Oxford unicompartmental knee prosthesis: a 5-year follow-up. *Knee Surg Sports Traumatol Arthrosc,* 8**,** 154-8.

WAANDERS, D., JANSSEN, D., MANN, K. A. & VERDONSCHOT, N. 2010. The mechanical effects of different levels of cement penetration at the cement–bone interface. *Journal of Biomechanics,* 43**,** 1167-1175.

WAANDERS, D., JANSSEN, D., MANN, K. A. & VERDONSCHOT, N. 2011. The behavior of the micro-mechanical cement–bone interface affects the cement failure in total hip replacement. *Journal of Biomechanics,* 44**,** 228-234.

WAANDERS, D., JANSSEN, D., MILLER, M. A., MANN, K. A. & VERDONSCHOT, N. 2009. Fatigue creep damage at the cement-bone interface: an experimental and a micro-mechanical finite element study. *J Biomech,* 42**,** 2513-9.

WADA, M., MAEZAWA, Y., BABA, H., SHIMADA, S., SASAKI, S. & NOSE, Y. 2001. Relationships among bone mineral densities, static alignment and dynamic load in patients with medial compartment knee osteoarthritis. *Rheumatology (Oxford),* 40**,** 499-505.

WALKER, P. S. & HAJEK, J. V. 1972. The load-bearing area in the knee joint. *J Biomech,* 5**,** 581-9.

WANG, J. W., KUO, K. N., ANDRIACCHI, T. P. & GALANTE, J. O. 1990. The influence of walking mechanics and time on the results of proximal tibial osteotomy. *J Bone Joint Surg Am,* 72**,** 905-9.

WAUGH, T. R. 1985. Total knee arthroplasty in 1984. *Clin Orthop Relat Res***,** 40-5.

WEALE, A. E., HALABI, O. A., JONES, P. W. & WHITE, S. H. 2001. Perceptions of Outcomes After Unicompartmental and Total Knee Replacements. *Clinical Orthopaedics and Related Research,* 382**,** 143-153.

WEALE, A. E., MURRAY, D. W., NEWMAN, J. H. & ACKROYD, C. E. 1999. The length of the patellar tendon after unicompartmental and total knee replacement. *The Journal of bone and joint surgery. British volume,* 81**,** 790-5.

WEINANS, H., HUISKES, R. & GROOTENBOER, H. J. 1992a. The behavior of adaptive bone-remodeling simulation models. *Journal of Biomechanics,* 25**,** 1425-41.

WEINANS, H., HUISKES, R. & GROOTENBOER, H. J. 1992b. Effects of material properties of femoral hip components on bone remodeling. *J Orthop Res,* 10**,** 845-53.

WEINANS, H., HUISKES, R., VAN RIETBERGEN, B., SUMNER, D. R., TURNER, T. M. & GALANTE, J. O. 1993. Adaptive bone remodeling around bonded noncemented total hip arthroplasty: a comparison between animal experiments and computer simulation. *J Orthop Res,* 11**,** 500-13.

WHITESIDE, L. A. 1994. Four screws for fixation of the tibial component in cementless total knee arthroplasty. *Clin Orthop Relat Res***,** 72-6.

WILLIS-OWEN, C. A., BRUST, K., ALSOP, H., MIRALDO, M. & COBB, J. P. 2009. Unicondylar knee arthroplasty in the UK National Health Service: An analysis of candidacy, outcome and cost efficacy. *The Knee,* 16**,** 473-478.

WRETENBERG, P., RAMSEY, D. K. & NEMETH, G. 2002. Tibiofemoral contact points relative to flexion angle measured with MRI. *Clin Biomech (Bristol, Avon),* 17**,** 477-85.

ZANT, N. P., WONG, C. K. & TONG, J. 2007. Fatigue failure in the cement mantle of a simplified acetabular replacement model. *Int J Fatigue,* 29**,** 1245-1252.

ZHAO, D., BANKS, S. A., MITCHELL, K. H., D'LIMA, D. D., COLWELL, C. W., JR. & FREGLY, B. J. 2007. Correlation between the knee adduction torque and medial contact force for a variety of gait patterns. *J Orthop Res,* 25**,** 789-97.